UNIVERSIDAD COMPLUTENSE DE MADRID

FACULTAD DE CIENCIAS FÍSICAS

DEPARTAMENTO DE ASTROFÍSICA Y CIENCIAS DE LA ATMÓSFERA

TESIS DOCTORAL

ANALISIS DE LA DISTRIBUCIÓN ESPACIAL DE ESTRELLAS, GAS Y POLVO EN GALAXIAS CERCANAS.
ANALYSIS OF THE SPTIAL DISTRIBUTION OF STARS, GAS AND DUST IN NEARBY GALAXIES

TESIS DOCTORAL

MEMORIA PARA OPTAR AL GRADO DE DOCTOR

PRESENTADA POR

Juan Carlos Muñoz Mateos

Directores:

Armando Gil de Paz
Jaime Zamorano Calvo

Madrid, 2010

ISBN: **978-84-693-8261-5**

UNIVERSIDAD COMPLUTENSE DE MADRID

FACULTAD DE CIENCIAS FÍSICAS
DEPARTAMENTO DE ASTROFÍSICA Y CIENCIAS DE LA ATMÓSFERA

Análisis de la distribución espacial de estrellas, gas y polvo en galaxias cercanas

Analysis of the spatial distribution of stars, gas and dust in nearby galaxies

Dirigida por:

D. Armando Gil de Paz
Investigador Ramón y Cajal
UCM

D. Jaime Zamorano Calvo
Profesor Titular
UCM

Memoria presentada por
D. Juan Carlos Muñoz Mateos
para aspirar al grado de
Doctor en Ciencias Físicas
Madrid, Junio 2010

Cover images credits:
Ultraviolet - *The GALEX Atlas of Nearby Galaxies* (Gil de Paz et al. 2007).
Optical - *Sloan Digital Sky Survey* (York et al. 2000).
Mid-infrared - *The Spitzer Infrared Nearby Galaxies Survey* (Kennicutt et a. 2003).
Far-infrared - Test image from the *Herschel* space telescope (ESA).
Molecular gas - CARMA array (Koda et al. 2009).
Atomic hydrogen - *The HI Nearby Galaxies Survey* (Walter et al. 2008).
Background image - *Millennium Simulation* (Springel et al. 2005).

Poets say science takes away from the beauty of the stars — mere globs of gas atoms. Nothing is "mere". I too can see the stars on a desert night, and feel them. But do I see less or more? The vastness of the heavens stretches my imagination — stuck on this carousel my little eye can catch one-million-year-old light. A vast pattern — of which I am a part... What is the pattern or the meaning or the "why"? It does not do harm to the mystery to know a little more about it. For far more marvelous is the truth than any artists of the past imagined it. Why do the poets of the present not speak of it? What men are poets who can speak of Jupiter if he were a man, but if he is an immense spinning sphere of methane and ammonia must be silent?

Richard Feynman, *Feynman Lectures on Physics*

There is a theory which states that if ever anybody discovers exactly what the Universe is for and why it is here, it will instantly disappear and be replaced by something even more bizarre and inexplicable. There is another theory which states that this has already happened.

Douglas Adams, *The Hitchhiker's Guide to the Galaxy*

A mis padres.

Contents

Agradecimientos

Me atrevería a decir que ésta es posiblemente la parte de la tesis que más me ha costado redactar. No en vano es la que he dejado para el último momento, no por falta de ganas, sino por la dif cultad que entraña darle el debido crédito a todas aquellas personas que de una u otra forma han contribuido a que esta aventura llegue a buen puerto. Quienes me conocen bien saben que no es raro que no recuerde cosas tan triviales como lo que he comido a mediodía o incluso mi edad (la tesis ha acabado con las pocas neuronas sanas que me quedaban tras la licenciatura). Por tanto, cualquier posible omisión en la retahíla de nombres que menciono a continuación es fruto del descuido y no es en modo alguno intencionada. En cualquier caso, todos aquellos que directa o indirectamente han jugado un papel importante en este viaje lo saben de sobra, por lo que vaya por delante mi agradecimiento hacia ellos.

En primer lugar, y como no podía ser de otra forma, quiero agradecer a mis directores de tesis, Armando y Jaime, el apoyo constante que me han brindado durante estos casi cinco años, tanto en los buenos momentos como en los malos. Conf aron en mí desde el principio para desarrollar un proyecto de tesis que se fue perf lando poco a poco a medida que iban surgiendo los resultados. Me siento orgulloso de decir que prácticamente han pasado más tiempo delante de mi ordenador que en sus propios despachos. Les debo muchas horas tanto de fructíferas discusiones científ cas como de "pedaleo", actividad imprescindible para conservar la salud mental durante la tesis. Además, no sólo me han orientado con su experiencia y sus consejos siempre que lo he necesitado, sino que en más de una ocasión se han manchado las manos para echarme un cable con alguna tarea tediosa. Pero por encima del aspecto profesional, lo que más aprecio es su calidez humana. Es una auténtica suerte poder af rmar que tus jefes son, por encima de eso, tus amigos.

Lo anterior es extensible a todos aquellos que han conseguido que este Departamento se haya convertido en mi segunda casa. Voy a echar de menos las multitudinarias comidas en la sala entre-cúpulas, las votaciones sobre temas absurdos y pintorescos, los chascarrillos de las tres menos cuarto o las partidas de Tetris con las bandejas en el ascensor. Por no hablar de las amenas reuniones del grupo G-Astronómico; dudo mucho que las hamburguesas y perritos calientes que me esperan puedan competir con las quiches, el tiramisú o el bizcocho de manzana. Muchas son las personas que han pasado por esta gran familia durante mi estancia en el Departamento: Jesús, África, Pablo, Sergio, Nicolás, Javier Gorgas, Guillermo, Elisa, Jaime Izquierdo, Esther, Víctor, Cristina, Maleni, Inés, Javier López, Antonio, Marta, Lucía, Raffaella, Néstor, Álex, Carmen, Alejandro, José Manuel, Santos, Mari Cruz y Javier Cenarro, entre otros. A todos vosotros, ya seáis estelares, galácticos o no-astrónomos —y por tanto cuerdos—, gracias por estar ahí.

A Jesús y África los puedo considerar mis directores de tesis no of ciales, dada la ayuda desinteresada que me han brindado siempre. En particular, África ha dedicado muchas horas de su tiempo a enseñarme pacientemente a reducir datos de espectroscopía bidimensional. A Pablo

también le agradezco los consejos prestados en más de una ocasión, amén de su confianza en mí como su proveedor oficial de Coca Cola. Por su paciencia a la hora de lidiar con nuestros problemas informáticos, Sergio se merece una estatua y una camiseta con el lema: *No, I will not fix your computer*. Con Guillermo y Jaime Izquierdo he compartido muchas horas de trabajo codo con codo —a veces en el sentido literal de la expresión— en los distintos despachos que hemos ocupado juntos durante estos años. Guillermo ha tenido que soportar alguna que otra broma sobre la naturaleza de sus supuestas galaxias y sobre *Lost*, la única serie conocida cuyo título ya es un *spoiler*. Y, como se dice por estos lares, "yo de mayor quiero ser como Jaime Izquierdo". Por otro lado, gracias a Elisa y Esther ya no pienso que las elípticas sean aburridas (aunque las galaxias con el mismo nombre sí lo sean). Además, Esther y Víctor me han enseñado que se puede sobrevivir con éxito a la recta final de la tesis. Este último tramo lo he recorrido junto a Inés y Maleni, que son estelares en todos los aspectos, no solo en el plano científico.

También quiero expresar mi agradecimiento al resto del personal del Departamento de Astrofísica y CC. de la Atmósfera de la Universidad Complutense de Madrid, incluyendo a los profesores Manuel Rego, Elisa de Castro, María José Fernández, Manuel Cornide y David Montes, por acogerme como doctorando y permitirme emplear los recursos del Departamento.

Una parte sustancial del trabajo presentado aquí se gestó y desarrolló durante una estancia de tres meses en el Laboratorio de Astrofísica de Marsella. Samuel Boissier, mi supervisor durante la estancia, se encargó eficientemente de todos los aspectos logísticos y me ayudó con mi proyecto científico, iniciando así una colaboración y una amistad que ha continuado desde entonces. Y no puedo olvidarme de Ángel López, por su inestimable ayuda durante mi breve —brevísima— estancia en Sydney.

Esta tesis se presenta como una recopilación de artículos. En este sentido, he tenido la suerte de contar con la experiencia de muchos coautores que leyeron detenidamente los borradores, detectando fallos y sugiriendo cambios que sin duda alguna mejoraron la calidad de los resultados obtenidos. Si bien sus nombres aparecen explícitamente en la lista de autores de cada artículo, quiero aprovechar estas líneas para reiterar mi agradecimiento. Además, durante estos años también he contado con la ayuda experta de personas como Alfonso Aragón o mi paisano Rafael Guzmán, cuyos sabios consejos han sido esenciales para comprender cómo hacer investigación de calidad.

No es posible completar con éxito casi cinco años de investigación sin tener a alguien que de vez en cuando te arranque el teclado de las manos y te arrastre al mundo exterior. Por ello estoy en deuda con Antonio, Irene, José Alberto e Irma, gracias a quienes he llegado hasta aquí algo menos loco de lo que podría estar ahora mismo. Con ellos he compartido viajes, comilonas, risas y largas charlas nocturnas (sí, no se me olvida, os la tengo jurada desde lo de aquella noche en Ribatejada). De Miriam me quedo con esa sonrisa capaz de animar al más alicaído. Y no quiero dejarme en el tintero a David, Begoña, Cris, Sandra, Irene, Pedro, Luis o Miguel. A pesar de la diáspora que nos ha llevado a estar repartidos por lugares dispares, espero que podamos seguir viéndonos con frecuencia a través del cristal de una buena jarra de cerveza.

Mi último agradecimiento, y el más importante, es para mi familia, y en particular para mis padres, Conchita y Juan Carlos. A ellos va dedicada esta tesis, por su cariño y por el esfuerzo indecible que han realizado durante tantos años para permitirme conseguir mi sueño. Hace ya unos doce o trece años me regalaron un pequeño telescopio refractor de 60 mm, que yo dirigía entusiasmado hacia el cielo cada noche, ávido de descubrir qué era cada nuevo punto brillante que veía. Uno de esos puntos resultó ser un disco borroso del que brotaron dos orejas a medida que

enfocaba la imagen. Se trataba de Saturno, y la visión tan nítida de sus anillos hizo que casi me matara bajando de cinco en cinco los escalones de la terraza para compartir mi "descubrimiento" con mis padres. La opción alternativa que barajaban para ese regalo era un microscopio, por lo que en algún universo paralelo mi otro yo acaba de terminar en estos momentos una tesis sobre paramecios y bacterias. En cualquier caso, sé que siempre podré contar con su apoyo incondicional. Por todo ello: gracias.

Madrid, 20 de abril de 2010

1

Introducción

1.1 Los dominios de las galaxias

El 26 de abril de 1920, el Museo Smithsonian de Historia Natural de Washington D.C. acogió un debate memorable que supuso un hito en la historia de la astronomía. El llamado "Gran Debate" giró en torno al controvertido asunto del tamaño del universo y, en particular, a la naturaleza de las nebulosas espirales como la de Andrómeda. ¿Estas débiles manchas difusas de luz formaban parte de la Vía Láctea, o se trataba de sistemas estelares completamente independientes? Harlow Shapley era partidario de la primera hipótesis, basándose en que si la Nebulosa de Andrómeda fuera una galaxia aparte, debería encontrarse a una distancia inconcebiblemente grande. Herber Curtis, por otro lado, creía que ésta y otras nebulosas eran en efecto sistemas estelares independientes. De otro modo sería difícil explicar el número anormalmente alto de novas observadas en la pequeña región del cielo ocupada por la Nebulosa de Andrómeda, así como el hecho de que fuesen sistemáticamente más débiles que otras novas vistas en otras zonas. Argumentó también que muchas nebulosas mostraban a lo largo de su ecuador bandas de polvo similares a las observadas en la Vía Láctea. Además, según las medidas del desplazamiento al rojo de Vesto Slipher, muchas de estas nebulosas parecían alejarse a velocidades tan altas que no podían ser retenidas por el pozo gravitacional de la Vía Láctea.

Edwin Hubble zanjó la cuestión en 1925 al medir el periodo de las oscilaciones de luminosidad de estrellas cefeidas en la galaxia irregular NGC 6822 (Hubble 1925). Concluyó que ésta se encontraba a unos 214 kpc, def nitivamente fuera de la Vía Láctea. Más tarde llegó a una conclusión similar con la galaxia del Triángulo (M 33; Hubble 1926a), y con la galaxia de Andrómeda (M 31; Hubble 1929). La Vía Láctea pasó de ser todo el universo conocido a sólo una entre incontables galaxias f otando en un espacio mucho más vasto que lo que anteriormente se pensaba, naciendo así la astronomía extragaláctica.

Dado que la astronomía es una disciplina altamente observacional, en la que no se pueden diseñar ni modif car dispositivos experimentales, una cuidadosa observación y clasif cación de los objetos bajo estudio es un primer paso importante para comprender cómo se formaron. Esto es particularmente cierto para las galaxias, y los astrónomos enseguida dedicaron grandes esfuerzos a diseñar un sistema para clasif car su morfología (véase Sandage 1975 para una revisión del tema). A f n de cuentas, las formas actuales de las galaxias son el resultado tanto de las condiciones iniciales en las que se formaron como de la acción conjunta de distintos procesos, tanto internos como externos, que han tenido lugar durante la vida de cada galaxia.

El esquema de clasif cación más ampliamente usado es el de Hubble (1926b, 1936), que

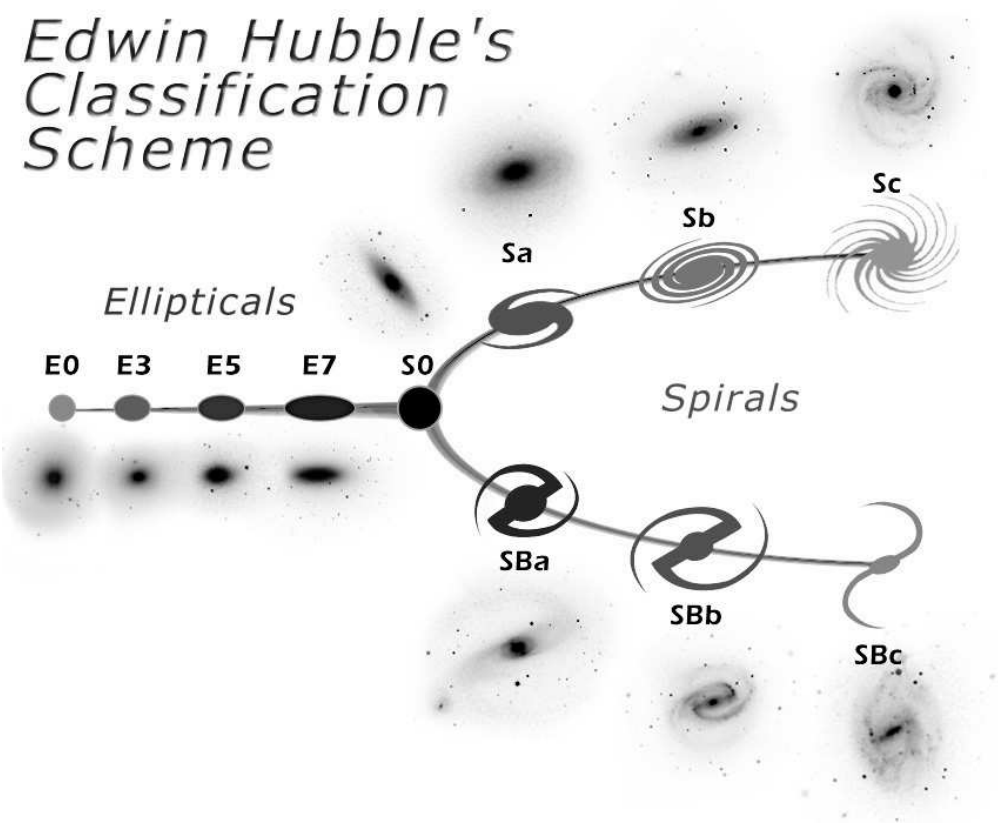

Figura 1.1: Diagrama de diapasón de Hubble para la clasif cación de galaxias.

está ilustrado en la Fig. 1.1. En este sistema, las galaxias se dividen en dos grupos principales: las elípticas y las espirales. Las primeras normalmente son estructuras esferoidales carentes de rasgos distintivos en las que la luz está distribuida uniformemente. Se denotan con la letra E, seguida de un número que depende de su elipticidad observada. Las estrellas de estas galaxias normalmente siguen movimientos desordenados, con muy poca o ninguna rotación organizada. Las galaxias espirales, por el contrario, poseen un disco plano giratorio en el que se pueden ver claramente brazos espirales. Se designan como galaxias Sa, Sb o Sc, de tal forma que los brazos espirales están cada vez menos arremolinados a medida que avanzamos en la secuencia. Las galaxias espirales también poseen una estructura central llamada bulbo, que es más prominente en las espirales Sa que en las Sc. En algunas galaxias, los brazos espirales parten de los extremos de una estructura central alargada. Este rasgo con forma de barra permite subdividir las espirales en barradas (SB) y no barradas (SA).

Siguiendo estos criterios, Hubble organizó las galaxias según el diagrama con forma de diapasón mostrado en la Fig. 1.1. En el punto de unión del diagrama de Hubble se encuentran las galaxias lenticulares (S0), que poseen un bulbo brillante y un disco plano carente de brazos espirales. Las galaxias situadas a la izquierda del diagrama se conocen como galaxias de tipos tempranos, mientras que las de tipos tardíos son las que se encuentran a la derecha. No obstante, nótese que estos términos no deben interpretarse en un sentido temporal. Otros astrónomos, como Gérard de Vaucouleurs, ref naron aún más la secuencia de Hubble añadiendo otros tipos más tardíos de espirales (Sd, Sm), el tipo de transición entre las galaxias barradas y no barradas (SAB) y la clase de galaxias irregulares, que carecen de una forma def nida y no encajan en ninguno de los tipos de

galaxias propuestos originalmente por Hubble.

La secuencia de Hubble extendida ha demostrado ser una herramienta extremadamente útil para estudiar la formación y evolución de las galaxias. No obstante, está basada únicamente en observaciones ópticas, que muestran sobre todo la ubicación de estrellas viejas y de edad intermedia. Se necesitan observaciones a otras longitudes de onda para localizar no sólo estrellas mucho más jóvenes, sino también los otros dos principales componentes luminosos de las galaxias: el polvo y el gas.

1.2 La estructura multi-longitud de onda de las galaxias

Los avances tecnológicos en el desarrollo de detectores y telescopios (tanto en tierra como en órbita) han hecho posible la exploración de otras regiones del espectro electromagnético a la hora de observar galaxias. En el caso particular de las galaxias cercanas, ahora nos encontramos en una posición privilegiada para delinear con gran detalle la distribución espacial de estrellas de distintas edades, del polvo y del gas.

Como ejemplo de la variedad de características que se pueden estudiar con datos multi-longitud de onda, en la Fig. 1.2 mostramos varias imágenes en diferentes bandas de la conocida galaxia espiral cercana M 51. El panel (a) muestra una imagen ultravioleta obtenida con el *Galaxy Evolution Explorer* (GALEX), y que forma parte del *Atlas GALEX de Galaxias Cercanas* (Gil de Paz et al. 2007). En el ultravioleta, los brotes de formación estelar reciente se aprecian nítidamente, y las bandas de polvo aparecen como manchas oscuras. Nótese que la galaxia compañera M 51b apenas es visible a estas longitudes de onda. En el panel (b) presentamos una imagen óptica clásica, elaborada con datos del *Sloan Digital Sky Survey* (SDSS; York et al. 2000). Los brazos espirales presentan una coloración azul debida a las estrellas jóvenes, mientras que otras más evolucionadas dan lugar a la emisión rojiza y difusa. La absorción debida al polvo todavía es importante en el rango óptico.

En el panel (c) mostramos una imagen en el infrarrojo medio de M 51, tomada con los instrumentos IRAC y MIPS a bordo de *Spitzer* como parte del *Spitzer Infrared Nearby Galaxies Survey* (SINGS; Kennicutt et al. 2003). La emisión a 3.6 μm, que aquí se muestra en azul, está distribuida más uniformemente que en el óptico, dado que traza la ubicación de poblaciones estelares evolucionadas. En M 51b la mayor parte de la emisión extensa y difusa procede de hecho de estrellas viejas, de ahí su color azul en esta imagen. Por el contrario, M 51a presenta abundantes estructuras a 8.0 μm y 24 μm, bandas mostradas aquí en verde y rojo, respectivamente. La emisión a 8.0 μm, que está producida por grandes moléculas orgánicas llamadas Hidrocarburos Aromáticos Policíclicos (PAHs), está distribuida siguiendo una estructura f lamentosa. El polvo calentado por formación estelar reciente domina la emisión a 24 μm, de ahí los grumos rojizos en esta imagen. Aunque el polvo próximo a regiones de formación estelar puede calentarse a temperaturas de varios centenares de grados, la mayor parte de los granos de polvo en las galaxias normales normalmente tienen temperaturas mucho más bajas, apenas unos 15-20 K, por lo que radian a longitudes de onda más largas. La distribución del polvo frío en M 51 se aprecia en la Fig. 1.2d, donde mostramos una imagen en el infrarrojo lejano tomada con el instrumento PACS, como parte de las pruebas de calibración del telescopio espacial Herschel lanzado recientemente. La emisión del polvo frío a 70 μm, 100 μm y 160 μm se muestra en azul, verde y rojo, respectivamente.

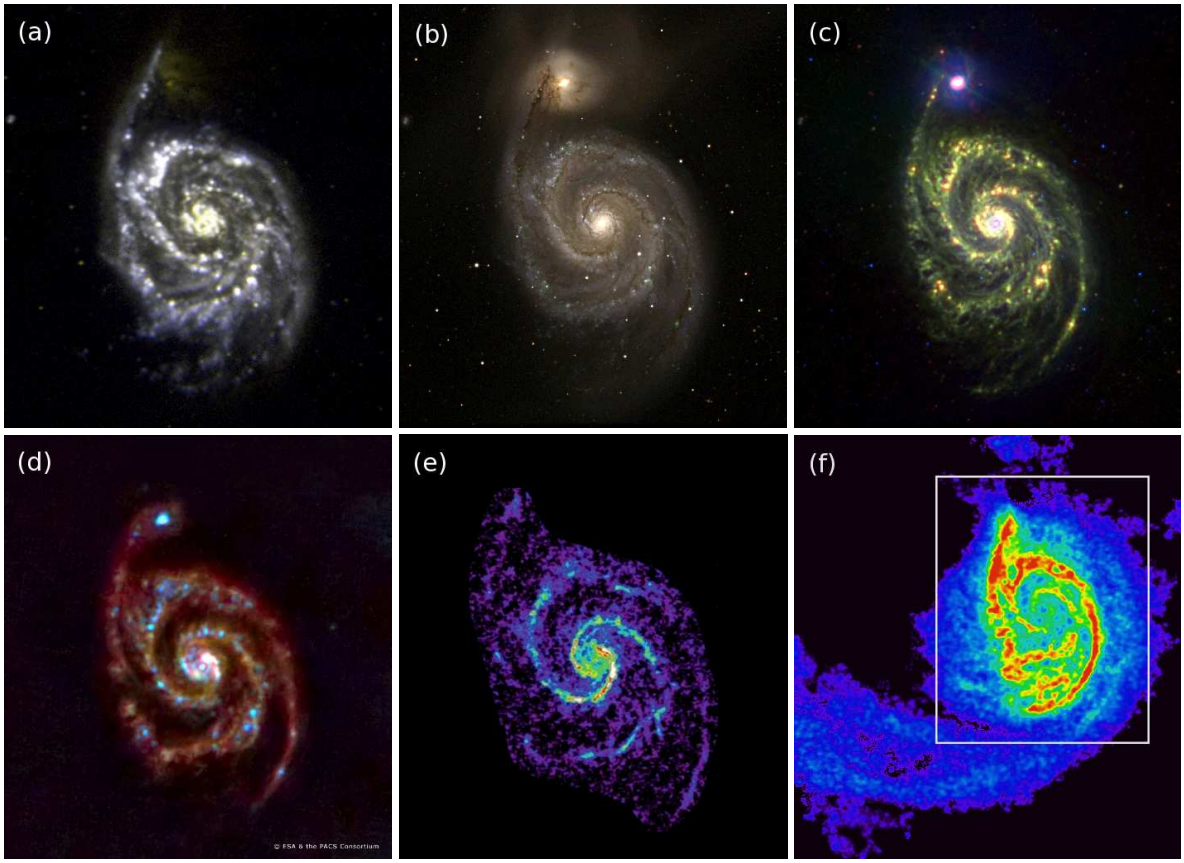

Figura 1.2: Imágenes de la galaxia M 51 en distintas bandas, en orden creciente de longitud de onda. (a): Imagen ultravioleta de GALEX, usando el ultravioleta lejano (FUV), el cercano (NUV) y una combinación lineal de ambas bandas en los canales azul, rojo y verde, respectivamente. (b): Imagen óptica del *Sloan Digital Sky Survey*. Los colores azul, verde y rojo corresponden a las bandas g, r e i. (c): Imagen de *Spitzer* en el infrarrojo medio, usando las bandas de 3.6 μm y 8.0 μm de IRAC como los canales azul y verde, y la banda de 24 μm de MIPS como el rojo. (d): Imagen en el infrarrojo lejano de Herschel tomada con el instrumento PACS, donde el azul, el verde y el rojo muestran la radiación emitida a 70 μm, 100 μm y 160 μm. (e): Mapa que muestra la emisión de la molécula de CO a 2.6 mm, tomada con el interferómetro CARMA. (f): Mapa de HI elaborado con datos del VLA, mostrando la emisión a 21 cm del hidrógeno neutro. El rectángulo blanco indica el área mostrada en los paneles anteriores.

Por último, pero no por ello menos importante, el gas se manifiesta a longitudes de onda mucho mayores (aparte de las conocidas líneas de emisión en el rango óptico, por supuesto). Normalmente se emplean observaciones en longitudes de onda milimétricas para trazar la distribución espacial del hidrógeno molecular. En realidad, dado que la molécula de H_2 es simétrica, carece de rasgos espectrales significativos, por lo que comúnmente se usan otras moléculas como el CO como trazadores de H_2. La Fig. 1.2e muestra un mapa de M 51 elaborado a partir de datos tomados con el *Combined Array for Research in Millimeter Astronomy* (CARMA; Koda et al. 2009). El gas interestelar normalmente adopta la forma molecular antes de que se inicie la formación estelar; por ello, los brazos espirales están definidos muy nítidamente en esta imagen. Sin embargo, la mayor parte del hidrógeno de las galaxias se encuentra en forma atómica, HI. El hidrógeno atómico se puede detectar fácilmente gracias a la línea de 21 cm, que se emite cada vez que ocurre una transición entre los dos niveles de la estructura hiperfina de su estado fundamental. La Fig. 1.2f muestra un mapa de HI de M 51 de *The HI Nearby Galaxies Survey* (THINGS; Walter et al. 2008), obtenido con el *Very Large Array* (VLA). El mapa cubre un área mucho mayor que las imágenes anteriores, mostrando estructuras extensas como una larga cola de marea, probablemente causada por la interacción entre M 51a y b.

Las imágenes mostradas en la Fig. 1.2 demuestran la importancia de cuantificar con precisión la distribución espacial de las estrellas, el polvo y el gas en galaxias cercanas, con el fin de proporcionar restricciones empíricas que cualquier modelo de evolución galáctica debe ser capaz de reproducir con éxito.

1.3 Modelando la formación y evolución de las galaxias

El modelo más ampliamente aceptado para describir la formación de estructuras en el universo es lo que se conoce como el paradigma ΛCDM (del inglés *Lambda-Cold Dark Matter*, materia oscura fría más constante cosmológica). Este modelo se elaboró para explicar simultáneamente la naturaleza y la estructura del fondo cósmico de microondas, la estructura a gran escala en la que se disponen las galaxias, las abundancias relativas de elementos ligeros y la expansión acelerada del universo que se infiere de las observaciones de supernovas en galaxias lejanas.

De acuerdo con el modelo ΛCDM, la mayor parte de la materia en el universo no se puede detectar a partir de radiación electromagnética, y es posiblemente de naturaleza no bariónica. La materia oscura parece ser necesaria para conciliar la relatividad general con las curvas de rotación de las galaxias y con sus movimientos relativos dentro de los cúmulos galácticos. El término "fría" en el paradigma ΛCDM se refiere al hecho de que las partículas de materia oscura no se mueven a velocidades relativistas. Se supone que no experimentan disipación, en el sentido de que no pueden enfriarse emitiendo fotones, ni tampoco sufren colisiones, ya que sólo interaccionan mediante la gravedad. La constante cosmológica Λ da cuenta de la llamada energía oscura, necesaria para explicar la expansión acelerada del universo. En el modelo actualmente aceptado que mejor se ajusta las observaciones, en torno al 70 % de la densidad de energía del universo se encuentra en forma de energía oscura, el 25 % como materia oscura, y el 5 % restante incluye la materia bariónica ordinaria.

En realidad, el escenario ΛCDM no describe la evolución de las galaxias, sino la de los halos de materia oscura en los que se supone que las galaxias se forman. Las simulaciones numéricas detalladas que se basan en el escenario ΛCDM producen una gran cantidad de halos de materia

oscura de diferentes masas y tamaños, que adquieren momento angular mediante interacciones de marea. Las partículas bariónicas de gas heredan el momento angular de sus halos correspondientes y colapsan dentro de ellos, dando lugar a estructuras que acabarán formando estrellas y convirtiéndose en galaxias.

En el caso particular de las galaxias espirales, la forma en la que la caída de gas tiene lugar hace que los discos galácticos se formen desde dentro hacia fuera (White & Frenk 1991; Mo, Mao & White 1998). El gas en las regiones externas posee un mayor momento angular, y por tanto se deposita sobre el disco en escalas de tiempo más largas que el gas en las zonas internas, que colapsa rápidamente. Además, el paso de las ondas espirales de densidad es menos frecuente en las zonas externas de los discos. En consecuencia, la formación estelar ocurre en escalas de tiempo mayores en las afueras de las galaxias. Como resultado de esta variación radial de la escala de tiempo en la que sucede la formación estelar, se supone que las galaxias de tipo disco crecen desde dentro hacia fuera. De aquí se deducen muchas predicciones importantes que se pueden contrastar observacionalmente:

1. La longitud de escala radial de los discos debería aumentar con el tiempo. Es decir, los discos deberían volverse más planos y extensos a medida que transcurre el tiempo. En términos absolutos, el gas de las zonas externas normalmente formará menos estrellas por año que el de las internas, pero esa formación estelar ocurrirá en lugares donde hay aún menos estrellas viejas, por lo que el disco crecerá hacia el exterior.

2. En consecuencia, el cociente entre la tasa de formación actual (SFR de sus siglas en inglés, *Star Formation Rate*) y la masa de las estrellas que ya se han formado —lo que se normalmente se conoce como la SFR específ ca, o sSFR— debería aumentar con la distancia al centro de la galaxia.

3. El argumento anterior implica que las estrellas deberían ser más jóvenes (en promedio) lejos del centro galáctico. Dado que las estrellas jóvenes emiten la mayor parte de su radiación en longitudes de onda más cortas que las viejas, el modelo de formación desde dentro hacia fuera es consistente con el hecho de que las galaxias espirales sean más azules en las regiones externas que en las internas.

4. Las estrellas transforman el hidrógeno en elementos más pesados como helio, carbono, nitrógeno, oxígeno, etc. mediante la nucleosíntesis estelar y explosiva. Estos elementos pesados acaban siendo inyectados en el medio interestelar, enriqueciendo el gas circundante. Si las galaxias espirales se forman desde dentro hacia fuera, la abundancia de elementos pesados debería disminuir hacia el exterior, donde se han formado menos generaciones de estrellas. Estas variaciones radiales de la metalicidad también pueden explicar parte de los gradientes de color que se observan en las galaxias.

5. No todos los átomos de elementos pesados permanecen en la fase gaseosa: muchos se condensan formando granos de polvo. Por el mismo razonamiento que antes, es esperable que la densidad superf cial de polvo también decaiga con el radio. Además, la subsiguiente variación radial de la extinción interna es el tercer factor que, junto con la edad estelar y la metalicidad, contribuye a los gradientes de color observados en las galaxias.

6. No sólo la cantidad neta de polvo debería disminuir a medida que nos alejamos del centro de una galaxia. Puesto que el polvo procede en última instancia del resultado de la nucleo-

síntesis estelar, y dado que las estrellas se forman a partir de gas, el cociente entre la masa de polvo y la de gas también debería disminuir con el radio.

7. Los granos de polvo están formados por una mezcla compleja de distintos elementos pesados, forjados originalmente en estrellas con diferentes masas y tiempos de vida. Algunos elementos puede que se hayan formado preferentemente en estrellas de baja masa que terminan sus días como nebulosas planetarias, mientras que otros pueden haber sido producidos en estrellas más masivas que f nalizan mucho antes su evolución en forma de supernovas. Por tanto, dado que los distintos elementos pesados se inyectan en el medio interestelar a ritmos diferentes, el escenario de formación de discos desde dentro a fuera predice que la composición química de los granos de polvo debería variar con la distancia al centro de cada galaxia.

Por tanto, medidas precisas de las variaciones radiales de todas estas propiedades def nitivamente arrojarán luz sobre el complejo proceso de la formación de galaxias.

1.4 Objetivos de esta tesis

El objetivo principal de esta tesis consiste en cuantif car la distribución espacial de las propiedades físicas de las estrellas, el gas y el polvo en galaxias cercanas, dado que son el registro fósil de su evolución pasada. En particular, nos centraremos sobre todo en las variaciones de estas propiedades con la distancia al centro de las galaxias espirales. Las preguntas clave que pretendemos responder son las siguientes:

1. **¿Aumenta con el radio la tasa de formación estelar específ ca en las espirales?** En caso af rmativo, ¿es posible usar el gradiente de la sSFR para inferir el ritmo de crecimiento radial de los discos?

2. **¿Qué aspecto presenta la secuencia de Hubble en longitudes de onda fuera del rango óptico?** Dada la estrecha conexión que sospechamos que debe existir entre la evolución de las galaxias y sus formas actuales, una caracterización homogénea de su morfología en diferentes bandas sería muy esclarecedora en este sentido.

3. **¿Cómo varían con el radio las propiedades físicas del polvo?** De la discusión presentada en la sección anterior resulta clara la relevancia de medir la variación radial de la extinción interna, de la densidad superf cial de polvo, de la composición química de los granos de polvo, de su temperatura o del cociente polvo/gas, entre otras propiedades.

4. **¿Es posible describir los perf les de luminosidad y de abundancias químicas de las galaxias espirales en un escenario auto-consistente?** Es decir, tomando el modelo ΛCDM como marco de referencia, e implementando de forma consistente mecanismos como la caída de gas, la formación estelar y la evolución química, ¿es posible reproducir los perf les radiales actuales de las espirales?

En el capítulo 2 trataremos el primer punto comparando los perf les en el UV y el IR cercano de una muestra de 161 espirales cercanas, junto con un sencillo modelo empírico para describir el crecimiento de los discos.

En los capítulos restantes haremos uso de los datos multi-longitud de onda de la ya mencionada muestra SINGS. La morfología de las galaxias SINGS en diferentes bandas se analizará en el capítulo 3. Allí mediremos los perfiles de brillo superficial de estas galaxias en todo el rango desde el UV lejano hasta el IR lejano. Además, determinaremos de manera cuantitativa su morfología en todas estas longitudes de onda mediante estimadores morfológicos usados habitualmente, como el índice de concentración, la asimetría, el momento de segundo orden de los píxeles más brillantes y el coeficiente de Gini.

En el capítulo 4 presentaremos un análisis exhaustivo de la distribución radial de las propiedades del polvo en las galaxias SINGS. Compararemos los perfiles en el IR total y el UV para obtener la variación radial de la extinción interna. Además, ajustaremos las distribuciones espectrales de energía infrarrojas a cada radio con los modelos de polvo de Draine & Li (2007), con el fin de determinar la variación espacial de las propiedades del polvo mencionadas en el punto 3 de la lista de objetivos.

El último aspecto de la lista se tratará en el capítulo 5. Combinando los perfiles de luminosidad presentados en el capítulo 3 con los perfiles de extinción interna obtenidos en el capítulo 4, recuperaremos la emisión intrínseca de las estrellas a cada longitud de onda a lo largo de los discos de las galaxias SINGS. Estos perfiles se ajustarán con los modelos de Boissier & Prantzos (1999; 2000), que tienen en cuenta la evolución química y espectro-fotométrica de las espirales de forma simultánea y auto-consistente.

Finalmente, las conclusiones globales de la tesis se resumen en el capítulo 6, y se proporciona un breve esquema del trabajo actual y futuro en el capítulo 7.

En los apéndices proporcionamos material adicional que no se incluye en el texto principal de la tesis. En el apéndice A mostramos imágenes multi-banda de todas las galaxias SINGS, junto con sus perfiles de brillo superficial y el resultado de ajustarlos con los modelos de polvo de Draine & Li (2007) y los modelos de evolución de discos de Boissier & Prantzos (1999; 2000). En el apéndice B citamos los valores de los estimadores morfológicos en cada longitud de onda para toda la muestra SINGS. Finalmente, en el apéndice C mostramos la distribución bidimensional de valores de χ^2 que obtenemos al ajustar los perfiles radiales con los modelos de evolución de discos.

Esta tesis se presenta como recopilación de artículos. En particular, el material que constituye los capítulos 2, 3 y 4 se ha publicado en el *Astrophysical Journal* como tres artículos independientes. Con el fin de facilitar la comprensión de estos artículos y situarlos dentro del contexto general de la tesis, cada uno incluye una breve introducción que proporciona información básica de los temas que se tratan después en los artículos. El análisis presentado en los capítulos 5 y 7 se publicará en breve en Muñoz-Mateos et al. (2010a, 2010b). Para terminar, todos los capítulos van precedidos por un breve resumen en español, y también se incluye una traducción completa de la introducción y el capítulo de conclusiones globales.

1

Introduction

1.1 The realm of galaxies

On April 26, 1920, the Smithsonian Museum of Natural History in Washington D.C. hosted a memorable debate that constituted a milestone in the history of astronomy. The so-called 'Great Debate' concerned the controversial issue of the size of the Universe and, in particular, the nature of spiral nebulae such as the Andromeda one. Were these faint and diffuse smudges of light part of the Milky Way, or were they entirely different stellar systems on their own? The former hypothesis was favored by Harlow Shapley, on the basis that were the Andromeda Nebula a separate galaxy, it must have lied at an inconceivably large distance. Herber Curtis, on the other hand, believed that this and other nebulae were indeed independent stellar systems. It would have been otherwise diff cult to explain the abnormally high number of novae found in the small patch of the sky occupied by the Andromeda Nebula, as well as the fact that they were systematically fainter than other novae seen elsewhere. Besides, he argued that many nebulae exhibited along their equators dust lanes similar to those observed in the Milky Way. Moreover, according to the redshift measurements of Vesto Slipher, most of these nebulae seemed to be receding at such large velocities that they could not be possibly retained by the Milky Way's gravitational well.

Edwin Hubble settled the question in 1925, when he measured the luminosity period of cepheid stars in the irregular galaxy NGC 6822 (Hubble 1925). He concluded that it lied roughly 214 kpc away from us, def nitely outside the Milky Way. He later reached similar conclusions for the Triangulum galaxy (M 33; Hubble 1926a) and the Andromeda galaxy (M 31; Hubble 1929). The Milky Way went therefore from being the whole known universe to merely one of the innumerable galaxies f oating in a much vaster space than previously thought, and extragalactic astronomy was born.

Since astronomy is a highly observational discipline, where one cannot directly design and modify experimental setups, a careful observation and classif cation of the subjects under study is an important f rst step to understand how they came to be. This is particularly true for galaxies, and astronomers soon devoted great efforts to design a system to classify their morphologies (see Sandage 1975 for a review). After all, the current shapes of galaxies are the result of both the initial conditions under which they f rst formed and the joint action of different processes, both internal and external, that have taken place during each galaxy's lifetime.

The most widely used classif cation scheme is that of Hubble (1926b, 1936), which is depicted in Fig. 1.1. In this system, galaxies are sorted out into two main groups: ellipticals and spirals. The former are usually featureless spheroidal structures in which light is uniformly dis-

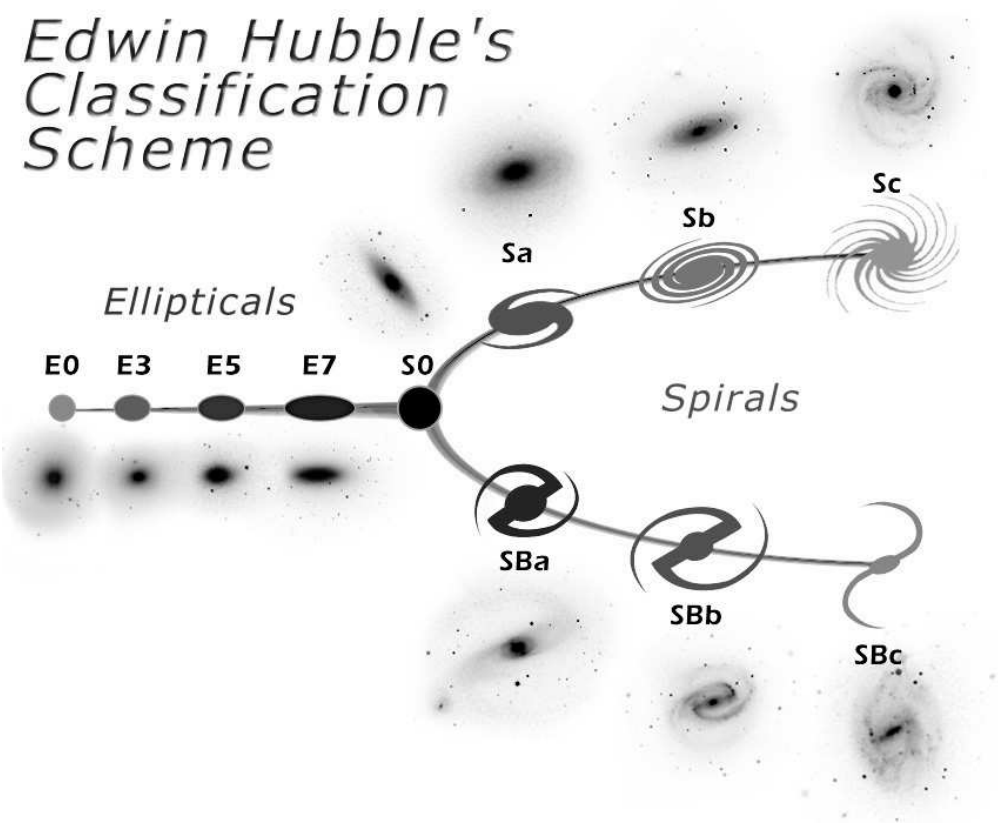

Figure 1.1: Hubble tuning-fork diagram for the classif cation of galaxies.

tributed. They are denoted with the letter E, followed by a number that depends on their observed ellipticity. Stars in these galaxies usually follow disordered motions, with little or no organized rotation. Spiral galaxies, on the other hand, exhibit a f at rotating disk in which spiral arms can be easily seen. They are designed as Sa, Sb or Sc galaxies, with the spiral arms becoming less tightly wound as we progress along the sequence. Spiral galaxies also have a central structure called bulge, which is more prominent in Sa spirals than in Sc ones. In some galaxies, the spiral arms begin from the ends of a central elongated structure. This bar-like feature is used to further subdivide spirals into barred (SB) and unbarred (SA).

Following these criteria, Hubble organized galaxies in the fork-like diagram shown in Fig. 1.1. The joint of the Hubble fork is occupied by lenticular galaxies (S0), which posses a bright bulge and a f at disk devoid of spiral arms. Galaxies located to the left of the diagram are known as early-type galaxies, while late-type ones are those to the right. Note, however, that these terms should not be understood in a temporal sense. Other astronomers, such as Gérard de Vaucouleurs, further ref ned the Hubble sequence by adding extra later types of spirals (Sd, Sm), the transition type between barred and unbarred galaxies (SAB) and the class of irregular galaxies, which lack a def ned form and do not f t any of the types of galaxies originally proposed by Hubble.

The extended Hubble sequence has proven to be an extremely useful guideline to study galaxy formation and evolution. However, it is solely based on optical observations of galaxies, which mainly trace the location of intermediate-age and old stars. Observations at other wavelengths are required to locate not only much younger stars, but also the other two main emitting

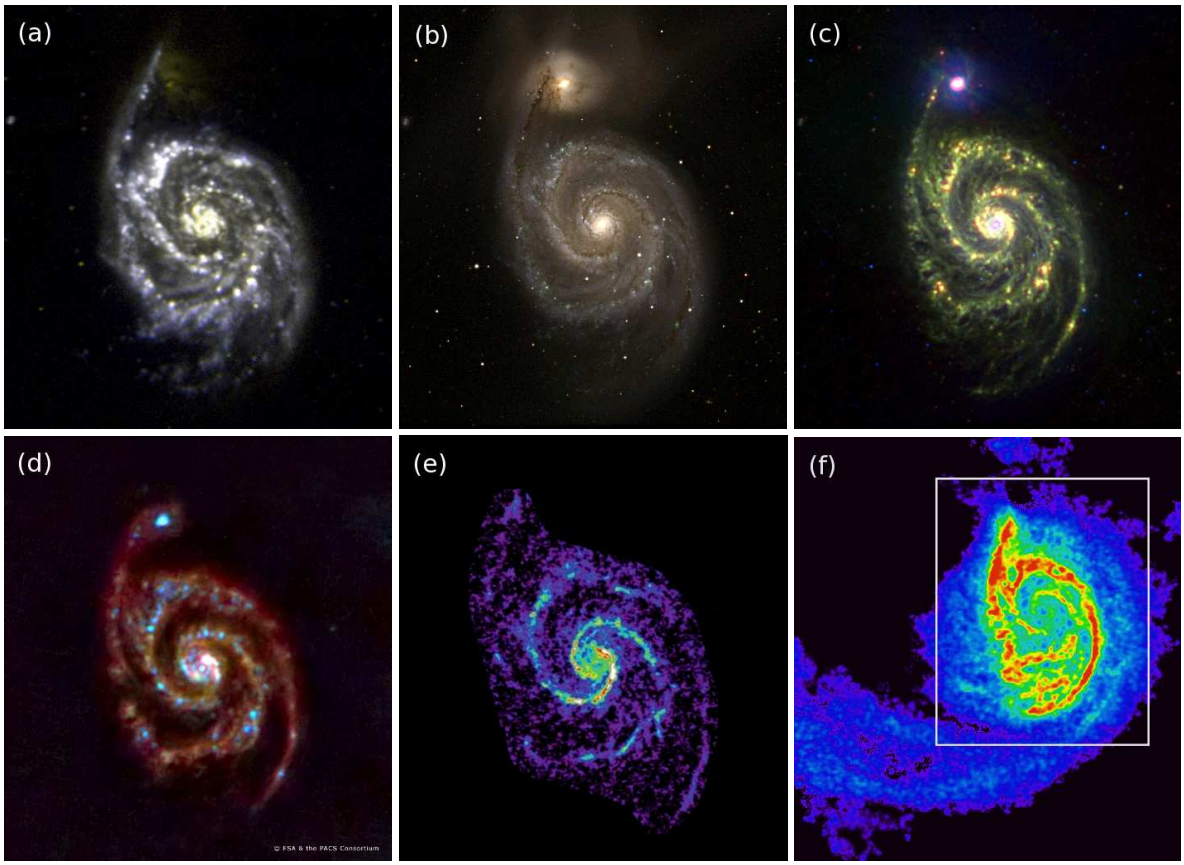

Figure 1.2: Images of the galaxy M 51 at different bands, in order of increasing wavelength. (a): Ultraviolet GALEX image, using the far-ultraviolet band (FUV), the near-utraviolet one (NUV) and a linear combination of both bands in the blue, red and green channels, respectively. (b): Optical image from the Sloan Digital Sky Survey. Blue, green and red correspond to the g, r and i bands. (c): *Spitzer* mid-infrared image, using the IRAC 3.6 μm and 8.0 μm bands as the blue and green channels, and the MIPS 24 μm band as the red one. (d): Far-IR image from Herschel taken with the PACS instrument, where blue, green and red show radiation emitted at 70 μm, 100 μm and 160 μm. (e): Map showing the 2.6 mm emission of the CO molecule, taken with the CARMA array. (f): HI map built from VLA data, showing the 21 cm emission of the neutral hydrogen. The white rectangular box corresponds to the area mapped in all previous panels.

components of galaxies: dust and gas.

1.2 The multi-wavelength structure of galaxies

Technological advances in the development of detectors and telescopes (both ground-based and in orbit) have made it possible to explore other regions of the electromagnetic spectrum when observing galaxies. In the particular case of nearby galaxies, we are now in a privileged position to map with great detail the spatial distribution of stars of different ages, dust and gas.

As an example of the variety of features that can be studied with multi-wavelength observations, in Fig. 1.2 we show several images at different bands of the well-known nearby spiral M 51. Panel (a) shows an ultraviolet color image obtained with the Galaxy Evolution Explorer (GALEX), which is part of the *GALEX Atlas of Nearby Galaxies* (Gil de Paz et al. 2007). Knots of recent

star formation neatly show up in the UV bands, with dust lanes appearing as dark features. Note that the companion galaxy M 51b is barely visible at these wavelengths. In panel (b) we present a classical optical image, built from data taken as part of the Sloan Digital Sky Survey (SDSS; York et al. 2000). Spiral arms exhibit a blue tint due to young stars, whereas more evolved ones constitute the redder and more diffuse emission. Dust absorption is still important in the optical range.

In panel (c) we show a mid-IR image of M 51, taken with the IRAC and MIPS instruments onboard *Spitzer* as part of the *Spitzer Infrared Nearby Galaxies Survey* (SINGS; Kennicutt et al. 2003). The emission at 3.6 μm, shown here in blue, is more uniformly distributed than in the optical, since it traces the old stellar populations. In M 51b most of the extended and diffuse emission does indeed come from old stars, hence its predominantly blue tint in this image. On the contrary, M 51a exhibits a wealth of features at 8.0 μm and 24 μm, shown in green and red, respectively. The 8.0 μm emission, which is produced by large organic molecules called Polycyclic Aromatic Hydrocarbons (PAHs), is distributed following a f lamentary structure. Very hot dust heated by recent star formation activity dominates the emission at 24 μm, hence the bright red knots in this image. Even though dust close to star-forming regions can be heated up to temperatures of several hundreds degrees, the bulk of dust grains in normal galaxies usually have much lower temperatures of just 15-20 K, thus radiating at longer wavelengths. The distribution of cold dust in M 51 is mapped in Fig. 1.2d, where we show a far-IR image taken with the PACS instrument, as part of the calibration tests of the recently launched Herschel space telescope. Cold dust emission at 70 μm, 100 μm and 160 μm is shown in blue, green and red, respectively.

Last, but not least, gas manifests itself at much longer wavelengths (besides the well known emission lines in the optical range, of course). Observations at millimetric wavelengths are employed to trace the spatial distribution of molecular hydrogen. Actually, since the H_2 molecule is symmetric, it lacks any signif cant spectral feature, so other molecules such as the CO one are commonly used as H_2 tracers. Fig. 1.2e shows a map of M 51 built from data taken with the Combined Array for Research in Millimeter Astronomy (CARMA; Koda et al. 2009). Interstellar gas usually goes through the molecular form before star formation is triggered; thus, the spiral arms are very neatly def ned in this image. However, the bulk of hydrogen in galaxies is in atomic form, HI. Atomic hydrogen can be easily detected thanks to the 21 cm line, which is emitted whenever a transition occurs between the two hyperf ne levels of its ground state. Fig. 1.2f shows an HI map of M 51 from *The HI Nearby Galaxies Survey* (THINGS; Walter et al. 2008) obtained with the Very Large Array (VLA). The map covers a much larger area than the previous images, showing extended features like a long tidal tail, likely caused by the interaction between M 51a and b.

The images shown in Fig. 1.2 demonstrate the importance of accurately quantifying the spatial distribution of stars, dust and gas in nearby galaxies, in order to provide empirical constraints that any successful model of galaxy evolution must be able to reproduce.

1.3 Modelling galaxy formation and evolution

The most widely accepted model describing the formation of structures in the universe is what is known as the Lambda-Cold Dark Matter paradigm (ΛCDM). This model was developed in order to simultaneously explain the nature and structure of the cosmic microwave background, the observed large scale structure in which galaxies are arranged, the relative abundances of light elements and

the accelerating expansion of the universe inferred from observations of supernovae in distant galaxies.

According to the ΛCDM model, most matter in the universe cannot be detected by electromagnetic emission, and is likely non-baryonic. Dark matter seems to be required to reconcile general relativity with the rotation curves of galaxies and the relative motion of galaxies within clusters. The term 'cold' in the ΛCDM paradigm refers to the fact that dark matter particles do not move at relativistic speeds. They are supposed to be dissipationless, in the sense that they cannot cool by emitting photons, and also collisionless, meaning that they only interact through gravity. The cosmological constant Λ accounts for the so-called dark energy, which is required to explain the accelerating expansion of the universe. In the currently accepted model that best fits the observations, about 70% of the energy density in the universe is in the form of dark energy, 25% is locked up in dark matter, and the remaining 5% comprises the ordinary baryonic matter.

The ΛCDM scenario does not actually describe the evolution of galaxies, but that of the dark matter haloes in which galaxies are supposed to get assembled. Detailed numerical simulations based on the ΛCDM scenario produce a wealth of dark matter haloes of different masses and sizes, that acquire angular momentum through tidal interactions. Gas baryons inherit the angular momentum of their parent haloes and then cool and collapse within them, yielding structures that will eventually form stars and become galaxies.

In the particular case of spiral galaxies, the way in which the gas infall takes place gives rise to the inside-out scenario of disk formation (White & Frenk 1991; Mo, Mao & White 1998). Gas in the outer regions has a larger angular momentum, and hence it settles onto the disk on much longer timescales than the gas in the central regions, which collapses quickly. Moreover, the passage of spiral density waves is less frequent in the outer zones of disks. In consequence, star formation takes place on longer timescales in the outskirts of galaxies. As a result of this radially-varying timescale of star formation, disk galaxies are supposed to grow from inside-out. This leads to many important predictions that can be observationally tested:

1. The radial scale-length of disks should increase with time. That is, disks should get fatter and more extended as time goes by. In absolute terms, gas in the outer regions will normally form less stars per year than in the central ones, but that star formation activity will occur in a place where even less older stars are already present, so the disk will grow outwards.

2. As a consequence, the ratio of the current star formation rate (SFR) and the mass of the already formed stars —usually called the *specific* SFR, or sSFR— should increase with galactocentric distance.

3. The previous argument implies that stars should be younger (on average) further away from the galactic center. Since young stars emit most of their light at shorter wavelengths that older ones, the inside-out scenario is consistent with spiral galaxies being bluer in the outer regions than in the central ones.

4. Stars transform hydrogen into heavier elements such as helium, carbon, nitrogen, oxygen, iron, etc. through stellar and explosive nucleosynthesis. These heavy elements are eventually injected into the interstellar medium (ISM), enriching the surrounding gas. If spiral galaxies are built from inside-out, the abundance of heavy elements should decrease outwards, where

less generations of stars have been born. These radial changes in metallicity can also account for part of the observed gradients in the colors of galaxies.

5. Not all heavy atoms remain in the gas phase: many condense to form dust grains. Because of the same argument as above, the dust mass surface density is expected to decay with radius. Moreover, the resulting radial variation in dust extinction is the third factor that, together with stellar age and metallicity, contributes to the observed color gradients of spirals.

6. Not only should the net amount of dust decrease as we move away from a galaxy's center. Since dust ultimately results from the outcome of stellar nucleosynthesis, and given that stars are born out of gas, the dust-to-gas ratio is also expected to decrease with radius.

7. Dust grains consist of a complex mixture of different heavy elements, originally forged in stars of different masses and lifetimes. Some elements may have been preferentially formed in low mass stars that end their lives as planetary nebulae, while others may have been produced in more massive stars that reach the end-point of their evolution much earlier as supernovae. Therefore, since different heavy elements are injected into the ISM at different rates, the inside-out scenario predicts that the chemical composition of dust grains should change with the distance to the galaxy's center.

Therefore, accurate measurements of the radial variations of all these properties will definitely shed light on the complex process of galaxy formation.

1.4 Aims of this thesis

The main goal of this thesis is to quantify the spatial distribution of the physical properties of stars, gas and dust in nearby galaxies, since they are the fossil record of their past evolution. In particular, we will mostly focus on the variations of these properties with the galactocentric distance in spiral galaxies. The key questions we intend to answer are the following:

1. **Does the specif c SFR increase with radius in spirals?** If so, is it possible to use the sSFR gradient to infer the radial growth rate of disks?

2. **What does the Hubble sequence look like at wavelengths beyond the optical range?** Given the strong connection that we suspect there must exist between the evolution of galaxies and their present-day shapes, an homogeneous characterization of their morphologies in different bands would be enlightening in this regard.

3. **How do the physical properties of dust vary with radius?** From the discussion in the previous section, it is clear the relevance of measuring the radial variation of the internal extinction, the dust mass surface density, the chemical composition of dust grains, their temperature or the dust-to-gas ratio, among other properties.

4. **Is it possible to describe the light and chemical prof les of spiral galaxies in a self-consistent scenario?** That is, taking the ΛCDM model as a reference framework, and implementing in a consistent way mechanisms like gas infall, star formation and chemical evolution, is it possible to reproduce the present-day radial prof les of spirals?

In chapter 2 we will address the first issue by comparing the UV and near-IR profiles of a sample of 161 nearby spirals, together with a simple empirically-motivated model of disk growth.

In the remaining chapters we will make use of the multi-wavelength data of the aforementioned SINGS survey. The morphology of the SINGS galaxies at different bands will be analyzed in chapter 3. There we will measure the surface brightness profiles of these galaxies all the way from the far-UV to the far-IR. Besides, we will quantitatively measure their morphology at all these wavelengths by means of commonly used morphological estimators, such as the concentration index, the asymmetry, the second order moment of the brightest pixels and the Gini coefficient.

In chapter 4 we will present a comprehensive analysis of the radial distribution of dust properties in the SINGS galaxies. We will compare the total-IR to UV profiles to derive the radial variation of the internal extinction. Moreover, we will fit the IR spectral energy distributions at each radius with the dust models of Draine & Li (2007) in order to determine the spatial variation of the dust properties mentioned in point 3 in the list of objectives.

The last issue of the list above will be dealt with in chapter 5. Combining the light profiles presented in chapter 3 with the internal extinction profiles obtained in chapter 4, we will recover the intrinsic multi-wavelength emission of stars across the disks of the SINGS galaxies. These profiles will be fit with the models of Boissier & Prantzos (1999; 2000), which take into account simultaneously and in a self-consistent way the chemical and spectro-photometric evolution of spirals.

Finally, the global conclusions of the thesis are summarized in chapter 6, and a brief outline of ongoing and future work is provided in chapter 7.

Additional material not included in the main body of the thesis is provided in several appendices at the end. In appendix A we present multi-wavelength images of all the SINGS galaxies, together with their surface brightness profiles and the result of fitting them with the dust models of Draine & Li (2007) and the disk evolution models of Boissier & Prantzos (1999; 2000). In appendix B we quote the values of the morphological estimators at each wavelength for the whole SINGS sample. Finally, in appendix C we display the two-dimensional χ^2 distributions obtained when fitting the radial profiles with the disk evolution models.

This thesis is presented as a compilation of papers. In particular, the material comprising chapters 2, 3 and 4 has been published in the Astrophysical Journal as three separate papers. In order to facilitate the comprehension of these chapters and put them into the general context of the thesis, each one includes a brief introduction that provides some basic information on the subjects addressed later in the papers. The analysis presented in chapters 5 and 7 will be soon published in Muñoz-Mateos et al. (2010a, 2010b). Finally, all chapters are preceded by a brief summary in Spanish, and a complete translation of the Introduction and Conclusions chapters is also provided.

2

Inside-out disk growth

Resumen

Tal y como se explicó en la sección 1.3, una predicción importante del modelo cosmológico ΛCDM es que las partes internas de los discos galácticos se forman en primer lugar, seguidas de las regiones externas (White & Frenk 1991; Mo, Mao & White 1998). Esto conduce de forma natural al crecimiento de los discos, es decir, a un aumento de su longitud de escala con el tiempo. Una consecuencia observacional inmediata es que la tasa de formación estelar específica debe aumentar con la distancia al centro de la galaxia. En particular, cabe preguntarse si dicha variación radial guarda alguna relación con la velocidad de crecimiento de los discos. En este capítulo hemos abordado este problema combinando perfiles de brillo superficial en el ultravioleta lejano, que trazan la distribución de estrellas jóvenes, con perfiles en el infrarrojo cercano, que muestran la distribución de estrellas más evolucionadas.

Hemos trabajado con una muestra de 161 galaxias espirales (con tipos entre S0/a y Sm) y con un ángulo de inclinación inferior a 45°, con el fin de minimizar los efectos de la extinción interna. Las galaxias fueron seleccionadas del *Atlas GALEX de Galaxias Cercanas* (Gil de Paz et al. 2007), donde ya se presentaron perfiles radiales en el ultravioleta lejano (FUV) y cercano (NUV). Reproduciendo el proceso seguido en Gil de Paz et al. (2007), medimos perfiles de brillo superficial en la banda K_S con la tarea `ellipse` en IRAF. Se empleó un incremento radial de $6''$, manteniendo constantes el ángulo de posición y la elipticidad, que fueron fijados a los valores correspondientes a la isofota a $\mu_B = 25\,\mathrm{mag\,arcsec^{-2}}$. El cálculo de errores se realizó siguiendo el método descrito en Gil de Paz & Madore (2005), incluyendo las variaciones de la intensidad a lo largo de cada isofota y el error del cielo (tanto la contribución poissoniana local como variaciones a gran escala).

Los perfiles fueron corregidos de extinción galáctica usando los excesos de color de Schlegel et al. (1998) y la curva de extinción de Cardelli et al. (1989). La corrección de extinción interna se llevó a cabo usando los resultados de Boissier et al. (2007), que combinaron datos de GALEX y IRAS para estudiar la atenuación del polvo en galaxias cercanas. Para las 16 galaxias comunes entre nuestra muestra y la de Boissier et al. (2007) empleamos perfiles de extinción derivados de la variación radial del cociente TIR/FUV. Para las galaxias restantes, la extinción interna se estimó indirectamente a partir de los perfiles de color $(\mathrm{FUV}-\mathrm{NUV})$. La tasa de formación estelar específica se calculó a partir del color $(\mathrm{FUV}-K_S)$, usando por un lado la calibración de Kennicutt (1998) para la SFR en función de la luminosidad en el FUV, y por otro la relación masa-luminosidad en banda K_S de Bell et al. (2003).

Para medir el gradiente radial de sSFR se aplicó un ajuste lineal a los perf les correspondientes, excluyendo el bulbo. Comprobamos que las galaxias poco masivas presentan un amplio rango de gradientes de sSFR, la mayoría positivos, aunque también algunos negativos. Las espirales más masivas poseen un gradiente apenas ligeramente positivo, indicando un ritmo de crecimiento modesto. Elaboramos un modelo sencillo de evolución de discos para relacionar estos gradientes con la tasa de crecimiento de las galaxias. En conjunto, concluimos que la distribución observada de gradientes de sSFR es consistente con un incremento promedio de un 25 % en la longitud de escala de los discos desde $z = 1$.

El modelo predice un límite superior para los posibles valores del gradiente de sSFR para un tamaño dado del disco. Sin embargo, en nuestra muestra encontramos galaxias con gradientes más pronunciados, y muchas de ellas muestran signos de intensa formación estelar en sus zonas externas. Es posible, por tanto, que estos discos estén experimentando episodios de crecimiento más acusados de lo que se espera en un escenario de crecimiento lineal y suave. Por el contrario, algunas galaxias poco masivas presentan gradientes negativos de sSFR. Esto puede indicar un crecimiento desde fuera hacia dentro, o bien puede ser el resultado de la pérdida de gas en las zonas externas en el caso de galaxias en cúmulos como el de Virgo.

2.1 Introduction

As explained in section 1.3, according to the sucessful ΛCDM scenario of galaxy formation the growth of galactic disks should proceed from inside out. As an example, in Fig. 2.1 we show the evolution of a massive disk galaxy simulated by Samland & Gerhard (2003). Their three-dimensional model follows the chemo-dynamical evolution of this galaxy in a ΛCDM universe. The simulation considers a two-phase ISM model, which is constituted by hot gas, heated and ionized by massive stars and supernovae, and embedded clouds of cold and warm gas.

The dissipation and collapse of the gas clearly takes place in an inside-out fashion. First, the stellar halo is formed early through an rapid collapse at $z > 1.5$. Between $z = 1.5$ and $z = 1$ a thick disk appears, and the bulk of the star formation at later times takes place mainly in the thin disk. This is nicely illustrated by the progressive f attening of the gas component and the associations of young OB stars. Due to its larger angular momentum, gas in the outer disk collapses on longer timescales than in the central regions. As a result, the distribution of newly born stars not only gets vertically f atter, but also more radially extended as star formation shifts outwards. Therefore, since $z = 1$ the overall evolution of the galaxy is dominated by the inside-out growth of its thin disk.

A direct prediction of this scenario is that, on average, stars should be younger in the outer disk than in the inner one, something that has been proposed to explain the observed color gradients of spirals (de Jong 1996). In other words: the SFR per unit of stellar mass should increase with radius. Despite the simplicity of this prediction, properly quantifying whether the specif c SFR actually varies with the galactocentric distance has not been an easy task. Up to now, most studies dealing with color gradients in spirals have relied mainly on optical measurements. However, neither the blue nor the red optical bands are accurate enough tracers of young and old stellar populations, respectively. The ultraviolet range is much more sensitive to the presence of recent star formation activity, and the near-IR bands are more reliable tracers of the accumulated stellar mass. Besides, radial variations in the dust content and metallicity can also lead to color gradients similar to those due to changes in the mean stellar age. Again, optical measurements alone do not allow to properly disentangle both effects.

In order to circumvent these problems, in the work presented in this chapter we combined FUV prof les from GALEX with near-IR ones in the K_S band from the *Two Micron All Sky Survey* (2MASS), for a sample of 161 nearly face-on galaxies. The resulting $(\mathrm{FUV} - K_S)$ color prof les were also corrected for internal extinction using the ratio of the total-IR (TIR) to the FUV emission, as well as the $(\mathrm{FUV} - \mathrm{NUV})$ color when TIR/FUV prof les were not available. The use of a wider wavelength baseline beyond the optical range, together with independent measurements of the radial variation of internal extinction, made it possible to directly translate these color prof les into specif c SFR ones.

Besides, we also developed a simple model that mimics the evolution of disk prof les predicted by more complex and physically motivated models. The basic assumption is that the radial scale-length of the SFR prof le grows smoothly and linearly as time goes by. Besides, the overall level of star formation is supposed to decay exponentially with time. This temporally varying SFR prof le can be then integrated in time to get the present-day stellar mass prof le. For each model galaxy we can therefore obtain the current sSFR gradient as a function of the initial disk size and its growth rate. The results of this simple model were compared to the distribution of sSFR gradi-

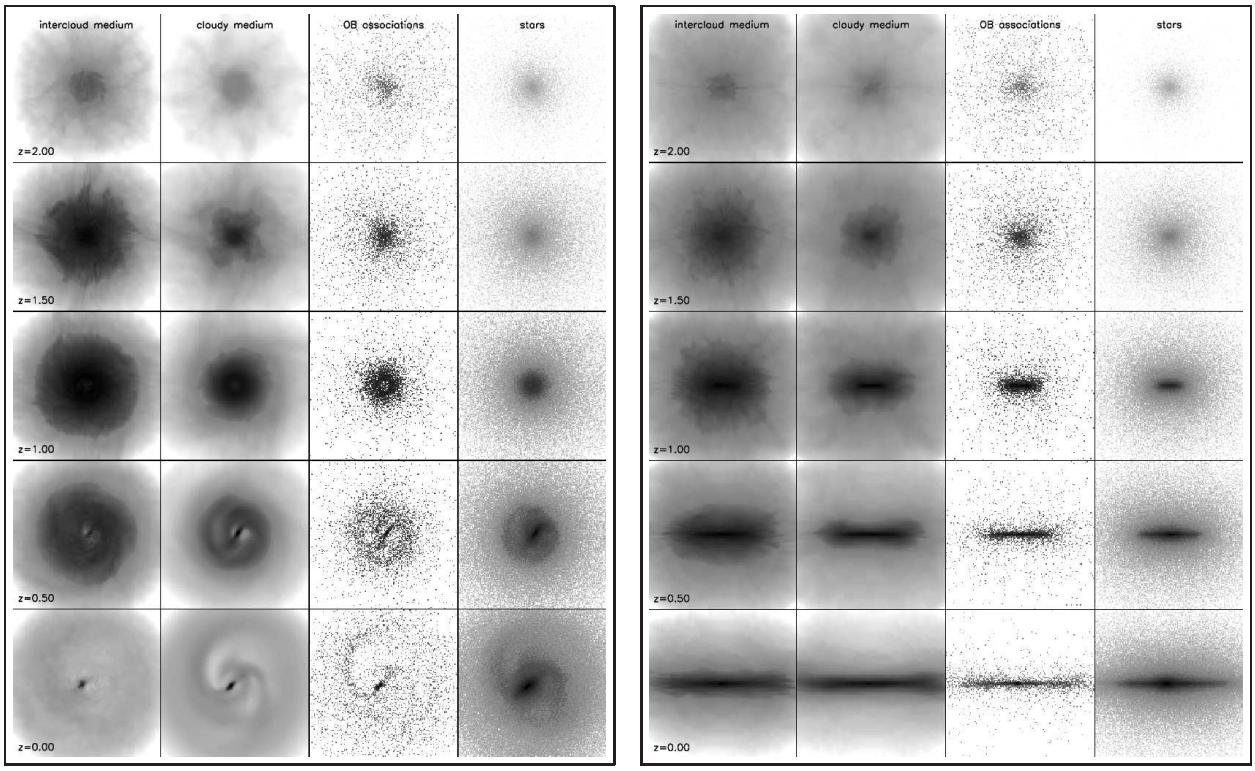

Figure 2.1: Results of the dynamical simulations of Samland & Gerhard (2003), showing the inside-out formation and evolution of a massive disk-like galaxy, viewed face-on (left panels) and edge-on (right panels). Each column shows the evolution with redshift of the spatial distribution of ionized gas, the cloudy medium, the associations of young OB stars and the total stellar mass surface density.

ents found in our sample, in order to interpret such gradients in terms of the radial growth rate of disks.

2.2 Muñoz-Mateos et al. (2007) ApJ, 658, 1006

The subsequent analysis of disk growth through sSFR profiles can be found in the following paper, originally published in the Astrophysical Journal:

➥ Muñoz-Mateos, J. C., Gil de Paz, A., Boissier, S., Zamorano, J., Jarrett, T., Gallego, J., & Madore, B. F., *Specific Star Formation Rate Profiles in Nearby Spiral Galaxies: Quantifying the Inside-Out Formation of Disks*, 2007, ApJ, 658, 1006

`http://iopscience.iop.org/0004-637X/658/2/1006/`

3

Multi-wavelength surface photometry and morphology

Resumen

En el capítulo anterior hemos demostrado cómo los datos en el ultravioleta lejano y el infrarrojo cercano pueden usarse para estimar el ritmo de crecimiento de los discos de las galaxias espirales, comparando la extensión actual de estrellas jóvenes y viejas. No obstante, para elaborar una descripción completa y detallada de la formación de las galaxias es esencial tener en cuenta dos ingredientes adicionales: el gas y el polvo.

Con el f n de estudiar simultáneamente la distribución de estrellas, polvo y gas en galaxias cercanas es imprescindible contar con observaciones multi-longitud de onda desde el UV lejano hasta el IR lejano y las radiofrecuencias. En este sentido, los datos de la muestra SINGS (del inglés *Spitzer Infrared Nearby Galaxies Survey*, Kennicutt et al. 2003) son perfectos para este propósito. La muestra SINGS está formada por 75 galaxias situadas a menos de 30 Mpc. Fueron seleccionadas con el f n de cubrir el rango de tipos morfológicos, luminosidades y cocientes FIR/óptico que se observan en el universo local. Además, también cubren un rango suf cientemente amplio en otras propiedades secundarias, como la actividad nuclear, la estructura de los brazos espirales y de las barras, la inclinación, el brillo superf cial y el entorno.

En este capítulo hemos analizado la morfología de las galaxias SINGS en todas las longitudes de onda mencionadas anteriormente. En primer lugar llevamos a cabo un cuidadoso proceso de detección y eliminación de estrellas de campo y galaxias de fondo en nuestras imágenes. Seguidamente medimos perf les de brillo superf cial en todas las longitudes de onda, siguiendo el mismo procedimiento descrito en el capítulo anterior. Los perf les resultantes muestran una enorme variedad de características, tales como truncamientos internos del disco (sobre todo en las espirales tempranas) o cambios bruscos de la pendiente en las zonas externas. Más aún, la intensidad de estos rasgos varía enormemente con la longitud de onda. Esto pone de manif esto las limitaciones de algunos prodecimientos clásicos como la descomposición bulbo-disco, que se han empleado habitualmente para estudiar la estructura de las galaxias.

Para comparar de manera consistente la morfología de las galaxias en todas las longitudes de onda, medimos sobre las distintas imágenes varios estimadores morfológicos: el índice de concentración, la asimetria, el momento de segundo orden de los píxeles más brillantes y el coef ciente de Gini. El índice de concentración y el momento de segundo orden miden el grado de concentración de la luz en las galaxias, aunque el momento es más sensible a la presencia de estructuras aisladas

lejos del centro, tales como brotes de formación estelar. La asimetría se calcula rotando 180° la imagen de una galaxia y comparando la imagen resultante con la original, por lo que nos da una idea del grado de simetría del objeto. Finalmente, el coef ciente de Gini es una magnitud usada comúnmente en economía para determinar cuán equitativa es la distribución de riqueza entre los individuos de una comunidad. Este coef ciente fue adaptado por Abraham et al. (2003) para su uso con galaxias, y permite determinar si la luminosidad de una galaxia está uniformemente repartida entre los píxeles que la componen, o si por el contrario la mayor parte de la luz procede de una pequeña fracción de píxeles muy brillantes.

Al analizar el comportamiento de estos cuatro coef cientes en función de la longitud de onda, observamos que las galaxias presentan un aspecto más asimétrico y menos concentrado en el ultravioleta, debido a la emisión de estrellas jóvenes esparcidas por todo el disco, así como en el infrarrojo medio, debido a la emisión de los PAHs a 8.0 μm y del polvo muy caliente a 24 μm. En el óptico y el infrarrojo lejano, por el contrario, la mayor parte de la radiación procede de estrellas más evolucionadas, sobre todo en el bulbo, pero también en el disco el disco. Esto conf ere a las galaxias un aspecto más simétrico y concentrado en esas bandas. En cuanto al coef ciente de Gini, concluimos que si bien está correlacionado con el índice de concentración en el óptico y el infrarrojo cercano, la correlación desaparece en el ultravioleta y el infrarrojo medio, donde las regiones más brillantes no se ubican necesariamente en las zonas centrales.

3.1 Introduction

In the previous chapter we have demonstrated how UV and near-IR data can be used to estimate the inside-out growth rate of spiral disks, by comparing the present-day extent of young and old stars. However, in order to elaborate a complete and detailed picture of the process of galaxy build-up, it is paramount to take into account two additional ingredients: gas and dust.

In order to simultaneously study the spatial distribution of stars, dust and gas in nearby galaxies, multiwavelength observations from the FUV to the FIR and radio are mandatory. In this regard, the data from the SINGS sample (*Spitzer Infrared Nearby Galaxies Survey*, Kennicutt et al. 2003) are perfectly suited for this purpose. The SINGS sample is comprised of 75 nearby galaxies at a distance closer than 30 Mpc. They were selected in order to cover the range in morphological type, luminosity and FIR/optical ratio observed in the nearby universe. Besides, they also span a wide enough range in other secondary properties, such as nuclear activity, spiral and bar structure, inclination, surface brightness and environment. Even though as a whole the SINGS sample lacks the statistical robustness of a magnitude- or volume-limited sample, the properties of its 75 galaxies are representative of those of typical nearby galaxies.

In this chapter we will numerically characterize the morphology of the SINGS galaxies at all wavelengths, in order to provide new insights into the Hubble sequence beyond the traditional optical-based classif cations. Once we understand how stars, dust and gas are spread within galaxies of different types, in chapter 4 we will focus on the radial variation of dust properties. Finally, the radial distribution of stars of different ages will be dealt with in chapter 5.

3.2 Quantifying the morphology of galaxies

As happens with any observational science, a taxonomical classif cation of the shapes of galaxies is an unavoidable f rst step prior to understanding the physical mechanisms driving their formation and evolution. The f rst classif cation schemes were highly subjective, and relied mainly on the visual inspection of optical images of nearby galaxies (Curtis 1918; Hubble 1926b, 1936; Sandage 1961). The Hubble classif cation scheme was soon embraced by the scientif c community, and was later ref ned by other authors (van den Bergh 1960a, 1960b; de Vaucouleurs 1959).

In an era when telescopes and detectors have considerably superseded those available decades ago in terms of collecting power and sensitivity, the number of galaxies in large surveys has increased exponentially. In such a scenario, carrying out a visual classif cation of galaxies is obviously an arduous task. Moreover, observations of distant galaxies have revealed that their morphology is severely distorted compared to that of nearby ones, making it diff cult to f t these objects into the classical Hubble scheme. Besides, since this morphological system is tied to optical images −where the emission of intermediate-age stars dominates−, it is not straightforward to apply it at wavelengths that trace recent star formation or dust.

Therefore, a system that can classify galaxies in a quantitative manner is highly desirable. It would make it possible to automatically classify a huge number of galaxies in large surveys, and it would also allow to compare the morphology of stars and the ISM at different bands in a self-consistent way.

The first quantitative morphological estimators were based on properties derived from a galaxy's surface photometry. Light profiles in elliptical galaxies and the bulges of spirals usually follow a de Vaucouleurs profile (de Vaucouleurs 1948):

$$I(r) = I_e e^{-7.67\left[(r/r_e)^{1/4}-1\right]} \tag{3.1}$$

where I_e is the surface brightness at r_e. Spiral disks, on the other side, can be approximated by an exponential law (Freeman 1970):

$$I(r) = I_0 e^{-r/R_d} \tag{3.2}$$

where I_0 is the central surface brightness and R_d the exponential scale-length of the disk. These equations can be used to fit the observed surface brightness profile of a galaxy and decompose it into a bulge and a disk component. The ratio between the luminosities of the bulge and the disk (B/D) decreases from early- to late-type galaxies, so it has been traditionally used as a morphological estimator.

Another common approach consists on fitting the radial profiles with a Sérsic law (Sérsic 1968):

$$I(r) = I_0 e^{-kr^n} \tag{3.3}$$

where the Sérsic index n controls the degree of curvature of the profile. Large values of n correspond to more centrally concentrated profiles. Indeed, it can be easily seen that the exponential and de Vaucouleurs laws are particular cases of a Sérsic profile with $n = 1$ and $n = 4$, respectively.

Even though B/D and n are known to be correlated with the Hubble type, their applicability to real galaxies is not devoid of problems. First of all, the observed profiles of galaxies usually exhibit a wealth of features that cannot be properly accounted for with the equations above. These include bars, rings, bright spiral arms, inner disk truncations, outer disk up- and down-bendings, etc. The multi-wavelength profiles presented in this chapter will show that this is indeed the case in many galaxies, with the prominence of these features varying wildly from the FUV to the FIR. Secondly, one-dimensional fits to radial profiles may not always yield the same results as bi-dimensional fits performed on the whole image of the galaxy (Byun & Freeman 1995; Wadadekar et al. 1999).

Non-parametric morphological estimators differ from the ones outlined above in that they do not assume a particular functional form for the distribution of light in galaxies. Here we make use of four of the most usual estimators commonly employed in the literature: the concentration index, the asymmetry, the second-order moment of the brightest 20% of the emission and the Gini coefficient. In order to facilitate the comprehension of the paper included in this chapter, a brief description of the graphical meaning of these estimators is provided in the sections that follow.

3.2.1 Concentration index

Several definitions of the concentration index can be found in the literature, although most of them are equivalent to some extent. Here we focus on the concentration index C_{42} defined by Kent (1985):

$$C_{42} = 5 \log \left(\frac{r_{80}}{r_{20}} \right) \tag{3.4}$$

where r_{80} and r_{20} are the radii along the semimajor axis of elliptical apertures that include 80% and 20% of the total emission of the galaxy.

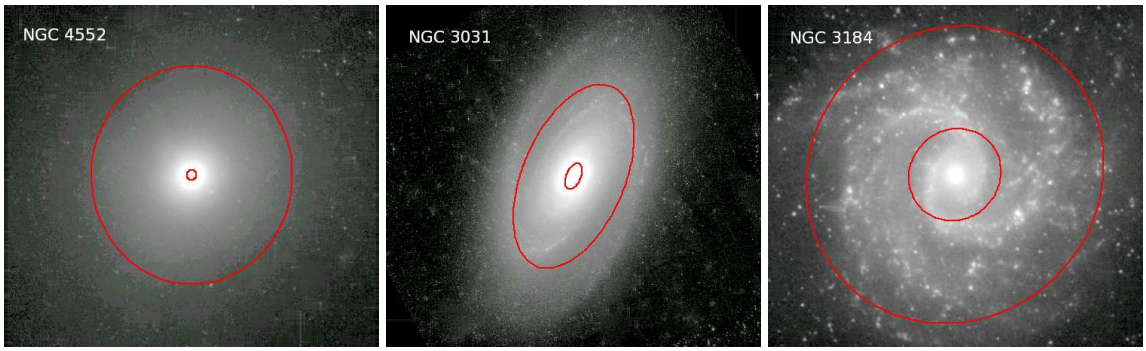

Figure 3.1: The apertures r_{80} and r_{20} for three sample galaxies at 3.6 μm: the elliptical galaxy NGC 4552 (E0), the early-type spiral NGC 3031 (Sab) and the late-type one NGC 3184 (Scd). Images are displayed with a square-root stretch.

As an example, in Fig. 3.1 we show the r_{80} and r_{20} elliptical apertures for three sample galaxies of different morphological types. The relative sizes of both apertures determines the corresponding concentration index. The images correspond to the 3.6 μm band, which traces the distribution of old stars. It is apparent from this f gure that C_{42} is correlated with the Hubble type, since it decreases monotonically from elliptical galaxies to late-type spirals. In the elliptical galaxy NGC 4552, the strongly peaked de Vaucouleurs prof le yields $C_{42} = 6.00$. The early-type spiral NGC 3031 has a prominent bulge and an exponential disk, so its concentration index is lower, $C_{42} = 4.26$. The light distribution in the late-type spiral NGC 3184 is almost entirely dominated by the exponential disk, yielding an even lower value of $C_{42} = 2.55$.

3.2.2 Asymmetry

As with the concentration index, different authors have proposed several mathematical def nitions for the asymmetry, although they rely on the same basic idea. Brief y speaking, the asymmetry is computed by rotating the image of a galaxy by 180° and comparing the resulting image with the original, unrotated one. More precisely, here we follow the def nition given by Abraham et al. (1996b):

$$A = \frac{1}{2}\left[\frac{\sum |I_{180^\circ} - I_0|}{\sum |I_0|} - \frac{\sum |B_{180^\circ} - B_0|}{\sum |I_0|}\right] \tag{3.5}$$

In this equation, I_0 and I_{180° are the intensities of the original and rotated images, respectively, and B_0 and B_{180° the intensities of background pixels and their rotationally-symmetric counterparts. This second term is needed to remove the extra positive signal that the random sky noise introduces in A.

The asymmetry also varies along the Hubble sequence, as can be readily seen in Fig. 3.2. Most elliptical galaxies lack any signif cant underlying structure, so their asymmetries tend to be very low. The presence of spiral arms and star-forming regions increases the asymmetry in spiral galaxies, but the effect is most noticeable in late-type spirals than in early-type ones, since the light distribution of the latter is still dominated by a prominent bulge. For the sample galaxies shown here we measured $A = 0.023$, 0.049 and 0.137 at 3.6 μm for NGC 4552, NGC 3031 and NGC 3184, respectively.

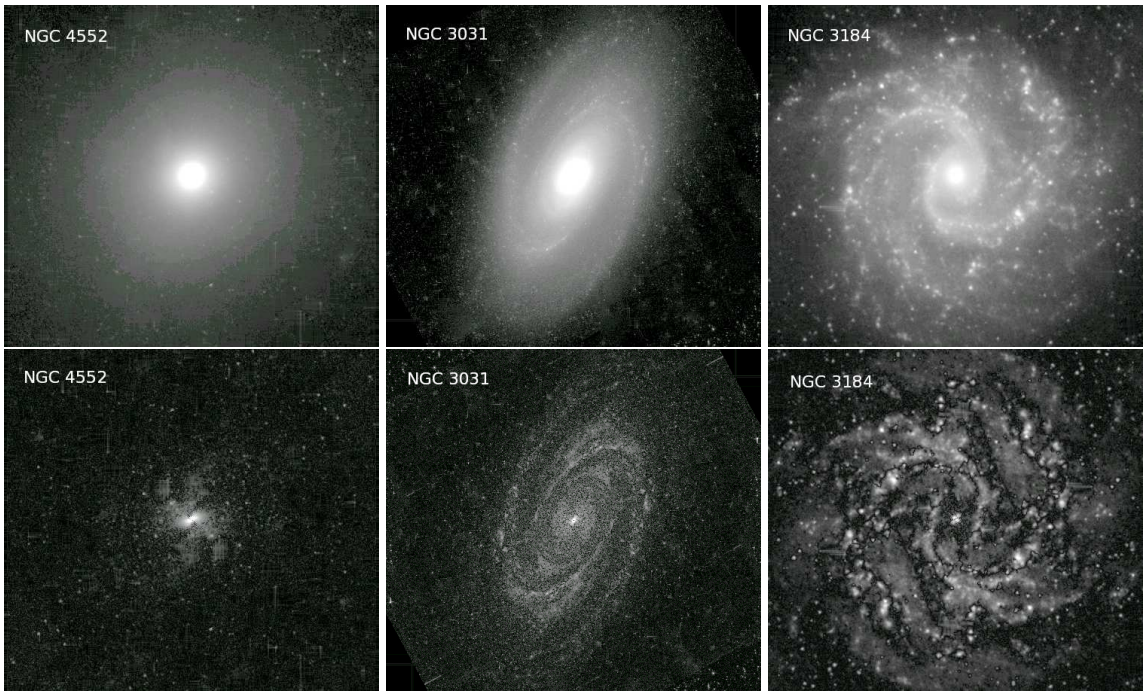

Figure 3.2: *Top row:* original 3.6 μm images of the galaxies NGC 4552, NGC 3031 and NGC 3184. *Bottom row:* absolute value of the difference between the original image and the rotated one. The same brightness cuts are used to display both the original images and the residuals.

3.2.3 Second-order moment

The total second-order moment of the light in a given galaxy is def ned as:

$$M_{\rm tot} = \sum_{i=1}^{n} M_i = \sum_{i=1}^{n} f_i \left[(x_i - x_c)^2 + (y_i - y_c)^2 \right] \tag{3.6}$$

where f_i is the f ux of the pixel at the position (x_i, y_i), and (x_c, y_c) are the coordinates of the galaxy's center. Lotz et al. (2004) suggest using the normalized second-order moment of the pixels constituting the brightest 20% of the total galaxy f ux:

$$\overline{M}_{20} = \log \left(M_{20} / M_{\rm tot} \right) \tag{3.7}$$

where M_{20} is computed by ranking the pixels in order of decreasing intensity, and then summing M_i over the brightest pixels until $\sum f_i = 0.2 f_{\rm tot}$. Since $M_{20} < M_{\rm tot}$, the normalized moment $\overline{M}_{20}$ is always negative, with lower −that is, more negative− values corresponding to more centralized emission.

Therefore, $\overline{M}_{20}$ can be understood as another way of measuring a galaxy's concentration, complementary to C_{42}. However, since $\overline{M}_{20}$ depends on the squared distance to the galaxy's center, it is more sensitive to the presence of bright regions in the outer parts of galaxies, while C_{42} tends to be more inf uenced by the central bulge.

In Fig. 3.3 we have highlighted the brightest pixels responsible of 20% of the total luminosity in our three sample galaxies. Those pixels are obviously spread across a larger area (relative to

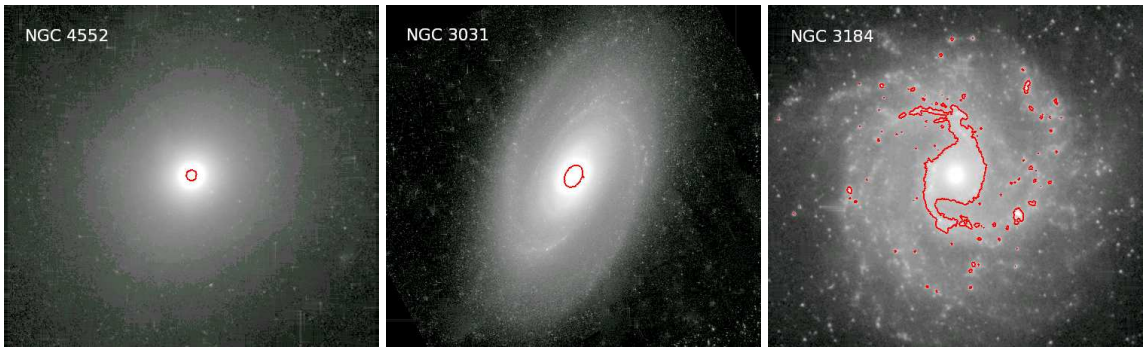

Figure 3.3: 3.6 μm images of NGC 4552 , NGC 3031 and NGC 3184, where the brightest pixels responsible of 20% of the total galaxy f ux are enclosed by the red contours.

the total galaxy's size) in late-type spirals than in early-type ones and ellipticals. Therefore, as happens with C_{42}, $\overline{M}_{20}$ is also correlated with the morphological type. After applying Eq. 3.7 to the 3.6 μm images of NGC 4552 , NGC 3031 and NGC 3184, we obtain $\overline{M}_{20} = -2.98$, -2.68 and -1.47, respectively.

3.2.4 Gini coeff cient

The Gini coeff cient G (Gini 1912) is a statistical parameter commonly used in econometrics to quantify how wealth is distributed in a given population. It is based on the Lorenz curve (Lorenz 1905), which is constructed by ranking individuals from the poorest to the richest, and then plotting the cumulative fraction of the total income as a function of population rank. In the case where all individuals have the same income, the Lorenz curve is simply a straight line with a slope of unity, since x% of the population will have x% of the population's total wealth. In the real case where some individuals are richer than others, the Lorenz curve will fall below the line of equality. In particular, if most of the total income is owned by just a few individuals, then the Lorenz curve will be almost f at and close to zero before rapidly rising at the very end.

Abraham et al. (2003) adapted this concept to study the distribution of light within galaxies, by substituting individuals with pixels and income with f ux. In Fig. 3.4 we show the Lorenz curves for the same galaxies as in the previous sections. The horizontal axis corresponds to the quantile of the distribution, with the faintest pixels to the left and the brightest ones to the right. The vertical axis shows the cumulative fraction $L(p)$ of the total galaxy's luminosity contributed by a given fraction p of pixels. The degree of inequality in the distribution of light among pixels (or of income among individuals) can be quantif ed with the Gini coeff cient. It is def ned as the ratio between the areas A and A + B, so it can range between zero and one. In general, large values of G mean that most of a galaxy's luminosity is arising from a small fraction of pixels. We can see in Fig. 3.4 that light is more equally distributed in late-type spirals than in galaxies with earlier Hubble types.

In practice, we compute the Gini coeff cient following the method described by Lotz et al. (2004). After ranking the pixels from the lowest absolute pixel intensity to the highest one, G is

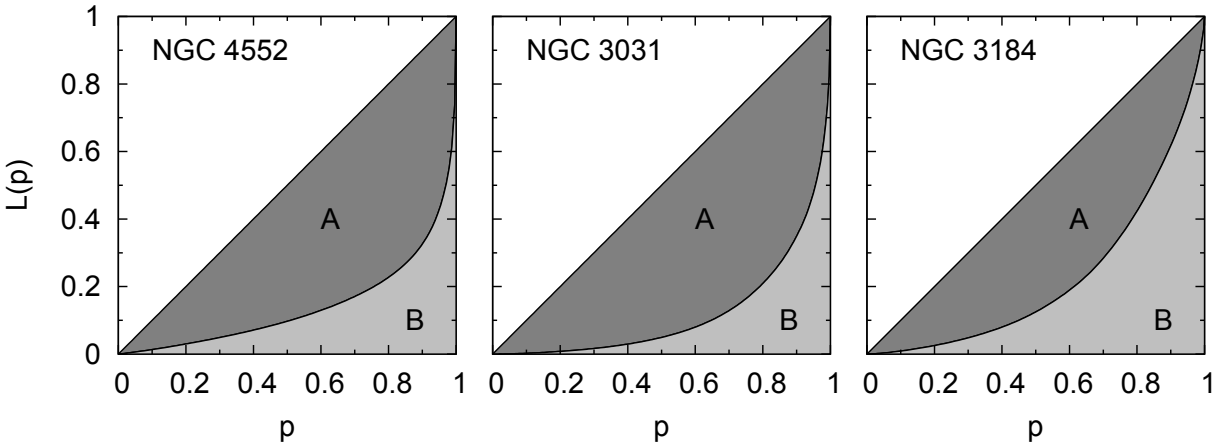

Figure 3.4: Lorenz curves computed on the 3.6 μm images of NGC 4552 , NGC 3031 and NGC 3184. The horizontal axis shows the quantile of the distribution, with pixels ranked in order of increasing brightness from left to right. The vertical axis corresponds to the cumulative fraction $L(p)$ of the galaxy's luminosity contributed by a fraction p of pixels. The diagonal line is the Lorenz curve in the particular case where the total luminosity is equally distributed among all pixels. The Gini coeff cient is, by def nition, the ratio between the area A and the total area below the line of equality, A + B.

computed as:

$$G = \frac{1}{\overline{|f|}n(n-1)} \sum_{i=1}^{n} (2i - n - 1)\,|f_i| \tag{3.8}$$

where n is the total number of pixels, $\overline{|f|}$ is the average absolute pixel intensity, and f_i is the intensity of the pixel i once all pixels have been ordered by their absolute brightness. For the galaxies in Fig. 3.4 we obtain $G = 0.720$, 0.761 and 0.553, respectively.

While the spatial information regarding the location of pixels within a galaxy is not taken into account, G has been traditionally used as an alternative estimate of a galaxy's degree of concentration. In the remaining of this chapter we shall demonstrate that this is only valid in the optical and near-IR regimes, where the brightest pixels of galaxies are located in their central regions, but not in the UV or the mid-IR, where luminous pixels might be associated to bright HII regions at any galactocentric distance.

In the paper included in this chapter we have obtained radial prof les for the SINGS galaxies at all bands between the FUV and the FIR. These prof les are shown in appendix A, together with images of each galaxy at selected wavelengths. We have also measured the morphological parameters described here at all wavelengths, in order to compare and quantify the morphology of stars, dust and gas in a consistent framework. The values of these estimators are quoted for just a few sample galaxies within the paper; a complete table with the values for the whole sample can be found in appendix B.

3.3 Muñoz-Mateos et al. (2009a) ApJ, 703, 1569

The description of the multi-wavelength morphology of the SINGS galaxies can be found in the following paper, originally published in the Astrophysical Journal:

➥ Muñoz-Mateos, J. C., Gil de Paz, A., Zamorano, J., Boissier, S., Dale, D. A., Pérez-González, P. G., Gallego, J., Madore, B. F., Bendo, G., Boselli, A., Buat, V., Calzetti, D., Moustakas, J., & Kennicutt, R. C., *Radial Distribution of Stars, Gas, and Dust in SINGS Galaxies. I. Surface Photometry and Morphology*, 2009, ApJ, 703, 1569

`http://iopscience.iop.org/0004-637X/703/2/1569/`

4

Radial distribution of dust properties

Resumen

El polvo interestelar juega un papel importante en los estudios de la formación y evolución de galaxias. De hecho, en el capítulo anterior hemos visto cómo el polvo interestelar moldea la apariecnia de las galaxias a lo largo del espectro electromagnético. Los granos de polvo absorben la luz de las estrellas en el ultravioleta y el óptico y la reemiten entre el infrarrojo medio y longitudes de onda submilimétricas. El polvo, por tanto, atenúa y enrojece la radiación estelar, limitando nuestra capacidad para calcular a partir de observaciones en el ultravioleta o el óptico magnitudes como la tasa de formación estelar, la edad de las estrellas o la metalicidad.

A pesar de sus serios efectos sobre la luz estelar, el polvo también constituye un ingrediente esencial en la evolución química de las galaxias. Después de todo, los granos de polvo están compuestos de elementos pesados producidos originalmente mediante nucleosíntesis estelar, e inyectados más tarde en el medio interestelar durante las fases tardías de la vida de las estrellas. Pueden actuar como catalizadores, proporcionando una superf cie sobre la que pueden formarse moléculas, incluyendo moléculas orgánicas complejas. Además, los gramos de polvo también pueden funcionar como termostatos, regulando la temperatura de las nubes de gas. Pueden calentar el gas liberando electrones mediante el efecto foto-eléctrico, o bien enfriarlo radiando en el infrarrojo, siendo este último un mecanismo esencial para acelerar la formación estelar.

El propósito de este capítulo es doble: por un lado, hemos obtenido perf les radiales de extinción interna para las galaxias SINGS. Estos perf les se usarán más adelante en el capítulo 5 para corregir los perf les en el ultravioleta, el óptico y el infrarrojo cercano, recuperando así la emisión intrínseca de estrellas de diferentes edades a lo largo de los discos galácticos. Por otro lado, hemos derivado la variación radial de otras propiedades físicas del polvo, que también pueden proporcionar pistas importantes sobre el proceso de evolución galaáctica.

Para este estudio, una vez eliminadas las estrellas de campo y las galaxias de fondo tal y como se explicó en el capitulo anterior, degradamos las imágenes de GALEX y *Spitzer* a la resolución de la banda de 160 μm de MIPS. Sobre estas imágenes degradadas medimos perf les de brillo superf cial con una resolución radial de 48″, algo superior a la anchura de la PSF a 160 μm.

Determinamos la variación radial de la extinción interna a partir del cociente entre la luminosidad infrarroja total y la ultravioleta, TIR/UV. Seguimos el procedimiento descrito por Cortese et al. (2008) para tener en cuenta el calentamiento adicional del polvo debido a estrellas evolucionadas. Encontramos que la extinción interna disminuye con la distancia al centro de la galaxia, siendo las espirales de tipos Sb-Sbc las más atenuadas, y las Sdm e irregulares las que menos extin-

ción interna presentan. Además, al igual que ocurre con las galaxias con formación estelar activa o *starbursts*, el cociente TIR/FUV está relacionado con el color $(\mathrm{FUV} - \mathrm{NUV})$, aunque con una dispersión mayor. Para un mismo cociente TIR/FUV las espirales normales presentan colores UV más rojos, debido seguramente a que su población estelar es intrínsecamente más vieja.

Por otro lado, ajustamos las distribuciones espectrales de energía infrarrojas a cada radio con los modelos de polvo de Draine & Li (2007). De dichos ajustes dedujimos la variación radial de varios parámetros físicos del polvo: la abundancia de PAHs, la fracción de polvo muy caliente, la intensidad del campo de radiación difuso y la densidad superf cial de masa de polvo. Vimos que la densidad de polvo disminuye con el radio de forma aproximadamente exponencial, con una longitud de escala prácticamente constante (comparada con el tamaño óptico) para las galaxias Sb-Sd. Encontramos también que muchas espirales de tipos tempranos presentan huecos centrales en sus perf les de polvo. Además, comprobamos que una misma densidad superf cial de polvo da lugar a diferentes atenuaciones en galaxias de distintos tipos morfológicos. Las nubes de polvo parecen ser más porosas en las galaxias de tipos Sc en adelante, dando lugar a menores atenuaciones que en las espirales de tipos más tempranos para una misma densidad superf cial de polvo.

La abundancia de PAHs presenta una compleja variación espacial en las galaxias SINGS. Del orden del 4 % de la masa total de polvo se encuentra en forma de PAHs en las espirales Sb-Sbc, mientras que en las Sdm e irregulares este porcentaje se sitúa en torno al 1 %. La abundancia de PAHs parece crecer con la metalicidad local hasta $12 + \log(O/H) \sim 8.9$, y luego la tendencia se aplana e incluso se invierte. Este comportamiento coincide de forma cualitativa con las prediciones de ciertos modelos de evolución del polvo (Galliano et al. 2008), aunque no podemos descartar la inf uencia de procesos de destrucción selectiva de PAHs.

Otro parámetro relevante en los estudios de evolución química de galaxias es el cociente entre la masa de polvo y la de gas. Para determinar la densidad total de gas a cada radio, empleamos perf les de hidrógeno atómico de la exploración THINGS (*The HI Nearby Galaxies Survey*, Walter et al. 2008), así como perf les de hidrógeno molecular de diversas fuentes. Constatamos que $M_{\mathrm{dust}}/M_{\mathrm{gas}}$ alcanza valores de 0.1-0.01 en las zonas centrales de los discos, y disminuye un orden de magnitud en las regiones externas. Además, este cociente está fuertemente correlacionado con la abundancia de oxígeno. No obstante, en las partes externas de algunos discos encontramos valores de $M_{\mathrm{dust}}/M_{\mathrm{gas}}$ inferiores a los esperados, indicando quizá la presencia de polvo a temperaturas inferiores a 15 K (más allá por tanto del límite de detección de MIPS), o bien la presencia de grandes masas de gas que aún no han sido transformadas en estrellas (ni por tanto en polvo).

4.1 Introduction

Interstellar dust plays an important role in studies of galaxy formation and evolution. Indeed, we have seen in the previous chapter how dust shapes the appearance of galaxies across the electromagnetic spectrum. Dust grains absorb light from stellar sources in the UV and optical spectral ranges, and re-emit it between mid-IR and submillimeter wavelengths. Dust dims and reddens starlight, thus limiting our ability to infer properties like the SFR, the stellar age or the metallicity from observations in the UV and optical windows. In this regard, in order to use the radial profiles obtained in the previous chapter to study the radial distribution of stars of different ages, we must first find a way to correct them for internal extinction.

Despite its serious effects on starlight, dust itself also constitutes a paramount ingredient in the chemical evolution of galaxies. After all, dust grains are composed of heavy elements originally produced by stellar nucleosynthesis, and later injected into the ISM in the last stages of a star's life. They can act as a catalyst, providing a surface on which molecules can form, including complex organic ones. Moreover, dust grains also serve as a thermostat in gas clouds. For instance, electrons released through the photo-electric effect can heat the gas. Besides, dust grains can also cool the gas by radiating IR photons that are able to escape from dense clouds. This latter process is key to speed up the process of star formation.

The purpose of this chapter is thus twofold: on one hand, we will derive radial attenuation profiles for the SINGS galaxies. These profiles will be later used in chapter 5 to correct the UV, optical and near-IR ones, thus recovering the intrinsic emission of stars of different ages across galactic disks. On the other hand, we will also derive the radial variation of several other physical properties of dust, which can also provide important clues on the process of galaxy evolution.

4.2 Measuring dust extinction

In Fig. 4.1 we illustrate the effect of dust grains on the radiation emitted by stars within a galaxy, as predicted by the models of Noll et al. (2009). The SEDs correspond to a stellar population with solar metallicity, an exponentially decaying SFH with a timescale of 10 Gyr, and an age of 1 Gyr[1]. In the absence of dust (black line), the SED is dominated by the emission of young stars at short wavelengths, and it smoothly decays in the near-IR following the Rayleigh-Jeans tail of the thermal emission. However, when dust is incorporated, the appearance of the SED is significantly altered: a great deal of UV, optical and −to a lesser extent− near-IR light is absorbed by dust grains and re-radiated at longer wavelengths. Large molecules called Polycyclic Aromatic Hydrocarbons (PAHs) are responsible for the emission lines seen between 3 and 20 μm (see section 4.3). The emission at longer wavelengths results from the superposition of the thermal spectra of dust grains at different temperatures.

Since absorption and scattering are more efficient at short wavelengths, the attenuated stellar spectra is not only dimmer, but also redder. Therefore, it is not straightforward to disentangle the effects of dust on a galaxy's SED from those due to variations in stellar ages and metallicities, especially when only photometric data are available.

[1] While such a young age is not representative of the average stellar populations of the galaxies in our sample, the purpose of this plot is simply to illustrate the effects of dust attenuation on the stellar SED.

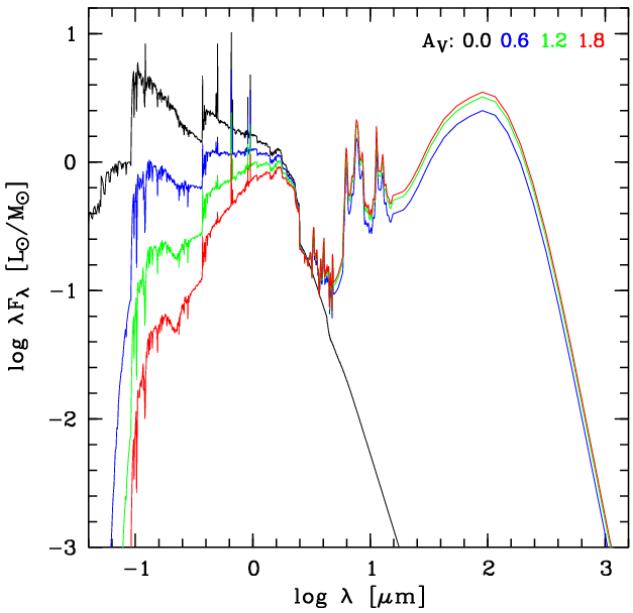

Figure 4.1: Effects of a varying degree of dust attenuation on starlight, using the models of Noll et al. (2009). All models correspond to a 1 Gyr old stellar population with solar metallicity, and an exponentially decaying SFH with a timescale of 10 Gyr. Each model has a different V-band attenuation, as labeled in the legend. (Image taken from Noll et al. 2009).

To overcome this problem, great efforts have been devoted to develop methods that provide independent measurements of dust attenuation in galaxies (see Calzetti 2001 for a review on the subject). In this regard, the ratio of the total-IR to UV light is known to be an excellent tracer of dust extinction. Indeed, as Fig. 4.1 demonstrates, larger values of the attenuation increase the ratio of the total infrared to UV light, as a result of a simple energy balance mechanism. Moreover, several radiative transfer simulations have shown that the relation between the TIR-to-UV ratio and extinction is quite insensitive to changes in the extinction law or in the relative arrangement of dust and stars (Buat & Xu 1996; Gordon et al. 2000; Witt & Gordon 2000; Buat et al. 2005; Cortese et al. 2008).

In this chapter we will use the radial variation of the TIR-to-UV ratio to obtain radial attenuation profiles. This will be done with state-of-the-art calibrations that take into account the extra dust heating due to old stars. Moreover, we will also provide empirical prescriptions to estimate the internal extinction in the lack of IR data.

4.3 Inferring the physical properties of dust

As argued before, besides quantifying the internal extinction in galaxies, IR data can be also used to study other interesting physical properties of dust, such as the abundance of PAHs, the intensity of the heating radiation field, the relative amounts of hot and cold dust or the total dust surface density.

To this end, in this chapter we will fit the IR SEDs of our galaxies at different radii with the dust models of Draine & Li (2007; DL07 hereafter). These models describe interstellar dust as a

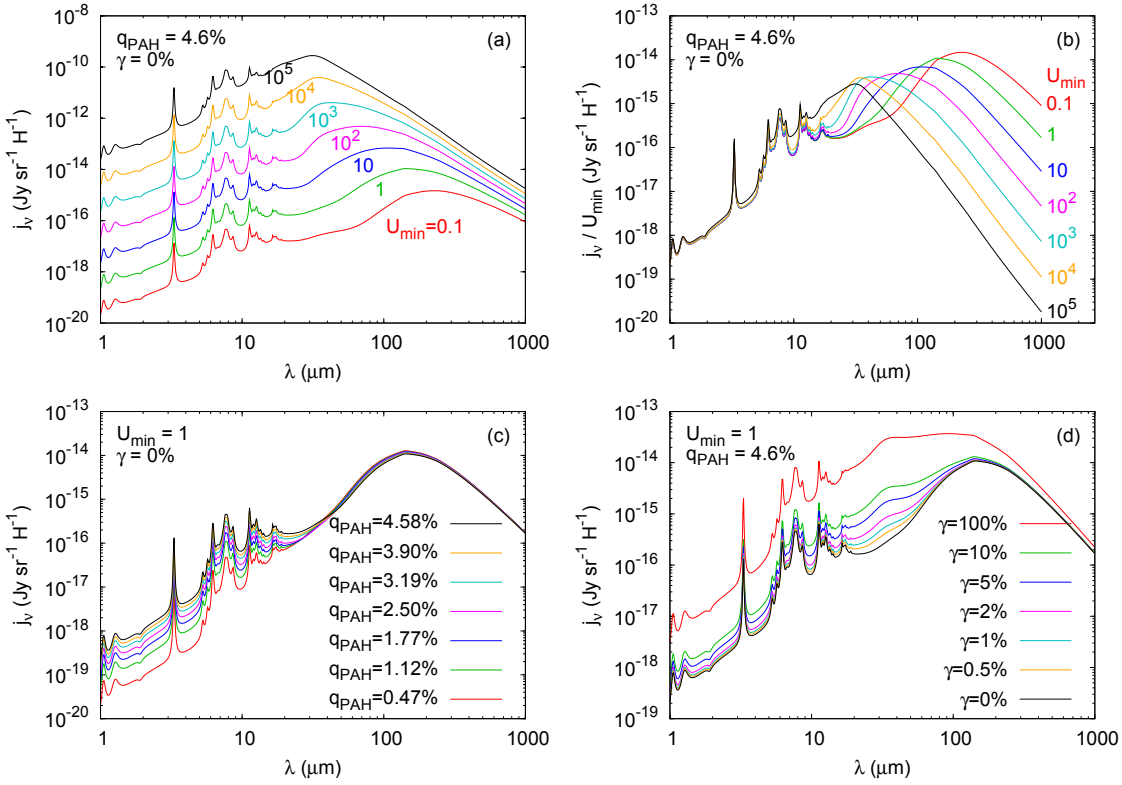

Figure 4.2: Inf uence of the parameters of the DL07 models on the f nal IR SED emitted by dust (note that the stellar emission in the near-IR is not included). The emissivity of the dust grains j_ν is expressed in janskys per steroradian and H nucleon. (a): Variations of the scale factor $U_{\rm min}$ that controls the intensity of the diffuse radiation f eld, in units of the MW f eld. (b): Same as (a), but after having normalized the SED by the value of $U_{\rm min}$. (c): Changes in the mass fraction of PAHS. (d): Variations in the fraction of hot dust heated by very intense starlight.

mixture of carbonaceous grains and amorphous silicate grains. The size distribution is chosen to be consistent with the extinction law in the Milky Way. The models predict the emitted SED of a given mixture of dust as a function of several free parameters:

1. **The intensity of the heating radiation f eld.** In the DL07 models, dust grains are heated by a certain radiation f eld, which is a scaled version of the local interstellar radiation f eld in the MW (Mathis et al. 1983). The scale factor is denoted by $U_{\rm min}$, so that $U_{\rm min} = 1$ would correspond to a heating starlight with the similar intensity as in the outskirts of the MW. In Fig. 4.2a we show the effect that changes this parameter have on the emitted SED. Increasing $U_{\rm min}$ makes large grains hotter, hence shifting the maximum of the SED towards shorter wavelengths. Small grains cool much faster than the incoming rate of photons, so instead of accumulating them and getting warmer, they respond to the increase in $U_{\rm min}$ simply by radiating more photons per second at each wavelength. For the sake of clarity, in panel (b) we have scaled down the SED by the corresponding value of $U_{\rm min}$.

2. **Abundance of PAHs.** The IR emission lines seen between 3 and 20 μm are produced by PAHs, which are large, f at molecules composed of a hexagonal grid of carbon atoms, surrounded by hydrogen ones. Following the absorption of a UV or an optical photon, PAHs molecules get vibrationally excited and re-emit the absorbed energy at selected wavelengths. The DL07 models parameterize the abundance of PAHs as $q_{\rm PAH}$, the fraction of the total dust

mass which is in the form of PAHs. As Fig. 4.2c shows, large values of $q_{\rm PAH}$ obviously yield more intense aromatic features.

3. **Fraction of very hot dust.** Dust grains close to or inside star-forming regions are exposed to much more intense starlight than that heating the diffuse dust clouds. The DL07 models assume that a small fraction γ of the total dust mass is heated by a radiation field whose intensity ranges from $U_{\rm min}$ to $U_{\rm max} = 10^6$, following a power law as described in Dale et al. (2001). The term γ thus mimics the contribution of very hot dust located in photodissociation regions (PDRs). The corresponding SED of one of these PDRs is shown with a red line ($\gamma = 100\%$) in Fig. 4.2d. In practice, the IR SED of a galaxy $-$or, as in our profiles, of a given area within a galaxy$-$ can be described as the combination of the IR light emitted by a fraction $1 - \gamma$ of diffuse dust, exposed to a constant radiation field $U_{\rm min}$, and a fraction γ of hot dust in PDRs, heated by very intense starlight.

4. **Total dust mass.** The three parameters described above control the shape of the SED. The total dust mass is computed afterwards by normalizing the SED. Since we apply these models to surface brightnes profiles, what we actually get after the normalization is the dust mass surface density, $\Sigma_{M_{\rm dust}}$.

In the paper that follows we measured the radial variation of all these properties in a large subset of SINGS galaxies (those detected and resolved at 160 μm). In appendix A we show the best-fitting DL07 model at each radius, as well as the resulting radial variation of each model parameter.

Besides, we combined all these radially varying properties of dust with existing profiles of other observables. In particular, we made use of the oxygen abundance profiles of Moustakas et al. (2010, in prep.), in order to analyze the link between dust properties and the local metallicity of the gas. Also, to study the radial variation of the dust-to-gas ratio, we relied on HI surface density profiles from *The HI Nearby Galaxies Survey* (THINGS; Walter et al. 2008). This survey has provided the scientific community with high quality 21 cm observations of a sample of 34 nearby galaxies, performed with the *Very Large Array* radio observatory. Whenever possible, we also complemented these measurements of the atomic gas column density with molecular gas profiles, in order to get the total amount of gas.

4.4 Muñoz-Mateos et al. (2009b) ApJ, 701, 1965

The full analysis of the radial distribution of dust properties can be found in the following paper, originally published in the Astrophysical Journal:

➥ Muñoz-Mateos, J. C., Gil de Paz, A., Boissier, S., Zamorano, J., Dale, D. A., Pérez-González, P. G., Gallego, J., Madore, B. F., Bendo, G., Thornley, M. D., Draine, B. T., Boselli, A., Buat, V., Calzetti, D., Moustakas, J., & Kennicutt, R. C., *Radial Distribution of Stars, Gas, and Dust in SINGS Galaxies. II. Derived Dust Properties*, 2009, ApJ, 701, 1965

`http://iopscience.iop.org/0004-637X/701/2/1965/`

5

Chemo-spectrophotometric evolution of spiral galaxies

Resumen

En el capítulo 2 combinamos perf les en el ultravioleta lejano y en banda K_S para analizar la variación radial de la SFR específ ca en galaxias cercanas. En general, la distribución de gradientes resultante resultó ser consitente con un incremento promedio de un 25 % en la longitud de escala radial de los discos desde $z = 1$ hasta ahora.

Aunque se trata ciertamente de una conclusión interesante, la metodología seguida en ese capítulo puede mejorarse en varios aspectos. En primer lugar, los detalles concretos de la historia de formación estelar pueden determinarse mejor incorporando datos en longitudes de onda intermedias además del ultravioleta lejano y el infrarrojo cercano. En segundo lugar, salvo para algunas galaxias con datos de IRAS disponibles, la corrección de extinción interna se llevó a cabo de forma indirecta, a partir del color $(\mathrm{FUV} - \mathrm{NUV})$. Finalmente, para interpretar los gradientes de SFR específ ca en términos del ritmo de crecimiento de los discos, usamos un modelo sencillo y esencialmente empírico que, aunque práctico, no fue desarrollado a partir de primeros principios.

Con los perf les multi-banda medidos en el capítulo 3 y los perf les de extinción interna obtenidos en el capítulo 4, podemos retomar el problema del crecimiento de los discos desde una perspectiva más detallada y compleja. En este capítulo hemos ajustado los perf les en el UV, el óptico y el IR cercano (corregidos de extinción interna) con los modelos de Boissier & Prantzos (1999, 2000). Estos modelos describen la evolución química y espectro-fotométrica de galaxias de tipo disco dentro de un marco unif cado, implementando procesos como la acreción de gas, la formación estelar y la evolución química de una manera auto consistente.

Los modelos están calibrados para reproducir ciertas propiedades observadas de la Vía Láctea (Boissier & Prantzos 1999). La generalización para otras galaxias se lleva a cabo mediante relaciones de escala deducidas del escenario ΛCDM (Boissier & Prantzos 2000). En particular, los modelos son capaces de reproducir los perf les multi-banda de las galaxias en base a dos parámetros: la máxima velocidad circular de la curva de rotación (V_C) y el espín (λ).

Realizamos un ajuste χ^2 sobre todas las bandas simultáneamente, desde el UV lejano hasta 4.5μm, implementando un procedimiento para estimar el error intrínseco de los modelos en cada banda. De cada ajuste obtuvimos tanto los mejores valores de V_C y λ como sus intervalos de incertidumbre correspondientes.

La mayoría de nuestras galaxias son similares a la Vía Láctea desde un punto de vista dinámico, con velocidades de rotación de unos 200-220 km/s y espines en torno a 0.03. Las velocidades de rotación resultantes del ajuste concuerdan con las observadas, aunque las primeras tienden a ser del orden de un 10-20 % mayores en algunos casos. La distribución de valores del espín es consistente con la que se encuentra en las simulaciones cosmológicas de N cuerpos, donde se ve que dicha distribución presenta un máximo alrededor de $\lambda \sim 0.04$, siendo prácticamente universal e independiente de la masa de los halos. Encontramos una correlación entre el tipo morfológico y la velocidad de rotación, en el sentido de que las espirales de tipos tardíos rotan más lentamente al ser menos masivas. Sin embargo, no observamos ninguna tendencia evidente entre el tipo morfológico y el espín.

Hemos visto que el modelo sobrestima la luminosidad ultravioleta de algunas espirales de tipos tempranos, aunque el motivo de tal desacuerdo aún no está claro. La función inicial de masas podría jugar un papel importante, aunque también es necesario considerar la presencia del bulbo o posibles errores en los f ujos UV de las bibliotecas estelares empleadas en los modelos.

En cualquier caso, el ajuste es siempre excelente en las demás bandas, por lo que en principio podemos suponer que en general los discos de nuestra muestra han evolucionado de la manera dictada por el modelo que mejor ajusta sus perf les actuales. En este sentido, hemos comprobado que la mayoría de nuestras galaxias han incrementado su longitud de escala radial a un ritmo de 0.05-0.06 kpc Gyr^{-1}. En términos relativos, la longitud de escala ha aumentado entre un 20 y un 25 % desde $z = 1$ según los modelos, reaf rmando las estimaciones iniciales presentadas en el capítulo 2.

5.1 Introduction

In chapter 2 we combined FUV and K_S-band profiles from GALEX and 2MASS data to analyze the radial variation of the specific SFR in nearby spirals. In general, the resulting distribution of gradients were consistent with an average increment of roughly 25% in the radial scale-lengths of disks since $z = 1$ until now.

While this is indeed an interesting conclusion, the methodology followed in that chapter can be improved in various aspects. First of all, we relied on FUV and K_S-band data alone. While these two bands are key to estimate the present to past-averaged SFR, the particular details of the SFH can be further constrained by adding data at intermediate wavelengths. Secondly, except for a few galaxies with available IRAS data, the correction for internal extinction was mostly done in an indirect way, by means of the FUV$-$NUV colour. In chapter 4 we demonstrated that this is actually a good solution in a statistical sense, but direct measurements of dust extinction are always desirable. Finally, in order to translate the specific SFR gradients into disk growth rates we made use of a simple model that mimics what is expected from the inside-out growth scenario. This model was, however, largely empirical and not built from first principles.

When that initial study was carried out, not all of the SINGS data had been released yet. Besides, even though our wavelength coverage was more limited back then, it should be noted that our analysis involved 161 galaxies, more than twice the number of objects in the SINGS sample.

With the multi-wavelength profiles measured in chapter 3 and the internal attenuation profiles obtained in chapter 4, we are now in the position to revisit the issue of disk growth from a more detailed and complex perspective. In this chapter we will fit the extinction-corrected UV, optical and near-IR profiles of the SINGS galaxies with the models of Boissier & Prantzos (1999, 2000; BP99 and BP00 hereafter). These models describe the chemical and spectro-photometric evolution of disk-like galaxies within a unified framework, by implementing processes such as gas infall, star formation and chemical enrichment in a self-consistent way. In particular, these models are able to reproduce the radial variation of several observable quantities as a function of the galaxy's maximum circular velocity and spin.

In this chapter we will first test the accuracy of the models at predicting the present-day properties of spiral galaxies in the SINGS sample. Afterwards, we will make use of these models in a backwards fashion to explore the properties of these galaxies at larger redshifts; in particular, we will focus on their size evolution. The analysis presented in this chapter will be published in brief in Muñoz-Mateos et al. (2010a).

5.2 Description of the models

In this section we broadly outline the main ingredients and underlying assumptions of the chemo-spectrophotometric models used to fit the multi-wavelength profiles of the SINGS galaxies. The reader is referred to BP99 and BP00 for a more in-depth description of the physical details of the models. Briefly speaking, an initial model was first developed and calibrated to reproduce several observed properties of our own galaxy (BP99). This model was then generalized to other spiral disks of different sizes and masses by means of several scaling laws deduced from the ΛCDM scenario of disk formation (BP00).

5.2.1 The Milky Way model

The Milky Way disk is modeled as several concentric rings, which are progressively built up by accretion of primordial gas from the halo. These annuli are supposed to evolve independently one from each other, in the sense that no radial mass flows are allowed. Such flows can actually take place in real galaxies as a result, for instance, of the presence of bars (Sellwood & Wilkinson 1993), redistribution of angular momentum due to viscosity (Yoshii & Sommer-Larsen 1989; Ferguson & Clarke 2001) and radial stellar migration (Rŏskar et al. 2008, Sánchez-Blázquez et al. 2009). Implementing these phenomena in an analytic way is not straightforward, and it would introduce many additional free parameters whose values might be difficult to constrain. Despite the simplifying assumption of independently-evolving rings, the model is still successful at reproducing the radial structure of the Milky Way.

The SFR at each radius r and time t depends on the local gas density $\Sigma_g(t,r)$ following a Schmidt law modulated by a dynamical term:

$$SFR(t,r) = \alpha \Sigma_g(t,r)^{1.5} V(r) r^{-1} \tag{5.1}$$

Here $V(r)$ is the rotational velocity at radius r. The term $V(r)r^{-1}$ is intended to mimic the conversion of gas into stars by the periodic passage of spiral density waves. It can be also seen as a dynamical timescale. The star formation efficiency α is fixed in order to reproduce the local gas fraction in the solar neighbourhood at $T = 13.5$ Gyr.

The gas infall rate $f(r,t)$ is supposed to decrease exponentially with time:

$$f(t,r) = A(r) e^{-t/\tau(r)} \tag{5.2}$$

The timescale of gas accretion $\tau(r)$ is assumed to increase with radius, from 1 Gyr at $r = 2$ kpc to 12 Gyr at $r = 17$ kpc. This allows reproducing the inside-out formation of disks, since gas takes longer to settle onto the disk in the outer regions given its larger angular momentum. At $r = 8$ kpc τ is set equal to 7 Gyr to reproduce the metallicity distribution of G-dwarf stars in the solar neighbourhood. The normalizing factor $A(r)$ can be deduced by integrating the infall rate until $T = 13.5$ Gyr, and then matching the result to the current stellar mass profile of the disk:

$$\int_0^T f(t,r) dt = \Sigma_{0\mathrm{G}} e^{-r/R_{\mathrm{dG}}} \tag{5.3}$$

The subscript G refers to the parameters of our galaxy. According to observations (see BP99), the central mass density of the Milky Way disk is set to $\Sigma_{0\mathrm{G}} = 1150\,\mathrm{M}_\odot\,\mathrm{pc}^{-2}$, and its radial scale-length is fixed to $R_{\mathrm{dG}} = 2.6$ kpc.

The mass distribution of stars for a given SFR follows a user-specified IMF. In this work we will compare the results obtained with the IMFs of Kroupa et al. (1993; K93 hereafter) and Kroupa (2001; K01 hereafter). The K93 IMF was used in the original models, and we are also interested in analyzing the results yielded by a more recent version of the IMF. The optical and near-IR fluxes, as well as the gas quantities, change by less than 20% between these two IMFs, which justifies not to totally recalibrate the model. It is the UV fluxes and metallicities that vary significantly, given the different content in high-mass stars of both IMFs (see section 5.6.2).

Stars of different masses enrich the ISM with varying amounts of different elements; in this regard, the model does not work under the *Instantaneous Recycling Approximation*, which assumes

that stars more massive than $1\,M_\odot$ die instantly, whereas less massive ones live forever. On the contrary, the model takes into account the finite lifetimes of stars of different masses when computing the chemical evolution within each ring. Moreover, the properties of each new generation of stars (lifetimes, stellar yields, evolutionary tracks and spectra) depend on the local metallicity at the corresponding radius and time of formation (see BP99). The spectrum of a given ring at time t can be then computed as the sum (both in time and mass) of the individual spectra of previously formed stars which are still alive at time t.

With the assumptions outlined above, BP99 showed that their Milky Way model is able to reproduce not only observables in the solar neighbourhood, but also radially-dependent ones, such as profiles of gas surface density, oxygen abundance, SFR and supernova rates, as well as luminosity profiles at different bands.

5.2.2 Extension to other disk-like galaxies

The previous model for the Milky Way was generalized to other disks in BP00, by making use of the scaling laws derived by MMW98 within the ΛCDM scenario. In this theoretical framework, galaxy formation is usually split into two different processes: the growth of non-baryonic dark matter haloes and the assembly of baryonic structures within them. Gravitational instabilities amplify the primordial density fluctuations, yielding dark matter clumps that merge and interact with each other, acquiring angular torques during the process. Meanwhile, baryonic gas cools and condenses within these haloes, leading to self-gravitating structures that are able to form stars, thus eventually giving rise to present-day galaxies.

The models of BP00 build on the mathematical formalism of MMW98, which establishes that under certain assumptions the scaling properties of disks depend only on two parameters: the maximum circular velocity of the rotation curve $V_{\rm C}$ and the dimensionless spin parameter λ:

$$V_{\rm C} = [10GH(z)M]^{1/3} \tag{5.4}$$

$$\lambda = J|E|^{1/2}G^{-1}M^{-5/2} \tag{5.5}$$

In the equations above, M, J and E are the total mass, angular momentum and energy of the halo, G is the gravitational constant and $H(z)$ is the Hubble parameter at the redshift z of halo formation. In order to express the properties of disks in terms of $V_{\rm C}$ and λ alone, the following assumptions need to be made:

(i) the masses of disks $M_{\rm d}$ are just a few percent of those of their corresponding haloes. The precise value of this ratio is unclear, but it must conform the baryonic fraction of the universe and the efficiency of disk formation. Following MMW98, the BP00 models assume $M_{\rm d} = 0.05M$ for all disks.

(ii) the specific angular momenta of disks are the same as those of their haloes (i.e., $J_{\rm d}/M_{\rm d} = J/M$). While this commonly used assumption is not strictly supported by numerical simulations, it is apparently required to produce acceptably large disks that match observations.

(iii) the effects of the formation time of the disks are ignored. It is now believed that the thin component of disks is assembled at $z \sim 1$ (Brook et al. 2006), and its evolution dominates

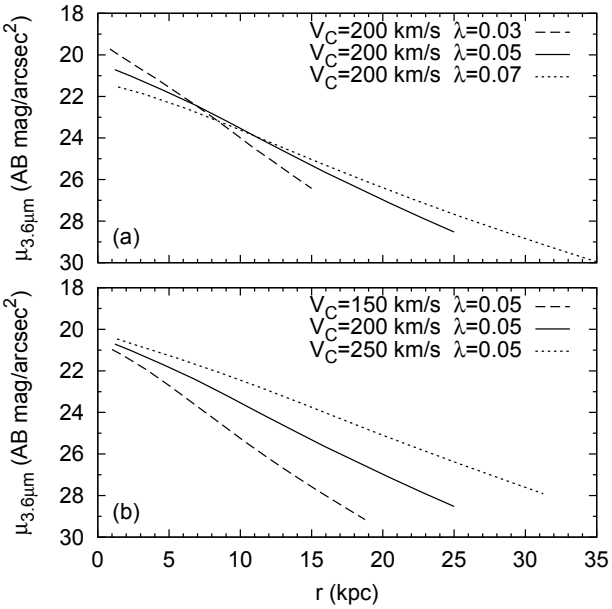

Figure 5.1: Sample surface brightness profiles generated by the model at 3.6 μm, showing the effect of varying the spin parameter (a) and the circular velocity (b).

the inside-out growth of spirals until $z = 0$ (Chiappini, Matteucci & Gratton 1997). However, disks might contain stellar populations formed much earlier. The concept of 'formation time' is thus somehow ill-defined, and the BP00 models simply assume that all disks started forming stars at the same time, having today a fixed age of 13.5 Gyr.

Under these assumptions, BP00 showed that the scale-length $R_{\rm d}$ and central mass density Σ_0 of a given disk can be derived from those of the Milky Way by means of their relative spins and circular velocities:

$$\frac{R_{\rm d}}{R_{\rm dG}} = \frac{\lambda}{\lambda_{\rm G}} \frac{V_{\rm C}}{V_{\rm CG}} \tag{5.6}$$

$$\frac{\Sigma_0}{\Sigma_{0\rm G}} = \left(\frac{\lambda}{\lambda_{\rm G}}\right)^{-2} \frac{V_{\rm C}}{V_{\rm CG}} \tag{5.7}$$

For the case of the Milky Way, the BP00 models assume that $V_{\rm CG} = 220\,{\rm km\,s^{-1}}$ and $\lambda_{\rm G} = 0.03$. Although both $V_{\rm C}$ and λ affect the final scale-length of a disk, they do it in different ways, as can be seen in Fig. 5.1. Larger values of $V_{\rm C}$ yield more extended and massive disks, while modifying λ alters the scale-length alone.

The scaling laws described above affect the way in which the SFR and the gas infall time-scale depend on galactocentric distance. The final rotation curve of a given simulated galaxy is computed as the sum of the contributions of the halo and the disk. The resulting function $V(r)$ is then used through Eq. 5.1 to determine the radial variation of the SFR. The time-scale for the gas infall is parameterized as a function of both the local mass surface surface density and the total galaxy's mass, in the sense that a deeper gravitational well leads to a more rapid infall of gas onto the disk (see Fig. 3 in BP00).

5.3 The data

From the original 75 objects of the SINGS sample we first exclude all ellipticals, lenticulars and dwarf irregulars, leaving only those galaxies with morphological types $1 \leq T \leq 9$. From the remaining list of galaxies we also exclude the following objects:

1. NGC 2798, an Sa galaxy with a severely distorted morphology due to its interaction with the neighbor galaxy NGC 2799.
2. NGC 3190 and NGC 4594 (The Sombrero Galaxy). These Sa galaxies are seen almost edge-on, with dense dust lanes heavily obscuring part of their disks. Besides, their prominent bulges modify the ellipticity of the isophotes used to measure their surface brightness profiles, which might not be then representative of their disk components alone.
3. NGC 4631, a completely edge-on Sd galaxy for which our elliptical isophotes probably mix light emitted at very different galactocentric distances.
4. NGC 5474, an Scd galaxy with a disturbed morphology, probably due to a tidal interaction with M 101. In the optical and near-IR, its main disk is significantly shifted southwards with respect to the bulge.

After applying these criteria we are left with 42 disk-like galaxies, whose main properties are summarized in Table 5.1.

5.4 Internal extinction correction

Prior to fitting the multi-wavelength profiles, we must first correct them for the radial variation of internal attenuation. In chapter 4 we computed internal attenuation profiles in the FUV and NUV bands independently from the TIR/FUV and TIR/NUV ratios, respectively. After $A_{\rm FUV}$ and $A_{\rm NUV}$ have been obtained, the attenuation at other wavelengths can be derived after assuming a given extinction law and a geometry for the distribution of stars and dust. Here we follow the prescriptions of Boselli et al. (2003) and adopt a sandwich model, where a thin layer of dust is embedded in a thicker layer of stars:

$$A_i(\lambda) = -2.5 \log \left(\left[\frac{1-\zeta(\lambda)}{2} \right] \left(1 + e^{-\tau(\lambda)\sec(i)} \right) + \left[\frac{\zeta(\lambda)}{\tau(\lambda)\sec(i)} \right] \left(1 - e^{-\tau(\lambda)\sec(i)} \right) \right) \quad (5.8)$$

Here $\tau(\lambda)$ is the face-on optical depth and i is the inclination angle. Note that we need not to care about them separately as $\tau(\lambda)\sec(i)$ is a joint quantity. The variable $\zeta(\lambda)$ denotes the ratio between the thickness of the dust and stars layers. Young stars, which dominate the emission in the UV range, are supposed to be immersed in a thin dust layer. More evolved ones, which emit most of their light predominantly in the optical and near-IR bands, migrate with time out of the galactic plane, and are thus supposed to lie within a thicker layer, partly above and below the thin dust layer. Therefore, Boselli et al. (2003) parameterize the dust-to-star scale-height ratio as a decreasing function of λ:

$$\zeta(\lambda) = 1.0867 - 5.501 \times 10^{-5} \lambda \quad (5.9)$$

Table 5.1: Main properties of the sample. (1): Galaxy name. (2), (3): RA(J2000) and DEC(J2000) of the galaxy center. (4), (5): Apparent major and minor isophotal diameters at μ_B=25 mag arcsec^{-2} from the RC3 catalog. (6): Position angle from RC3. †The PA and axis ratio of NGC 5194 adopted here differ from those in the RC3, which are affected by the presence of NGC 5195. (7): Galactic color excess from Schlegel et al. (1998). (8): Distance to the galaxy, rounded to the nearest Mpc when larger than 10 Mpc, taken from Gil de Paz et al. (2007) and Kennicutt et al. (2003). ‡The distances to NGC 4826 and NGC 7793 have been updated with respect to those used in MM09a and MM09b. (9): Morphological type T as given in the RC3 catalog. (10): Full description of the morphological type from the RC3. (11), (12): Inner and outer limits along the semimajor axis used to restrict the f tting procedure.

Object name	RA_{2000}	DEC_{2000}	$2a$	$2b$	P.A.	E(B−V)	dist	T	Morphological	$r_{\rm in}$	$r_{\rm out}$
	(h:m:s)	(d:m:s)	(arcmin)	(arcmin)	(deg)	(mag)	(Mpc)	type	type	(arcsec)	(arcsec)
(1)	(2)	(3)	(4)	(5)	(6)	(7)	(8)	(9)	(10)	(11)	(12)
NGC 0024	00 09 56.5	−24 57 47.3	5.8	1.3	46	0.020	8.2	5	SA(s)	48	···
NGC 0337	00 59 50.1	−07 34 40.7	2.9	1.8	310	0.112	25	7	SB(s)d	30	···
NGC 0628	01 36 41.8	15 47 00.5	10.5	9.5	25	0.070	11	5	SA(s)c	54	···
NGC 0925	02 27 16.9	33 34 45.0	10.5	5.9	282	0.076	9.3	7	SAB(s)d	66	···
NGC 1097	02 46 19.1	−30 16 29.7	9.3	6.3	310	0.027	15	3	SB(s)b	54	···
NGC 1512	04 03 54.3	−43 20 55.9	8.9	5.6	90	0.011	10	1	SB(r)a	48	300
NGC 1566	04 20 00.4	−54 56 16.1	8.3	6.6	60	0.009	17	4	SAB(s)bc	30	···
NGC 2403	07 36 51.4	65 36 09.2	21.9	12.3	307	0.040	3.2	6	SAB(s)cd	24	···
NGC 2841	09 22 02.6	50 58 35.5	8.1	3.5	327	0.016	14	3	SA(r)b	90	···
NGC 2976	09 47 15.5	67 54 59.0	5.9	2.7	323	0.069	3.6	5	SAc pec	···	···
NGC 3049	09 54 49.7	09 16 17.9	2.2	1.4	25	0.038	22	2	SB(rs)ab	18	···
NGC 3031	09 55 33.2	69 03 55.1	26.9	14.1	337	0.080	3.6	2	SA(s)ab	204	900
NGC 3184	10 18 17.0	41 25 28.0	7.4	6.9	135	0.017	8.6	6	SAB(rs)cd	48	···
NGC 3198	10 19 54.9	45 32 59.0	8.5	3.3	35	0.012	17	5	SB(rs)c	48	···
IC 2574	10 28 23.5	68 24 43.7	13.2	5.4	50	0.036	4.0	9	SAB(s)m	···	···
NGC 3351	10 43 57.7	11 42 13.0	7.4	5.0	13	0.028	12	3	SB(r)b	48	···
NGC 3521	11 05 48.6	−00 02 09.1	11.0	5.1	343	0.058	9.0	4	SAB(rs)bc	48	···
NGC 3621	11 18 16.5	−32 48 50.6	12.3	7.1	339	0.080	8.3	7	SA(s)d	48	230
NGC 3627	11 20 15.0	12 59 29.6	9.1	4.2	353	0.032	9.1	3	SAB(s)b	48	···
NGC 3938	11 52 49.4	44 07 14.6	5.4	4.9	15	0.021	12	5	SA(s)c	48	···
NGC 4236	12 16 42.1	69 27 45.3	21.9	7.2	342	0.015	4.5	8	SB(s)dm	···	···
NGC 4254	12 18 49.6	14 24 59.4	5.4	4.7	35	0.039	17	5	SA(s)c	48	···
NGC 4321	12 22 54.9	15 49 20.6	7.4	6.3	30	0.026	18	4	SAB(s)bc	60	···
NGC 4450	12 28 29.6	17 05 05.8	5.2	3.9	355	0.028	17	2	SA(s)ab	48	···
NGC 4536	12 34 27.1	02 11 16.4	7.6	3.2	310	0.018	15	4	SAB(rs)bc	48	···
NGC 4559	12 35 57.7	27 57 35.1	10.7	4.4	330	0.018	17	6	SAB(rs)cd	48	···
NGC 4569	12 36 49.8	13 09 46.3	9.5	4.4	23	0.046	17	2	SAB(rs)ab	48	···
NGC 4579	12 37 43.6	11 49 05.1	5.9	4.7	275	0.041	17	3	SAB(rs)b	48	···
NGC 4625	12 41 52.7	41 16 25.4	2.2	1.9	330	0.018	9.5	9	SAB(rs)m pec	···	50
NGC 4725	12 50 26.6	25 30 02.7	10.7	7.6	35	0.012	17	2	SAB(r)ab pec	96	···
NGC 4736	12 50 53.1	41 07 13.6	11.2	9.1	285	0.018	5.2	2	(R)SA(r)ab	75	230
NGC 4826 ‡	12 56 43.8	21 40 51.9	10.0	5.4	295	0.041	7.5	2	(R)SA(rs)ab	96	···
NGC 5033	13 13 27.5	36 35 38.0	10.7	5.0	170	0.011	13	5	SA(s)c	96	···
NGC 5055	13 15 49.3	42 01 45.4	12.6	7.2	285	0.018	8.2	4	SA(rs)bc	96	···
NGC 5194 †	13 29 52.7	47 11 42.6	11.2	9.0	0	0.035	8.4	4	SA(s)bc pec	48	400
TOL 89	14 01 21.6	−33 03 49.6	2.8	1.7	352	0.066	16	8.1	(R')SB(s)dm pec	···	···
NGC 5713	14 40 11.5	−00 17 21.2	2.8	2.5	10	0.039	27	4	SAB(rs)bc pec	···	···
IC 4710	18 28 38.0	−66 58 56.0	3.6	2.8	5	0.089	8.5	9	SB(s)m	···	···
NGC 6946	20 34 52.3	60 09 14.2	11.5	9.8	75	0.342	5.5	6	SAB(rs)cd	48	400
NGC 7331	22 37 04.1	34 24 56.3	10.5	3.7	351	0.091	15	3	SA(s)b	96	···
NGC 7552	23 16 10.8	−42 35 05.4	3.4	2.7	1	0.014	22	2	(R')SB(s)ab	24	···
NGC 7793 ‡	23 57 49.8	−32 35 27.7	9.3	6.3	278	0.019	3.9	7	SA(s)d	48	···

where λ is measured in Å. In the UV ($\lambda \simeq 2000$Å), this ratio is $\zeta = 1$, so Eq. 5.8 reduces to a slab model and can be numerically inverted:

$$\begin{aligned} \tau(UV)\sec(i) &= 0.0259 + 1.2002 \times A_i(UV) + 1.5543 \times A_i(UV)^2 \\ &\quad - 0.7409 \times A_i(UV)^3 + 0.2246 \times A_i(UV)^4 \end{aligned} \tag{5.10}$$

Once the optical depth in the UV is known, the corresponding value at any other wavelength is given by a particular extinction law $k(\lambda)$:

$$\tau(\lambda) = \tau(UV) \times k(\lambda)/k(UV) \tag{5.11}$$

which plugged into Eq. 5.8 gives us the attenuation at the desired band.

The conversion between the TIR/FUV and TIR/NUV ratios into $A_{\rm FUV}$ and $A_{\rm NUV}$, respectively, is rather insensitive to the adopted extinction law (Cortese et al. 2008). Nevertheless, to compute the extinction at other wavelengths we must not only choose a particular extinction law, but also decide whether to determine $A(\lambda)$ by extrapolating from $A_{\rm FUV}$ or $A_{\rm NUV}$ in the equations above. Here we use the MW extinction law of Li & Draine (2001), assuming $R_V = 3.1$. Other extinction curves are possible, but most of them agree pretty well from the near-IR to the NUV bands (Gordon et al. 2003). It is beyond the 2175 Å bump that large differences arise. Therefore, in order to minimize the impact of our particular choice of extinction law, we use the NUV band rather than the FUV one in Eqs. 5.10 and 5.11.

5.5 Fitting procedure

In order to find the model that best fits the observed multiwavelength profiles for each galaxy, a χ^2 minimization procedure was followed. We started with an initial coarse grid of 40 models with $0.02 \leq \lambda \leq 0.09$, in steps of 0.01, and $V_{\rm C} = 80, 150, 220, 290$ and $360\,{\rm km\,s^{-1}}$. After applying an initial fit to our multi-wavelength profiles, we identified the region of the $(\lambda, V_{\rm C})$ parameter space most populated by the galaxies in the sample. We generated a second set of models with additional values of the circular velocity between 130 and 250 $\rm km\,s^{-1}$, in steps of 10 $\rm km\,s^{-1}$, plus an extra velocity of 40 $\rm km\,s^{-1}$ to better cover the low-mass end of our sample. The 'resolution' in λ was kept the same, since the χ^2 variations along λ were found to be milder than along $V_{\rm C}$. Nevertheless, in order to properly fit some high-spin galaxies found in the sample, additional values of $\lambda = 0.10, 0.15$ and 0.20 were also considered.

Taking this new set of 176 pre-computed models as our starting point, we used a 2D interpolation algorithm to generate a finer grid of models with steps of 0.001 in λ and 1 $\rm km\,s^{-1}$ in $V_{\rm C}$. We verified that any given property of a model galaxy at a certain radius varies smoothly enough with λ and $V_{\rm C}$, so that the corresponding value for a model with an intermediate spin and velocity can be indeed approximated by means of a 2D interpolation.

The total χ^2 of each model was computed by summing over data-points at all bands and galactocentric distances. By visually inspecting the multi-wavelength profiles, we excluded from the fit those radial ranges in which the overall emission is dominated by the bulge. In those galaxies with sharp outer truncations or anti-truncations −which the BP00 models cannot reproduce by construction− the outermost regions were excluded as well. The radial range used for the fit is quoted in table 5.1.

The resulting distribution of χ^2 values are shown in appendix C. If they are to be used to derive confidence intervals for the fitted parameters, rather than just to find the best-fitting values, then a proper determination of the uncertainties of each data-point and of the models is mandatory. In principle, the χ^2 method assumes that any deviation of the observed values with respect to the model predictions is entirely due to measurement errors. If these errors are properly accounted for when computing χ^2, then the confidence intervals for the fitted parameters are defined by all models with $\chi^2 < \chi^2_{\rm min} + \Delta\chi^2$, where $\Delta\chi^2$ depends on the confidence level and the number of parameters that are being estimated simultaneously (see e.g. Avni 1976; Press et al. 1992).

However, we cannot strictly follow this approach in our case, since the models do not reproduce the small-scale structures of real disks. In an attempt to overcome this problem, we first run our fitting code assuming that the total uncertainty for each data-point is the quadratic sum of the photometric and zero-point errors, plus an extra uncertainty of 10%. This additional term serves as an initial guess for the intrinsic error of the model, and also avoids giving excessive weight to any particular band and/or data-point. The typical reduced χ^2 at this stage is of the order of ~ 5. We then compute the relative rms of the best-fitting model with respect to the galaxy's profiles, both as a function of radius and wavelength. In this way we can estimate how well we can expect the model to fit that particular galaxy at each band. These 'error profiles' are then fed to the code in a second run, in place of the initial uncertainties. The new reduced χ^2 values are now close to 1, as expected. However, the purpose of this two-stage fitting process is not to just artificially bring the reduced χ^2 closer to unity, but to properly take into account deviations due to features that the models, by construction, are not able to reproduce.

Even after following this process, we found that the technique of adding a constant $\Delta\chi^2$ offset to the total (i.e. not reduced) χ^2 still yielded unrealistically small confidence intervals for $V_{\rm C}$ and λ. A visual inspection confirmed that indeed many models outside these confidence regions were still in very good agreement with the observed profiles. Thus, we finally opted for defining the boundaries of the confidence intervals with those models whose total χ^2 is twice the minimum one. Therefore, although the resulting errors in λ and $V_{\rm C}$ cover the range of models that visually agree with the galaxy's profiles, they should not be understood in a strict statistical way (see also Boselli et al. 2006 in this regard).

As an example, in Fig. 5.2 we show the resulting fit for the Sc spiral NGC 3198 using the K01 IMF (see appendix A for similar plots for the remaining galaxies). The gray data-points show the observed profiles, corrected only for MW extinction, while the black ones are also corrected for internal extinction. Both profiles have been deprojected to their face-on values by means of the galaxy's morphological axis ratio[1]. The fit is applied to the profiles corrected for internal extinction, and only to those points beyond the red dashed line, which separates the bulge- and disk-dominated regions of the profiles. In the few cases where we had to exclude the outer regions (due to strong up-bendings, for instance), the outer limit is marked with a blue dashed line. The best-fitting model is shown with a red line, and the band with a lighter shade of red contains all models with $\chi^2 \leq 2\chi^2_{\rm min}$.

However, the fit is not always equally good at all wavelengths. In Fig. 5.3 we show the best fitting model for the Sb galaxy NGC 2841. Even though the quality of the fit is excellent all the

[1]Note that, strictly speaking, this deprojection is only valid for the profiles corrected for internal extinction. In the observed ones, the difference between the inclined and face-on values would not just owe to a simple geometrical projection effect, since the interaction between starlight and dust along a different line of sight would also play a role.

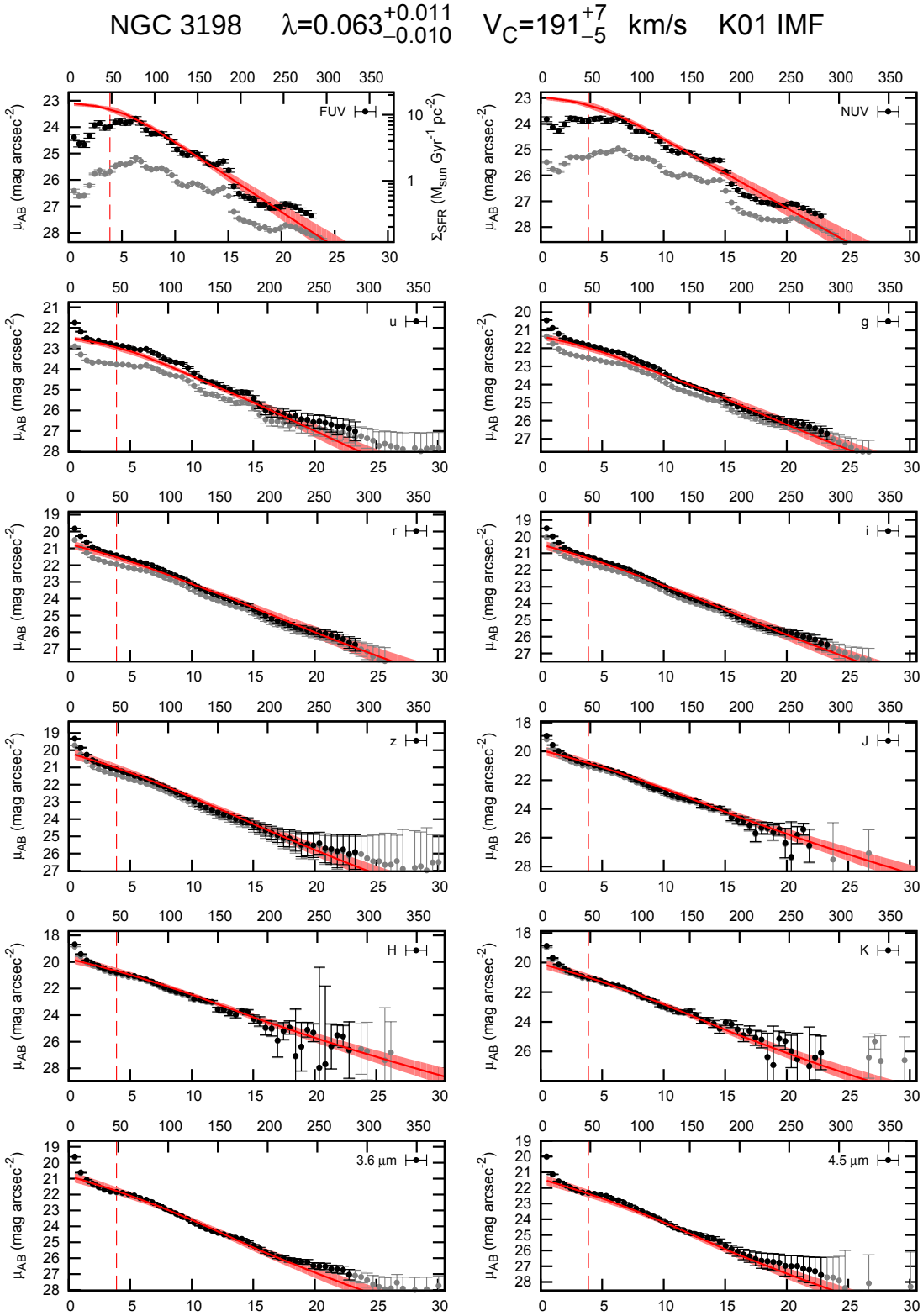

Figure 5.2: Best-f tting model for the Sc galaxy NGC 3198, using the K01 IMF. The gray points show the observed prof les, corrected only for Milky way extinction, while the black ones also include a correction for the radial variation of internal extinction. Both prof les have been deprojected to their face-on values using the galaxy's morphological axis ratio. In each panel, the radius along the semimajor axis is expressed both in arcseconds (top x axis) and in kpc (bottom x axis). The f t is applied to those points in the extinction-corrected prof les beyond the dashed red line, in order to exclude the bulge. The red curve corresponds to the best-f tting model, and the background band contains all models with $\chi^2 \leq 2\chi^2_{\rm min}$.

way from 4.5 μm to the u band, the model overpredicts the luminosity of the galaxy in the GALEX bands. This tends to happen mostly in early-type spirals, as will be discussed in section 5.6.2.

5.6 Results

5.6.1 Global properties

The results of the fitting procedure are quoted in Table 5.2. Prior to analyzing the temporal evolution of our galaxies, we will briefly describe the statistical distribution of the model parameters λ and $V_{\rm C}$. As mentioned before, for each galaxy we have run our fitting code using both the K93 and K01 IMFs. Given their different content in high-mass stars at a fixed total mass, the resulting profiles differ in the UV bands, but agree in the optical and near-IR ones. The effects of choosing one IMF or another will be discussed in detail in section 5.6.2, but for now it will suffice to say that neither λ nor $V_{\rm C}$ are significantly affected by our particular choice of IMF. Therefore, in the remaining of this work we shall use the K93 IMF as our default choice, otherwise mentioned.

5.6.1.1 Statistical distribution of the model parameters

In Fig. 5.4 we show the resulting histograms of both fitting parameters. It can be seen that most galaxies exhibit values of λ and $V_{\rm C}$ similar to those of the Milky Way. In particular, the distribution of rotational velocities peaks at 200-220 km s^{-1}. It should be noted, however, that neither the SINGS sample nor the smaller subsample of disks considered here are complete. The well-known Schechter (1976) function can be used to fit not only the mass and luminosity functions of nearby galaxies (Bell et al. 2003), but also their circular velocity distribution (González et al. 2000). In this sense, low-mass slow-rotating disks are known to outnumber more massive and faster-rotating ones. Therefore, the velocity distribution shown in Fig. 5.4 obviously underestimates the number of low-velocity galaxies that would be found in a volume-limited sample.

Regarding the spin parameter, most disks in our sample have $\lambda \sim 0.03$. This is in agreement with a key prediction of ΛCDM simulations of galaxy formation: the fact that most haloes exhibit the same angular momentum per unit of mass at any epoch, regardless of their total mass and their particular history of mass assembly. In this sense, the following analytic expression is known to fit the distribution of λ obtained in computer simulations (see e.g. Barnes & Efstathiou 1987; Warren et al. 1992; Gardner 2001; Bullock et al. 2001; Vitvitska et al. 2002):

$$p(\lambda)d\lambda = \frac{1}{\sqrt{2\pi}\sigma_\lambda} \exp\left[-\frac{\ln^2(\lambda/\overline{\lambda})}{2\sigma_\lambda^2}\right] \frac{d\lambda}{\lambda} \tag{5.12}$$

In particular, MMW98 adopt $\overline{\lambda} = 0.05$ and $\sigma_\lambda = 0.5$. Since it is a log-normal function, these values should not be understood as the mean and width of the distribution. In fact, this function peaks around $\lambda \sim 0.04$, and has a width of ~ 0.05. Interestingly, the distribution of spin values of our galaxies agrees well with Eq. 5.12. This implies that even though our sample is not representative of a complete one, to some extent it behaves as if it was with regard to λ and, by extension, to any other quantity that depends primarily on λ rather than on $V_{\rm C}$.

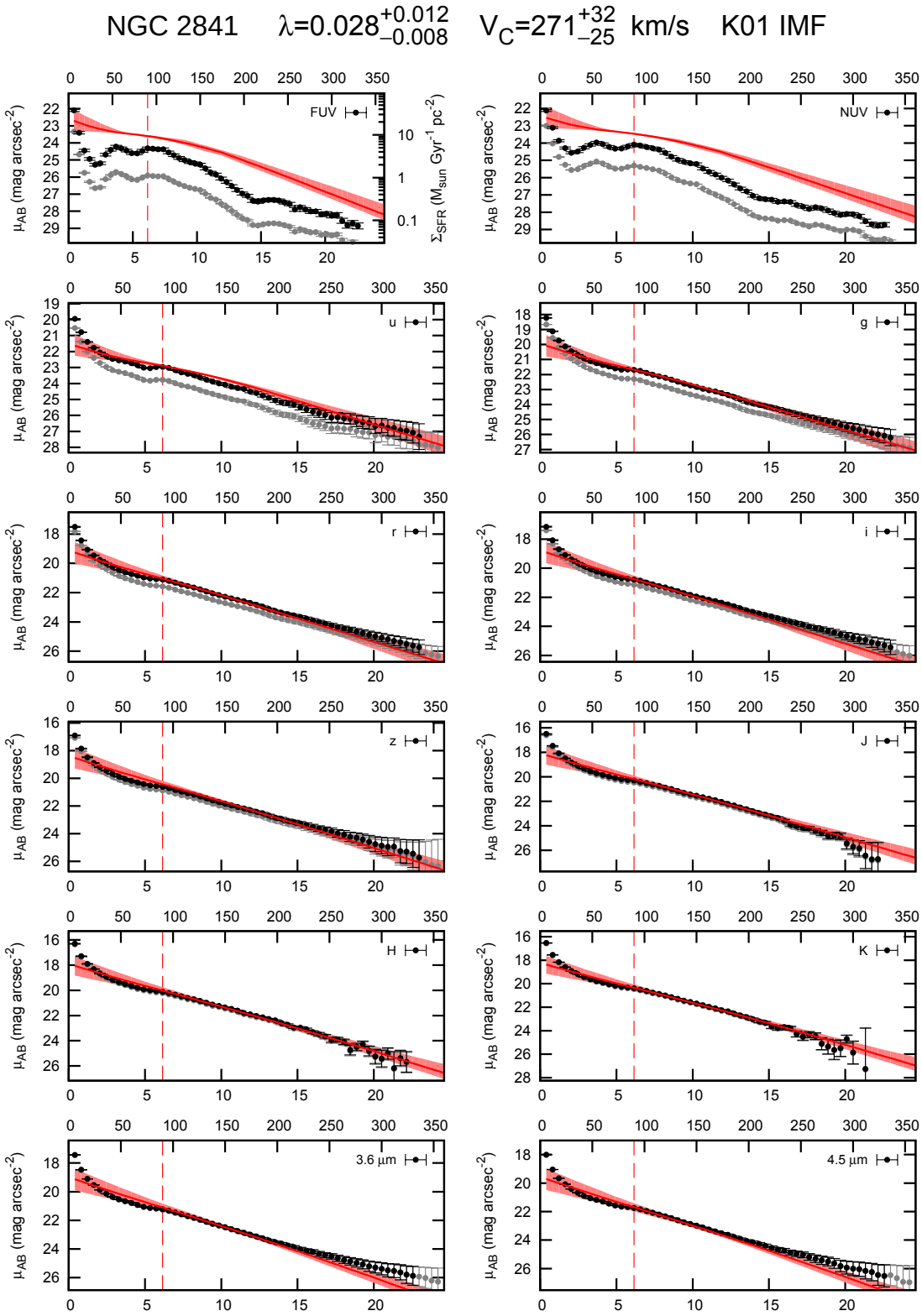

Figure 5.3: Same as Fig. 5.2, but for the Sb spiral NGC 2841. The f t is excellent at all wavelengths except in the FUV and NUV bands.

Table 5.2: Results from the model fitting. (1): Galaxy name. (2), (6): Dimensionless spin parameter. (3), (7): Maximum circular velocity. (4), (8): Central value of $12 + \log(O/H)$. (5), (9): Radial metallicity gradient. (10): Temporal growth rate of the stellar disk scale-length, obtained by fitting $R_{\rm d}(t)$ between $z = 1$ and $z = 0$. (11): Ratio of the stellar disk scale-lengths at $z = 0$ and $z = 1$. Neither (10) nor (11) vary noticeably with the IMF.

	Kroupa et al. (1993) IMF				Kroupa (2001) IMF					
Object name	λ	$V_{\rm C}$ (km s^{-1})	Metallicity at $r = 0$	Gradient (dex kpc^{-1})	λ	$V_{\rm C}$ (km s^{-1})	Metallicity at $r = 0$	Gradient (dex kpc^{-1})	$dR_{\rm d}/dt$ (kpc Gyr^{-1})	$\frac{R_{\rm d}(z=0)}{R_{\rm d}(z=1)}$
(1)	(2)	(3)	(4)	(5)	(6)	(7)	(8)	(9)	(10)	(11)
NGC 0024	$0.066^{+0.015}_{-0.014}$	100^{+5}_{-5}	$8.92^{+0.08}_{-0.07}$	$-0.118^{+0.014}_{-0.015}$	$0.067^{+0.015}_{-0.014}$	98^{+5}_{-5}	$9.49^{+0.09}_{-0.08}$	$-0.128^{+0.016}_{-0.017}$	0.029	1.14
NGC 0337	$0.037^{+0.011}_{-0.010}$	169^{+9}_{-6}	$9.26^{+0.09}_{-0.12}$	$-0.085^{+0.014}_{-0.009}$	$0.036^{+0.013}_{-0.010}$	165^{+14}_{-9}	$9.87^{+0.10}_{-0.10}$	$-0.086^{+0.011}_{-0.009}$	0.052	1.26
NGC 0628	$0.057^{+0.014}_{-0.012}$	208^{+12}_{-11}	$9.17^{+0.11}_{-0.11}$	$-0.046^{+0.009}_{-0.012}$	$0.055^{+0.012}_{-0.011}$	199^{+12}_{-10}	$9.84^{+0.07}_{-0.06}$	$-0.057^{+0.008}_{-0.008}$	0.069	1.19
NGC 0925	$0.081^{+0.027}_{-0.011}$	163^{+11}_{-17}	$8.72^{+0.29}_{-0.11}$	$-0.042^{+0.013}_{-0.023}$	$0.095^{+0.020}_{-0.016}$	152^{+16}_{-10}	$9.50^{+0.07}_{-0.07}$	$-0.060^{+0.011}_{-0.010}$	0.050	1.11
NGC 1097	$0.057^{+0.021}_{-0.017}$	257^{+20}_{-15}	$9.32^{+0.07}_{-0.09}$	$-0.036^{+0.005}_{-0.004}$	$0.056^{+0.021}_{-0.017}$	256^{+22}_{-17}	$9.94^{+0.09}_{-0.11}$	$-0.041^{+0.006}_{-0.005}$	0.086	1.18
NGC 1512	$0.056^{+0.013}_{-0.012}$	144^{+9}_{-6}	$9.10^{+0.07}_{-0.07}$	$-0.078^{+0.009}_{-0.008}$	$0.058^{+0.017}_{-0.014}$	141^{+8}_{-7}	$9.68^{+0.10}_{-0.10}$	$-0.085^{+0.012}_{-0.010}$	0.047	1.18
NGC 1566	$0.052^{+0.022}_{-0.017}$	247^{+23}_{-18}	$9.33^{+0.07}_{-0.09}$	$-0.040^{+0.008}_{-0.007}$	$0.049^{+0.018}_{-0.014}$	242^{+23}_{-16}	$9.96^{+0.08}_{-0.10}$	$-0.048^{+0.007}_{-0.006}$	0.080	1.20
NGC 2403	$0.052^{+0.009}_{-0.008}$	121^{+4}_{-4}	$9.05^{+0.05}_{-0.05}$	$-0.102^{+0.010}_{-0.010}$	$0.051^{+0.009}_{-0.008}$	116^{+4}_{-5}	$9.64^{+0.06}_{-0.06}$	$-0.117^{+0.010}_{-0.010}$	0.037	1.19
NGC 2841	$0.027^{+0.011}_{-0.007}$	276^{+31}_{-27}	$9.41^{+0.02}_{-0.04}$	$-0.039^{+0.005}_{-0.004}$	$0.028^{+0.012}_{-0.008}$	271^{+32}_{-25}	$10.04^{+0.03}_{-0.05}$	$-0.046^{+0.005}_{-0.004}$	0.063	1.22
NGC 2976	$0.030^{+0.007}_{-0.005}$	76^{+2}_{-2}	$9.04^{+0.06}_{-0.05}$	$-0.202^{+0.024}_{-0.020}$	$0.033^{+0.007}_{-0.006}$	75^{+2}_{-2}	$9.62^{+0.05}_{-0.04}$	$-0.219^{+0.025}_{-0.017}$	0.021	1.26
NGC 3049	$0.082^{+0.028}_{-0.026}$	144^{+34}_{-17}	$8.95^{+0.08}_{-0.39}$	$-0.059^{+0.058}_{-0.025}$	$0.091^{+0.037}_{-0.031}$	150^{+56}_{-24}	$9.50^{+0.10}_{-0.04}$	$-0.058^{+0.025}_{-0.032}$	0.049	1.11
NGC 3031	$0.033^{+0.009}_{-0.009}$	199^{+17}_{-9}	$9.35^{+0.05}_{-0.08}$	$-0.068^{+0.007}_{-0.005}$	$0.028^{+0.014}_{-0.008}$	203^{+24}_{-18}	$10.00^{+0.06}_{-0.11}$	$-0.076^{+0.008}_{-0.005}$	0.055	1.27
NGC 3184	$0.041^{+0.014}_{-0.010}$	148^{+12}_{-6}	$9.17^{+0.11}_{-0.10}$	$-0.081^{+0.013}_{-0.018}$	$0.045^{+0.014}_{-0.013}$	145^{+8}_{-7}	$9.75^{+0.11}_{-0.08}$	$-0.088^{+0.013}_{-0.015}$	0.048	1.22
NGC 3198	$0.061^{+0.009}_{-0.010}$	198^{+6}_{-6}	$9.12^{+0.10}_{-0.10}$	$-0.049^{+0.007}_{-0.007}$	$0.063^{+0.011}_{-0.010}$	191^{+7}_{-5}	$9.78^{+0.06}_{-0.06}$	$-0.057^{+0.005}_{-0.004}$	0.066	1.17
IC 2574	$0.141^{+0.030}_{-0.021}$	103^{+21}_{-16}	$8.52^{+0.08}_{-0.08}$	$-0.075^{+0.023}_{-0.022}$	$0.144^{+0.037}_{-0.026}$	98^{+26}_{-18}	$9.03^{+0.10}_{-0.10}$	$-0.081^{+0.029}_{-0.029}$	0.027	1.06
NGC 3351	$0.037^{+0.011}_{-0.009}$	197^{+10}_{-9}	$9.32^{+0.06}_{-0.09}$	$-0.065^{+0.010}_{-0.007}$	$0.038^{+0.012}_{-0.011}$	193^{+14}_{-10}	$9.92^{+0.09}_{-0.08}$	$-0.069^{+0.009}_{-0.009}$	0.061	1.24
NGC 3521	$0.031^{+0.012}_{-0.009}$	226^{+26}_{-17}	$9.37^{+0.04}_{-0.06}$	$-0.053^{+0.006}_{-0.006}$	$0.031^{+0.015}_{-0.011}$	224^{+32}_{-20}	$10.00^{+0.06}_{-0.10}$	$-0.061^{+0.006}_{-0.006}$	0.062	1.25
NGC 3621	$0.032^{+0.008}_{-0.007}$	161^{+8}_{-9}	$9.30^{+0.07}_{-0.09}$	$-0.102^{+0.012}_{-0.009}$	$0.031^{+0.008}_{-0.007}$	156^{+12}_{-7}	$9.91^{+0.09}_{-0.08}$	$-0.105^{+0.011}_{-0.011}$	0.048	1.29
NGC 3627	$0.030^{+0.010}_{-0.007}$	219^{+21}_{-12}	$9.35^{+0.03}_{-0.04}$	$-0.053^{+0.006}_{-0.007}$	$0.032^{+0.009}_{-0.008}$	215^{+20}_{-13}	$9.98^{+0.04}_{-0.06}$	$-0.061^{+0.005}_{-0.004}$	0.061	1.25
NGC 3938	$0.045^{+0.013}_{-0.012}$	157^{+10}_{-10}	$9.15^{+0.13}_{-0.16}$	$-0.079^{+0.021}_{-0.020}$	$0.046^{+0.014}_{-0.013}$	149^{+8}_{-5}	$9.75^{+0.10}_{-0.08}$	$-0.084^{+0.014}_{-0.014}$	0.049	1.22
NGC 4236	$0.127^{+0.017}_{-0.018}$	118^{+8}_{-8}	$8.65^{+0.07}_{-0.06}$	$-0.067^{+0.010}_{-0.011}$	$0.125^{+0.020}_{-0.019}$	113^{+11}_{-9}	$9.19^{+0.08}_{-0.07}$	$-0.074^{+0.013}_{-0.013}$	0.033	1.07
NGC 4254	$0.029^{+0.014}_{-0.009}$	239^{+30}_{-21}	$9.38^{+0.03}_{-0.06}$	$-0.047^{+0.006}_{-0.005}$	$0.028^{+0.014}_{-0.008}$	240^{+31}_{-24}	$10.02^{+0.03}_{-0.08}$	$-0.055^{+0.007}_{-0.006}$	0.060	1.24
NGC 4321	$0.041^{+0.017}_{-0.013}$	295^{+22}_{-14}	$9.38^{+0.03}_{-0.04}$	$-0.030^{+0.005}_{-0.004}$	$0.040^{+0.017}_{-0.013}$	293^{+27}_{-13}	$10.03^{+0.02}_{-0.05}$	$-0.036^{+0.005}_{-0.004}$	0.084	1.20
NGC 4450	$0.041^{+0.011}_{-0.010}$	212^{+8}_{-6}	$9.31^{+0.05}_{-0.08}$	$-0.052^{+0.008}_{-0.005}$	$0.042^{+0.013}_{-0.011}$	209^{+10}_{-7}	$9.92^{+0.07}_{-0.07}$	$-0.058^{+0.008}_{-0.007}$	0.068	1.23
NGC 4536	$0.060^{+0.014}_{-0.014}$	200^{+9}_{-7}	$9.12^{+0.14}_{-0.15}$	$-0.047^{+0.011}_{-0.009}$	$0.059^{+0.017}_{-0.014}$	196^{+10}_{-9}	$9.81^{+0.10}_{-0.10}$	$-0.056^{+0.007}_{-0.006}$	0.067	1.18
NGC 4559	$0.080^{+0.010}_{-0.014}$	223^{+10}_{-7}	$9.18^{+0.07}_{-0.12}$	$-0.039^{+0.004}_{-0.004}$	$0.080^{+0.010}_{-0.013}$	220^{+9}_{-8}	$9.76^{+0.08}_{-0.06}$	$-0.043^{+0.004}_{-0.004}$	0.076	1.13
NGC 4569	$0.046^{+0.011}_{-0.009}$	256^{+14}_{-12}	$9.38^{+0.04}_{-0.05}$	$-0.042^{+0.003}_{-0.003}$	$0.048^{+0.011}_{-0.010}$	253^{+15}_{-11}	$9.99^{+0.06}_{-0.07}$	$-0.046^{+0.004}_{-0.003}$	0.082	1.20
NGC 4579	$0.029^{+0.010}_{-0.008}$	264^{+23}_{-18}	$9.38^{+0.02}_{-0.03}$	$-0.038^{+0.004}_{-0.004}$	$0.028^{+0.010}_{-0.008}$	267^{+24}_{-21}	$10.03^{+0.02}_{-0.03}$	$-0.045^{+0.005}_{-0.004}$	0.063	1.22
NGC 4625	$0.026^{+0.011}_{-0.006}$	72^{+4}_{-4}	$9.08^{+0.07}_{-0.09}$	$-0.265^{+0.070}_{-0.063}$	$0.027^{+0.014}_{-0.007}$	71^{+4}_{-5}	$9.67^{+0.09}_{-0.11}$	$-0.287^{+0.082}_{-0.073}$	0.019	1.30
NGC 4725	$0.044^{+0.016}_{-0.013}$	290^{+27}_{-15}	$9.42^{+0.04}_{-0.06}$	$-0.035^{+0.003}_{-0.003}$	$0.043^{+0.018}_{-0.015}$	288^{+36}_{-15}	$10.05^{+0.05}_{-0.09}$	$-0.041^{+0.005}_{-0.003}$	0.086	1.20
NGC 4736	$0.020^{+0.008}_{-0.001}$	146^{+8}_{-7}	$9.34^{+0.02}_{-0.07}$	$-0.125^{+0.017}_{-0.006}$	$0.020^{+0.009}_{-0.001}$	143^{+8}_{-10}	$9.96^{+0.01}_{-0.10}$	$-0.140^{+0.020}_{-0.010}$	0.036	1.35
NGC 4826	$0.020^{+0.006}_{-0.001}$	209^{+6}_{-11}	$9.39^{+0.00}_{-0.01}$	$-0.069^{+0.004}_{-0.005}$	$0.020^{+0.005}_{-0.001}$	208^{+5}_{-12}	$10.03^{+0.00}_{-0.03}$	$-0.079^{+0.004}_{-0.004}$	0.043	1.27
NGC 5033	$0.081^{+0.030}_{-0.016}$	196^{+10}_{-10}	$8.89^{+0.18}_{-0.12}$	$-0.036^{+0.009}_{-0.011}$	$0.087^{+0.024}_{-0.020}$	188^{+11}_{-8}	$9.64^{+0.11}_{-0.10}$	$-0.049^{+0.008}_{-0.007}$	0.063	1.12
NGC 5055	$0.050^{+0.016}_{-0.013}$	215^{+13}_{-9}	$9.26^{+0.08}_{-0.15}$	$-0.047^{+0.009}_{-0.006}$	$0.049^{+0.017}_{-0.013}$	212^{+15}_{-10}	$9.89^{+0.09}_{-0.09}$	$-0.054^{+0.008}_{-0.006}$	0.072	1.21
NGC 5194	$0.026^{+0.009}_{-0.006}$	239^{+21}_{-18}	$9.39^{+0.02}_{-0.04}$	$-0.051^{+0.006}_{-0.004}$	$0.025^{+0.008}_{-0.005}$	240^{+20}_{-20}	$10.03^{+0.02}_{-0.04}$	$-0.058^{+0.005}_{-0.005}$	0.054	1.24
TOL 89	$0.066^{+0.012}_{-0.011}$	117^{+8}_{-6}	$8.96^{+0.05}_{-0.05}$	$-0.092^{+0.015}_{-0.014}$	$0.070^{+0.018}_{-0.014}$	114^{+14}_{-10}	$9.51^{+0.07}_{-0.07}$	$-0.101^{+0.025}_{-0.025}$	0.035	1.14
NGC 5713	$0.020^{+0.007}_{-0.001}$	226^{+17}_{-19}	$9.40^{+0.00}_{-0.03}$	$-0.060^{+0.010}_{-0.010}$	$0.020^{+0.010}_{-0.001}$	224^{+18}_{-25}	$10.04^{+0.00}_{-0.06}$	$-0.070^{+0.012}_{-0.012}$	0.044	1.25
IC 4710	$0.078^{+0.022}_{-0.014}$	99^{+23}_{-17}	$8.84^{+0.05}_{-0.06}$	$-0.107^{+0.033}_{-0.033}$	$0.087^{+0.028}_{-0.018}$	99^{+28}_{-20}	$9.37^{+0.07}_{-0.08}$	$-0.110^{+0.042}_{-0.038}$	0.029	1.10
NGC 6946	$0.030^{+0.008}_{-0.006}$	189^{+12}_{-10}	$9.34^{+0.02}_{-0.06}$	$-0.073^{+0.012}_{-0.009}$	$0.029^{+0.008}_{-0.007}$	186^{+13}_{-11}	$9.95^{+0.04}_{-0.06}$	$-0.078^{+0.011}_{-0.008}$	0.053	1.28
NGC 7331	$0.059^{+0.027}_{-0.021}$	265^{+20}_{-16}	$9.33^{+0.09}_{-0.10}$	$-0.035^{+0.006}_{-0.005}$	$0.059^{+0.029}_{-0.023}$	263^{+22}_{-16}	$9.94^{+0.11}_{-0.13}$	$-0.039^{+0.008}_{-0.006}$	0.089	1.17
NGC 7552	$0.034^{+0.019}_{-0.014}$	223^{+35}_{-17}	$9.34^{+0.05}_{-0.13}$	$-0.048^{+0.007}_{-0.008}$	$0.033^{+0.020}_{-0.013}$	222^{+37}_{-19}	$9.98^{+0.05}_{-0.13}$	$-0.057^{+0.009}_{-0.006}$	0.064	1.25
NGC 7793	$0.040^{+0.009}_{-0.008}$	104^{+6}_{-5}	$9.06^{+0.06}_{-0.05}$	$-0.133^{+0.019}_{-0.017}$	$0.039^{+0.010}_{-0.009}$	101^{+5}_{-5}	$9.66^{+0.07}_{-0.07}$	$-0.153^{+0.021}_{-0.021}$	0.031	1.24

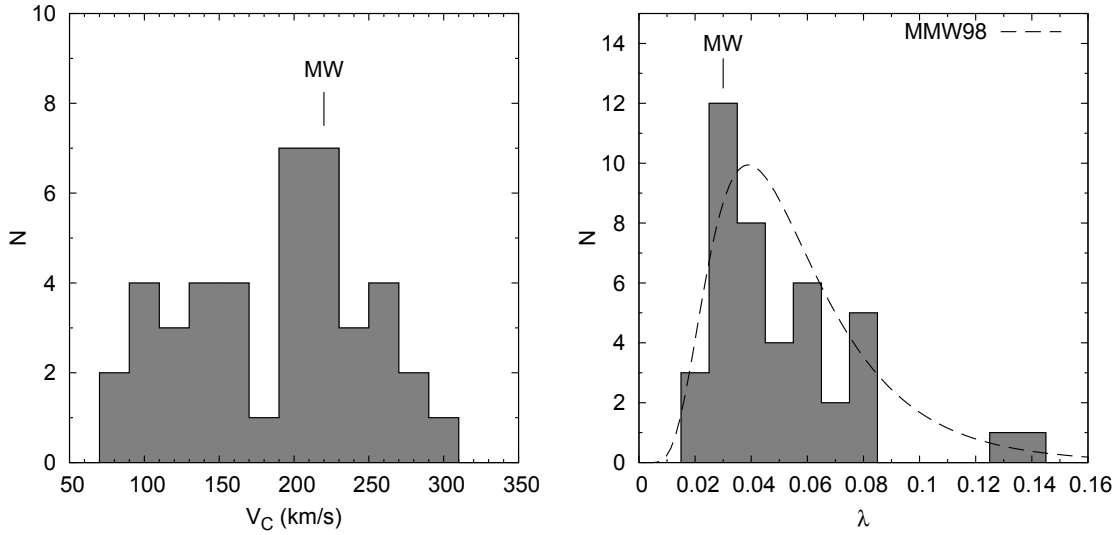

Figure 5.4: Distribution of the circular velocity (left) and spin (right) in our sample. The values adopted for the Milky-Way ($\lambda = 0.03$ and $V_{\rm C} = 220\,{\rm km\,s^{-1}}$) have been marked in both panels. The dashed curve corresponds to the probability distribution of λ proposed by Mo, Mao & White (1998), scaled to match our histogram.

5.6.1.2 Comparison with observed values

Before further proceeding with any detailed analysis, we must first verify that the values of λ and $V_{\rm C}$ that our fitting code yields for each galaxy conform with the observed ones. This is not a straightforward task in the case of the spin parameter, since it is not a directly measurable quantity in real galaxies. Nevertheless, as commented above Fig. 5.4 shows that the distribution of λ in our sample resembles the one usually found in numerical N-body simulations.

In order to check the accuracy of our circular velocities, in Fig. 5.5a we compare the theoretical values given by the model with the observed rotational velocities retrieved from the Lyon-Meudon Extragalactic Database[2] (LEDA; Paturel et al. 2003). The latter are determined from the width of the 21 cm hydrogen line at different levels and/or from rotation curves, usually Hα ones. The final values provided by LEDA are homogenized and corrected for inclination. In general, our theoretical values for the circular velocity are in agreement with the observed ones, although ours tend to be about 25% larger in many cases.

The most discrepant outlier in this plot is the Sc spiral NGC 0628, for which our fitting code yields $V_{\rm C} = 208\,{\rm km\,s^{-1}}$, while in LEDA we find a much lower value of $38\,{\rm km\,s^{-1}}$. This latter velocity is surprisingly small given that NGC 0628 has an absolute K_S-band magnitude of -21.64 mags, for which one should expect a rotational velocity of $\sim 175\,{\rm km\,s^{-1}}$ according to the Tully-Fisher relation (see below). The fact that this galaxy is almost face-on might introduce large uncertainties in the inclination correction, thus possibly making the LEDA velocity very uncertain for this galaxy. We note, however, that the LEDA values for many other face-on galaxies in the sample agree well with the ones obtained from the model.

Another way to check the validity of our model rotational velocities consists on trying to

[2] `http://leda.univ-lyon1.fr`

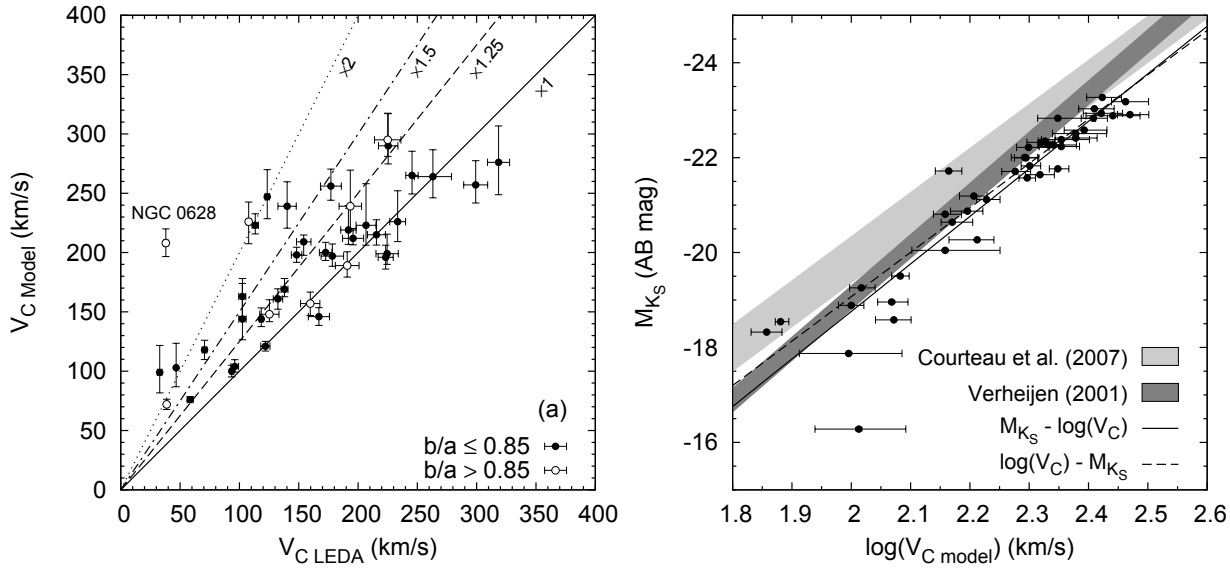

Figure 5.5: (a): Comparison between the circular velocities derived from the model fitting and the observed ones compiled in the LEDA database. Filled symbols correspond to galaxies with a minor to major axis ratio $b/a \leq 0.85$, while open ones show show almost face-on galaxies with $b/a > 0.85$. (b): Absolute K_S-band magnitude of our galaxies as a function of the circular velocity of the corresponding best-fitting model. The absolute magnitudes have been derived from the asymptotic values, and are corrected for internal extinction. The shaded band corresponds to the empirical TF relation of Verheijen (2001). The width of the band shows the 1σ scatter of their fit. The solid and dashed lines show direct and reverse linear fits to our data, respectively.

reproduce the Tully-Fisher (TF) relation (Tully & Fisher 1977). This tight empirical relation links the intrinsic luminosity of a galaxy with the amplitude of its rotation curve. The former quantity traces the stellar mass, while the latter probes the total gravitational mass. Therefore, any successful model of disk evolution must be able to reproduce this observed correlation.

The scaling laws adopted by BP00 imprint a built-in TF relation in the models through Eq. 5.4. However, once star formation is implemented in a self-consistent way, the resulting slope and zero-point of the TF relation might vary. When comparing the TF relation resulting from the models with several empirical ones in the I band from different authors, BP00 found a good agreement, although their theoretical TF relation yielded somewhat larger velocities for a given absolute I-band magnitude.

In Fig. 5.5b we plot the K_S-band absolute magnitude of our galaxies as a function of the circular velocity resulting from the model fitting. The absolute magnitudes were computed from the asymptotic values presented in chapter 3. Here we rely on the K_S band rather than on optical ones in order to minimize the effects of internal extinction. Nevertheless, we used the integrated TIR-to-UV ratio to derive the global internal extinction for each object, using a MW extinction curve combined with a sandwich model, in a similar way as we did for the radial profiles (section 5.4). The resulting median extinction in the K_S band is just ~ 0.03 mag. We compare our results with the empirical K_S-band TF of Verheijen (2001). The model TF relation lies slightly below the observed ones, with values of V_C roughly 0.05-0.1 dex larger for a given absolute magnitude. This translates into a relative offset of 10-20%, thus explaining part (but not all) of the systematic shift towards larger velocities seen in Fig. 5.5a. After applying a direct and a reverse weighted linear fit

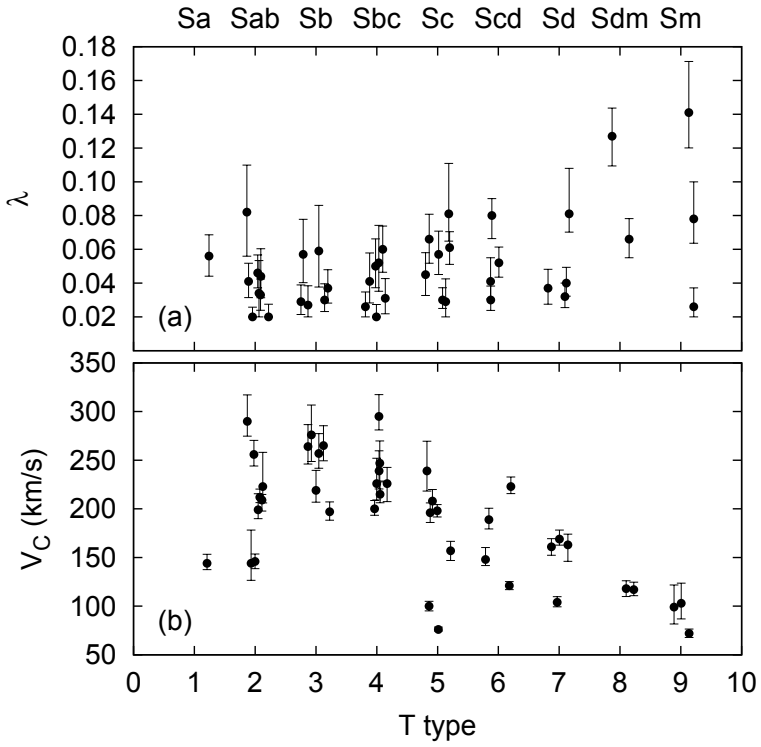

Figure 5.6: Dependence of the spin parameter (a) and the circular velocity (b) on the morphological type T. Given that the T types are integer values, small random horizontal offsets have been applied for the sake of clarity.

to our data-points, the following relations are obtained:

$$M_{K_S} = 1.3 \pm 1.4 - (10.01 \pm 0.60) \times \log V_{\rm C} \quad (rms = 0.61\,{\rm mag}) \quad (5.13)$$

$$\log V_{\rm C} = -0.04 \pm 0.10 - (0.1069 \pm 0.0049) \times M_{K_S} \quad (rms = 0.068\,{\rm dex}) \quad (5.14)$$

where M_{K_S} is expressed in AB magnitudes and $V_{\rm C}$ in km s^{-1}.

5.6.1.3 Trends along the Hubble sequence

It is illustrative to discuss whether the derived values of λ and $V_{\rm C}$ depend on the morphological type or not. In Fig. 5.6 we plot the model parameters as a function of the Hubble type. The rotational velocity is clearly correlated with the morphology of the galaxies, with early-type disks rotating faster −and hence being more massive− than late-type ones. However, there is no apparent trend between the spin parameter and the Hubble type, except maybe an increased scatter in Sdm-Sm galaxies.

Although the fact that the Hubble type does not seem to depend on the spin parameter might look surprising at f rst glance, it supports the f ndings of numerical simulations. The number density of galaxies per velocity interval can be parameterized with a generalized form of the Schechter function, resulting from the combination of the luminosity function and the TF relation at a given band (González et al. 2000). This distribution is obviously monotonic, with massive disks being

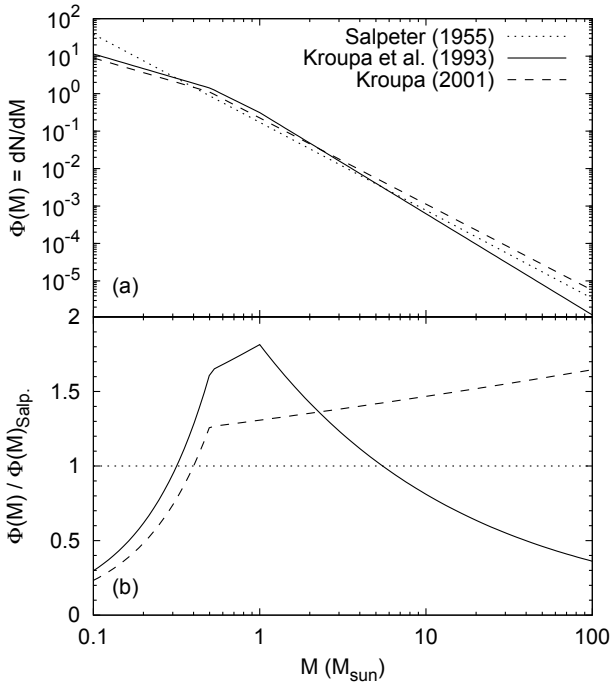

Figure 5.7: (a): The IMFs of Salpeter (1955), Kroupa et al. (1993) and Kroupa (2001), normalized to a total stellar mass of 1 $M_\odot$. (b): Ratio of the K93 and K01 IMFs to the Salpeter one.

rather scarce compared to low-mass ones. Given that $V_{\rm C}$ depends on the Hubble type, the probability distribution of λ would be also monotonic if this parameter was also correlated with the morphological type. However, we have seen that numerical N-body simulations conclude that most haloes usually exhibit the same 'universal' spin value $\lambda \sim 0.04$ quite irrespective of their mass. Therefore, the lack of correlation between λ and the Hubble type agrees with this result.

5.6.2 The influence of the IMF

The IMF, usually denoted as $\Phi(M)$, indicates the number of stars in the mass interval M to $M + dM$ formed in a given burst. The classical IMF of Salpeter (1955) consists of a single power-law across the whole stellar mass range, $\Phi(M) \propto m^{-\alpha}$, where $\alpha = 2.35$. In this work we have used two grid of models with the K93 and K01 IMFs, which are multi-sloped:

$$\begin{aligned} 0.1 \leq M/M_\odot < 0.5 \qquad & \alpha_{\rm K93} = 1.3 \; ; \; \alpha_{\rm K01} = 1.3 \\ 0.5 \leq M/M_\odot < 1.0 \qquad & \alpha_{\rm K93} = 2.2 \; ; \; \alpha_{\rm K01} = 2.3 \\ 1.0 \leq M/M_\odot \qquad & \alpha_{\rm K93} = 2.7 \; ; \; \alpha_{\rm K01} = 2.3 \end{aligned} \tag{5.15}$$

These IMFs are shown in Fig. 5.7, where they have been normalized such that:

$$\int_{M_{\rm min}}^{M_{\rm max}} \Phi(M) M dM = 1 \tag{5.16}$$

where the integration is carried out between $M_{\rm min} = 0.1\,{\rm M}_\odot$ and $M_{\rm max} = 100\,{\rm M}_\odot$. The K01 IMF has more short-lived massive stars for a given total stellar mass, so it yields larger UV fluxes for the

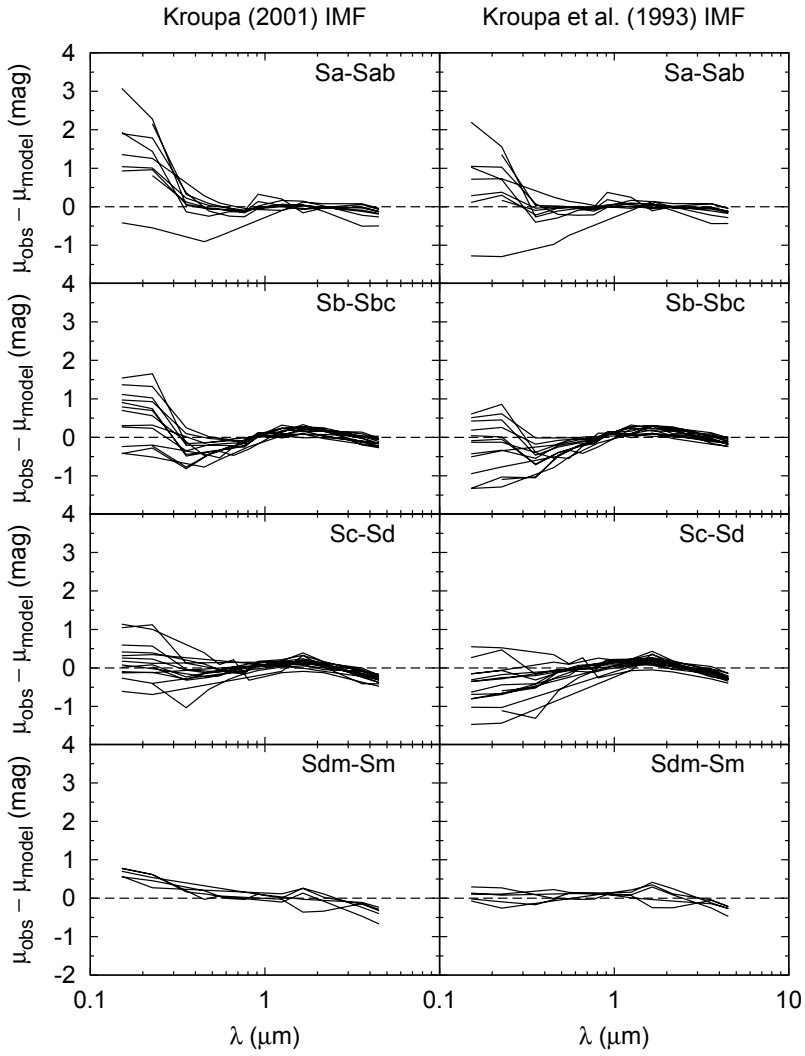

Figure 5.8: Average difference between the observed and model surface brightness prof les for each galaxy at different wavelengths. The average offset was computed within the radial range used during the f tting procedure.

same near-IR and optical luminosities. Therefore, choosing one IMF or another obviously affects the ability of the model to simultaneously f t all the multi-wavelength prof les.

In order to quantify the discrepancy between the model predictions and the actual prof les, for each galaxy and wavelength we have computed the average difference between the observed and model surface brightness within the radial range considered in the f tting procedure. The results are shown in Fig. 5.8 for each IMF and morphological type.

It is clear that neither IMF provides an equally good f t at all wavelengths for all morphological types. The largest discrepancies are found in the UV range, as expected. The K01 IMF yields an excellent f t for most Sc-Sd spirals, as well as for some Sb-Sbc ones. However, it signif cantly overestimates the UV f ux in early-type disks. The K93 IMF, on the other hand, mitigates the problem in Sb-Sbc galaxies, but the perfect agreement between model and observations found in Sc-Sd disks is partially lost. Very late-type disks, however, are better f t with the K93 IMF than with the K01 one.

Elucidating whether a varying IMF is the actual reason behind these discrepancies is not straightforward, as other mechanisms could introduce similar systematic biases in the UV profiles. In the case of Sdm-Sm galaxies, an IMF-related explanation could be indeed viable. Since the canonical stellar IMFs are always determined within star clusters, their application at galaxy-wide scales might not be appropriate. Indeed, it is now believed that the so-called Integrated Galactic Initial Mass Function (IGIMF) is steeper than the canonical IMF, especially in galaxies with low levels of global star formation (Weidner & Kroupa 2005). This is due to the fact that the mass of the most massive star in a young cluster is a function of the total mass of the cluster itself (Weidner & Kroupa 2006). Moreover, the mass of the most massive cluster in a galaxy is also a function of the global SFR of the galaxy (Weidner, Kroupa & Larsen 2004). The combination of these two effects leads to a scarcity of massive stars in galaxies with low global SFR.

While the previous arguments are purely statistical, a physical explanation to the apparent dearth of massive stars in low-density regions has been brought forward by Krumholz & McKee (2008). If star-forming clouds collapse in a isothermal way due to radiative cooling, they will keep fragmenting into progressively smaller clouds, yielding stars of one solar mass or less. The energy released by the accretion of low-mass stars within the cloud could heat the gas and avoid fragmentation. However, these authors found that gas column densities of at least $1\,\mathrm{g\,cm^{-2}}$ are required to halt fragmentation and produce massive stars.

This mechanism has been proposed to explain the observed discrepancies between the UV and Hα-derived SFR in dwarf galaxies (Pflamm-Altenburg et al. 2007, 2009; Lee et al. 2009). In this regard, even though both the K93 and K01 IMFs are canonical, it would make sense that Sdm-Sm disks are better fit with a top-light IMF like the K93 one rather than with the K01 one.

However, we cannot appeal to these mechanisms to explain the discrepancies in the UV bands found in early-type disks. The largest deviations are seen in galaxies like NGC 4826 or NGC 4569, which are anemic spirals that have lost most of their gas probably as a result of ram pressure stripping (Boselli et al. 2006). Consequently, the recent star formation activity in these galaxies has been quenched, yielding anomalously low UV fluxes. However, the model also fails at fitting the UV profiles of many normal early-type spirals, like NGC 3031 or NGC 2841. The origin of such mismatch in the UV range has not been elucidated, although it might be related to the bulge. Its presence could somehow alter the overall gas infall rate, modifying the SFH with respect to the model predictions, which only consider the disk component.

Nevertheless, it is worth asking whether our particular choice of IMF affects the results of the fitting. Thanks to our two-step fitting procedure, which estimates the intrinsic error of the model for each galaxy and band after a first run, the UV bands are automatically assigned a relatively large error whenever large discrepancies are found. This prevents the UV bands from biasing the fit at longer wavelengths. In Fig. 5.9 we compare the values of λ and V_{C} obtained with both IMFs. The differences are obviously negligible and much smaller than the estimated uncertainties, since the fit is still excellent in the optical and near-IR bands even when it fails in the UV. Therefore, even if the very recent level of SF (either massive or total) predicted by the models for the last few Gyr is not entirely reliable, the overall SFH across longer timescales can still be trusted.

Besides modifying the emitted UV flux, changing the IMF also has a significant impact in the resulting metallicity profiles predicted by the model. In Fig. 5.10 we compare the central abundances and radial gradients obtained with both IMFs. Since the K01 IMF is richer in massive stars than the K93 one, it produces more Type II supernovae and metals, leading to oxygen abundances

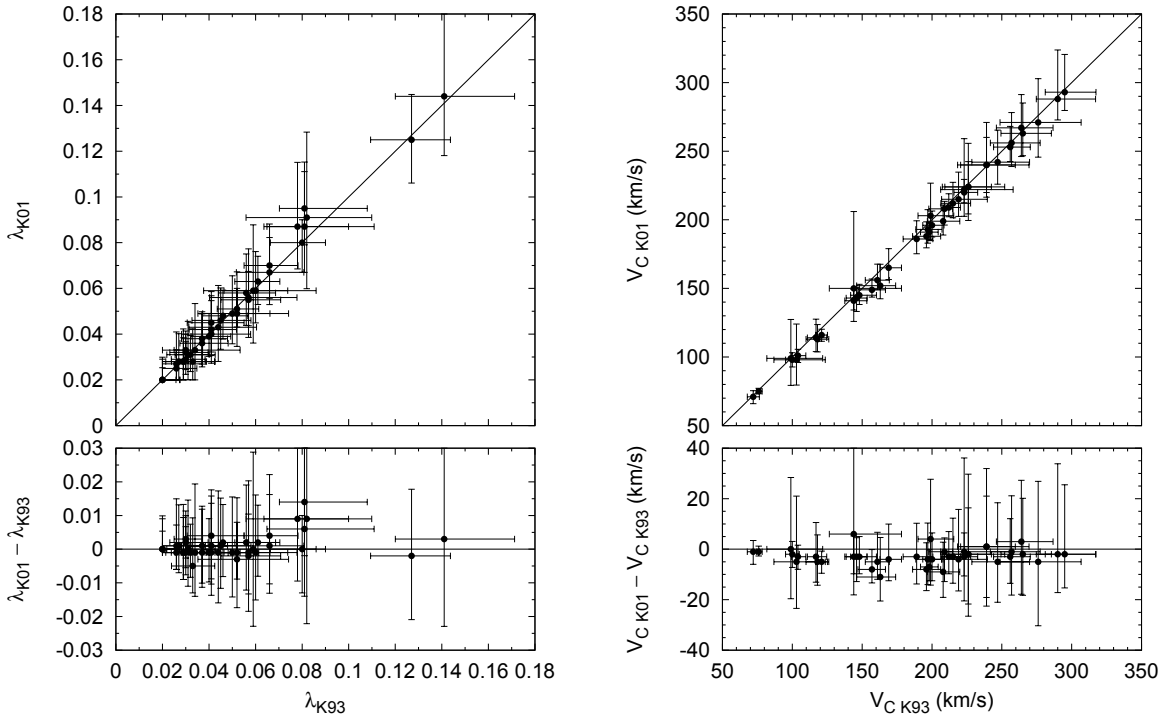

Figure 5.9: Comparison of the values of the spin parameter and circular velocities obtained when using the IMFs of Kroupa et al. (1993) and Kroupa (2001). The solid line show the corresponding 1:1 relations.

which are ~ 0.62 dex larger than those resulting from the K93 IMF. The radial gradients, on the other hand, remain nearly unchanged, the K01 ones being just mildly steeper.

We must also check whether the oxygen abundance profiles predicted by the model are in agreement with the observed ones. As in the previous chapter, here we rely on the metallicity zero-points and gradients measured by Moustakas et al. (2010, in prep.), using the calibration of Kobulnicky & Kewley (2004). In Fig. 5.11 we plot the central oxygen abundances as a function of the predicted values using both IMFs. The values computed with the K93 IMF are totally consistent with the observed central abundances, whereas those yielded by the K01 IMF are roughly 0.7 dex larger.

As for the radial gradients, they are plotted in Fig. 5.12. The gradients predicted by the model are always steeper than the observed ones, although for most galaxies the difference is just about ~ 0.015 dex kpc^{-1}. While this offset is probably not significant, it is worth mentioning that recent numerical N-body simulations have shown that radial stellar migration can flatten the final metallicity profiles (Rŏskar et al. 2008; Sánchez-Blázquez et al. 2009).

In brief, most Sc-Sd spirals require the K01 IMF to be used in order not to underestimate the UV luminosity, but at the expense of ending up with oxygen abundances much larger than the observed ones. Conversely, the K93 IMF provides a better fit for the remaining Hubble types, and is able to reproduce the correct present-day abundances. Whether the better agreement with the observed metallicities should be given a special importance is unclear, since neither the measured values nor the predicted ones are devoid of possible sources of large systematic errors. On one hand, the different existing calibrations used to compute the oxygen abundance from observed

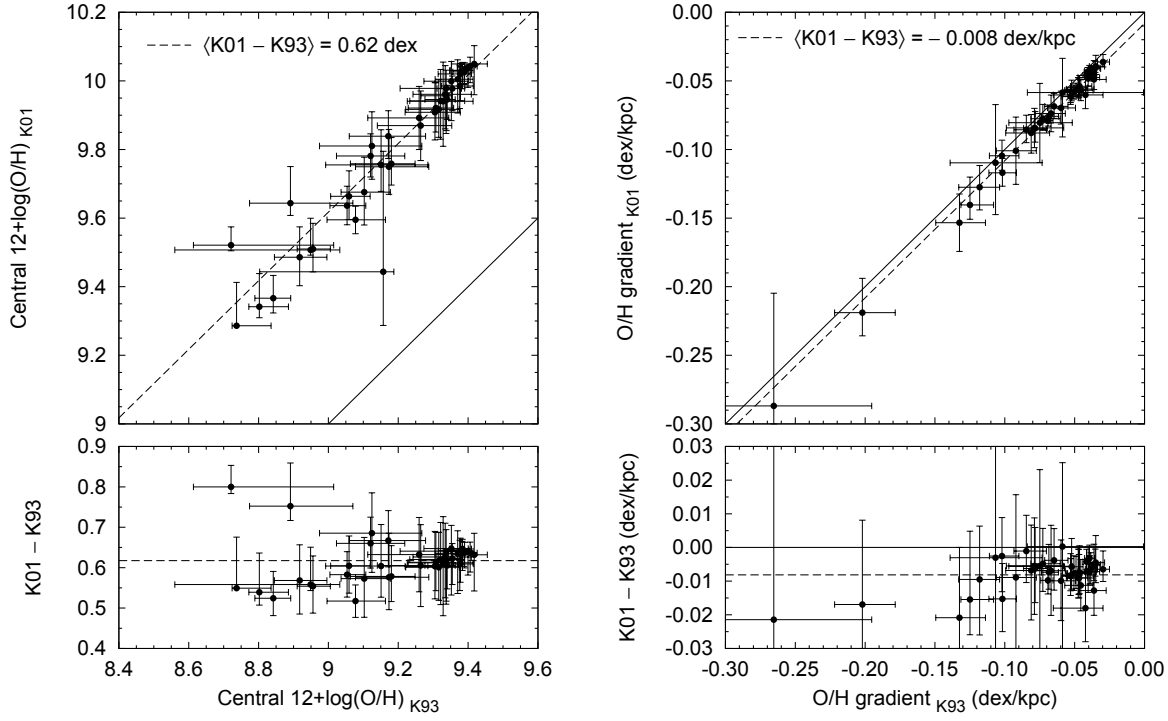

Figure 5.10: Comparison of the central abundances and gradients obtained when using the IMFs of Kroupa et al. (1993) and Kroupa (2001). The solid lines in each panel correspond to the 1:1 relation, while the dashed lines show linear f ts where only the zero-point has been left as a free parameter. The corresponding offset is quoted in each panel.

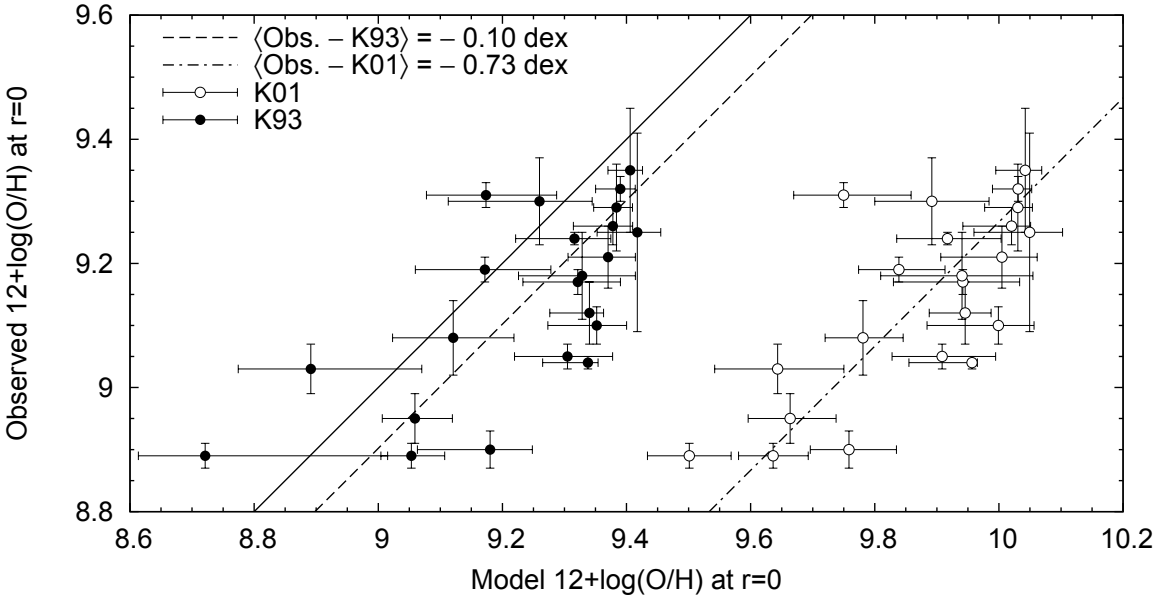

Figure 5.11: Comparison between the observed and predicted central abundances for those SINGS galaxies with metallicity prof les available in the compilation of Moustakas et al. (2010, in prep.). The average offsets for the K93 and K01 IMFs are shown with a dashed and dot-dashed line, respectively, while the solid one corresponds to the line of equality.

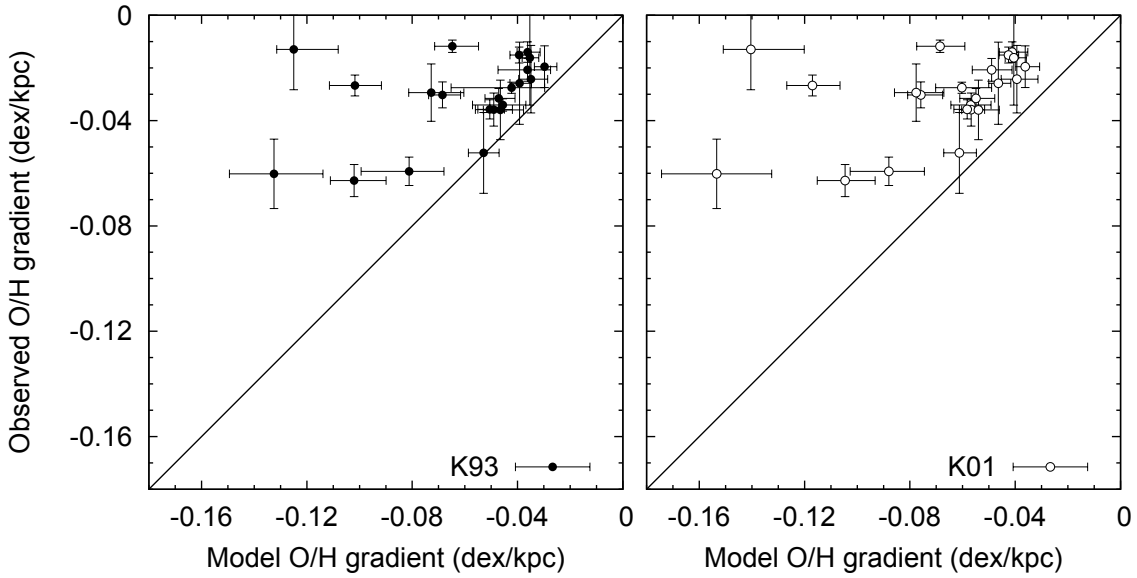

Figure 5.12: Comparison between the observed and predicted abundance gradients for those galaxies in the sample of Moustakas et al. (2010, in prep.). The solid line marks the 1:1 relation.

spectra may lead to systematically different values (see e.g. Moustakas & Kennicutt 2006). On the other hand, uncertainties in the stellar yields used in the disk evolution models will affect the predicted metallicities. Besides, we cannot neglect the possibility that the library of synthetic spectra used to compute the multiwavelength prof les could be quite off in the UV range.

In consequence, we opt for a compromise solution and adopt the K93 IMF as our default choice, while keeping in mind that the origin of the discrepancies at UV wavelengths must be elucidated in future works. This will be key if one wishes to use the models to infer the very recent SFH of present-day galaxies, in particular when studying possible departures from the smooth inside-out growth expected for an isolated galaxy. Anyway, we remark that given the excellent quality of the f ts in the optical and near-IR bands, the model predictions on disk evolution should be accurate enough on longer timescales of several Gyrs.

5.6.3 Implications for the inside-out growth of disks

After having checked that the model is able to reproduce the observed circular velocities of our galaxies, as well as the expected values of the spin parameter −both of which seem to be unaffected by our particular choice of IMF−, we can now proceed to study the evolution of the objects in our sample. We will do so by assuming that our disks have evolved in a similar way as the corresponding model that best f ts its present-day multiwavelength prof les (see also Boissier & Prantzos 2001 for a detailed analysis of the evolution with z of several physical properties of galaxies).

For each model characterized with a particular pair of values of λ and $V_{\rm C}$, we determine the disk scale-length $R_{\rm d}$ at each epoch t by f tting an exponential law to the total stellar mass density prof le:

$$\Sigma_{\rm stars}(r,t) = \Sigma_{\rm stars}(0,t)e^{-r/R_{\rm d}(t)} \tag{5.17}$$

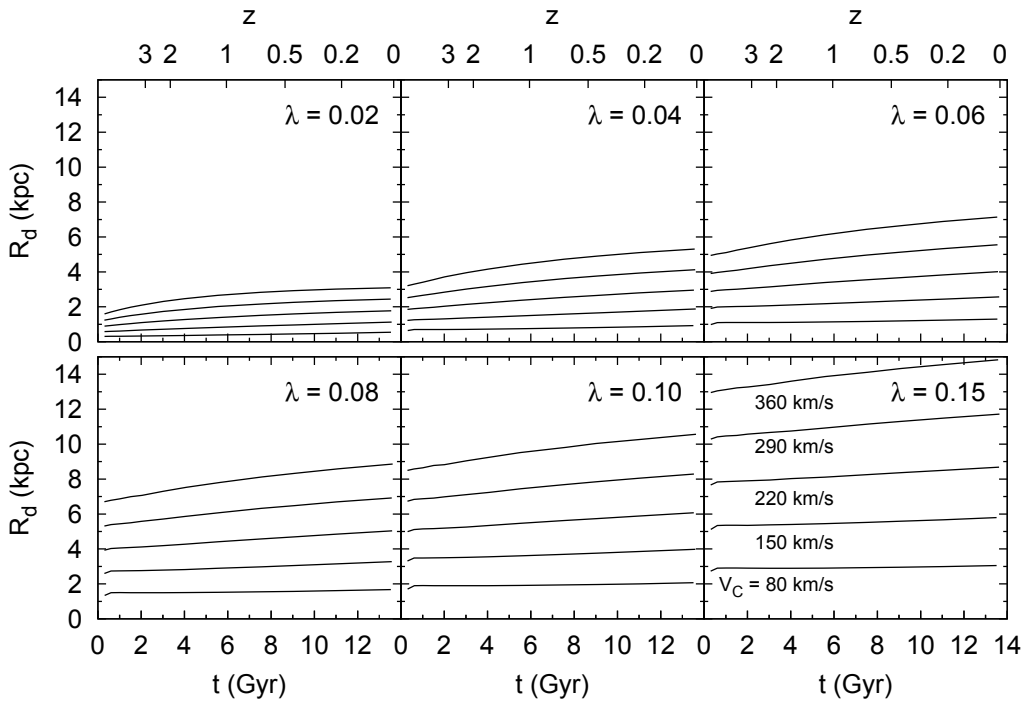

Figure 5.13: Temporal evolution of the exponential scale-length $R_{\rm d}$ of the total stellar mass density profiles. For each value of the spin parameter λ we have plotted the curves corresponding to five selected circular velocities, as labeled in the bottom right panel.

In Fig. 5.13 we show the temporal evolution of the disk scale-length for selected values of λ and $V_{\rm C}$. As expected, $R_{\rm d}$ increases with time in all cases. At any given epoch, the most extended disks are those with larger values of either parameter, as we already pointed out in Fig. 5.1.

The curves describing the growth rate of $R_{\rm d}$ seem to get steeper with increasing $V_{\rm C}$ at fixed λ. In order to quantify the slope of these curves, we have applied a linear fit to the $R_{\rm d}(t)$ functions between $z = 1$ and $z = 0$. Disk growth seems to be approximately linear since $z = 1$ and, as mentioned in the previous sections, it is not clear whether the models can describe disk evolution beyond that redshift, when mergers were more frequent and the thin disk was not fully assembled.

In Fig. 5.14 we plot the disk growth rate $dR_{\rm d}/dt$ as a function of both the spin parameter and the rotational velocity. The growth rate increases up to $\lambda \sim 0.06$, but for larger values it seems to be largely insensitive to the particular spin of the galaxy. It is clear that $dR_{\rm d}/dt$ mainly depends on the circular velocity, while the spin parameter only seems to be relevant at large velocities. In general, very late-type disks appear to grow at a rate of 0.02-0.04 kpc Gyr^{-1}; early-type spirals, on the other hand, can increase their scale-lengths at a rate up to ~ 0.01 kpc Gyr^{-1}, depending on their spin.

Rather than describing disk evolution in terms of their *absolute* growth rate in kpc Gyr^{-1}, it is perhaps more illustrative to focus on their *relative* size increase. We have plotted in Fig. 5.15 the ratio of the scale-length of the stellar mass profiles at $z = 0$ and $z = 1$. Interestingly, this size ratio is essentially a unique function of the spin, with almost no dependence on $V_{\rm C}$ −and hence on mass. It might seem striking that high-spin galaxies experience almost no change in size since

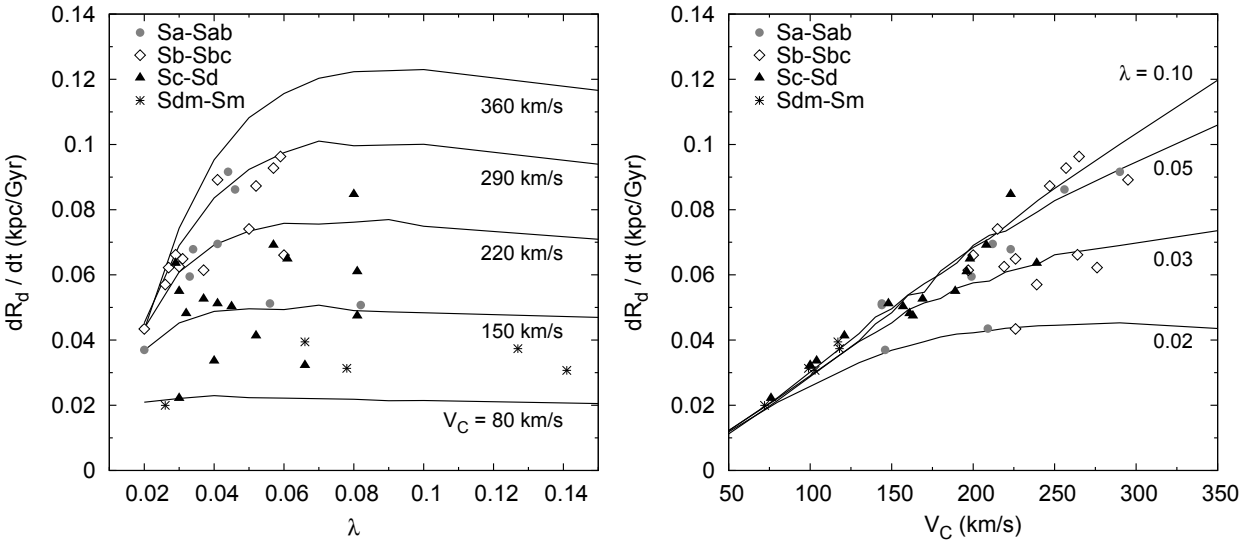

Figure 5.14: Growth rate of the scale-length of the stellar mass density profiles, as a function of λ and $V_{\rm C}$. The growth rate has been computed by fitting $R_{\rm d}$ as a function of t between $z = 1$ and $z = 0$. Morphological types are coded with different symbols.

$z = 1$. However, as Fig. 5.13 demonstrates, these galaxies will already exhibit extended stellar mass profiles at $z = 1$. Therefore, even if the absolute growth rate is high, it will not have a significant impact on the relative increment in size.

Can we extrapolate the conclusions obtained for our sample to the general population of disk-like galaxies? The histograms in Fig. 5.16 show the distribution of both the absolute and relative growth rates in our sample. Both distributions peak around the values typical for galaxies similar to the Milky Way, with an absolute growth rate of about 0.05-0.06 kpc Gyr^{-1} and a relative size increase roughly equal to 20-25% since $z = 1$.

We should not blindly extend these results to the whole population of spiral galaxies. The absolute growth rate depends primarily on $V_{\rm C}$ and, as we discussed in section 5.6.1.1, low-mass disks are considerably underrepresented in our sample. Therefore, most disks in a volume-limited sample would likely grow at slower rates than the peak value in Fig. 5.16.

However, the situation is different regarding the relative increment in size. As we stated in section 5.6.1.1, the distribution of spin values in our sample matches reasonably well the one found in N-body simulations of disk formation. Therefore, we can treat our sample as being representative of a complete one regarding any λ-dependent quantity. This is precisely the case of the relative size ratio, which depends almost entirely on λ alone according to Fig. 5.15. Therefore, we can safely conclude that most disks have probably undergone an increase of 20-25% in their scale-lengths since $z = 1$ until now, regardless of their total mass. This result is in perfect agreement with the growth rate estimated in chapter 2.

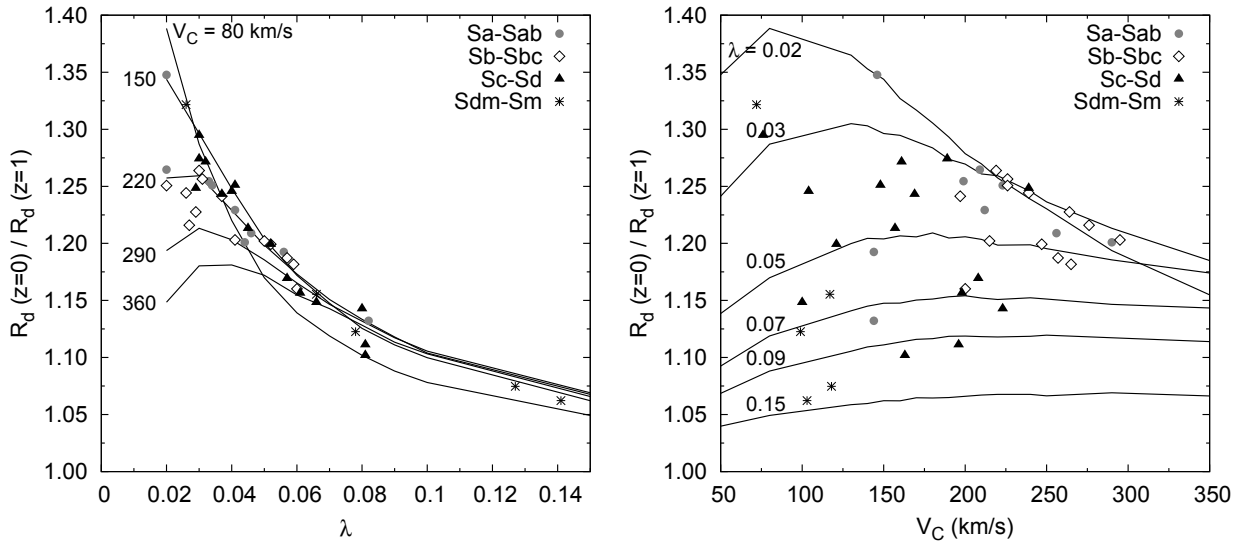

Figure 5.15: Ratio of the stellar disk scale-lengths at $z = 0$ and $z = 1$ as a function of the spin and the rotational velocity. Morphological types are coded with different symbols.

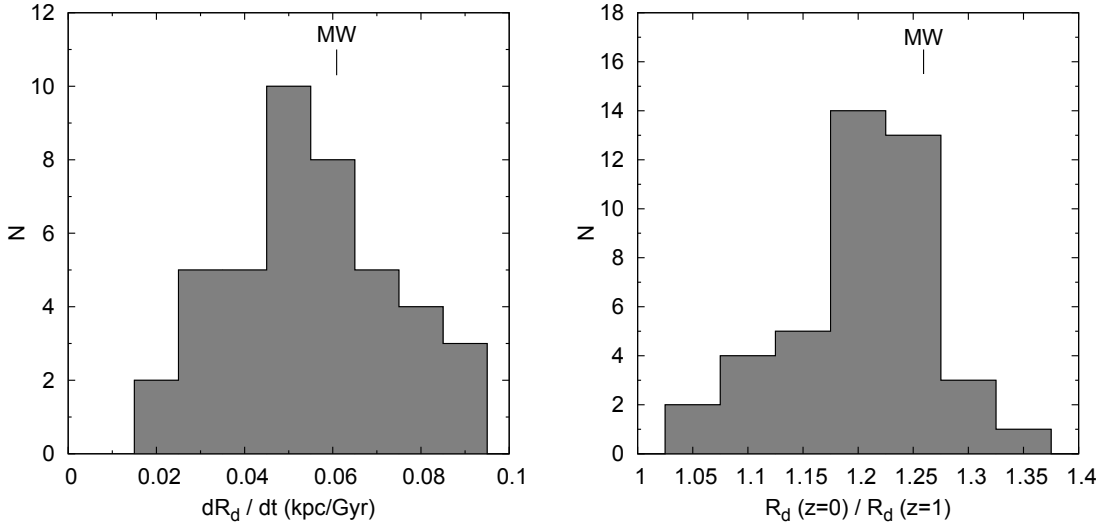

Figure 5.16: Distribution of the absolute growth rate (left) and relative size increase (right) in our sample. The values for a MW-like galaxy, with $\lambda = 0.03$ and $V_{\rm C} = 220\,{\rm km\,s^{-1}}$, have been marked as a reference.

5.7 Conclusions

In this chapter we have f tted the UV, optical and near-IR prof les of 42 disk-like galaxies of the SINGS sample with the models of Boissier & Prantzos (1999, 2000). In order to recover the unattenuated starlight prof les at each wavelength, we have used the radially-varying TIR/UV ratio as tracer of the internal extinction. The disk evolution models are calibrated on the Milky Way (BP99) and further extended to other disk-like galaxies through scaling laws derived from the ΛCDM scenario (BP00). By considering in a consistent framework the gas infall, the star formation activity and the subsequent chemical evolution, the models are capable of predicting the current multi-band prof les of spirals as a function of only two parameters: the maximum circular velocity of the rotation curve, $V_{\rm C}$, and the dimensionless spin parameter, λ. By f tting the prof les of the SINGS galaxies with those predicted by the models, we have not only checked the accuracy of the models themselves, but have also used them to infer the size evolution of the SINGS galaxies. The main conclusions of this work can be summarized as follows:

1. The rotational velocities are in good agreement with those measured from observed rotation curves, as well as with those estimated from the Tully-Fisher relation. There is some systematic scatter in both cases, in the sense that the values of $V_{\rm C}$ derived from the model f tting tend to be 10-20% larger than the empirical ones.

2. Most galaxies in our sample exhibit spin values of $\lambda \sim 0.03$. In fact, even though the sample is not volume-limited, the statistical distribution of spin values closely resembles the narrow distributions usually found in N-body simulations, which typically have an almost universal peak value of 0.03-0.04.

3. There is a clear, well-known trend between $V_{\rm C}$ and Hubble type, in the sense that early-type disks have larger circular velocities $-$and are hence more massive$-$ than late-type ones. There is not, however, any evident trend between the morphological type and λ, which supports the f ndings of numerical simulations that most haloes posses the same spin, regardless of their total mass or mass assembly history.

4. While there is an excellent agreement between the model predictions and the observed prof les in the optical and near-IR bands, signif cant departures may arise in the UV bands, depending on the morphological type and the particular choice of IMF. The Kroupa (2001) yields excellent results in Sc-Sd spirals, but overestimates the UV luminosity in early-type disks, and to a much lesser extent in Sdm-Sm ones. The Kroupa et al. (1993) IMF brings the UV model prof les into better agreement with the observed ones in Sb-Sbc spirals, as well as in Sdm-Sm ones, but at the expense of losing the excellent f ts for Sc-Sd disks. While differences in the high-mass end of the IMF might indeed play a role in very late-type galaxies, it is doubtful that the IMF is behind the discrepancies in the UV predictions for early-type disks. Rather, the presence of massive bulges could have a larger impact. Anyway, the values of λ and $V_{\rm C}$ are largely unaffected by the specif c IMF chosen.

5. The models successfully predict the metallicity gradients, which are just $\sim 0.015\,{\rm dex\,kpc^{-1}}$ steeper than the observed ones. The central oxygen abundances depend on the IMF: the values yielded by the K93 IMF are in perfect agreement with the observed central metallicities, but those obtained with the K01 one overestimate the real values by ~ 0.07 dex.

6. According to the models, the absolute growth rate (in kpc Gyr^{-1}) of the exponential scale-length of disks depends mainly on V_{C}, with rapidly rotating disks expanding faster. In our sample, most galaxies see their scale-lengths increased by about 0.05-0.06 kpc each Gyr. Still, this is not representative of the overall population of disks, since low-mass ones are underrepresented in our sample.

7. The ratio between the current disk scale-length and that at $z = 1$ is a decreasing function of λ, with little dependence on V_{C}. Even though high-spin disks grow faster in absolute terms, such a rapid radial expansion does not signif cantly increase their scale-lengths, which are already considerably large at $z = 1$. On average, most disks in our sample are now 20-25% larger than at $z = 1$. This value can be treated as being representative of a volume-limited sample, given that our galaxies have the λ distribution expected for such a kind of sample.

6

Conclusiones

En esta tesis hemos realizado un análisis detallado y exhaustivo de la distribución espacial de las estrellas, el gas y el polvo en galaxias cercanas. Al cuantif car de forma precisa cómo cambian sus propiedades físicas a medida que nos desplazamos a lo largo de los discos galácticos, hemos podido obtener pistas importantes sobre el proceso de formación y evolución de las galaxias.

Como primera aproximación a este problema complejo, en primer lugar estudiamos la variación radial de la tasa de formación estelar específ ca en una muestra de 161 discos cercanos y prácticamente de cara. Para ello, medimos perf les de brillo superf cial en imágenes en banda K_S de estas galaxias, y los combinamos con perf les en el UV lejano publicados en el *Atlas GALEX de Galaxias Cercanas* (Gil de Paz et al. 2007). Los perf les en banda K_S trazan la distribución radial de estrellas evolucionadas, mientras que los perf les UV muestran la actividad de formación estelar reciente. Además, corregimos los perf les de color $(\mathrm{FUV} - K_S)$ del efecto de la variación radial de la extinción interna, usando perf les del cociente TIR/FUV o, en su defecto, perf les de color $(\mathrm{FUV} - \mathrm{NUV})$. Las conclusiones principales de ese trabajo son:

1. Los gradientes de sSFR dependen de la masa y el tamaño total de las galaxias. Las galaxias de baja masa presentan una gran variedad de gradientes de sSFR, la mayoría positivos, pero también algunos negativos. El rango de gradientes de sSFR se estrecha en discos más grandes y masivos, la mayoría de los cuales presentan un gradiente casi plano, pero ligeramente positivo, consistente con un crecimiento de dentro hacia fuera moderado.

2. Esta tendencia se puede describir con un modelo sencillo de evolución de discos, en el que la longitud de escala del perf l de SFR aumenta linealmente con el tiempo, a la vez que el nivel global de formación estelar decae exponencialmente con el tiempo a medida que se consume el gas. Este modelo sencillo reproduce el rango de gradientes de sSFR progresivamente más estrecho que observamos a medida que nos centramos en discos cada vez más grandes y masivos.

3. Aunque en este modelo la longitud de escala radial del perf l de SFR es siempre mayor que la del perf l de masa estelar, no puede ser *arbitrariamente* mayor, dado que los ritmos crecimiento de ambos discos están acoplados. Como resultado de ello, el modelo predice un límite superior del gradiente de sSFR para cualquier valor dado de la longitud de escala del perf l de masa. No obstante, encontramos muchos discos cuyos gradientes de sSFR son más pronunciados que este límite superior teórico. Esto podría ser una señal de episodios recientes de formación estelar anormalmente alta en las regiones externas, como los que parece que tienen lugar en algunos discos extensos en el ultravioleta.

4. Las galaxias en las que la sSFR disminuye con el radio suelen ser pequeñas y de baja masa. Sus dicos puede que hayan evolucionado por tanto desde fuera hacia dentro. Fenómenos como la pérdida de gas debida a la interacción con el gas intergaláctico (*ram pressure stripping*) o episodios transitorios de formación estelar intensa en las regiones centrales dan lugar también a gradientes negativos de sSFR.

5. En general, la distribución de los gradientes de sSFR respecto a la masa y el tamaño parece indicar que la longitud de escala de los discos es ahora del orden de un 25 % mayor que a $z = 1$, en promedio.

Aunque la distribución radial de estrellas jóvenes en relación a las viejas proporciona una restricción observacional robusta para los diferentes escenario de evolución galáctica, la ubicación espacial del polvo y del gas también se debe considerar. Aquí lo hicimos centrando todo nuestro análisis posterior en las galaxias de la muestra SINGS, explotando las numerosas imágenes multi-longitud de onda disponibles para estas galaxias. Comenzamos este análisis simultáneo de la distribución espacial de las estrellas, el gas y el polvo midiendo perf les de brillo superf cial desde el UV lejano hasta el IR lejano. También calculamos diversos estimadores morfológicos en todas estas longitudes de onda: el índice de concentración (C_{42}), la asimetría (A), el momento de segundo orden del 20 % de los píxeles más brillantes ($\overline{M}_{20}$) y el coef ciente de Gini. De ese estudio surgieron varios resultados importantes:

1. Los perf les multi-banda presentan una gran variedad de rasgos como truncamientos internos y externos que no se pueden tener en cuenta con descomposiciones bulbo-disco clásicas. La intensidad de estas características varía no sólo de galaxia a galaxia, sino también con la longitud de onda para una galaxia dada. En particular, los truncamientos externos son más marcados en el UV y el óptico en en el IR cercano, debido posiblemente a diferentes niveles de formación estelar a ambos lados del radio de truncamiento, y/o a migración estelar radial.

2. La concentración de la luz, medida con C_{42} y $\overline{M}_{20}$, está estrechamente relacionada con el tipo morfológico de las galaxias. Las galaxias elípticas y lenticulares siempre presentan índices de concentración altos independientemente de la longitud de onda. Al atravesar la discontinuidad de 4000 Å la concentración aumenta bruscamente, dado que la mayor parte de la luminosidad en las bandas ópticas y en el IR cercano está dominada por el bulbo. Finalmente, la concentración disminuye de nuevo en el IR medio, debido a la emisión de los PAHs a 8 μm y la del polvo caliente a 24 μm. La amplitud de estas dos discontinuidades en el índice de concentración disminuye desde los discos tempranos a los tardíos.

3. La asimetría está anti-correlacionada con el grado de concentración. De nuevo, las elípticas y lenticulares tienen una morfología extremadamente simétrica en todas las longitudes de onda. En las espirales, sin embargo, la asímetría alcanza su valor máximo en el UV, debido a la distribución desigual de galaxias recién nacidadas. En el óptico y el IR cercano disminuye progresivamente, debido a la contribución cada vez más dominante del bulbo y del disco uniforme de estrellas viejas. Finalmente, aumenta otra vez en el IR medio como resultado de la distribución grumosa y desorganizada de los PAHs y del polvo caliente.

4. Aunque el coef ciente de Gini no depende de la distribución espacial de los píxeles, está correlacionado con C_{42} y $\overline{M}_{20}$, pero sólo en las bandas del óptico y el IR cercano. A estas

longitudes de onda, el grueso de la luminosidad total de una galaxia emerge de una pequeña fracción de píxeles en el bulbo central, dando lugar simultáneamente a valores altos de la concentración y de G. Este acoplamiento se rompe en el UV y el IR medio, donde los píxeles más brillantes ya no se encuentran en las zonas centrales, sino por todo el disco, especialmente en regiones de formación estelar.

Seguidamente decidimos centrarnos en la distribución de las propiedades del polvo por sí solo. Hay dos razones que nos llevaron a realizar un estudio tan particularizado. En primer lugar, necesitábamos investigar la variación radial de la extinción interna, con el f n de recuperar los perf les de luminosidad estelar para análisis posteriores. Para ello calculamos la extinción interna a partir del cociente TIR/FUV, usando recetas actualizadas que tienen en cuenta el calentamiento del polvo debido a estrellas viejas (Cortese et al. 2008). En segundo lugar, teníamos la intención de examinar si la propia variación radial de las propiedades del polvo podía arrojar algo de luz sobre la evolución de los discos. Abordamos este segundo aspecto ajustando las distribuciones espectrales de energía infrarrojas a cada radio con los modelos de polvo de Draine & Li (2007), de donde derivamos la abundancia de PAHs ($q_{\rm PAH}$), la intensidad del campo de radiación (U), la fracción de polvo muy caliente (γ) y la densidad superf cial de polvo ($\Sigma_{M_{\rm dust}}$). Las conclusiones más relevantes a las que llegamos en ese análisis son las siguientes:

1. En general, la extinción interna disminuye con la distancia galactocéntrica. Las galaxias con mayor atenuación son las espirales Sb-Sbc, en las que $A_{\rm FUV}$ típicamente disminuye desde ~ 2.5 mag en el centro a ~ 1.5 mag en el radio óptico R25. En el extremo opuesto, $A_{\rm FUV}$ casi nunca aumenta por encima de ~ 0.5 mag en las espirales Sdm y en las irregulares.

2. El cociente TIR/FUV está correlacionado con el color $({\rm FUV}-{\rm NUV})$, siguiendo una curva IRX-β similar a la de las galaxias con formación estelar activa (*starbursts*), pero desplazada hacia colores UV más rojos para el mismo cociente TIR/FUV. Esto se debe seguramente al hecho de que la radiación UV en las espirales normales no está completamente dominada for formación estelar reciente como en las galaxias *starburst*. Parte del enrojecimiento en el UV en las espirales normales se debe a la emisión de estrellas algo más evolucionadas, que son intrínsecamente más rojas. No obstante, aunque el desplazamiento hacia colores UV más rojos es más acusado en los bulbos y en las zonas externas de las espirales anémicas, otros factores como la geometría del polvo o la curva de extinción puden dominar la dispersión en entornos no tan extremos.

3. Tanto el cociente TIR/FUV como color $({\rm FUV}-{\rm NUV})$ a cada radio aumentan con la abundancia local de oxígeno. Para una metalidad dada, las galaxias más inclinadas muestran cocientes TIR/FUV mayores y colores UV más rojos, de forma que los puntos se desplazan diagonalmente a lo largo de la distribución IRX-β.

4. Los PAHs son más abundantes en las espirales Sb-Sbc, donde suponen el 3-4.5 % de la masa total de polvo. En las partes externas de las galaxias Sdm y en las irregulares, por el contrario, hay una gran escasez de PAHs, con abundancias típicamente inferiores al 1 %. La abundancia de PAHs aumenta con la metalicidad local hasta $12+\log(O/H)\simeq 9$, pero esta tendencia se aplana e incluso se invierte para abundancias de oxígeno mayores. Esto encaja con algunos modelos de evolución del polvo, en los que las AGBs producen e inyectan en el medio interestelar la mayoría de los átomos de carbono de los PAHs, mientras que el resto

de los componentes del polvo se condensan a partir del material ejectado por las supernovas en escalas de tiempo mucho más cortas. Esta inyección retrasada de carbono explicaría el aumento inicial de $q_{\rm PAH}$ con la metalicidad. El hecho de que las AGBs de baja masa y/o las más metálicas son más ricas en oxígeno que en carbono explicaría la inversión de la tendencia a metalicidades mayores.

5. La intensidad promedio de la radiación estelar que calienta el polvo decae con el radio, y en las regiones externas es similar al campo de radiación local de la Vía Láctea. El polvo difuso expuesto a esta radiación estelar presenta temperaturas de unos 20 K. No obstante, parece que del orden del 1 % de la cantidad total de polvo está calentado por campos de radiación muy intensos, emitiendo aproximadamente el 10 % de la luminosidad IR total radiada por el polvo.

6. La densidad superf cial de polvo normalmente sigue perf les exponenciales. Para las espirales con tipos entre Sb y Sd, la longitud de escala radial permanece asombrosamente constante una vez que se normaliza al radio óptico (0.2-0.3$\times$R25). Las densidades más altas se encuentran en las galaxias Sb-Sbc, donde $\Sigma_{M_{\rm dust}}$ varía entre 10^6 y $10^4\,{\rm M}_\odot\,{\rm kpc}^{-2}$ a lo largo del disco óptico. Por el contrario, en las galaxias Sdm e irregulares, permanece por debajo de $10^4\,{\rm M}_\odot\,{\rm kpc}^{-2}$. Además, algunos discos tempranos presentan huecos o truncamientos internos en sus perf les de masa de polvo.

7. Para cualquier densidad de polvo dada encontramos un valor mínimo para la atenuación. Esta envolvente inferior está def nida por galaxias de tipos Sc y más tardíos, mientras que espirales de tipos más tempranos presentan atenuaciones mayores para la misma densidad de columna de polvo. Las nubes de polvo probablemente son más porosas en las espirales tardías que en las tempranas, permitiendo que más fotones UV y ópticos escapen, lo que disminuiría la atenuación global para una densidad de polvo dada.

8. El cociente polvo/gas disminuye con la distancia galactocéntrica, variando desde 0.1-0.01 en las zonas más internas hasta 0.01-0.001 en las más externas. Más aún, está fuertemente correlacionado con la abundancia local de oxígeno a cada radio. Cuando la metalicidad cae por debajo de aproximadamente $12 + \log(O/H) = 8.9$ en las zonas externas, muchas espirales presentan cocientes polvo/gas menores de lo que se esperaría para esas abundancias. Esto podría apuntar a la existencia de grandes reservas de gas que todavía no se han transformado en estrellas (ni por tanto en polvo). Por el contrario, grandes cantidades de polvo frío no detectado en nuestros datos conseguirían que los cocientes polvo/gas observados estuvieran en mejor acuerdo con los valores esperados.

Finalmente, retomamos el estudio del crecimiento galáctico desde dentro hacia fuera desde una perspectiva más teórica. Para ello, ajustamos los perf les desde el UV hasta el IR cercano (corregidos de extinción interna) de 42 espirales de la muestra SINGS con los modelos de evolución de discos de Boissier & Prantzos (1999; 2000). Estos modelos predicen los perf les multi-banda de los discos galácticos en función de su velocidad circular $V_{\rm C}$ y su espín λ. Los resultados más relevantes que podemos resaltar son:

1. En promedio, la mayoría de nuestras galaxias son dinámicamente similares a la Vía Láctea, con velocidades de rotación en torno a $220\,{\rm km\,s}^{-1}$ y valores del espín del orden de 0.03.

Los valores teóricos de $V_{\rm C}$ concuerdan con los medidos y con los estimados a partir de la relación de Tully-Fisher, aunque tienden a ser un 10-20 % mayores. La distribución de valores del espín se asemeja a la que se obtiene en simulaciones numéricas de N cuerpos basadas en el marco ΛCDM.

2. Aunque $V_{\rm C}$ disminuye desde los discos tempranos a los tardíos, no se aprecia ninguna correlación evidente entre λ y el tipo de Hubble. Esto es consistente con los resultados de las simulaciones numéricas, en las que la mayor parte de los halos de materia oscura tienen valores de espín cercanos a 0.03-0.04 independientemente de su masa.

3. La IMF influye en la capacidad del modelo para ajustar los perfiles UV y los de metalicidad. La IMF de Kroupa (2001) proporciona un ajuste excelente para los discos Sc-Sd, pero sobrestima la luminosidad UV en discos de tipo temprano. También produce demasiados metales, aunque los gradientes de metalicidad son próximos a los observados. La IMF de Kroupa et al. (1993) da lugar luminosidades UV y metalicidades más bajas para la misma masa estelar, mejorando el ajuste en discos de tipo temprano (y también en los más tardíos), pero fallando en las espirales Sc-Sd.

4. La mayoría de los discos de nuestra muestra crecen a un ritmo de unos 0.05-0.06 kpc Gyr^{-1}, cantidad que aumenta con $V_{\rm C}$ y, en menor medida, con λ. No obstante, este valor no es representativo de una muestra limitada en volumen, que contendría muchos más discos con baja velocidad de rotación que nuestra submuestra de galaxias SINGS.

5. En términos relativos, las longitudes de escala de los discos son hoy aproximadamente un 20-25 % mayores que a $z = 1$, corroborando nuestras estimaciones originales. Dado que esta variación relativa depende casi exclusivamente de λ, un parámetro respecto al que nuestra muestra no parece estar sesgada, esta conclusión puede extenderse a una muestra completa limitada en volumen.

Consideraciones finales

En resumen, los resultados de este trabajo suponen una contribución importante al panorama actual de la evolución de galaxias. No sólo hemos verificado de manera cuantitativa muchas predicciones clave de este escenario, sino que también hemos obtenido nuevos resultados que pueden someterse a prueba con instrumentos ya existentes o disponibles en el futuro.

Hemos cuantificado la formación de los discos desde dentro hacia fuera en el universo local, corroborando anteriores mediciones directas de la evolución del tamaño de las galaxias a diferentes desplazamientos al rojo. De la misma forma, exploraciones que ya están o estarán en marcha con los telescopios espaciales Hubble y Herschel permitirán resolver estrellas individuales en galaxias cercanas, proporcionando así medidas independientes de la historia de la formación estelar de los discos a distintos radios que podrían confirmar nuestros resultados.

Aunque el problema de la formación y evolución de las galaxias se ha enfocado tradicionalmente desde una perspectiva estelar, hemos recurrido también al polvo y al gas como trazadores fósiles de la evolución galáctica. Por ejemplo, la disminución radial del cociente polvo/gas representa una prueba independiente del escenario de formación desde dentro hacia fuera. Los estudios

previos sobre la distribución espacial del polvo en galaxias cercanas se habían centrado generalmente en unos pocos objetos. Por el contrario, en este trabajo hemos medido por primera vez la variación radial de muchas propiedades físicas del polvo en una muestra razonablemente grande de galaxias de diferentes tipos. Hemos esclarecido algunos aspectos complejos como el posible origen de la variación de la abundancia de PAHs dentro de las galaxias, el papel de la geometría del polvo a la hora de determinar la extinción interna, o la posible presencia de polvo frío en las zonas externas de algunos discos. Estos resultados sobre galaxias representativas constituyen un excelente banco de pruebas para futuros estudios con Herschel y ALMA, no sólo en el campo de las galaxias cercanas, sino también como una referencia local para estudios a altos desplazamientos al rojo.

Para terminar, además de los resultados puramente científicos de esta tesis, los datos que hemos generado y proporcionado podrán ser empleados en muchos otros estudios de evolución galáctica que no hemos explorado aquí. En particular, los perfiles multi-banda y los de extinción interna son esenciales para trazar la estructura de las galaxias. Además, la variación de los estimadores morfológicos con la longitud de onda puede resultar útil para refinar los algoritmos de clasificación de galaxias en grandes exploraciones.

6

Conclusions

In this thesis we have carried out a detailed and comprehensive analysis of the spatial distribution of stars, gas and dust in nearby galaxies. By accurately quantifying how their physical properties change as we move across galactic disks, we have been able to infer important clues on the process of galaxy assembly and evolution.

As an initial approach to this complex problem, we first studied the radial variation of the specific SFR in a sample of 161 nearby, almost face-on disks. In order to do so, we measured surface brightness profiles in K_S-band images of these galaxies, and combined them with the FUV profiles published in the *GALEX Atlas of Nearby Galaxies* (Gil de Paz et al. 2007). The former trace the radial distribution of evolved stars, while the latter probe recent star formation activity. Besides, we corrected the $(\mathrm{FUV} - K_S)$ color profiles for the effect of radially-varying internal extinction, using TIR/FUV profiles or, in their absence, $(\mathrm{FUV} - \mathrm{NUV})$ ones. The main conclusions of that work are:

1. The sSFR gradients depend on the total mass and size of the galaxies. Low-mass galaxies exhibit a wealth of possible sSFR gradients, most of them positive, but also some negative. The range of possible sSFR gradients narrows in larger and more massive disks, most of which present an almost flat, but slightly positive sSFR gradient, consistent with a moderate inside-out growth.

2. This trend can be described with a simple model of disk evolution, in which the scale-length of the SFR profile increases linearly with time, while in the meantime the overall level of star formation decreases exponentially with time as the gas is consumed. This simple model reproduces the progressively narrower range in sSFR that we observe as we focus on larger and more massive disks.

3. While in this model the radial scale-length of the SFR profile is always larger than that of the stellar mass profile, in cannot be *arbitrarily* larger, since the growth rates of both profiles are coupled. As a result, the model predicts an upper limit for the sSFR gradient for any given scale-length of the mass profile. We find, however, many disks whose sSFR gradients are steeper than this predicted upper limit. This might be a telltale of recent episodes of enhanced star formation in the outer regions, as those apparently taking place in some XUV disks.

4. Galaxies in which the sSFR decreases with radius tend to be small, low-mass ones. Their disks may have thus evolved in a outside-in fashion. Ram pressure stripping or transitory episodes of intense star formation in the central regions also yield negative sSFR gradients.

5. All in all, the distribution of sSFR gradients with galactic mass and size seems to be consistent with disk scale-lengths being now roughly 25% larger than at $z = 1$, on average.

While the radial distribution of young stars relative to old ones provides already a robust observational constraint on different scenarios of disk evolution, the spatial location of dust and gas must be also considered. We did so by focusing all our subsequent analysis on the SINGS galaxies, exploiting the large data-set of multiwavelength images available for these objects. We began this simultaneous analysis of the spatial distribution of stars, dust and gas by measuring surface brightness profiles from the FUV to the FIR. We also computed several morphological estimators at all these wavelengths: the concentration index (C_{42}), the asymmetry (A), the second-order moment of the brightest 20% of the emission ($\overline{M}_{20}$) and the Gini coefficient (G). Several important results arose from that study:

1. The multi-wavelength radial profiles exhibit a wealth of features like inner and outer disk truncations that cannot be accounted for with classical bulge-disk decompositions. The prominence of these features varies not only among galaxies, but also with wavelength for a given galaxy. In particular, outer disk truncations are sharper in the UV and optical bands than in the near-IR, possibly due to different levels of star formation at both sides of the truncation radius, and/or to radial stellar migration.

2. Light concentration, as measured with C_{42} and $\overline{M}_{20}$, is tightly related to the morphological type of galaxies. Ellipticals and lenticulars always exhibit high concentration indices quite irrespective of wavelength. Spiral ones are much more extended in the UV, since young stars tend to be distributed all over their disks. As we go through the 4000 Å break the concentration rises abruptly, since most of the luminosity in the optical and near-IR bands is dominated by the bulge. Finally, light concentration decreases again in the mid-IR, due to the emission of PAHs at 8 μm and hot dust at 24 μm. The amplitude of these two breaks in light concentration diminishes from early- to late-type disks.

3. The asymmetry is anti-correlated with the degree of concentration. Again, elliptical galaxies and lenticulars have an extremely symmetric morphology at all wavelengths. In spiral ones, however, the asymmetry is largest in the UV, due to the patchy distribution of newly born stars. It progressively decreases in the optical and reaches a minimum in the near-IR, due to the increasingly dominant contribution of the bulge and the smooth disk of old stars. Finally, it rises again in the mid-IR as a result of the clumpier and more disorganized distribution of PAHs and hot dust.

4. Even though the Gini coefficient does not depend on the spatial distribution of pixels, it is correlated with C_{42} and $\overline{M}_{20}$, but only in the optical and near-IR bands. At these wavelengths, the bulk of a galaxy's total luminosity emerges from a small fraction of pixels in the central bulge, yielding simultaneously large concentration indices and values of G. This coupling is broken in the UV and mid-IR ranges, where the brightest pixels are no longer found in the central zones, but all over the disk, especially in star-forming regions.

We then shifted our main subject of interest to the radial distribution of dust properties alone. The reasons for such a particularized study were twofold. First, we needed to investigate the radial variation of internal extinction, in order to recover the intrinsic starlight profiles for subsequent

analysis. This issue was addressed by computing the internal extinction from the TIR-to-FUV ratio, using state-of-the-art recipes that consider the extra dust heating of old stars (Cortese et al. 2008). Secondly, we intended to explore whether the radial variation of dust properties themselves could shed light on disk evolution. We pursued this second goal by f tting the radially varying IR SEDs with the dust models of Draine & Li (2007), from which we derived the abundance of PAHs ($q_{\rm PAH}$), the intensity of the heating starlight (U), the fraction of very hot dust (γ) and the dust mass surface density ($\Sigma_{M_{\rm dust}}$). The most relevant conclusions reached in that analysis are the following:

1. In general, internal extinction decreases with galactocentric distance. The most heavily attenuated galaxies are Sb-Sbc spirals, were $A_{\rm FUV}$ typically decreases from ~ 2.5 mag in the center to ~ 1.5 mag at the optical radius R25. At the opposite extreme, $A_{\rm FUV}$ is hardly ever rises above ~ 0.5 mag in Sdm spirals and irregulars.

2. The TIR/FUV ratio is correlated with the $({\rm FUV}-{\rm NUV})$ color, following an IRX-β trend similar to that of starburst galaxies, but displaced to redder UV colors for the same TIR/FUV ratio. This is most likely due to the fact the UV light in normal spirals is not entirely dominated by recent star formation as in starbursts. Part of the UV reddening in normal star-forming galaxies is due to the emission of somewhat more evolved −and hence intrinsically redder− stars. However, even though the shift towards redder UV colors is more pronounced in bulges and the outer regions of anemic spirals, other factors like the dust geometry or the extinction law might dominate the scatter in not so extreme environments.

3. Both the TIR/FUV ratio and the $({\rm FUV}-{\rm NUV})$ color at each radius increase with the local oxygen abundance. At f xed metallicity, more inclined galaxies exhibit larger TIR/FUV ratios and redder UV colors, in such a way that data-points are roughly shifted along the IRX-β relation.

4. The abundance of PAHs is largest in Sb-Sbc spirals, where 3-4.5% of the total dust mass is contributed by these molecules. In the outer parts of Sdm galaxies and in irregular ones, on the contrary, there is a dearth of PAHs, with abundances typically below 1%. The PAH abundance increases with the local metallicity up to $12+\log(O/H)\simeq 9$, but the trend f attens and even reverses at larger oxygen abundances. This is in agreement with some models of dust evolution, in which most carbon atoms in PAHs are produced and injected into the ISM by AGB stars, while the rest of dust species would condense out of supernovae ejecta in much shorter timescales. This delayed injection of carbon would account for the initial increase of $q_{\rm PAH}$ with metallicity. The fact that low-mass and/or more metallic AGBs are oxygen-rich rather than carbon-rich would explain the bending over at larger metallicities.

5. The average intensity of the heating starlight decreases with radius, and in the outer parts it is similar to the local MW radiation f eld. Diffuse dust exposed to this starlight has temperatures of about 20 K. However, around 1% of the total amount of dust seems to be heated by very intense radiation f elds, accounting for roughly 10% of the total IR luminosity radiated by dust.

6. The dust mass surface density prof les are usually exponential. From Sb to Sd spirals, the radial scale-length holds surprisingly constant once normalized to the optical radius (0.2-0.3×R25). The highest densities are found in Sb-Sbc galaxies, where $\Sigma_{M_{\rm dust}}$ varies from 10^6 to $10^4\,{\rm M}_\odot\,{\rm kpc}^{-2}$ across the optical size. In Sdm and irregular galaxies, on the contrary, it

lies below $10^4\,\mathrm{M}_\odot\,\mathrm{kpc}^{-2}$. Besides, some early-type disks present central truncations in their $\Sigma_{M_{\mathrm{dust}}}$ profiles.

7. For any given dust surface density we find a minimum value for the attenuation. This lower envelope is defined by Sc galaxies and later, while spirals of earlier types present larger attenuations for the same dust column density. Dust clouds are probably more porous in late-type spirals than in early-type ones, thus allowing more UV and optical photons to escape, which would lower the overall attenuation for a given dust surface density.

8. The dust-to-gas ratio decreases with the galactocentric distance, ranging from 0.1-0.01 in the innermost regions to 0.01-0.001 in the outermost ones. Moreover, it is tightly correlated with the local oxygen abundance at each radius. When the metallicity drops below roughly $12 + \log(O/H) = 8.9$ in the outer zones, many spirals exhibit lower dust-to-gas ratios than would be expected for such oxygen abundances. This might point toward the existence of large reservoirs of gas that have not been yet transformed into stars (and later into dust). Conversely, large amounts of cold dust undetected by our data would bring the observed dust-to-gas ratio into better agreement with the expected values.

Finally, we returned to the topic of galactic inside-out growth from a more theoretical perspective. To that aim, we fitted the UV, optical and near-IR profiles of 42 SINGS spirals (corrected for internal extinction as summarized above) with the disk models of Boissier & Prantzos (1999; 2000). These models predict the current multi-wavelength profiles of galactic disks as a function of their circular velocity V_{C} and their spin λ. The foremost results we can remark from that study are:

1. On average, most of our galaxies are dynamically similar to the Milky Way, with rotational velocities around $220\,\mathrm{km\,s}^{-1}$ and spin values of about 0.03. The theoretical values of V_{C} are in good agreement with the measured ones and those estimated from the Tully-Fisher relation, if just 10-20% larger. The distribution of spin values neatly resembles the one obtained in numerical N-body simulations based on the ΛCDM framework.

2. While V_{C} decreases as we progress from early- to late-type disks, there is not any significant correlation between λ and Hubble type. This is consistent with the findings of numerical simulations, in which most dark matter haloes have spin values close to 0.03-0.04 quite irrespective of their mass.

3. The IMF affects the ability of the model to fit the UV and metallicity profiles. The Kroupa (2001) IMF provides an excellent fit for Sc-Sd disks, but overestimates the UV luminosity in early-type disks. It also produces too many metals, although the metallicity gradients are close to the observed ones. The Kroupa et al. (1993) IMF yields lower UV luminosities and metallicities for the same stellar mass, improving the fit in early-type disks (and also in the latest ones), but failing in Sc-Sd spirals.

4. Most disks in our sample grow at a rate of about $0.05\text{-}0.06\,\mathrm{kpc\,Gyr}^{-1}$, a quantity that increases with V_{C} and, to a lesser extent, with λ. This value, however, is not representative of a volume-limited sample, which would have many more slow-rotating disks than our subsample of SINGS galaxies.

5. In relative terms, disk scale-lengths are now roughly 20-25% larger than they were at $z = 1$, thus supporting our original estimates. Since the scale-length ratio depends almost exclusively on λ, a parameter regarding which our sample seems to be numerically unbiased, this conclusion may be extended to a complete volume-limited sample.

Concluding remarks

In brief, the results of this work constitute an important contribution to the current picture of galaxy evolution. Not only have we quantitatively verif ed many key predictions of this scenario, but have also obtained new results that can be tested with existing and future instruments.

We have quantif ed the inside-out formation of disks in the local universe, corroborating previous direct measurements of the size evolution of galaxies at different redshifts. Likewise, already ongoing and future surveys with the Hubble and James Webb space telescopes will make it possible to resolve individual stars in nearby galaxies, thus allowing independent measurements of the SFH of disks at different radii that might conf rm our results.

While the issue of galaxy assembly and evolution has been traditionally addressed from a stellar perspective, here we have also resorted to dust and gas as fossil tracers of galaxy evolution. For instance, the radial decrease of the dust-to-gas ratio represents an independent proof of the inside-out scenario. Previous studies of the spatial distribution of dust in nearby galaxies had mostly dealt with just a few objects. Conversely, in this work we have measured for the f rst time the radial variation of many physical dust properties in a reasonably large sample of galaxies of different types. We have shed light on several complex issues such as the possible origin of the varying PAH abundance within galaxies, the role of dust geometry in determining the internal extinction, or the possible presence of cold dust in the outskirts of some disks. These results on representative galaxies constitute an excellent benchmark for future studies with Herschel and ALMA, not only in the f eld of nearby galaxies, but also as a local reference for high redshift studies.

Last, but not least, besides the purely scientif c outcome of this thesis, the dataset generated and provided here can be further exploited in many other unanticipated studies on galaxy evolution. In particular, our multi-wavelength prof les and those of internal extinction are key to trace galactic structure. Besides, the variation with wavelength of the morphological estimators can prove useful to ref ne galaxy classif cation algorithms in large surveys.

7

Future work

Resumen

El análisis de la distribución espacial de estrellas, gas y polvo presentado en esta tesis se ha centrado principalmente en el estudio de variaciones con la distancia al centro de cada galaxia. El siguiente paso natural consiste en extender este análisis unidimensional hacia un estudio bidimensional, analizando las distribuciones espectrales de energía de regiones individuales en lugar de promediar a lo largo de isofotas elípticas. Esto podría revelar diferencias en las propiedades físicas de las estrellas y el medio interestelar en los brazos y en las zonas entre éstos, por ejemplo.

Sin embargo, este tipo de estudios existe adolecen de una grave limitación: la ausencia de espectros individuales para cada región de interés. Los datos espectroscópicos son un complemento ideal para la fotometría de banda ancha, dado que pueden proporcionar información muy detallada de las propiedades físicas de las poblaciones estelares (edad, tasa de formación estelar, historia de la formación estelar, metalicidad...) y del medio interestelar (extinción, abundancias químicas...).

La obtención de espectros en dos dimensiones espaciales es posible ahora gracias a una nueva técnica observacional conocida como espectroscopía de campo integral (o IFS, de sus siglas en inglés). Los instrumentos que permiten obtener espectros de diferentes partes de un objeto simultáneamente se conocen como unidades de campo integral (o IFUs), y aunque pueden construirse siguiendo distintos diseños, todos ellos producen como salida un cubo de datos con una medida del f ujo para cada posición espacial (x, y) y longitud de onda.

Para explorar con más detalle la interconexión entre las estrellas y el medio interestelar, hemos llevado a cabo una exploración de galaxias cercanas con dos IFUs: el instrumento VIMOS, instalado en uno de los telescopios de 8.2 m en el VLT (Paranal), y el instrumento PPAK, que opera en el telescopio de 3.5 m de Calar Alto. Las galaxias de nuestra muestra serán observadas a 250 μm, 360 μm y 520 μm con el instrumento SPIRE, como parte del *Herschel Galaxy Reference Survey* (Boselli et al. 2010), que es uno de los programas aprobados de tiempo garantizado de Herschel. Además, nuestras galaxias también disponen de datos de GALEX y *Spitzer*, junto con imágenes en banda ancha y estrecha adquiridas por nuestro equipo en el Telescopio Óptico Nórdico en La Palma.

En este capítulo se presentan los resultados provisionales obtenidos con PPAK para una galaxia de nuestra muestra, NGC 4654, una espiral Scd que pertenece al cúmulo de Virgo. Dado que el campo de visión de PPAK es de $74'' \times 65''$, se necesitaron siete apuntados para cubrir la mayor parte de la galaxia. Las observaciones se realizaron con la red V300, que muestrea el rango óptico desde 3600 Å hasta 7000 Å con una escala de dispersión de 1.6 Å por píxel y una resolu-

ción espectral de 10.7 ÅĽos datos se redujeron con el paquete R3D (Sánchez 2006), junto con la herramienta de visualización E3D (Sánchez 2004) y algunas tareas en IRAF. Muy brevemente, el proceso de reducción incluye la sustracción del bias, la eliminación de rayos cósmicos, la localización y extracción de los espectros, la corrección de distorsión, la calibración en longitud de onda y la corrección de la respuesta relativa entre las f bras. Seguidamente se sustrae el espectro del cielo, medido con mazos de f bras que rodean al mazo principal. Los espectros resultantes se calibran en f ujo mediante comparación con una estrella estándar, y se construye el mosaico acoplando los siete apuntados.

El cubo de datos resultante es de gran calidad, y hemos comprobado que es posible detectar las estructuras complejas y detalladas que muestran las imágenes convencionales, con la ventaja de que en este caso disponemos de un espectro completo en cada posición espacial. Actualmente estamos estudiando los resultados obtenidos, y publicaremos el análisis correspondiente en Muñoz-Mateos et al. (2010b).

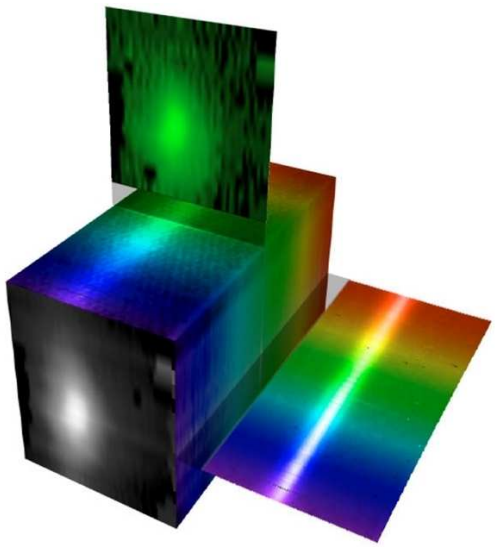

Figure 7.1: Schematic depiction of a data-cube obtained with an IFU.

7.1 Introduction

The analysis of the spatial distribution of stars, dust and gas presented in this thesis has been mainly focused on variations with the galactocentric distance. The next natural step consists of extending this one-dimensional work into a full two-dimensional study, by analyzing the SEDs of individual regions of galaxies rather than averaging within elliptical isophotes. This might reveal differences in the physical properties of stars and the ISM in the arms and inter-arms zones, for instance.

This region-by-region approach has been already explored by several authors in some nearby galaxies (see, e.g., Calzetti et al. 2005; Pérez-González et al. 2006; Bendo et al. 2006; Thilker et al. 2007b). However, when studying the spatially-resolved SEDs of galaxies a severe limitation arises: the lack of individual spectra for every region of interest. Spectroscopic data are a key complement to broadband photometry, since they can provide very detailed information on the physical properties of the stellar populations (age, SFR, SFH, metallicity...) and the ISM (extinction, chemical abundances...). Up to now, spatially resolved spectroscopic observations were usually limited to individual spectra for a handful of bright HII regions within a galaxy, or long-slit spectra along a given axis. However, a full two-dimensional spectroscopic coverage of galaxies is desirable in order to probe the whole range in physical conditions found in each galaxy. This is also critical in kinematic studies, where long-slit spectra only provide two dimensions (the spatial one along the slit and the line-of-sight velocity) of the intrinsically six-dimensional phase space of a galaxy.

Two-dimensional spectral mapping of galaxies is now possible thanks to an observational technique known as Integral Field Spectroscopy (IFS). Instruments that allow recording spectra of different parts of an object simultaneously are called Integral Field Units (IFUs), and even though they can be built following different designs, their outcome is usually a data-cube with one flux measurement for each spatial position (x, y) and wavelength (Fig. 7.1).

In order to explore in more detail the interplay between stars and the ISM, we have pursued an survey of nearby galaxies with two IFUs: the VIMOS instrument, mounted on one of the 8.2 m telescopes in the Very Large Telescope facility in Paranal, and the PPAK one, operating at the 3.5 m

telescope in Calar Alto. The galaxies in our sample[1] will be eventually observed at 250 μm, 360 μm and 520 μm with the SPIRE instrument as part of the *Herschel Galaxy Reference Survey* (Boselli et al. 2010), which is one of the approved Herschel Guaranteed-time Key programs. Besides, our galaxies were selected to have available GALEX and *Spitzer* IRAC and MIPS images, a dataset that we have further completed with custom broadband and narrowband optical images taken at the Nordic Optical Telescope in La Palma. In this chapter we will brief y outline the f rst results obtained with PPAK for one of the galaxies in the sample, NGC 4654, a Scd spiral that belongs to the Virgo cluster.

7.2 Data reduction and first results

The focal plane of PPAK consists of an hexagonal bundle of 331 f bers, each one $2.7''$ in diameter, f lling a total f eld of view of $74'' \times 65''$. In order to map the main optical disk of NGC 4654 we used seven pointings as shown in Fig. 7.2. We allowed for a certain overlap between them, so that we could later match the f ux levels of adjacent pointings when building the complete mosaic. Each pointing was split into three separate exposures of 20 minutes each to allow for cosmic ray removal, adding up to one hour per pointing.

Besides the main f bers, PPAK has also six small IFUs comprising six f bers each. These mini-bundles are placed around the main IFU, lying $72''$ away from its center, and are intended to sample the sky background while observing the main target. Finally, there are 15 more f bers that can be lit with calibration lamps at the same time the main target is being observed, although we preferred to take the calibration exposures separately.

The observations were performed over three nights between February 26 and March 1 2008. We employed a 300 line mm^{-1} grating (V300), which samples the optical range from 3600 Å to 7000 Å with a dispersion scale of 1.6 Å per pixel and a spectral resolution of 10.7 Å (FWHM). The data reduction was performed with the R3D package (Sánchez 2006), together with the E3D visualization tool (Sánchez 2004) and several standard tasks in IRAF. The main steps followed during the data reduction process are the following:

1. **Bias subtraction and cosmic ray removal.** A master bias was subtracted to all frames. Besides, the three individual exposures of each pointing were then combined using a standard rejection algorithm to remove cosmic rays.

2. **Spectra location and extraction.** The position of each spectrum on the detector was traced by illuminating the focal plane with a continuum lamp.

3. **Distortion correction.** The C-shaped distortion of the spectra on the detector was mapped and corrected using a He-Hg-Cd lamp.

[1]Note that pursuing an IFS survey of the SINGS sample would require prohibitively long exposure times, given the large apparent sizes of the SINGS galaxies. Nevertheless, some of them have been already observed with PPAK as part of the PPAK IFS Nearby Galaxies Survey (PINGS; Rosales-Ortega et al. 2010). Moreover, a large fraction of the SINGS sample will be observed with 3D-NTT, a double Fabry-Pérot IFS to be mounted on the New Technology Telescope (NTT) in La Silla (Marcelin et al. (2008).

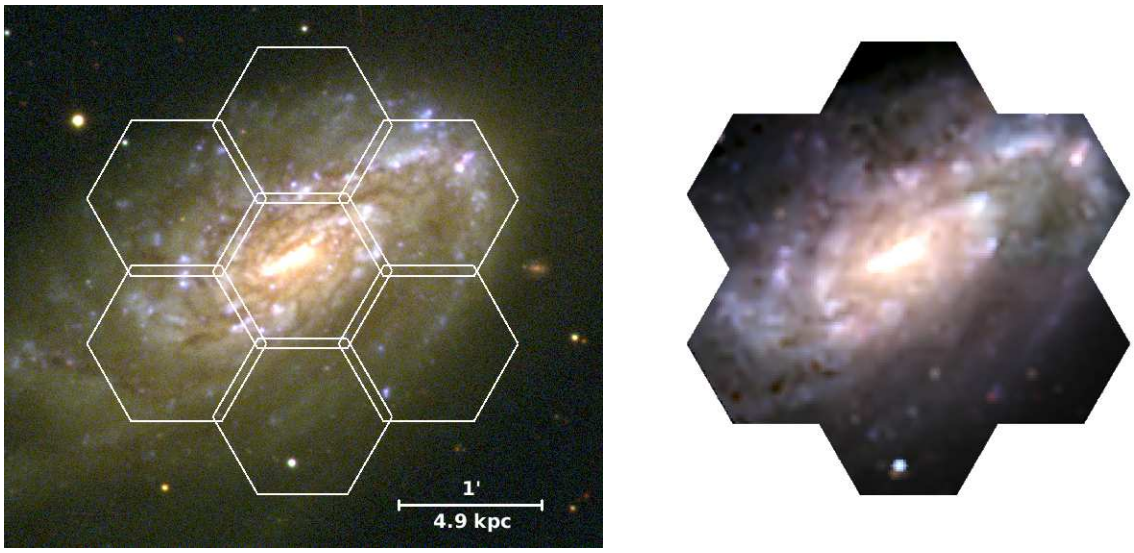

Figure 7.2: Left: ugr color image of NGC 4654 from the SDSS (north is up and east is left). The overlaid white hexagons correspond to the seven PPAK pointings used here. Right: synthetic three-color image reconstructed from the PPAK data-cube.

4. **Wavelength calibration.** Using ~ 15 lines with known wavelengths in the He-Hg-Cd lamp, we computed a dispersion solution that was later refined by double-checking the wavelength of several sky lines.

5. **Fiber to fiber correction.** In order to account for the different transmission exhibited by each fiber, we took a sky exposure at dusk. This frame was then smoothed along the dispersion axis, and all scientific frames were normalized by this image.

6. **Sky subtraction.** For the six outermost pointings, the background was determined by combining the sky spectra of the mini-bundles located furthest away from the galaxy in each case. As for the central pointing, all of the surrounding mini-bundles are still embedded within the galaxy light, so a separate sky exposure was taken.

7. **Flux calibration.** The standard spectro-photometric star Feige 34 was observed using the same instrumental setup. The response curve resulting from the ratio between the real and observed spectra was applied to the NGC 4654 data.

8. **Mosaic construction.** All pointings share an entire row of overlapping fibers with each adjacent pointing. These common fibers were used to rescale the global flux level of each pointing, in order to get an overall light distribution as even as possible once all pointings were stitched together.

The resulting mosaic is roughly $3'$ wide, and contains over 2000 individual spectra. In Fig. 7.2 we show a synthetic three-color image created from the spectral data-cube, which is remarkably similar to the optical SDSS image. Despite its lower spatial resolution, imposed by the fiber size, the PPAK image still exhibits a wealth of small structures such as HII regions and dust lanes.

Even though the spatial resolution is somewhat poorer than in standard broadband and narrowband images (or even in Fabry-Pérot ones), it should be noted that each spaxel —which is the

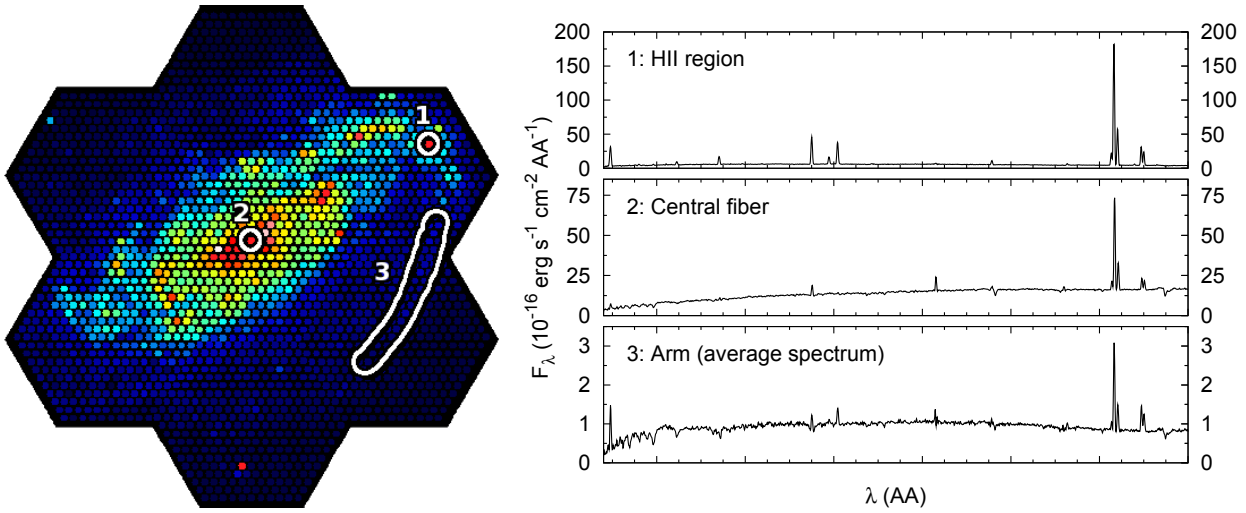

Figure 7.3: Sample PPAK spectra extracted from selected zones in NGC 4654: a bright HII region (1), the central f ber (2) and part of one of the spiral arms (3).

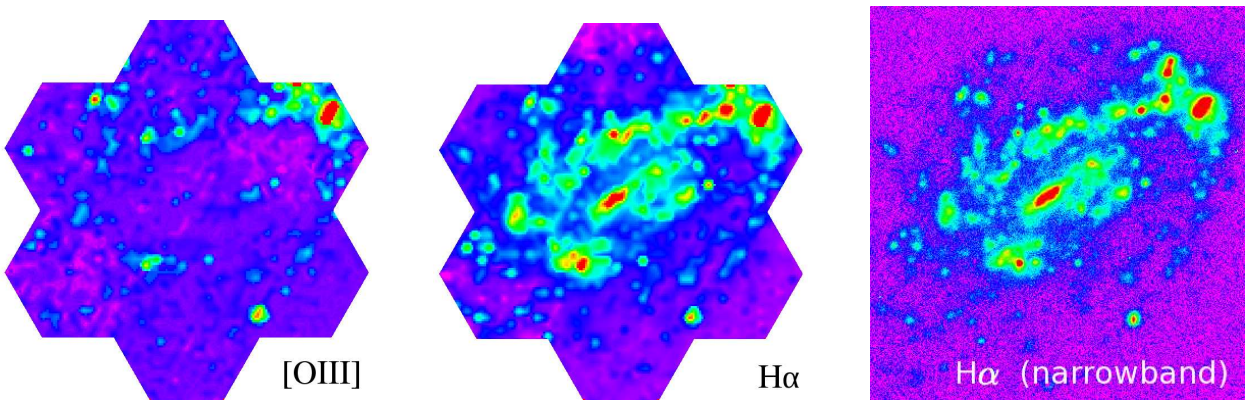

Figure 7.4: Left: [OIII] 5007 map. Middle: Hα map. Right: conventional narrowband Hα image retrieved from the GOLDMine database (Gavazzi et al. 2003). The maps and the narrowband image are continuum-subtracted.

usual name given to IFU pixels– contains a whole spectra, rather than just a single photometric measurement as in conventional images. Therefore, the incredible amount of physical information that can be obtained from each individual spaxel is worth the small loss in spatial resolution.

As an example, in Fig. 7.3 we present some sample spectra of different regions within the galaxy: a bright star-forming complex north-west of the main disk, the nucleus of the galaxy and the faint spiral arm extending south-west. In Fig. 7.4 we plot two continuum-subtracted maps, one at Hα and another one at 5007 Å showing the emission of the [OIII] forbidden line. The Hα map closely resembles the narrowband Hα image shown in that f gure, demonstrating the capability of our data to resolve and detect even faint regions.

As mentioned above, these IFU data will be combined with images at different wavelengths, in order to better describe the two-dimensional distribution of stars of different ages, dust and gas in this and the remaining galaxies in our sample. The possible topics that can be investigated with such a dataset are manifold. In the particular case of NGC 4654, this galaxy is known to be moving north-west into the Virgo cluster. As a result from the interaction with the intracluster

medium, ram pressure stripping is removing gas out of the main disk, as clearly shown by HI maps (Phookun & Mundy 1995). Therefore, it will be interesting to look for any evidence of star formation quenching along the movement direction. We are currently carrying out the analysis of this dataset and the results will be soon published in Muñoz-Mateos et al. (2010b).

A

Additional graphical material

In this appendix we provide multi-wavelength images of all SINGS galaxies, together with additional plots showing the multi-wavelength profiles and the fits to the models of Draine & Li (2007) and Boissier & Prantzos (2000). The material presented here is thus intended to complement the discussion presented in chapters 3, 4 and 5.

A.1 Multi-wavelength images

For each SINGS galaxy we show 12 images at selected wavelengths: the two GALEX bands (FUV and NUV), four optical bands (either the $ugri$ ones from the SDSS or the original $BVRI$ images from SINGS when the former were not available), the three 2MASS bands (J, H and K_S), the IRAC 3.6 μm and 8.0 μm bands and the MIPS 24 μm one.

The images are displayed following the stretch method proposed by Jarrett et al. (2003):

$$P' = \sqrt{\log[1 + P/(n\sigma)]} \tag{A.1}$$

where P and P' are the original and final pixel values, σ is the local background noise and n is a threshold throttle which we fix at $n = 10$. This stretching algorithm boosts the intensity of low-S/N pixels while reducing the overall dynamic range spanned by bright and faint pixels. This allows displaying faint and diffuse structures while preventing the brightest ones from being saturated.

A.2 Multi-wavelength radial profiles

Next to the images we show the multi-wavelength surface brightness profiles of each galaxy. They were measured on the original images at their native resolution, with a radial step of $6''$. The profiles have been shifted for displaying purposes; the corresponding offsets in magnitudes are quoted next to each label. The profiles are arranged in order of decreasing wavelength, from top to bottom, as shown by the labels. For the sake of clarity, black and gray lines are used to group both the profiles and their labels according to their wavelength range (GALEX, optical, 2MASS, IRAC and MIPS, respectively). Note that the optical profiles of the original $BVRI$ SINGS images are not displayed (even if the images themselves are) in the few cases where we could not properly recalibrate the photometric zero-point, as explained in chapter 3.

Errorbars are not shown for clarity. The solid profiles have been truncated when $\Delta\mu > 0.3$ mag, and then continue with dashed lines until $\Delta\mu > 1$ mag. Note that the large uncertainties

in the outermost spatial regions (i.e. those marked with dashed lines) are mostly due to large-scale errors in the background estimation, but do not necessarily imply non-detections. Emission from the galaxy can be clearly seen in these regions above the local noise, although large-scale background variations preclude a more reliable determination of the azimuthally-averaged flux density along these outer isophotes.

A.3 Radial profiles of dust properties

For those galaxies analyzed in chapter 4 with the dust models of Draine & Li (2007), we also display the radial distribution of the dust properties resulting from the fitting. The different lines show the best-fitting values at each radius, and the gray bands show the estimated uncertainties.

(a) Fraction of the dust mass in the form of PAHs. Regions in which the stellar emission at 8 μm is more than twice the one from PAHs are marked (when present) with a dotted line instead of a solid one. The FWHM of the MIPS 160 μm band (38″) is marked with an horizontal segment along the major axis.

(b) Fraction γ of the total dust mass heated by very intense starlight. The right vertical axis shows the fraction of the dust luminosity contributed by regions exposed to radiation fields with $U > U_{\rm min}$ and $U > 10^2$ (their errors are not shown for clarity).

(c) Scale factor of the minimum ($U_{\rm min}$) and average ($\langle U \rangle$) starlight intensity heating the dust, in units of the local MW radiation field. The errors of $\langle U \rangle$ are not shown.

(d) Dust mass (left y-axis) and luminosity (right y-axis) surface densities, both corrected for inclination. The open circles show the dust luminosity profiles obtained with the photometric estimator of DL07.

A.4 Fits of the IR SEDs with the dust models

Below the radial profiles of dust properties, we plot the observed IR SEDs at different galactocentric distances, without correcting for inclination, together with the best-fitting model in each case. The observed flux densities are marked with rectangular boxes, their width showing the corresponding bandpass and their height showing the observational errors. The best-fitting model spectra (solid line) results from the combination of a diffuse component (dashed line), the emission from hot dust (dash-dotted line) and the stellar emission (dotted line). The filled circles correspond to the model spectra convolved with each bandpass.

A.5 Fits of the radial profiles with the disk evolution models

For those spiral galaxies studied in chapter 5, we provide the models of Boissier & Prantzos (2000) that best fit the multi-wavelength radial profiles. For each galaxy we show two different fits, using the IMFs of Kroupa et al. (1993) and Kroupa (2001), as indicated on top of each set of panels. We

also quote the best-fitting values of the circular velocity $V_{\rm C}$ and the spin parameter λ, together with their estimated uncertainties, determined by all models with $\chi^2 \leq 2\chi^2_{\rm min}$.

The gray points show the observed profiles, corrected only for Milky way extinction, while the black ones also include a correction for the radial variation of internal extinction. Both profiles have been deprojected to their face-on values using the galaxy's morphological axis ratio. In each panel, the radius along the semimajor axis is expressed both in arcseconds (top x axis) and in kpc (bottom x axis). The fit is applied to those points in the extinction-corrected profiles between the vertical dashed lines. The red dashed line excludes the bulge, and the blue one the outermost regions, in the few cases where severe up-bendings are present. The red curve corresponds to the best-fitting model, and the background band contains all models with $\chi^2 \leq 2\chi^2_{\rm min}$.

NGC 0024
FUV
NUV
B
V
R
I
J
H
K
3.6 um
8.0 um
24 um
2 kpc

r (kpc)
NGC 0024
160 μm – 14.5 mag
70 μm – 13.5 mag
24 μm – 15 mag
8.0 μm – 13 mag
5.8 μm – 12 mag
4.5 μm – 10.5 mag
3.6 μm – 8.5 mag
K_S – 6.5 mag
H – 5 mag
J – 4 mag
I – 2.5 mag
R – 2 mag
V – 1 mag
B – 0.5 mag
NUV – 1 mag
FUV
μ (AB mag/arcsec²)
log F_ν (Jy/arcsec²)
r (arcsec)

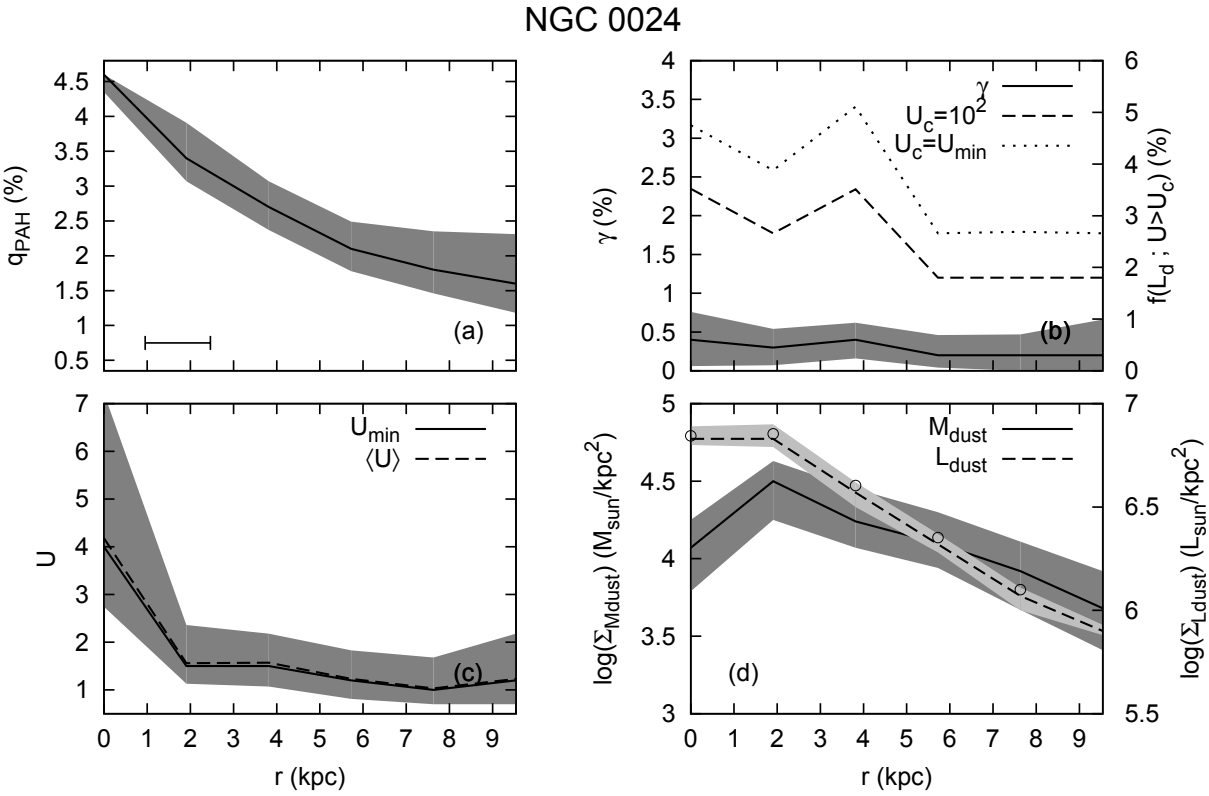
NGC 0024
q_{PAH} (%)
(a)
γ (%)
$f(L_d ; U>U_c)$ (%)
γ
$U_c=10^2$
$U_c=U_{min}$
(b)
U
U_{min}
⟨U⟩
(c)
r (kpc)
$\log(\Sigma_{Mdust})$ (M_{sun}/kpc^2)
$\log(\Sigma_{Ldust})$ (L_{sun}/kpc^2)
M_{dust}
L_{dust}
(d)
r (kpc)

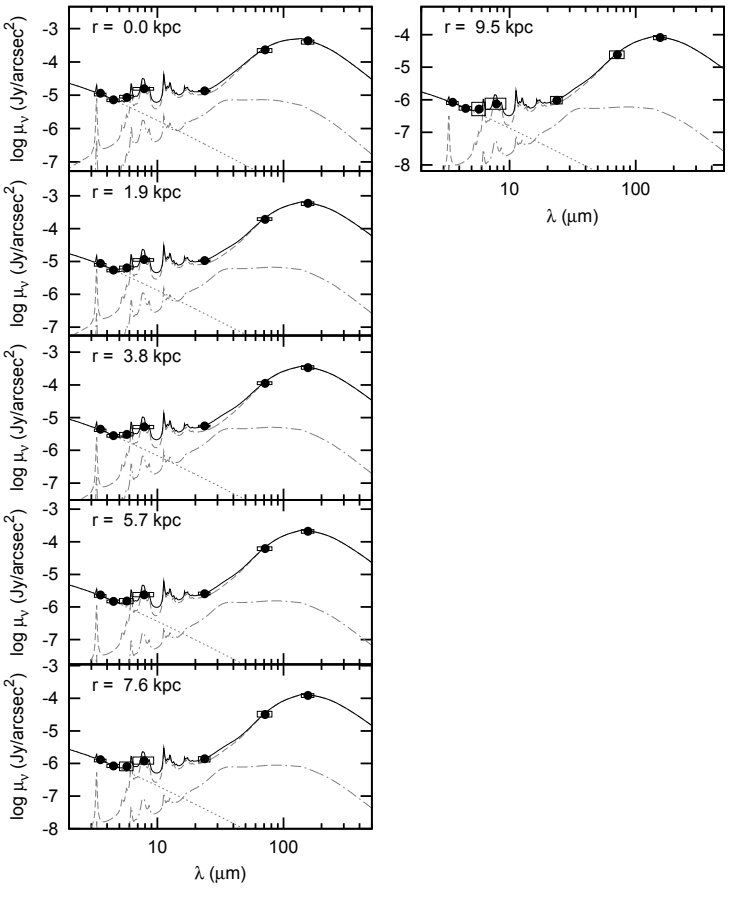
r = 0.0 kpc
r = 1.9 kpc
r = 3.8 kpc
r = 5.7 kpc
r = 7.6 kpc
r = 9.5 kpc
log μ_ν (Jy/arcsec^2)
λ (μm)

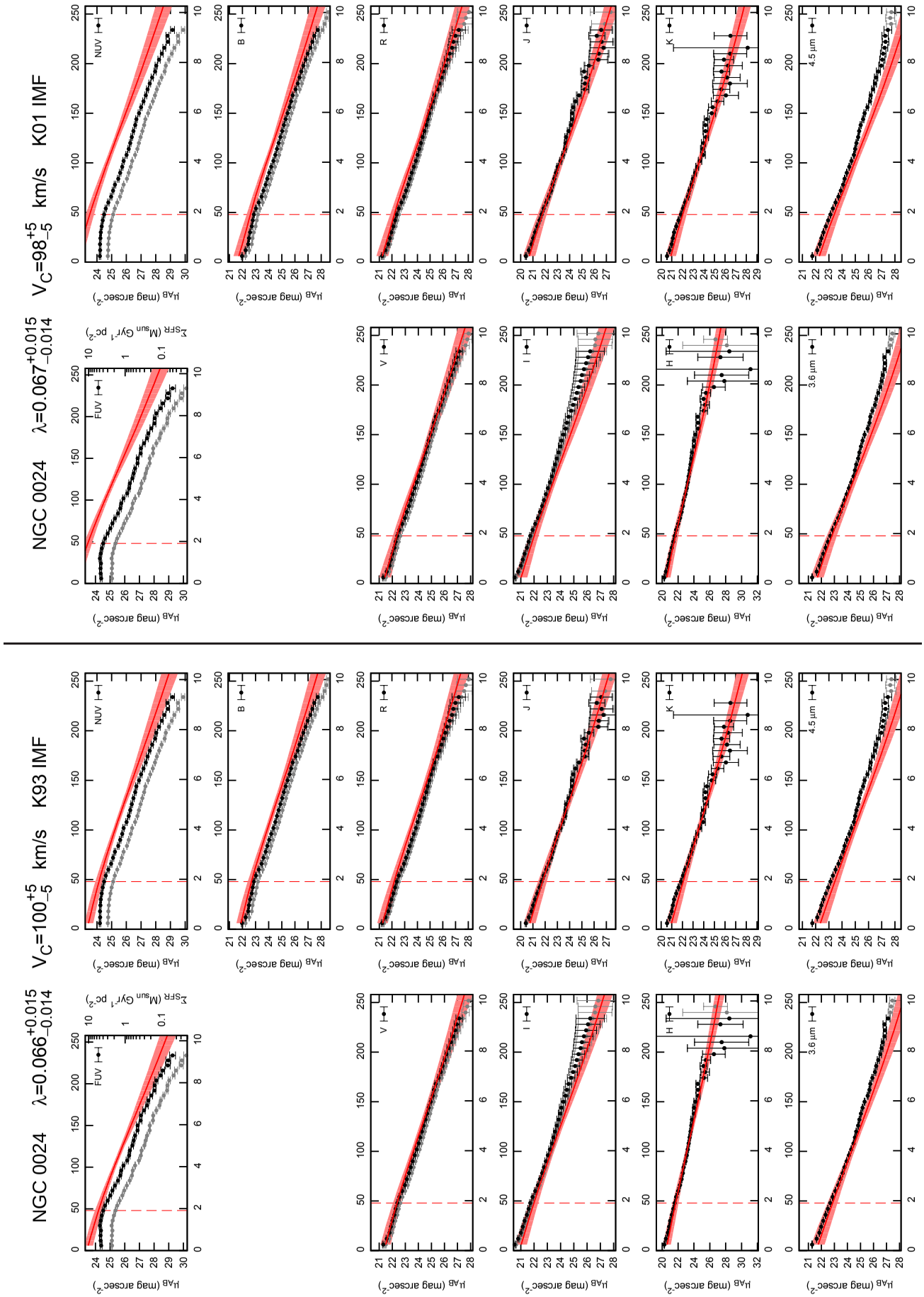
NGC 0024 λ=0.067+0.015−0.014 VC=98+5−5 km/s K01 IMF
NGC 0024 λ=0.066+0.015−0.014 VC=100+5−5 km/s K93 IMF
NUV
FUV
B
V
R
I
J
H
K
3.6 μm
4.5 μm
μAB (mag arcsec-2)
ΣSFR (Msun Gyr-1 pc-2)

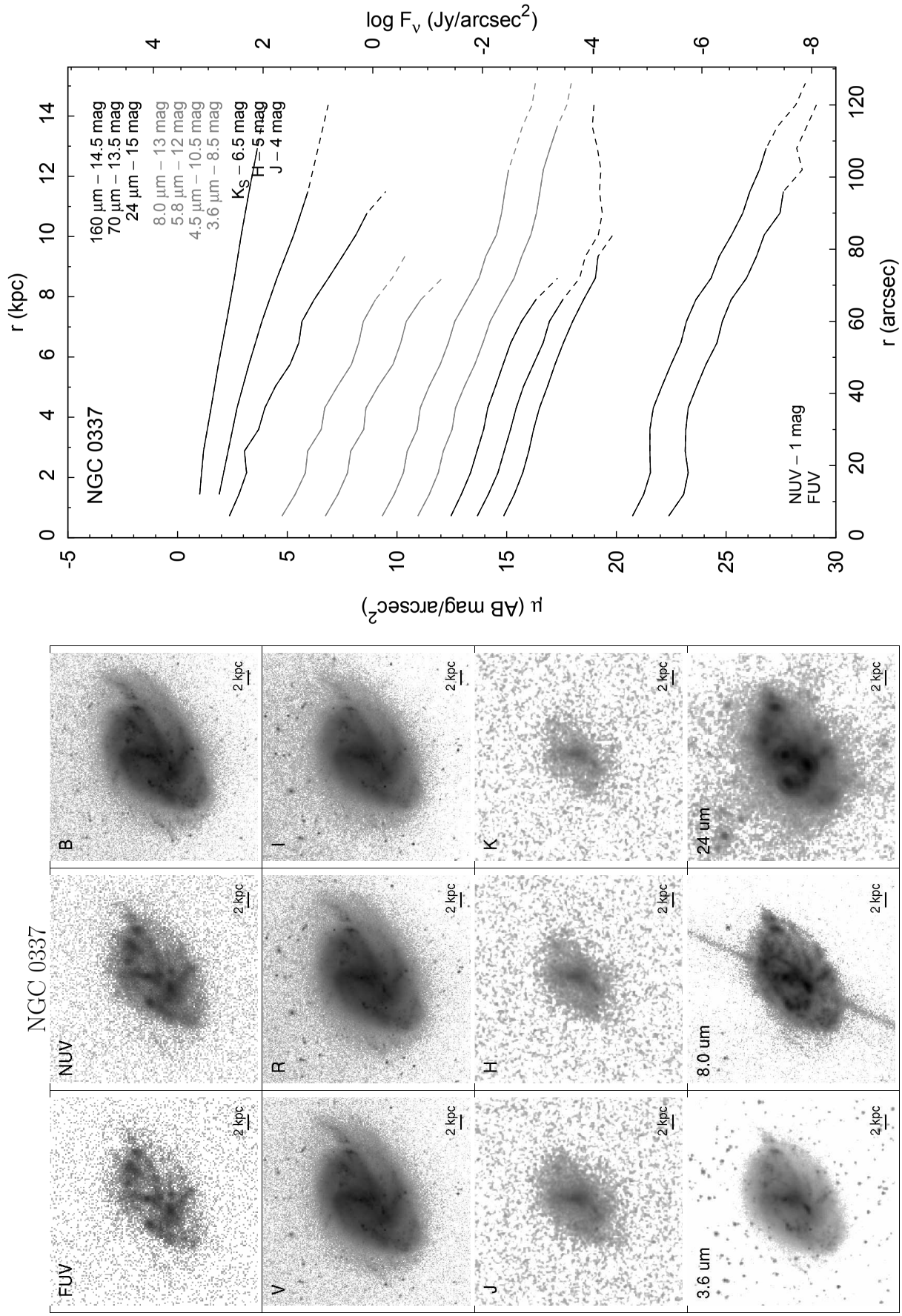
NGC 0337
FUV
NUV
B
V
R
I
J
H
K
3.6 um
8.0 um
24 um
2 kpc
μ (AB mag/arcsec²)
log F_ν (Jy/arcsec²)
r (kpc)
r (arcsec)
NGC 0337
160 μm – 14.5 mag
70 μm – 13.5 mag
24 μm – 15 mag
8.0 μm – 13 mag
5.8 μm – 12 mag
4.5 μm – 10.5 mag
3.6 μm – 8.5 mag
K_S – 6.5 mag
H – 5 mag
J – 4 mag
NUV – 1 mag
FUV

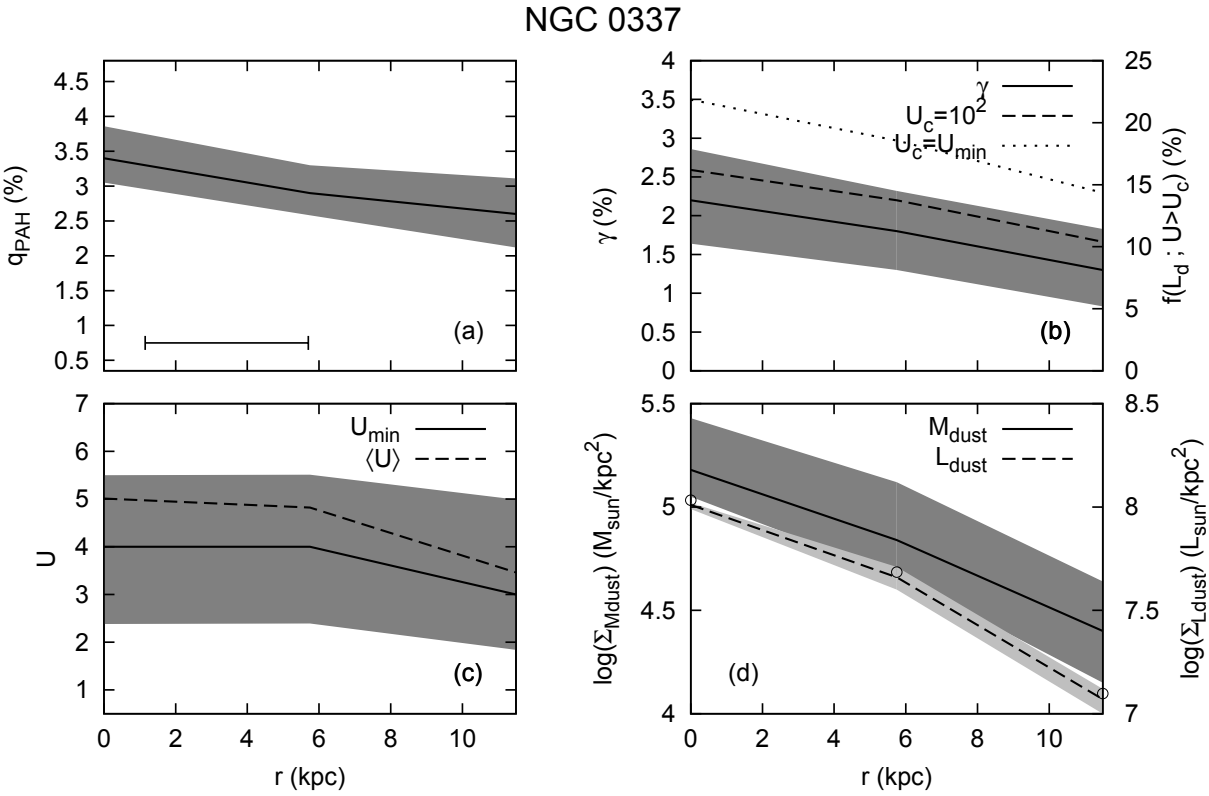
NGC 0337
q_{PAH} (%)
(a)
γ (%)
$U_c=10^2$
$U_c=U_{min}$
$f(L_d ; U>U_c)$ (%)
(b)
U
U_{min}
⟨U⟩
(c)
r (kpc)
$\log(\Sigma_{Mdust})$ (M_{sun}/kpc^2)
M_{dust}
L_{dust}
$\log(\Sigma_{Ldust})$ (L_{sun}/kpc^2)
(d)
r (kpc)

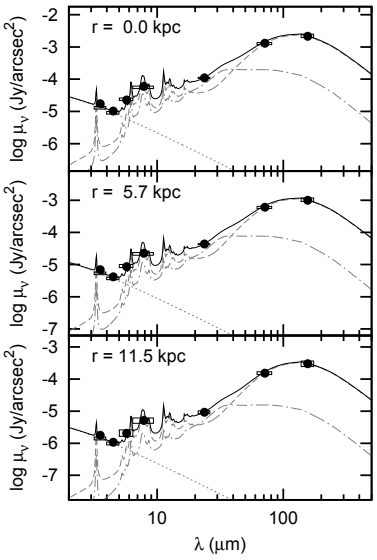
r = 0.0 kpc
r = 5.7 kpc
r = 11.5 kpc
log μ_ν (Jy/arcsec^2)
λ (μm)

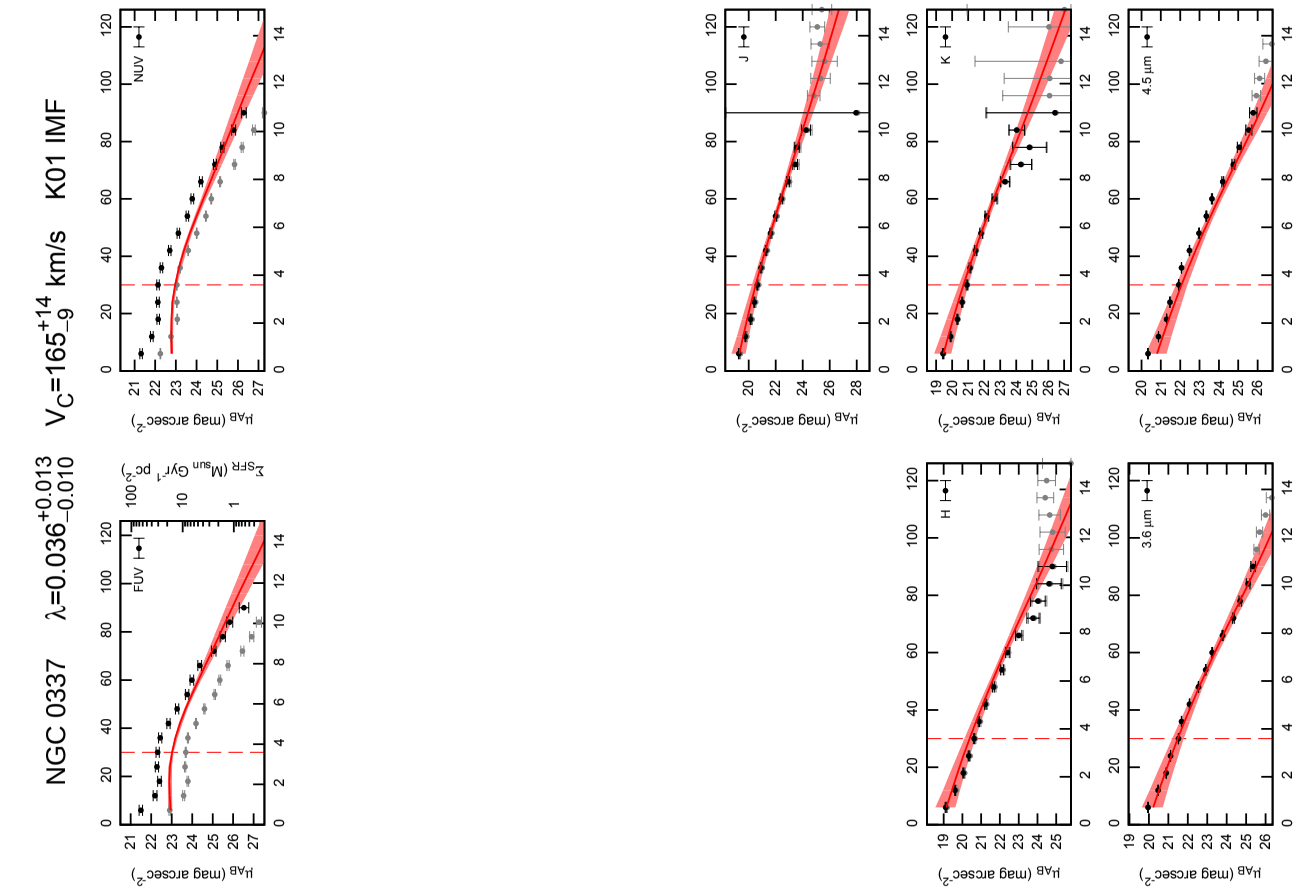
NGC 0337 λ=0.036+0.013−0.010 VC=165+14−9 km/s K01 IMF
NUV
FUV
J
K
H
4.5 μm
3.6 μm
μAB (mag arcsec-2)
ΣSFR (Msun Gyr-1 pc-2)

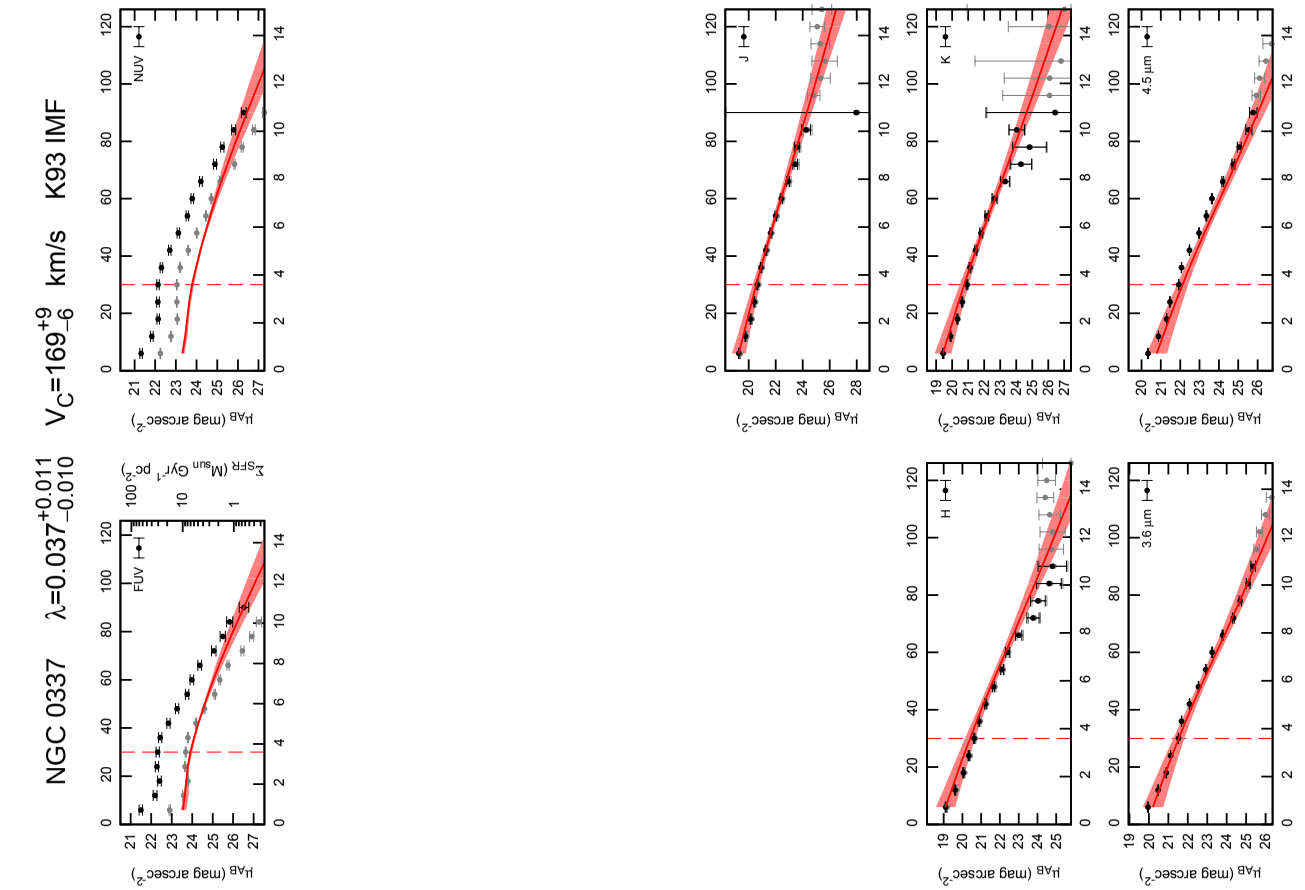
NGC 0337 λ=0.037+0.011−0.010 VC=169+9−6 km/s K93 IMF
NUV
FUV
J
K
H
4.5 μm
3.6 μm
μAB (mag arcsec-2)
ΣSFR (Msun Gyr-1 pc-2)

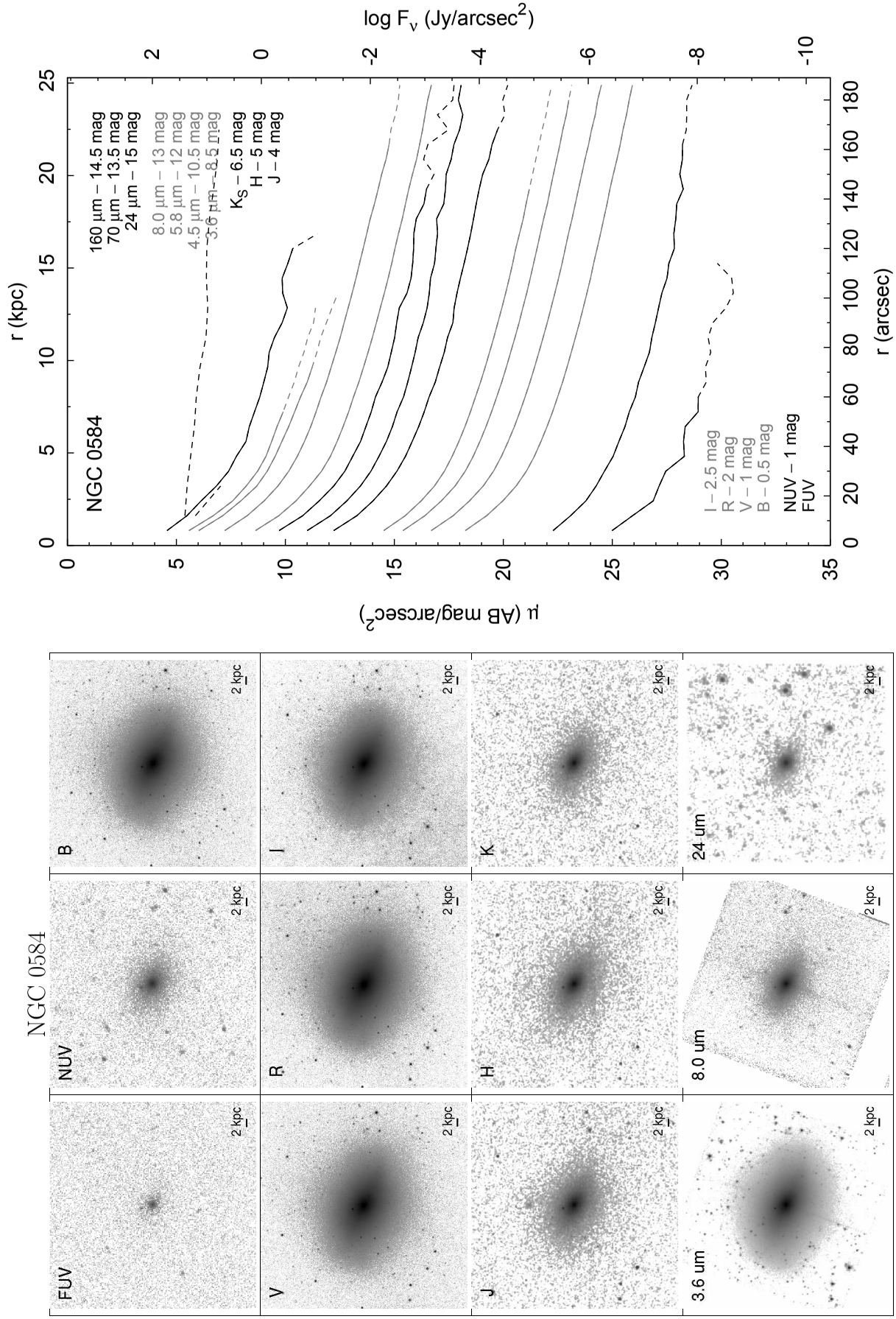
NGC 0584
FUV
NUV
B
V
R
I
J
H
K
3.6 um
8.0 um
24 um
2 kpc
r (kpc)
r (arcsec)
μ (AB mag/arcsec²)
log F_ν (Jy/arcsec²)
NGC 0584
160 μm – 14.5 mag
70 μm – 13.5 mag
24 μm – 15 mag
8.0 μm – 13 mag
5.8 μm – 12 mag
4.5 μm – 10.5 mag
3.6 μm – 8.5 mag
K_S – 6.5 mag
H – 5 mag
J – 4 mag
I – 2.5 mag
R – 2 mag
V – 1 mag
B – 0.5 mag
NUV – 1 mag
FUV

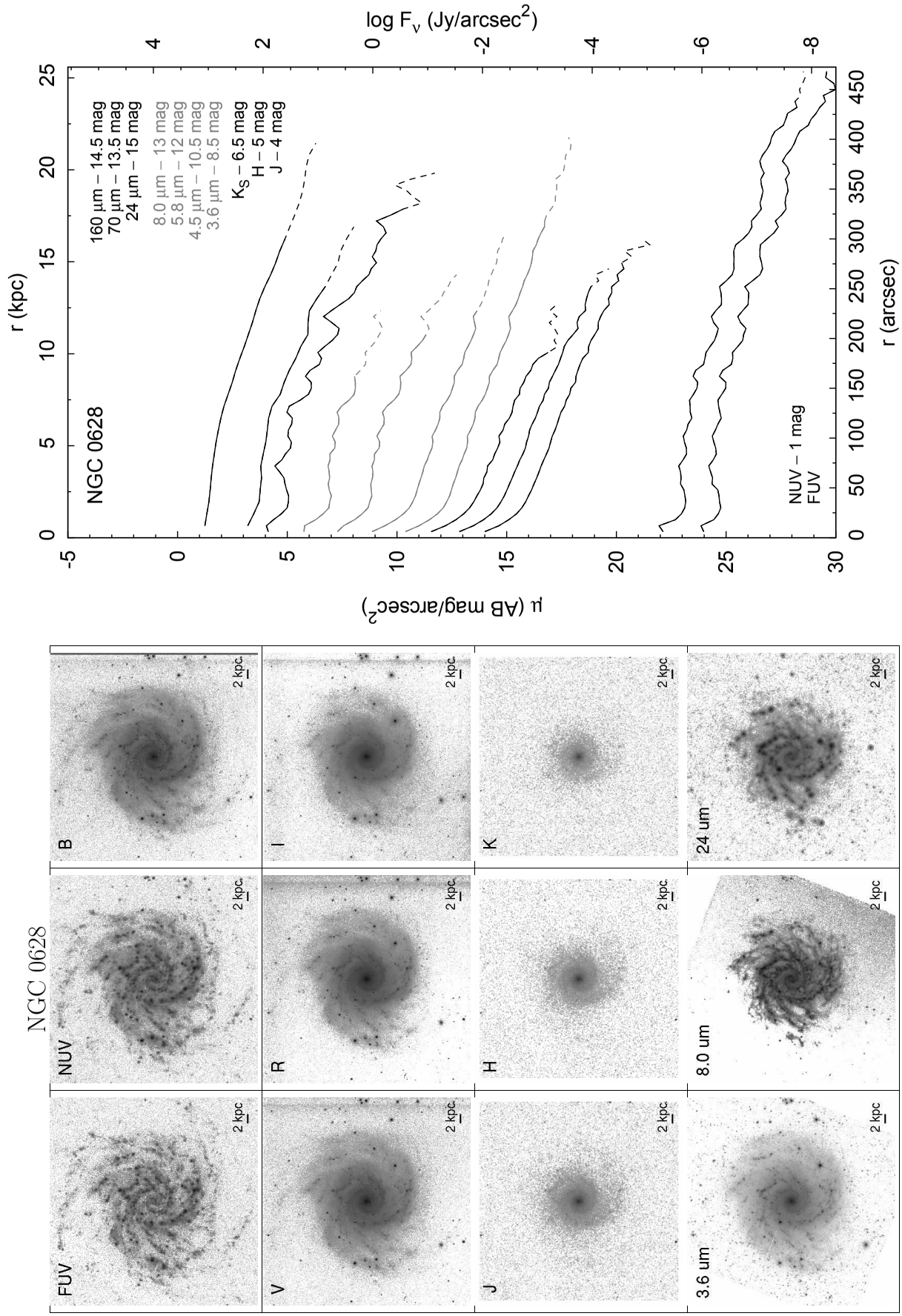
NGC 0628
FUV
NUV
B
V
R
I
J
H
K
3.6 um
8.0 um
24 um
2 kpc
μ (AB mag/arcsec²)
log F_ν (Jy/arcsec²)
r (kpc)
r (arcsec)
NGC 0628
160 μm – 14.5 mag
70 μm – 13.5 mag
24 μm – 15 mag
8.0 μm – 13 mag
5.8 μm – 12 mag
4.5 μm – 10.5 mag
3.6 μm – 8.5 mag
K_S – 6.5 mag
H – 5 mag
J – 4 mag
NUV – 1 mag
FUV

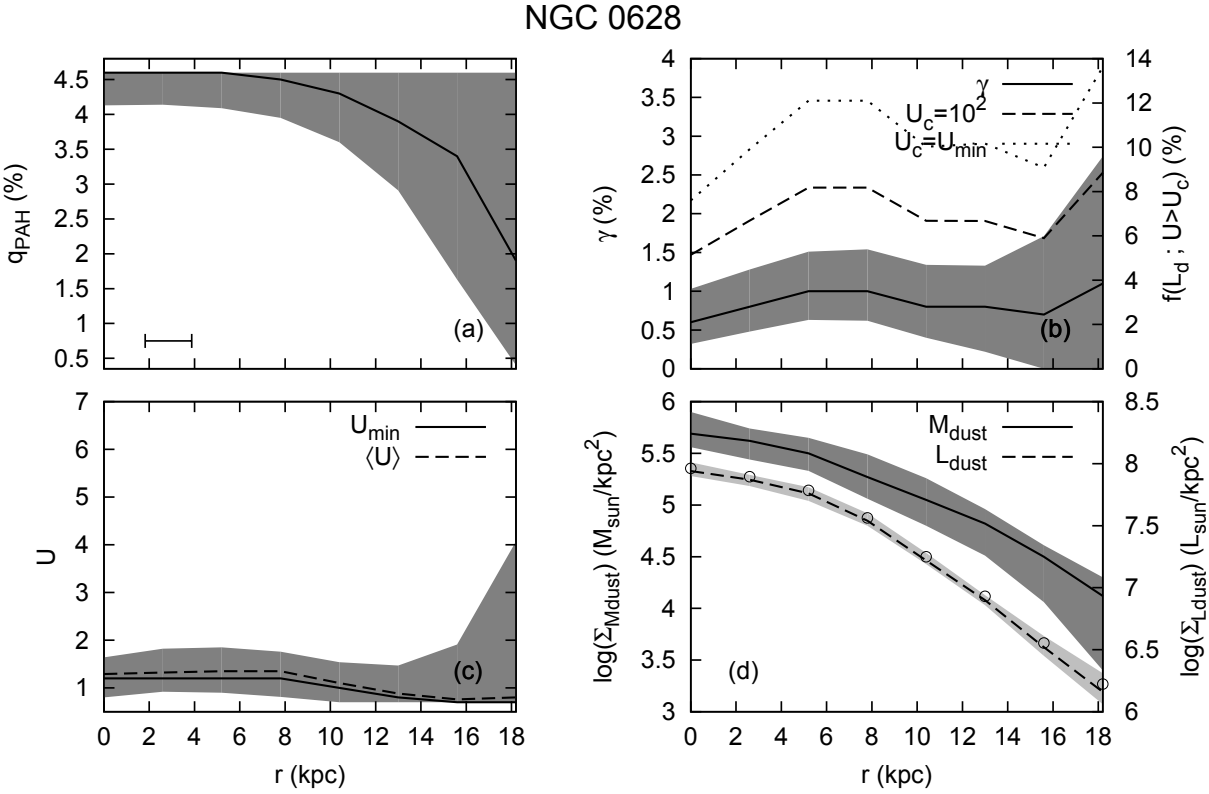
NGC 0628
q_{PAH} (%)
(a)
γ (%)
$U_c=10^2$
$U_c=U_{min}$
$f(L_d ; U>U_c)$ (%)
(b)
U
U_{min}
⟨U⟩
(c)
r (kpc)
$\log(\Sigma_{Mdust})$ (M_{sun}/kpc^2)
M_{dust}
L_{dust}
$\log(\Sigma_{Ldust})$ (L_{sun}/kpc^2)
(d)
r (kpc)

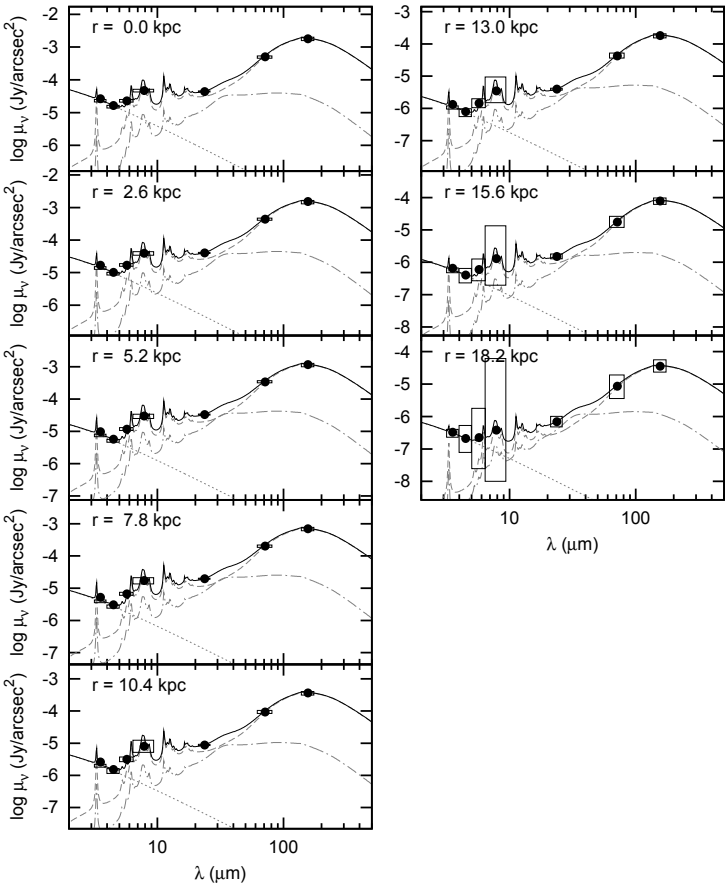
r = 0.0 kpc
r = 2.6 kpc
r = 5.2 kpc
r = 7.8 kpc
r = 10.4 kpc
r = 13.0 kpc
r = 15.6 kpc
r = 18.2 kpc
log μν (Jy/arcsec²)
λ (μm)

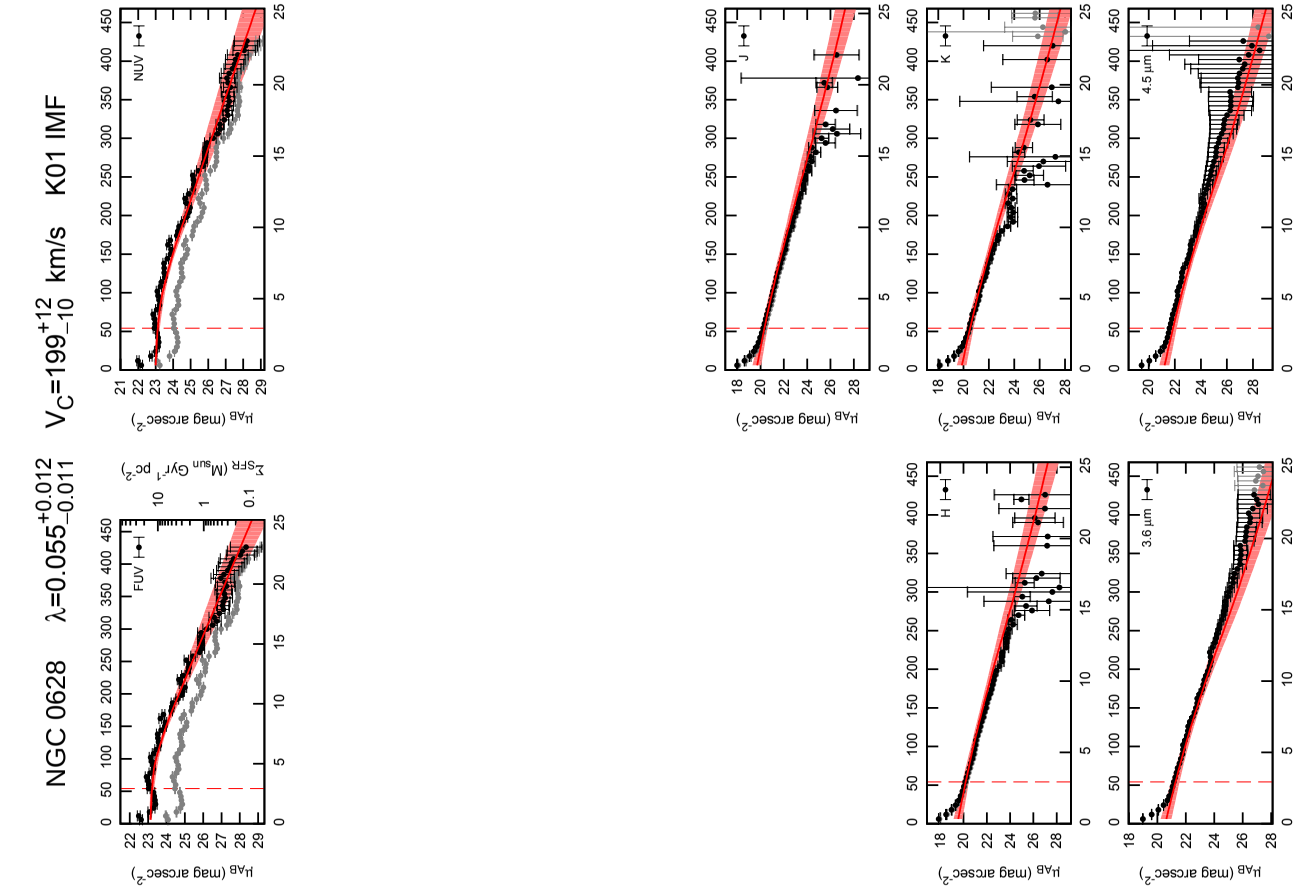
NGC 0628 λ=0.055+0.012−0.011 VC=199+12−10 km/s K01 IMF
NUV
FUV
J
K
H
4.5 μm
3.6 μm
μAB (mag arcsec-2)
ΣSFR (Msun Gyr-1 pc-2)

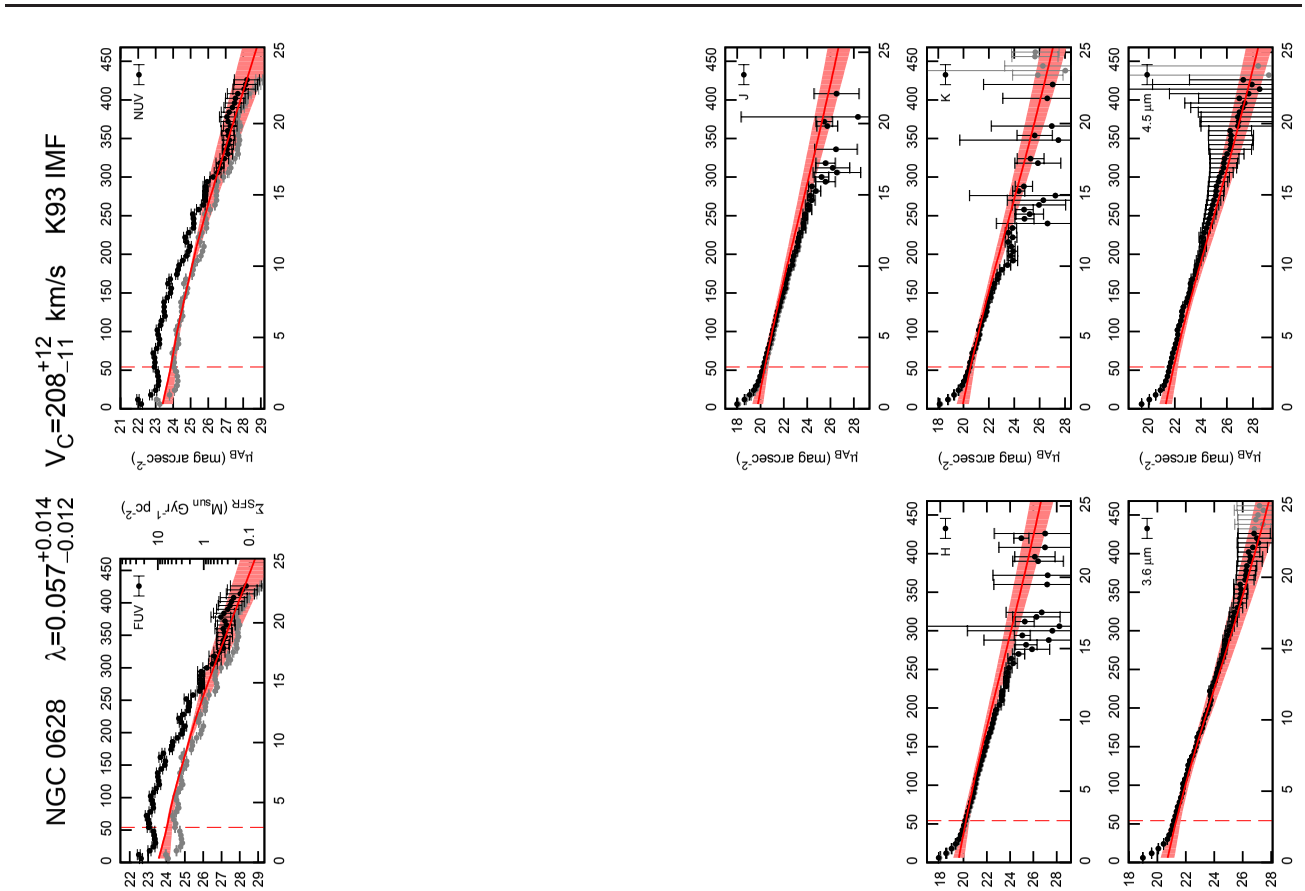
NGC 0628 λ=0.057+0.014−0.012 VC=208+12−11 km/s K93 IMF
NUV
FUV
J
K
H
4.5 μm
3.6 μm
μAB (mag arcsec-2)
ΣSFR (Msun Gyr-1 pc-2)

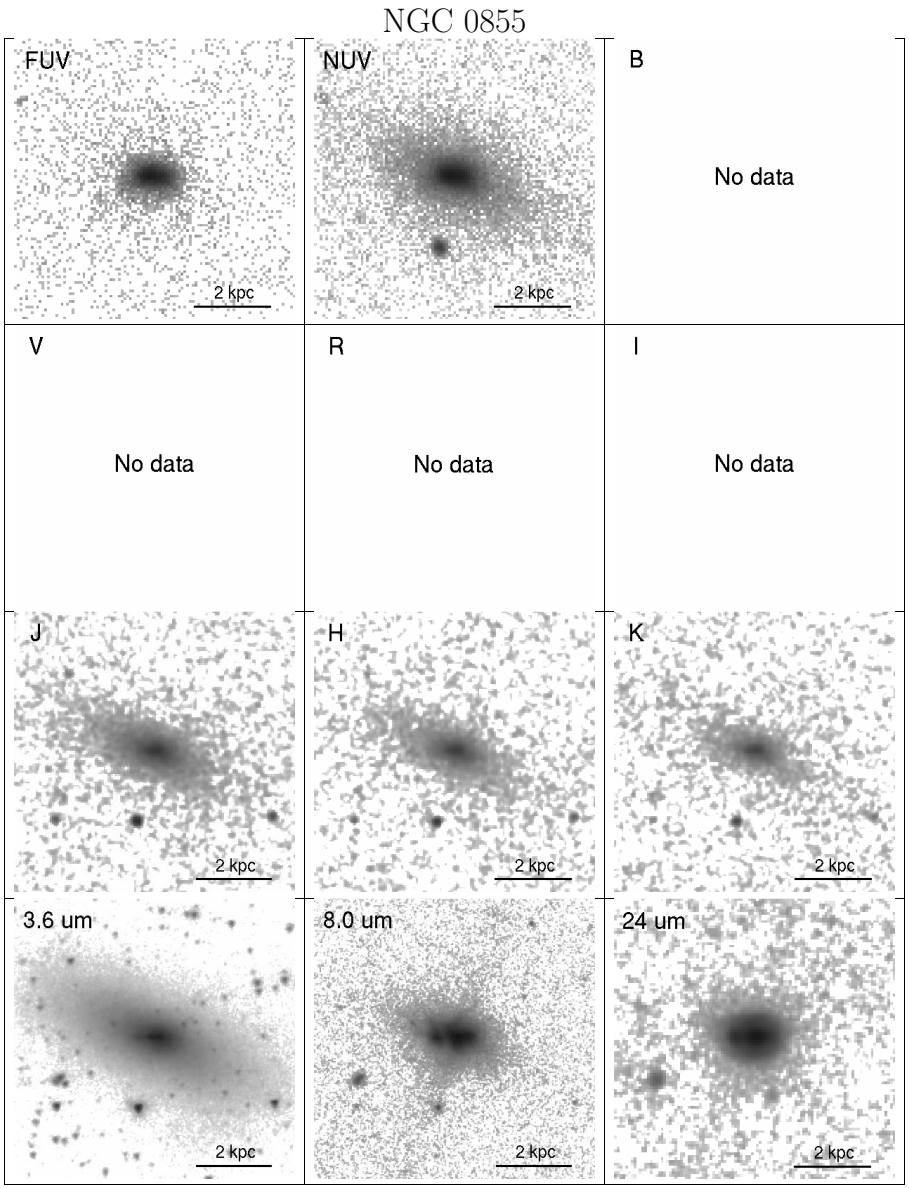
NGC 0855
FUV
NUV
B
No data
2 kpc
V
R
I
No data
No data
No data
J
H
K
3.6 um
8.0 um
24 um

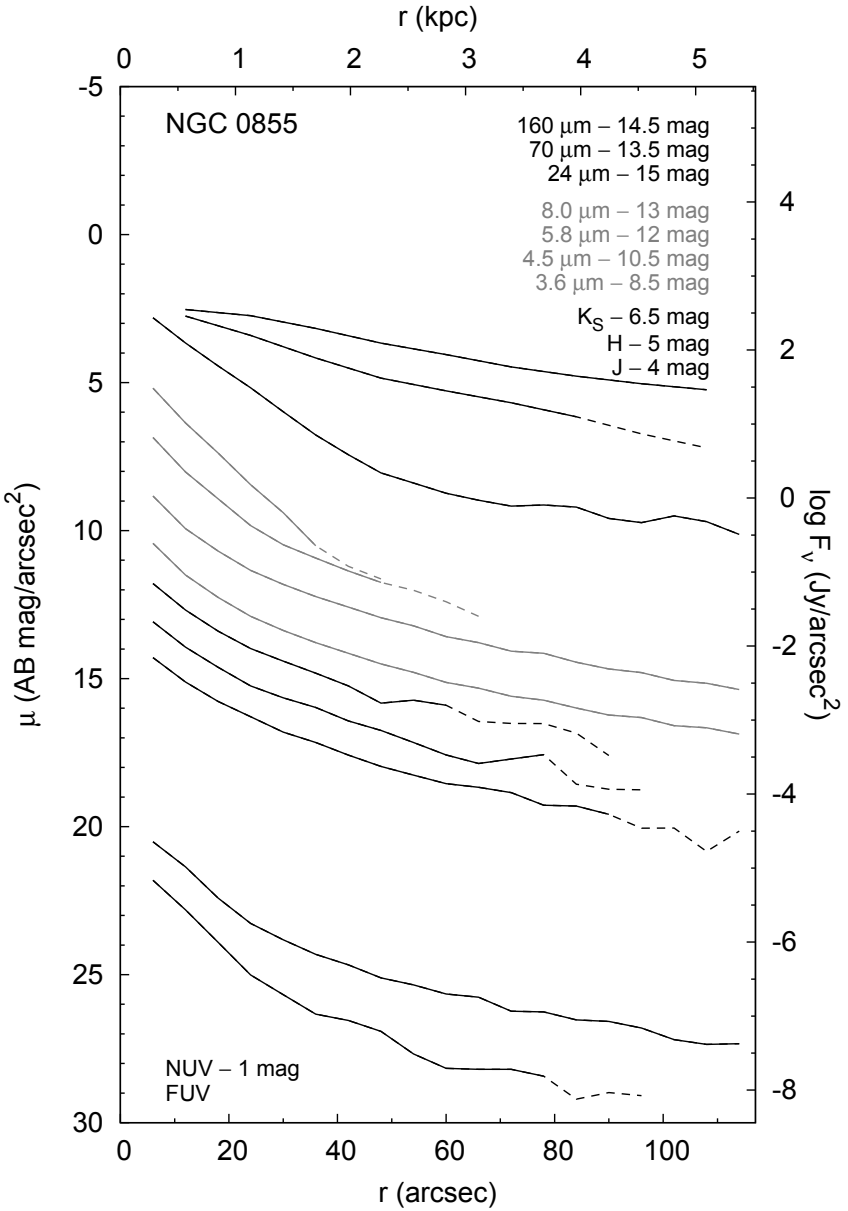
r (kpc)
NGC 0855
160 μm – 14.5 mag
70 μm – 13.5 mag
24 μm – 15 mag
8.0 μm – 13 mag
5.8 μm – 12 mag
4.5 μm – 10.5 mag
3.6 μm – 8.5 mag
K_S – 6.5 mag
H – 5 mag
J – 4 mag
NUV – 1 mag
FUV
μ (AB mag/arcsec²)
log F_ν (Jy/arcsec²)
r (arcsec)

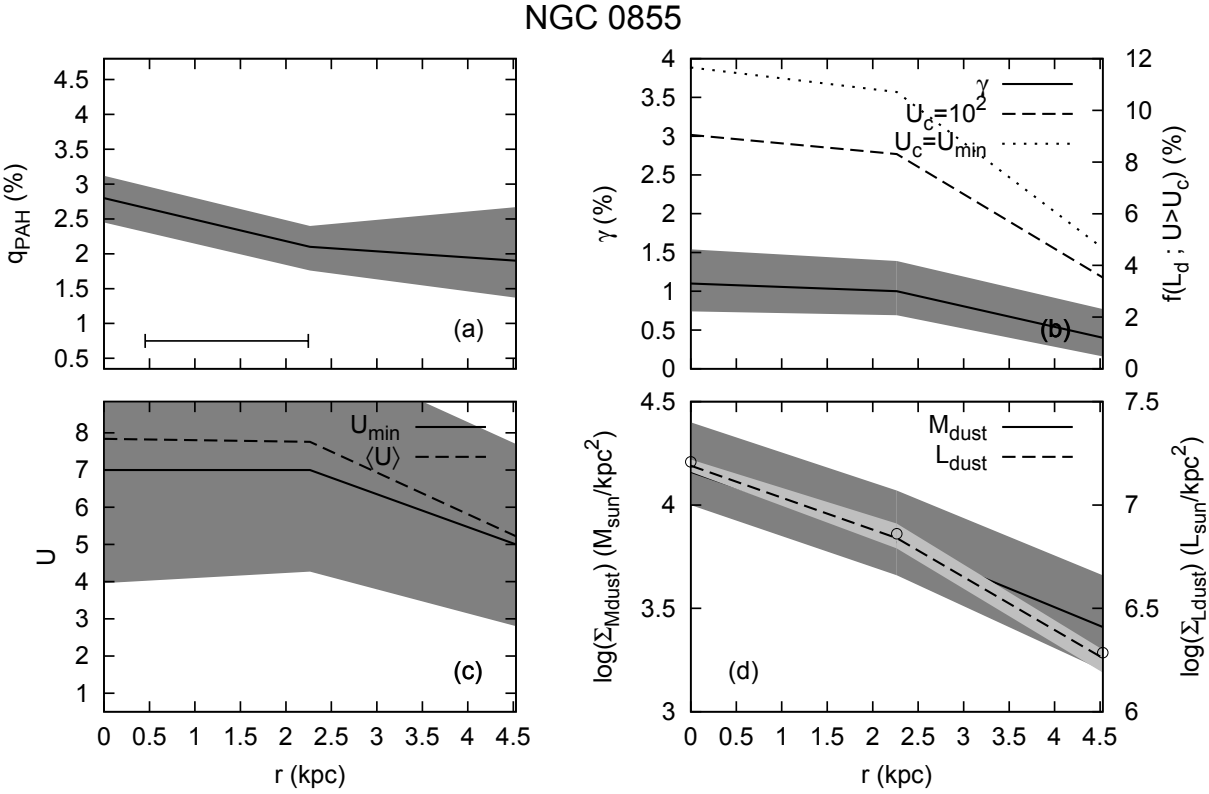
NGC 0855
q_{PAH} (%)
(a)
γ (%)
$U_c=10^2$
$U_c=U_{min}$
$f(L_d ; U>U_c)$ (%)
(b)
U
U_{min}
⟨U⟩
(c)
r (kpc)
$\log(\Sigma_{Mdust})$ (M_{sun}/kpc^2)
M_{dust}
L_{dust}
$\log(\Sigma_{Ldust})$ (L_{sun}/kpc^2)
(d)
r (kpc)

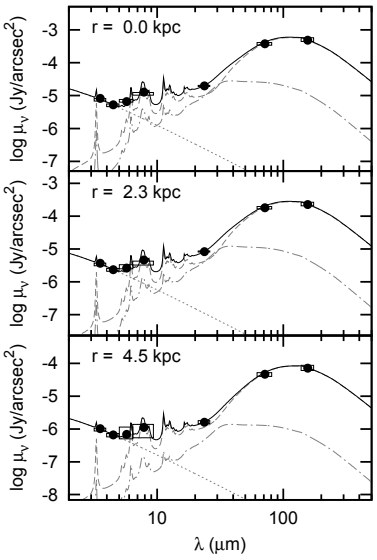
r = 0.0 kpc
r = 2.3 kpc
r = 4.5 kpc
log μ_ν (Jy/arcsec^2)
λ (μm)

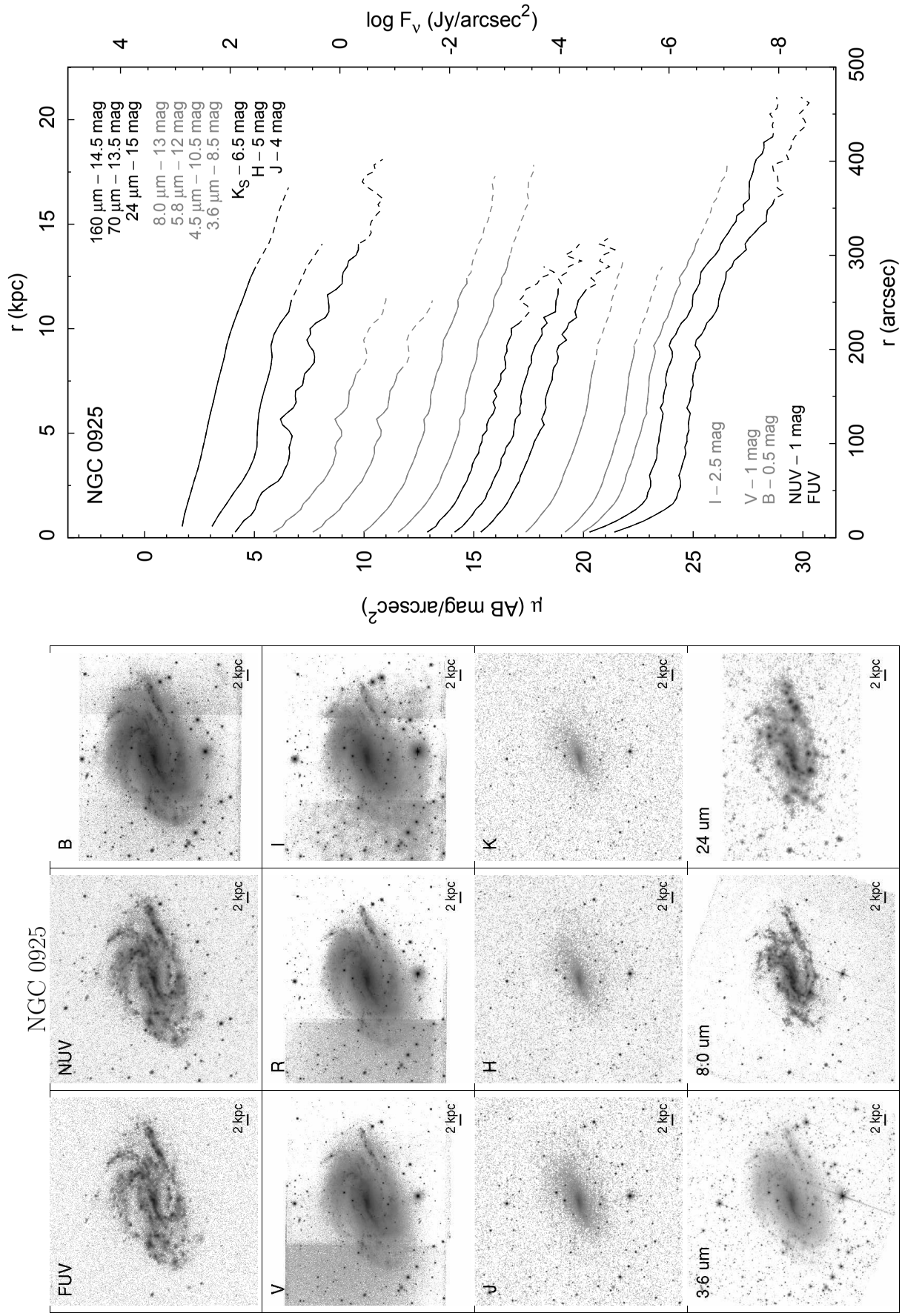
NGC 0925
FUV
NUV
B
V
R
I
J
H
K
3.6 um
8.0 um
24 um
2 kpc
μ (AB mag/arcsec²)
r (kpc)
r (arcsec)
log F_ν (Jy/arcsec²)
NGC 0925
160 μm – 14.5 mag
70 μm – 13.5 mag
24 μm – 15 mag
8.0 μm – 13 mag
5.8 μm – 12 mag
4.5 μm – 10.5 mag
3.6 μm – 8.5 mag
K_S – 6.5 mag
H – 5 mag
J – 4 mag
I – 2.5 mag
V – 1 mag
B – 0.5 mag
NUV – 1 mag
FUV

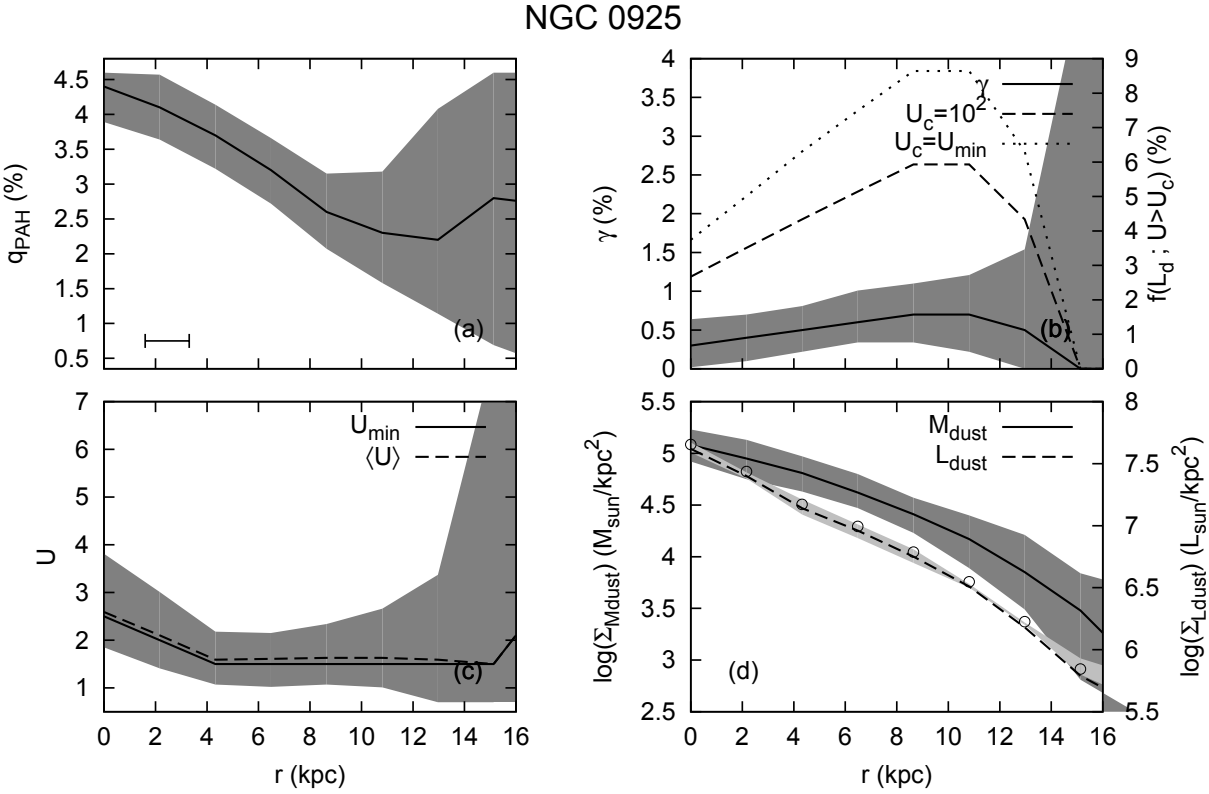
NGC 0925
q_{PAH} (%)
(a)
γ (%)
$f(L_d ; U>U_c)$ (%)
$U_c=10^2$
$U_c=U_{min}$
(b)
U
U_{min}
⟨U⟩
(c)
r (kpc)
$\log(\Sigma_{Mdust})$ (M_{sun}/kpc^2)
$\log(\Sigma_{Ldust})$ (L_{sun}/kpc^2)
M_{dust}
L_{dust}
(d)
r (kpc)

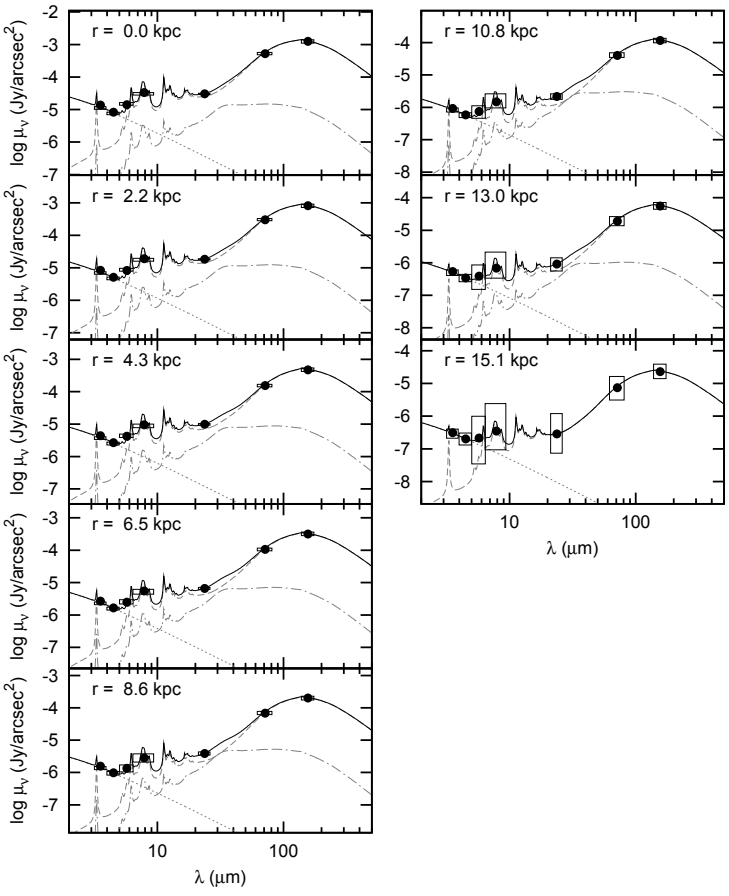
r = 0.0 kpc
r = 2.2 kpc
r = 4.3 kpc
r = 6.5 kpc
r = 8.6 kpc
r = 10.8 kpc
r = 13.0 kpc
r = 15.1 kpc
log μ_ν (Jy/arcsec^2)
λ (μm)

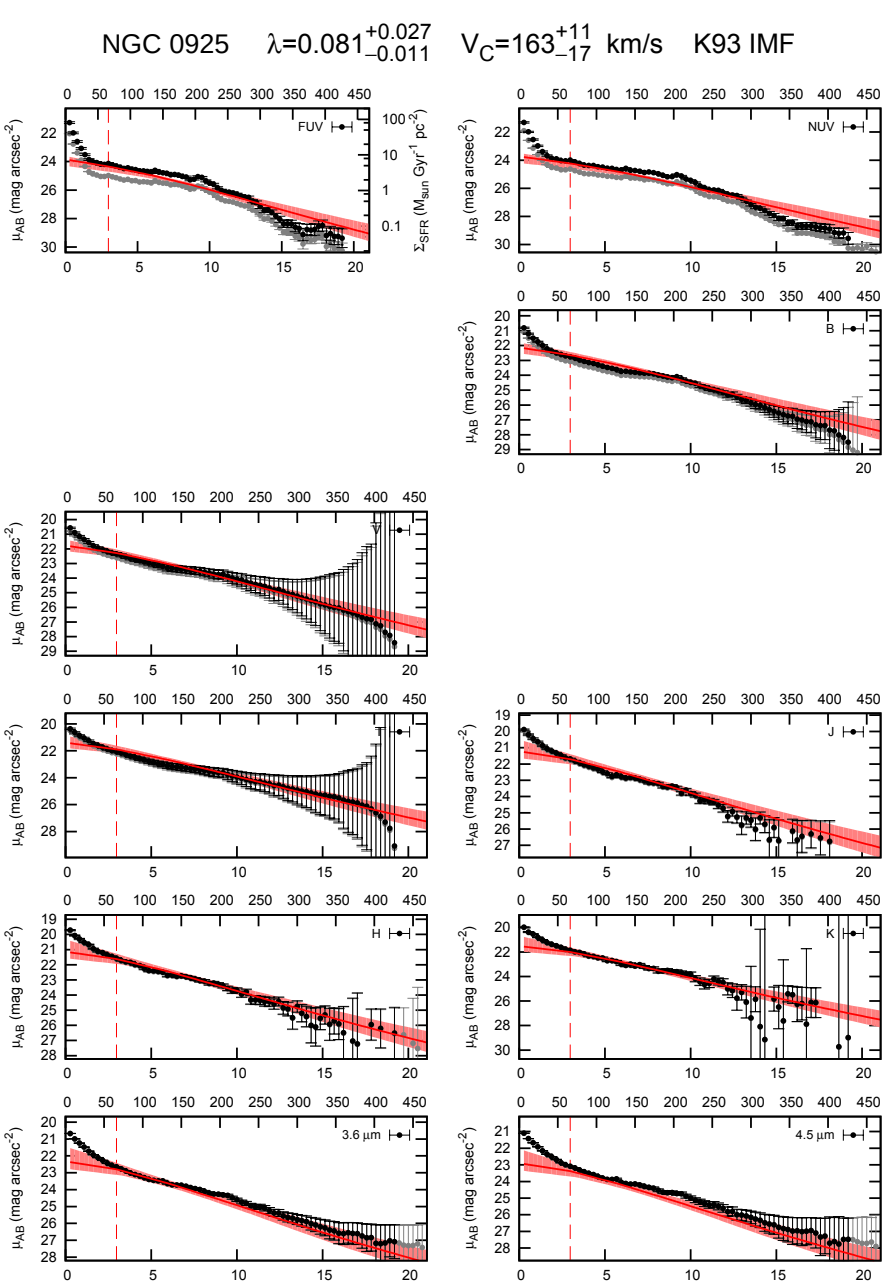
NGC 0925 λ=0.081+0.027−0.011 VC=163+11−17 km/s K93 IMF
NGC 0925 λ=0.095+0.020−0.016 VC=152+16−10 km/s K01 IMF
FUV
NUV
B
V
J
H
K
3.6 μm
4.5 μm
μAB (mag arcsec−2)
ΣSFR (Msun Gyr−1 pc−2)

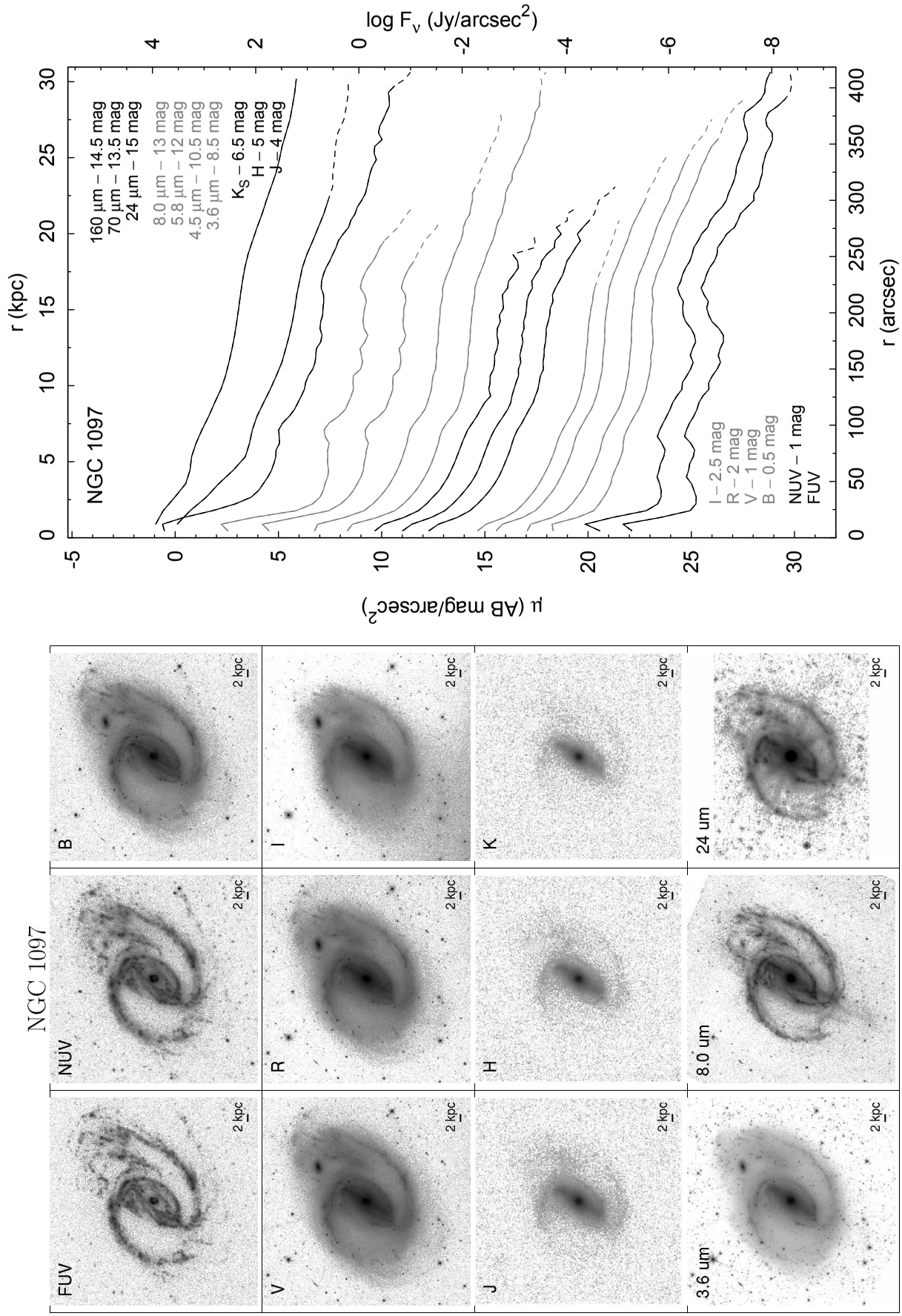
NGC 1097
FUV
NUV
B
V
R
I
J
H
K
3.6 um
8.0 um
24 um
2 kpc
μ (AB mag/arcsec²)
log F_ν (Jy/arcsec²)
r (kpc)
r (arcsec)
NGC 1097
160 μm – 14.5 mag
70 μm – 13.5 mag
24 μm – 15 mag
8.0 μm – 13 mag
5.8 μm – 12 mag
4.5 μm – 10.5 mag
3.6 μm – 8.5 mag
K_S – 6.5 mag
H – 5 mag
J – 4 mag
I – 2.5 mag
R – 2 mag
V – 1 mag
B – 0.5 mag
NUV – 1 mag
FUV

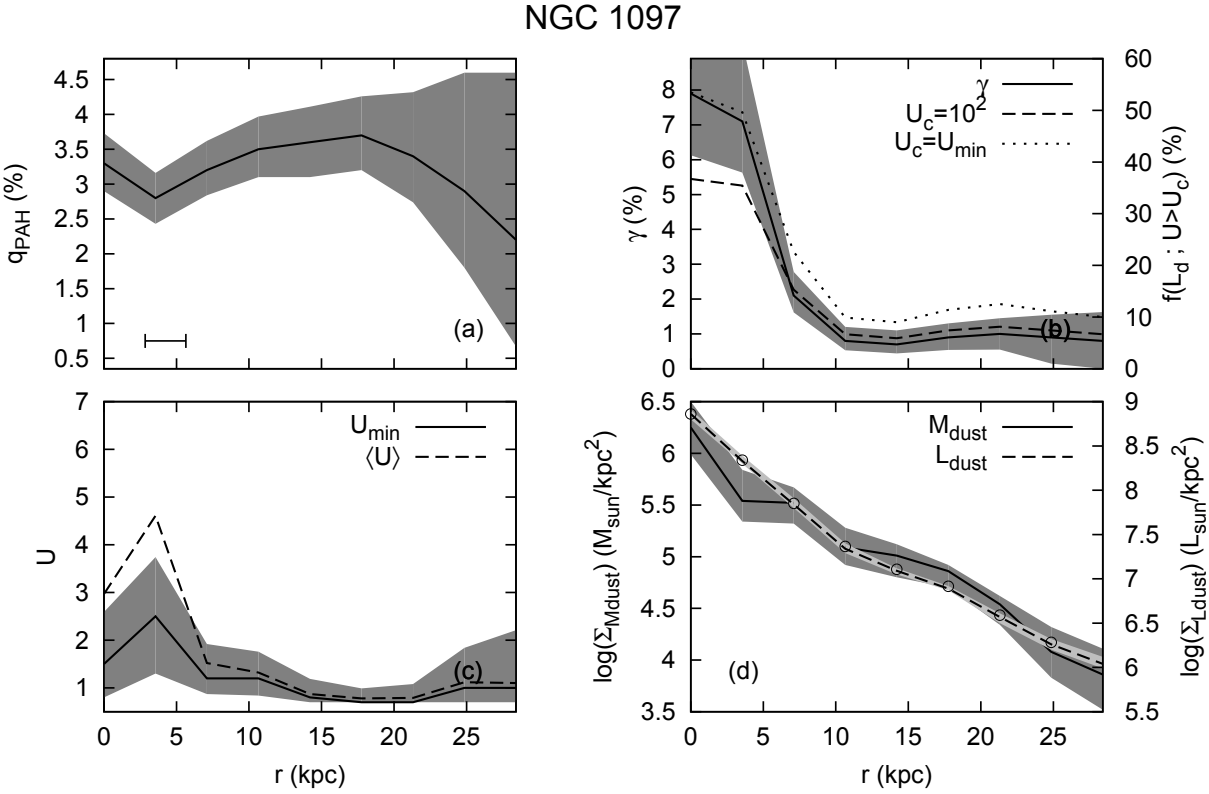
NGC 1097
q_{PAH} (%)
(a)
γ
$U_c=10^2$
$U_c=U_{min}$
γ (%)
$f(L_d ; U>U_c)$ (%)
(b)
U_{min}
⟨U⟩
U
(c)
r (kpc)
M_{dust}
L_{dust}
$\log(\Sigma_{Mdust})$ (M_{sun}/kpc^2)
$\log(\Sigma_{Ldust})$ (L_{sun}/kpc^2)
(d)
r (kpc)

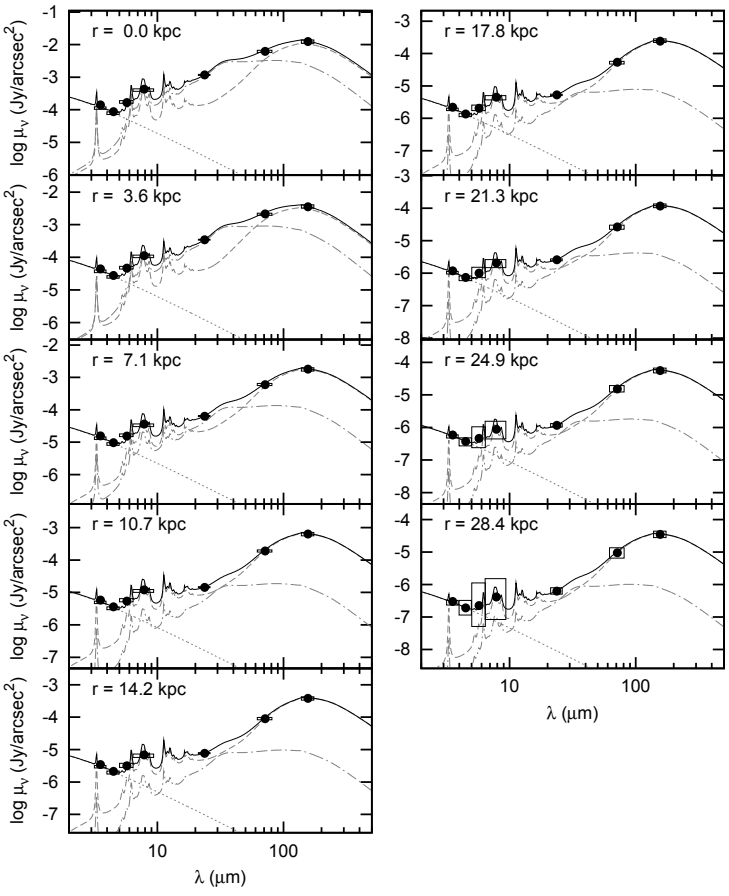
r = 0.0 kpc
r = 3.6 kpc
r = 7.1 kpc
r = 10.7 kpc
r = 14.2 kpc
r = 17.8 kpc
r = 21.3 kpc
r = 24.9 kpc
r = 28.4 kpc
log μ_ν (Jy/arcsec^2)
λ (μm)

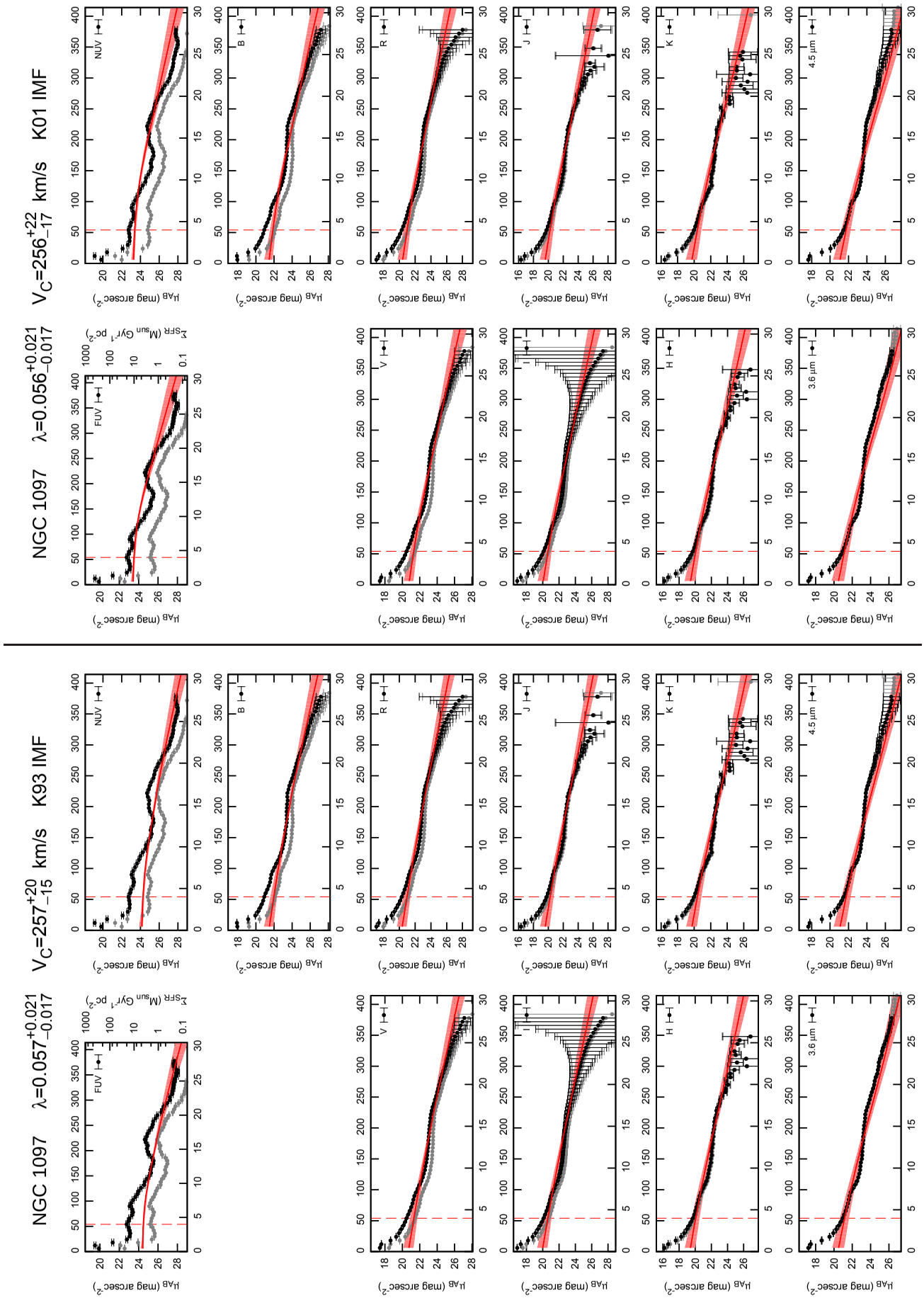
NGC 1097 λ=0.056+0.021−0.017 VC=256+22−17 km/s K01 IMF
NGC 1097 λ=0.057+0.021−0.017 VC=257+20−15 km/s K93 IMF
FUV
NUV
B
V
R
I
J
H
K
3.6 μm
4.5 μm
μAB (mag arcsec-2)
ΣSFR (Msun Gyr-1 pc-2)

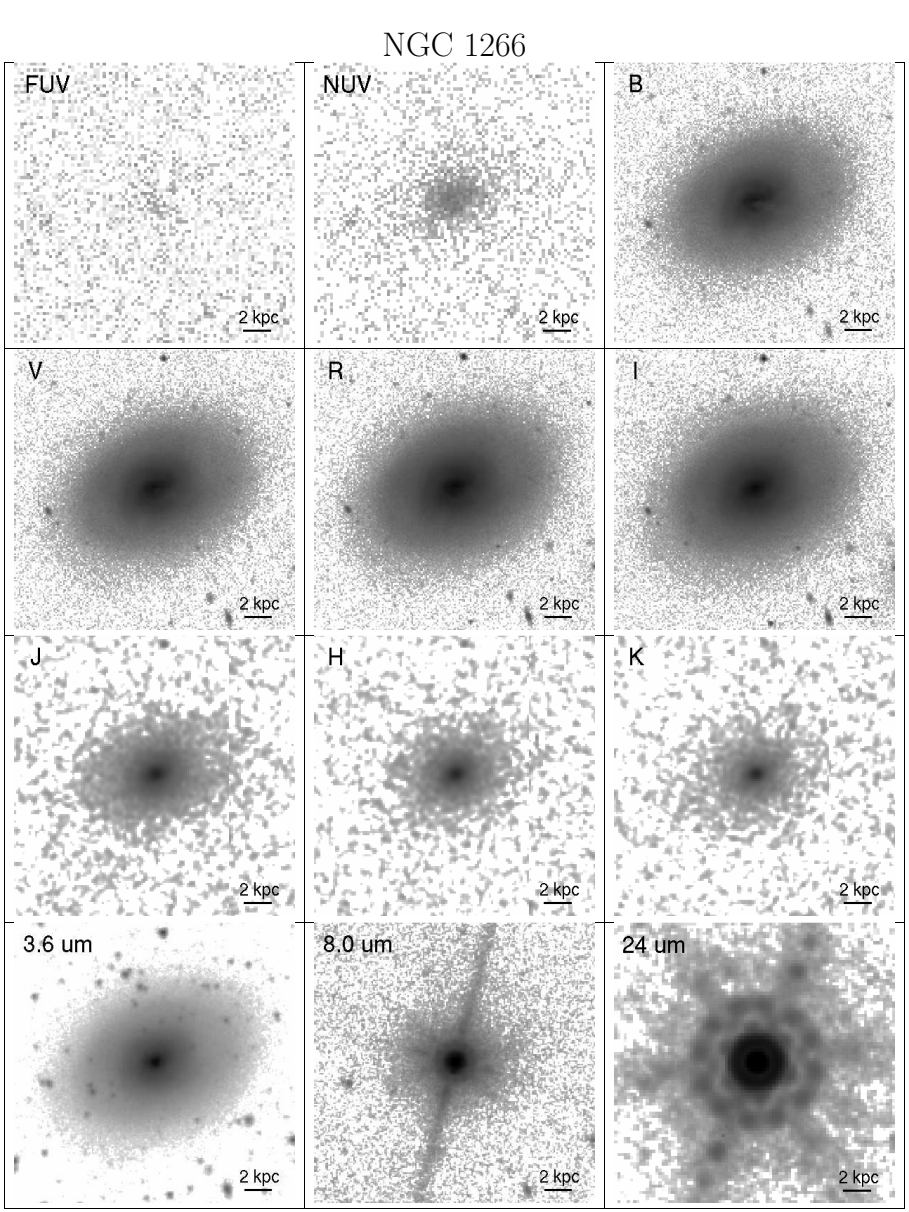
NGC 1266
FUV
NUV
B
V
R
I
J
H
K
3.6 um
8.0 um
24 um
2 kpc

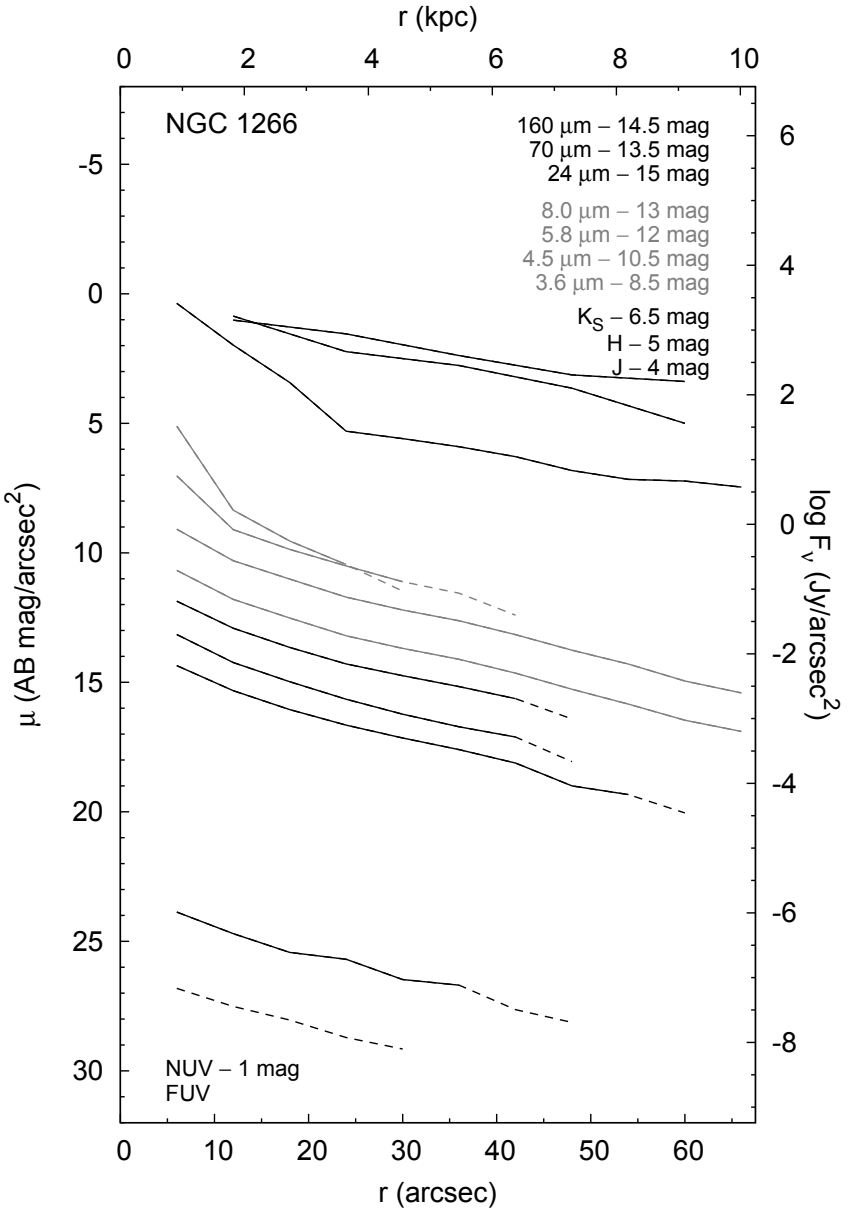
NGC 1266
r (kpc)
r (arcsec)
μ (AB mag/arcsec²)
log F_ν (Jy/arcsec²)
160 μm – 14.5 mag
70 μm – 13.5 mag
24 μm – 15 mag
8.0 μm – 13 mag
5.8 μm – 12 mag
4.5 μm – 10.5 mag
3.6 μm – 8.5 mag
K_S – 6.5 mag
H – 5 mag
J – 4 mag
NUV – 1 mag
FUV

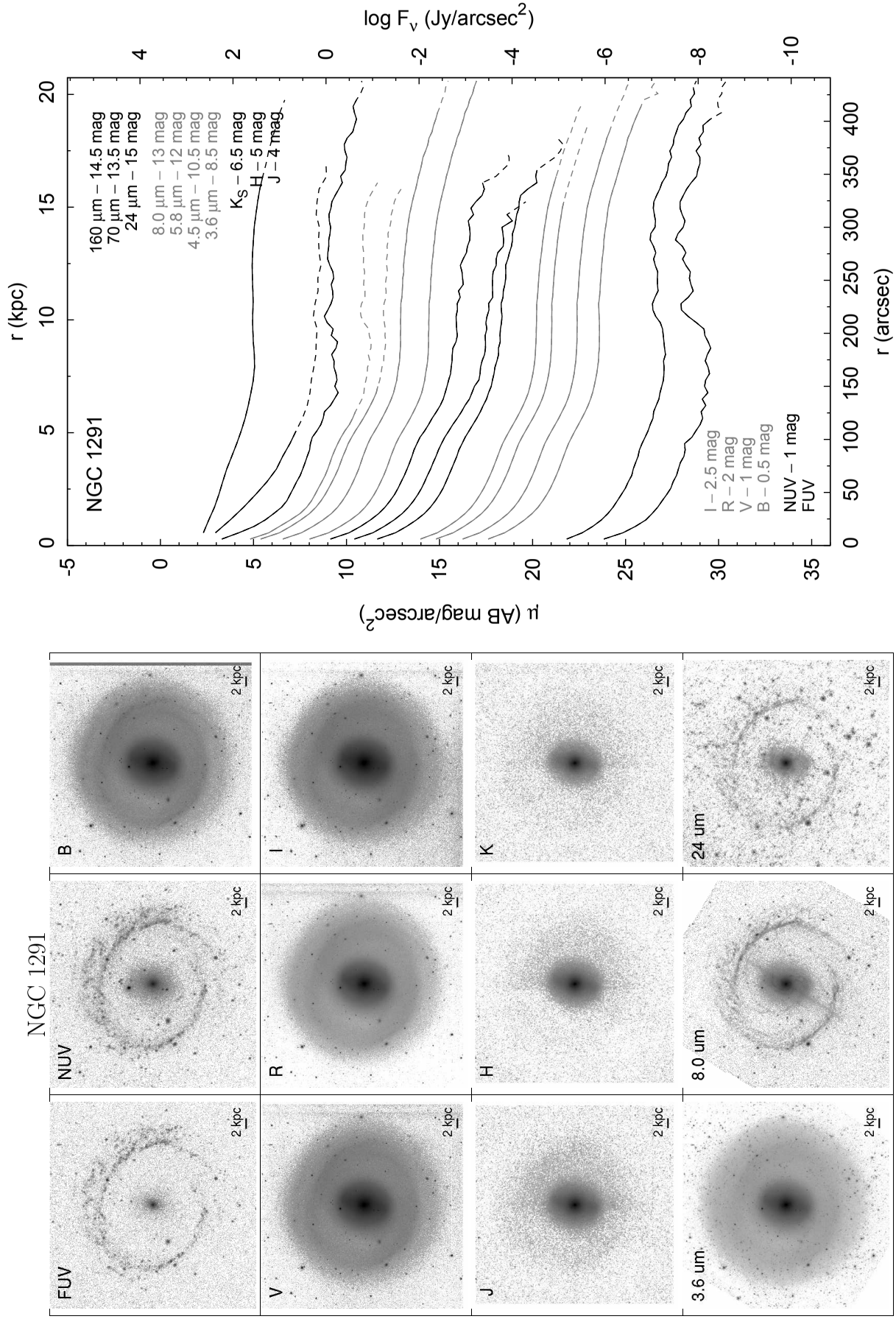
NGC 1291
FUV
NUV
B
V
R
I
J
H
K
3.6 um
8.0 um
24 um
2 kpc
μ (AB mag/arcsec²)
log F_ν (Jy/arcsec²)
r (kpc)
r (arcsec)
NGC 1291
160 μm – 14.5 mag
70 μm – 13.5 mag
24 μm – 15 mag
8.0 μm – 13 mag
5.8 μm – 12 mag
4.5 μm – 10.5 mag
3.6 μm – 8.5 mag
K_S – 6.5 mag
H – 5 mag
J – 4 mag
I – 2.5 mag
R – 2 mag
V – 1 mag
B – 0.5 mag
NUV – 1 mag
FUV

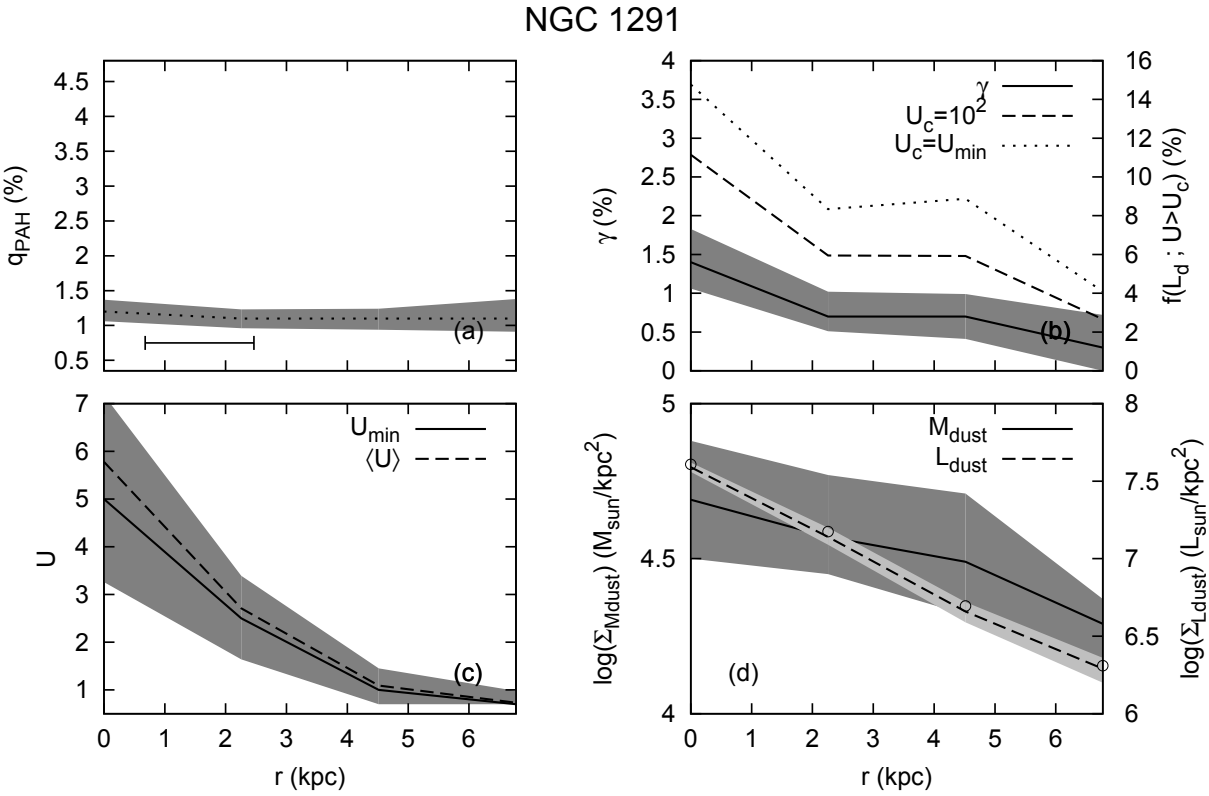
NGC 1291
q_{PAH} (%)
(a)
γ (%)
$f(L_d ; U>U_c)$ (%)
γ
$U_c=10^2$
$U_c=U_{min}$
(b)
U
U_{min}
⟨U⟩
(c)
r (kpc)
$\log(\Sigma_{Mdust})$ (M_{sun}/kpc^2)
$\log(\Sigma_{Ldust})$ (L_{sun}/kpc^2)
M_{dust}
L_{dust}
(d)
r (kpc)

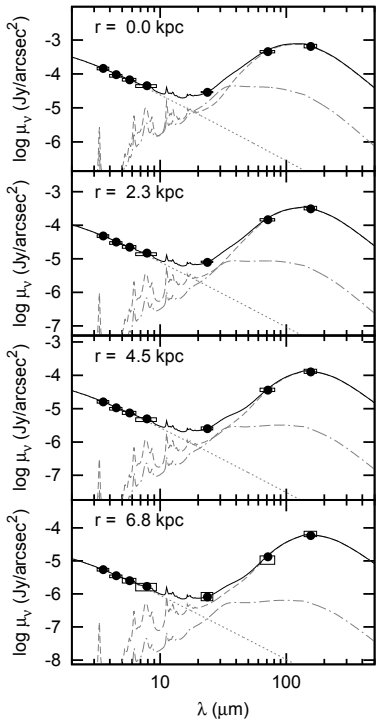
r = 0.0 kpc
r = 2.3 kpc
r = 4.5 kpc
r = 6.8 kpc
log μ_ν (Jy/arcsec^2)
λ (μm)

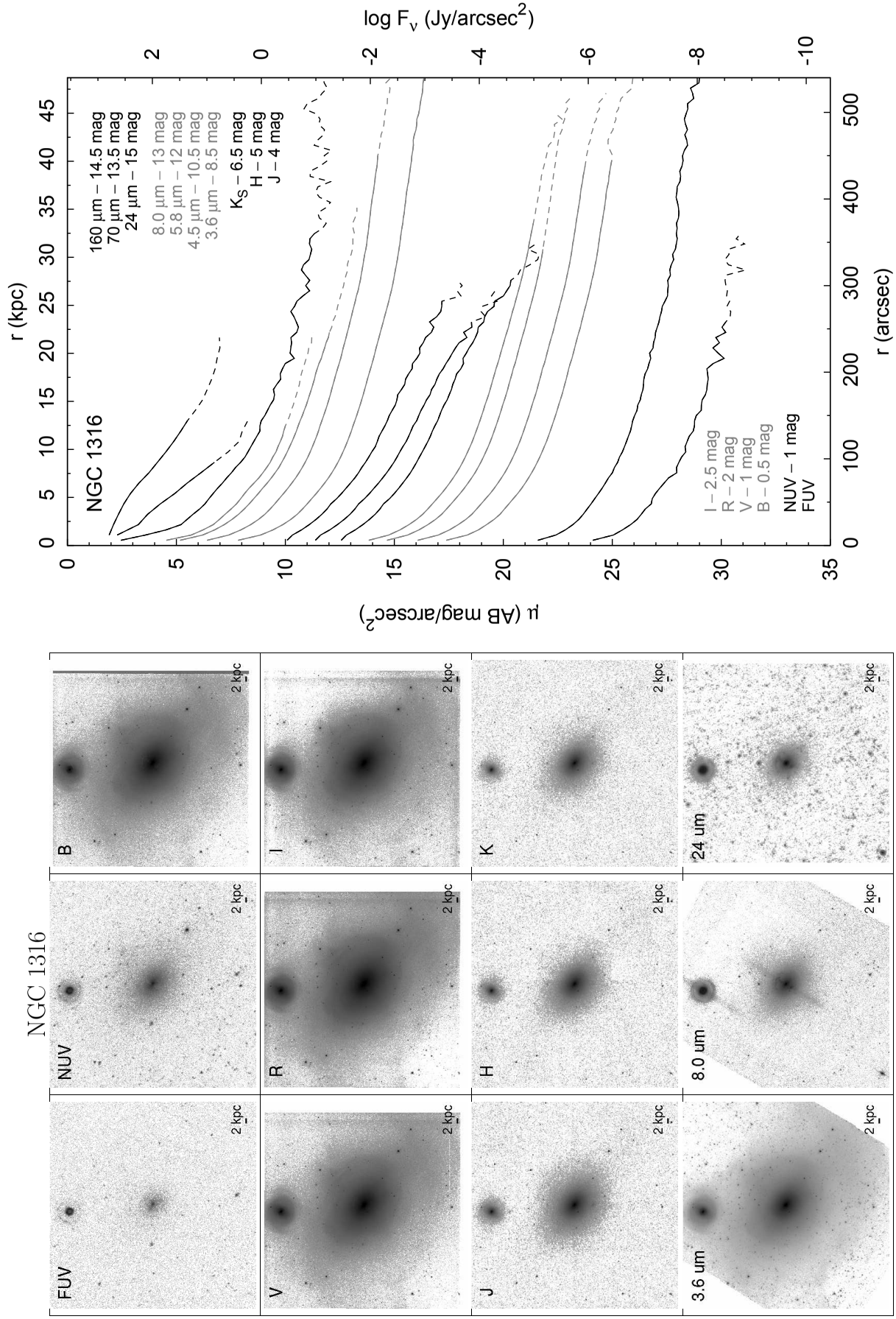
NGC 1316
FUV
NUV
B
V
R
I
J
H
K
3.6 um
8.0 um
24 um
2 kpc
μ (AB mag/arcsec²)
log F_ν (Jy/arcsec²)
r (kpc)
r (arcsec)
NGC 1316
160 μm – 14.5 mag
70 μm – 13.5 mag
24 μm – 15 mag
8.0 μm – 13 mag
5.8 μm – 12 mag
4.5 μm – 10.5 mag
3.6 μm – 8.5 mag
K_S – 6.5 mag
H – 5 mag
J – 4 mag
I – 2.5 mag
R – 2 mag
V – 1 mag
B – 0.5 mag
NUV – 1 mag
FUV

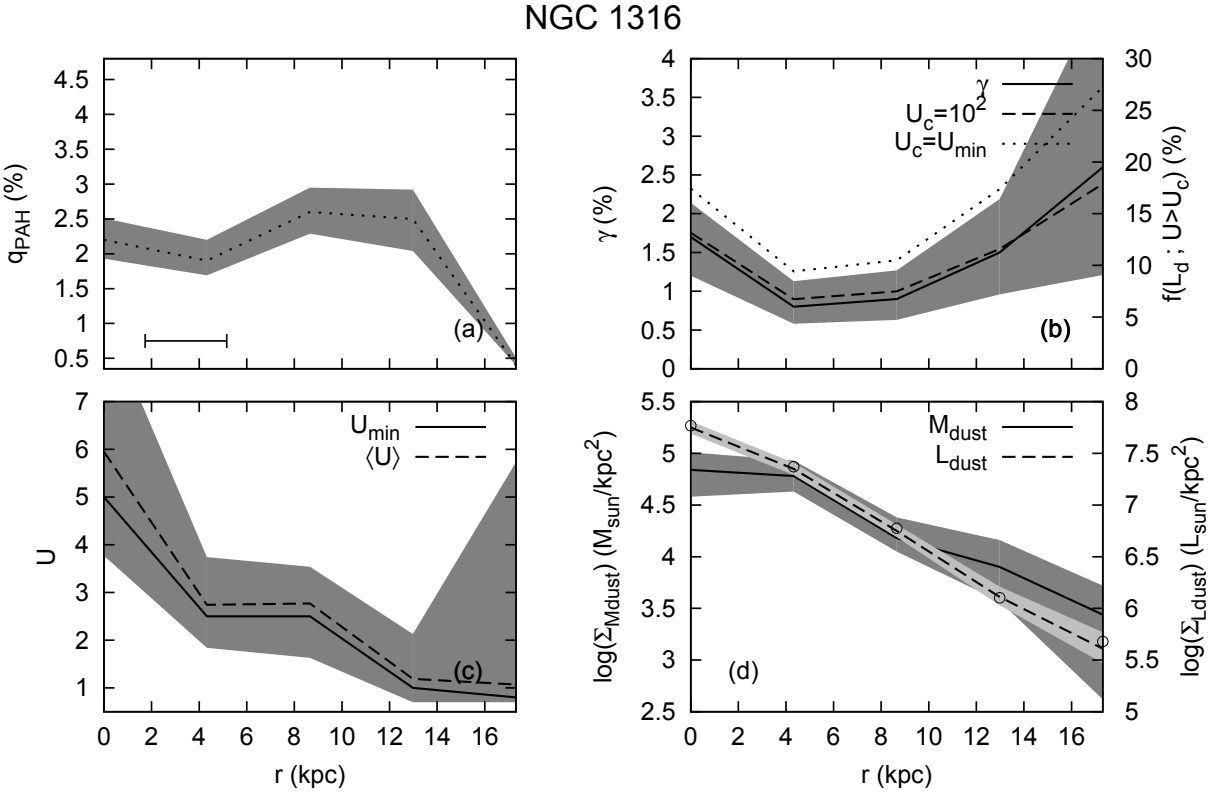
NGC 1316
q_{PAH} (%)
(a)
γ
$U_c=10^2$
$U_c=U_{min}$
γ (%)
$f(L_d ; U>U_c)$ (%)
(b)
U_{min}
⟨U⟩
U
(c)
r (kpc)
M_{dust}
L_{dust}
$\log(\Sigma_{Mdust})$ (M_{sun}/kpc^2)
$\log(\Sigma_{Ldust})$ (L_{sun}/kpc^2)
(d)
r (kpc)

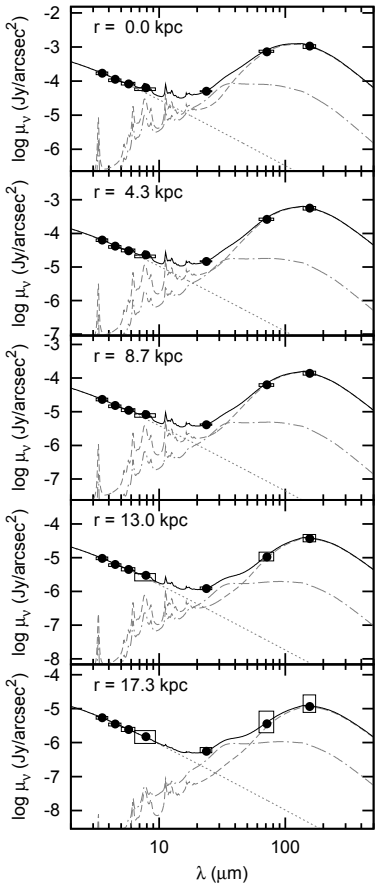
r = 0.0 kpc
r = 4.3 kpc
r = 8.7 kpc
r = 13.0 kpc
r = 17.3 kpc
log μ_ν (Jy/arcsec^2)
λ (μm)

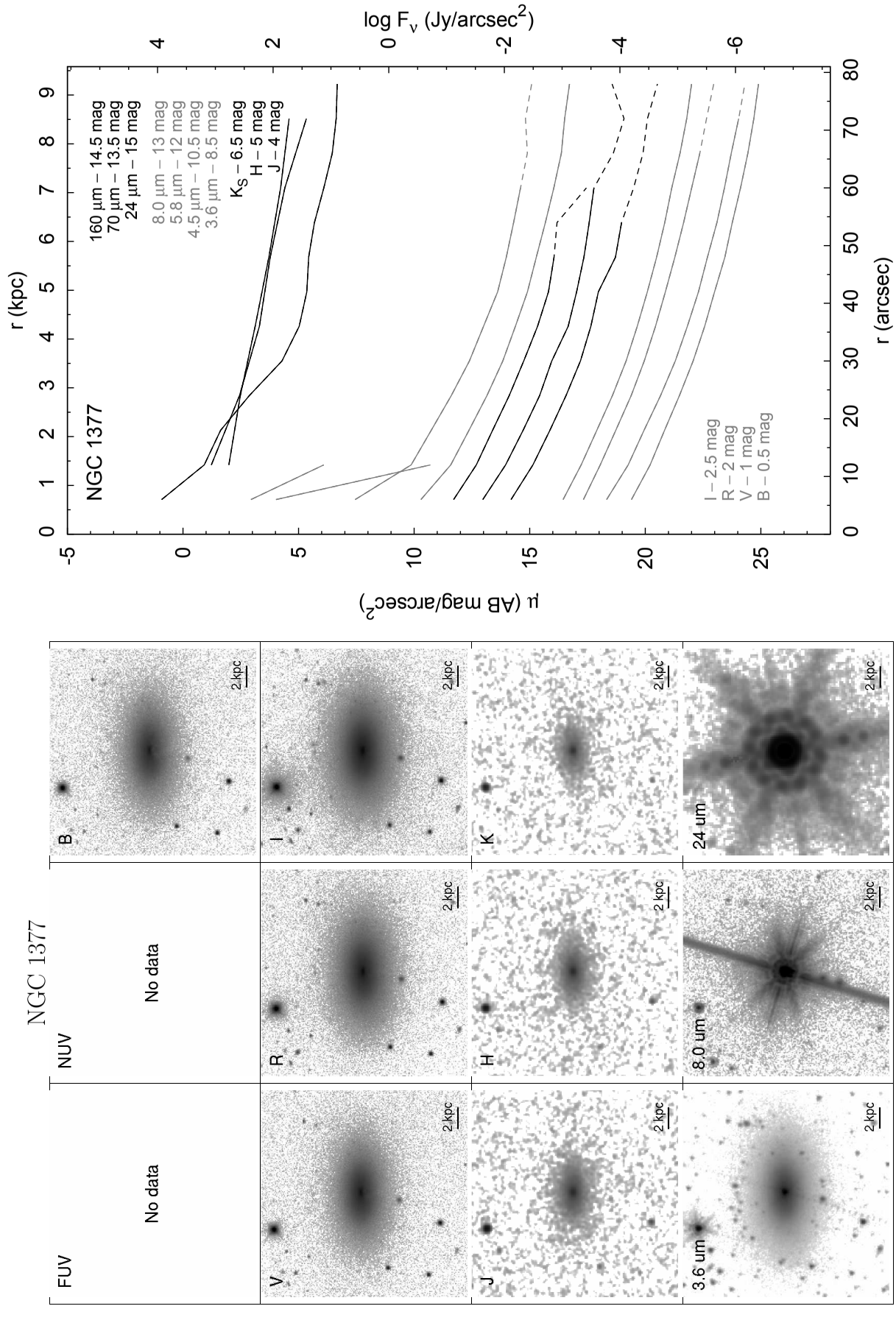
NGC 1377
FUV
NUV
No data
No data
B
I
R
K'
V
H
J
24 um
8.0 um
3.6 um
2 kpc
NGC 1377
160 μm – 14.5 mag
70 μm – 13.5 mag
24 μm – 15 mag
8.0 μm – 13 mag
5.8 μm – 12 mag
4.5 μm – 10.5 mag
3.6 μm – 8.5 mag
K_S – 6.5 mag
H – 5 mag
J – 4 mag
I – 2.5 mag
R – 2 mag
V – 1 mag
B – 0.5 mag
r (kpc)
r (arcsec)
log F_ν (Jy/arcsec²)
μ (AB mag/arcsec²)

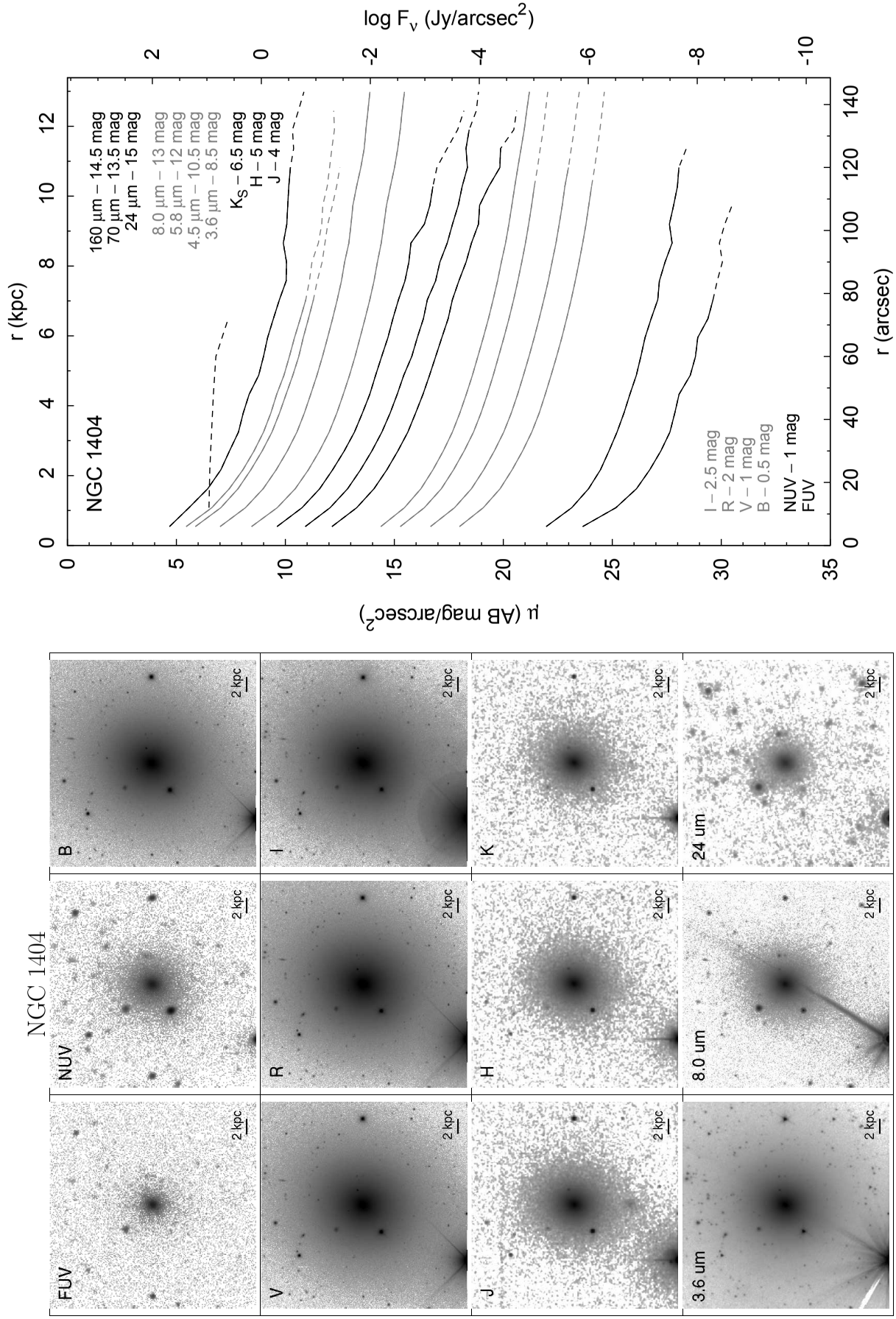
NGC 1404
FUV
NUV
B
V
R
I
J
H
K
3.6 um
8.0 um
24 um
2 kpc
μ (AB mag/arcsec²)
log F_ν (Jy/arcsec²)
r (kpc)
r (arcsec)
NGC 1404
160 μm – 14.5 mag
70 μm – 13.5 mag
24 μm – 15 mag
8.0 μm – 13 mag
5.8 μm – 12 mag
4.5 μm – 10.5 mag
3.6 μm – 8.5 mag
K_S – 6.5 mag
H – 5 mag
J – 4 mag
I – 2.5 mag
R – 2 mag
V – 1 mag
B – 0.5 mag
NUV – 1 mag
FUV

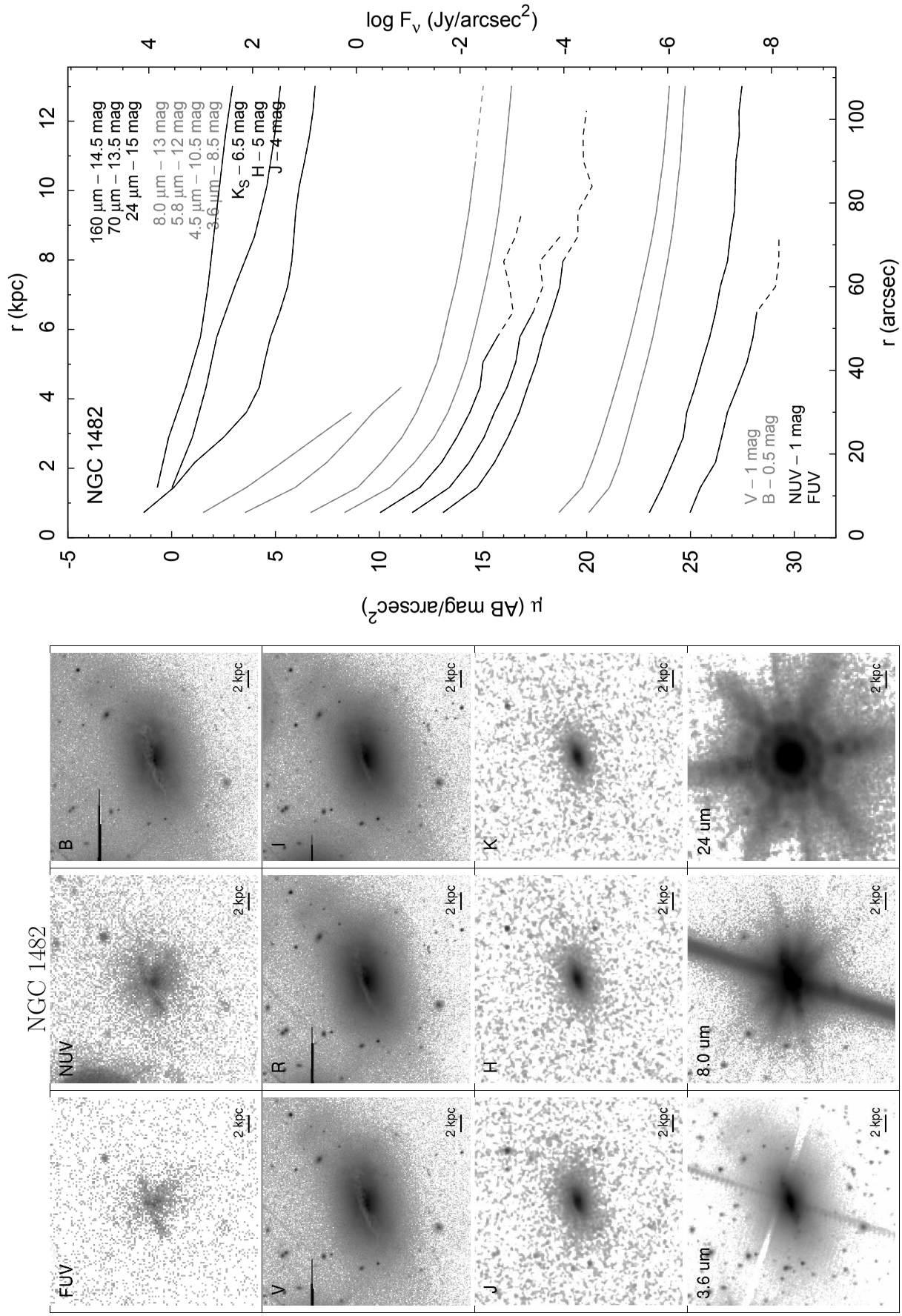
NGC 1482
NUV
B
R
I
V
H
J
K'
3.6 um
8.0 um
24 um
2 kpc
μ (AB mag/arcsec²)
log F_ν (Jy/arcsec²)
r (kpc)
r (arcsec)
NGC 1482
160 μm – 14.5 mag
70 μm – 13.5 mag
24 μm – 15 mag
8.0 μm – 13 mag
5.8 μm – 12 mag
4.5 μm – 10.5 mag
3.6 μm – 8.5 mag
K_S – 6.5 mag
H – 5 mag
J – 4 mag
V – 1 mag
B – 0.5 mag
NUV – 1 mag
FUV

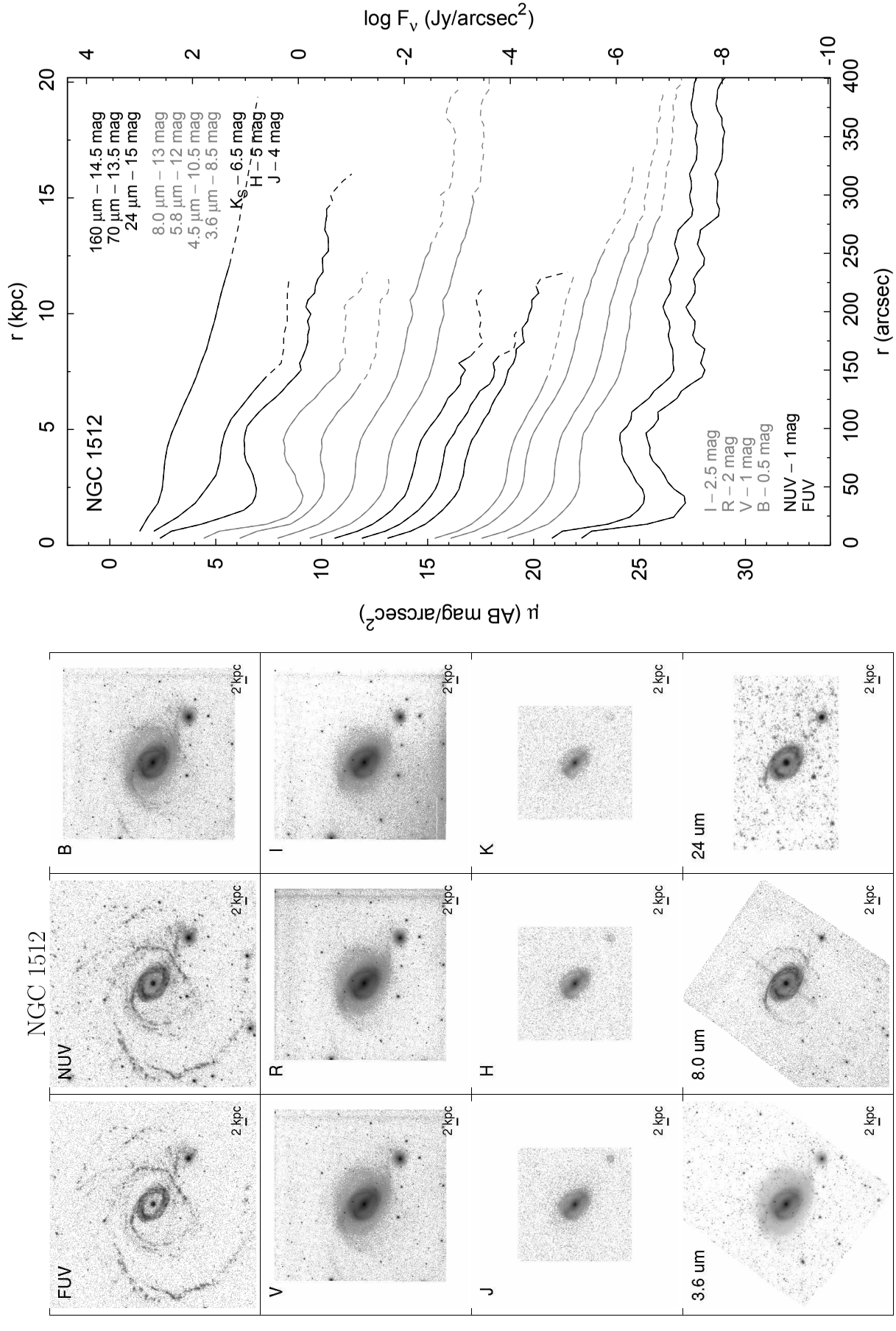
NGC 1512
FUV
NUV
B
V
R
I
J
H
K
3.6 um
8.0 um
24 um
2 kpc
NGC 1512
160 µm – 14.5 mag
70 µm – 13.5 mag
24 µm – 15 mag
8.0 µm – 13 mag
5.8 µm – 12 mag
4.5 µm – 10.5 mag
3.6 µm – 8.5 mag
Ks – 6.5 mag
H – 5 mag
J – 4 mag
I – 2.5 mag
R – 2 mag
V – 1 mag
B – 0.5 mag
NUV – 1 mag
FUV
r (kpc)
r (arcsec)
log Fν (Jy/arcsec2)
µ (AB mag/arcsec2)

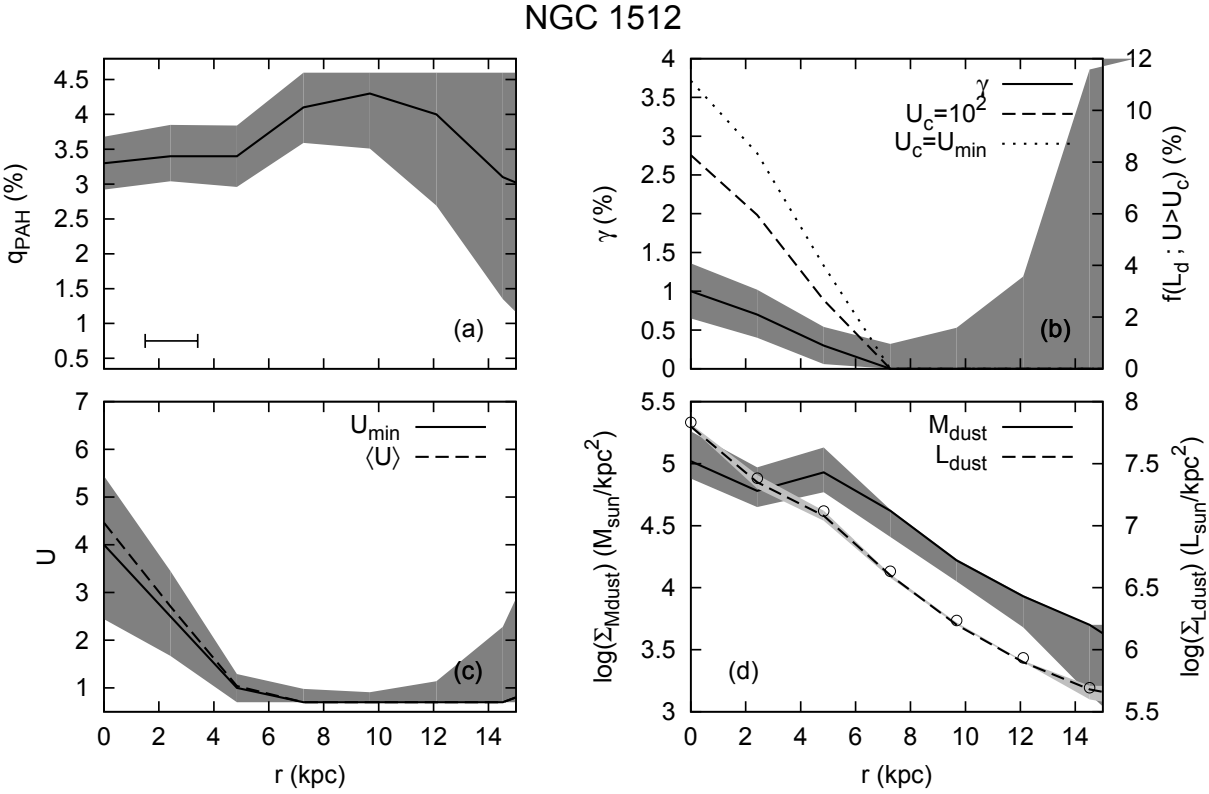
NGC 1512
q_{PAH} (%)
(a)
γ (%)
$U_c=10^2$
$U_c=U_{min}$
(b)
$f(L_d ; U>U_c)$ (%)
U
U_{min}
⟨U⟩
(c)
r (kpc)
$\log(\Sigma_{Mdust})$ (M_{sun}/kpc^2)
M_{dust}
L_{dust}
(d)
$\log(\Sigma_{Ldust})$ (L_{sun}/kpc^2)
r (kpc)

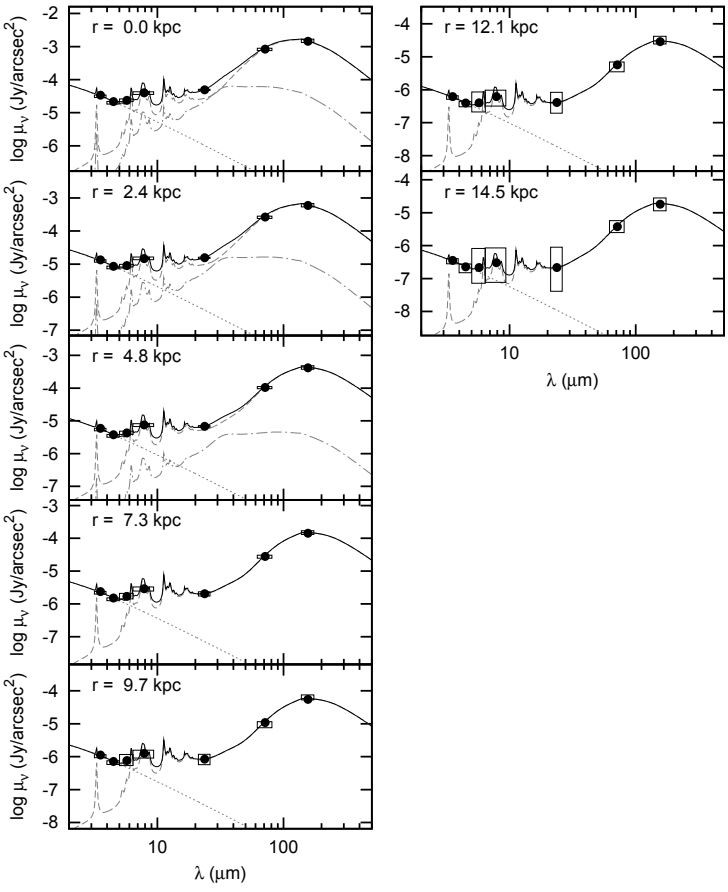
r = 0.0 kpc
r = 2.4 kpc
r = 4.8 kpc
r = 7.3 kpc
r = 9.7 kpc
r = 12.1 kpc
r = 14.5 kpc
log μν (Jy/arcsec²)
λ (μm)

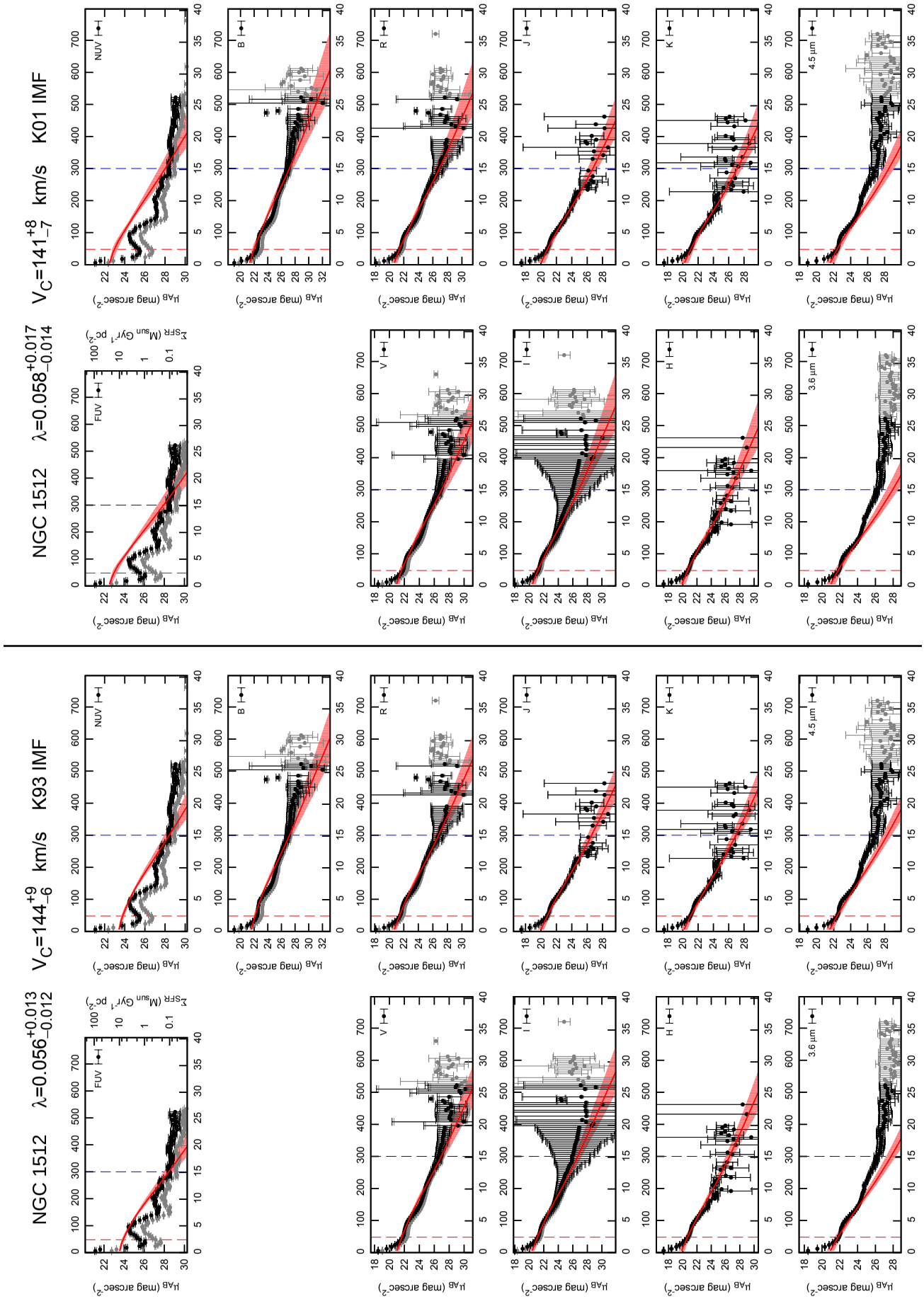
NGC 1512 λ=0.058+0.017−0.014 VC=141+8−7 km/s K01 IMF
NGC 1512 λ=0.056+0.013−0.012 VC=144+9−6 km/s K93 IMF
μAB (mag arcsec-2)
ΣSFR (Msun Gyr-1 pc-2)
FUV
NUV
B
V
R
I
J
H
K
3.6 μm
4.5 μm

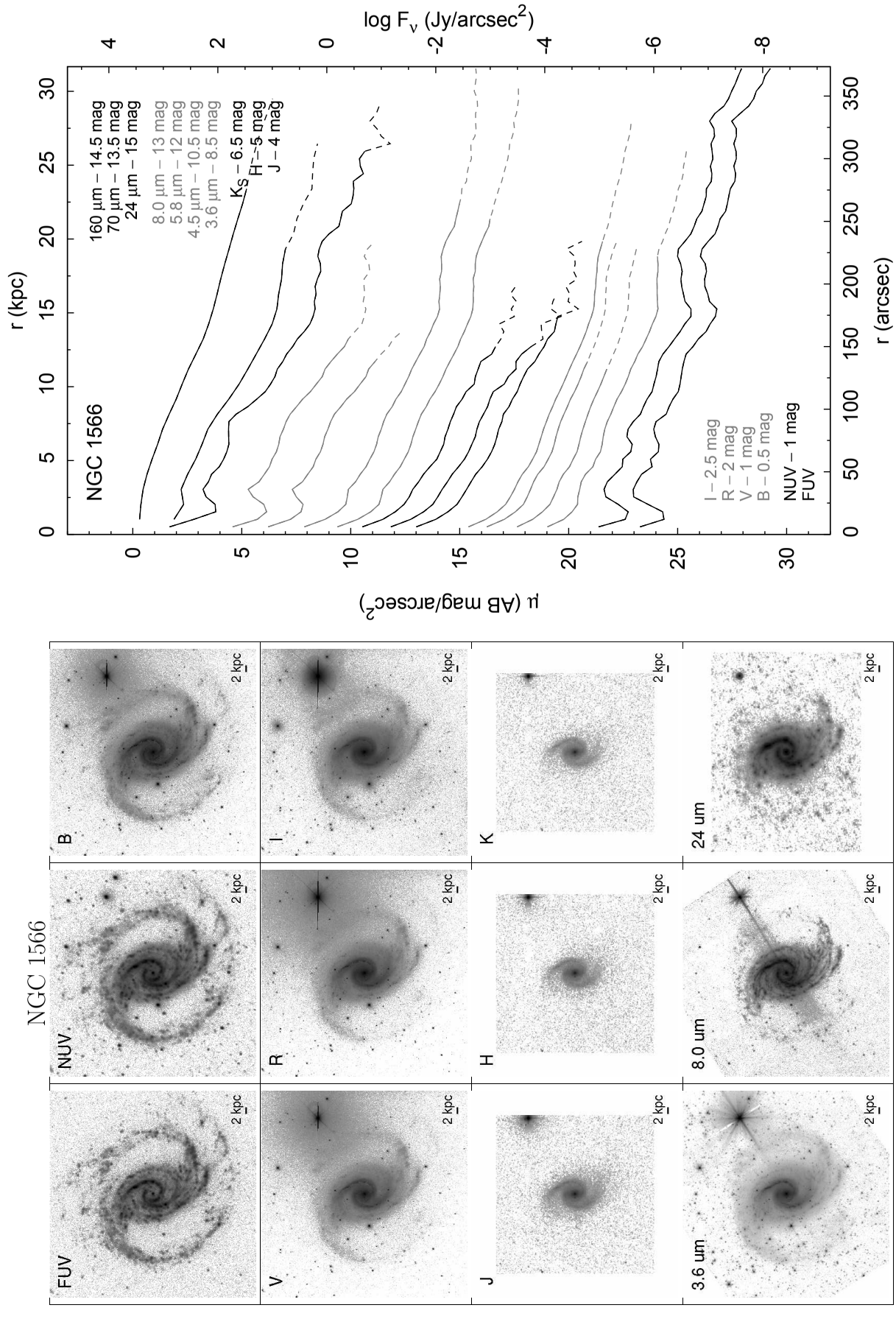
NGC 1566
r (kpc)
log F$_\nu$ (Jy/arcsec^2)
μ (AB mag/arcsec^2)
r (arcsec)
160 μm – 14.5 mag
70 μm – 13.5 mag
24 μm – 15 mag
8.0 μm – 13 mag
5.8 μm – 12 mag
4.5 μm – 10.5 mag
3.6 μm – 8.5 mag
K$_S$ – 6.5 mag
H – 5 mag
J – 4 mag
I – 2.5 mag
R – 2 mag
V – 1 mag
B – 0.5 mag
NUV – 1 mag
FUV
FUV
NUV
B
V
R
I
J
H
K
3.6 um
8.0 um
24 um
2 kpc

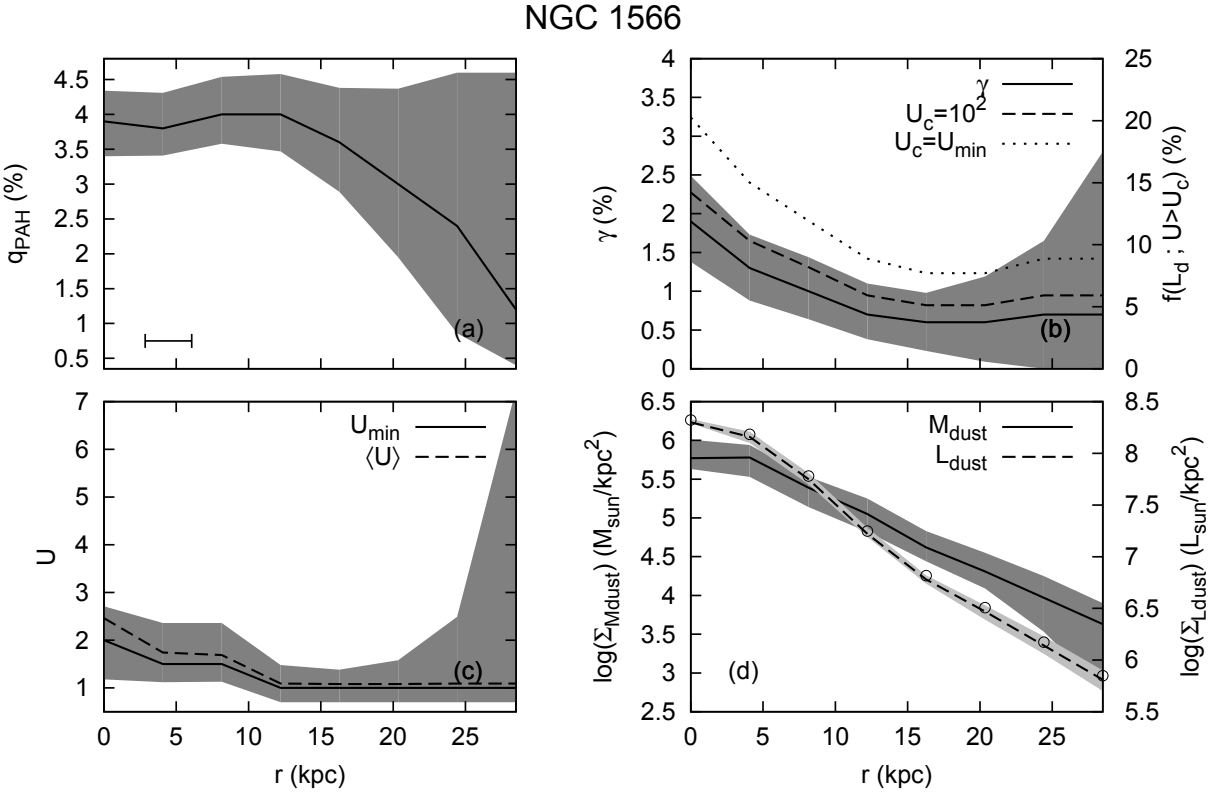
NGC 1566
q_{PAH} (%)
(a)
γ
$U_c=10^2$
$U_c=U_{min}$
γ (%)
$f(L_d ; U>U_c)$ (%)
(b)
U_{min}
⟨U⟩
U
(c)
r (kpc)
M_{dust}
L_{dust}
$\log(\Sigma_{Mdust})$ (M_{sun}/kpc^2)
$\log(\Sigma_{Ldust})$ (L_{sun}/kpc^2)
(d)
r (kpc)

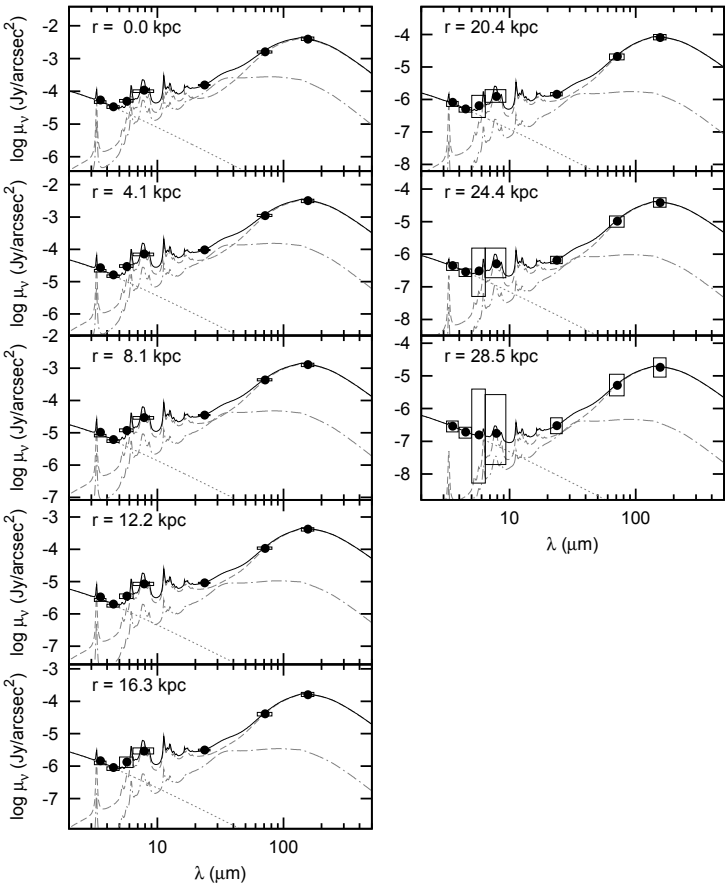
r = 0.0 kpc
r = 4.1 kpc
r = 8.1 kpc
r = 12.2 kpc
r = 16.3 kpc
r = 20.4 kpc
r = 24.4 kpc
r = 28.5 kpc
log μ_ν (Jy/arcsec^2)
λ (μm)

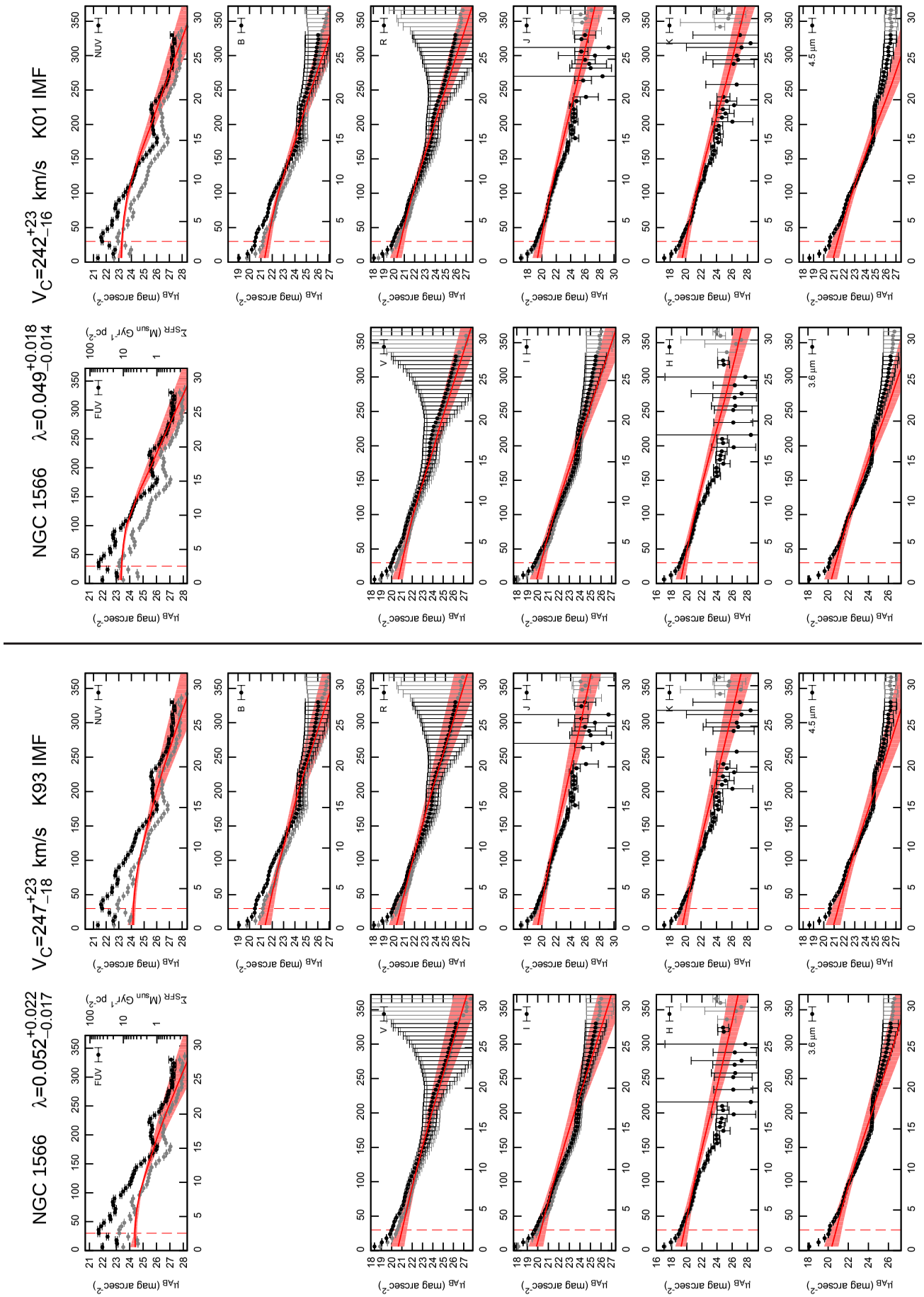
NGC 1566 λ=0.049+0.018−0.014 VC=242+23−16 km/s K01 IMF
NGC 1566 λ=0.052+0.022−0.017 VC=247+23−18 km/s K93 IMF
NUV
FUV
B
V
R
I
J
H
K
3.6 μm
4.5 μm
μAB (mag arcsec-2)
ΣSFR (Msun Gyr-1 pc-2)

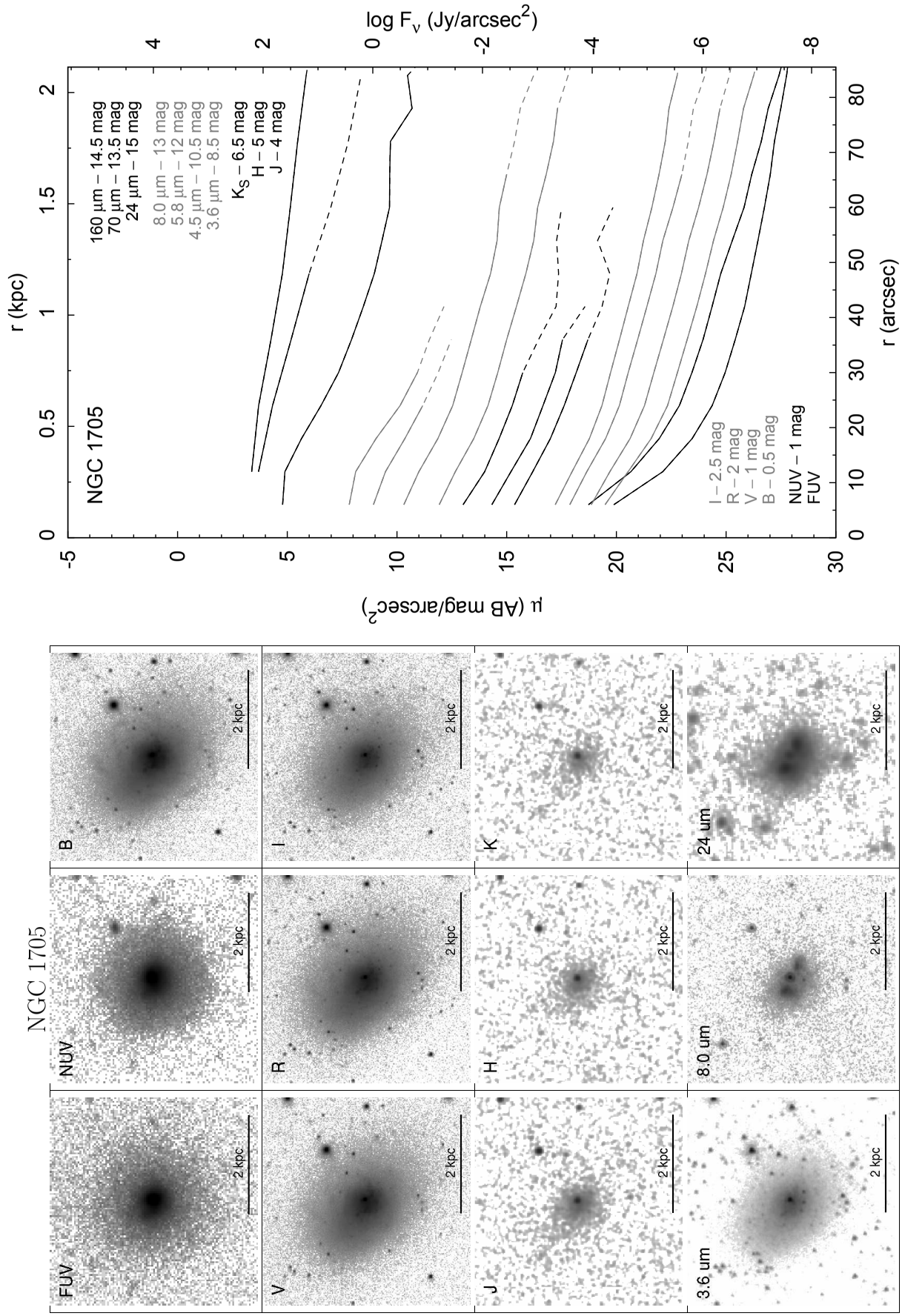
NGC 1705
FUV
NUV
B
V
R
I
J
H
K
3.6 um
8.0 um
24 um
2 kpc
μ (AB mag/arcsec²)
log F_ν (Jy/arcsec²)
r (kpc)
r (arcsec)
NGC 1705
160 μm – 14.5 mag
70 μm – 13.5 mag
24 μm – 15 mag
8.0 μm – 13 mag
5.8 μm – 12 mag
4.5 μm – 10.5 mag
3.6 μm – 8.5 mag
K_S – 6.5 mag
H – 5 mag
J – 4 mag
I – 2.5 mag
R – 2 mag
V – 1 mag
B – 0.5 mag
NUV – 1 mag
FUV

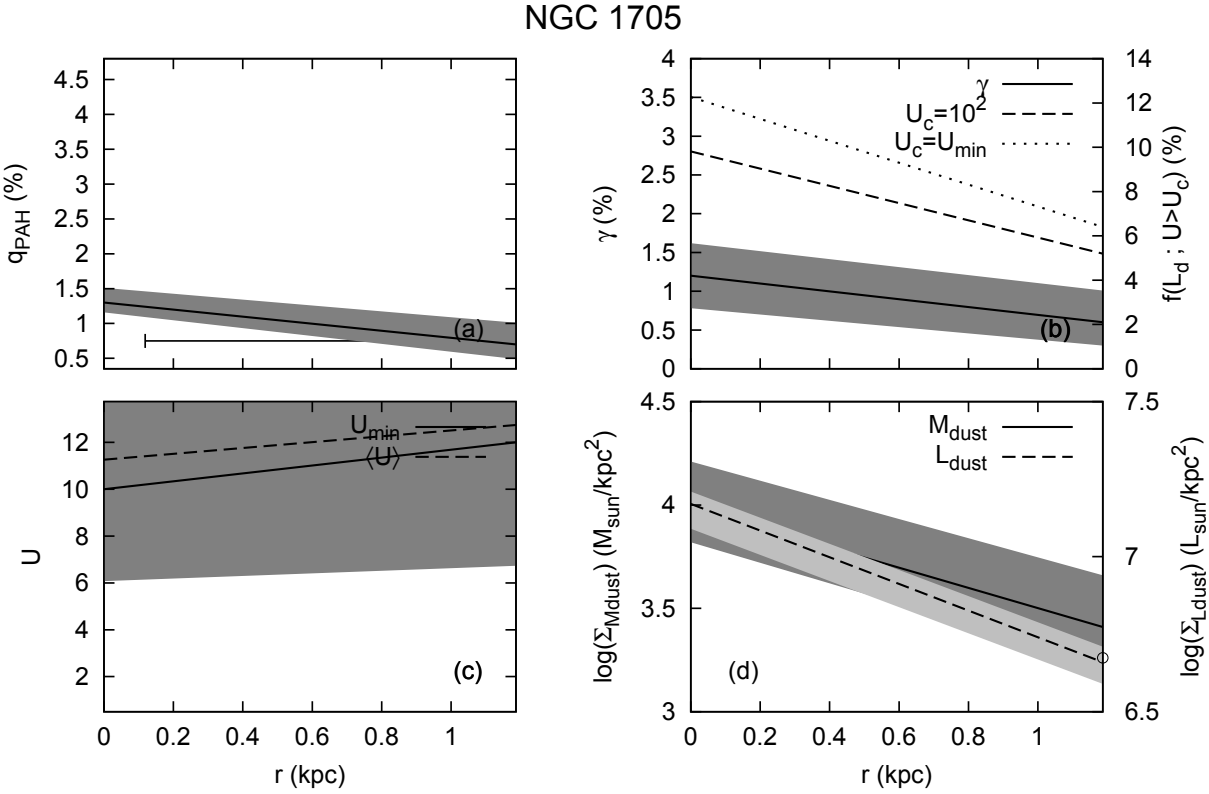
NGC 1705
q_{PAH} (%)
(a)
γ (%)
$U_c=10^2$
$U_c=U_{min}$
$f(L_d ; U>U_c)$ (%)
(b)
U
U_{min}
⟨U⟩
(c)
$\log(\Sigma_{Mdust})$ (M_{sun}/kpc^2)
M_{dust}
L_{dust}
$\log(\Sigma_{Ldust})$ (L_{sun}/kpc^2)
(d)
r (kpc)
r (kpc)

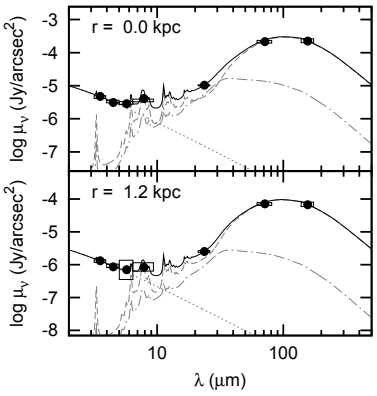
r = 0.0 kpc
r = 1.2 kpc
log μ_ν (Jy/arcsec^2)
log μ_ν (Jy/arcsec^2)
λ (μm)

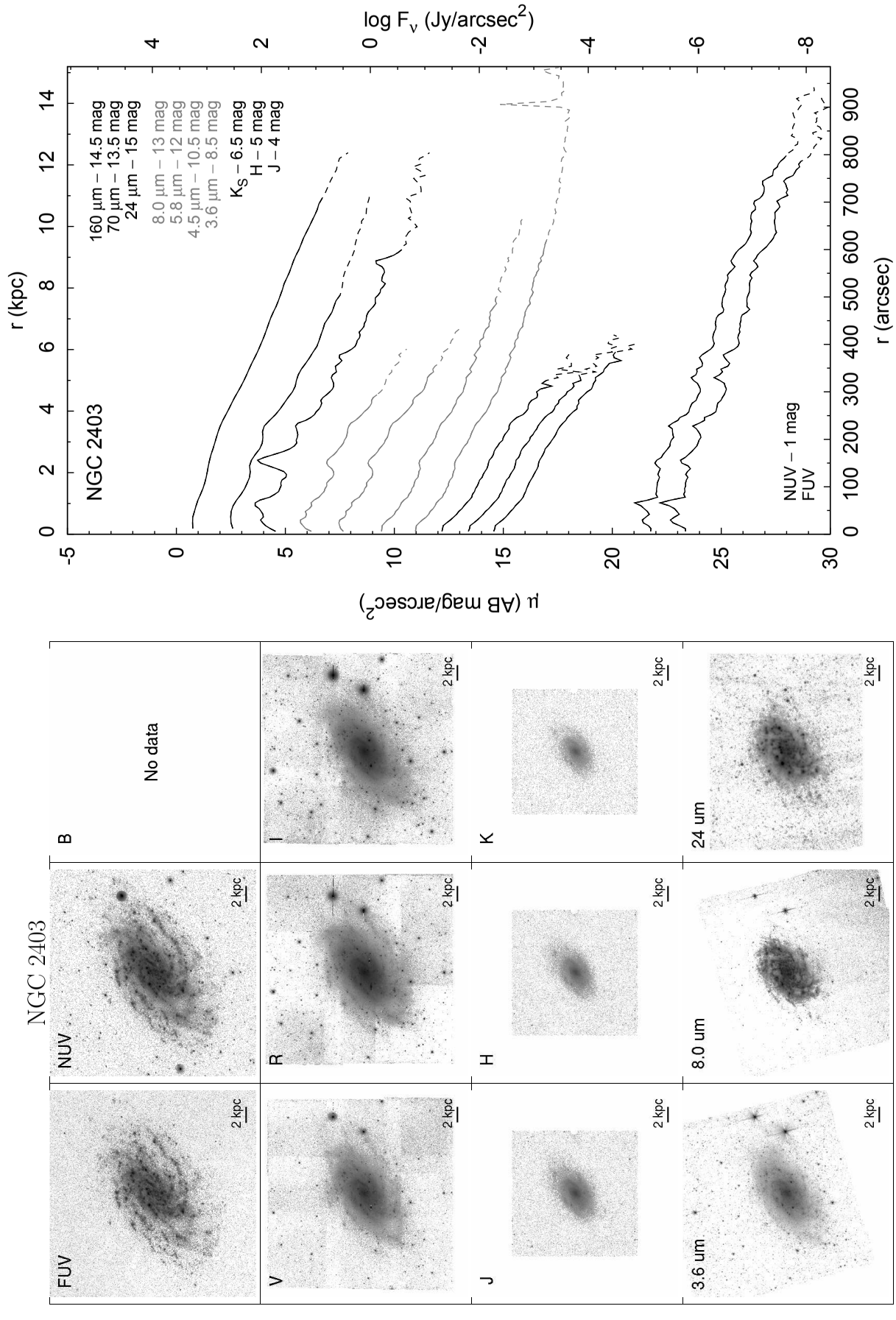
NGC 2403
FUV
NUV
B
No data
V
R
I
J
H
K
3.6 um
8.0 um
24 um
2 kpc
μ (AB mag/arcsec²)
log F_ν (Jy/arcsec²)
r (kpc)
r (arcsec)
NGC 2403
160 μm – 14.5 mag
70 μm – 13.5 mag
24 μm – 15 mag
8.0 μm – 13 mag
5.8 μm – 12 mag
4.5 μm – 10.5 mag
3.6 μm – 8.5 mag
K_S – 6.5 mag
H – 5 mag
J – 4 mag
NUV – 1 mag
FUV

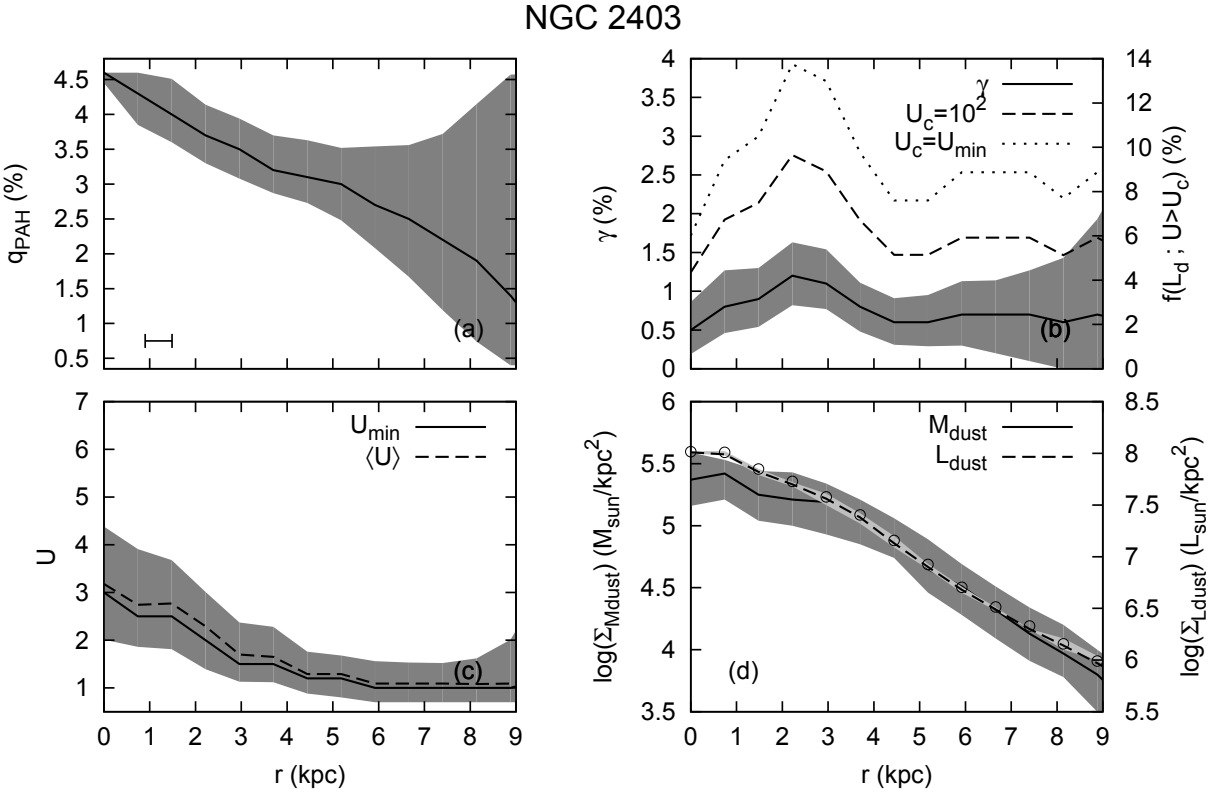
NGC 2403
q_{PAH} (%)
(a)
γ (%)
$U_c=10^2$
$U_c=U_{min}$
$f(L_d ; U>U_c)$ (%)
(b)
U
U_{min}
⟨U⟩
(c)
r (kpc)
$\log(\Sigma_{Mdust})$ (M_{sun}/kpc^2)
M_{dust}
L_{dust}
(d)
$\log(\Sigma_{Ldust})$ (L_{sun}/kpc^2)
r (kpc)

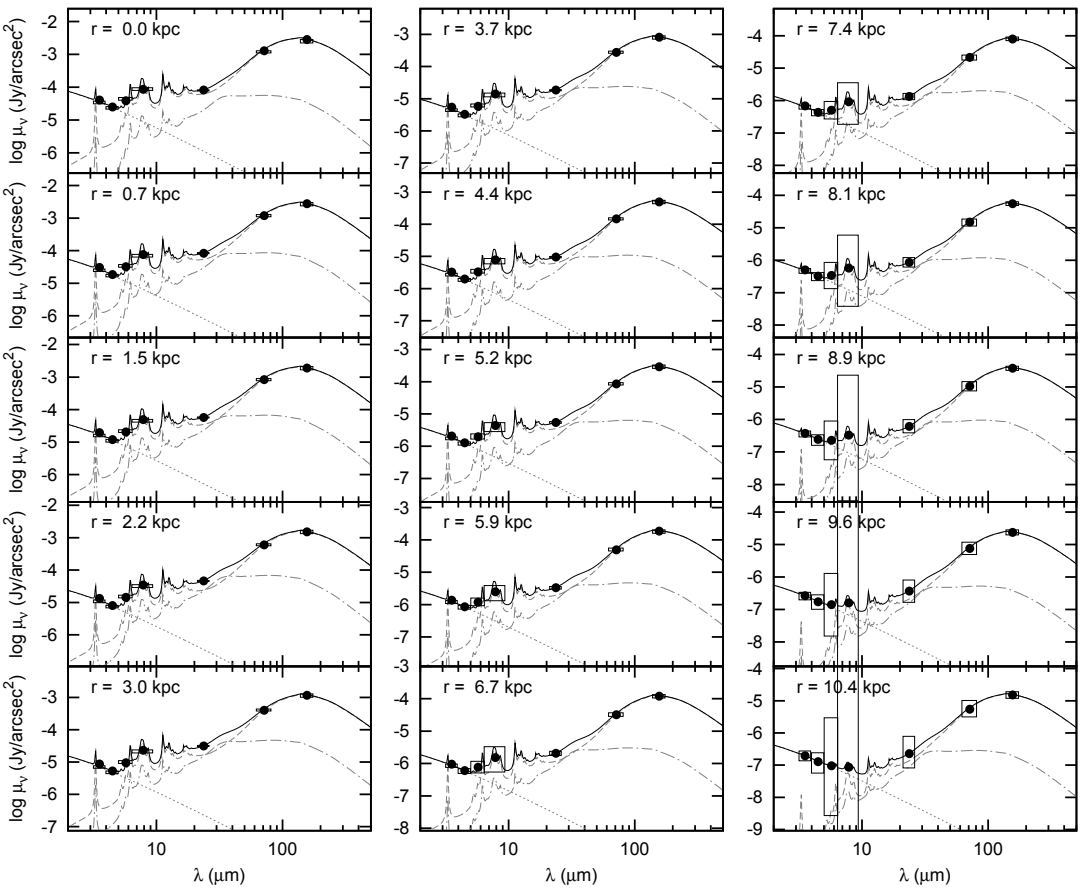
r = 0.0 kpc
r = 0.7 kpc
r = 1.5 kpc
r = 2.2 kpc
r = 3.0 kpc
r = 3.7 kpc
r = 4.4 kpc
r = 5.2 kpc
r = 5.9 kpc
r = 6.7 kpc
r = 7.4 kpc
r = 8.1 kpc
r = 8.9 kpc
r = 9.6 kpc
r = 10.4 kpc
log μ_ν (Jy/arcsec^2)
λ (μm)

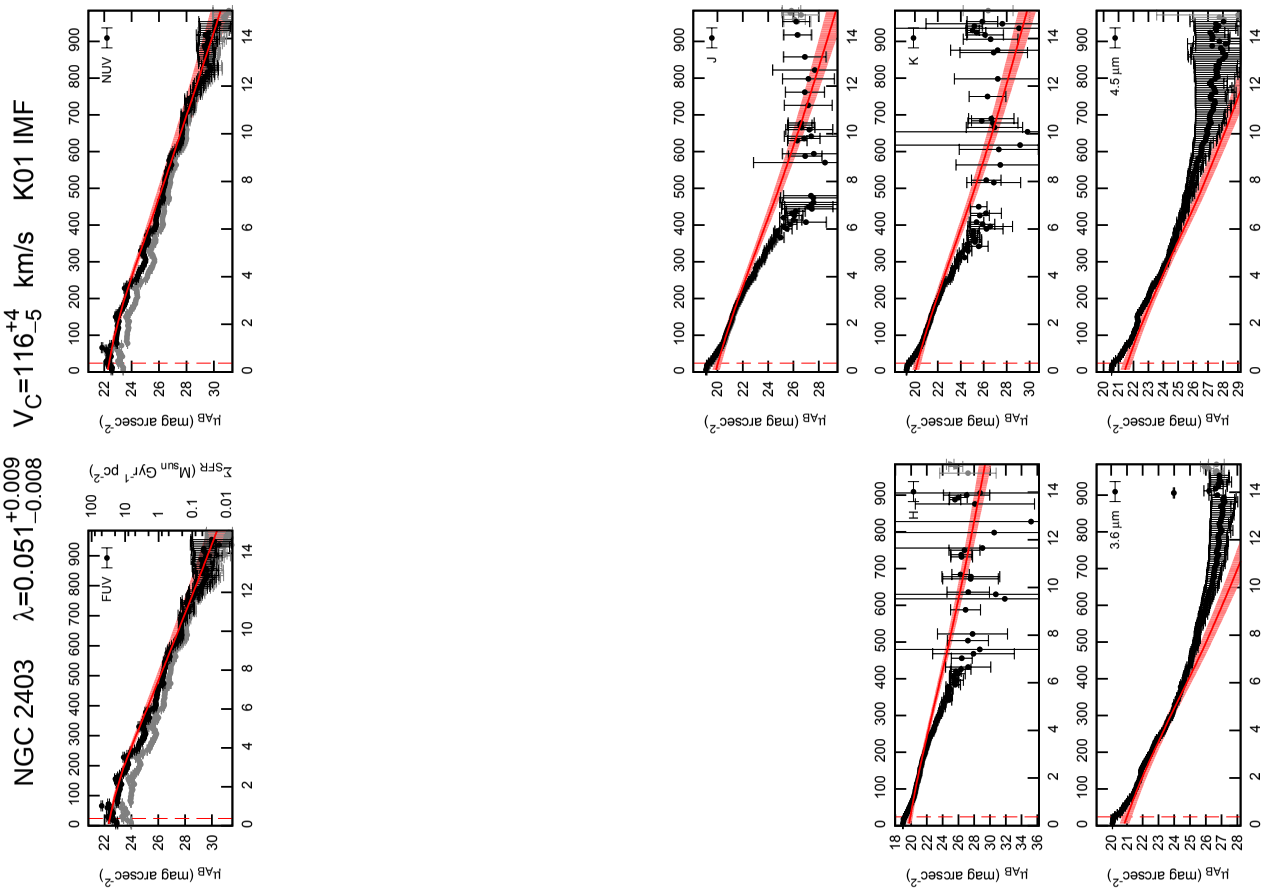
NGC 2403 λ=0.051+0.009−0.008 VC=116+4−5 km/s K01 IMF
NUV
FUV
J
K
4.5 μm
3.6 μm
H
μAB (mag arcsec-2)
ΣSFR (Msun Gyr-1 pc-2)

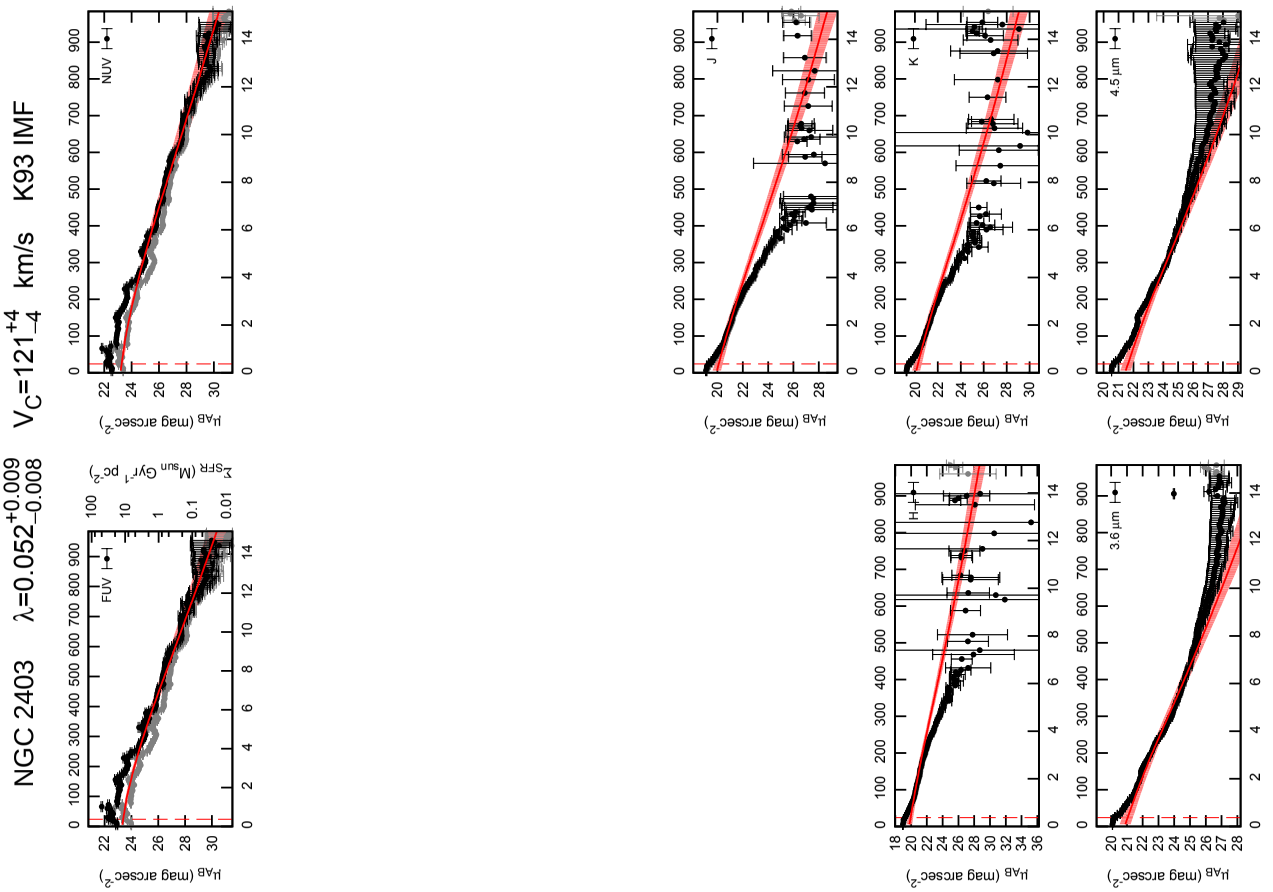
NGC 2403 λ=0.052+0.009−0.008 VC=121+4−4 km/s K93 IMF
NUV
FUV
J
K
4.5 μm
3.6 μm
H
μAB (mag arcsec-2)
ΣSFR (Msun Gyr-1 pc-2)

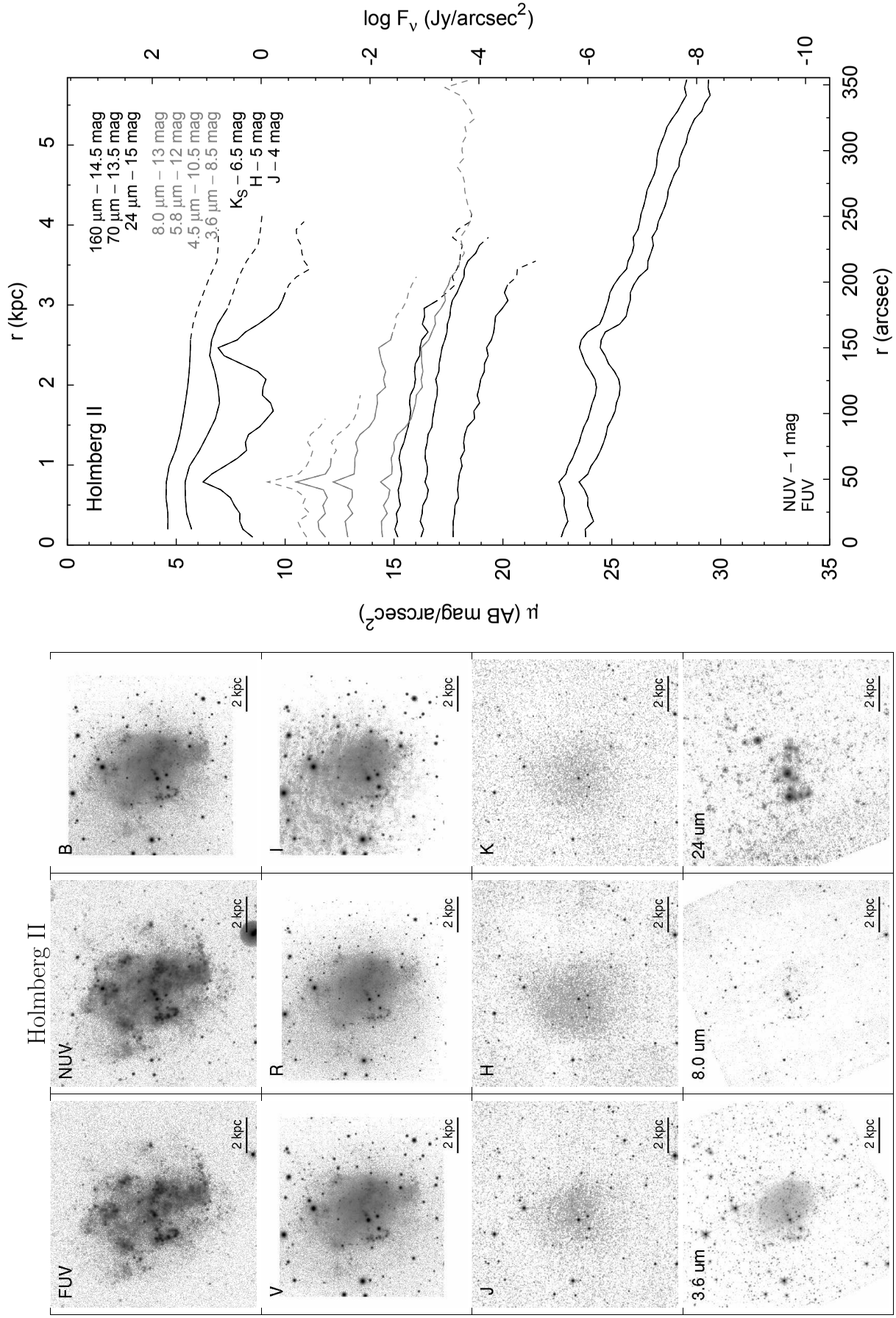
Holmberg II
FUV
NUV
B
V
R
I
J
H
K
3.6 um
8.0 um
24 um
2 kpc
μ (AB mag/arcsec²)
log F_ν (Jy/arcsec²)
r (kpc)
r (arcsec)
Holmberg II
160 μm – 14.5 mag
70 μm – 13.5 mag
24 μm – 15 mag
8.0 μm – 13 mag
5.8 μm – 12 mag
4.5 μm – 10.5 mag
3.6 μm – 8.5 mag
K_S – 6.5 mag
H – 5 mag
J – 4 mag
NUV – 1 mag
FUV

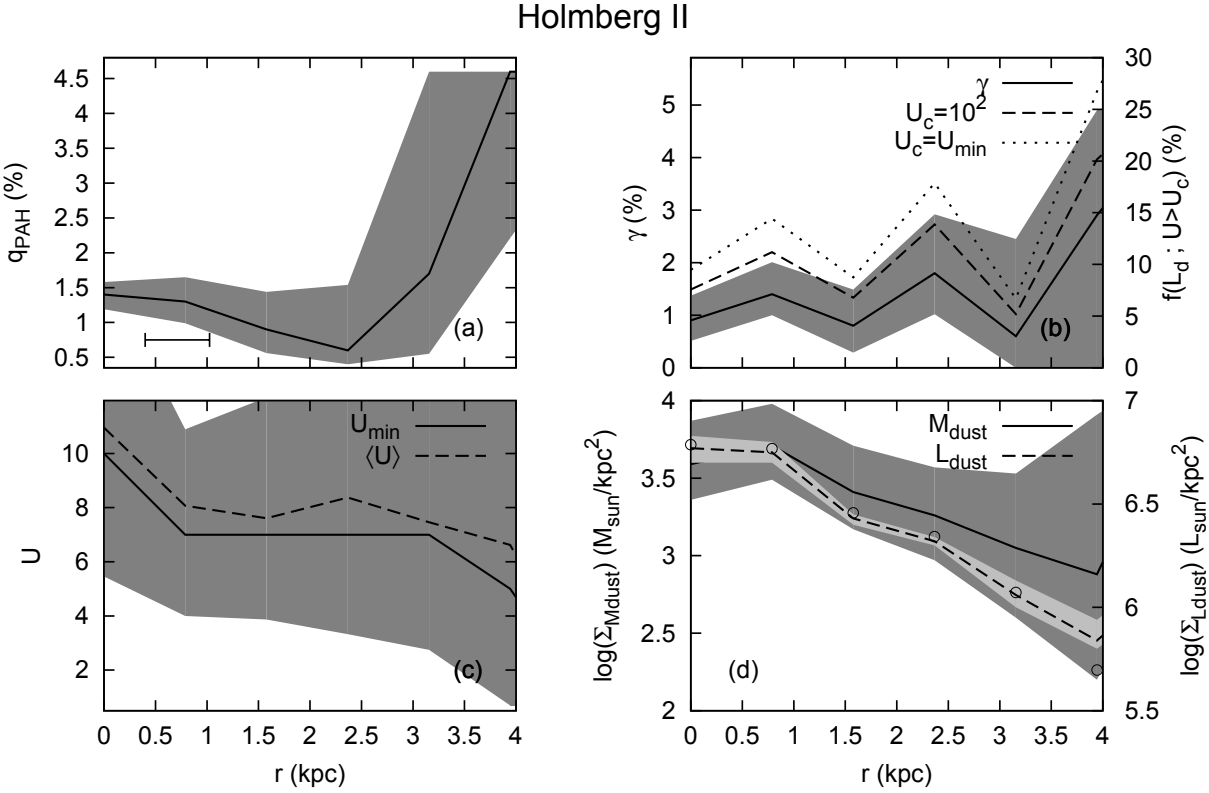
Holmberg II
q_{PAH} (%)
(a)
γ
$U_c=10^2$
$U_c=U_{min}$
γ (%)
$f(L_d ; U>U_c)$ (%)
(b)
U_{min}
⟨U⟩
U
(c)
r (kpc)
M_{dust}
L_{dust}
$\log(\Sigma_{Mdust})$ (M_{sun}/kpc^2)
$\log(\Sigma_{Ldust})$ (L_{sun}/kpc^2)
(d)
r (kpc)

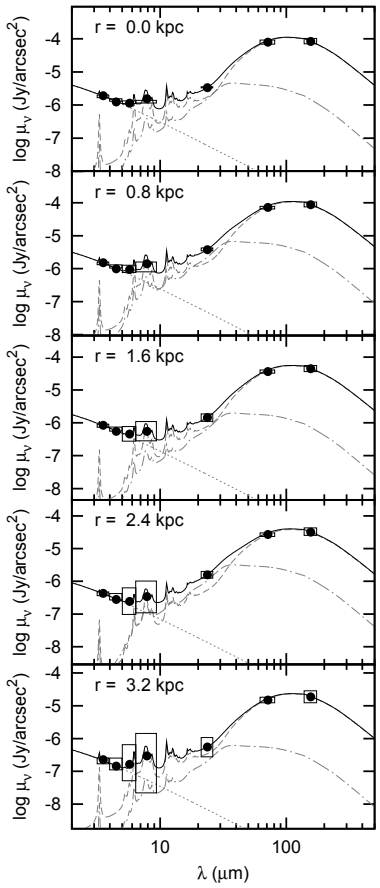
r = 0.0 kpc
r = 0.8 kpc
r = 1.6 kpc
r = 2.4 kpc
r = 3.2 kpc
log μ_ν (Jy/arcsec^2)
λ (μm)

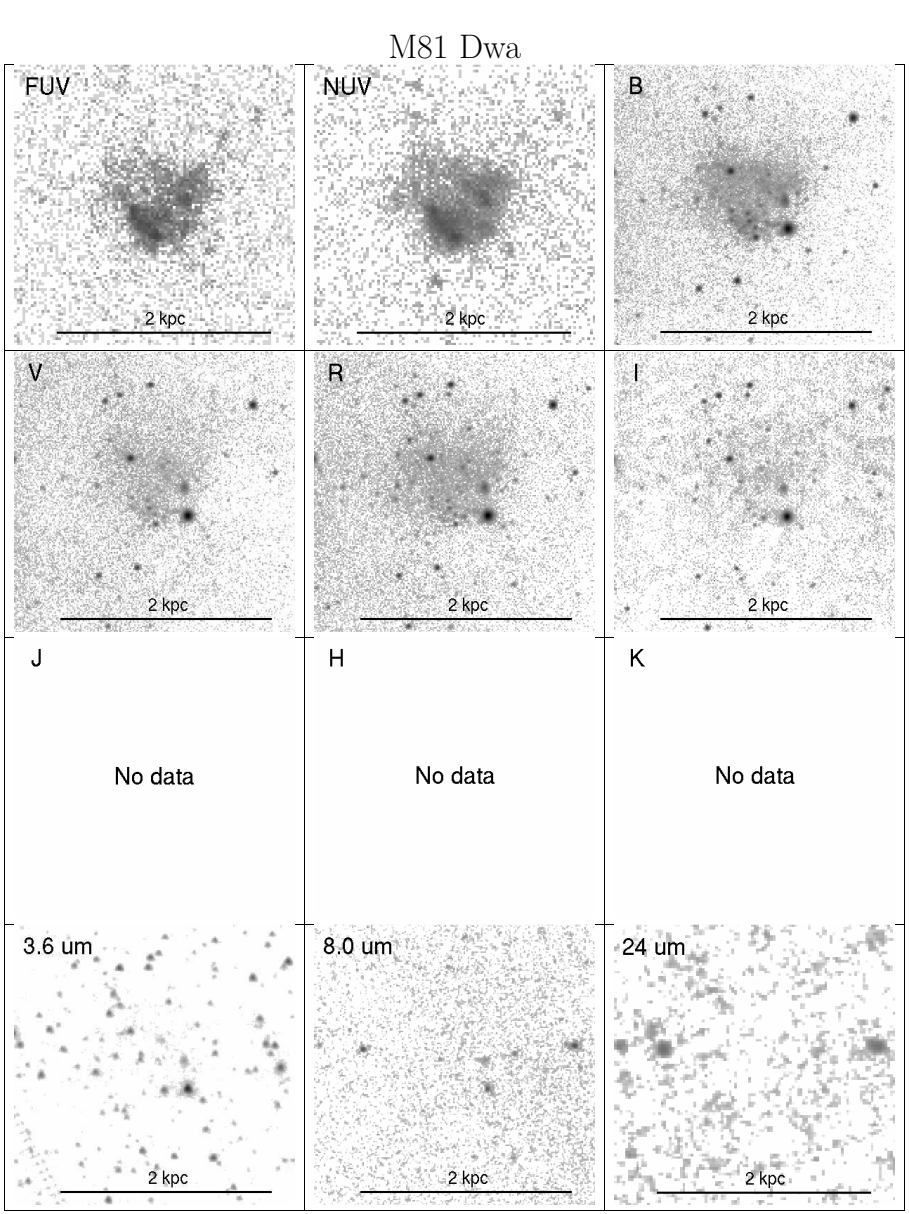
M81 Dwa
FUV
NUV
B
V
R
I
J
H
K
3.6 um
8.0 um
24 um
2 kpc
No data

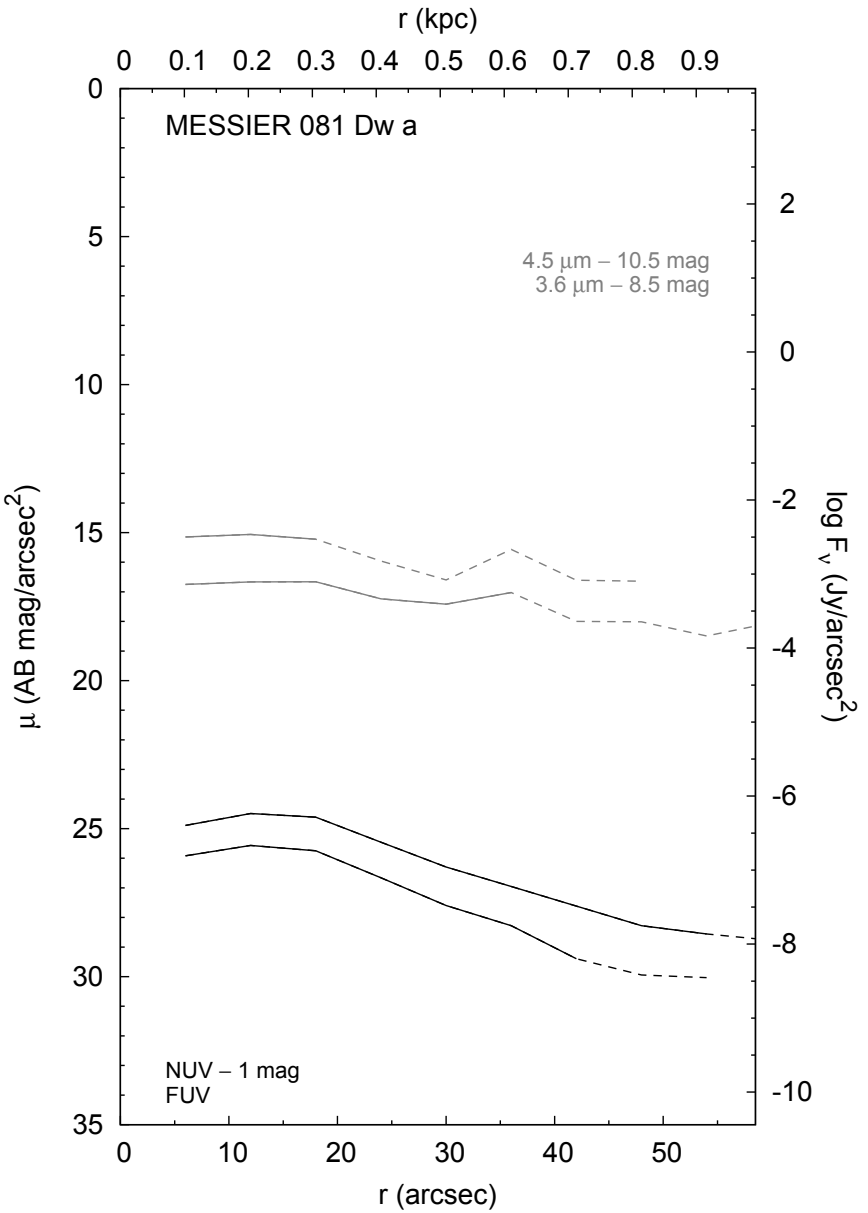
r (kpc)
MESSIER 081 Dw a
4.5 μm – 10.5 mag
3.6 μm – 8.5 mag
NUV – 1 mag
FUV
μ (AB mag/arcsec²)
log F_ν (Jy/arcsec²)
r (arcsec)

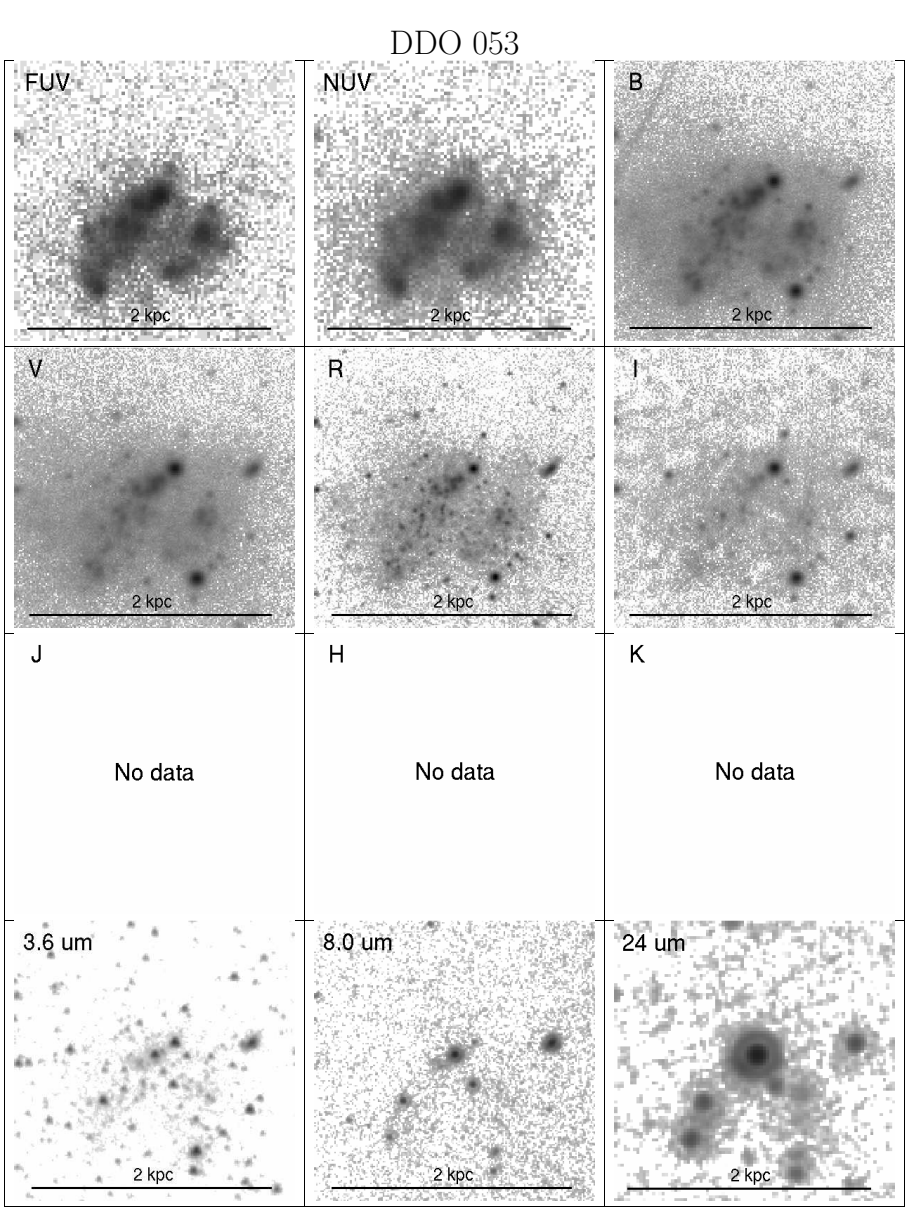
DDO 053
FUV
NUV
B
V
R
I
J
H
K
No data
No data
No data
3.6 um
8.0 um
24 um
2 kpc

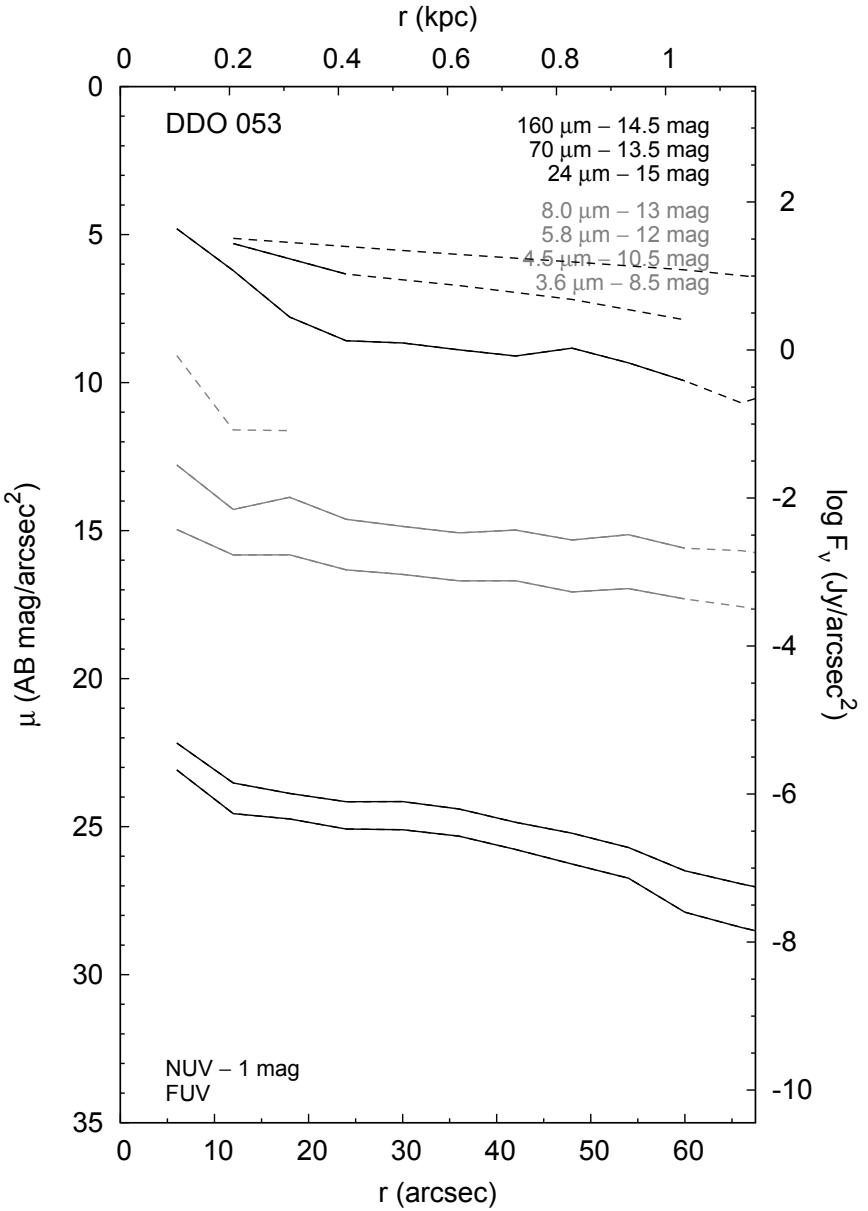
r (kpc)
DDO 053
160 μm – 14.5 mag
70 μm – 13.5 mag
24 μm – 15 mag
8.0 μm – 13 mag
5.8 μm – 12 mag
4.5 μm – 10.5 mag
3.6 μm – 8.5 mag
NUV – 1 mag
FUV
μ (AB mag/arcsec²)
log F_ν (Jy/arcsec²)
r (arcsec)

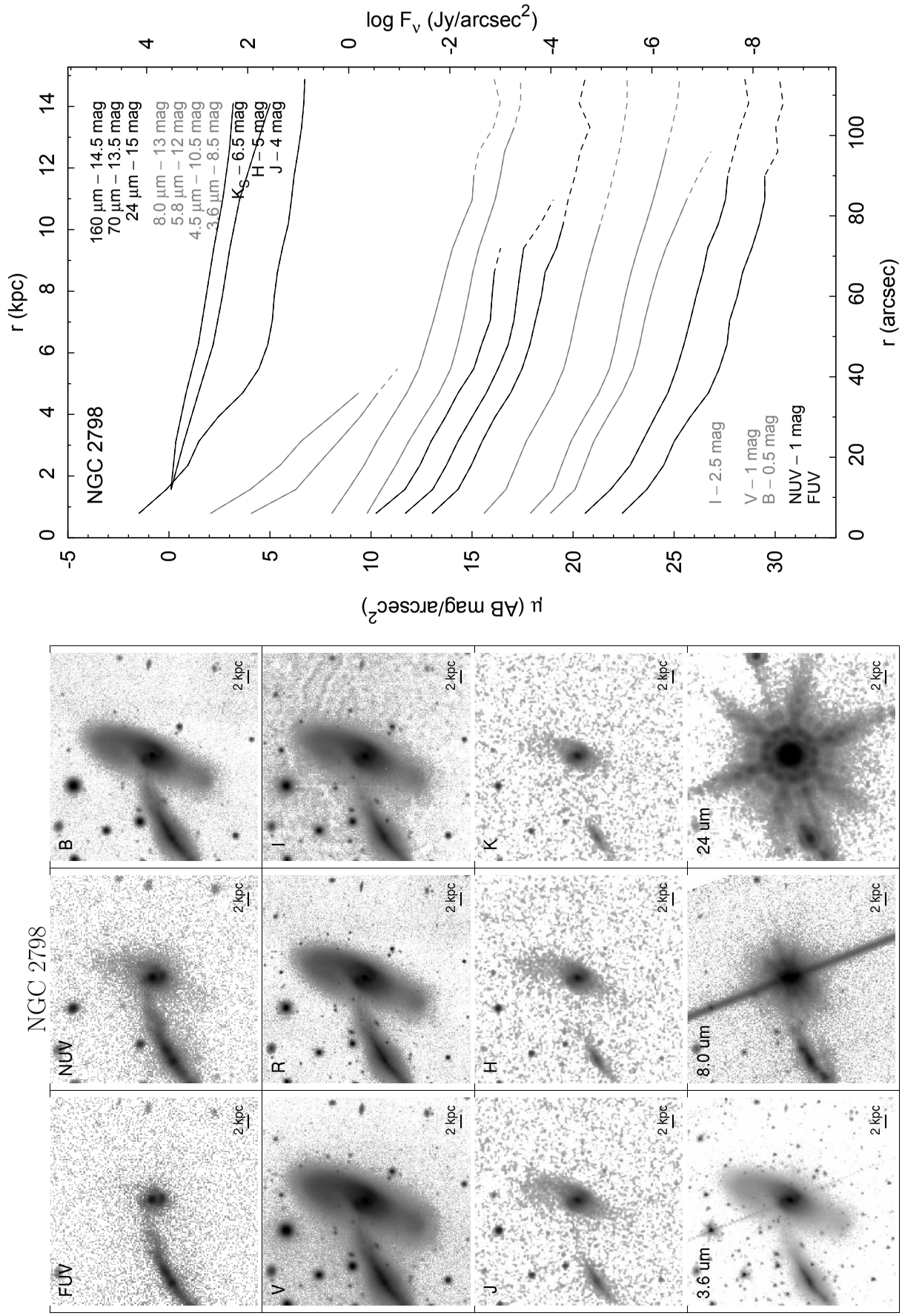
NGC 2798
FUV
NUV
B
V
R
I
J
H
K
3.6 um
8.0 um
24 um
2 kpc
μ (AB mag/arcsec²)
r (kpc)
r (arcsec)
log F_ν (Jy/arcsec²)
NGC 2798
160 μm – 14.5 mag
70 μm – 13.5 mag
24 μm – 15 mag
8.0 μm – 13 mag
5.8 μm – 12 mag
4.5 μm – 10.5 mag
3.6 μm – 8.5 mag
K_S – 6.5 mag
H – 5 mag
J – 4 mag
I – 2.5 mag
V – 1 mag
B – 0.5 mag
NUV – 1 mag
FUV

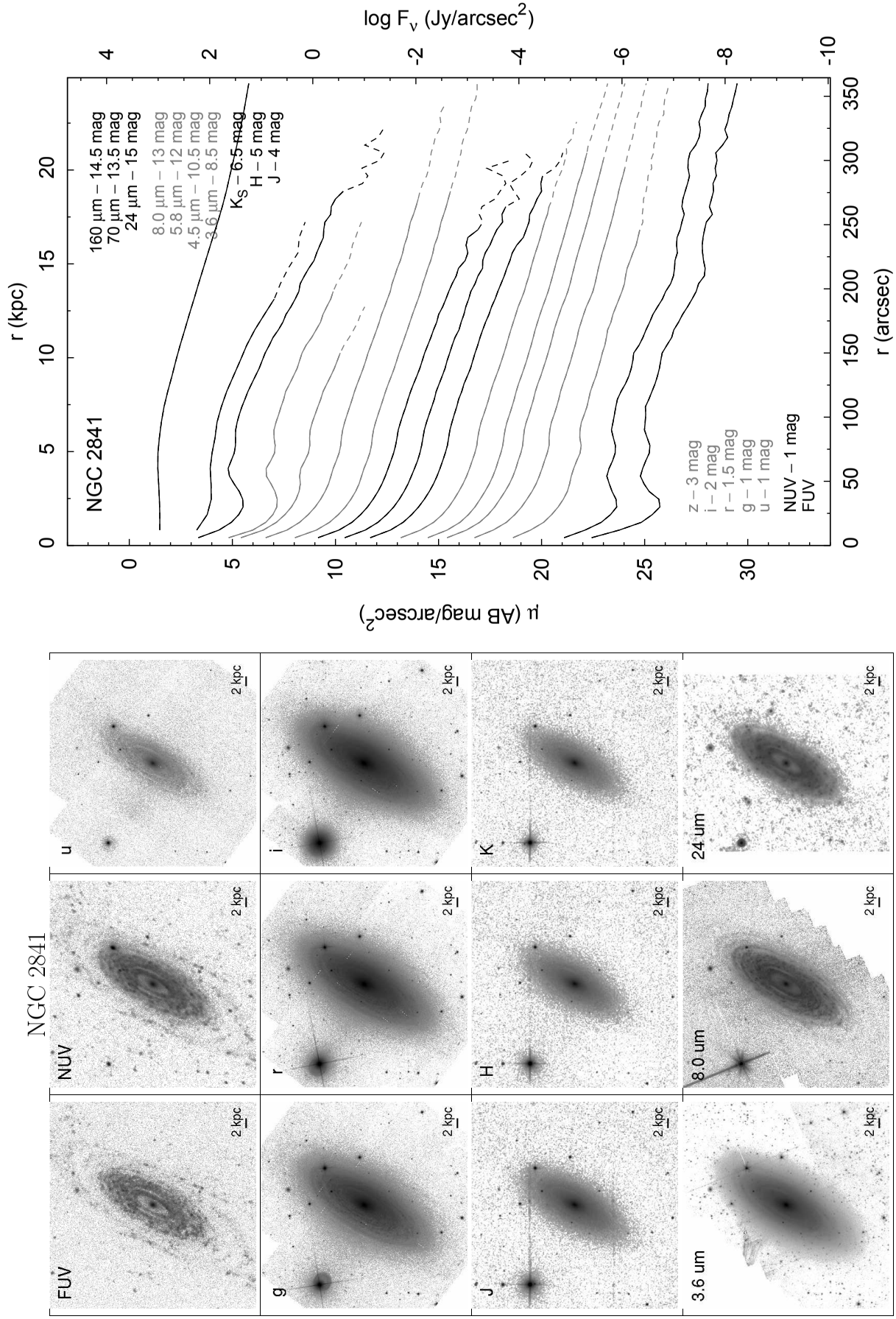
NGC 2841
FUV
NUV
u
g
r
i
J
H
K
3.6 um
8.0 um
24 um
2 kpc
μ (AB mag/arcsec²)
log F_ν (Jy/arcsec²)
r (kpc)
r (arcsec)
NGC 2841
160 μm – 14.5 mag
70 μm – 13.5 mag
24 μm – 15 mag
8.0 μm – 13 mag
5.8 μm – 12 mag
4.5 μm – 10.5 mag
3.6 μm – 8.5 mag
K_S – 6.5 mag
H – 5 mag
J – 4 mag
z – 3 mag
i – 2 mag
r – 1.5 mag
g – 1 mag
u – 1 mag
NUV – 1 mag
FUV

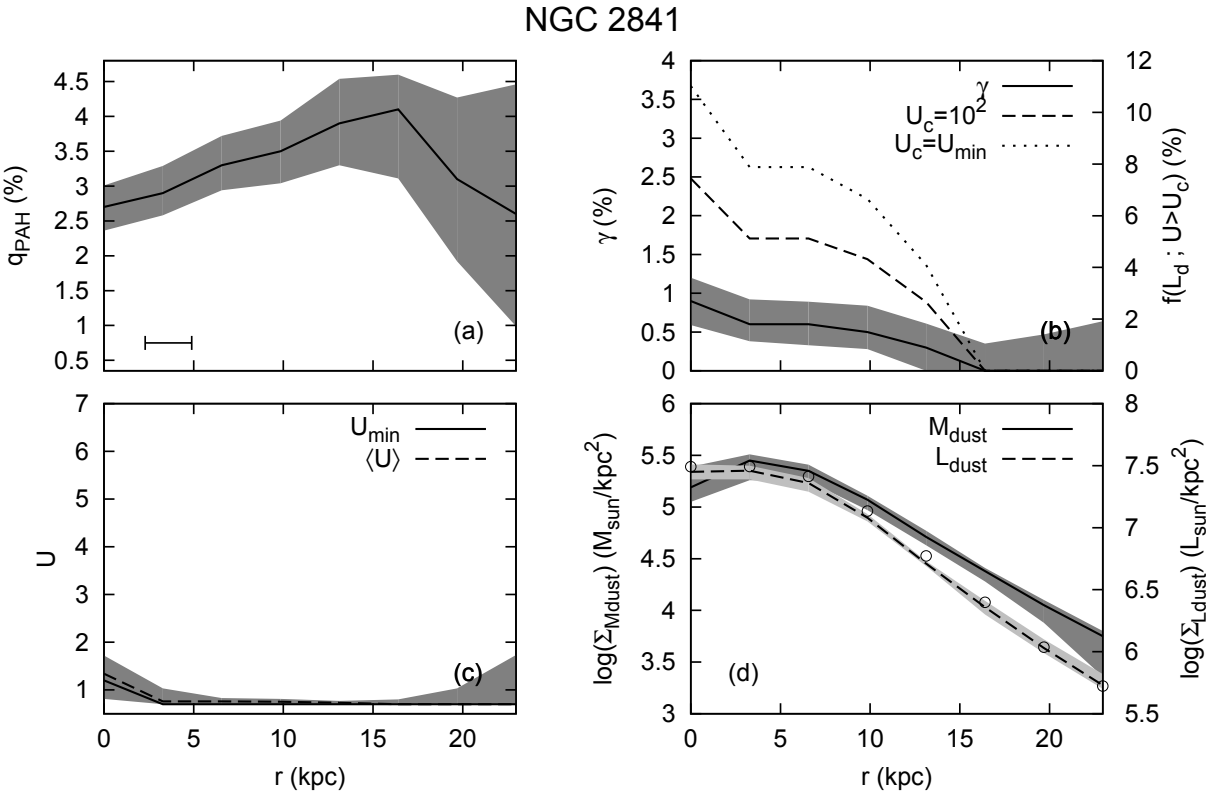
NGC 2841
q_{PAH} (%)
(a)
γ
$U_c=10^2$
$U_c=U_{min}$
γ (%)
$f(L_d ; U>U_c)$ (%)
(b)
U_{min}
⟨U⟩
U
(c)
M_{dust}
L_{dust}
$\log(\Sigma_{Mdust})$ (M_{sun}/kpc^2)
$\log(\Sigma_{Ldust})$ (L_{sun}/kpc^2)
(d)
r (kpc)
r (kpc)

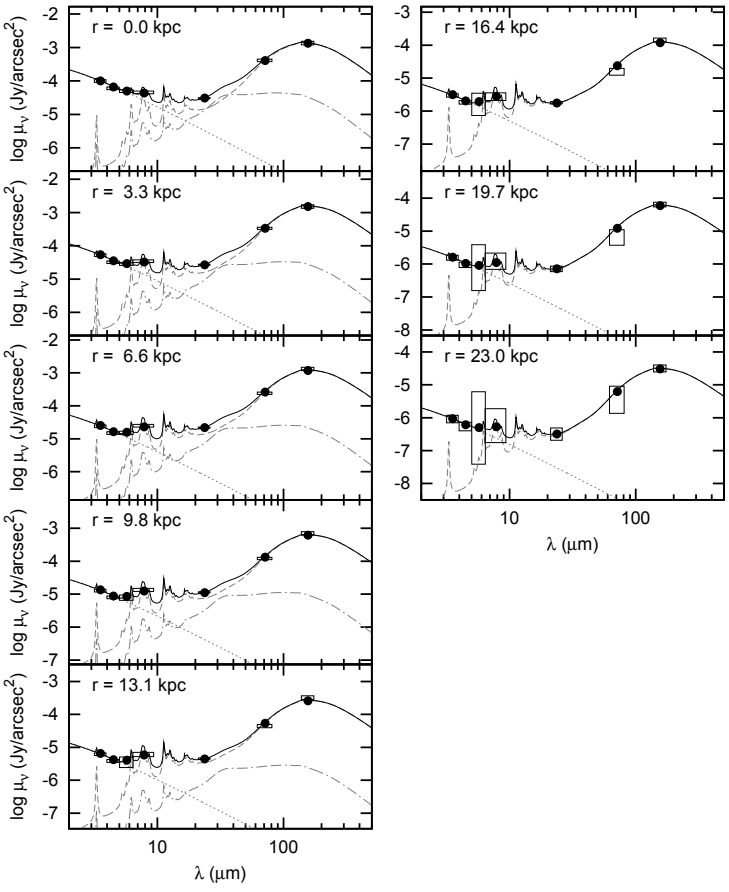
r = 0.0 kpc
r = 3.3 kpc
r = 6.6 kpc
r = 9.8 kpc
r = 13.1 kpc
r = 16.4 kpc
r = 19.7 kpc
r = 23.0 kpc
log μ_ν (Jy/arcsec^2)
λ (μm)

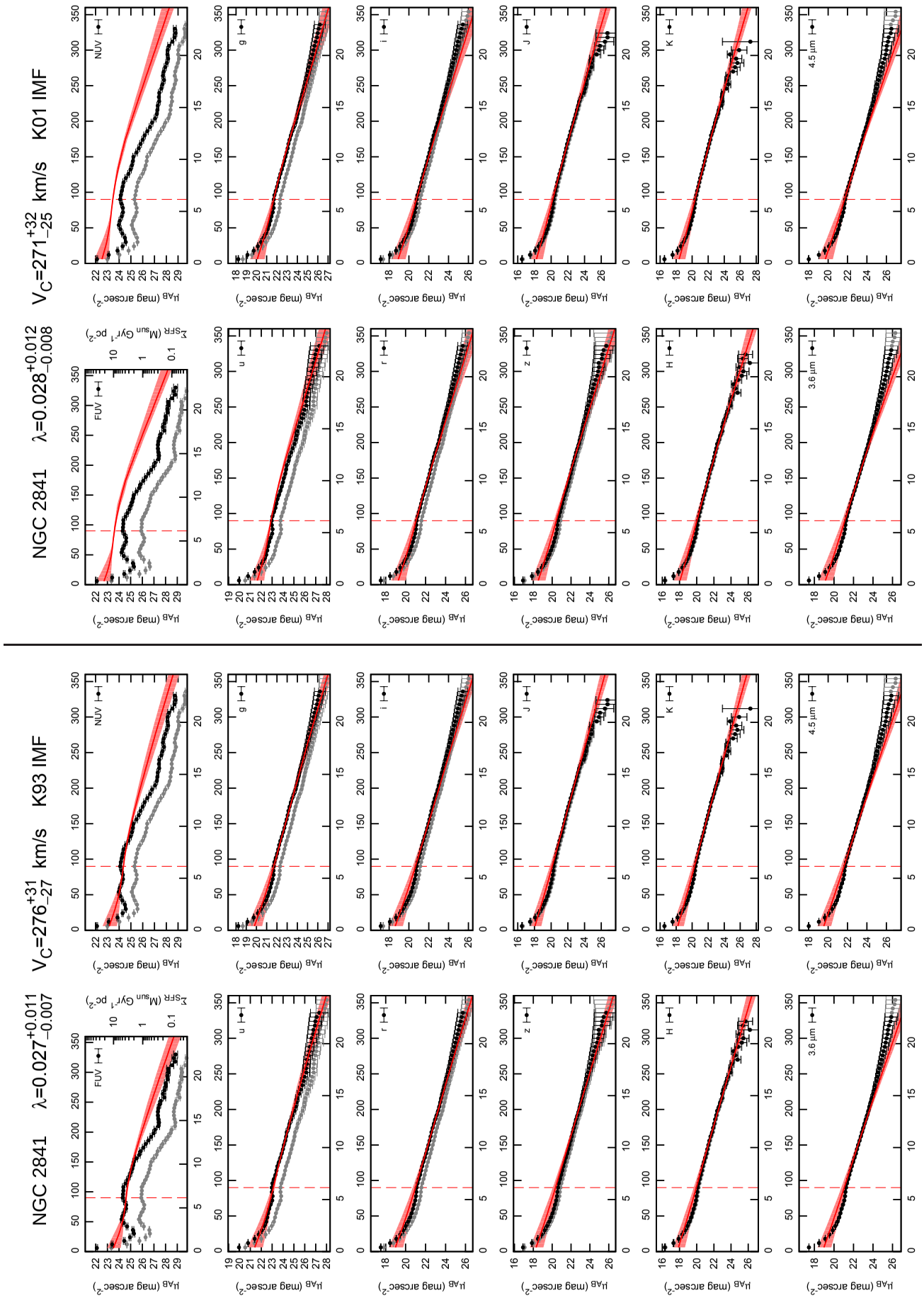
NGC 2841 λ=0.028+0.012−0.008 VC=271+32−25 km/s K01 IMF
NGC 2841 λ=0.027+0.011−0.007 VC=276+31−27 km/s K93 IMF
FUV
NUV
u
g
r
i
z
H
J
K
3.6 μm
4.5 μm
μAB (mag arcsec-2)
ΣSFR (Msun Gyr-1 pc-2)

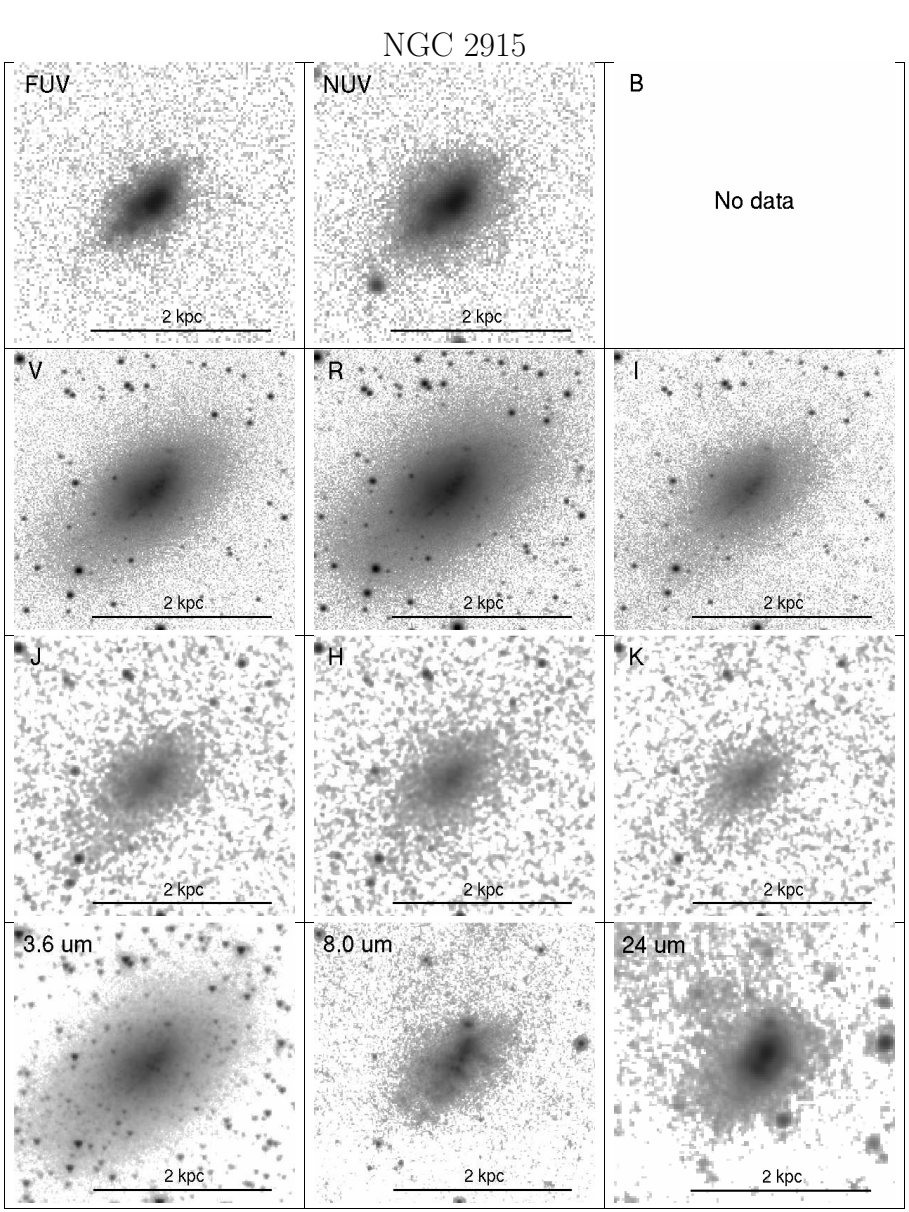
NGC 2915
FUV
NUV
B
No data
V
R
I
J
H
K
3.6 um
8.0 um
24 um
2 kpc

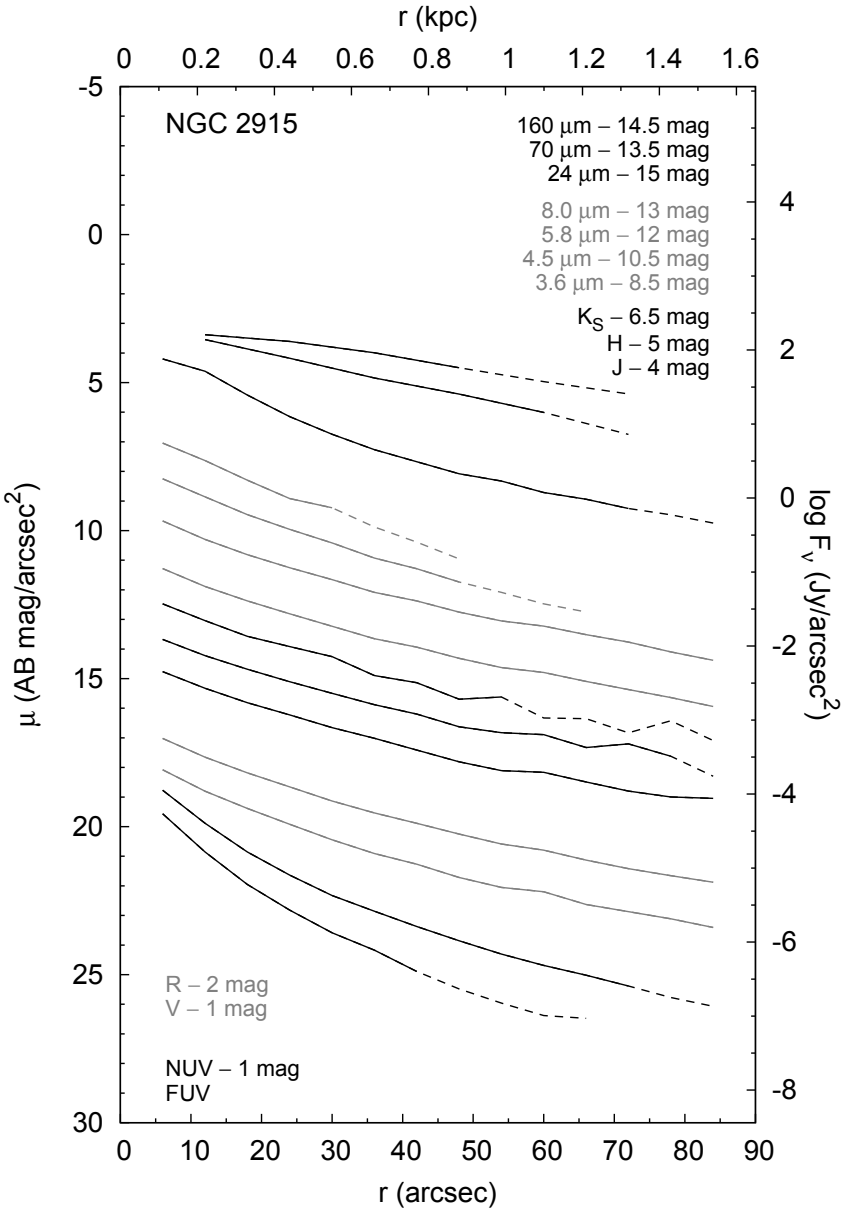
r (kpc)
NGC 2915
160 μm – 14.5 mag
70 μm – 13.5 mag
24 μm – 15 mag
8.0 μm – 13 mag
5.8 μm – 12 mag
4.5 μm – 10.5 mag
3.6 μm – 8.5 mag
K_S – 6.5 mag
H – 5 mag
J – 4 mag
R – 2 mag
V – 1 mag
NUV – 1 mag
FUV
μ (AB mag/arcsec²)
log F_ν (Jy/arcsec²)
r (arcsec)

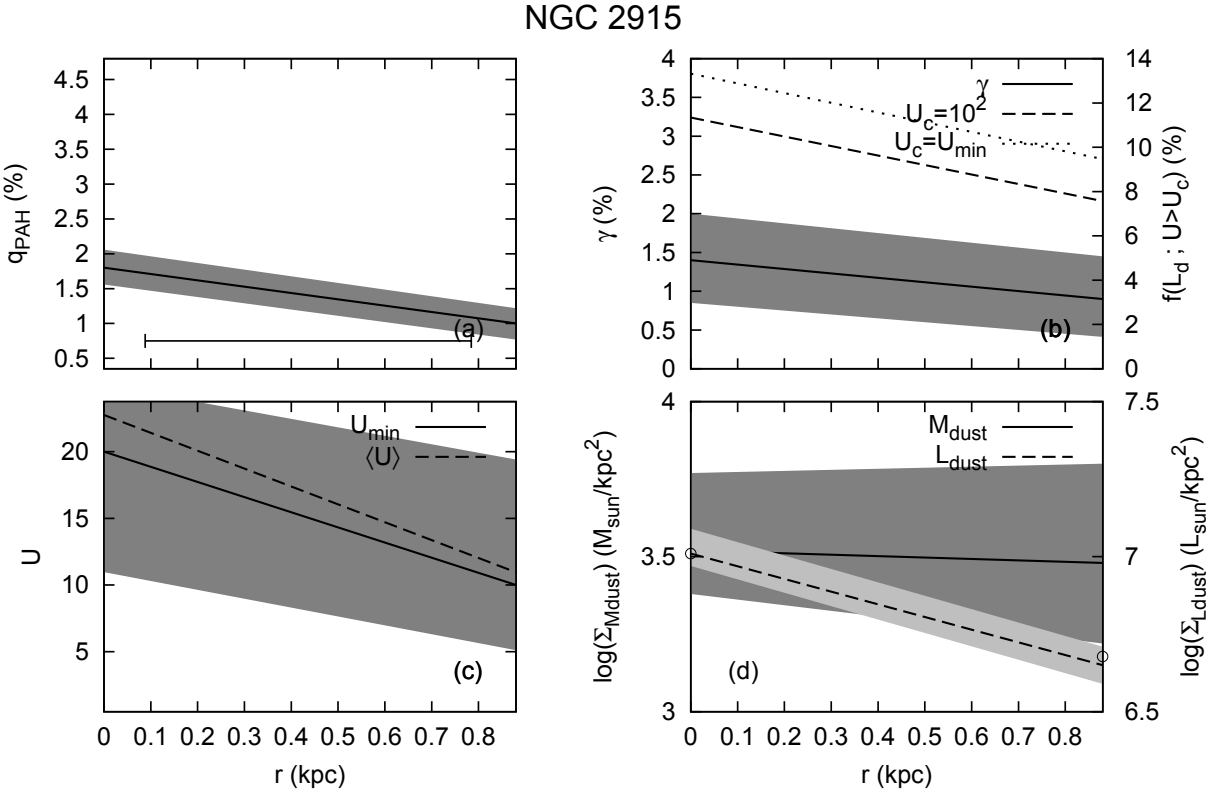
NGC 2915
q_{PAH} (%)
(a)
γ (%)
$f(L_d ; U>U_c)$ (%)
γ
$U_c=10^2$
$U_c=U_{min}$
(b)
U
U_{min}
⟨U⟩
(c)
$\log(\Sigma_{Mdust})$ (M_{sun}/kpc^2)
$\log(\Sigma_{Ldust})$ (L_{sun}/kpc^2)
M_{dust}
L_{dust}
(d)
r (kpc)
r (kpc)

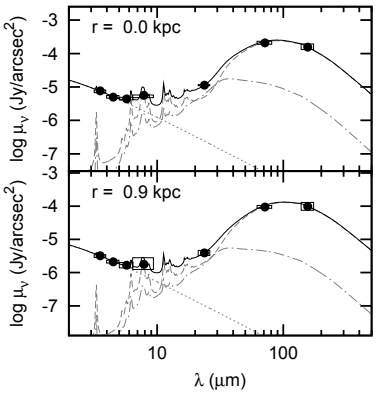
r = 0.0 kpc
r = 0.9 kpc
log μ_ν (Jy/arcsec^2)
log μ_ν (Jy/arcsec^2)
λ (μm)

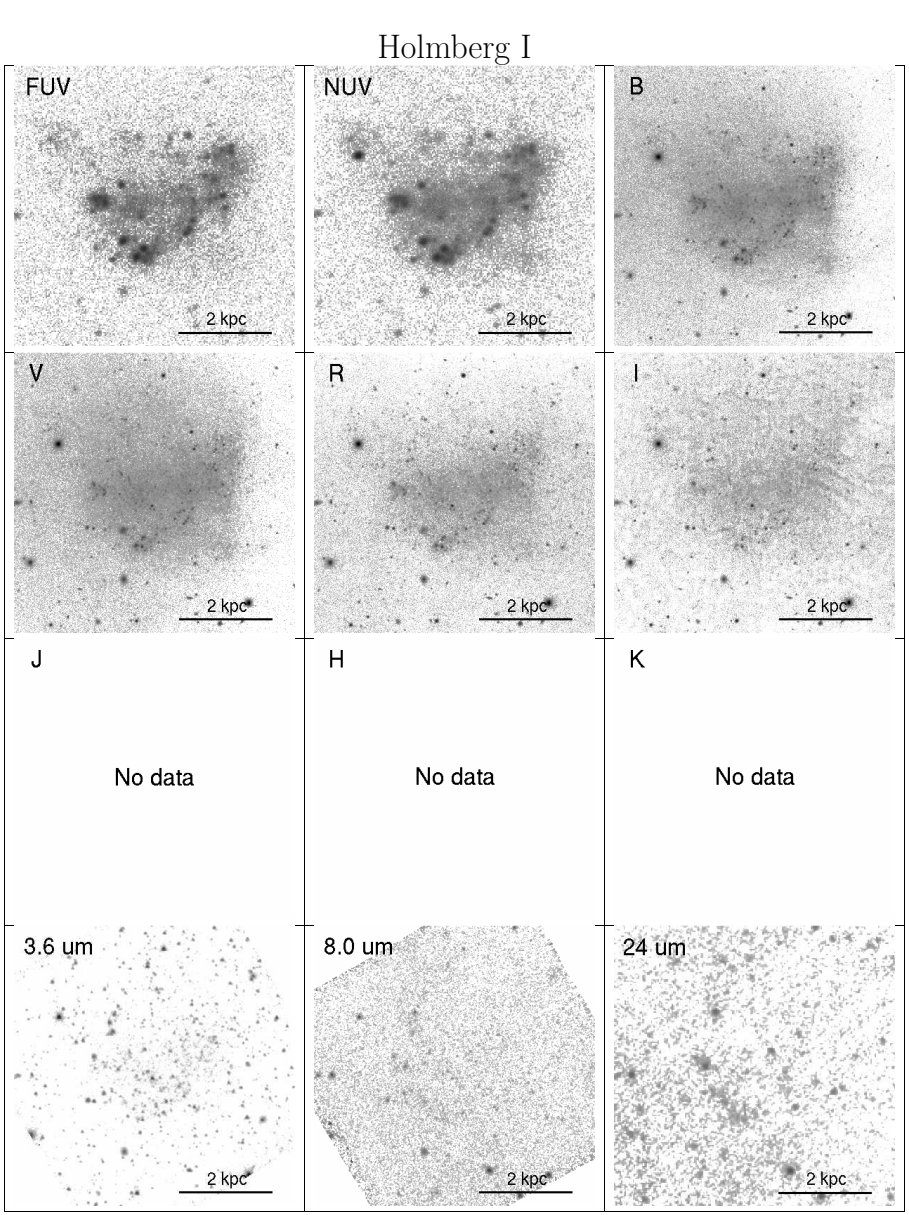
Holmberg I
FUV
NUV
B
V
R
I
J
H
K
No data
No data
No data
3.6 um
8.0 um
24 um
2 kpc

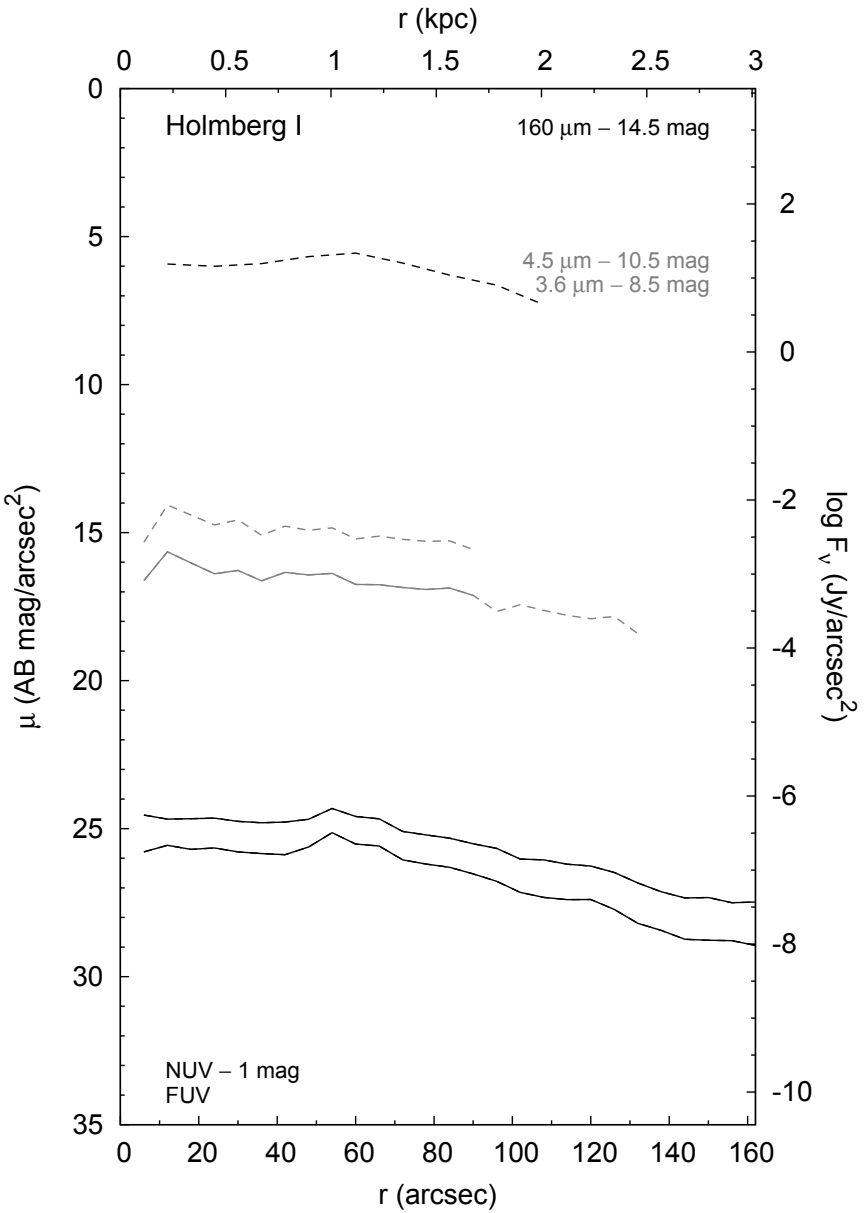
r (kpc)
Holmberg I
160 μm – 14.5 mag
4.5 μm – 10.5 mag
3.6 μm – 8.5 mag
NUV – 1 mag
FUV
μ (AB mag/arcsec²)
log F_ν (Jy/arcsec²)
r (arcsec)

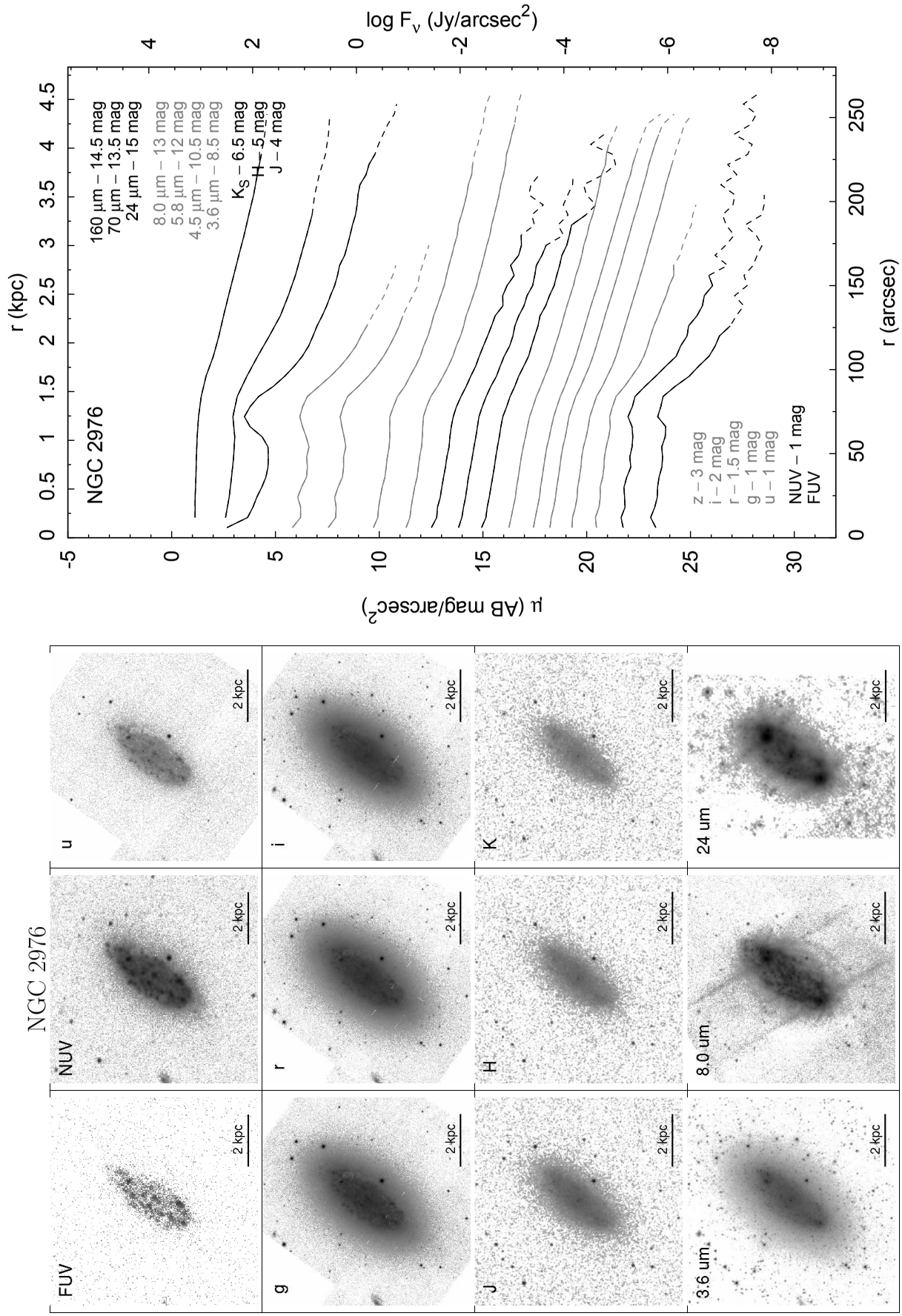
NGC 2976
FUV
NUV
u
g
r
i
J
H
K
3.6 um
8.0 um
24 um
2 kpc
μ (AB mag/arcsec²)
r (kpc)
r (arcsec)
log F_ν (Jy/arcsec²)
NGC 2976
160 μm – 14.5 mag
70 μm – 13.5 mag
24 μm – 15 mag
8.0 μm – 13 mag
5.8 μm – 12 mag
4.5 μm – 10.5 mag
3.6 μm – 8.5 mag
K_S – 6.5 mag
H – 5 mag
J – 4 mag
z – 3 mag
i – 2 mag
r – 1.5 mag
g – 1 mag
u – 1 mag
NUV – 1 mag
FUV

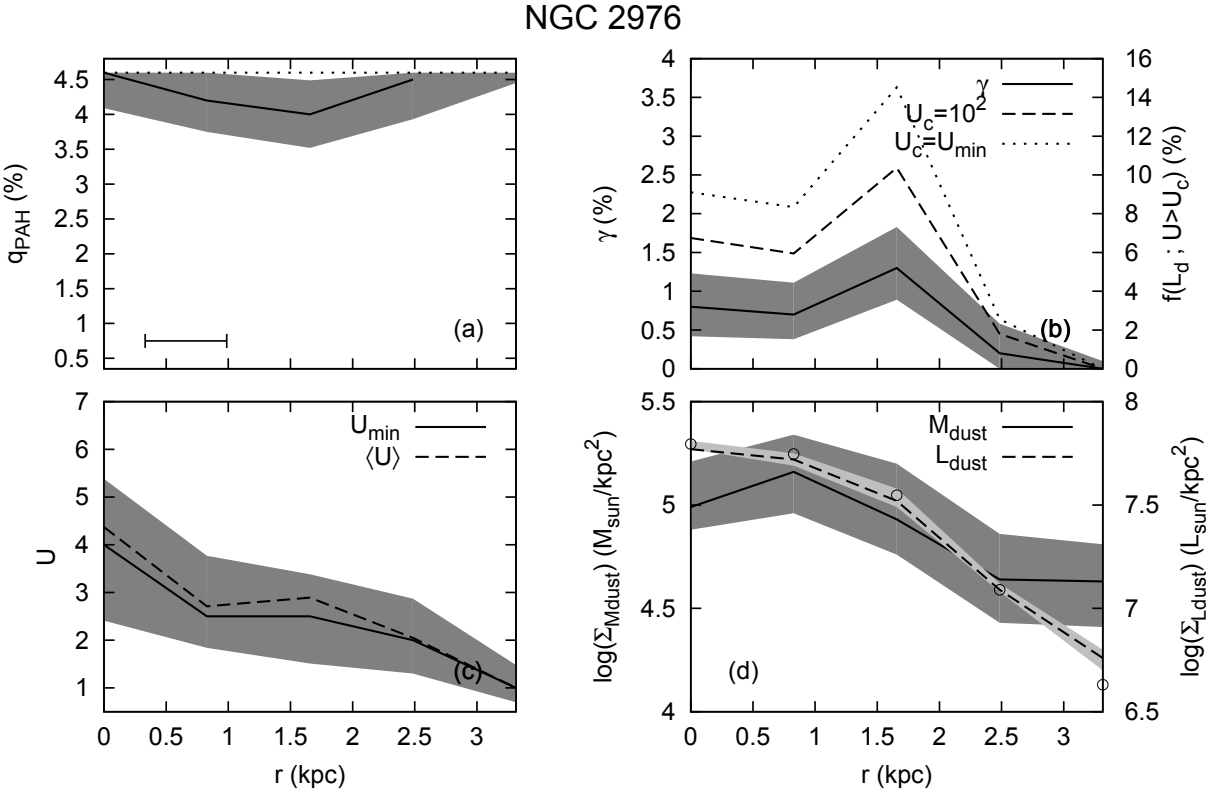
NGC 2976
q_{PAH} (%)
(a)
γ
$U_c=10^2$
$U_c=U_{min}$
γ (%)
$f(L_d ; U>U_c)$ (%)
(b)
U_{min}
⟨U⟩
U
(c)
r (kpc)
M_{dust}
L_{dust}
$\log(\Sigma_{Mdust})$ (M_{sun}/kpc^2)
$\log(\Sigma_{Ldust})$ (L_{sun}/kpc^2)
(d)
r (kpc)

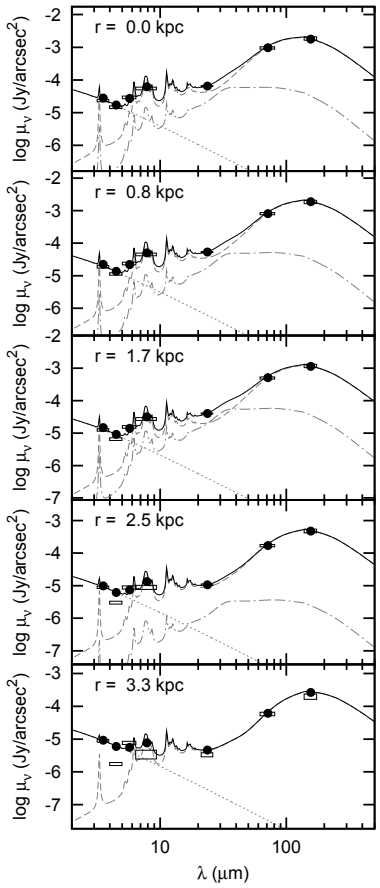
r = 0.0 kpc
r = 0.8 kpc
r = 1.7 kpc
r = 2.5 kpc
r = 3.3 kpc
log μ_ν (Jy/arcsec^2)
λ (μm)

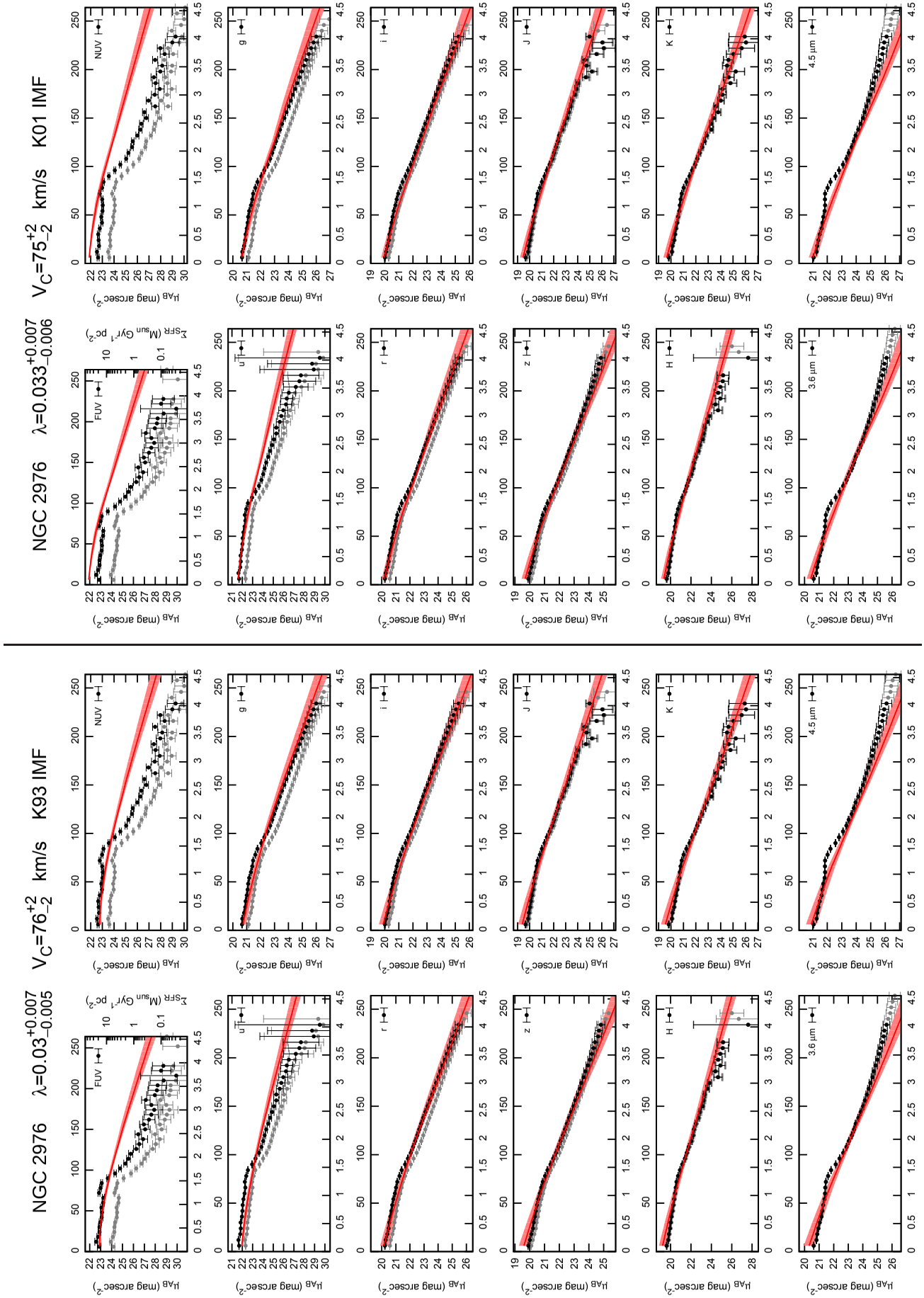
NGC 2976 λ=0.033+0.007−0.006 VC=75+2−2 km/s K01 IMF
NGC 2976 λ=0.03+0.007−0.005 VC=76+2−2 km/s K93 IMF
μAB (mag arcsec-2)
ΣSFR (Msun Gyr-1 pc-2)
FUV
NUV
u
g
r
i
z
J
H
K
3.6 μm
4.5 μm

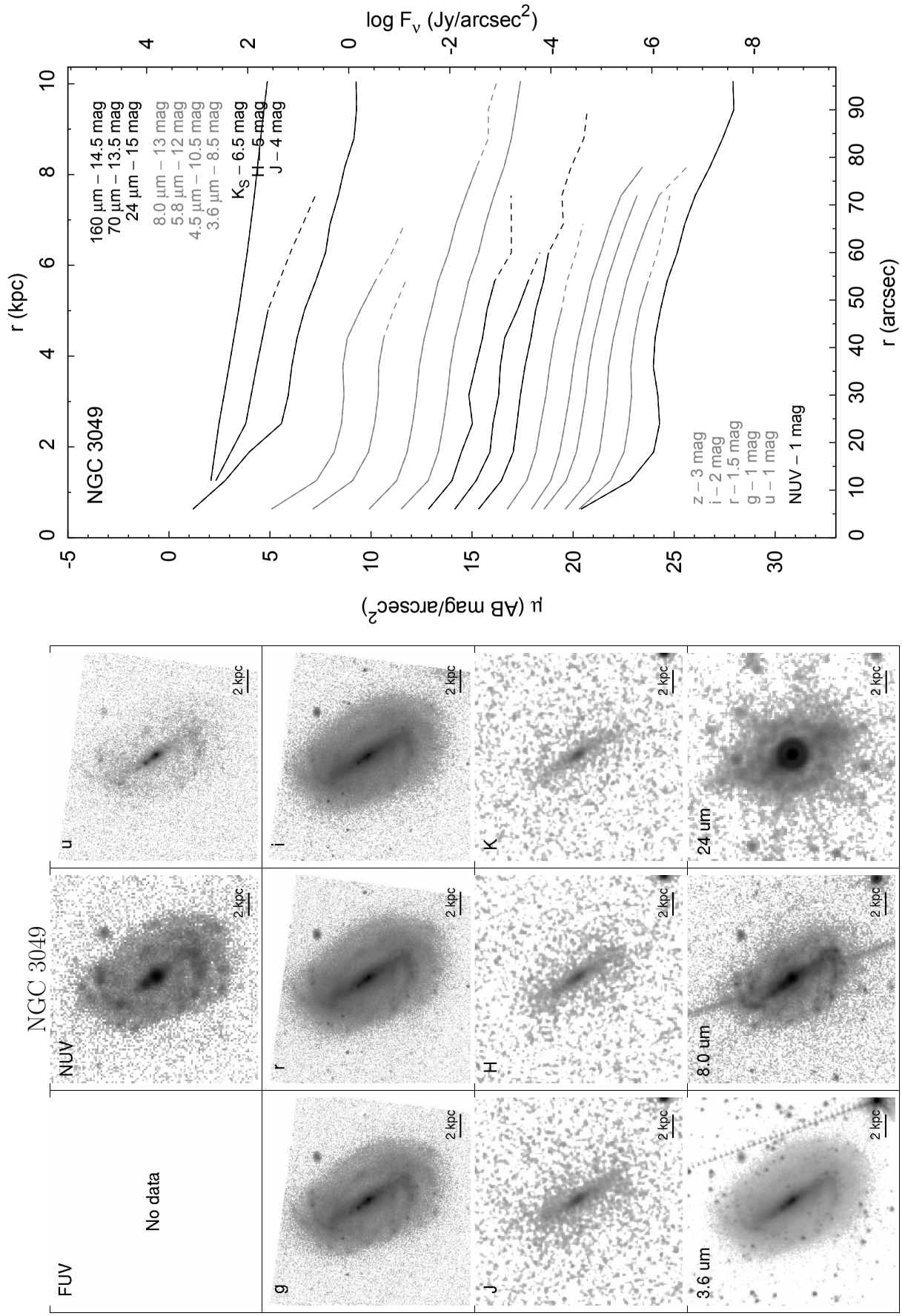
NGC 3049
FUV
No data
NUV
u
g
r
i
H
K
J
24 um
8.0 um
3.6 um
2 kpc
μ (AB mag/arcsec²)
log F_ν (Jy/arcsec²)
r (kpc)
r (arcsec)
160 μm – 14.5 mag
70 μm – 13.5 mag
24 μm – 15 mag
8.0 μm – 13 mag
5.8 μm – 12 mag
4.5 μm – 10.5 mag
3.6 μm – 8.5 mag
K_S – 6.5 mag
H – 5 mag
J – 4 mag
z – 3 mag
i – 2 mag
r – 1.5 mag
g – 1 mag
u – 1 mag
NUV – 1 mag

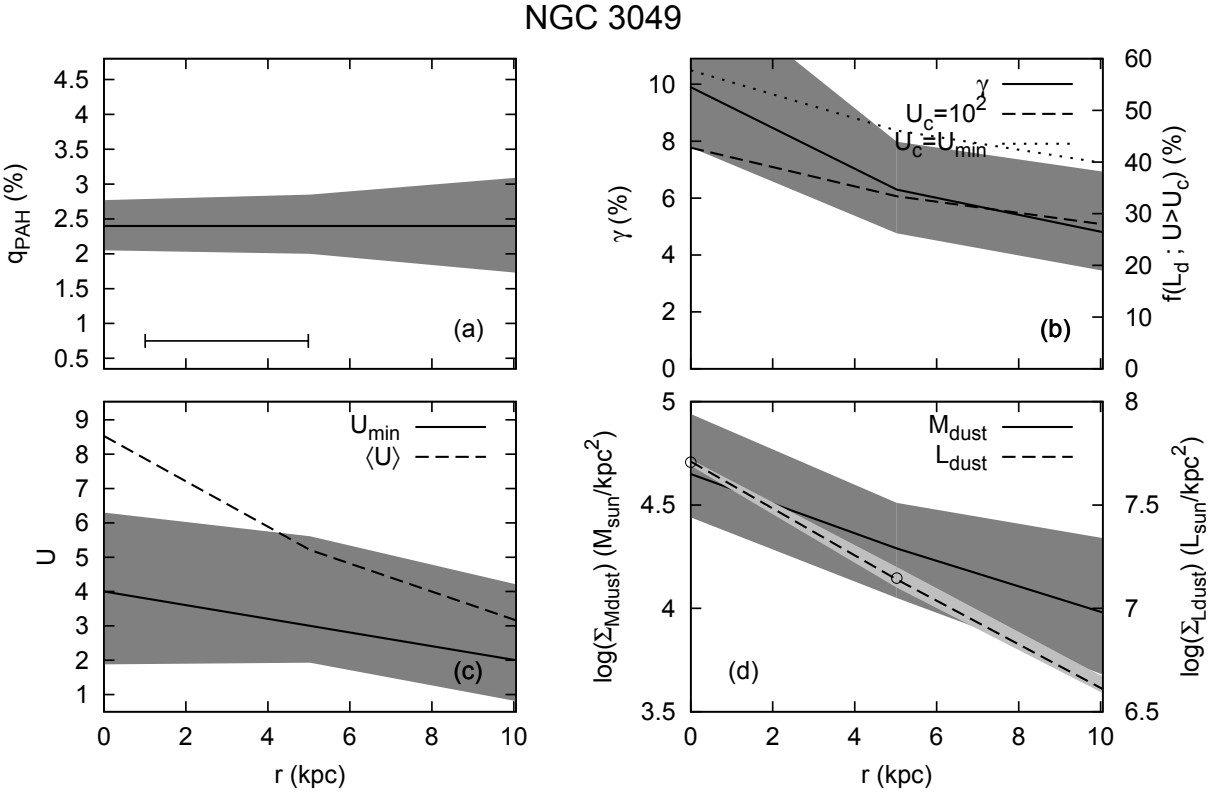
NGC 3049
q_{PAH} (%)
(a)
γ
$U_c=10^2$
$U_c=U_{min}$
γ (%)
$f(L_d ; U>U_c)$ (%)
(b)
U_{min}
⟨U⟩
U
(c)
r (kpc)
M_{dust}
L_{dust}
$\log(\Sigma_{Mdust})$ (M_{sun}/kpc^2)
$\log(\Sigma_{Ldust})$ (L_{sun}/kpc^2)
(d)
r (kpc)

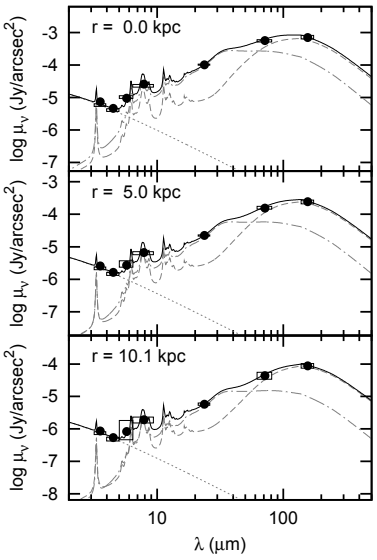
r = 0.0 kpc
r = 5.0 kpc
r = 10.1 kpc
log μ_ν (Jy/arcsec^2)
λ (μm)

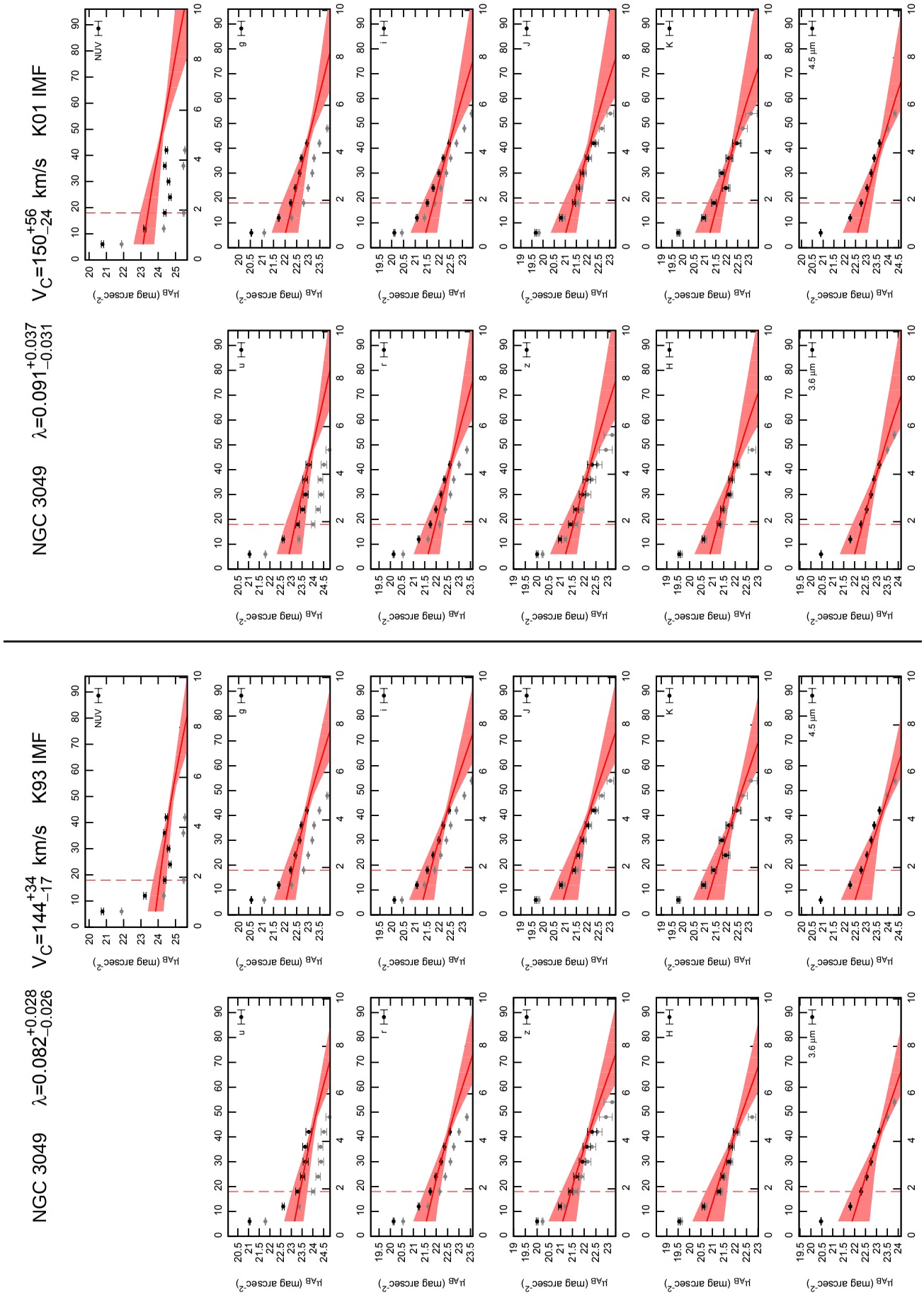
NGC 3049 λ=0.091+0.037−0.031 VC=150+56−24 km/s K01 IMF
NGC 3049 λ=0.082+0.028−0.026 VC=144+34−17 km/s K93 IMF
NUV
u
g
r
i
z
J
H
K
3.6 μm
4.5 μm
μAB (mag arcsec-2)

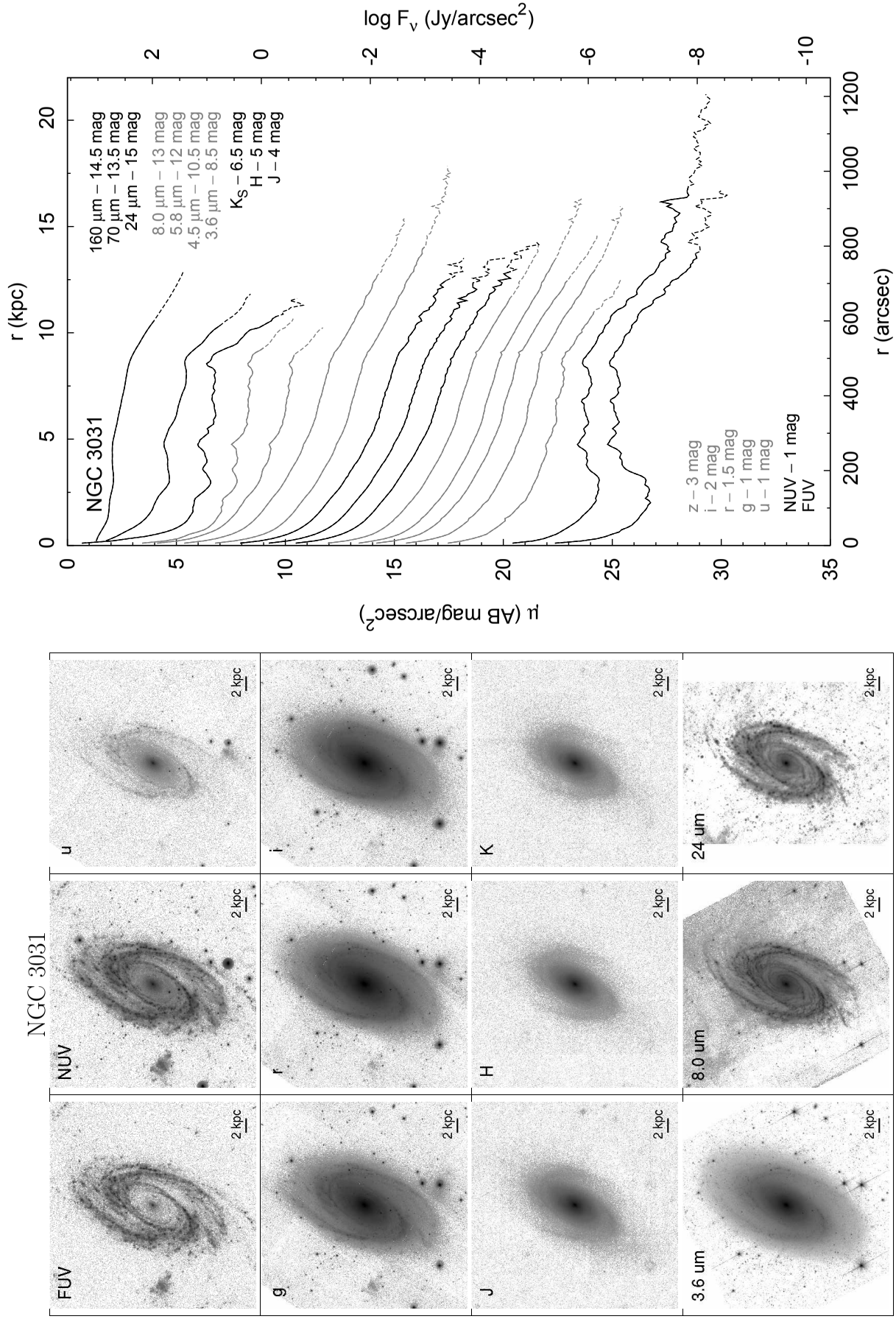
NGC 3031
FUV
NUV
u
g
r
i
J
H
K
3.6 um
8.0 um
24 um
2 kpc
μ (AB mag/arcsec²)
log F_ν (Jy/arcsec²)
r (kpc)
r (arcsec)
NGC 3031
160 μm – 14.5 mag
70 μm – 13.5 mag
24 μm – 15 mag
8.0 μm – 13 mag
5.8 μm – 12 mag
4.5 μm – 10.5 mag
3.6 μm – 8.5 mag
K_S – 6.5 mag
H – 5 mag
J – 4 mag
z – 3 mag
i – 2 mag
r – 1.5 mag
g – 1 mag
u – 1 mag
NUV – 1 mag
FUV

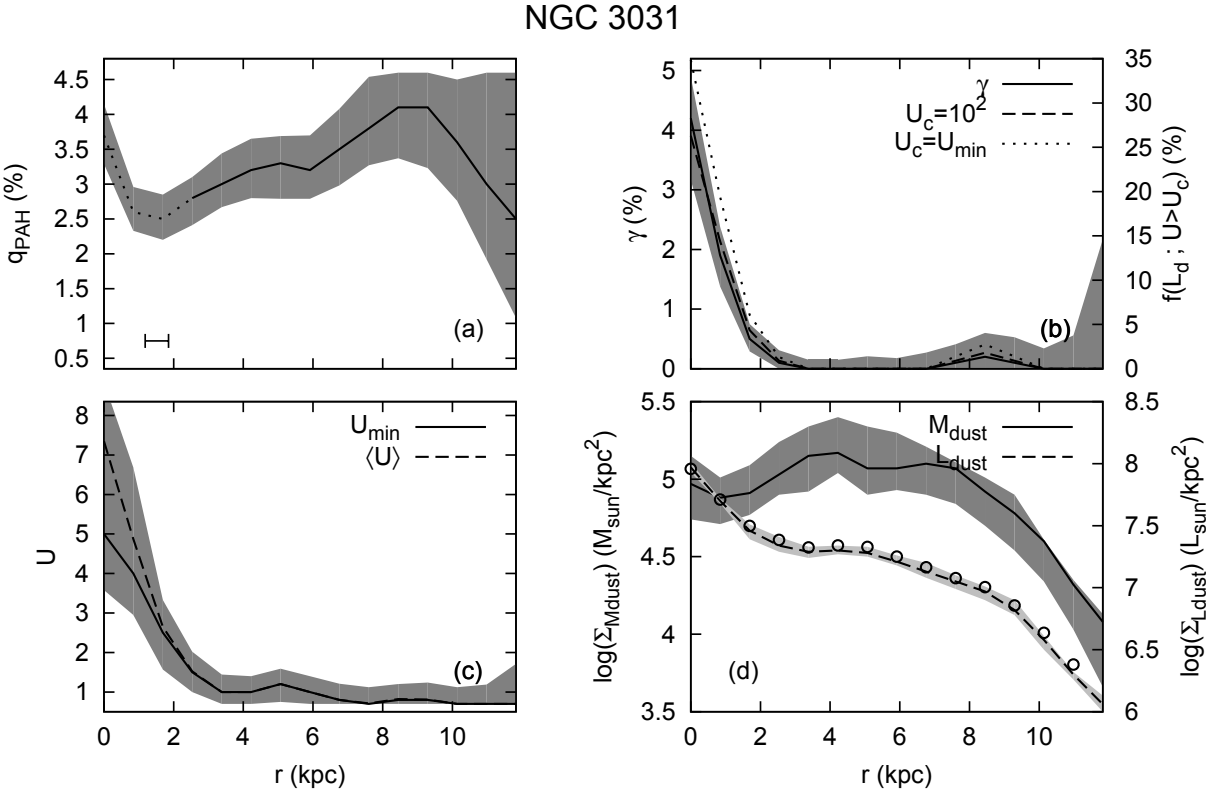
NGC 3031
q_{PAH} (%)
(a)
γ
$U_c=10^2$
$U_c=U_{min}$
γ (%)
$f(L_d ; U>U_c)$ (%)
(b)
U_{min}
⟨U⟩
U
(c)
r (kpc)
M_{dust}
L_{dust}
$\log(\Sigma_{Mdust})$ (M_{sun}/kpc^2)
$\log(\Sigma_{Ldust})$ (L_{sun}/kpc^2)
(d)
r (kpc)

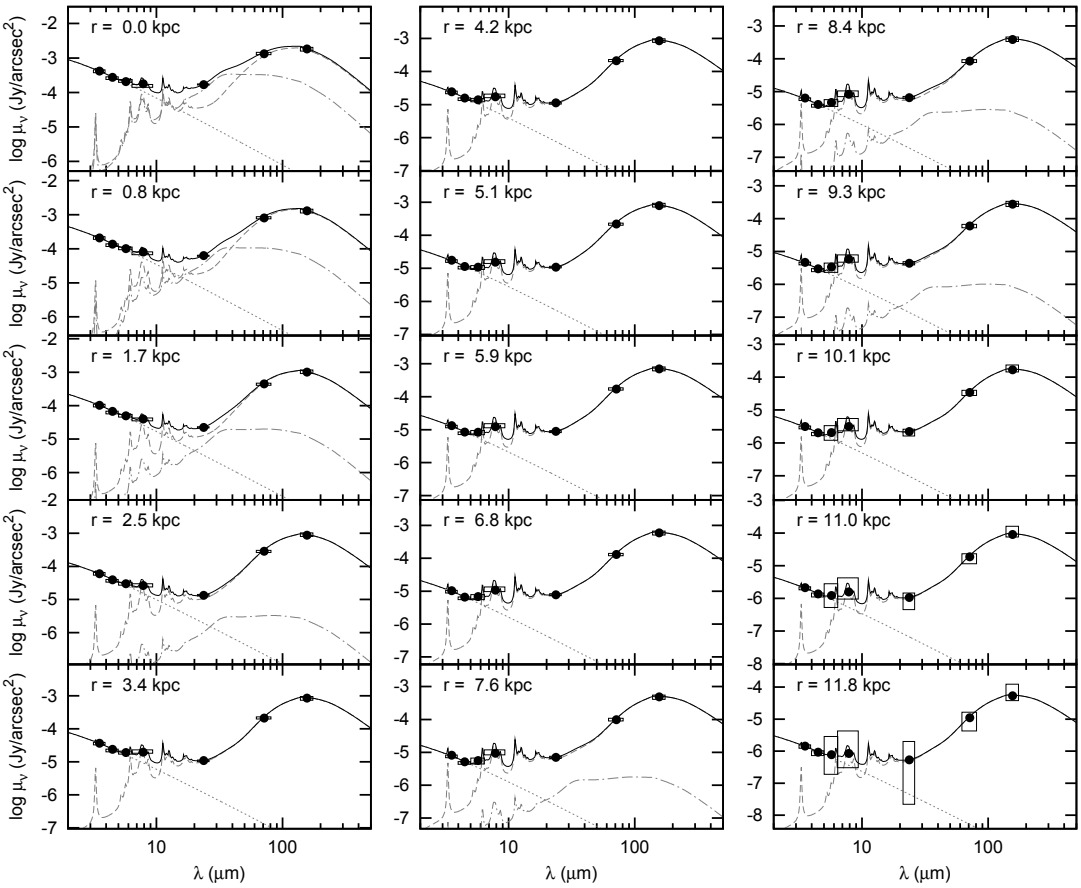
r = 0.0 kpc
r = 0.8 kpc
r = 1.7 kpc
r = 2.5 kpc
r = 3.4 kpc
r = 4.2 kpc
r = 5.1 kpc
r = 5.9 kpc
r = 6.8 kpc
r = 7.6 kpc
r = 8.4 kpc
r = 9.3 kpc
r = 10.1 kpc
r = 11.0 kpc
r = 11.8 kpc
log μ_ν (Jy/arcsec^2)
λ (μm)

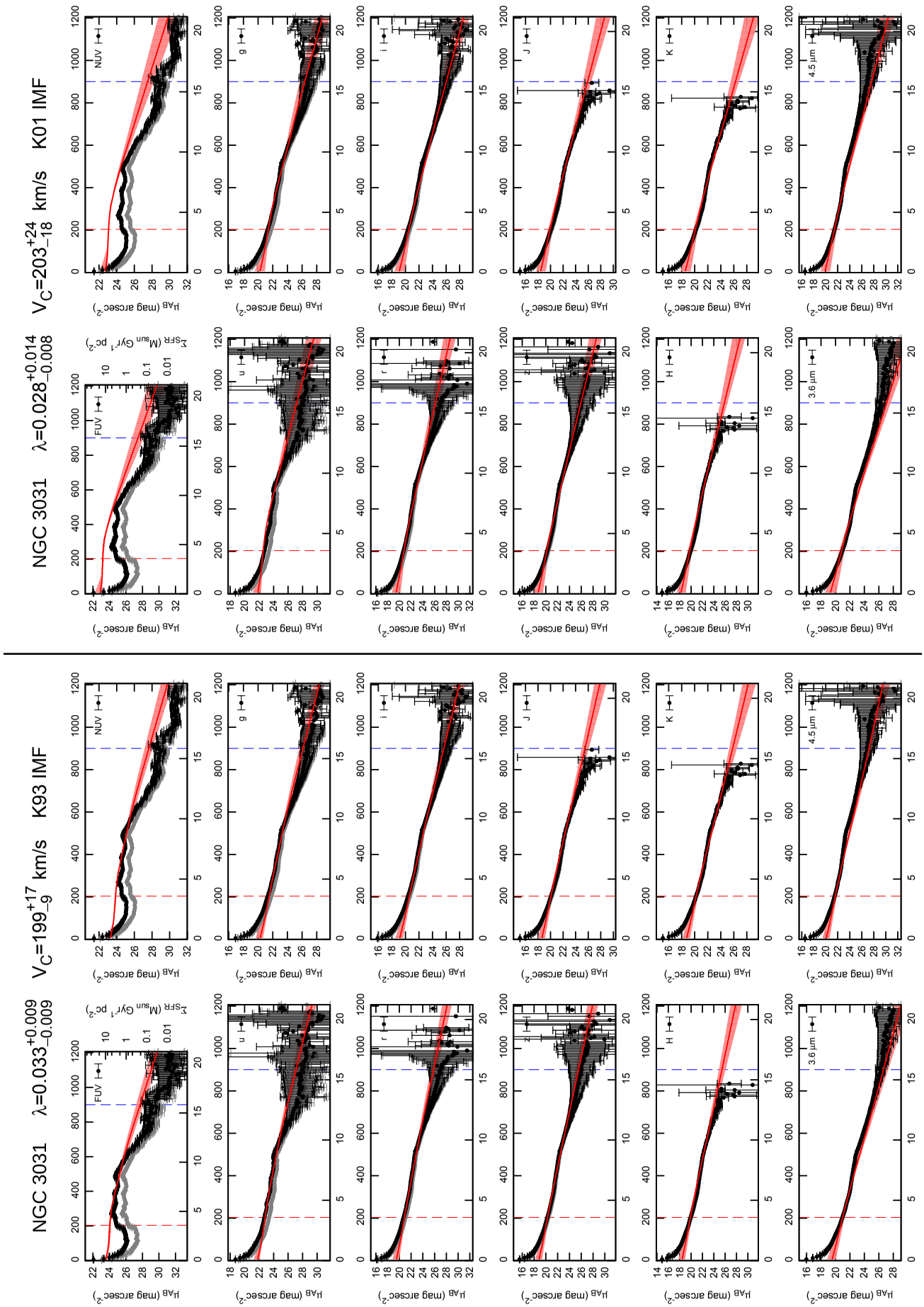
NGC 3031 λ=0.033+0.009−0.009 VC=199+17−9 km/s K93 IMF
NGC 3031 λ=0.028+0.014−0.008 VC=203+24−18 km/s K01 IMF
μAB (mag arcsec-2)
ΣSFR (Msun Gyr-1 pc-2)
FUV
NUV
u
g
r
i
J
H
K
3.6 μm
4.5 μm

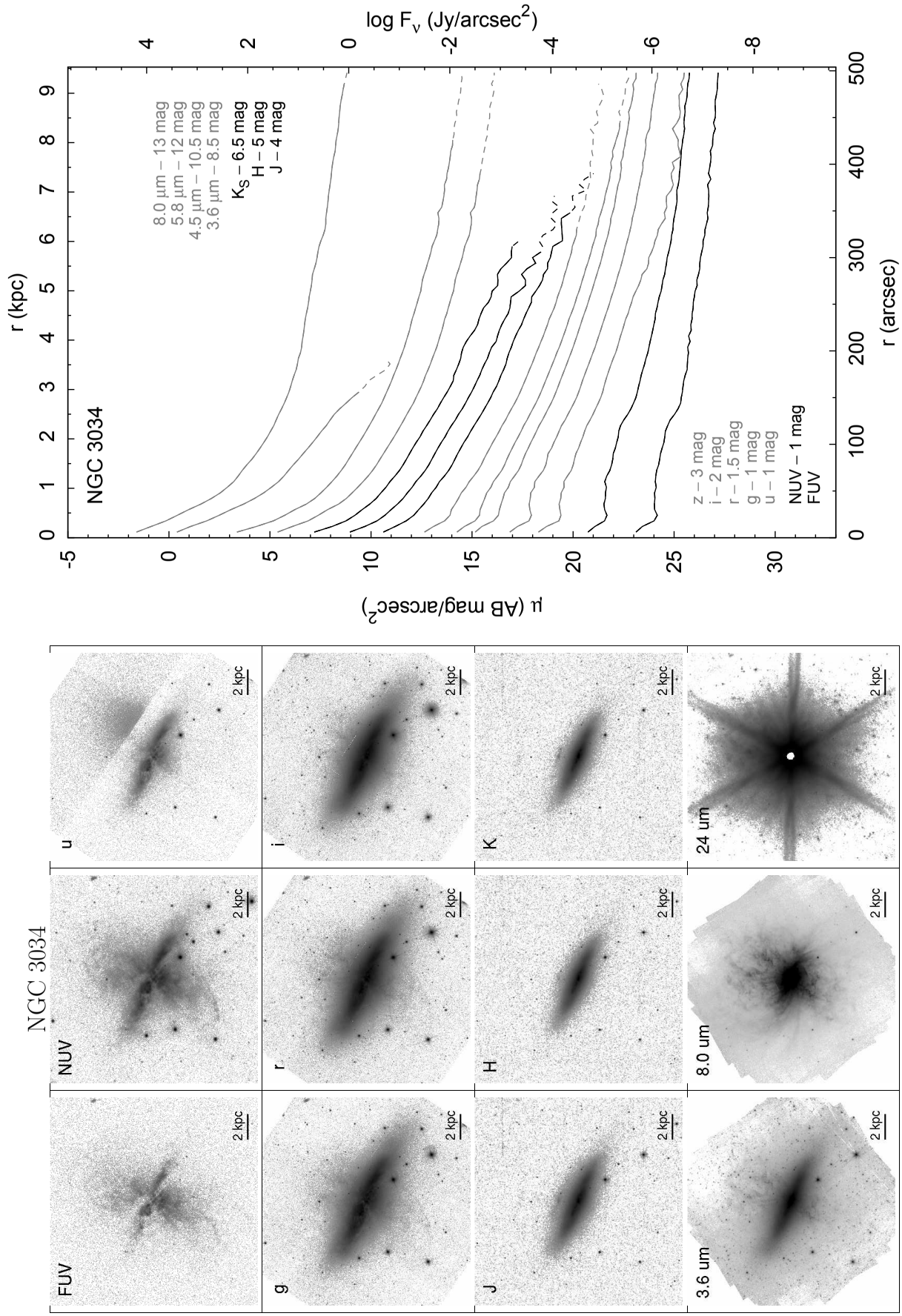
NGC 3034
FUV
NUV
u
g
r
i
J
H
K
3.6 um
8.0 um
24 um
2 kpc
μ (AB mag/arcsec²)
r (kpc)
r (arcsec)
log F_ν (Jy/arcsec²)
NGC 3034
8.0 μm – 13 mag
5.8 μm – 12 mag
4.5 μm – 10.5 mag
3.6 μm – 8.5 mag
K_S – 6.5 mag
H – 5 mag
J – 4 mag
z – 3 mag
i – 2 mag
r – 1.5 mag
g – 1 mag
u – 1 mag
NUV – 1 mag
FUV

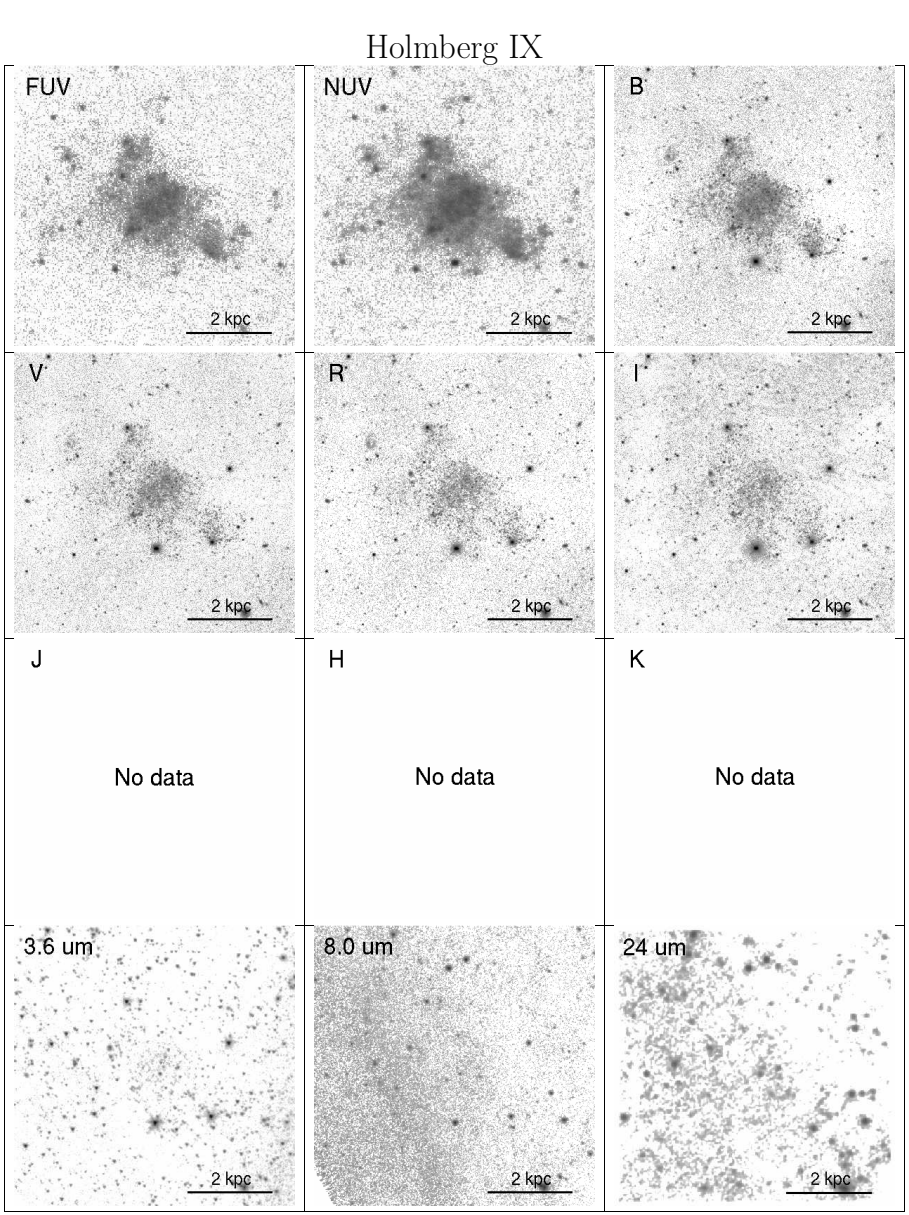
Holmberg IX
FUV
NUV
B
V
R
I
J
H
K
No data
No data
No data
3.6 um
8.0 um
24 um
2 kpc

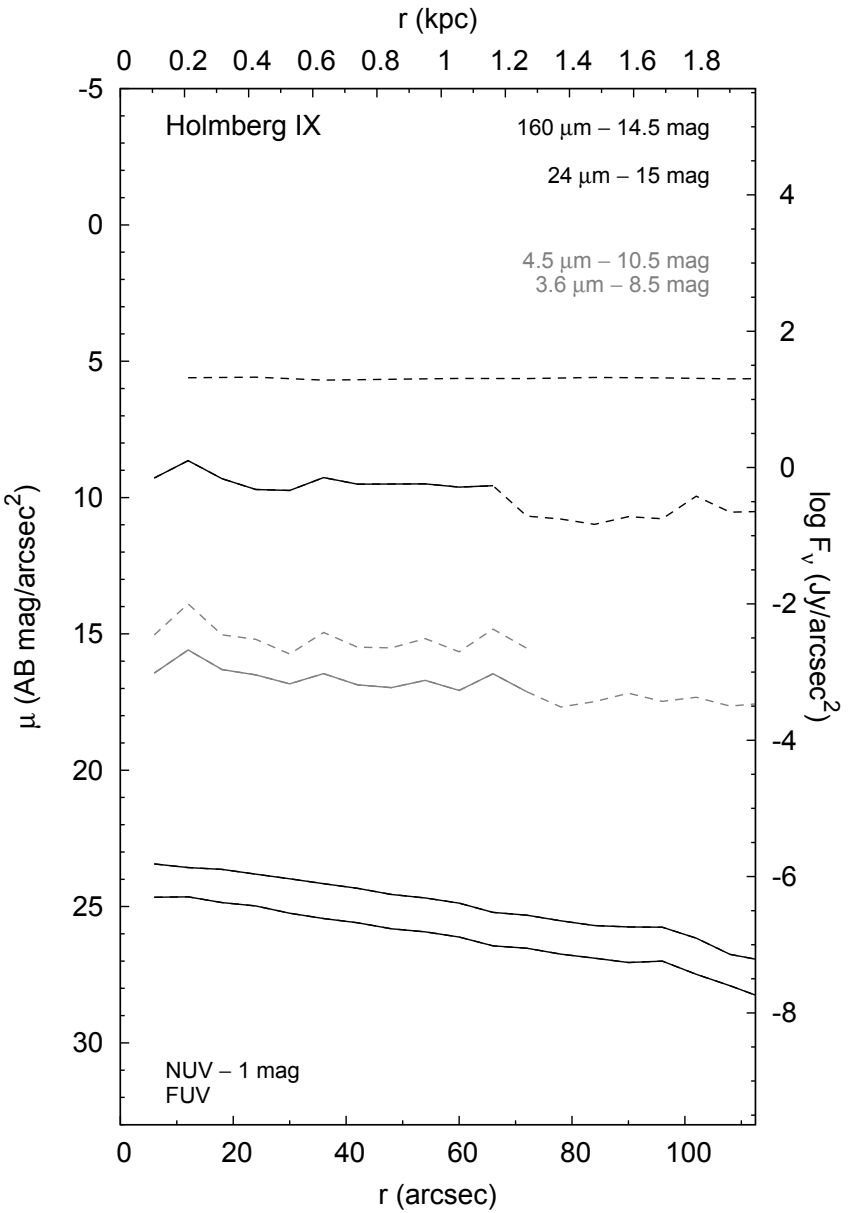
r (kpc)
0 0.2 0.4 0.6 0.8 1 1.2 1.4 1.6 1.8
Holmberg IX
160 μm – 14.5 mag
24 μm – 15 mag
4.5 μm – 10.5 mag
3.6 μm – 8.5 mag
NUV – 1 mag
FUV
μ (AB mag/arcsec²)
log F_ν (Jy/arcsec²)
r (arcsec)
0 20 40 60 80 100

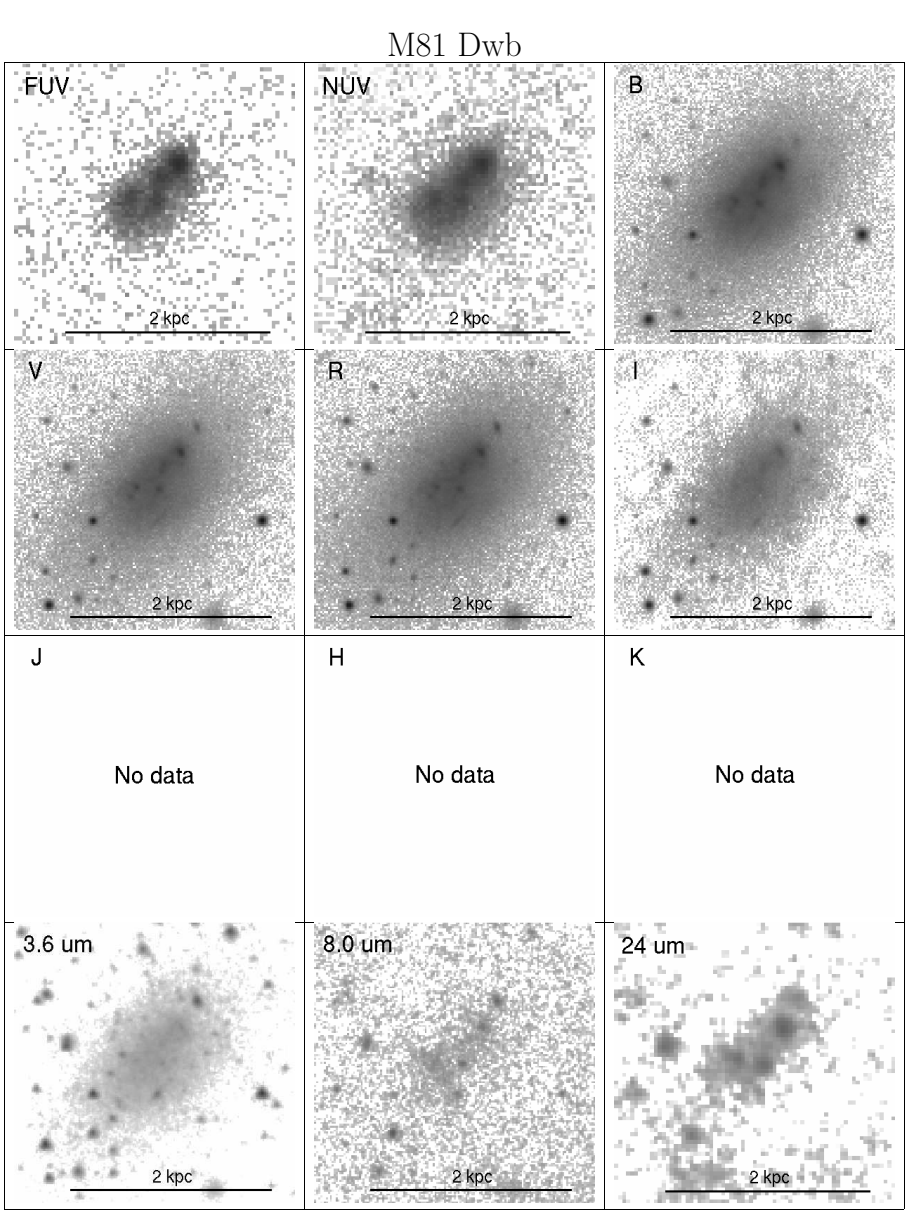
M81 Dwb
FUV
NUV
B
V
R
I
J
H
K
No data
No data
No data
3.6 um
8.0 um
24 um
2 kpc

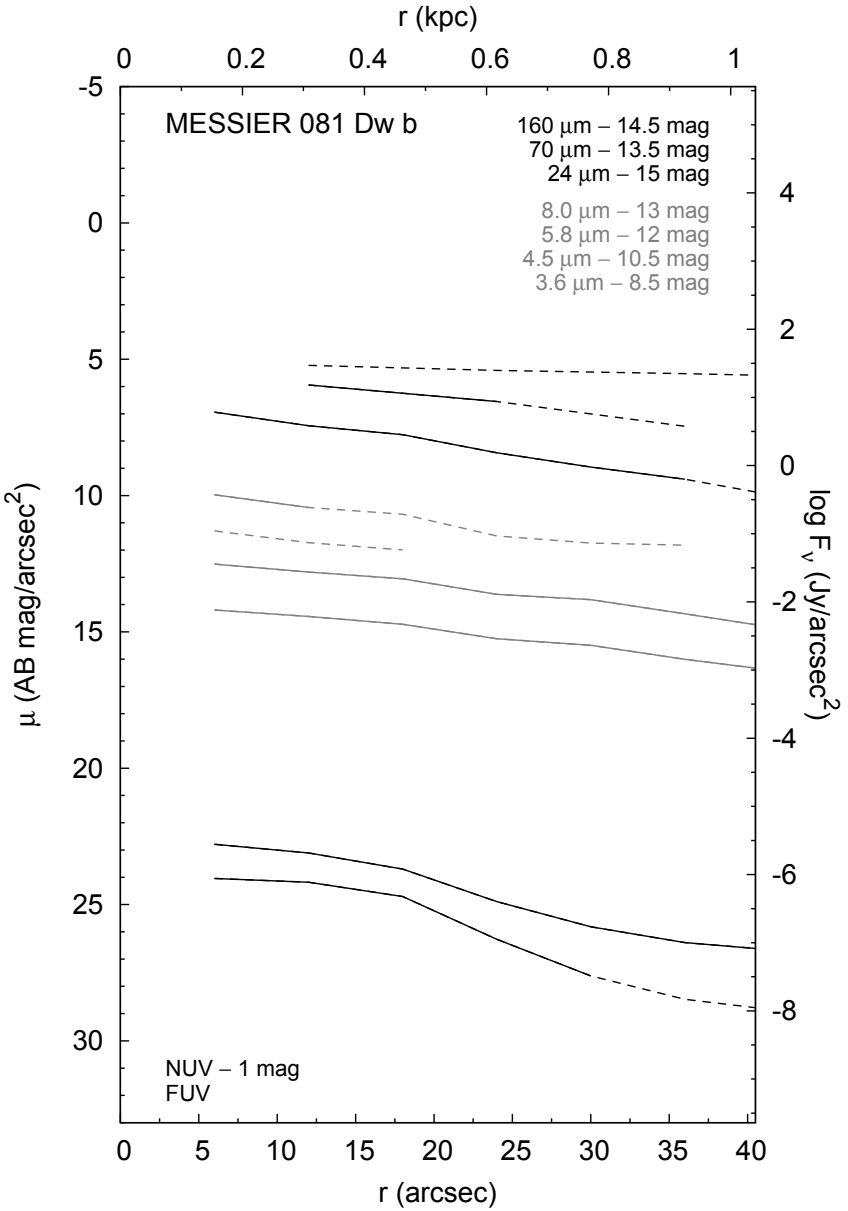
r (kpc)
MESSIER 081 Dw b
160 μm – 14.5 mag
70 μm – 13.5 mag
24 μm – 15 mag
8.0 μm – 13 mag
5.8 μm – 12 mag
4.5 μm – 10.5 mag
3.6 μm – 8.5 mag
NUV – 1 mag
FUV
μ (AB mag/arcsec²)
log F_ν (Jy/arcsec²)
r (arcsec)

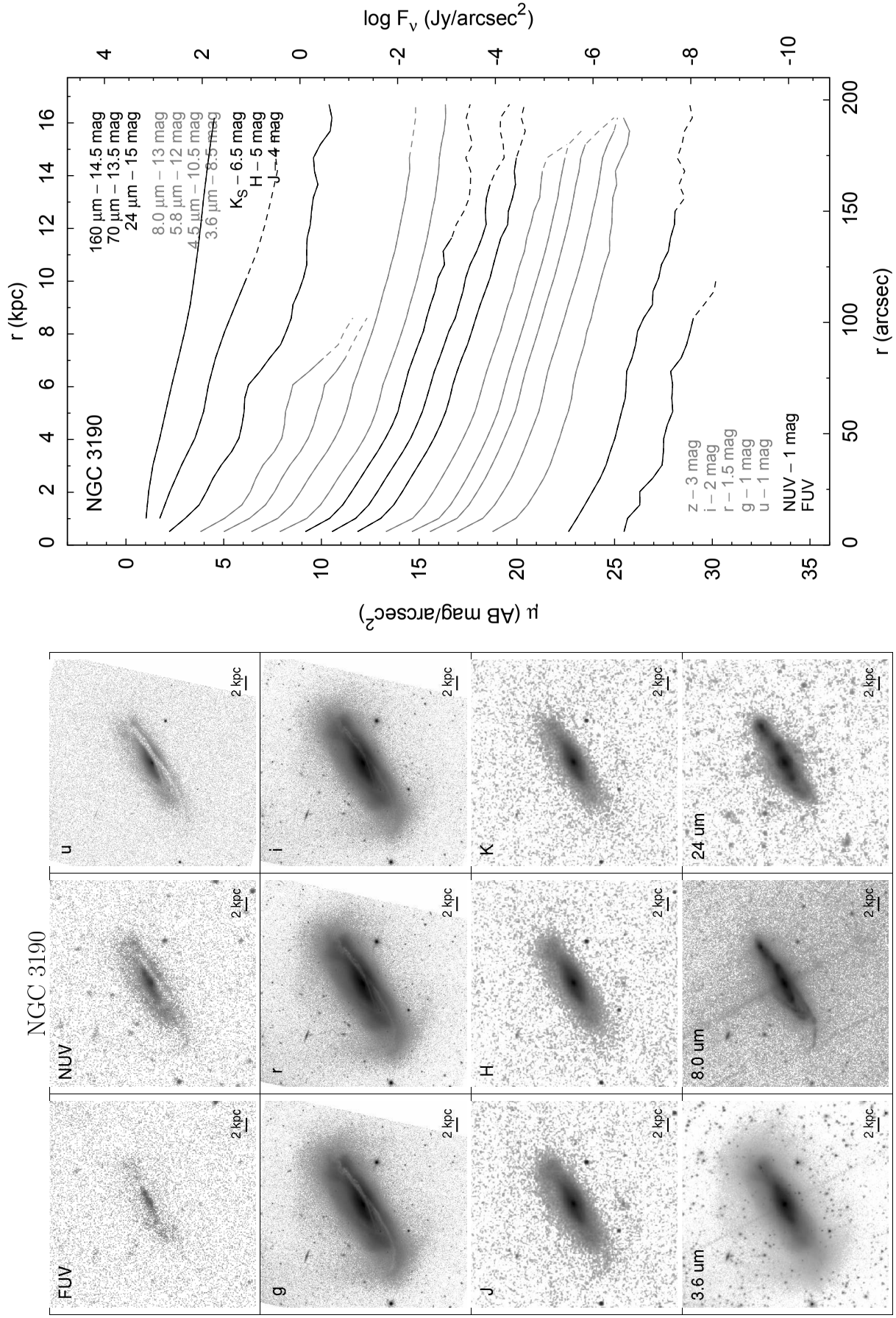
NGC 3190
FUV
NUV
u
g
r
i
J
H
K
3.6 um
8.0 um
24 um
2 kpc
μ (AB mag/arcsec²)
log F_ν (Jy/arcsec²)
r (kpc)
r (arcsec)
NGC 3190
160 μm – 14.5 mag
70 μm – 13.5 mag
24 μm – 15 mag
8.0 μm – 13 mag
5.8 μm – 12 mag
4.5 μm – 10.5 mag
3.6 μm – 8.5 mag
K_S – 6.5 mag
H – 5 mag
J – 4 mag
z – 3 mag
i – 2 mag
r – 1.5 mag
g – 1 mag
u – 1 mag
NUV – 1 mag
FUV

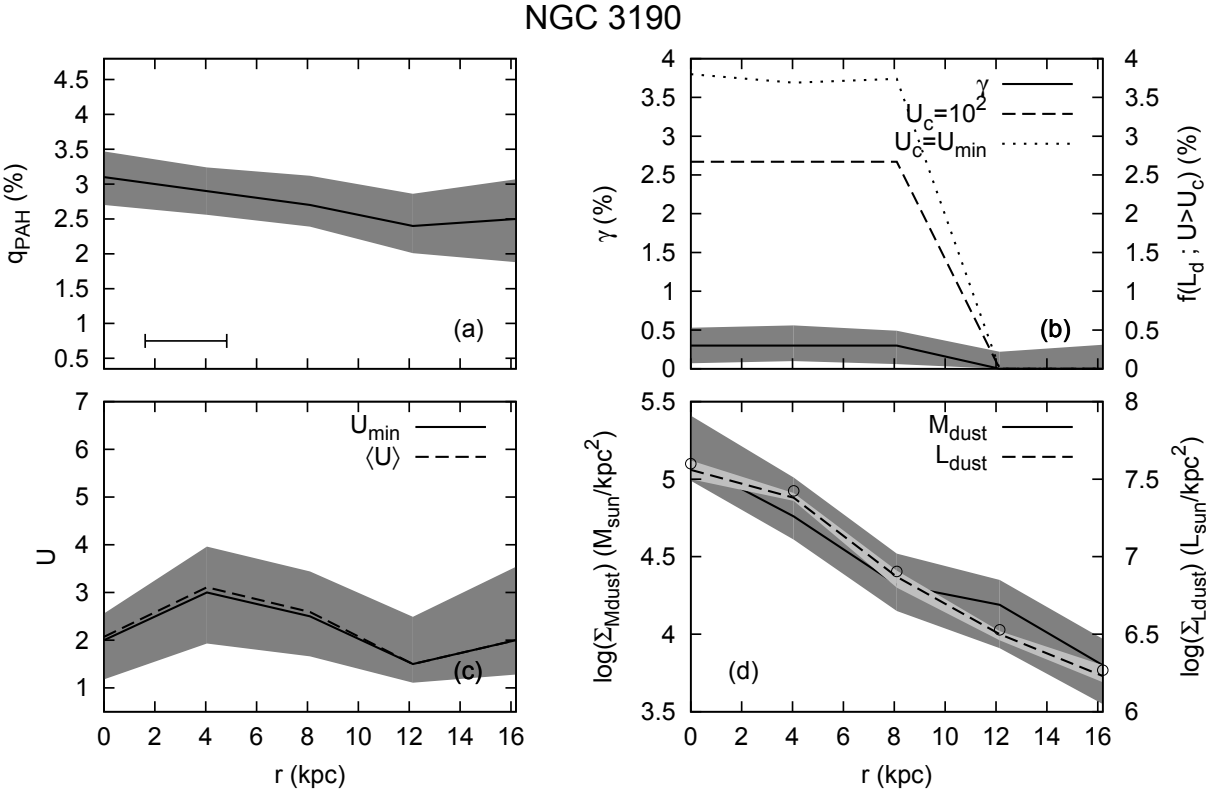
NGC 3190
q_{PAH} (%)
(a)
γ (%)
$U_c=10^2$
$U_c=U_{min}$
(b)
f(L_d ; U>U_c) (%)
U
U_{min}
⟨U⟩
(c)
r (kpc)
log(Σ_{Mdust}) (M_{sun}/kpc^2)
M_{dust}
L_{dust}
(d)
log(Σ_{Ldust}) (L_{sun}/kpc^2)
r (kpc)

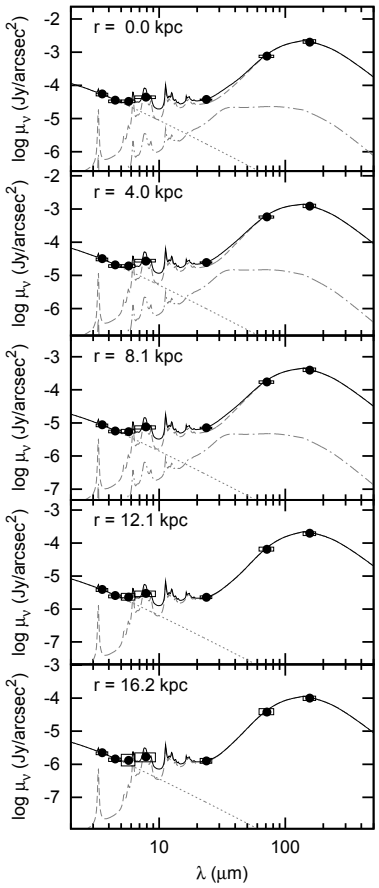
r = 0.0 kpc
r = 4.0 kpc
r = 8.1 kpc
r = 12.1 kpc
r = 16.2 kpc
log μ_ν (Jy/arcsec^2)
λ (μm)

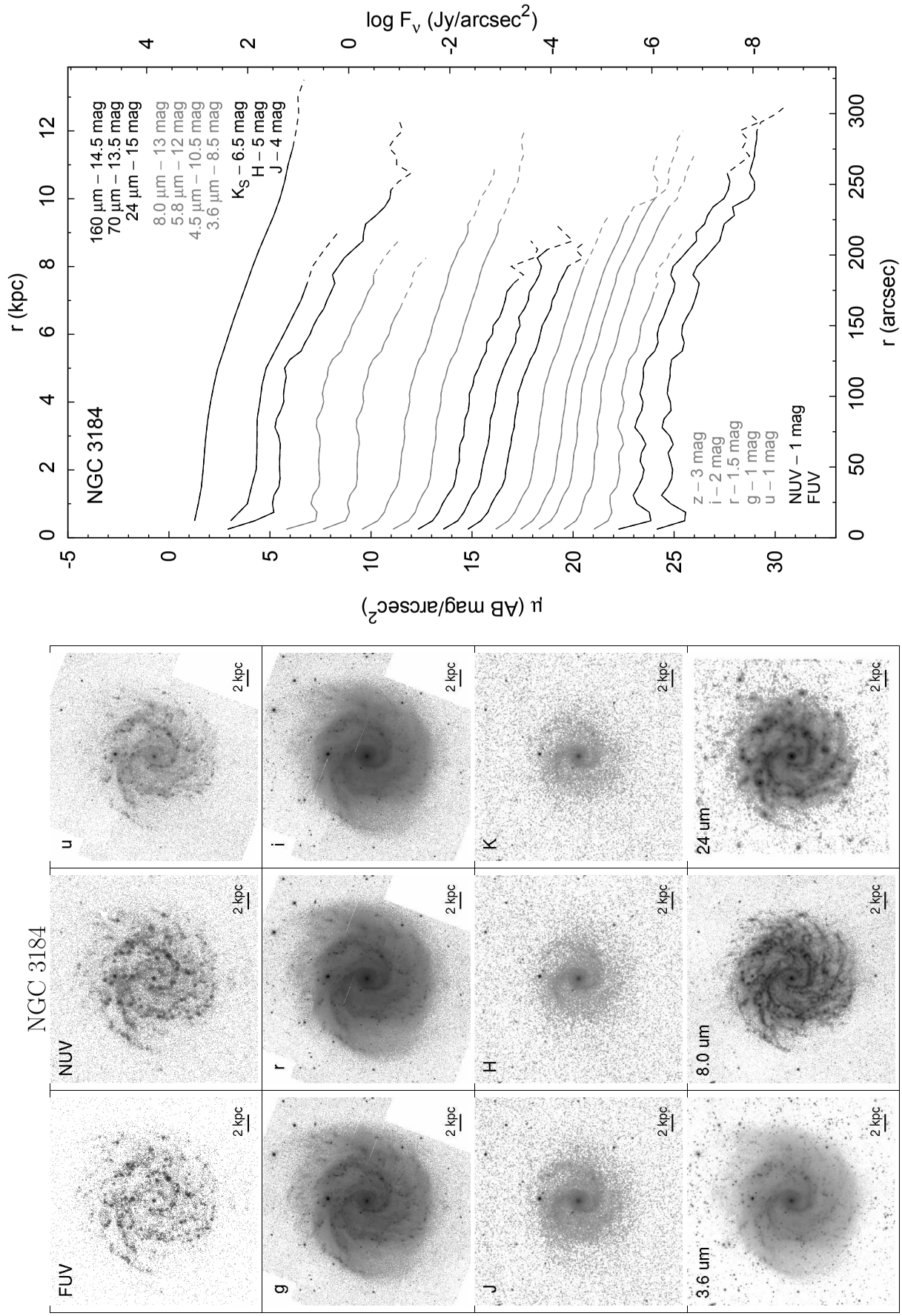
NGC 3184
FUV
NUV
u
g
r
i
J
H
K
3.6 um
8.0 um
24 um
2 kpc
μ (AB mag/arcsec²)
log F_ν (Jy/arcsec²)
r (kpc)
r (arcsec)
NGC 3184
160 μm – 14.5 mag
70 μm – 13.5 mag
24 μm – 15 mag
8.0 μm – 13 mag
5.8 μm – 12 mag
4.5 μm – 10.5 mag
3.6 μm – 8.5 mag
K_S – 6.5 mag
H – 5 mag
J – 4 mag
z – 3 mag
i – 2 mag
r – 1.5 mag
g – 1 mag
u – 1 mag
NUV – 1 mag
FUV

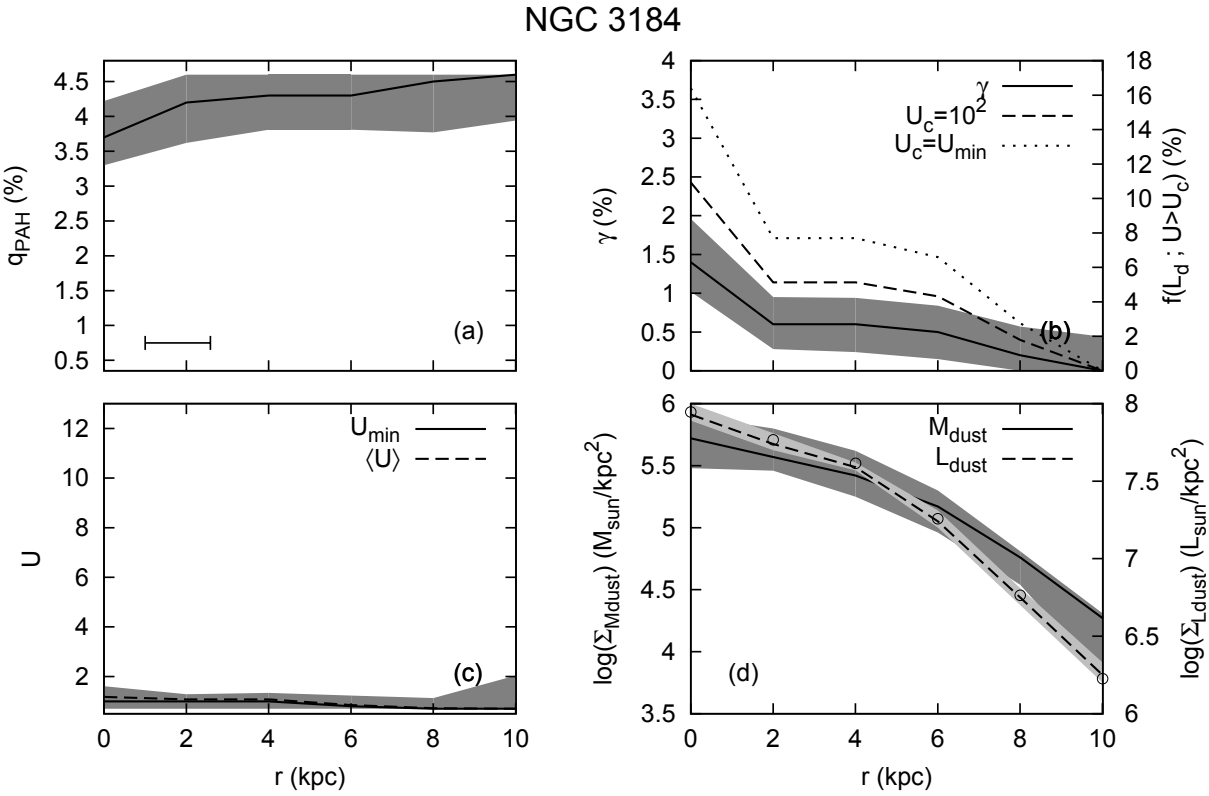
NGC 3184
q_{PAH} (%)
(a)
γ (%)
$U_c=10^2$
$U_c=U_{min}$
$f(L_d ; U>U_c)$ (%)
(b)
U
U_{min}
⟨U⟩
(c)
r (kpc)
$\log(\Sigma_{Mdust})$ (M_{sun}/kpc^2)
M_{dust}
L_{dust}
$\log(\Sigma_{Ldust})$ (L_{sun}/kpc^2)
(d)
r (kpc)

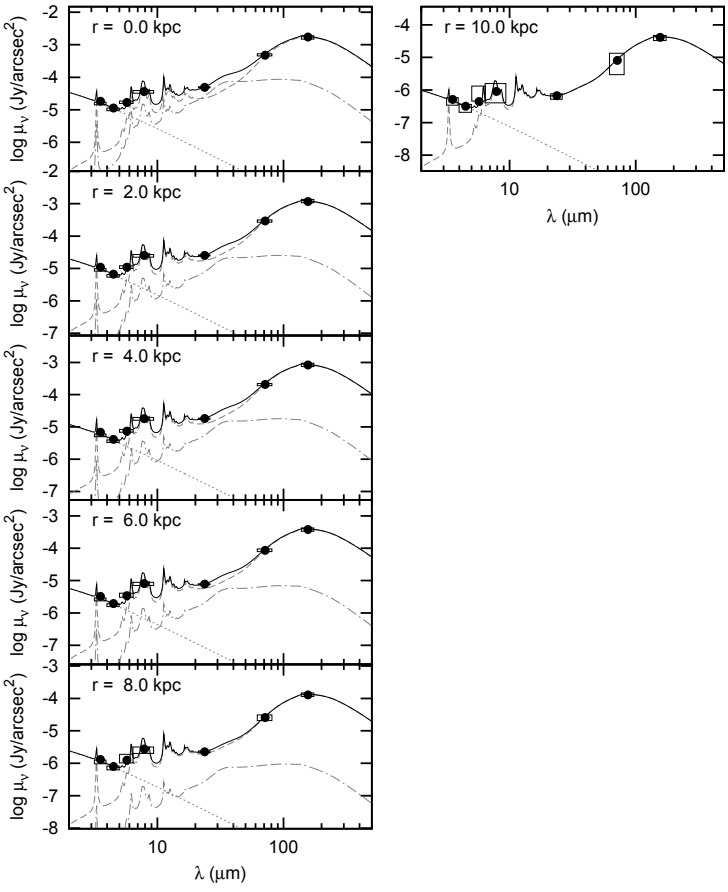
r = 0.0 kpc
r = 2.0 kpc
r = 4.0 kpc
r = 6.0 kpc
r = 8.0 kpc
r = 10.0 kpc
log μ_ν (Jy/arcsec^2)
λ (μm)

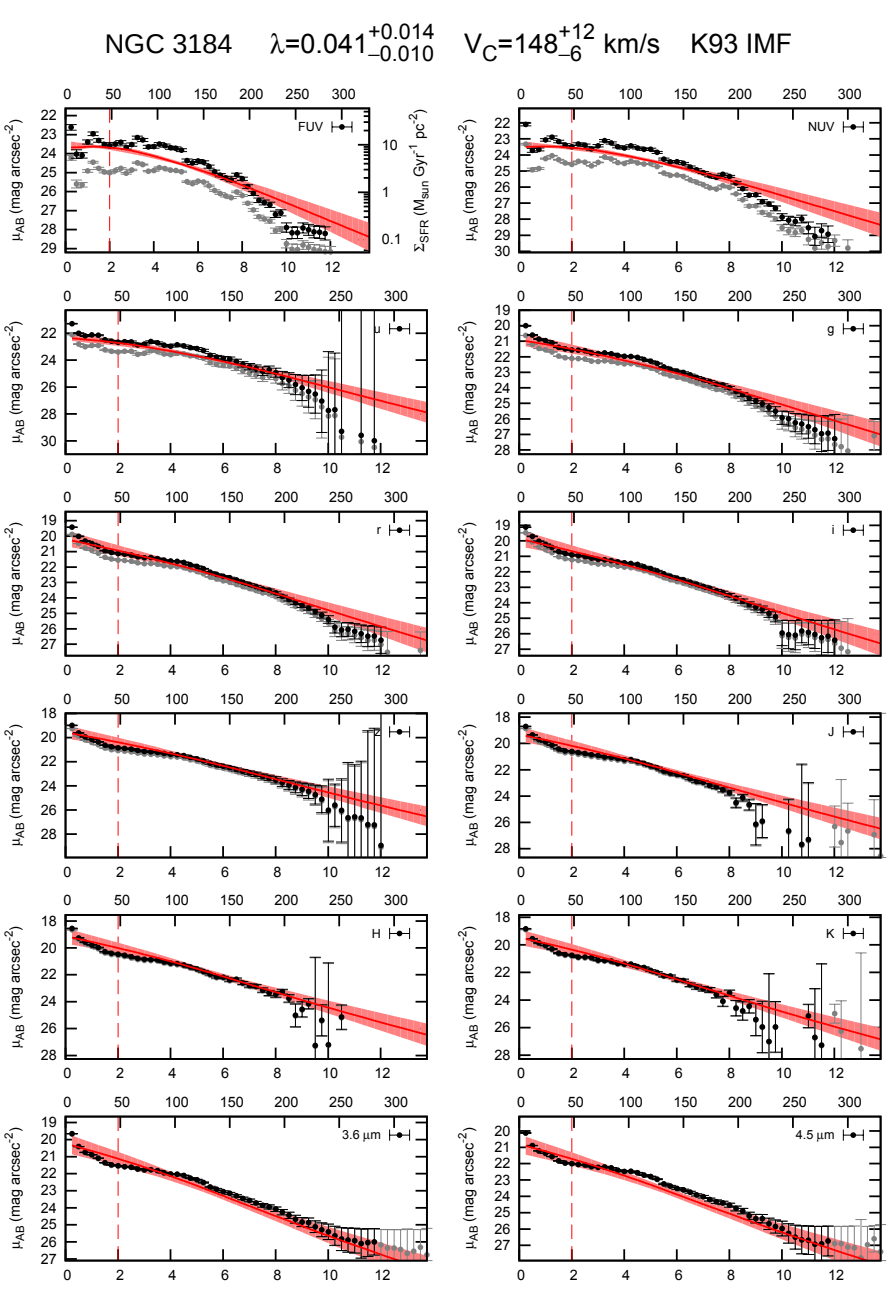
NGC 3184 λ=0.041+0.014−0.010 VC=148+12−6 km/s K93 IMF
FUV
NUV
u
g
r
i
J
H
K
3.6 μm
4.5 μm
μAB (mag arcsec−2)
ΣSFR (Msun Gyr−1 pc−2)

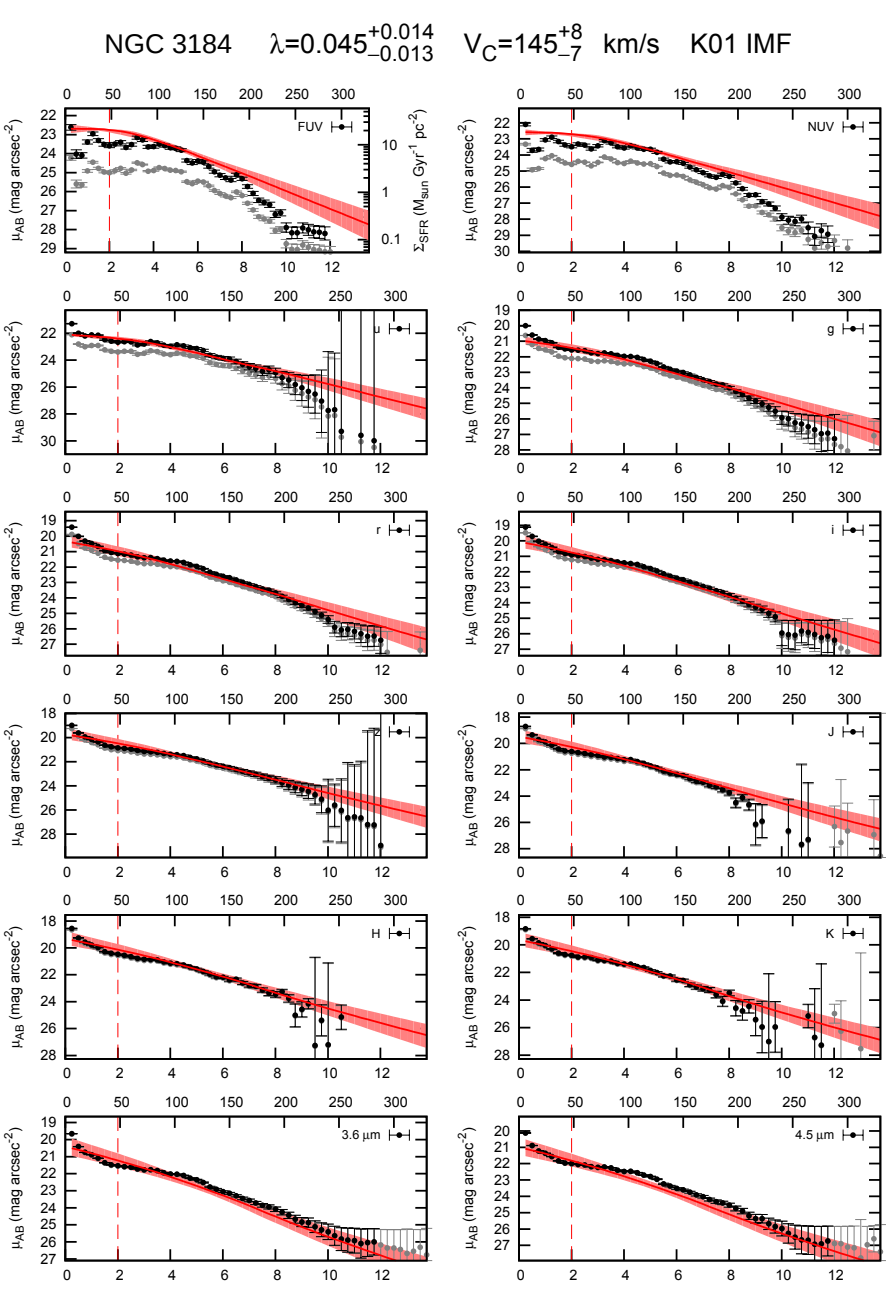
NGC 3184 λ=0.045+0.014−0.013 VC=145+8−7 km/s K01 IMF
FUV
NUV
u
g
r
i
J
H
K
3.6 μm
4.5 μm
μAB (mag arcsec−2)
ΣSFR (Msun Gyr−1 pc−2)

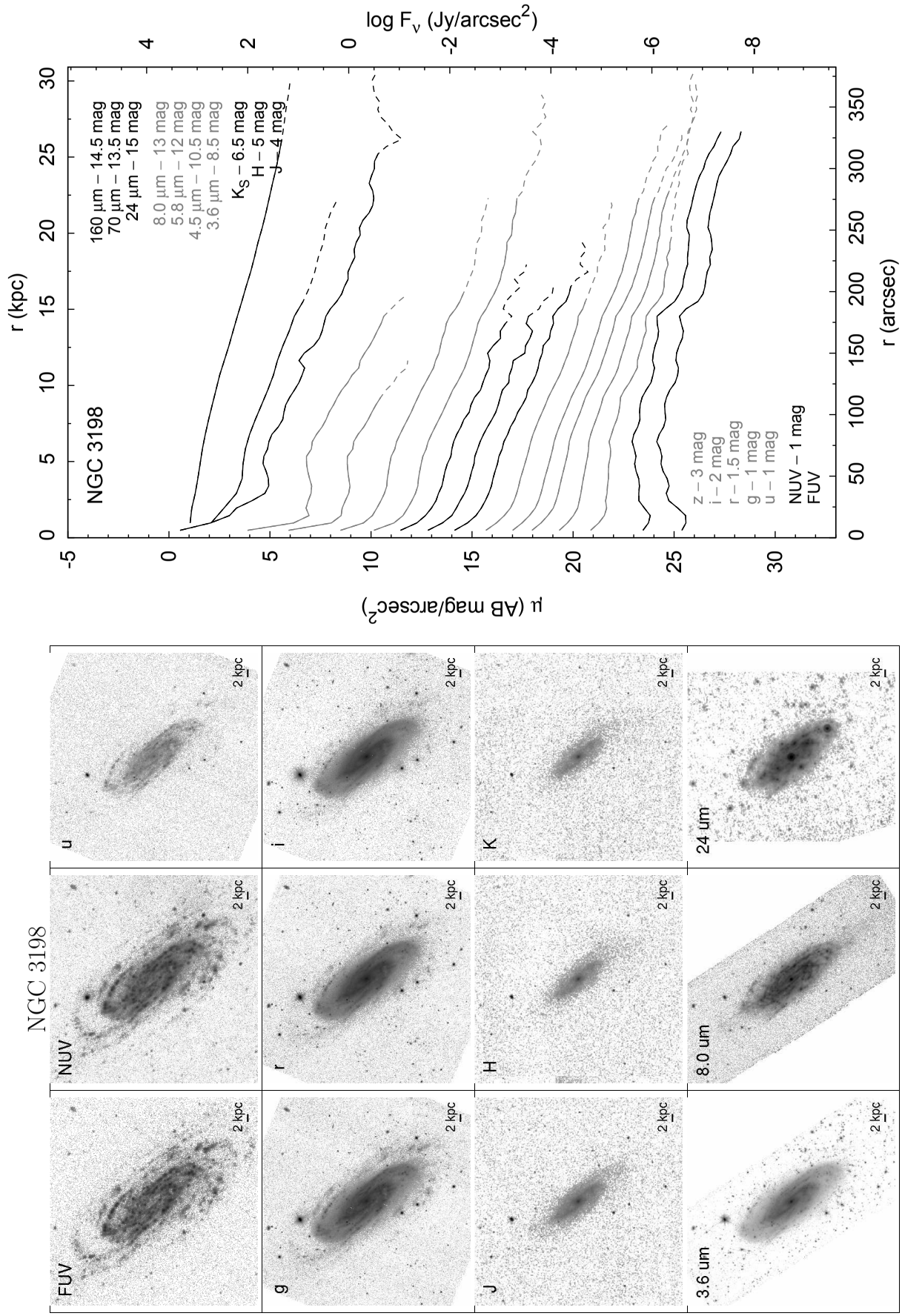
NGC 3198
160 μm – 14.5 mag
70 μm – 13.5 mag
24 μm – 15 mag
8.0 μm – 13 mag
5.8 μm – 12 mag
4.5 μm – 10.5 mag
3.6 μm – 8.5 mag
K_S – 6.5 mag
H – 5 mag
J – 4 mag
z – 3 mag
i – 2 mag
r – 1.5 mag
g – 1 mag
u – 1 mag
NUV – 1 mag
FUV
r (kpc)
log F_ν (Jy/arcsec^2)
μ (AB mag/arcsec^2)
r (arcsec)
NGC 3198
FUV
NUV
u
g
r
i
J
H
K
3.6 um
8.0 um
24 um
2 kpc

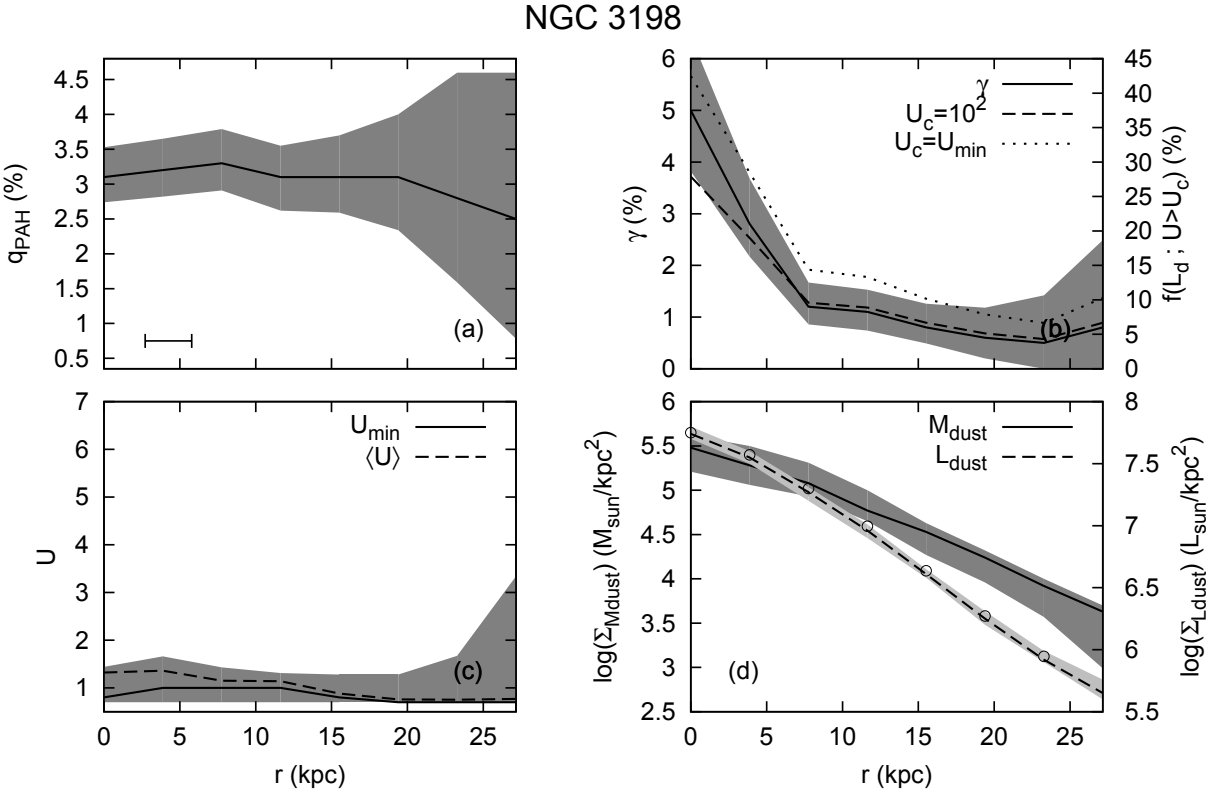
NGC 3198
q_{PAH} (%)
(a)
γ (%)
$f(L_d ; U>U_c)$ (%)
$U_c=10^2$
$U_c=U_{min}$
(b)
U
U_{min}
⟨U⟩
(c)
r (kpc)
$\log(\Sigma_{Mdust})$ (M_{sun}/kpc^2)
$\log(\Sigma_{Ldust})$ (L_{sun}/kpc^2)
M_{dust}
L_{dust}
(d)
r (kpc)

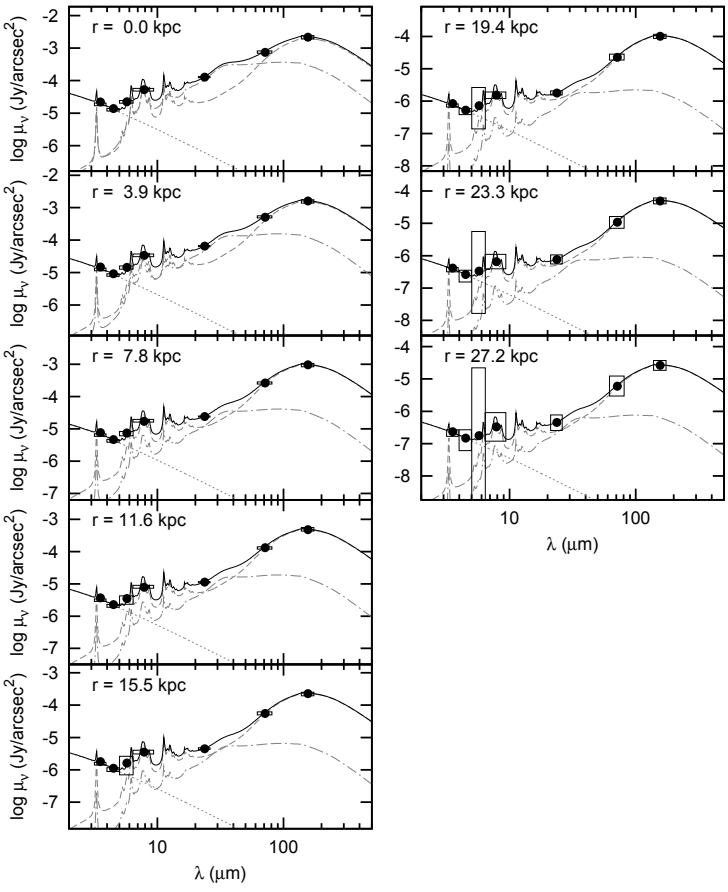
r = 0.0 kpc
r = 3.9 kpc
r = 7.8 kpc
r = 11.6 kpc
r = 15.5 kpc
r = 19.4 kpc
r = 23.3 kpc
r = 27.2 kpc
log μ_ν (Jy/arcsec^2)
λ (μm)

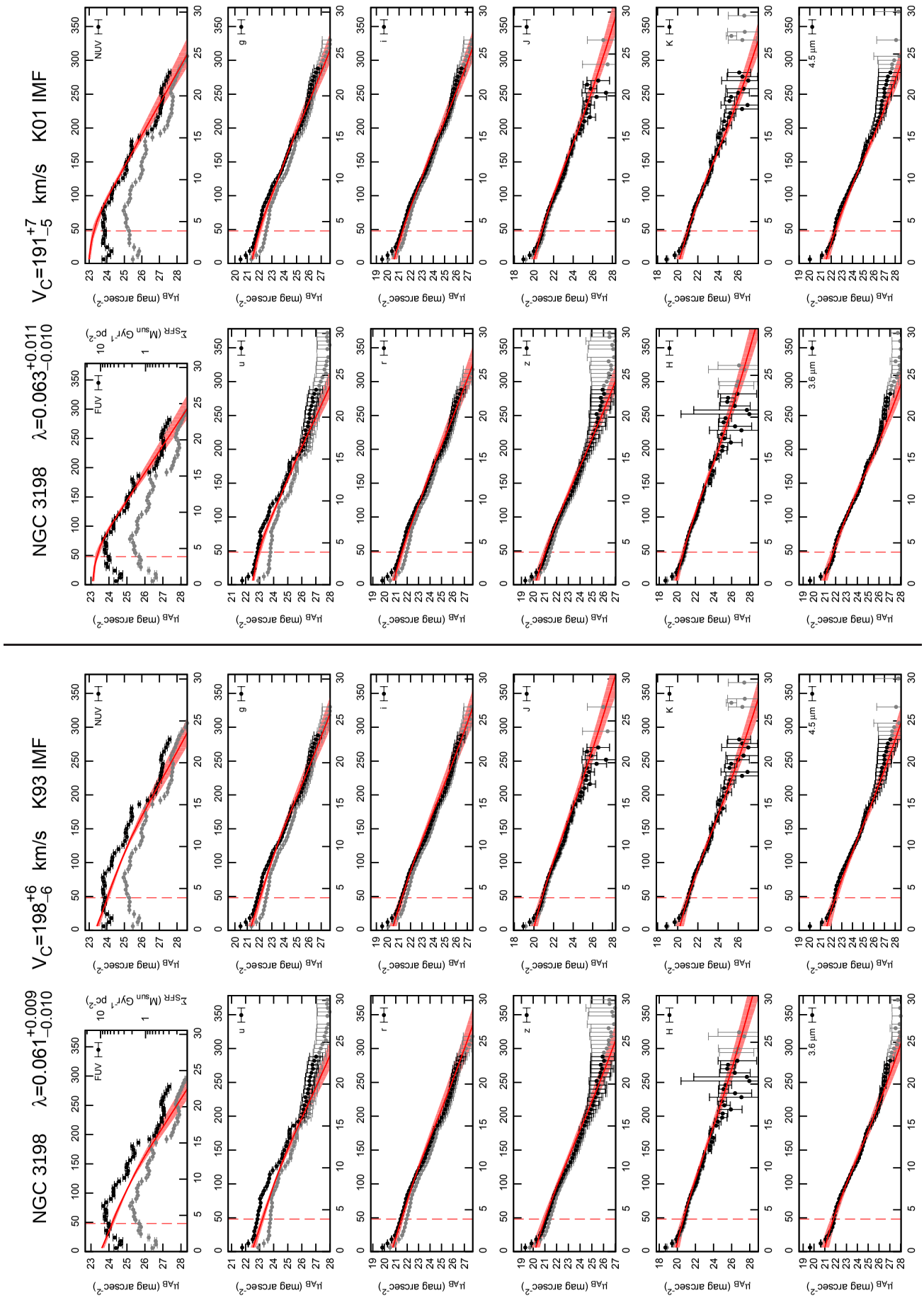
NGC 3198 λ=0.063$^{+0.011}_{-0.010}$ V_C=191$^{+7}_{-5}$ km/s K01 IMF
NGC 3198 λ=0.061$^{+0.009}_{-0.010}$ V_C=198$^{+6}_{-6}$ km/s K93 IMF
FUV
NUV
u
g
r
i
z
J
H
K
3.6 μm
4.5 μm
μ_AB (mag arcsec^{-2})
Σ_SFR (M_sun Gyr^{-1} pc^{-2})

IC 2574
FUV
NUV
B
V
R
I
J
H
K
3.6 um
8.0 um
24 um
2 kpc

r (kpc)
IC 2574
160 μm – 14.5 mag
70 μm – 13.5 mag
24 μm – 15 mag
8.0 μm – 13 mag
5.8 μm – 12 mag
4.5 μm – 10.5 mag
3.6 μm – 8.5 mag
K_S – 6.5 mag
H – 5 mag
J – 4 mag
V – 1 mag
B – 0.5 mag
NUV – 1 mag
FUV
μ (AB mag/arcsec²)
log F_ν (Jy/arcsec²)
r (arcsec)

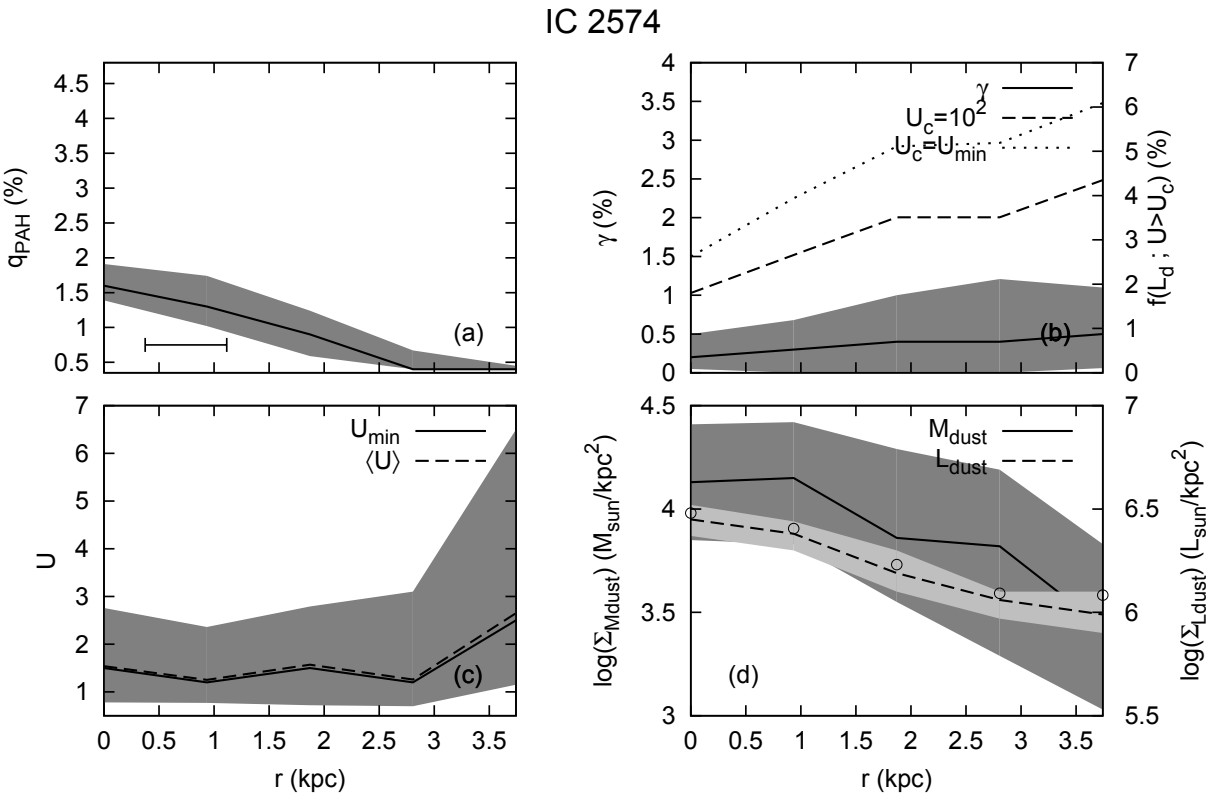
IC 2574
q_{PAH} (%)
(a)
γ (%)
$U_c=10^2$
$U_c=U_{min}$
$f(L_d ; U>U_c)$ (%)
(b)
U
U_{min}
⟨U⟩
(c)
r (kpc)
$\log(\Sigma_{Mdust})$ (M_{sun}/kpc^2)
M_{dust}
L_{dust}
$\log(\Sigma_{Ldust})$ (L_{sun}/kpc^2)
(d)
r (kpc)

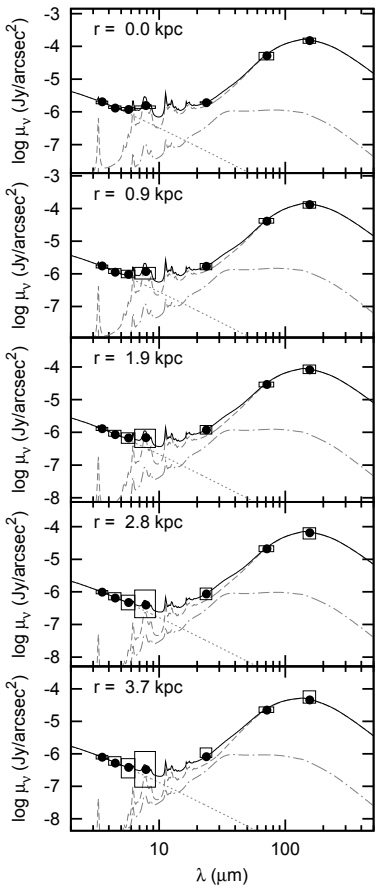
r = 0.0 kpc
r = 0.9 kpc
r = 1.9 kpc
r = 2.8 kpc
r = 3.7 kpc
log μ_ν (Jy/arcsec^2)
λ (μm)

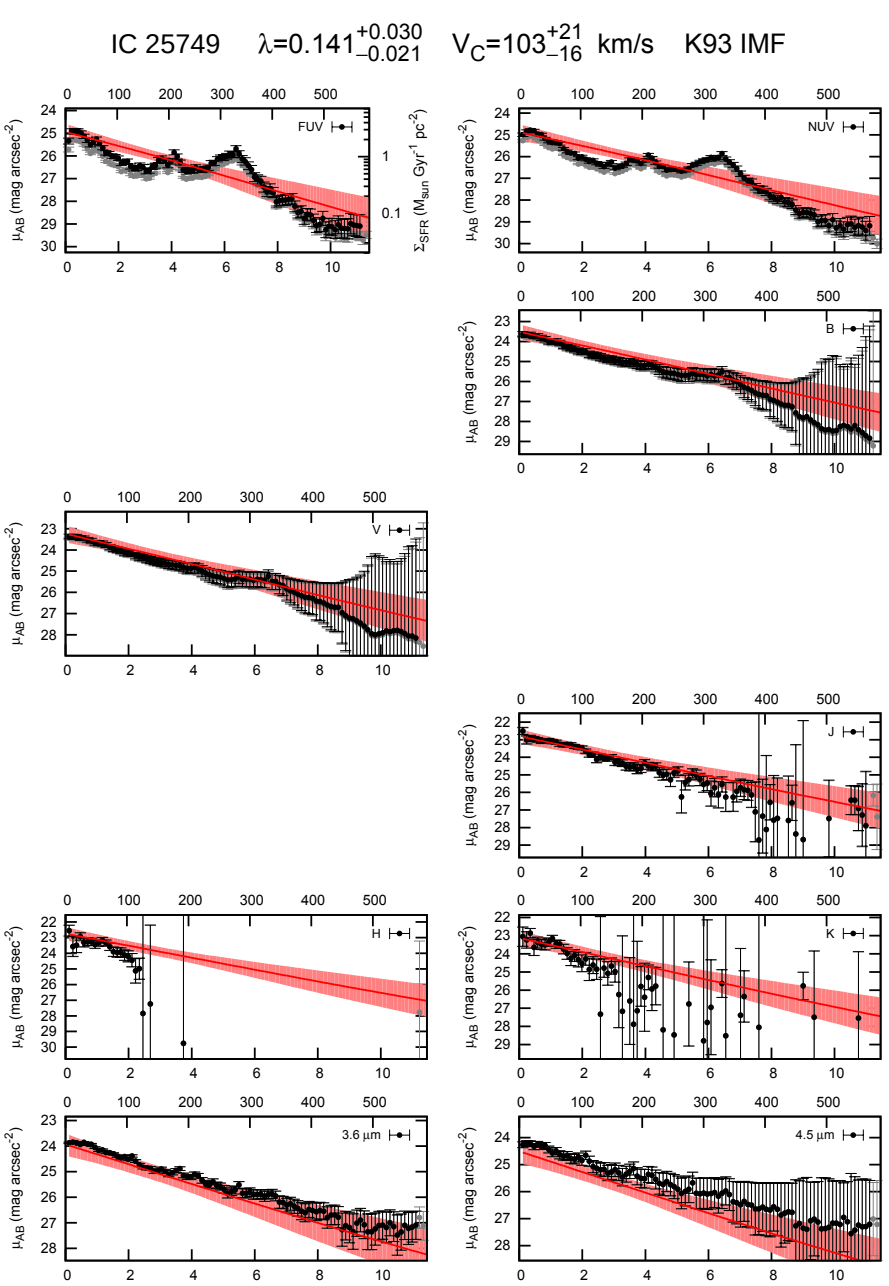
IC 25749 λ=0.141 +0.030 −0.021 V_C=103 +21 −16 km/s K93 IMF
FUV
NUV
B
V
J
H
K
3.6 μm
4.5 μm
μ_AB (mag arcsec^-2)
Σ_SFR (M_sun Gyr^-1 pc^-2)

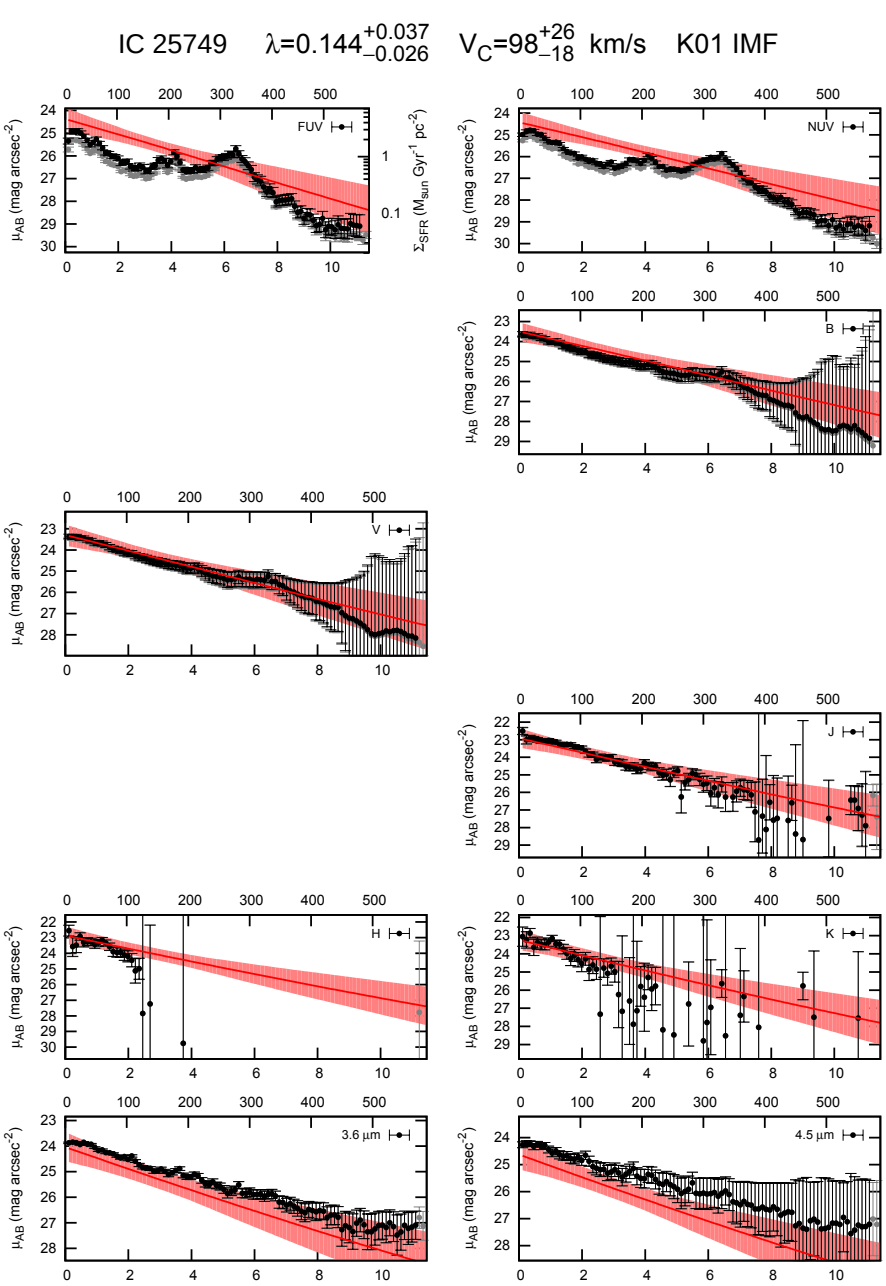
IC 25749 λ=0.144 +0.037 −0.026 V_C=98 +26 −18 km/s K01 IMF
FUV
NUV
B
V
J
H
K
3.6 μm
4.5 μm
μ_AB (mag arcsec^-2)
Σ_SFR (M_sun Gyr^-1 pc^-2)

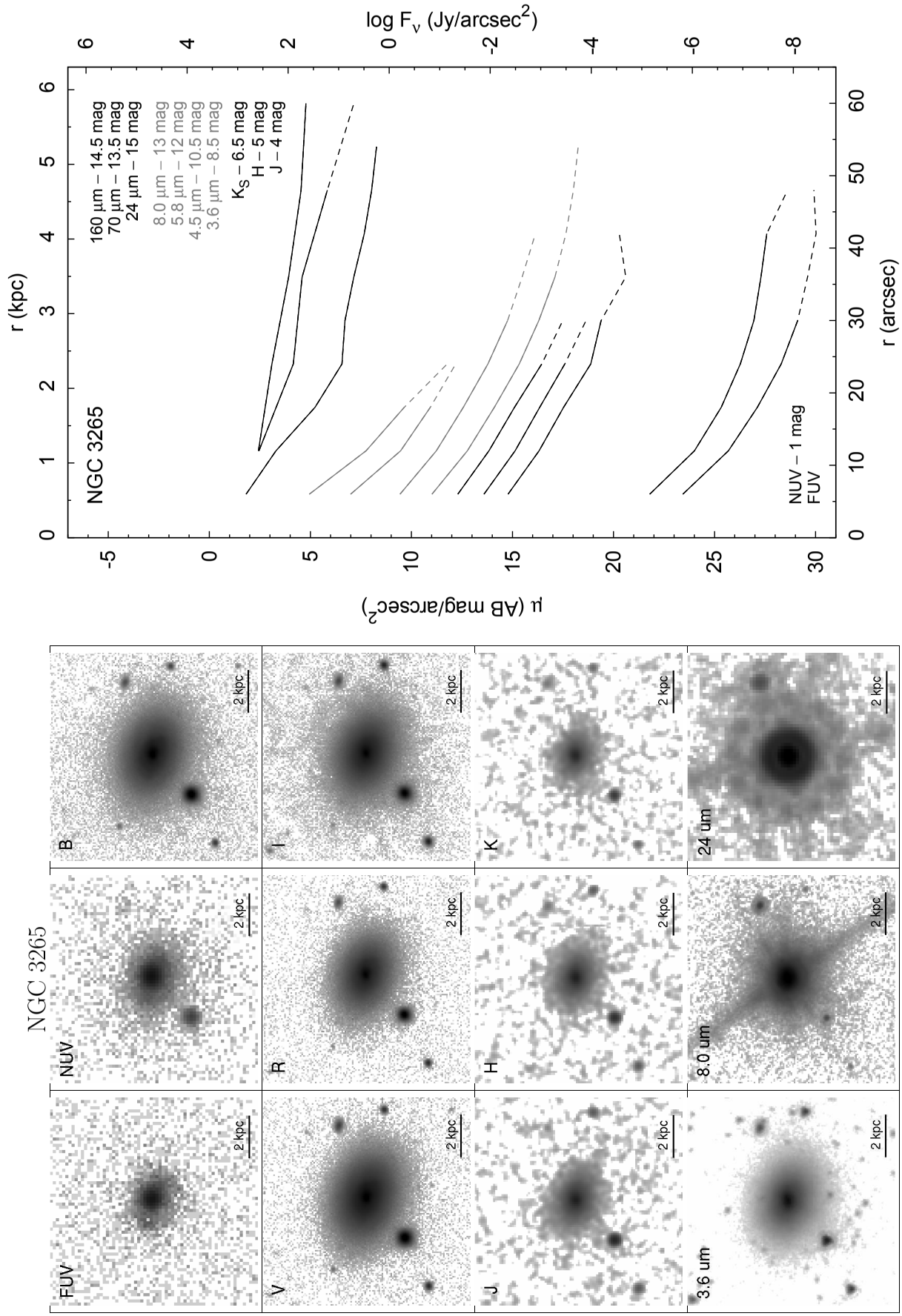
NGC 3265
FUV
NUV
B
V
R
I
J
H
K
3.6 um
8.0 um
24 um
2 kpc
μ (AB mag/arcsec²)
log F_ν (Jy/arcsec²)
r (kpc)
r (arcsec)
NGC 3265
160 μm – 14.5 mag
70 μm – 13.5 mag
24 μm – 15 mag
8.0 μm – 13 mag
5.8 μm – 12 mag
4.5 μm – 10.5 mag
3.6 μm – 8.5 mag
K_S – 6.5 mag
H – 5 mag
J – 4 mag
NUV – 1 mag
FUV

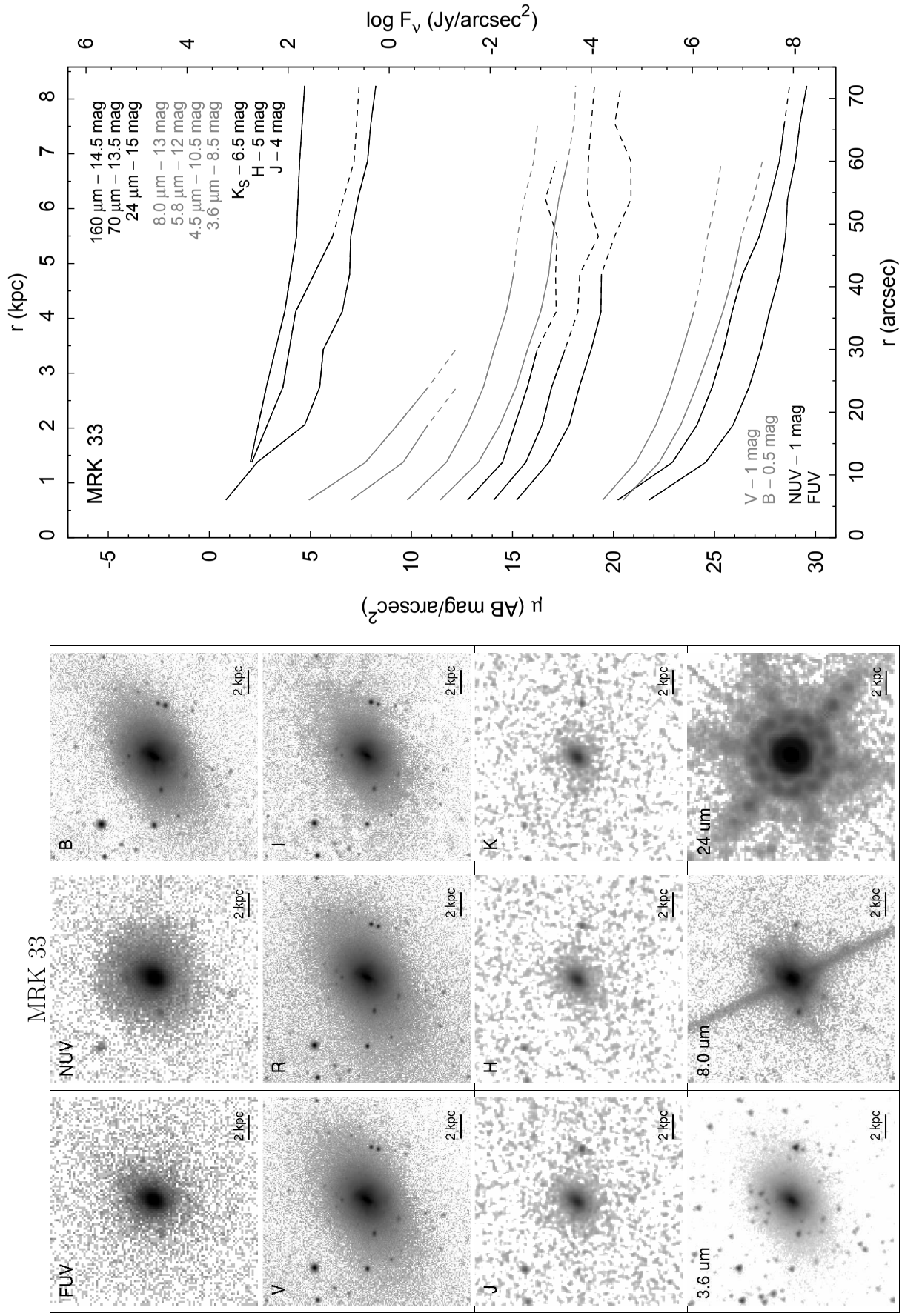
MRK 33
FUV
NUV
B
V
R
I
J
H
K
3.6 um
8.0 um
24 um
2 kpc
MRK 33
160 μm – 14.5 mag
70 μm – 13.5 mag
24 μm – 15 mag
8.0 μm – 13 mag
5.8 μm – 12 mag
4.5 μm – 10.5 mag
3.6 μm – 8.5 mag
K_S – 6.5 mag
H – 5 mag
J – 4 mag
V – 1 mag
B – 0.5 mag
NUV – 1 mag
FUV
r (kpc)
r (arcsec)
log F_ν (Jy/arcsec²)
μ (AB mag/arcsec²)

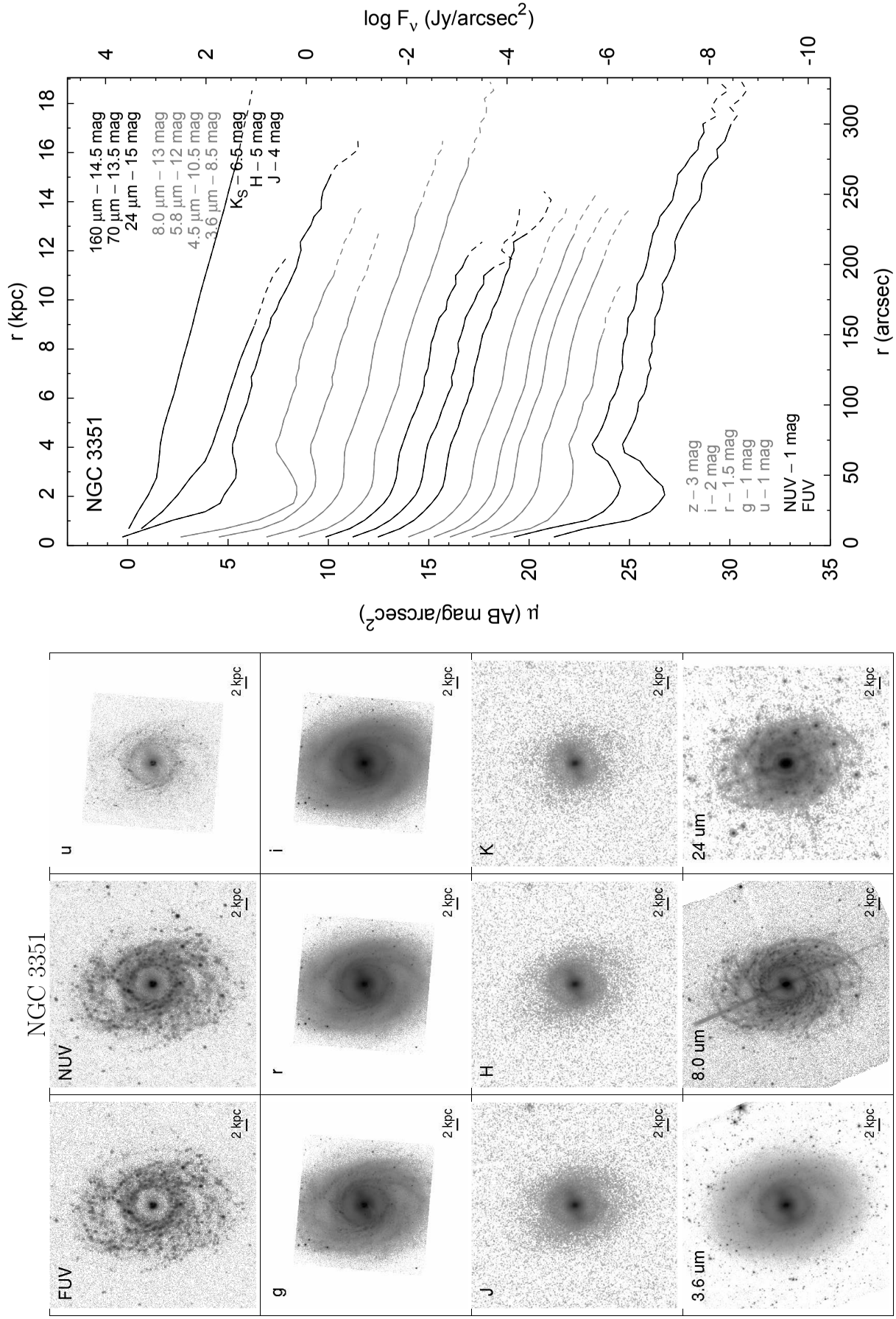
NGC 3351
FUV
NUV
u
g
r
i
J
H
K
3.6 um
8.0 um
24 um
2 kpc
μ (AB mag/arcsec²)
log F_ν (Jy/arcsec²)
r (kpc)
r (arcsec)
NGC 3351
160 μm – 14.5 mag
70 μm – 13.5 mag
24 μm – 15 mag
8.0 μm – 13 mag
5.8 μm – 12 mag
4.5 μm – 10.5 mag
3.6 μm – 8.5 mag
K_S – 6.5 mag
H – 5 mag
J – 4 mag
z – 3 mag
i – 2 mag
r – 1.5 mag
g – 1 mag
u – 1 mag
NUV – 1 mag
FUV

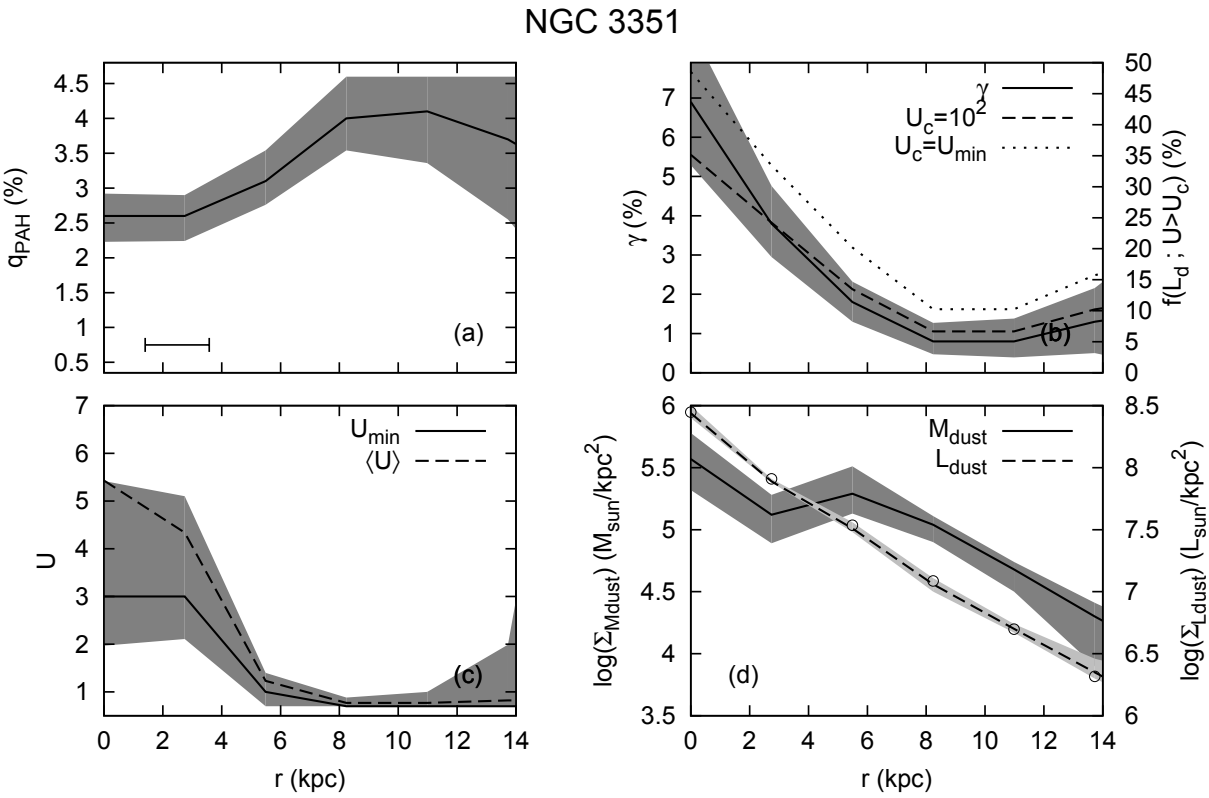
NGC 3351
q_{PAH} (%)
(a)
γ
$U_c=10^2$
$U_c=U_{min}$
γ (%)
$f(L_d ; U>U_c)$ (%)
(b)
U_{min}
⟨U⟩
U
(c)
r (kpc)
M_{dust}
L_{dust}
$\log(\Sigma_{Mdust})$ (M_{sun}/kpc^2)
$\log(\Sigma_{Ldust})$ (L_{sun}/kpc^2)
(d)
r (kpc)

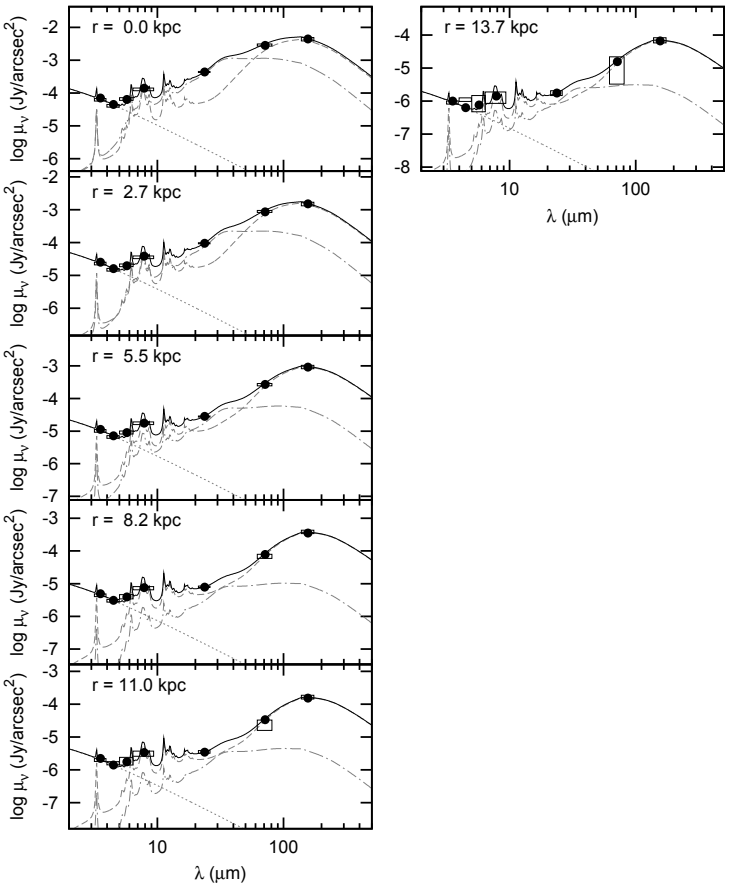
r = 0.0 kpc
r = 2.7 kpc
r = 5.5 kpc
r = 8.2 kpc
r = 11.0 kpc
r = 13.7 kpc
log μ_ν (Jy/arcsec^2)
λ (μm)

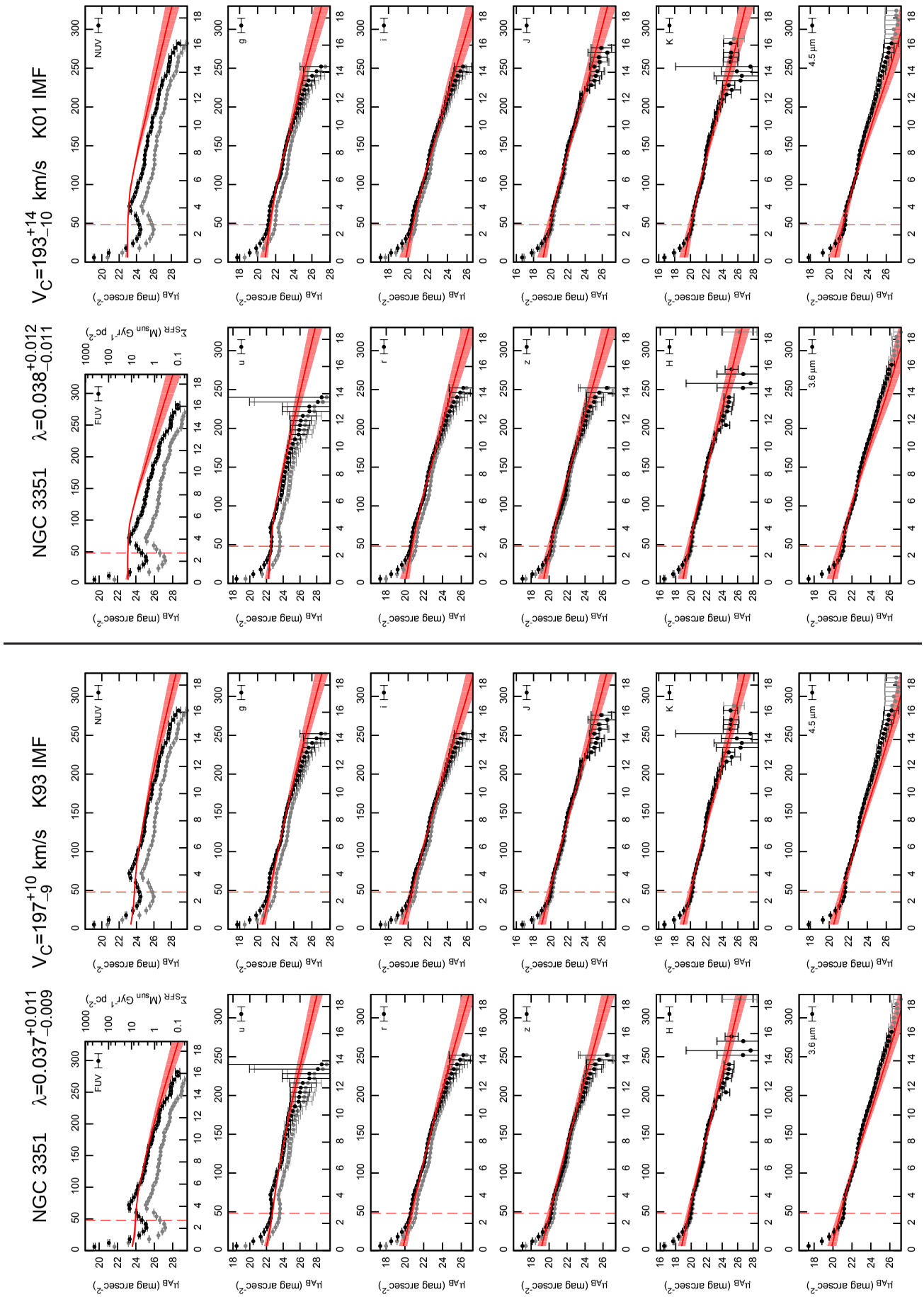
NGC 3351 λ=0.038+0.012−0.011 VC=193+14−10 km/s K01 IMF
NGC 3351 λ=0.037+0.011−0.009 VC=197+10−9 km/s K93 IMF
μAB (mag arcsec-2)
ΣSFR (Msun Gyr-1 pc-2)
FUV
NUV
u
g
r
i
z
J
H
K
3.6 μm
4.5 μm

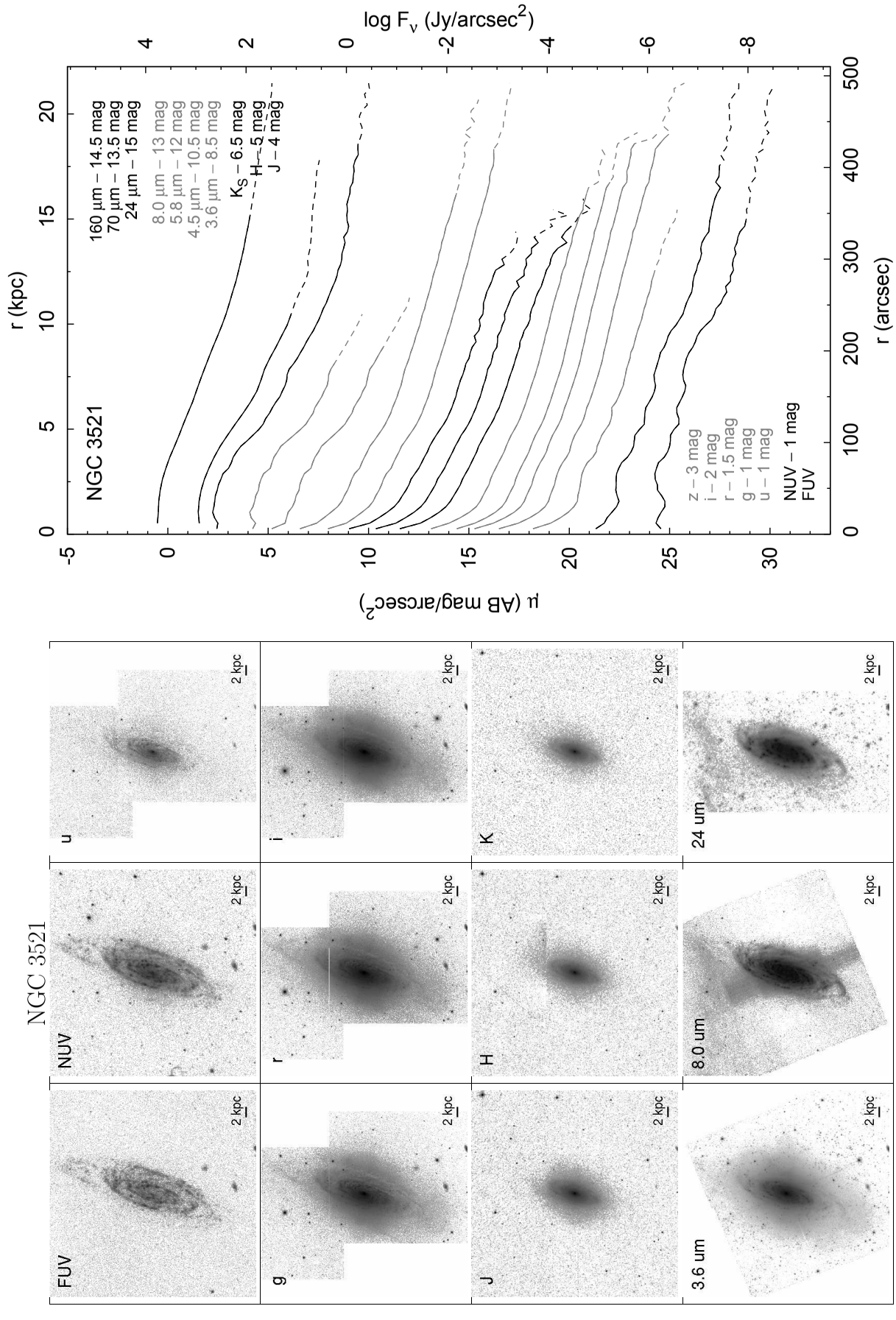
NGC 3521
FUV
NUV
u
g
r
i
J
H
K
3.6 um
8.0 um
24 um
2 kpc
μ (AB mag/arcsec²)
r (kpc)
r (arcsec)
log F_ν (Jy/arcsec²)
NGC 3521
160 μm – 14.5 mag
70 μm – 13.5 mag
24 μm – 15 mag
8.0 μm – 13 mag
5.8 μm – 12 mag
4.5 μm – 10.5 mag
3.6 μm – 8.5 mag
K_S – 6.5 mag
H – 5 mag
J – 4 mag
z – 3 mag
i – 2 mag
r – 1.5 mag
g – 1 mag
u – 1 mag
NUV – 1 mag
FUV

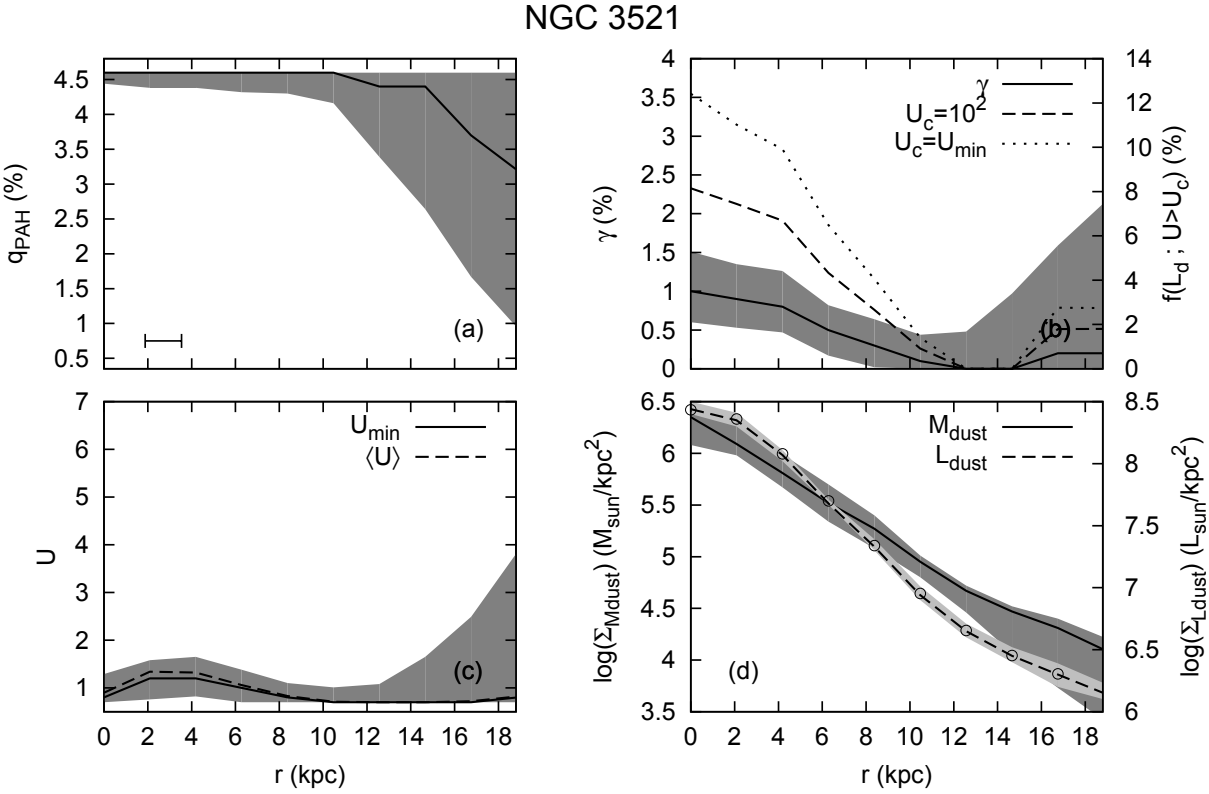
NGC 3521
q_{PAH} (%)
(a)
γ
$U_c=10^2$
$U_c=U_{min}$
γ (%)
$f(L_d ; U>U_c)$ (%)
(b)
U_{min}
⟨U⟩
U
(c)
r (kpc)
M_{dust}
L_{dust}
$\log(\Sigma_{Mdust})$ (M_{sun}/kpc^2)
$\log(\Sigma_{Ldust})$ (L_{sun}/kpc^2)
(d)
r (kpc)

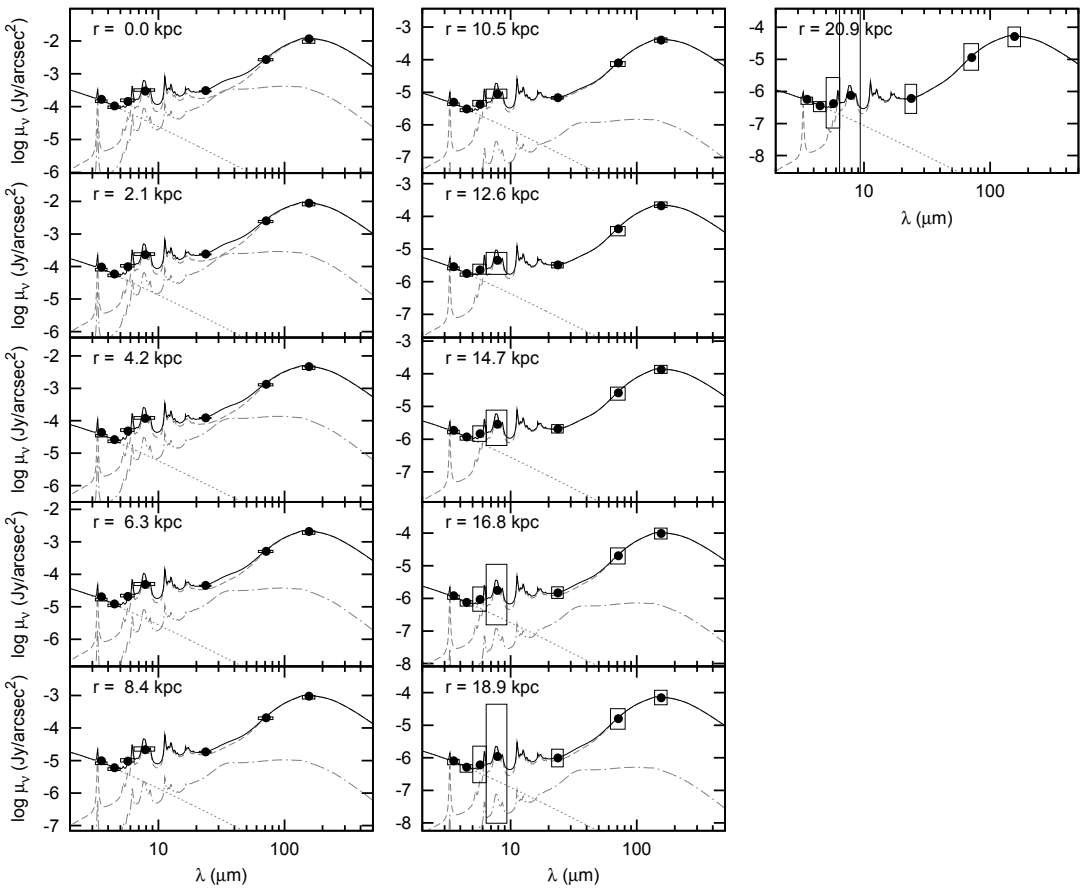
r = 0.0 kpc
r = 2.1 kpc
r = 4.2 kpc
r = 6.3 kpc
r = 8.4 kpc
r = 10.5 kpc
r = 12.6 kpc
r = 14.7 kpc
r = 16.8 kpc
r = 18.9 kpc
r = 20.9 kpc
log μν (Jy/arcsec²)
λ (μm)

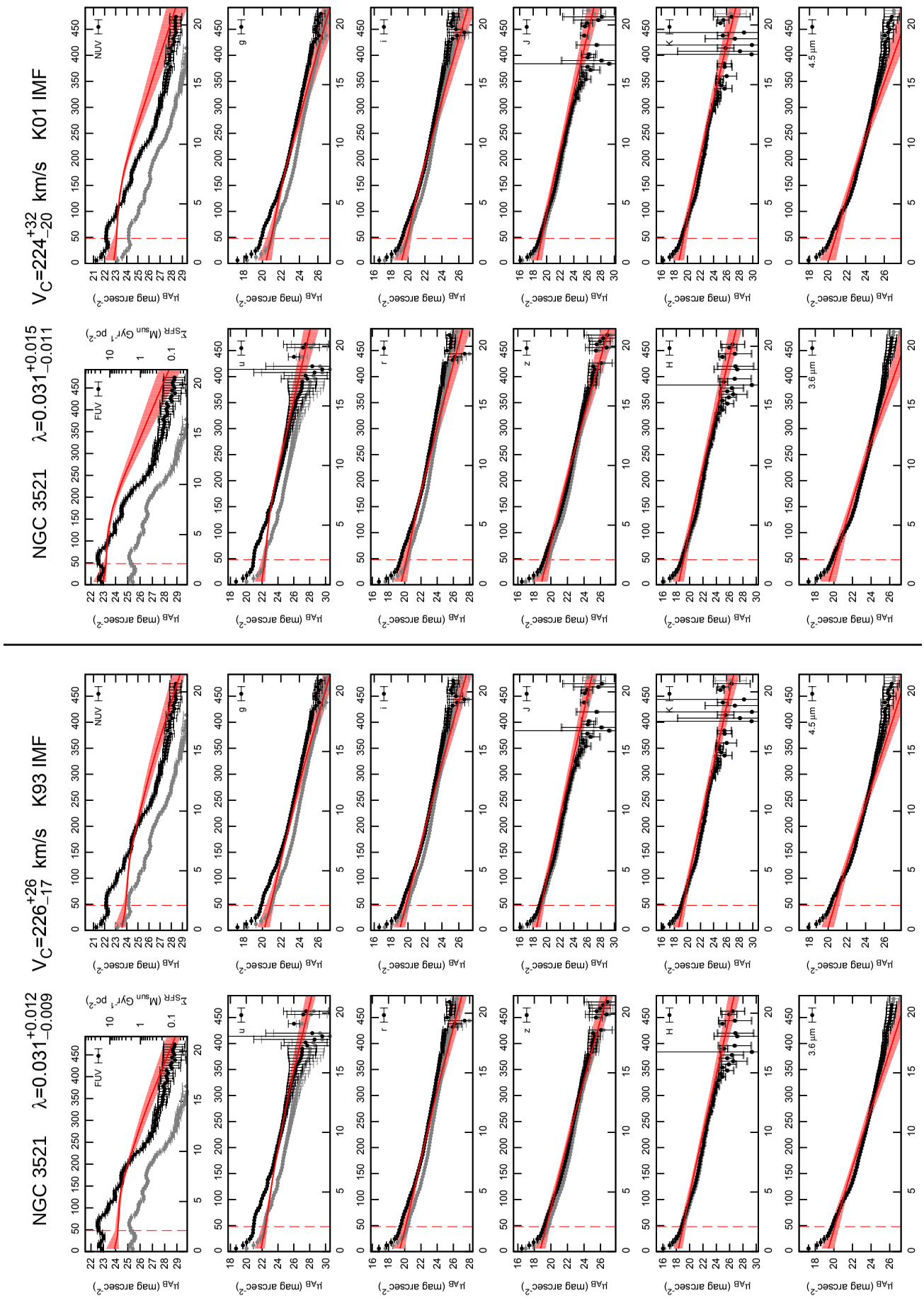
NGC 3521 λ=0.031+0.015−0.011 VC=224+32−20 km/s K01 IMF
NGC 3521 λ=0.031+0.012−0.009 VC=226+26−17 km/s K93 IMF
μAB (mag arcsec-2)
ΣSFR (Msun Gyr-1 pc-2)
FUV
NUV
u
g
r
i
z
J
H
K
3.6 μm
4.5 μm

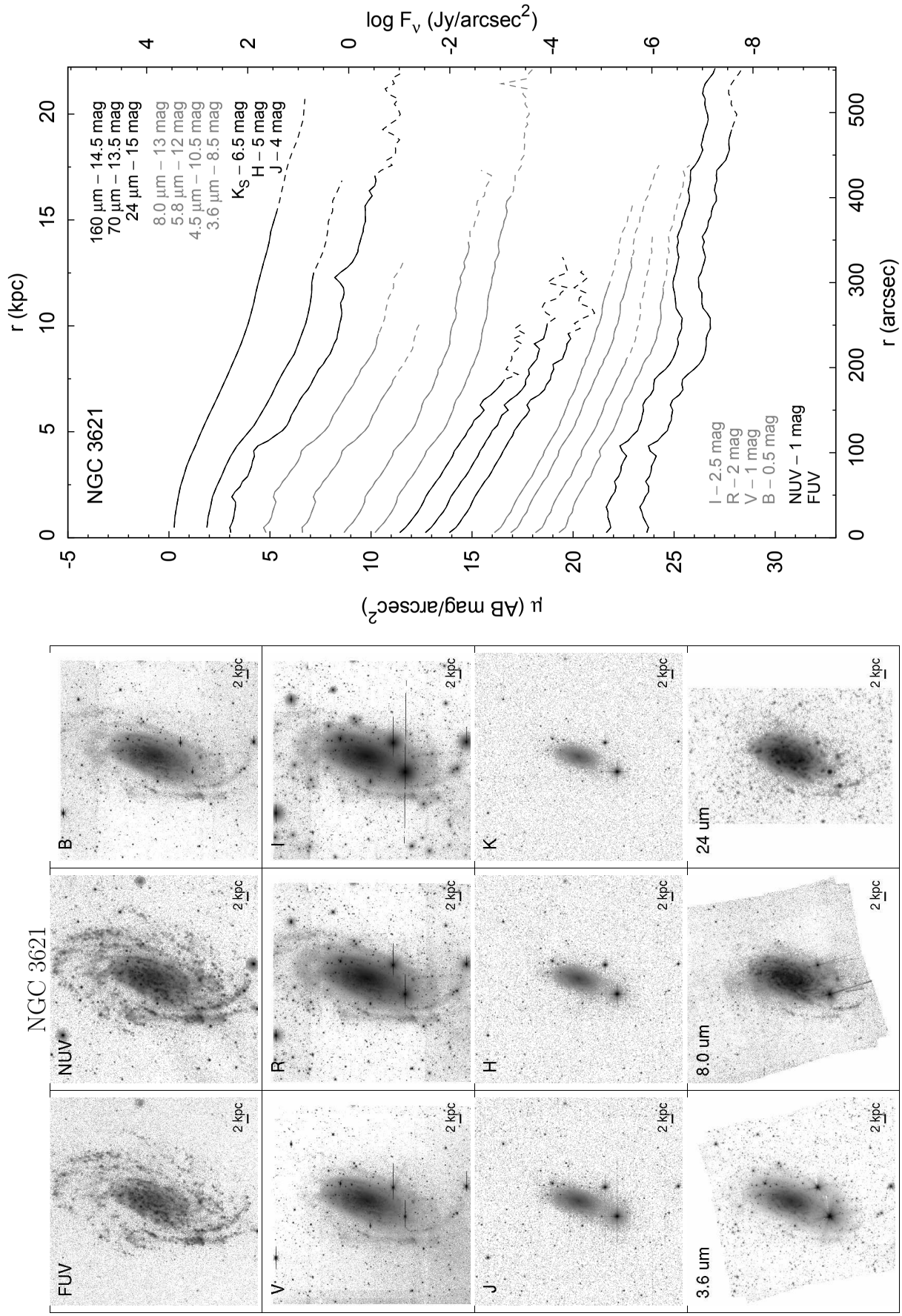
NGC 3621
FUV
NUV
B
V
R
I
J
H
K'
3.6 um
8.0 um
24 um
2 kpc
μ (AB mag/arcsec²)
log F_ν (Jy/arcsec²)
r (kpc)
r (arcsec)
NGC 3621
160 μm – 14.5 mag
70 μm – 13.5 mag
24 μm – 15 mag
8.0 μm – 13 mag
5.8 μm – 12 mag
4.5 μm – 10.5 mag
3.6 μm – 8.5 mag
K_S – 6.5 mag
H – 5 mag
J – 4 mag
I – 2.5 mag
R – 2 mag
V – 1 mag
B – 0.5 mag
NUV – 1 mag
FUV

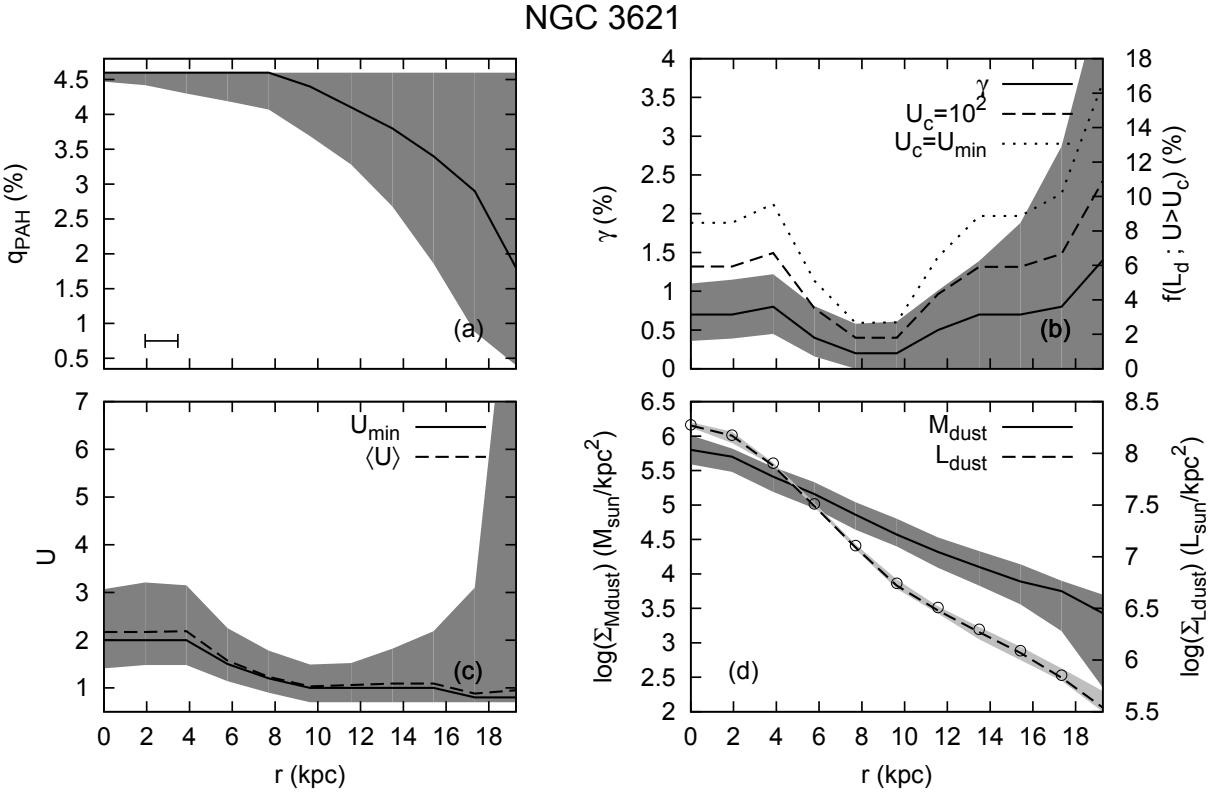
NGC 3621
q_{PAH} (%)
(a)
γ (%)
$U_c=10^2$
$U_c=U_{min}$
$f(L_d ; U>U_c)$ (%)
(b)
U
U_{min}
⟨U⟩
(c)
r (kpc)
$\log(\Sigma_{Mdust})$ (M_{sun}/kpc^2)
M_{dust}
L_{dust}
$\log(\Sigma_{Ldust})$ (L_{sun}/kpc^2)
(d)
r (kpc)

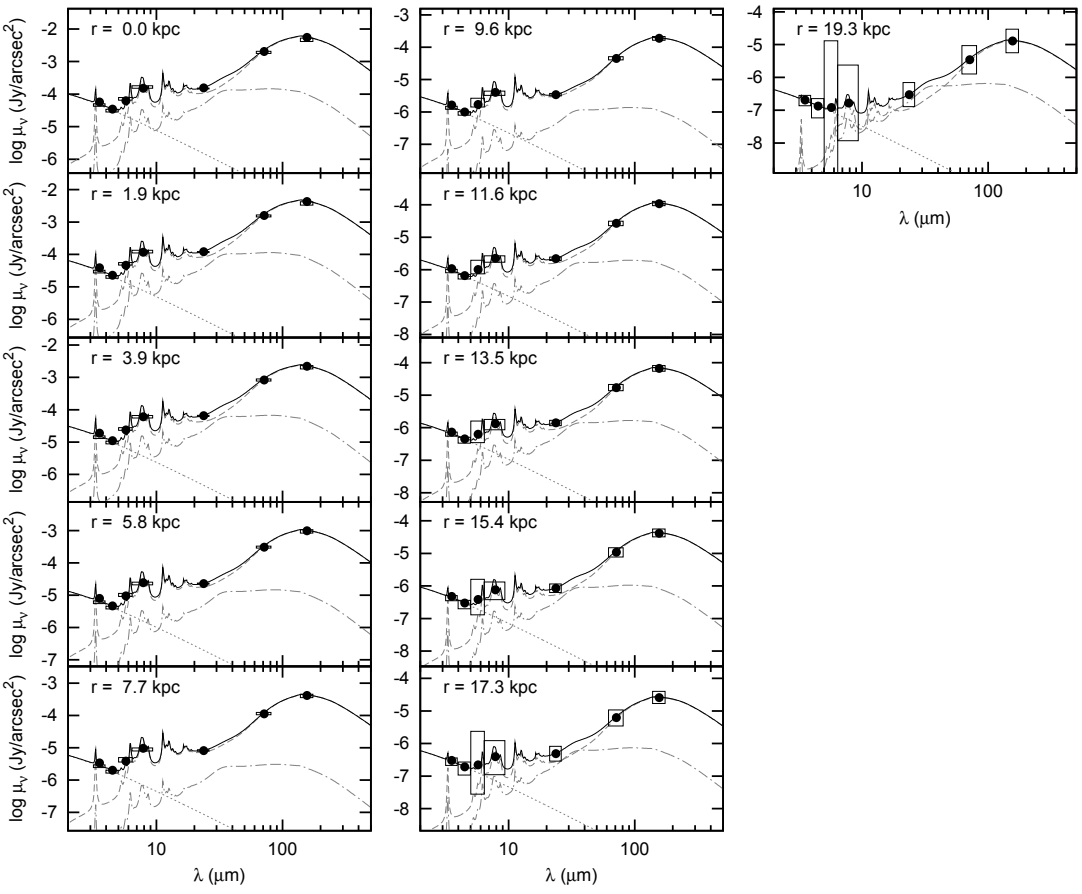
r = 0.0 kpc
r = 1.9 kpc
r = 3.9 kpc
r = 5.8 kpc
r = 7.7 kpc
r = 9.6 kpc
r = 11.6 kpc
r = 13.5 kpc
r = 15.4 kpc
r = 17.3 kpc
r = 19.3 kpc
log μν (Jy/arcsec²)
λ (μm)

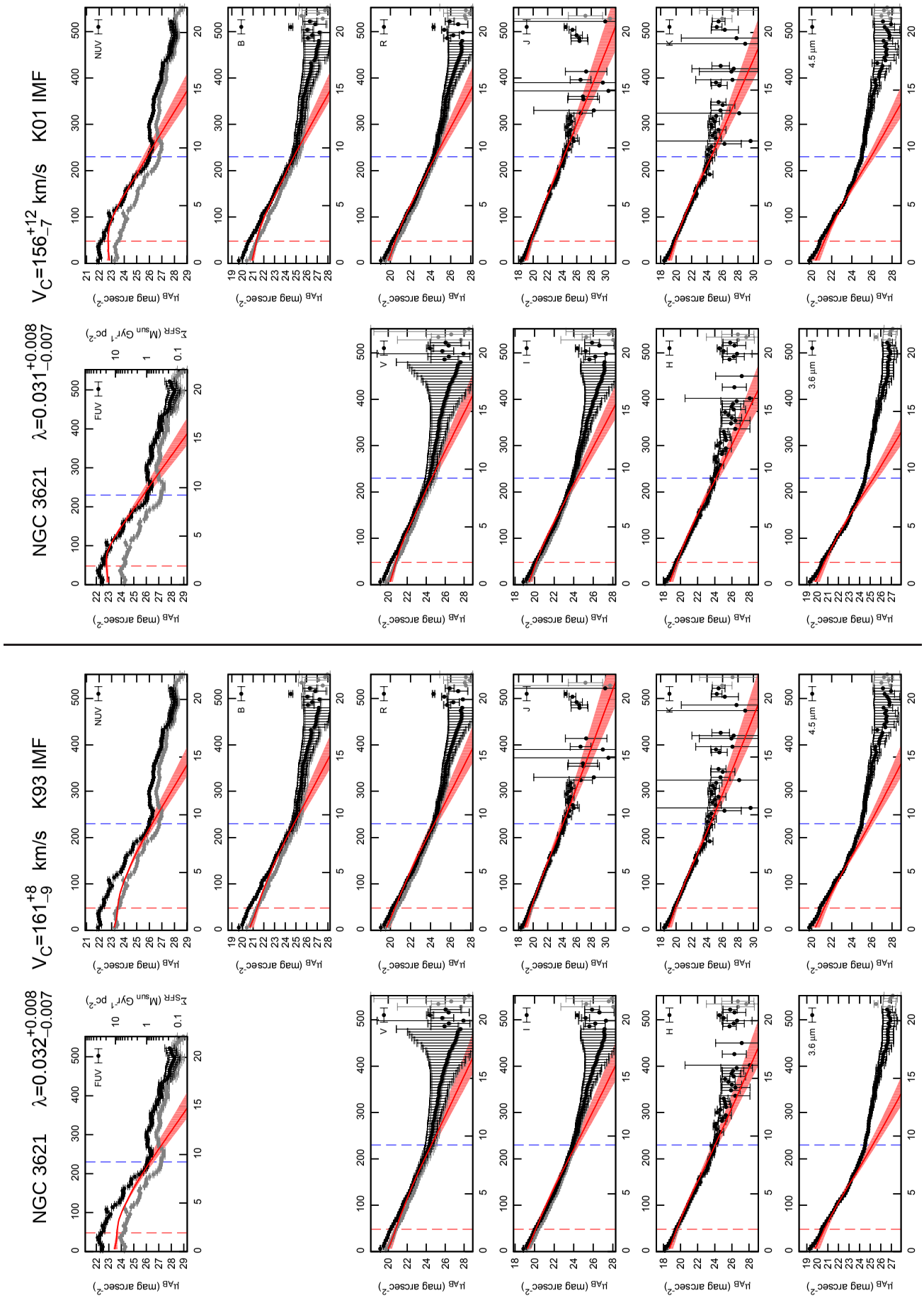
NGC 3621 λ=0.031+0.008−0.007 VC=156+12−7 km/s K01 IMF
NGC 3621 λ=0.032+0.008−0.007 VC=161+8−9 km/s K93 IMF
NUV
FUV
B
V
R
I
J
H
K
3.6 μm
4.5 μm
μAB (mag arcsec-2)
ΣSFR (Msun Gyr-1 pc-2)

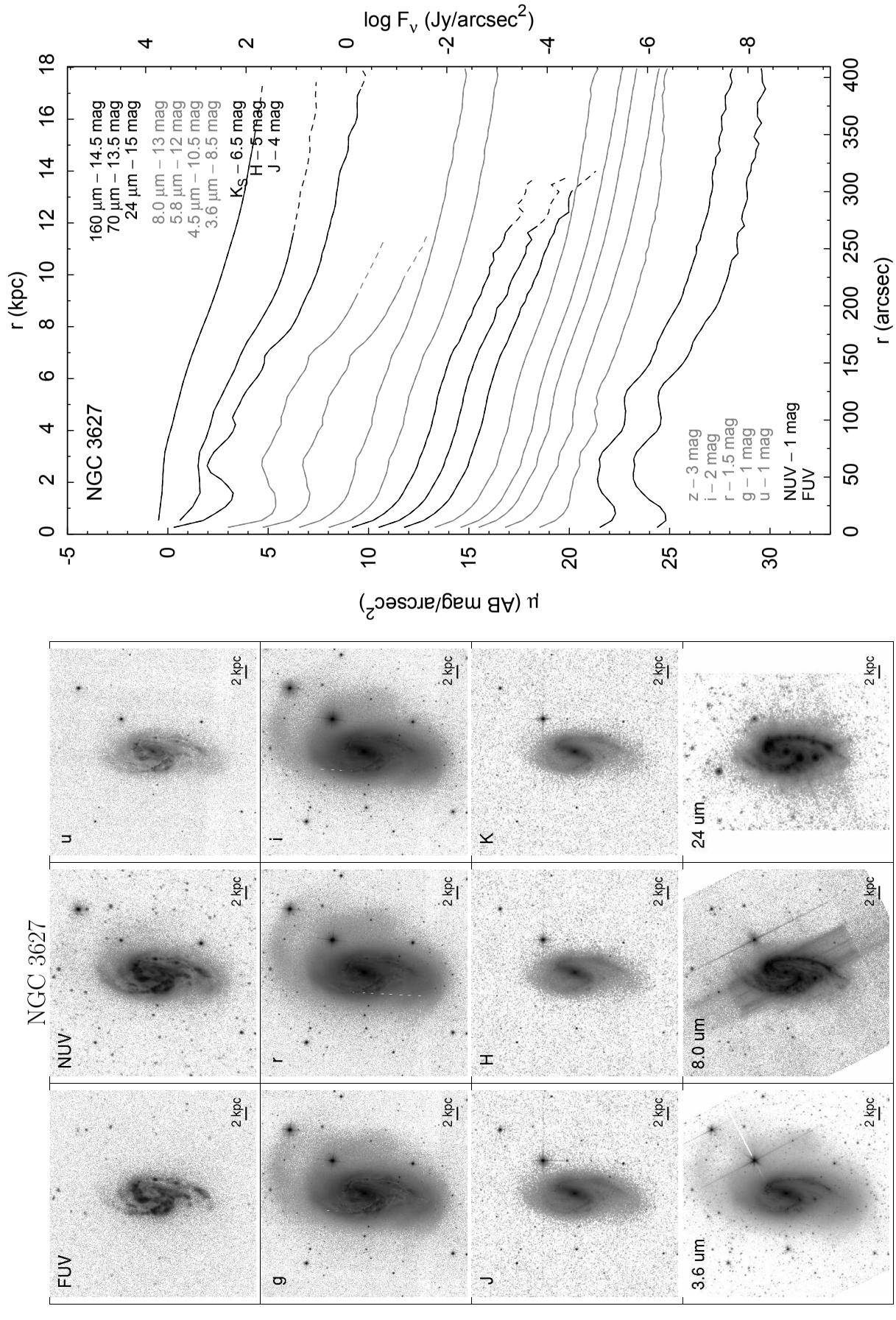
NGC 3627
FUV
NUV
u
g
r
i
J
H
K
3.6 um
8.0 um
24 um
2 kpc
μ (AB mag/arcsec²)
r (kpc)
r (arcsec)
log F_ν (Jy/arcsec²)
NGC 3627
160 μm – 14.5 mag
70 μm – 13.5 mag
24 μm – 15 mag
8.0 μm – 13 mag
5.8 μm – 12 mag
4.5 μm – 10.5 mag
3.6 μm – 8.5 mag
K_S – 6.5 mag
H – 5 mag
J – 4 mag
z – 3 mag
i – 2 mag
r – 1.5 mag
g – 1 mag
u – 1 mag
NUV – 1 mag
FUV

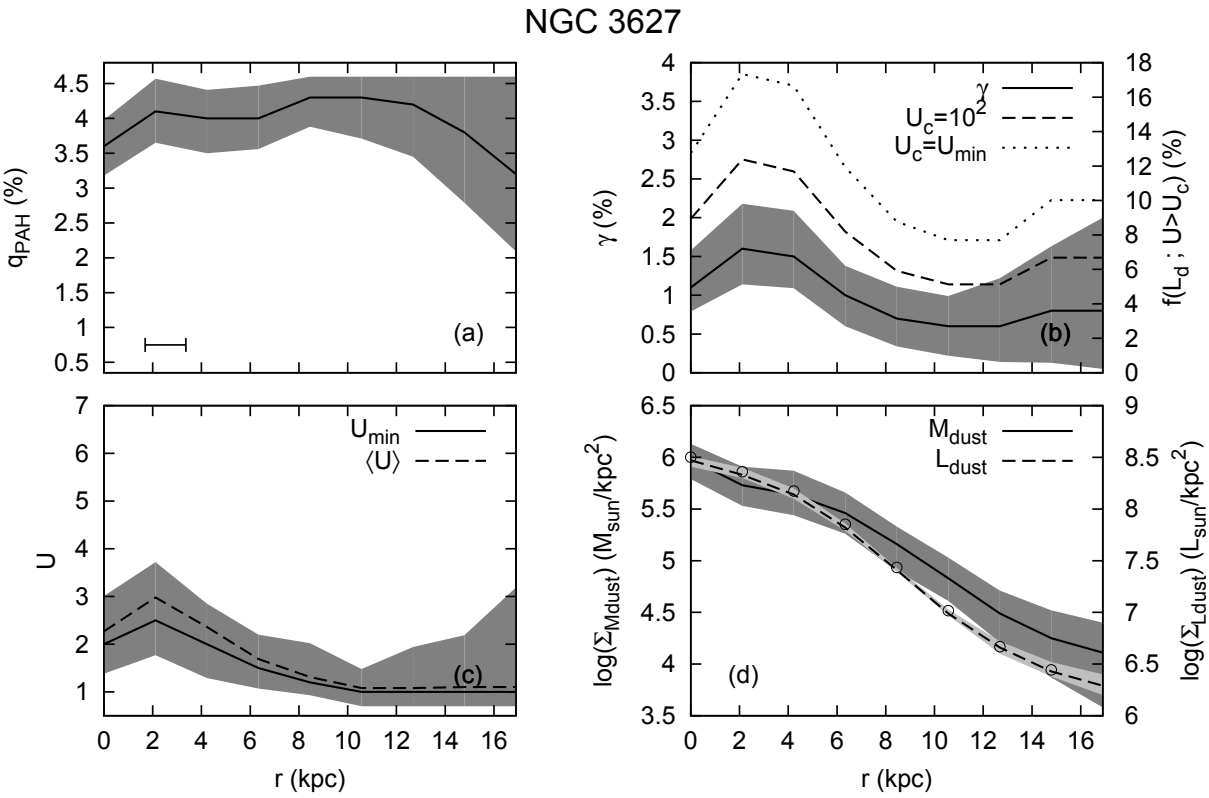
NGC 3627
q_{PAH} (%)
(a)
γ (%)
$U_c=10^2$
$U_c=U_{min}$
γ
$f(L_d ; U>U_c)$ (%)
(b)
U
U_{min}
⟨U⟩
(c)
r (kpc)
$\log(\Sigma_{Mdust})$ (M_{sun}/kpc^2)
M_{dust}
L_{dust}
(d)
$\log(\Sigma_{Ldust})$ (L_{sun}/kpc^2)
r (kpc)

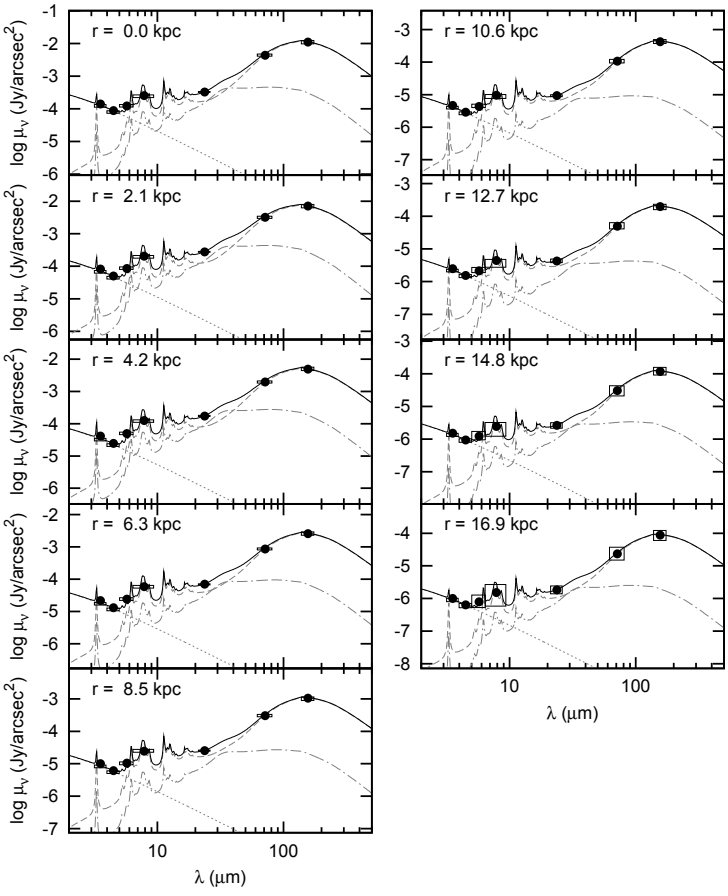
r = 0.0 kpc
r = 2.1 kpc
r = 4.2 kpc
r = 6.3 kpc
r = 8.5 kpc
r = 10.6 kpc
r = 12.7 kpc
r = 14.8 kpc
r = 16.9 kpc
log μν (Jy/arcsec²)
λ (μm)

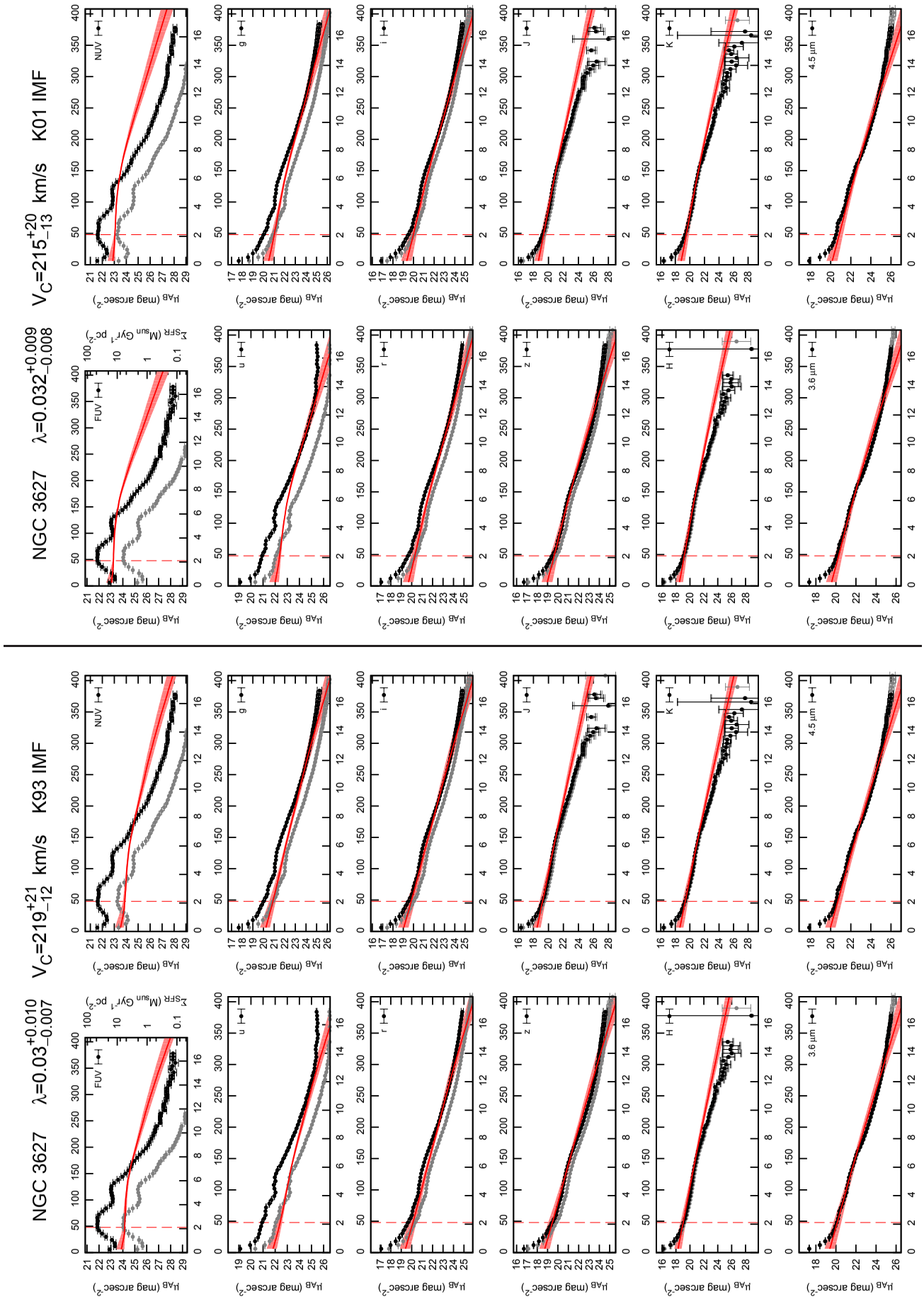
NGC 3627 λ=0.03+0.010−0.007 VC=219+21−12 km/s K93 IMF
NGC 3627 λ=0.032+0.009−0.008 VC=215+20−13 km/s K01 IMF
FUV
NUV
u
g
r
i
z
J
H
K
3.6 μm
4.5 μm
μAB (mag arcsec-2)
MSFR (Msun Gyr-1 pc-2)

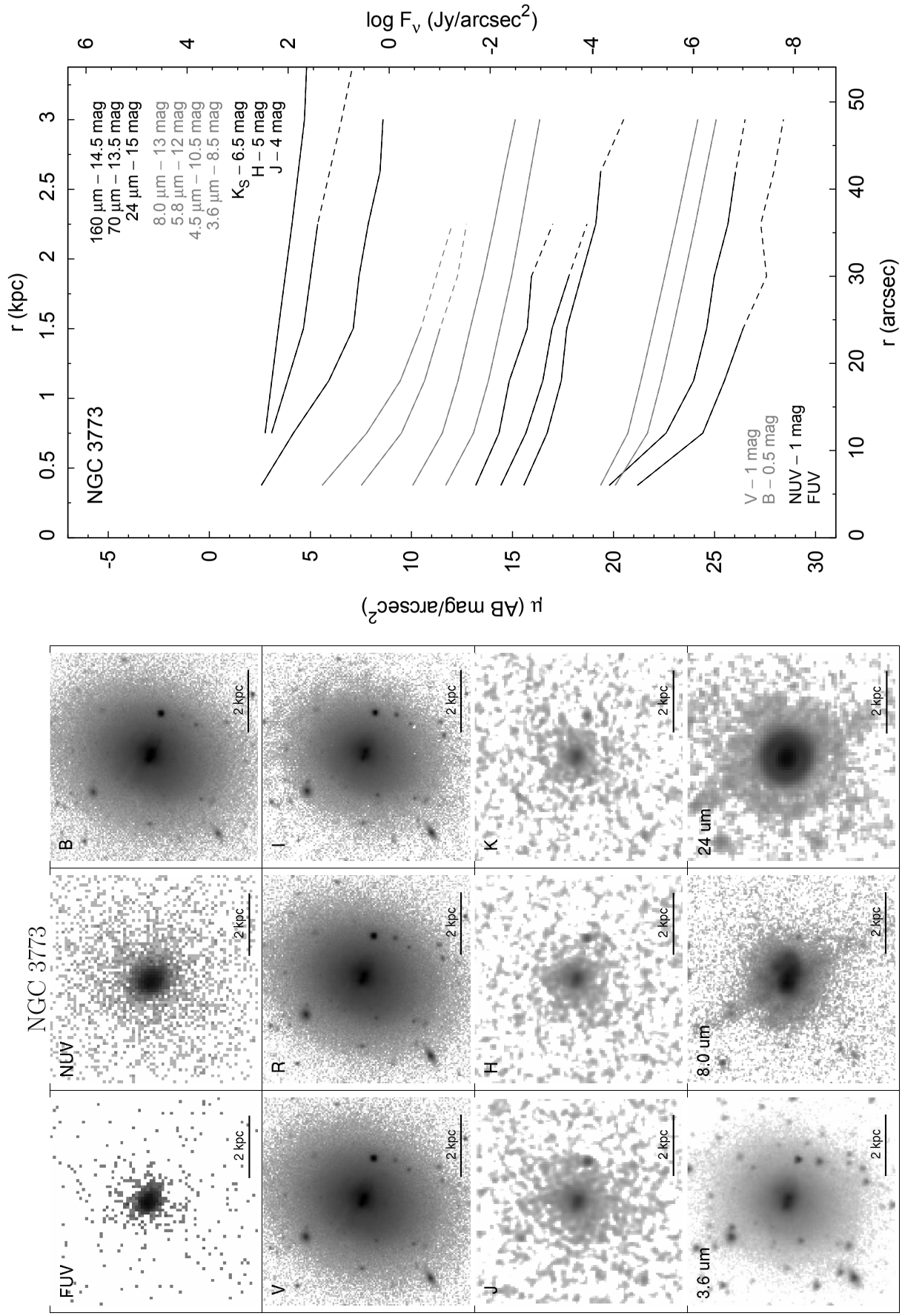
NGC 3773
FUV
NUV
B
V
R
I
J
H
K
3.6 um
8.0 um
24 um
2 kpc
μ (AB mag/arcsec²)
log F_ν (Jy/arcsec²)
r (kpc)
r (arcsec)
NGC 3773
160 μm – 14.5 mag
70 μm – 13.5 mag
24 μm – 15 mag
8.0 μm – 13 mag
5.8 μm – 12 mag
4.5 μm – 10.5 mag
3.6 μm – 8.5 mag
K_S – 6.5 mag
H – 5 mag
J – 4 mag
V – 1 mag
B – 0.5 mag
NUV – 1 mag
FUV

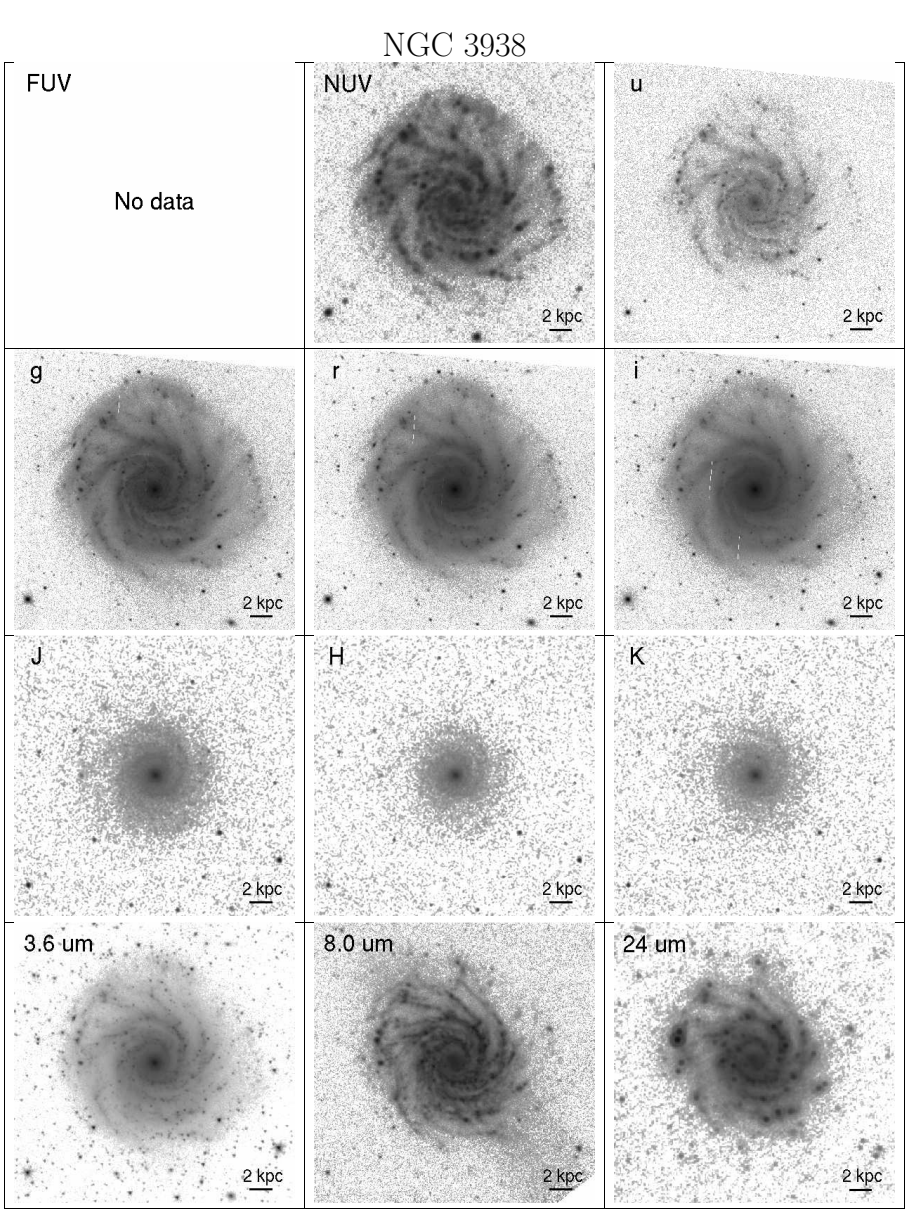
NGC 3938
FUV
No data
NUV
u
g
r
i
J
H
K
3.6 um
8.0 um
24 um
2 kpc

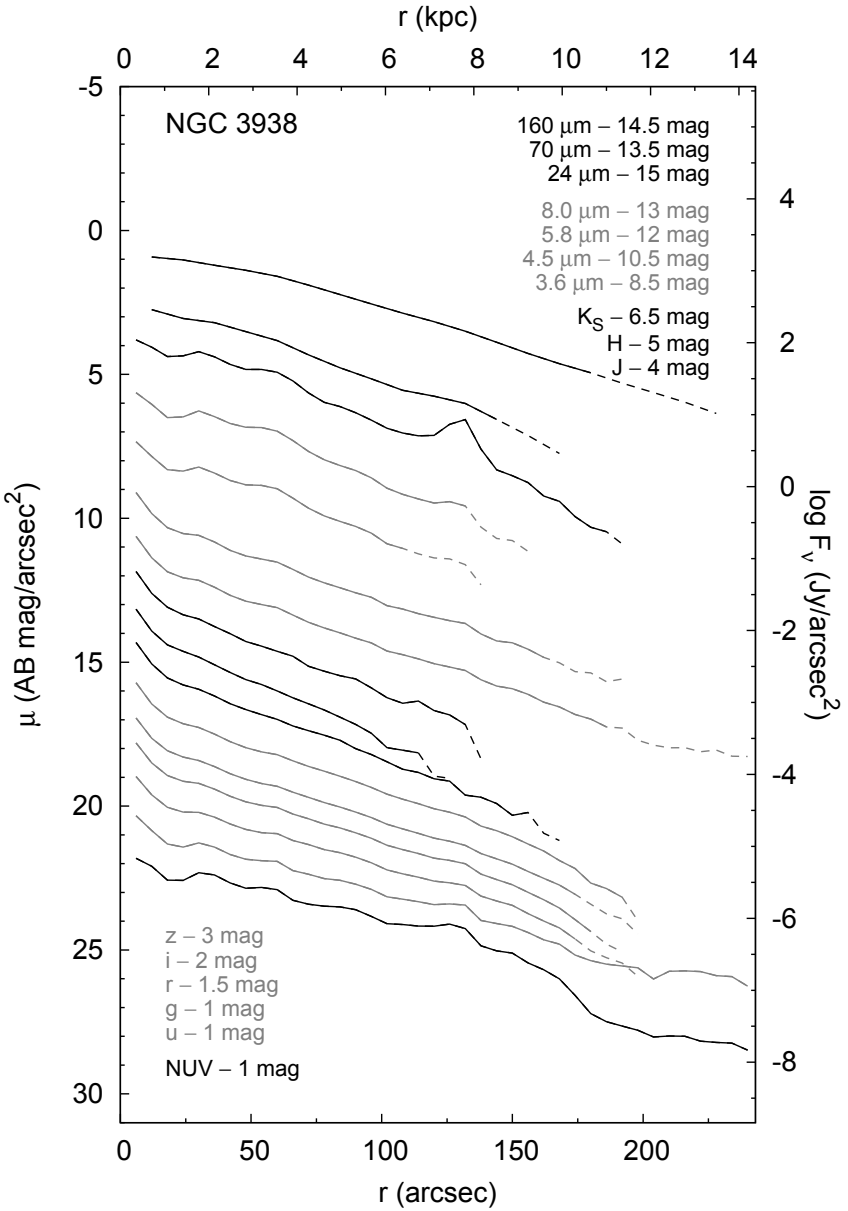
NGC 3938
r (kpc)
r (arcsec)
μ (AB mag/arcsec^2)
log F_ν (Jy/arcsec^2)
160 μm – 14.5 mag
70 μm – 13.5 mag
24 μm – 15 mag
8.0 μm – 13 mag
5.8 μm – 12 mag
4.5 μm – 10.5 mag
3.6 μm – 8.5 mag
K_S – 6.5 mag
H – 5 mag
J – 4 mag
z – 3 mag
i – 2 mag
r – 1.5 mag
g – 1 mag
u – 1 mag
NUV – 1 mag

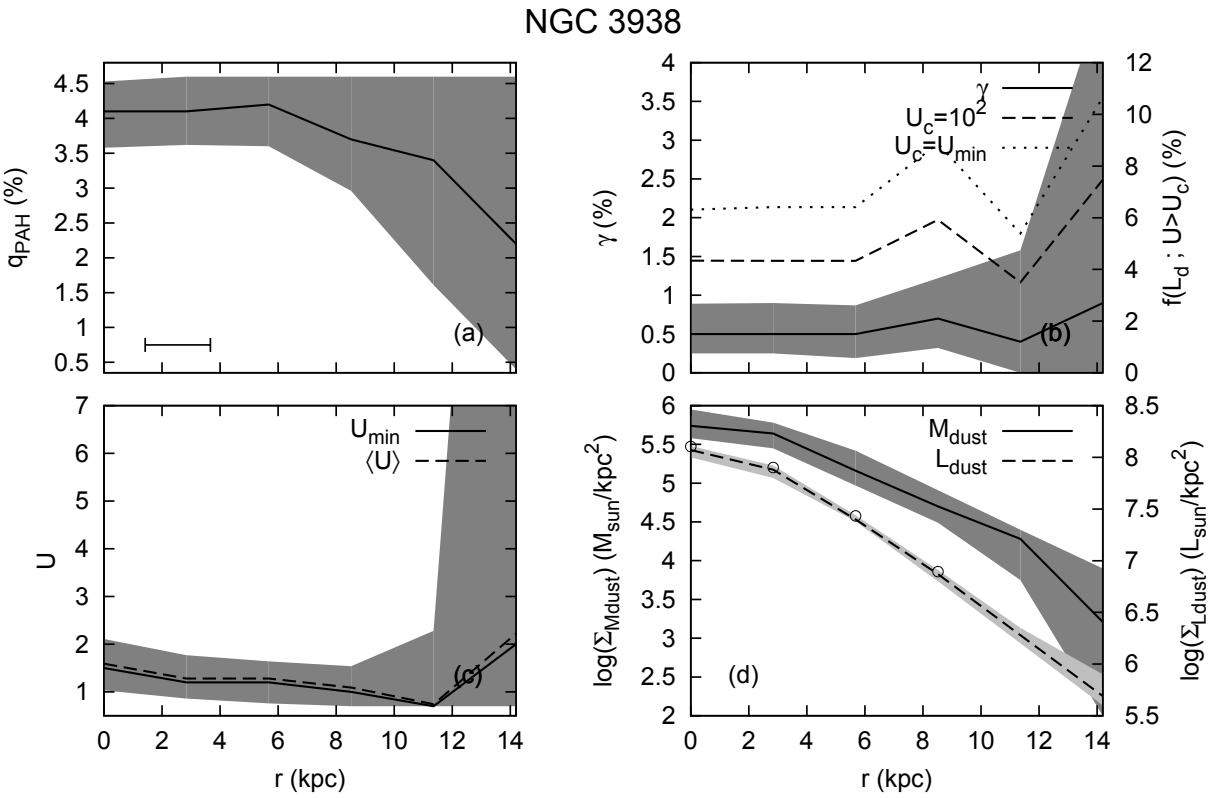
NGC 3938
q_{PAH} (%)
(a)
γ
$U_c=10^2$
$U_c=U_{min}$
γ (%)
$f(L_d ; U>U_c)$ (%)
(b)
U_{min}
⟨U⟩
U
(c)
M_{dust}
L_{dust}
$\log(\Sigma_{Mdust})$ (M_{sun}/kpc^2)
$\log(\Sigma_{Ldust})$ (L_{sun}/kpc^2)
(d)
r (kpc)
r (kpc)

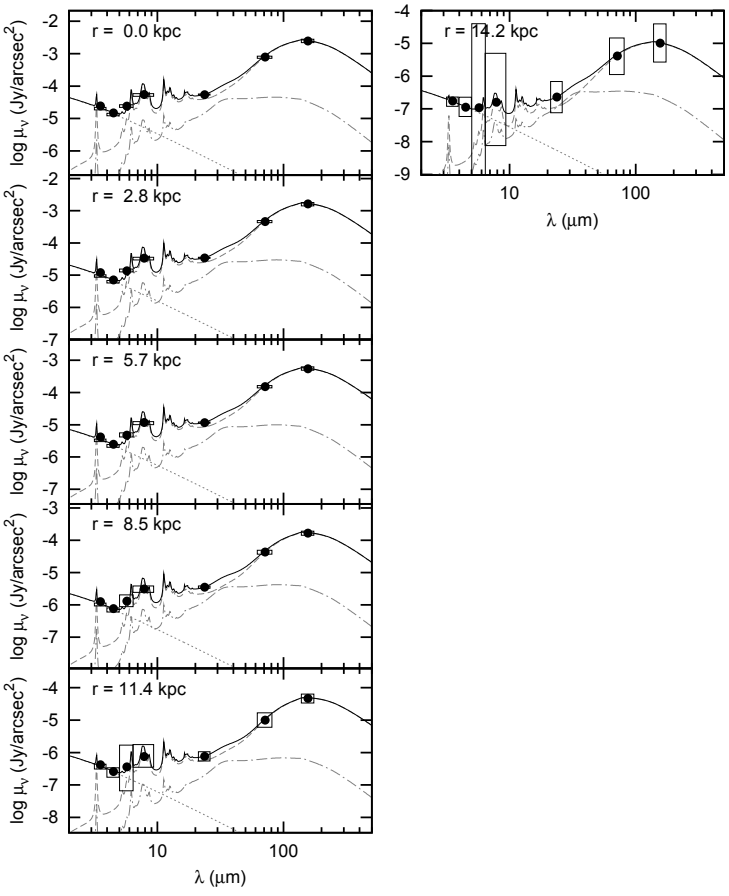
r = 0.0 kpc
r = 2.8 kpc
r = 5.7 kpc
r = 8.5 kpc
r = 11.4 kpc
r = 14.2 kpc
log μ_ν (Jy/arcsec^2)
λ (μm)

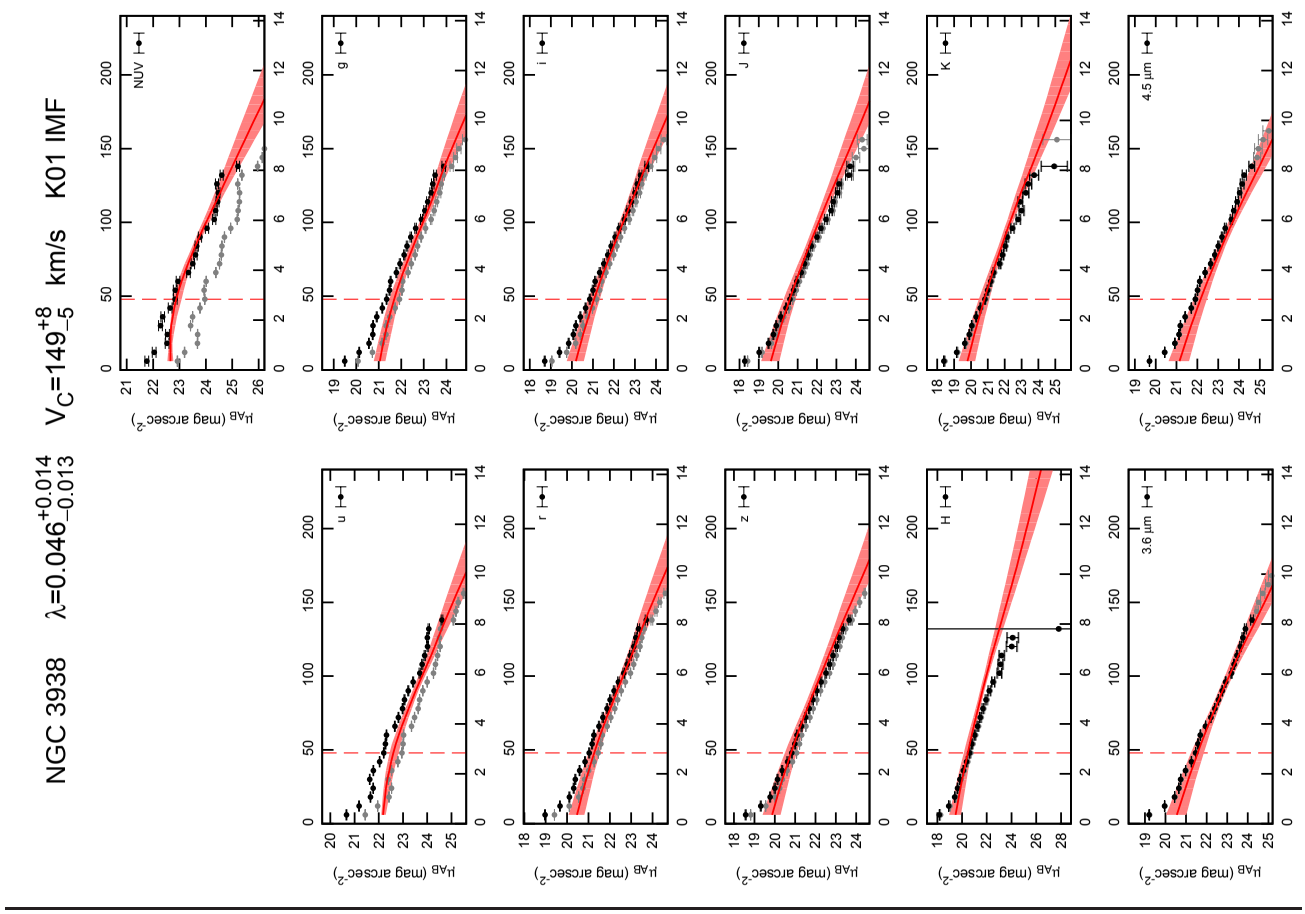
NGC 3938 λ=0.046+0.014−0.013 VC=149+8−5 km/s K01 IMF
NUV
g
i
J
K
4.5 μm
u
r
z
H
3.6 μm
μAB (mag arcsec-2)

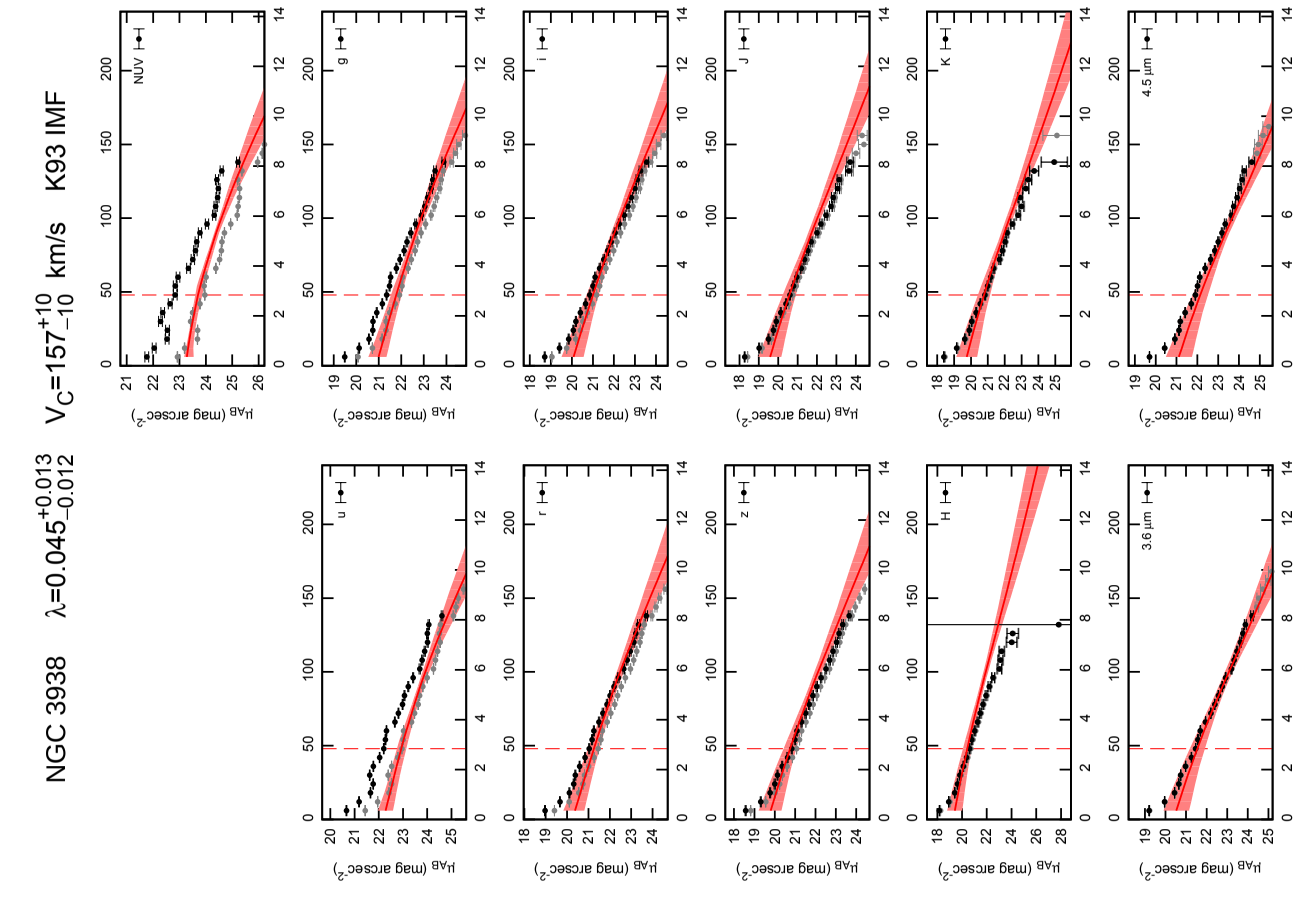
NGC 3938 λ=0.045+0.013−0.012 VC=157+10−10 km/s K93 IMF
NUV
g
i
J
K
4.5 μm
u
r
z
H
3.6 μm
μAB (mag arcsec-2)

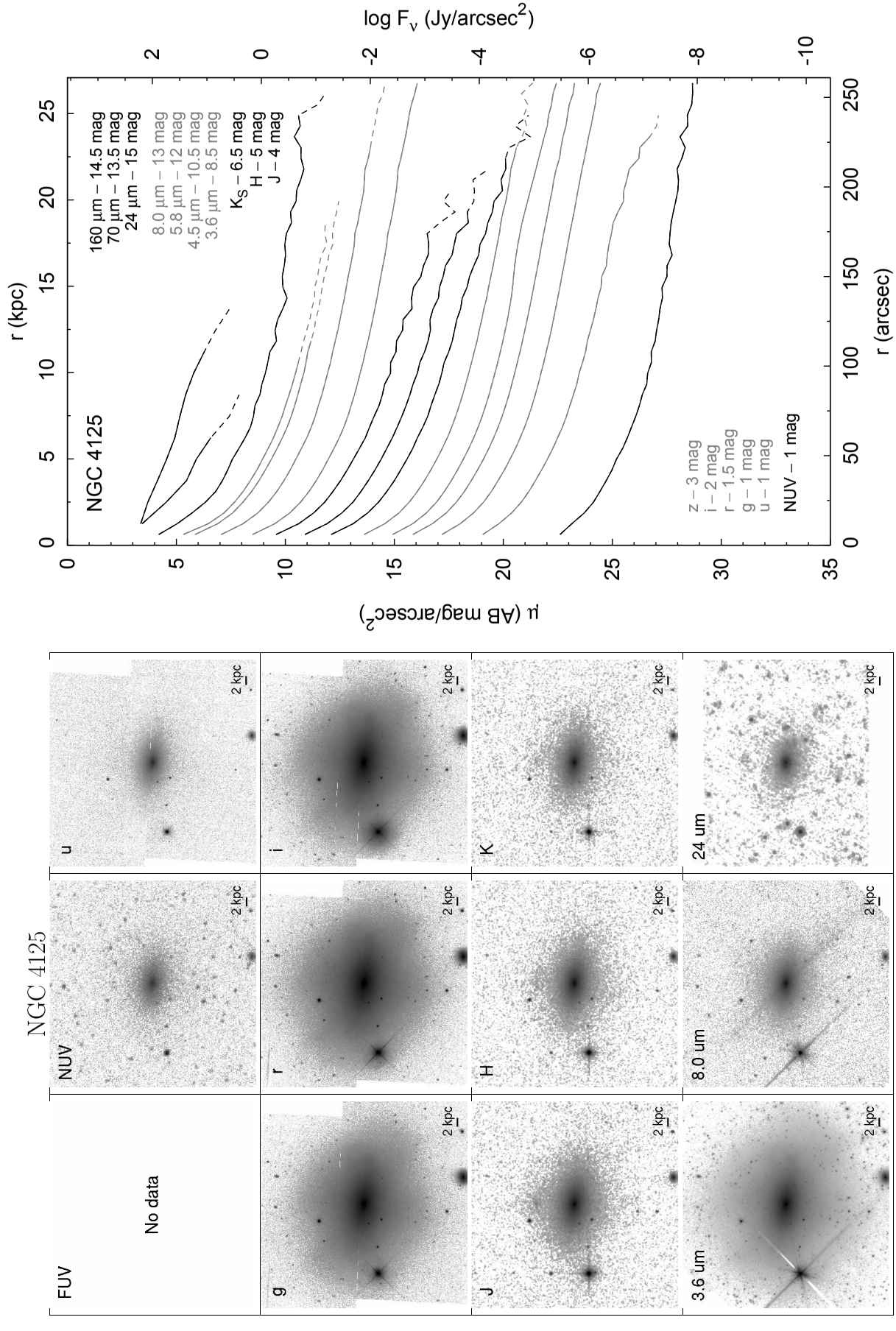
NGC 4125
FUV
No data
NUV
u
g
r
i
J
H
K
3.6 um
8.0 um
24 um
2 kpc
μ (AB mag/arcsec²)
log F_ν (Jy/arcsec²)
r (kpc)
r (arcsec)
NGC 4125
160 μm – 14.5 mag
70 μm – 13.5 mag
24 μm – 15 mag
8.0 μm – 13 mag
5.8 μm – 12 mag
4.5 μm – 10.5 mag
3.6 μm – 8.5 mag
K_S – 6.5 mag
H – 5 mag
J – 4 mag
z – 3 mag
i – 2 mag
r – 1.5 mag
g – 1 mag
u – 1 mag
NUV – 1 mag

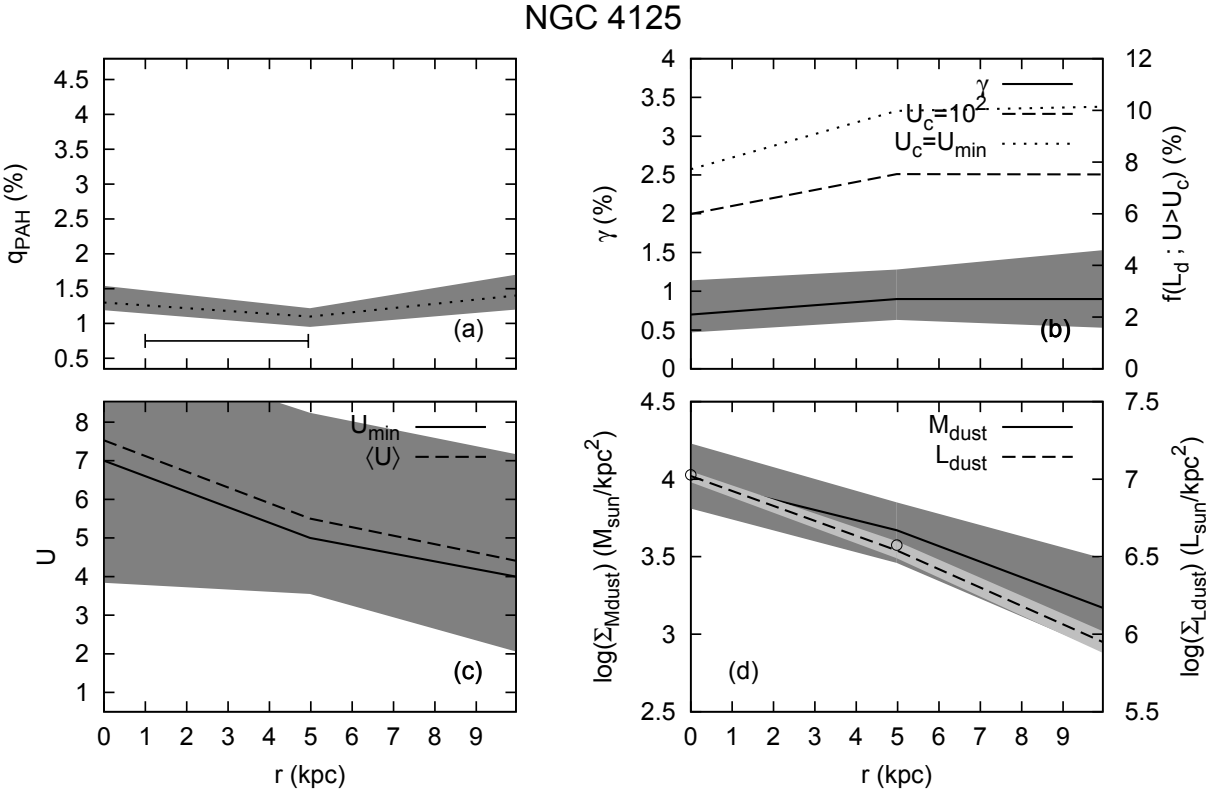
NGC 4125
q_{PAH} (%)
(a)
γ
$U_c=10^2$
$U_c=U_{min}$
γ (%)
$f(L_d ; U>U_c)$ (%)
(b)
U_{min}
⟨U⟩
U
(c)
r (kpc)
M_{dust}
L_{dust}
$\log(\Sigma_{Mdust})$ (M_{sun}/kpc^2)
$\log(\Sigma_{Ldust})$ (L_{sun}/kpc^2)
(d)
r (kpc)

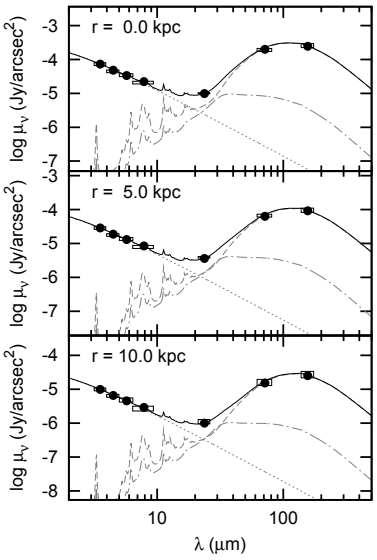
r = 0.0 kpc
r = 5.0 kpc
r = 10.0 kpc
log μ_ν (Jy/arcsec^2)
λ (μm)

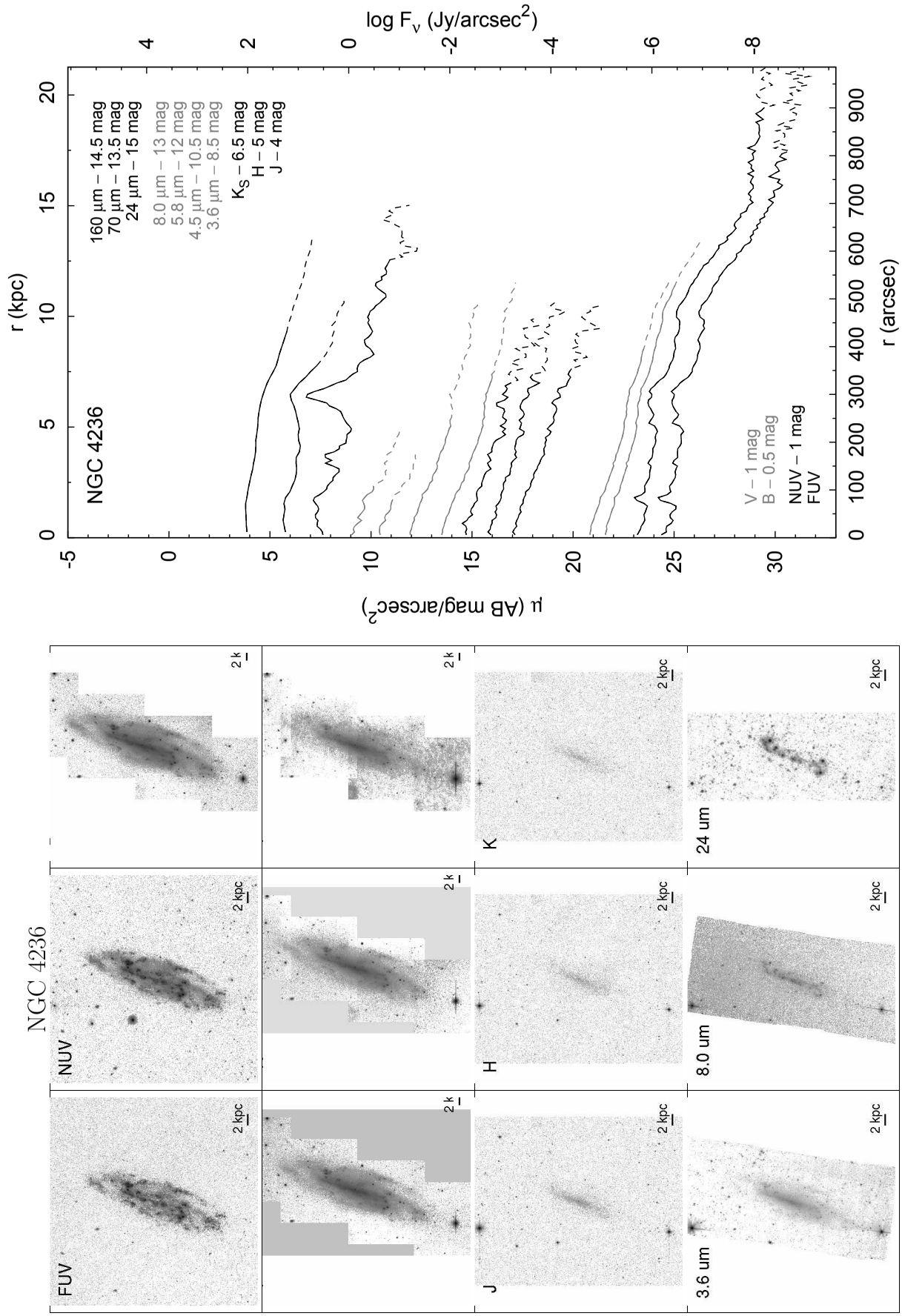
NGC 4236
FUV
NUV
J
H
K
3.6 um
8.0 um
24 um
2 kpc
μ (AB mag/arcsec²)
log F_ν (Jy/arcsec²)
r (kpc)
r (arcsec)
NGC 4236
160 μm – 14.5 mag
70 μm – 13.5 mag
24 μm – 15 mag
8.0 μm – 13 mag
5.8 μm – 12 mag
4.5 μm – 10.5 mag
3.6 μm – 8.5 mag
K_S – 6.5 mag
H – 5 mag
J – 4 mag
V – 1 mag
B – 0.5 mag
NUV – 1 mag
FUV

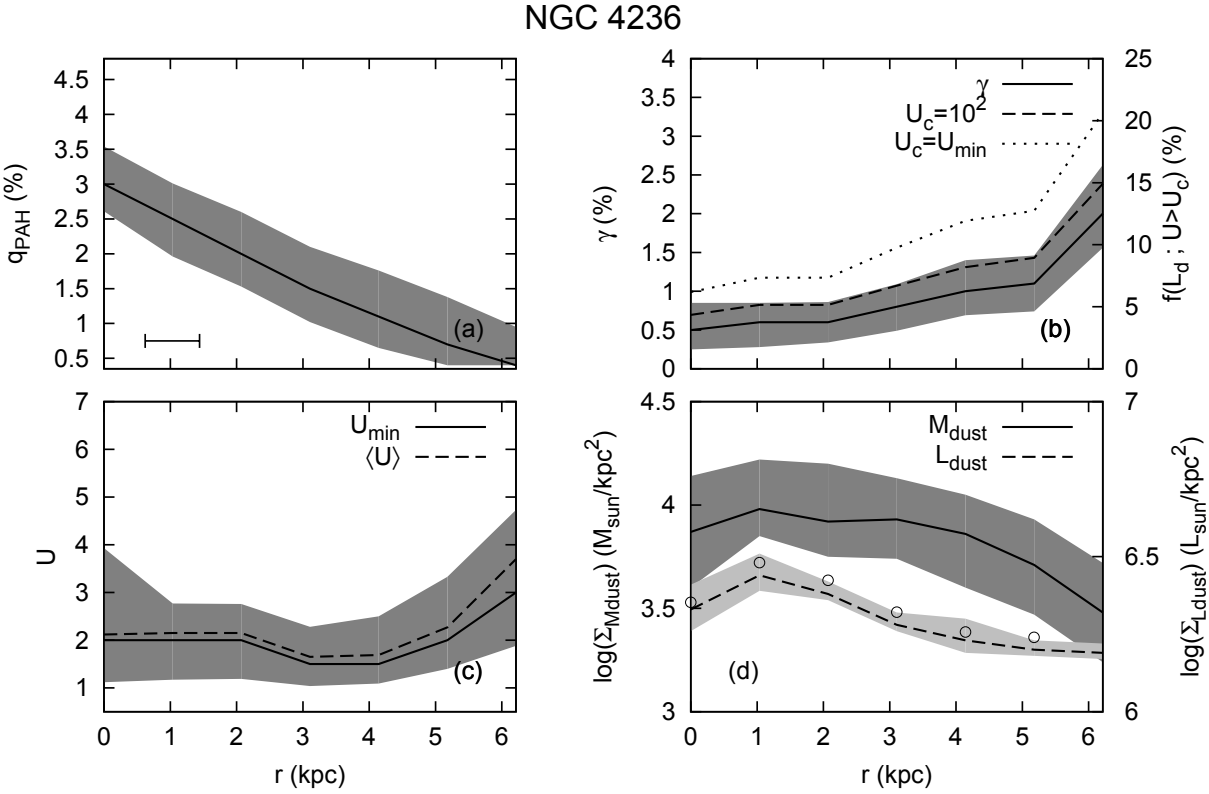
NGC 4236
q_{PAH} (%)
(a)
γ
$U_c=10^2$
$U_c=U_{min}$
γ (%)
$f(L_d\,;U>U_c)$ (%)
(b)
U_{min}
$\langle U\rangle$
U
(c)
r (kpc)
M_{dust}
L_{dust}
$\log(\Sigma_{Mdust})$ (M_{sun}/kpc^2)
$\log(\Sigma_{Ldust})$ (L_{sun}/kpc^2)
(d)
r (kpc)

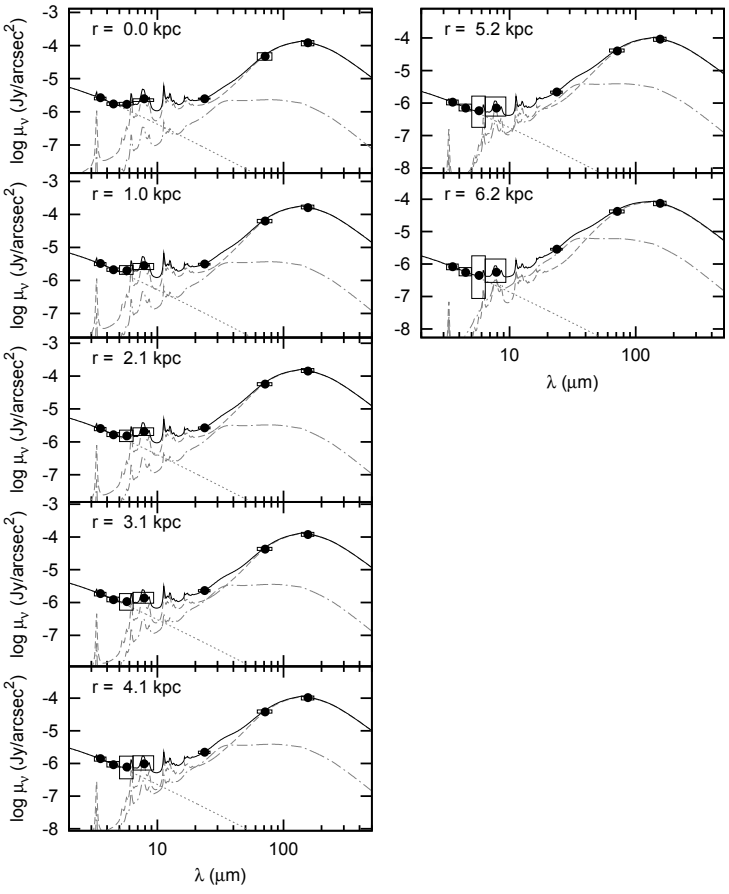
r = 0.0 kpc
r = 1.0 kpc
r = 2.1 kpc
r = 3.1 kpc
r = 4.1 kpc
r = 5.2 kpc
r = 6.2 kpc
log μ_ν (Jy/arcsec^2)
λ (μm)

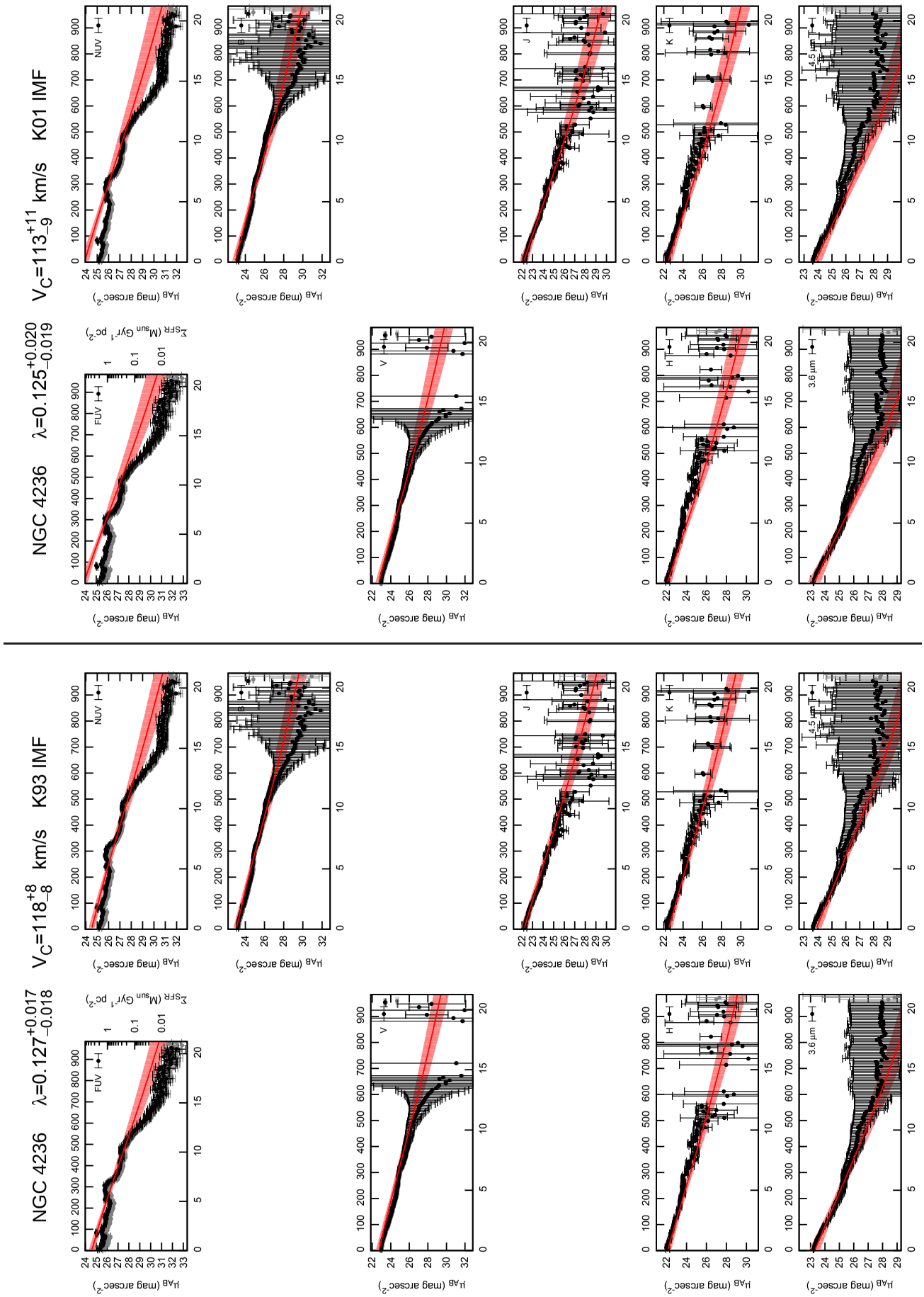
NGC 4236 λ=0.125+0.020−0.019 VC=113+11−9 km/s K01 IMF
NGC 4236 λ=0.127+0.017−0.018 VC=118+8−8 km/s K93 IMF
μAB (mag arcsec-2)
ΣSFR (Msun Gyr-1 pc-2)
NUV
FUV
B
V
H
J
K
4.5
3.6 μm

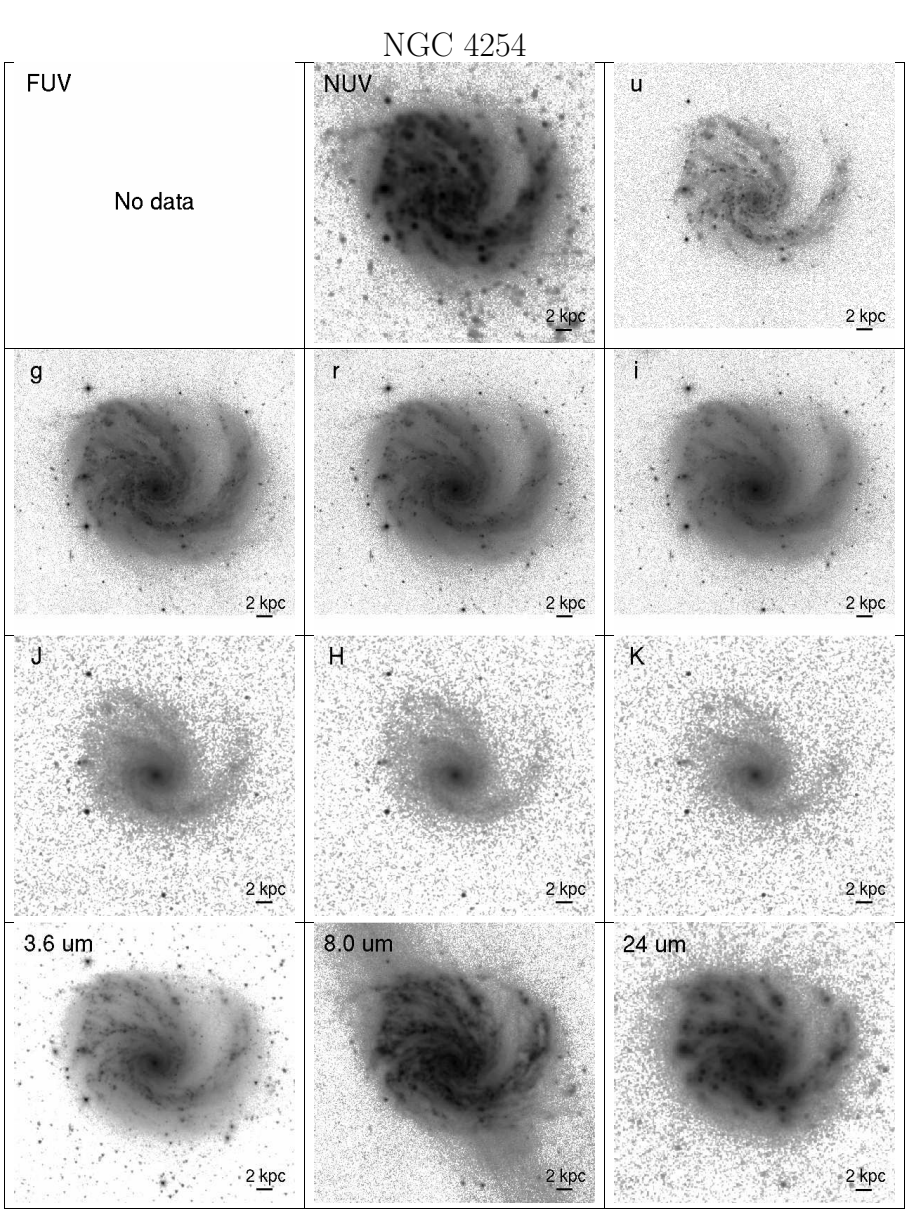
NGC 4254
FUV
No data
NUV
u
g
r
i
J
H
K
3.6 um
8.0 um
24 um
2 kpc

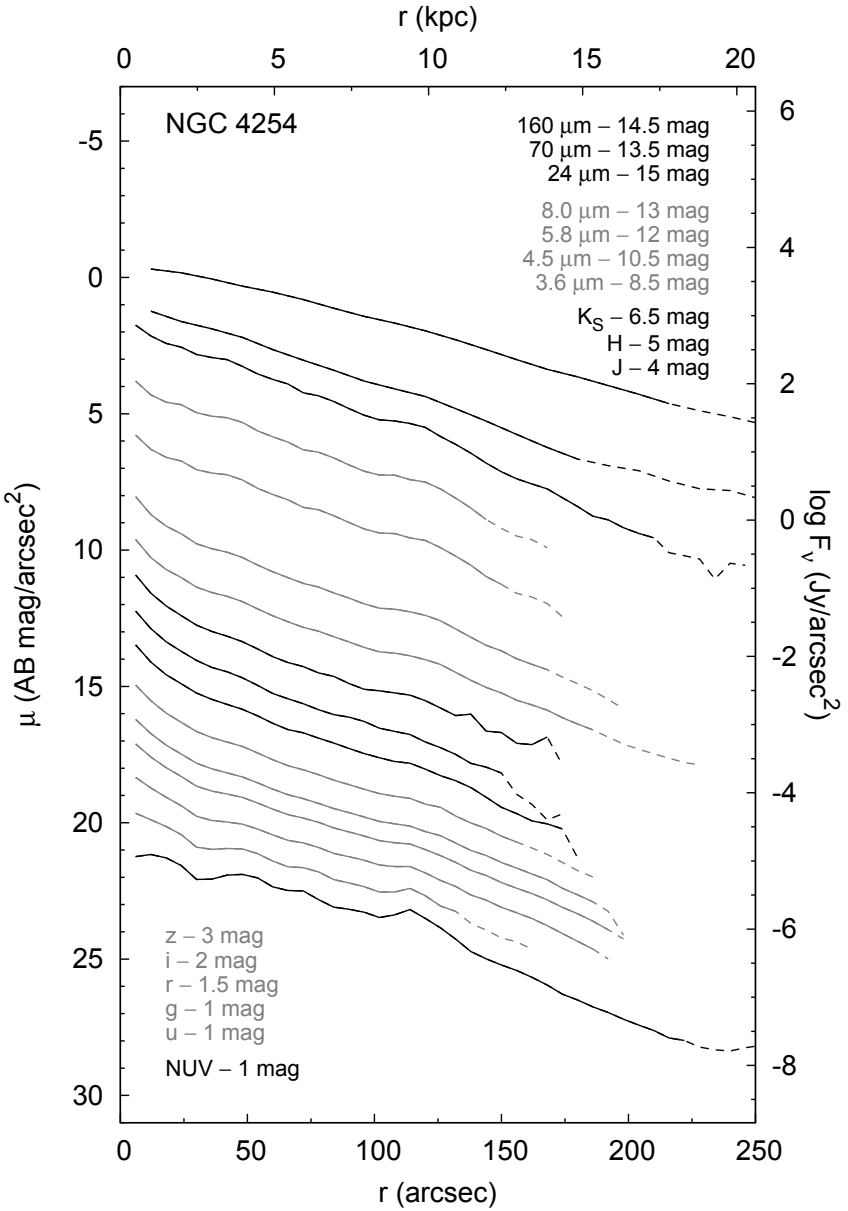
NGC 4254
r (kpc)
r (arcsec)
μ (AB mag/arcsec²)
log F_ν (Jy/arcsec²)
160 μm – 14.5 mag
70 μm – 13.5 mag
24 μm – 15 mag
8.0 μm – 13 mag
5.8 μm – 12 mag
4.5 μm – 10.5 mag
3.6 μm – 8.5 mag
K_S – 6.5 mag
H – 5 mag
J – 4 mag
z – 3 mag
i – 2 mag
r – 1.5 mag
g – 1 mag
u – 1 mag
NUV – 1 mag

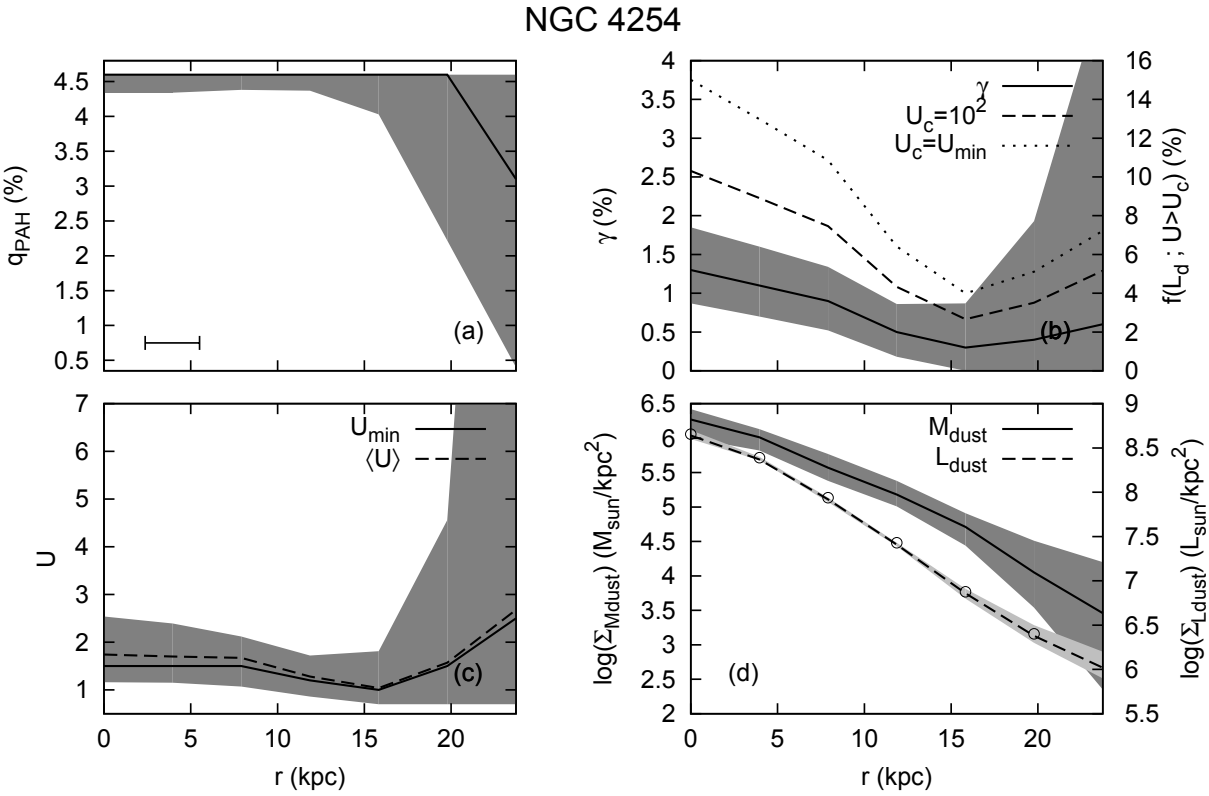
NGC 4254
q_{PAH} (%)
(a)
γ
$U_c=10^2$
$U_c=U_{min}$
γ (%)
$f(L_d ; U>U_c)$ (%)
(b)
U_{min}
⟨U⟩
U
(c)
r (kpc)
M_{dust}
L_{dust}
$\log(\Sigma_{Mdust})$ (M_{sun}/kpc^2)
$\log(\Sigma_{Ldust})$ (L_{sun}/kpc^2)
(d)
r (kpc)

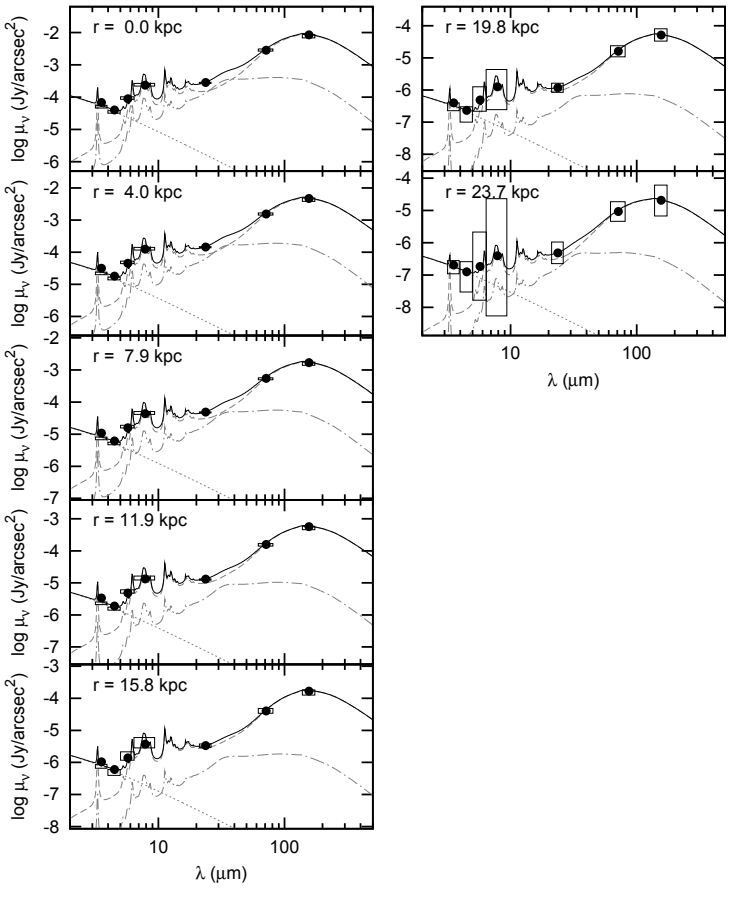
r = 0.0 kpc
r = 4.0 kpc
r = 7.9 kpc
r = 11.9 kpc
r = 15.8 kpc
r = 19.8 kpc
r = 23.7 kpc
log μ_ν (Jy/arcsec^2)
λ (μm)

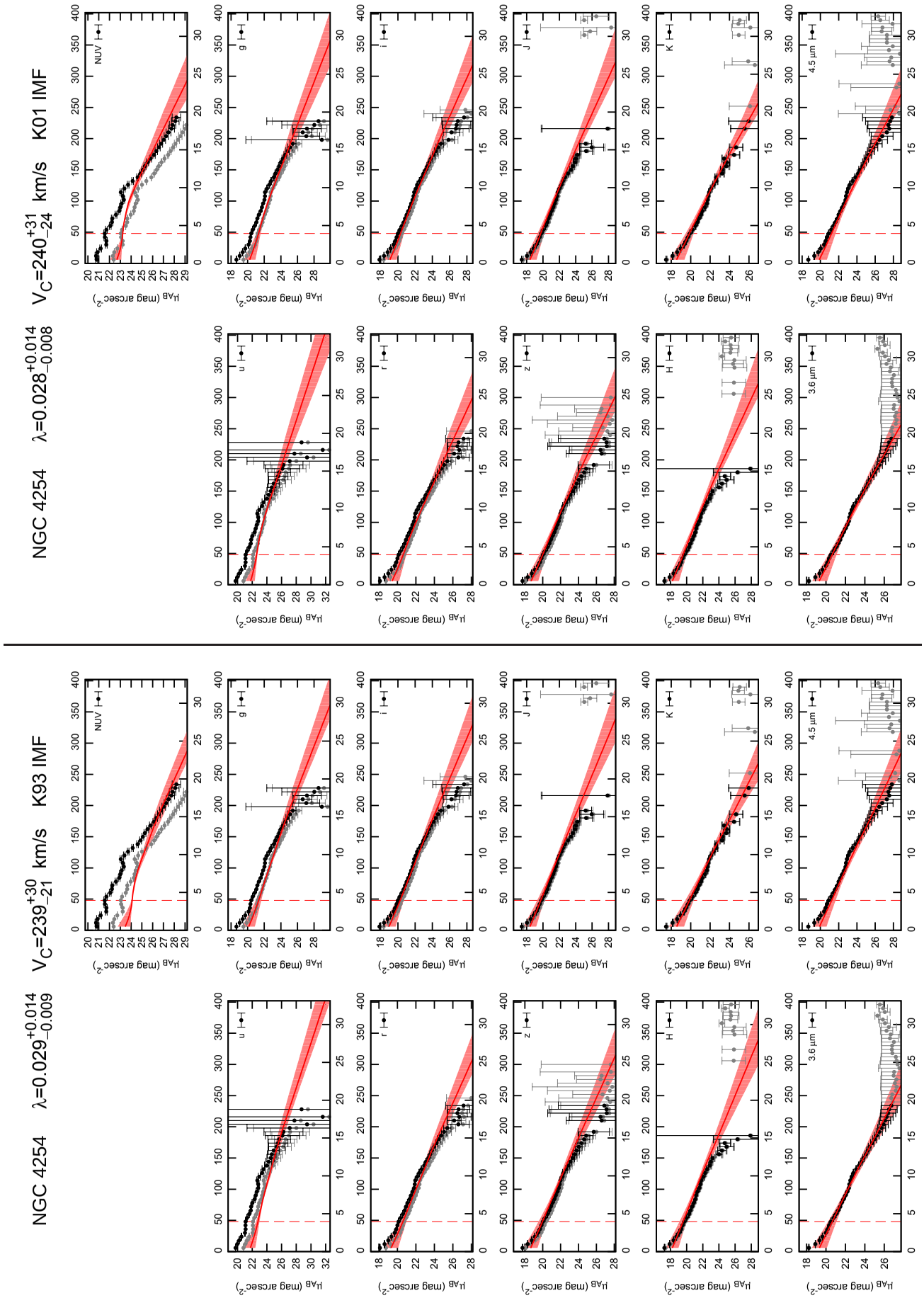
NGC 4254 λ=0.028+0.014−0.008 VC=240+31−24 km/s K01 IMF
NGC 4254 λ=0.029+0.014−0.009 VC=239+30−21 km/s K93 IMF
NUV
u
g
r
i
z
J
H
K
3.6 μm
4.5 μm
μAB (mag arcsec-2)

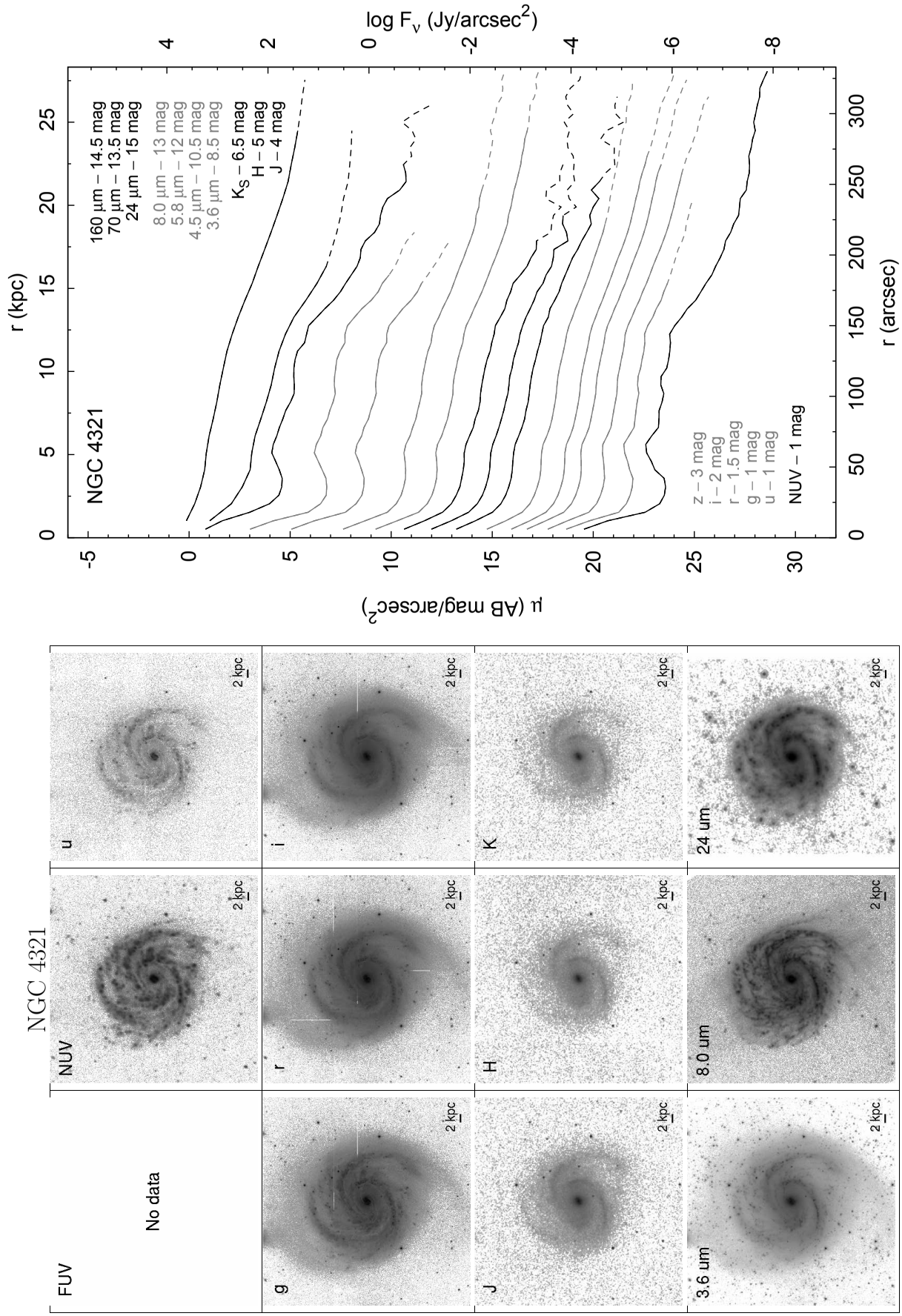
NGC 4321
FUV
No data
NUV
u
g
r
i
J
H
K
3.6 um
8.0 um
24 um
2 kpc
μ (AB mag/arcsec²)
r (kpc)
r (arcsec)
log F_ν (Jy/arcsec²)
NGC 4321
160 μm – 14.5 mag
70 μm – 13.5 mag
24 μm – 15 mag
8.0 μm – 13 mag
5.8 μm – 12 mag
4.5 μm – 10.5 mag
3.6 μm – 8.5 mag
K_S – 6.5 mag
H – 5 mag
J – 4 mag
z – 3 mag
i – 2 mag
r – 1.5 mag
g – 1 mag
u – 1 mag
NUV – 1 mag

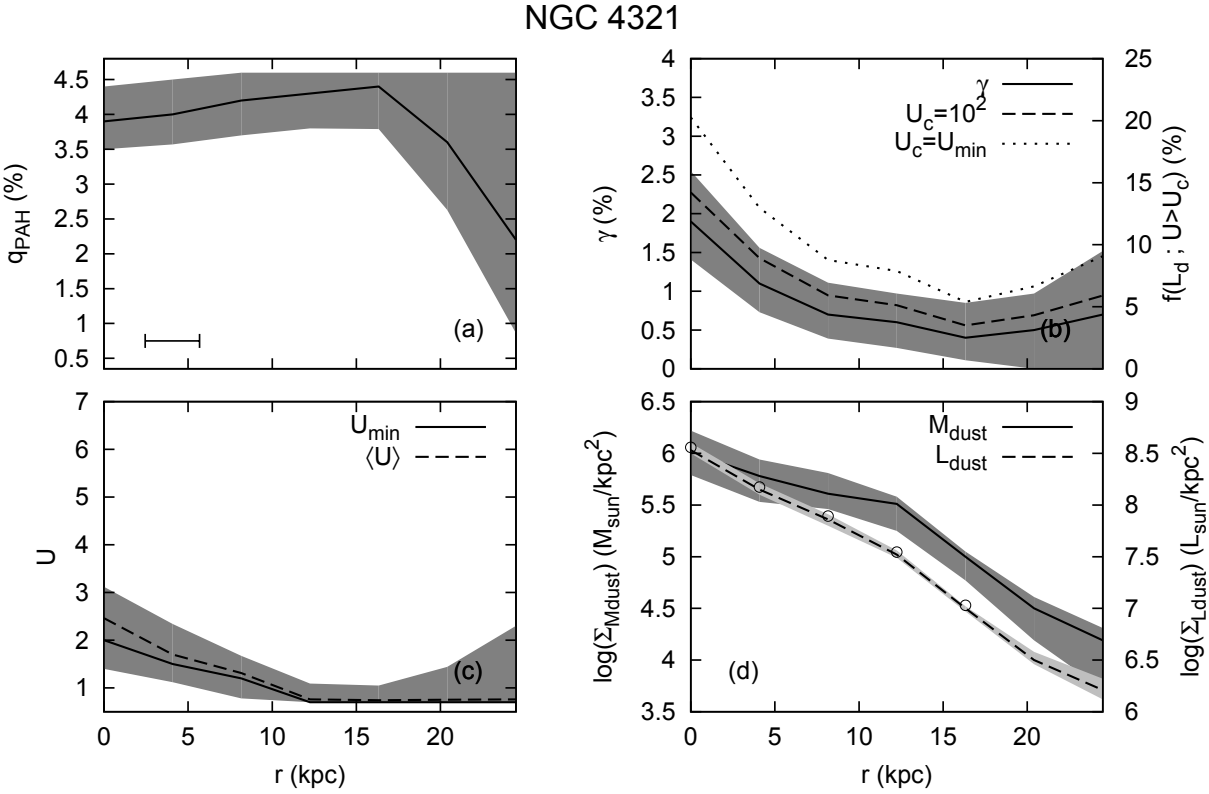
NGC 4321
q_{PAH} (%)
(a)
γ
$U_c=10^2$
$U_c=U_{min}$
γ (%)
$f(L_d ; U>U_c)$ (%)
(b)
U_{min}
⟨U⟩
U
(c)
r (kpc)
M_{dust}
L_{dust}
$\log(\Sigma_{Mdust})$ (M_{sun}/kpc^2)
$\log(\Sigma_{Ldust})$ (L_{sun}/kpc^2)
(d)
r (kpc)

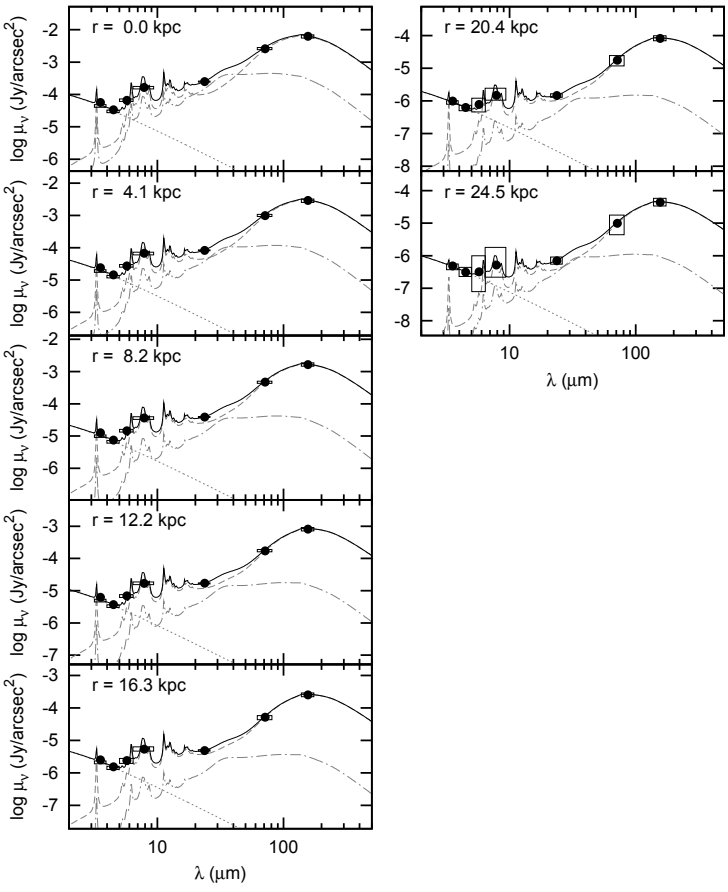
r = 0.0 kpc
r = 4.1 kpc
r = 8.2 kpc
r = 12.2 kpc
r = 16.3 kpc
r = 20.4 kpc
r = 24.5 kpc
log μ_ν (Jy/arcsec^2)
λ (μm)

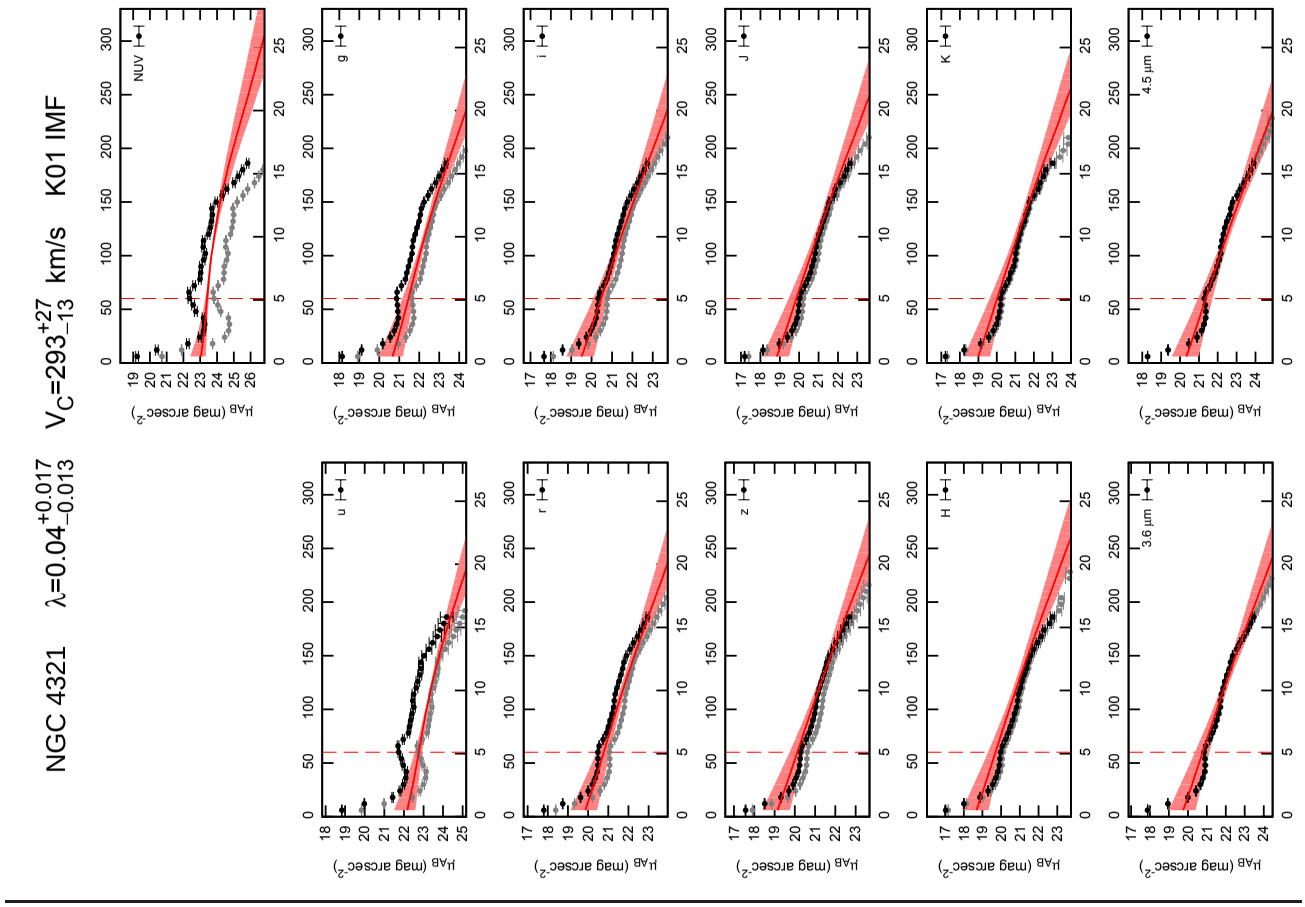
NGC 4321 λ=0.04+0.017−0.013 VC=293+27−13 km/s K01 IMF
NUV
g
i
J
K
4.5 μm
u
r
z
H
3.6 μm
μAB (mag arcsec-2)

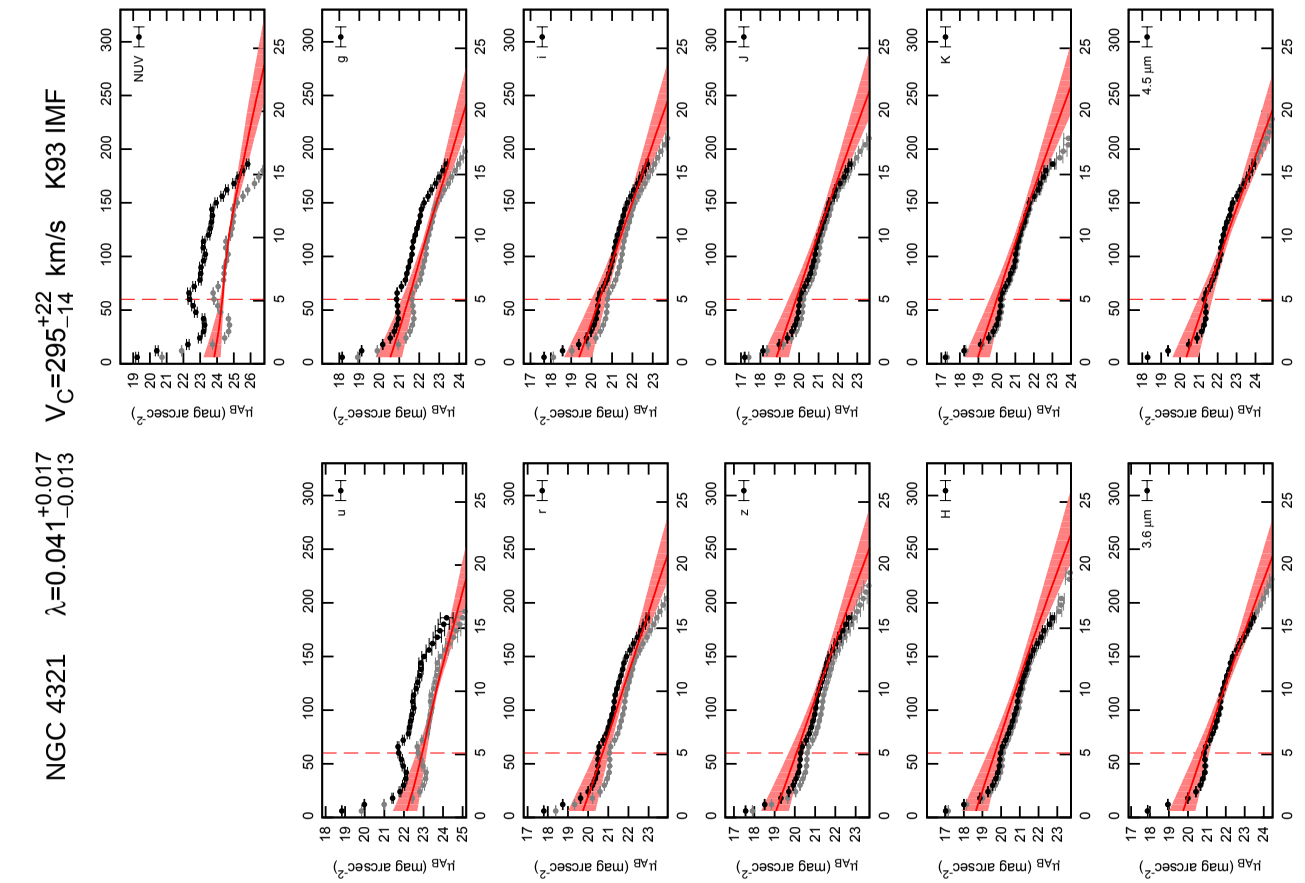
NGC 4321 λ=0.041+0.017−0.013 VC=295+22−14 km/s K93 IMF
NUV
g
i
J
K
4.5 μm
u
r
z
H
3.6 μm
μAB (mag arcsec-2)

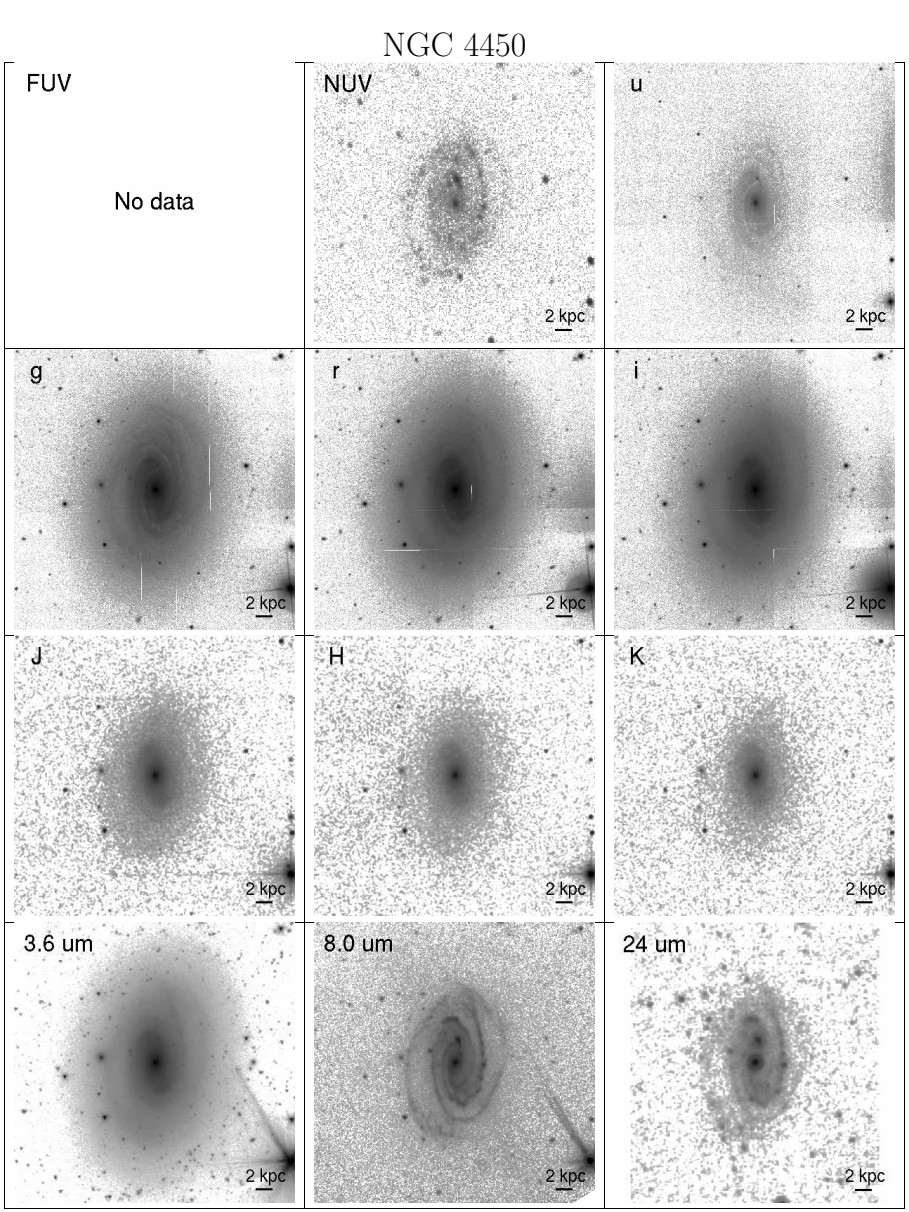
NGC 4450
FUV
No data
NUV
u
g
r
i
J
H
K
3.6 um
8.0 um
24 um
2 kpc

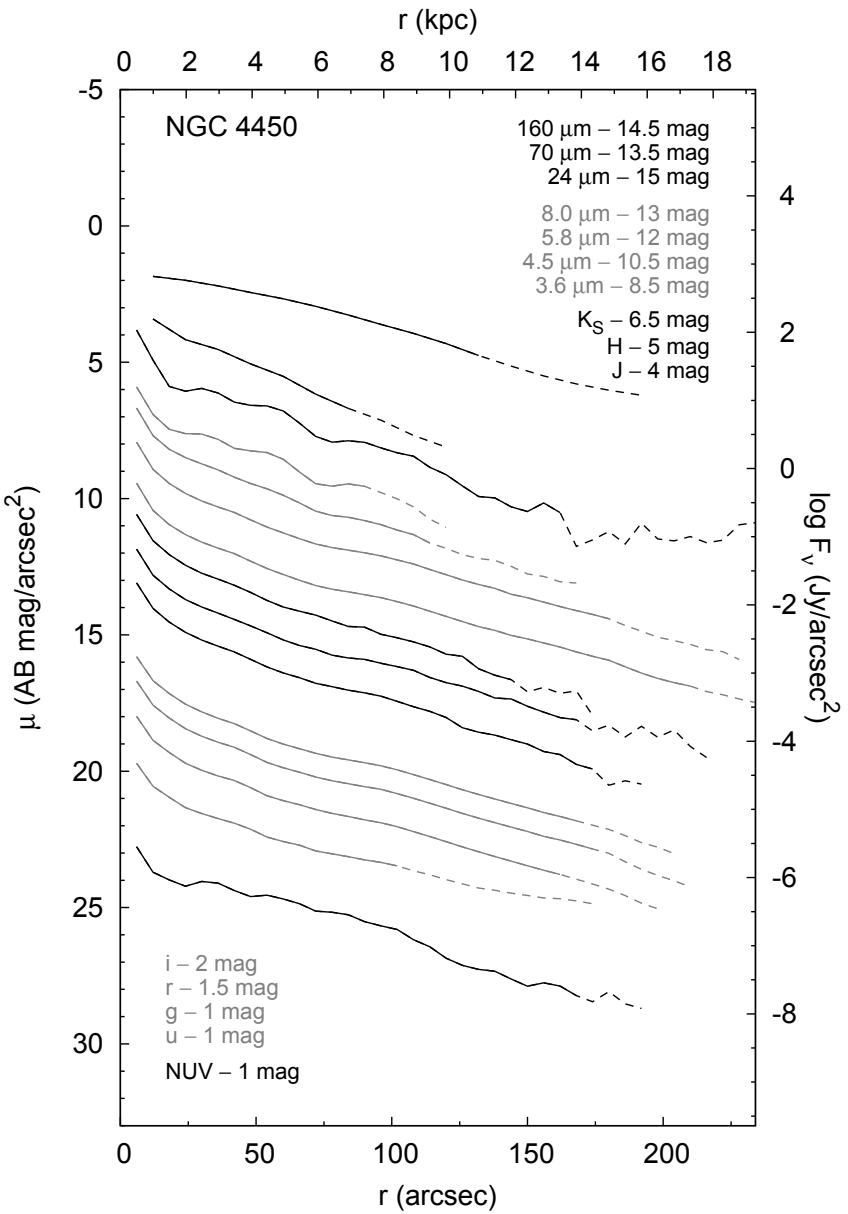
NGC 4450
r (kpc)
r (arcsec)
μ (AB mag/arcsec²)
log F_ν (Jy/arcsec²)
160 μm – 14.5 mag
70 μm – 13.5 mag
24 μm – 15 mag
8.0 μm – 13 mag
5.8 μm – 12 mag
4.5 μm – 10.5 mag
3.6 μm – 8.5 mag
K_S – 6.5 mag
H – 5 mag
J – 4 mag
i – 2 mag
r – 1.5 mag
g – 1 mag
u – 1 mag
NUV – 1 mag

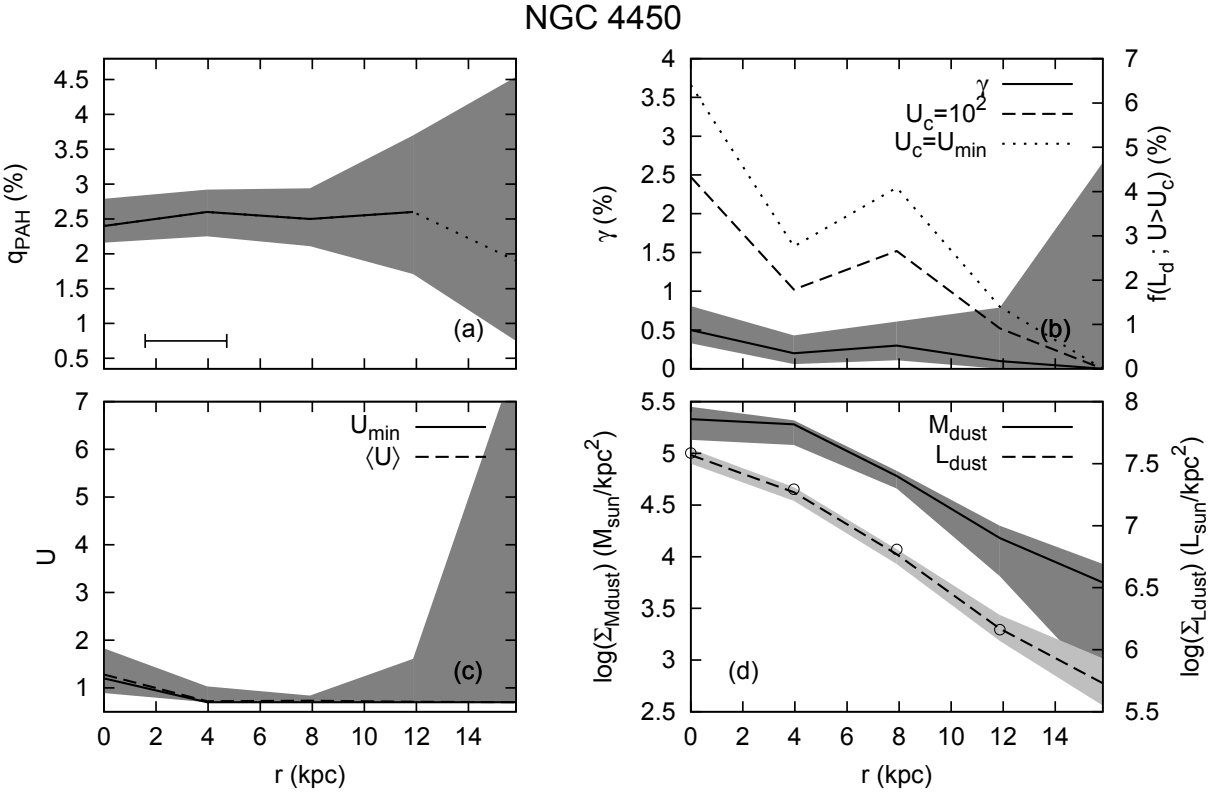
NGC 4450
q_{PAH} (%)
(a)
γ
$U_c=10^2$
$U_c=U_{min}$
γ (%)
$f(L_d ; U>U_c)$ (%)
(b)
U_{min}
⟨U⟩
U
(c)
M_{dust}
L_{dust}
$\log(\Sigma_{Mdust})$ (M_{sun}/kpc^2)
$\log(\Sigma_{Ldust})$ (L_{sun}/kpc^2)
(d)
r (kpc)
r (kpc)

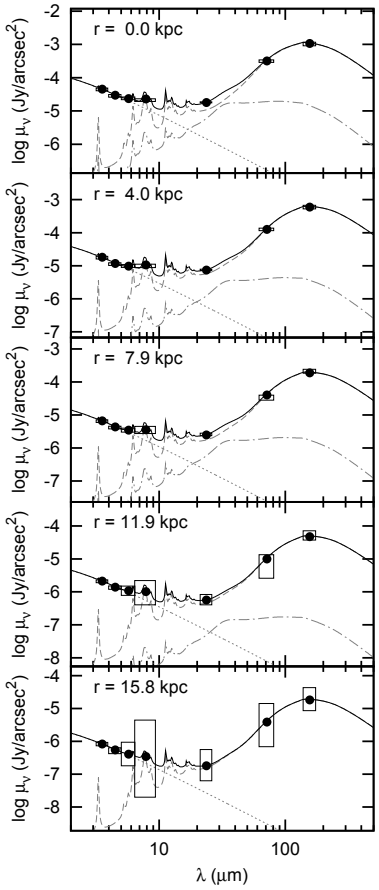
r = 0.0 kpc
r = 4.0 kpc
r = 7.9 kpc
r = 11.9 kpc
r = 15.8 kpc
log μ_ν (Jy/arcsec^2)
λ (μm)

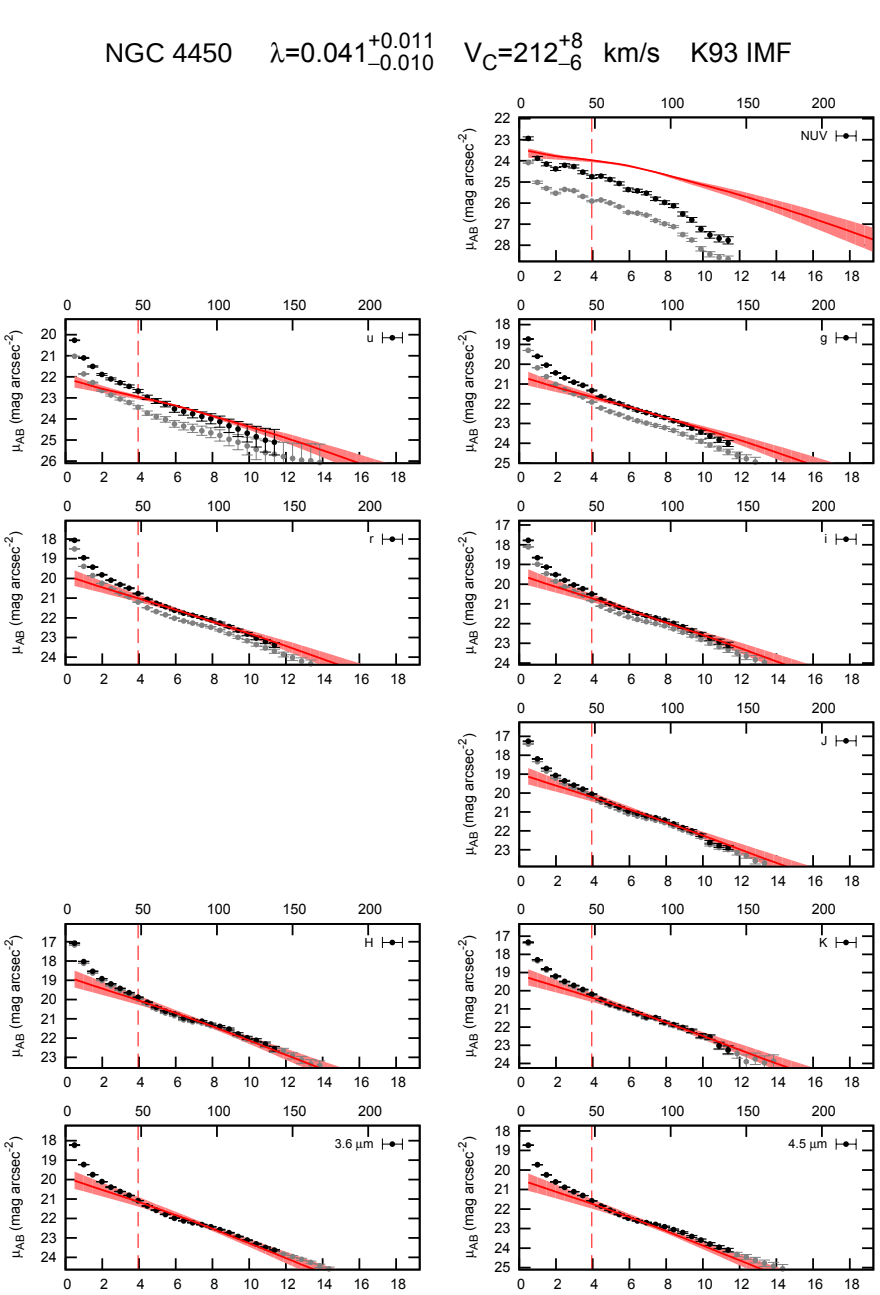
NGC 4450 λ=0.041+0.011−0.010 VC=212+8−6 km/s K93 IMF
NUV
u
g
r
i
J
H
K
3.6 μm
4.5 μm
μAB (mag arcsec−2)

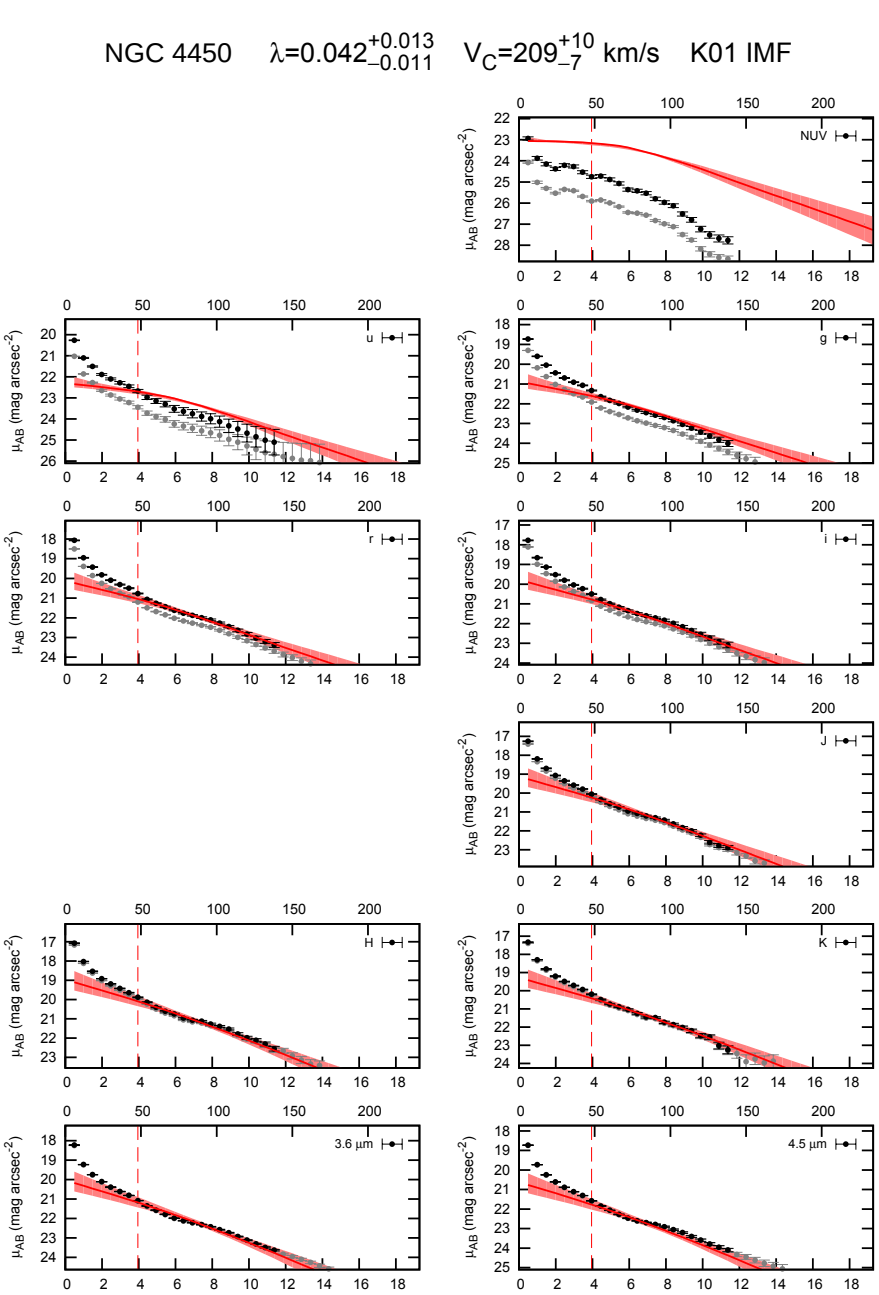
NGC 4450 λ=0.042+0.013−0.011 VC=209+10−7 km/s K01 IMF
NUV
u
g
r
i
J
H
K
3.6 μm
4.5 μm
μAB (mag arcsec−2)

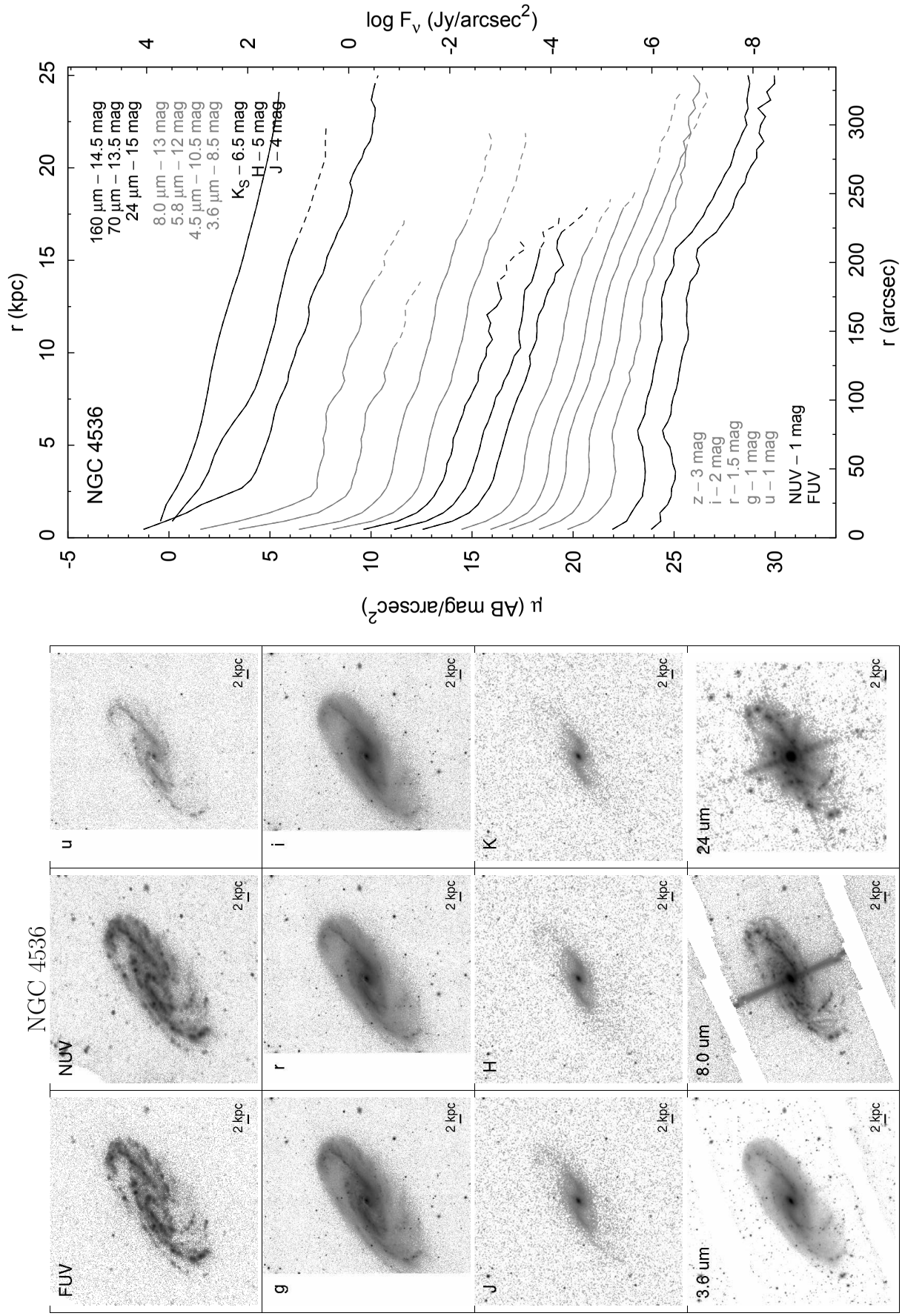
NGC 4536
160 µm – 14.5 mag
70 µm – 13.5 mag
24 µm – 15 mag
8.0 µm – 13 mag
5.8 µm – 12 mag
4.5 µm – 10.5 mag
3.6 µm – 8.5 mag
K_S – 6.5 mag
H – 5 mag
J – 4 mag
z – 3 mag
i – 2 mag
r – 1.5 mag
g – 1 mag
u – 1 mag
NUV – 1 mag
FUV
r (kpc)
r (arcsec)
log F_ν (Jy/arcsec^2)
µ (AB mag/arcsec^2)
FUV
NUV
u
g
r
i
J
H
K
3.6 um
8.0 um
24 um
2 kpc

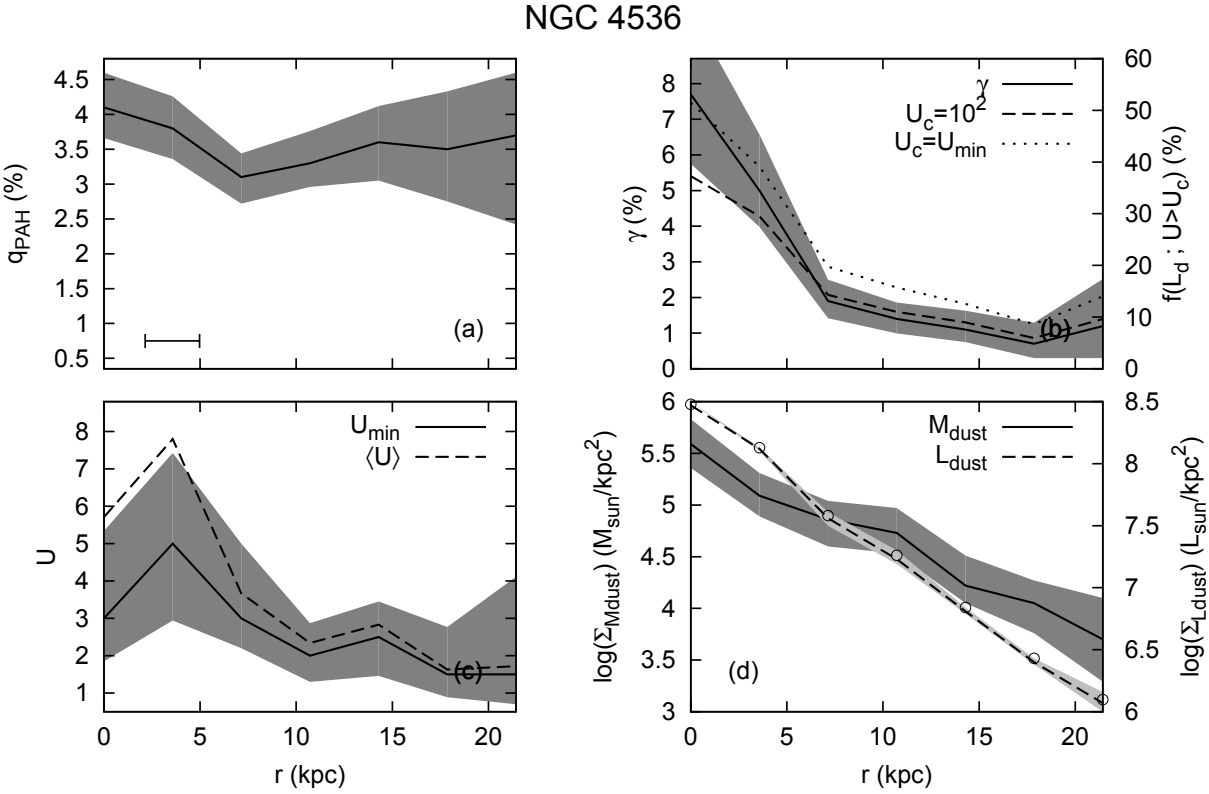
NGC 4536
q_{PAH} (%)
(a)
γ
$U_c=10^2$
$U_c=U_{min}$
γ (%)
$f(L_d ; U>U_c)$ (%)
(b)
U_{min}
⟨U⟩
U
(c)
r (kpc)
M_{dust}
L_{dust}
$\log(\Sigma_{Mdust})$ (M_{sun}/kpc^2)
$\log(\Sigma_{Ldust})$ (L_{sun}/kpc^2)
(d)
r (kpc)

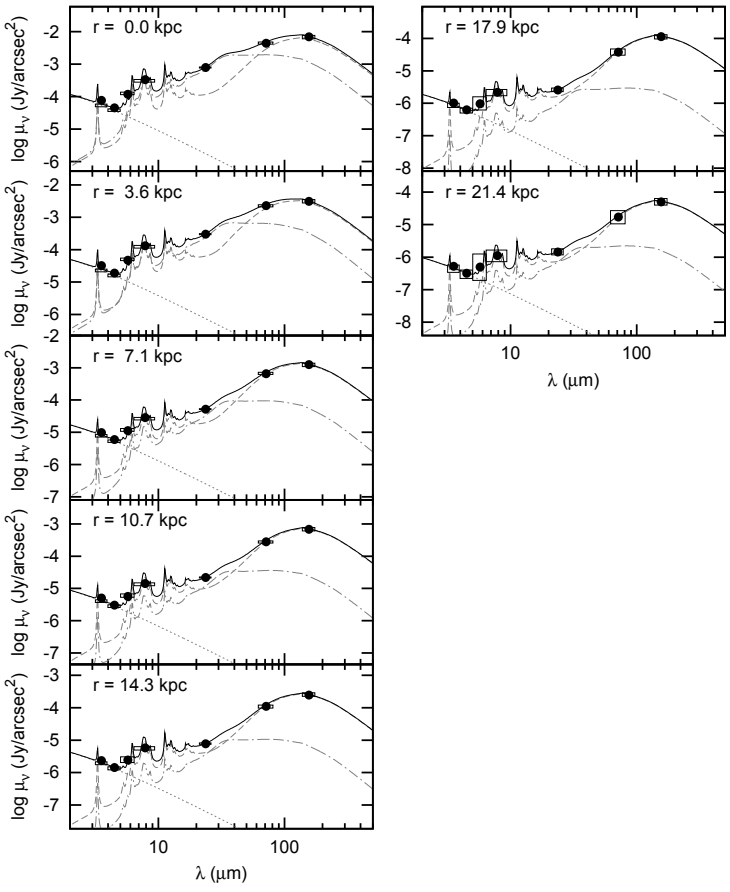
r = 0.0 kpc
r = 3.6 kpc
r = 7.1 kpc
r = 10.7 kpc
r = 14.3 kpc
r = 17.9 kpc
r = 21.4 kpc
log μ_ν (Jy/arcsec^2)
λ (μm)

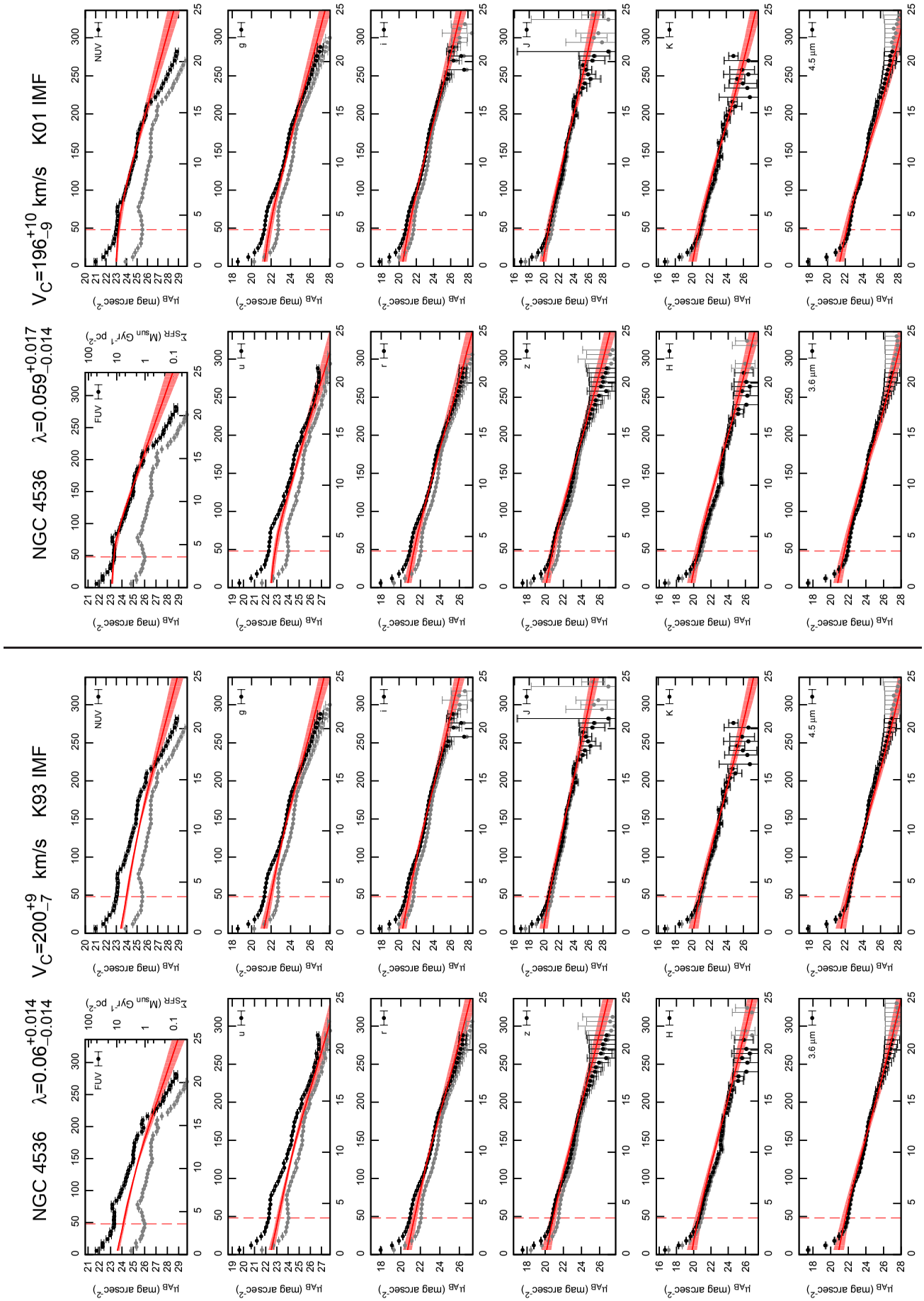
NGC 4536 λ=0.06+0.014−0.014 VC=200+9−7 km/s K93 IMF
NGC 4536 λ=0.059+0.017−0.014 VC=196+10−9 km/s K01 IMF
μAB (mag arcsec-2)
ΣSFR (Msun Gyr-1 pc-2)
FUV
NUV
u
g
r
i
z
J
H
K
3.6 μm
4.5 μm

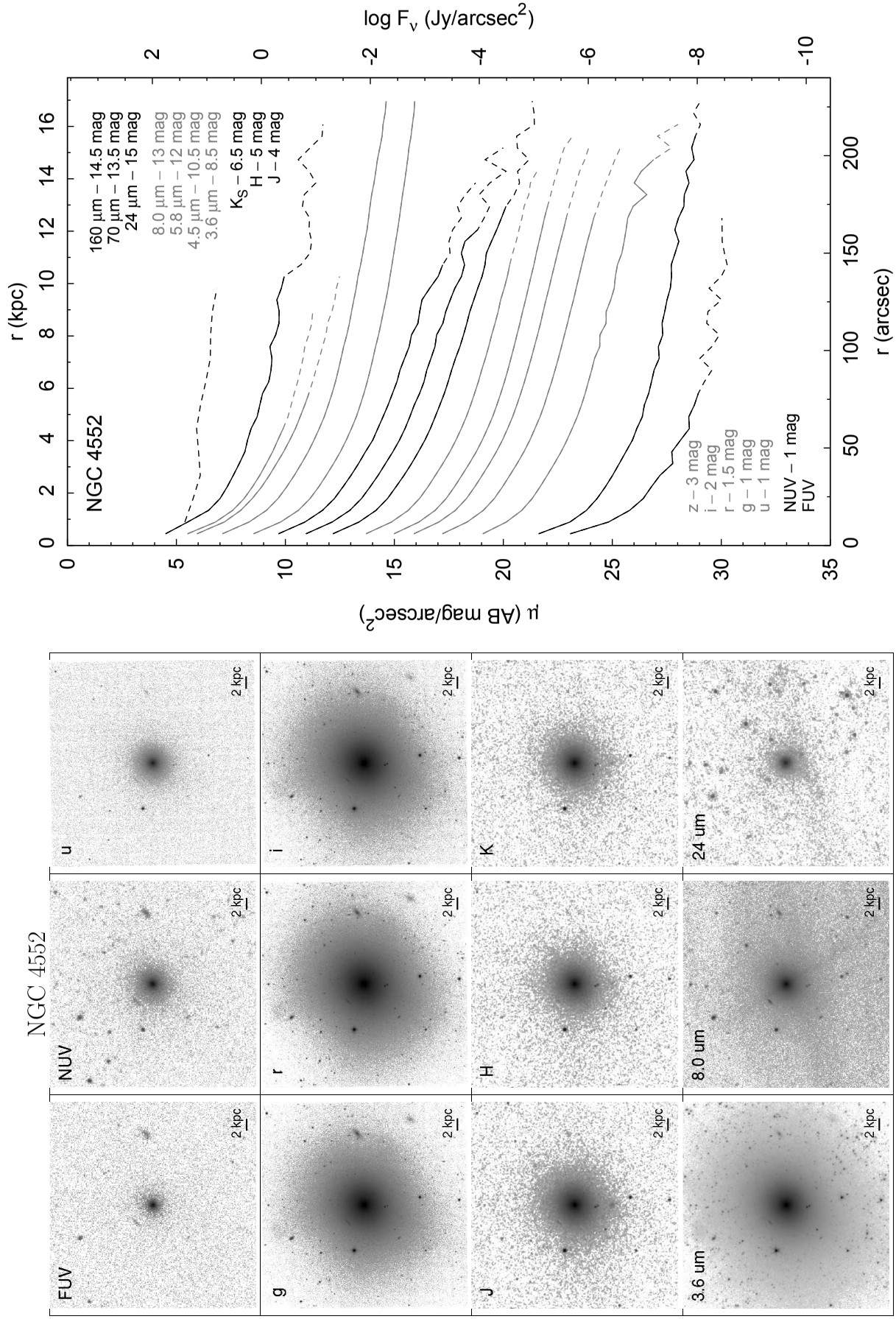
NGC 4552
FUV
NUV
u
g
r
i
J
H
K
3.6 um
8.0 um
24 um
2 kpc
μ (AB mag/arcsec²)
log F_ν (Jy/arcsec²)
r (kpc)
r (arcsec)
NGC 4552
160 μm – 14.5 mag
70 μm – 13.5 mag
24 μm – 15 mag
8.0 μm – 13 mag
5.8 μm – 12 mag
4.5 μm – 10.5 mag
3.6 μm – 8.5 mag
K_S – 6.5 mag
H – 5 mag
J – 4 mag
z – 3 mag
i – 2 mag
r – 1.5 mag
g – 1 mag
u – 1 mag
NUV – 1 mag
FUV

NGC 4559
FUV
NUV
u
g
r
i
J
H
K
3.6 um
8.0 um
24 um
2 kpc

r (kpc)
NGC 4559
160 μm – 14.5 mag
70 μm – 13.5 mag
24 μm – 15 mag
8.0 μm – 13 mag
5.8 μm – 12 mag
4.5 μm – 10.5 mag
3.6 μm – 8.5 mag
K_S – 6.5 mag
H – 5 mag
J – 4 mag
z – 3 mag
i – 2 mag
r – 1.5 mag
g – 1 mag
u – 1 mag
NUV – 1 mag
FUV
μ (AB mag/arcsec²)
log F_ν (Jy/arcsec²)
r (arcsec)

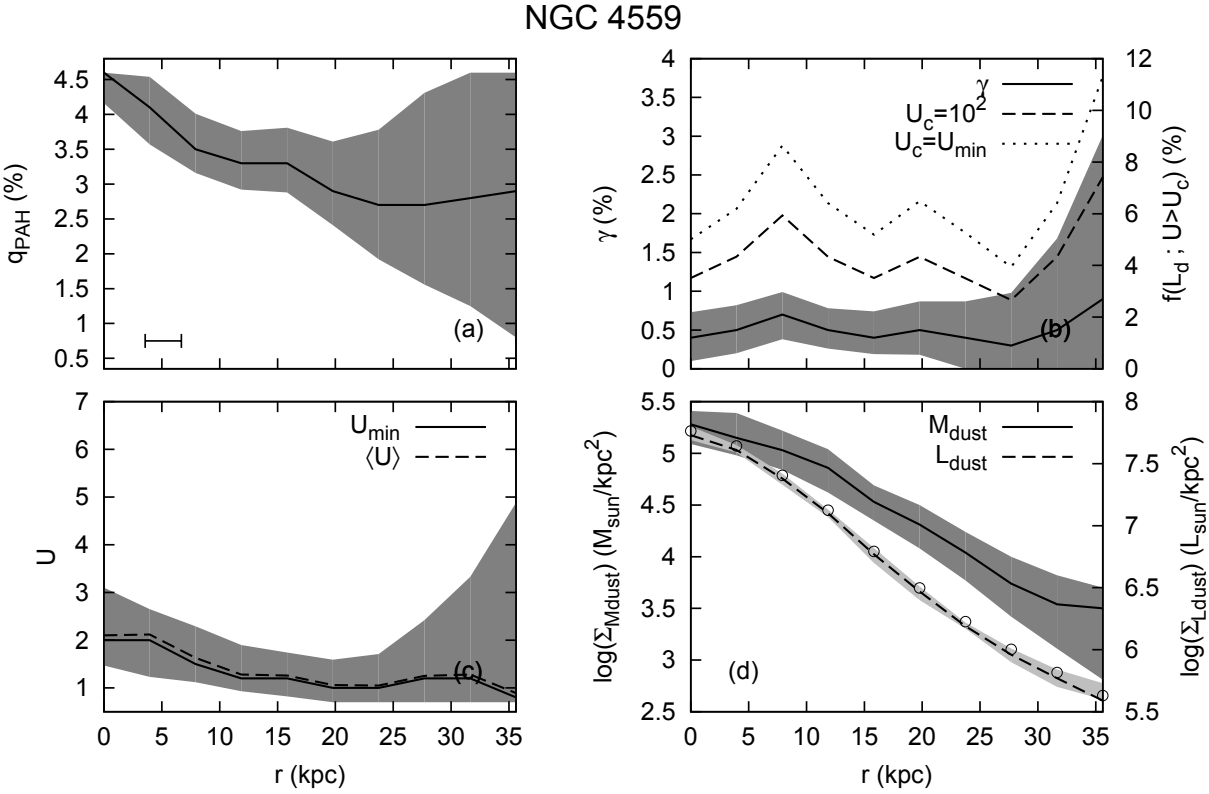
NGC 4559
q_{PAH} (%)
(a)
γ (%)
γ
$U_c=10^2$
$U_c=U_{min}$
$f(L_d ; U>U_c)$ (%)
(b)
U
U_{min}
⟨U⟩
(c)
r (kpc)
$\log(\Sigma_{Mdust})$ (M_{sun}/kpc^2)
M_{dust}
L_{dust}
(d)
$\log(\Sigma_{Ldust})$ (L_{sun}/kpc^2)
r (kpc)

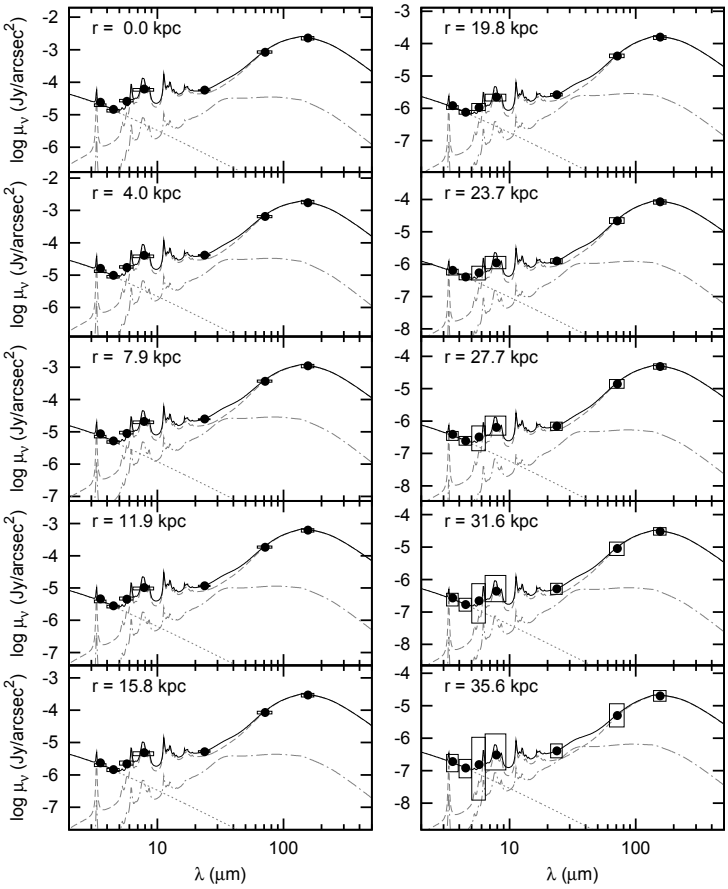
r = 0.0 kpc
r = 4.0 kpc
r = 7.9 kpc
r = 11.9 kpc
r = 15.8 kpc
r = 19.8 kpc
r = 23.7 kpc
r = 27.7 kpc
r = 31.6 kpc
r = 35.6 kpc
log μν (Jy/arcsec^2)
λ (μm)

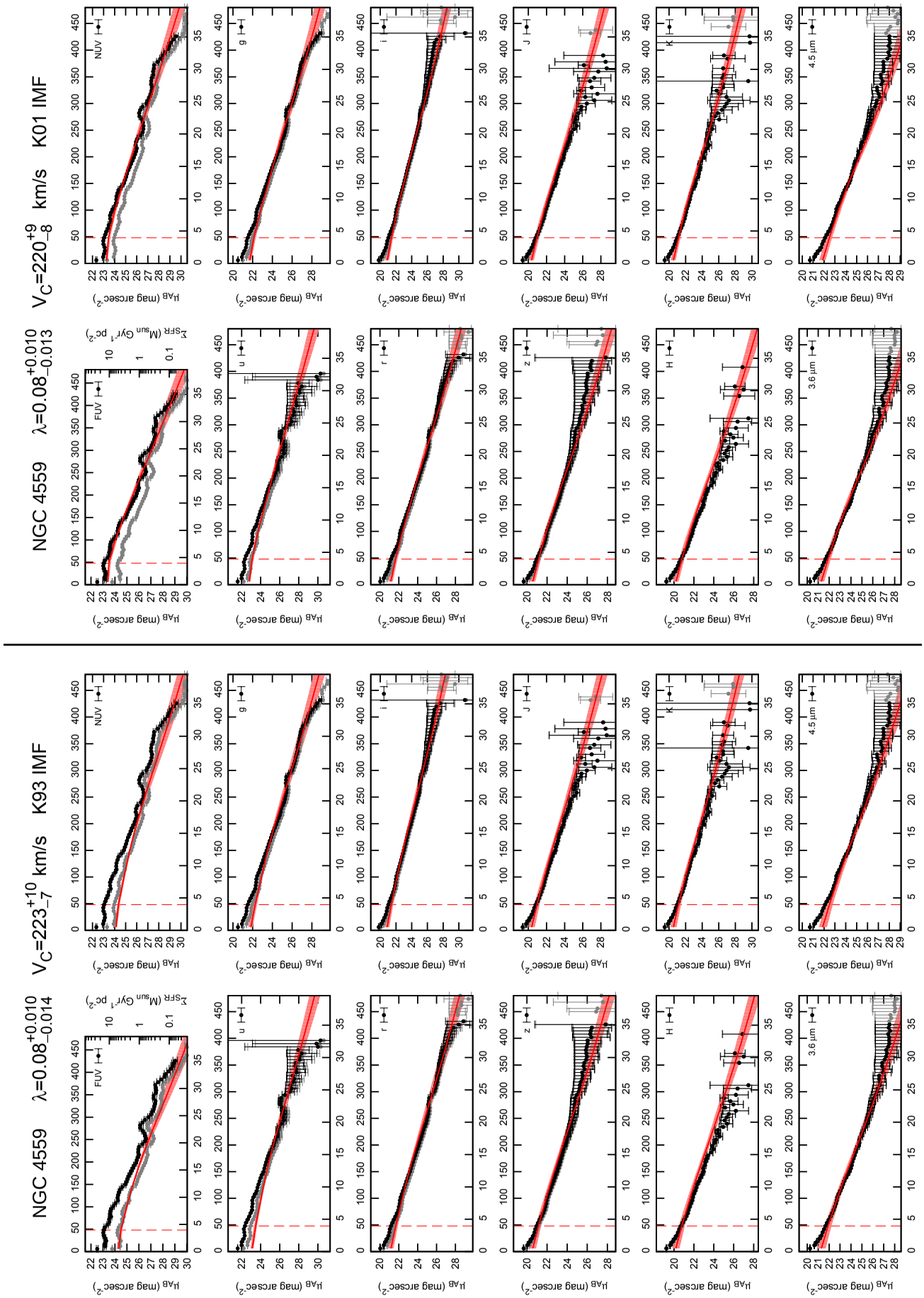
NGC 4559 λ=0.08+0.010−0.013 VC=220+9−8 km/s K01 IMF
NGC 4559 λ=0.08+0.010−0.014 VC=223+10−7 km/s K93 IMF
FUV
NUV
u
g
r
i
z
J
H
K
3.6 μm
4.5 μm
μAB (mag arcsec-2)
ΣSFR (Msun Gyr-1 pc-2)

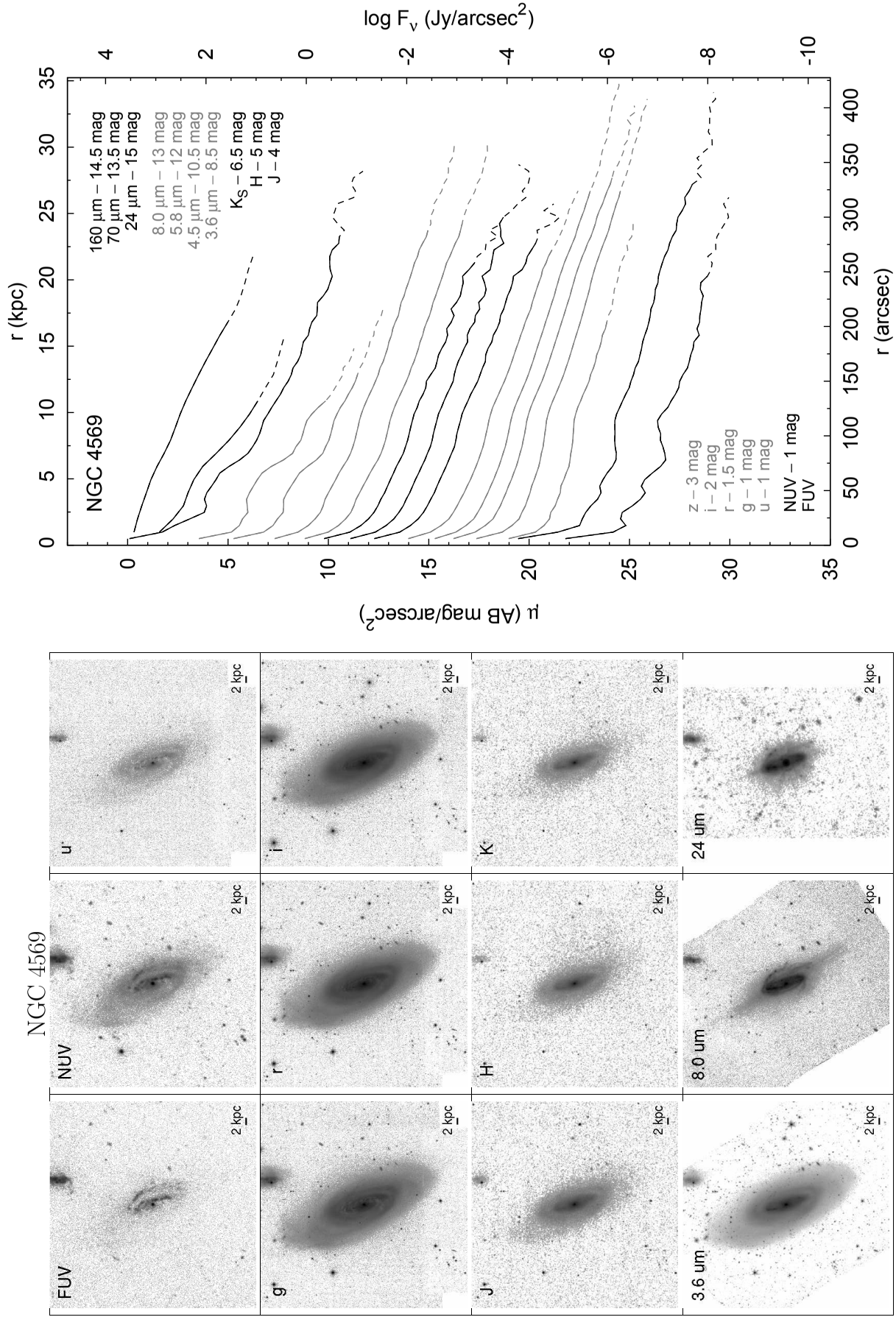
NGC 4569
FUV
NUV
u'
g'
r'
i'
J
H
K'
3.6 um
8.0 um
24 um
2 kpc
μ (AB mag/arcsec²)
log F_ν (Jy/arcsec²)
r (kpc)
r (arcsec)
NGC 4569
160 μm – 14.5 mag
70 μm – 13.5 mag
24 μm – 15 mag
8.0 μm – 13 mag
5.8 μm – 12 mag
4.5 μm – 10.5 mag
3.6 μm – 8.5 mag
K_S – 6.5 mag
H – 5 mag
J – 4 mag
z – 3 mag
i – 2 mag
r – 1.5 mag
g – 1 mag
u – 1 mag
NUV – 1 mag
FUV

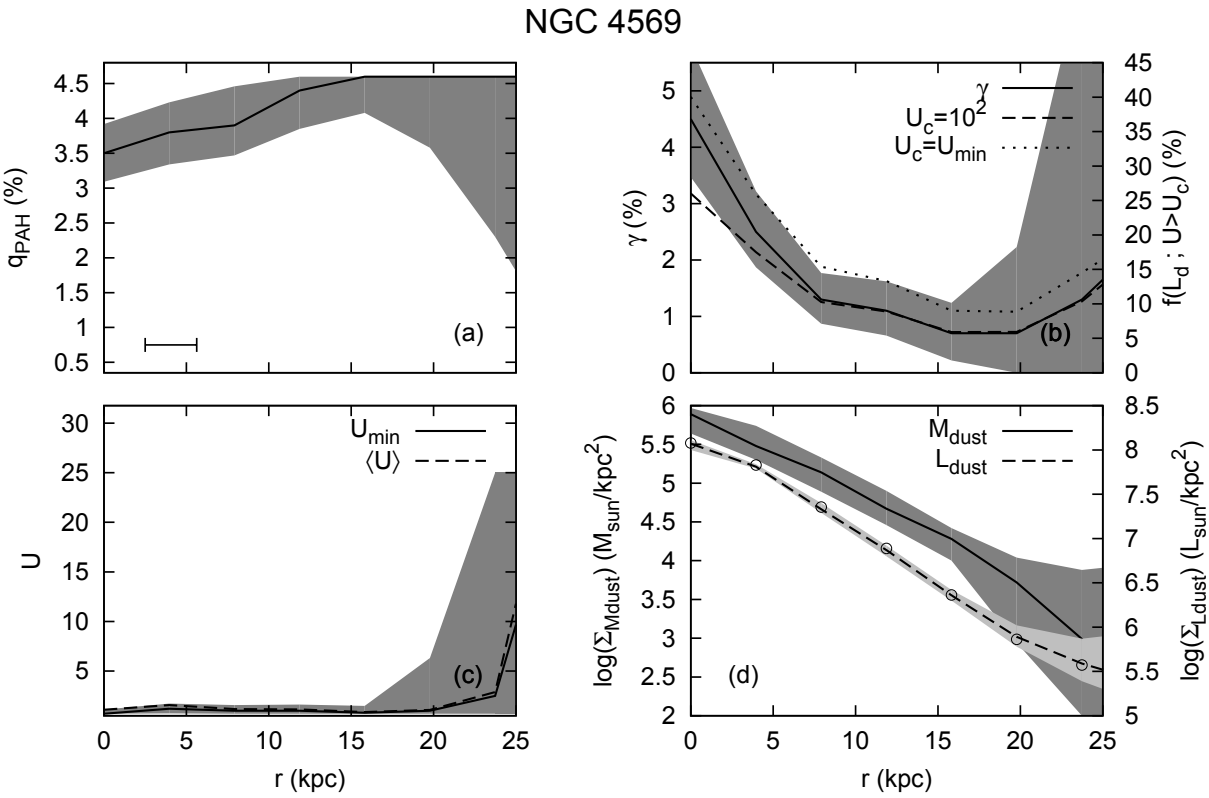
NGC 4569
q_{PAH} (%)
(a)
γ
$U_c=10^2$
$U_c=U_{min}$
γ (%)
$f(L_d ; U>U_c)$ (%)
(b)
U_{min}
⟨U⟩
U
(c)
r (kpc)
M_{dust}
L_{dust}
$\log(\Sigma_{Mdust})$ (M_{sun}/kpc^2)
$\log(\Sigma_{Ldust})$ (L_{sun}/kpc^2)
(d)
r (kpc)

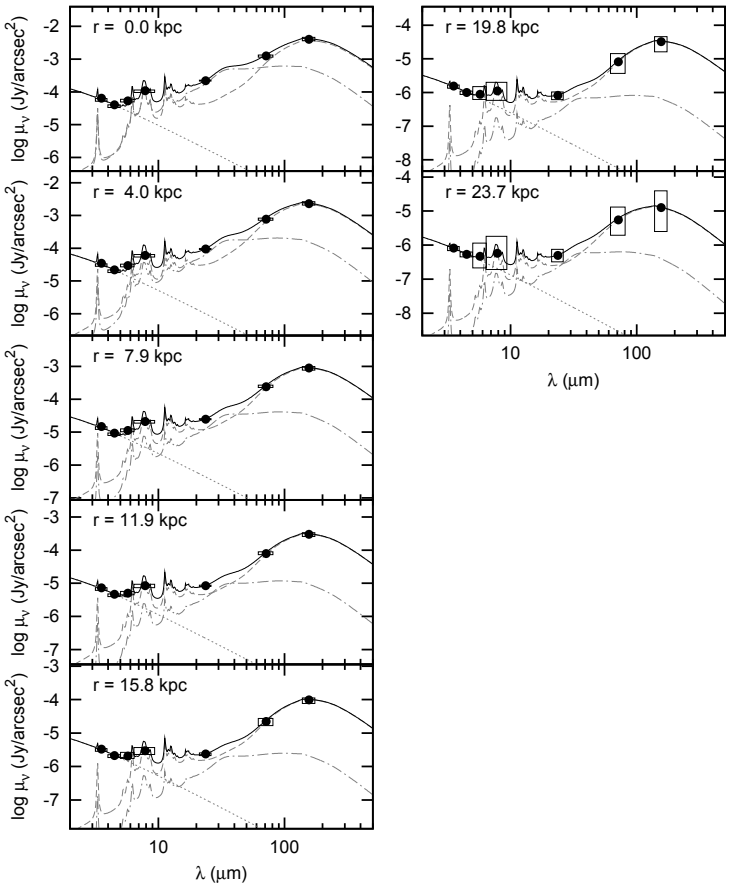
r = 0.0 kpc
r = 4.0 kpc
r = 7.9 kpc
r = 11.9 kpc
r = 15.8 kpc
r = 19.8 kpc
r = 23.7 kpc
log μ_ν (Jy/arcsec^2)
λ (μm)

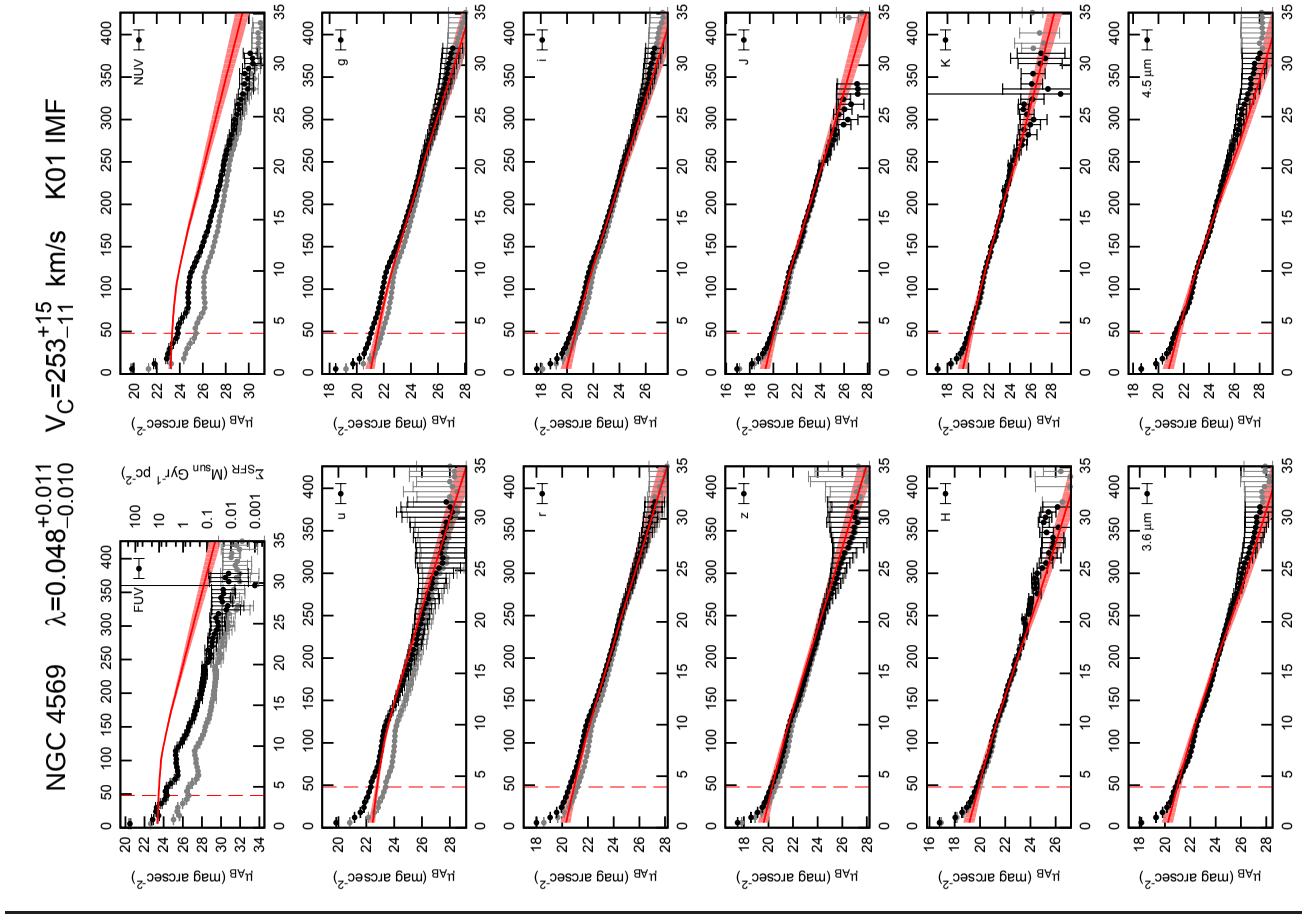
NGC 4569 λ=0.048+0.011−0.010 VC=253+15−11 km/s K01 IMF
NGC 4569 λ=0.046+0.011−0.009 VC=256+14−12 km/s K93 IMF
μAB (mag arcsec-2)
ΣSFR (Msun Gyr-1 pc-2)
FUV
NUV
u
g
r
i
z
J
H
K
3.6 μm
4.5 μm

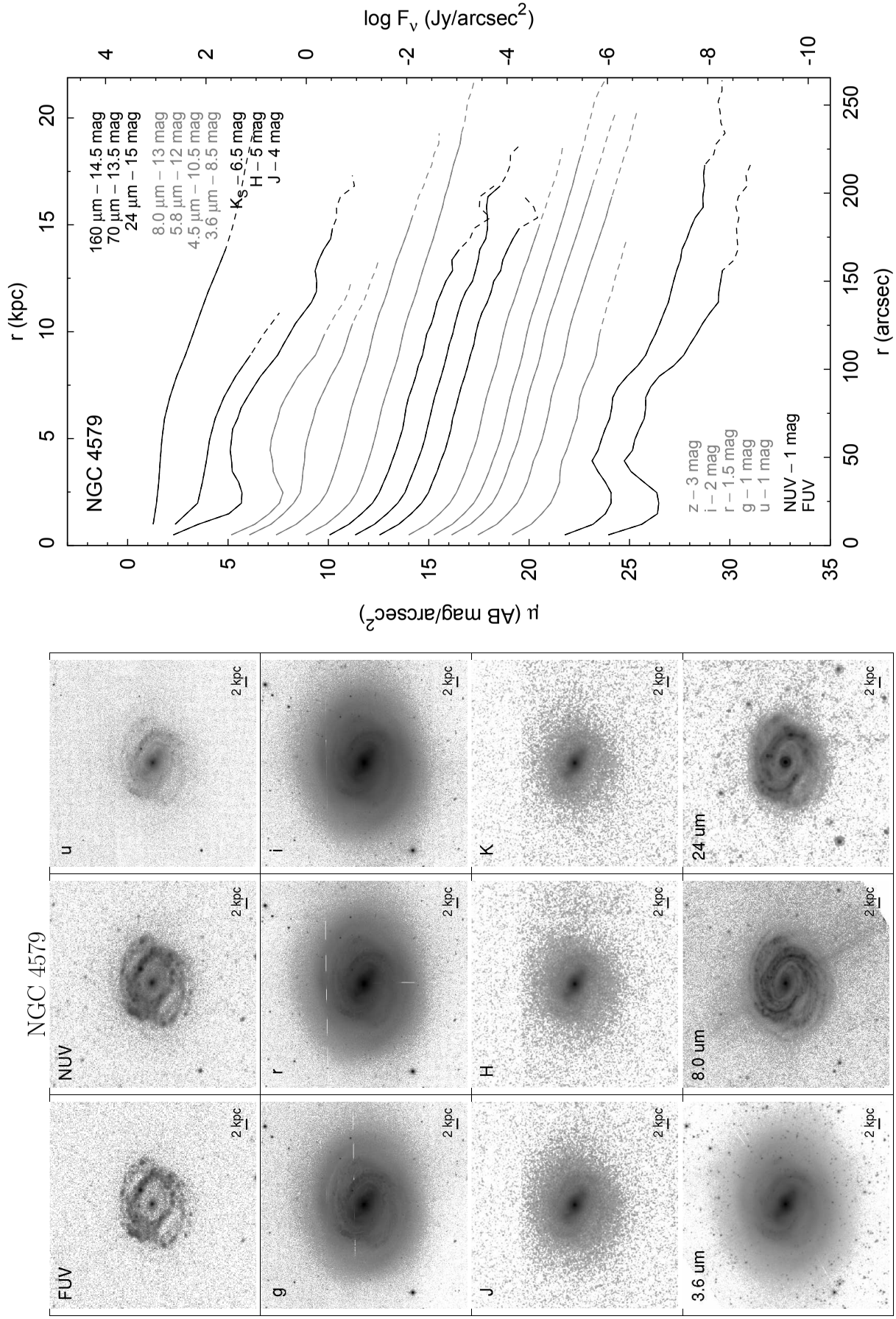
NGC 4579
FUV
NUV
u
g
r
i
J
H
K
3.6 um
8.0 um
24 um
2 kpc
μ (AB mag/arcsec²)
log F_ν (Jy/arcsec²)
r (kpc)
r (arcsec)
NGC 4579
160 μm – 14.5 mag
70 μm – 13.5 mag
24 μm – 15 mag
8.0 μm – 13 mag
5.8 μm – 12 mag
4.5 μm – 10.5 mag
3.6 μm – 8.5 mag
K_s – 6.5 mag
H – 5 mag
J – 4 mag
z – 3 mag
i – 2 mag
r – 1.5 mag
g – 1 mag
u – 1 mag
NUV – 1 mag
FUV

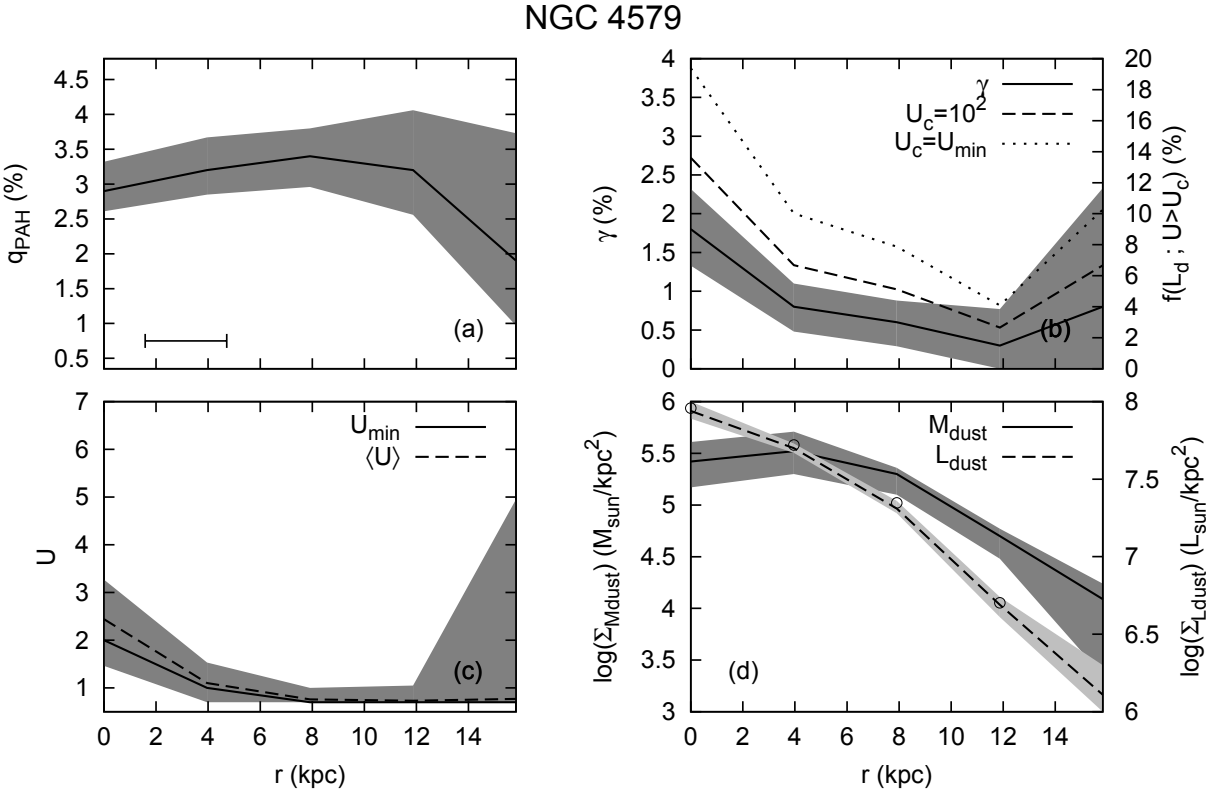
NGC 4579
q_{PAH} (%)
(a)
γ (%)
γ
$U_c=10^2$
$U_c=U_{min}$
$f(L_d ; U>U_c)$ (%)
(b)
U
U_{min}
⟨U⟩
(c)
r (kpc)
$\log(\Sigma_{Mdust})$ (M_{sun}/kpc^2)
M_{dust}
L_{dust}
(d)
$\log(\Sigma_{Ldust})$ (L_{sun}/kpc^2)
r (kpc)

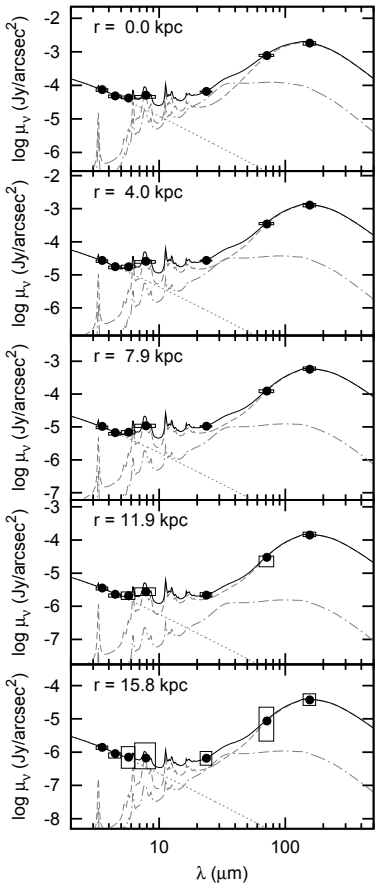
r = 0.0 kpc
r = 4.0 kpc
r = 7.9 kpc
r = 11.9 kpc
r = 15.8 kpc
log μ_ν (Jy/arcsec^2)
λ (μm)

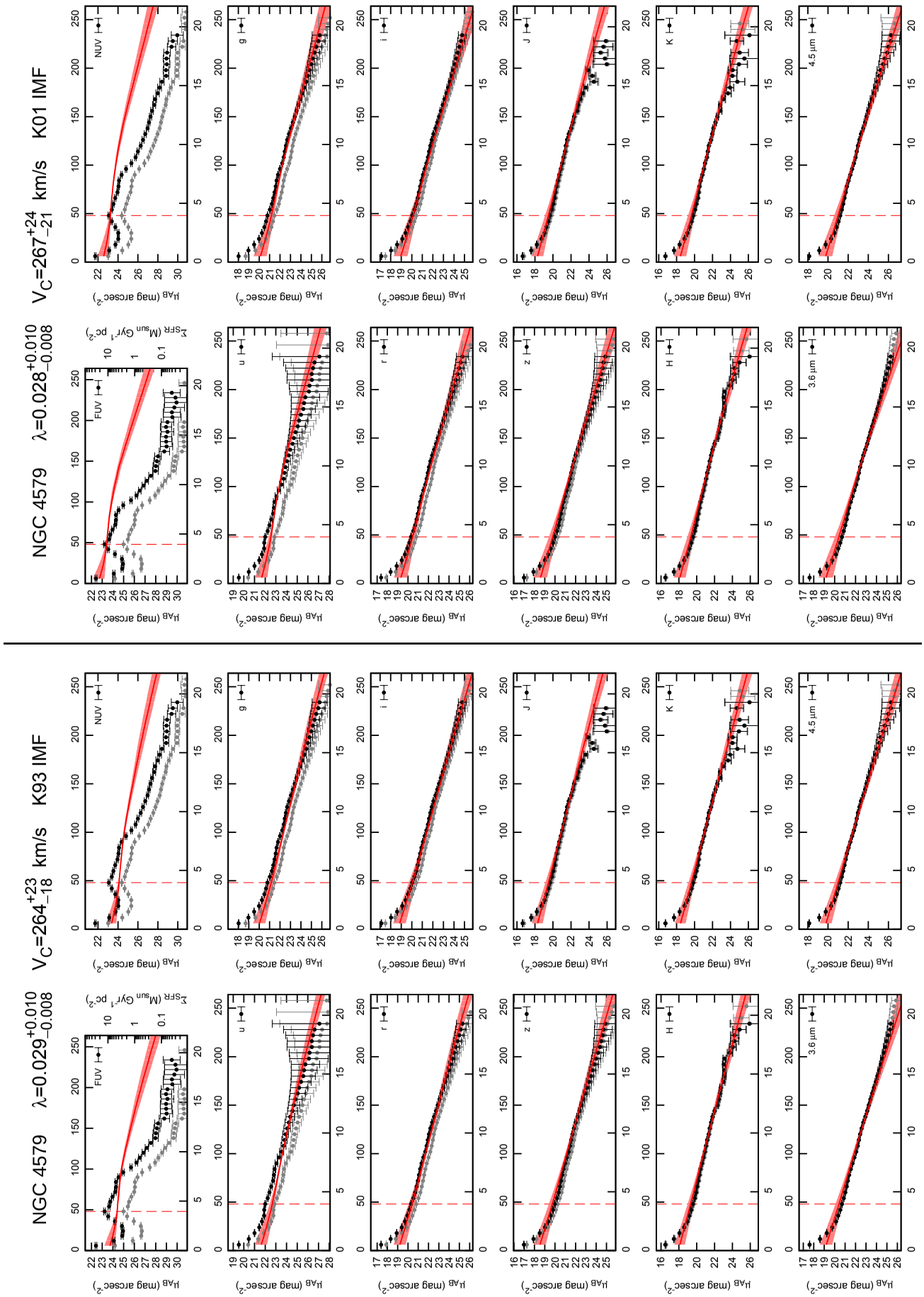
NGC 4579 λ=0.028+0.010−0.008 VC=267+24−21 km/s K01 IMF
NGC 4579 λ=0.029+0.010−0.008 VC=264+23−18 km/s K93 IMF
FUV
NUV
u
g
r
i
z
J
H
K
3.6 μm
4.5 μm
μAB (mag arcsec-2)
ΣSFR (MSun Gyr-1 pc-2)

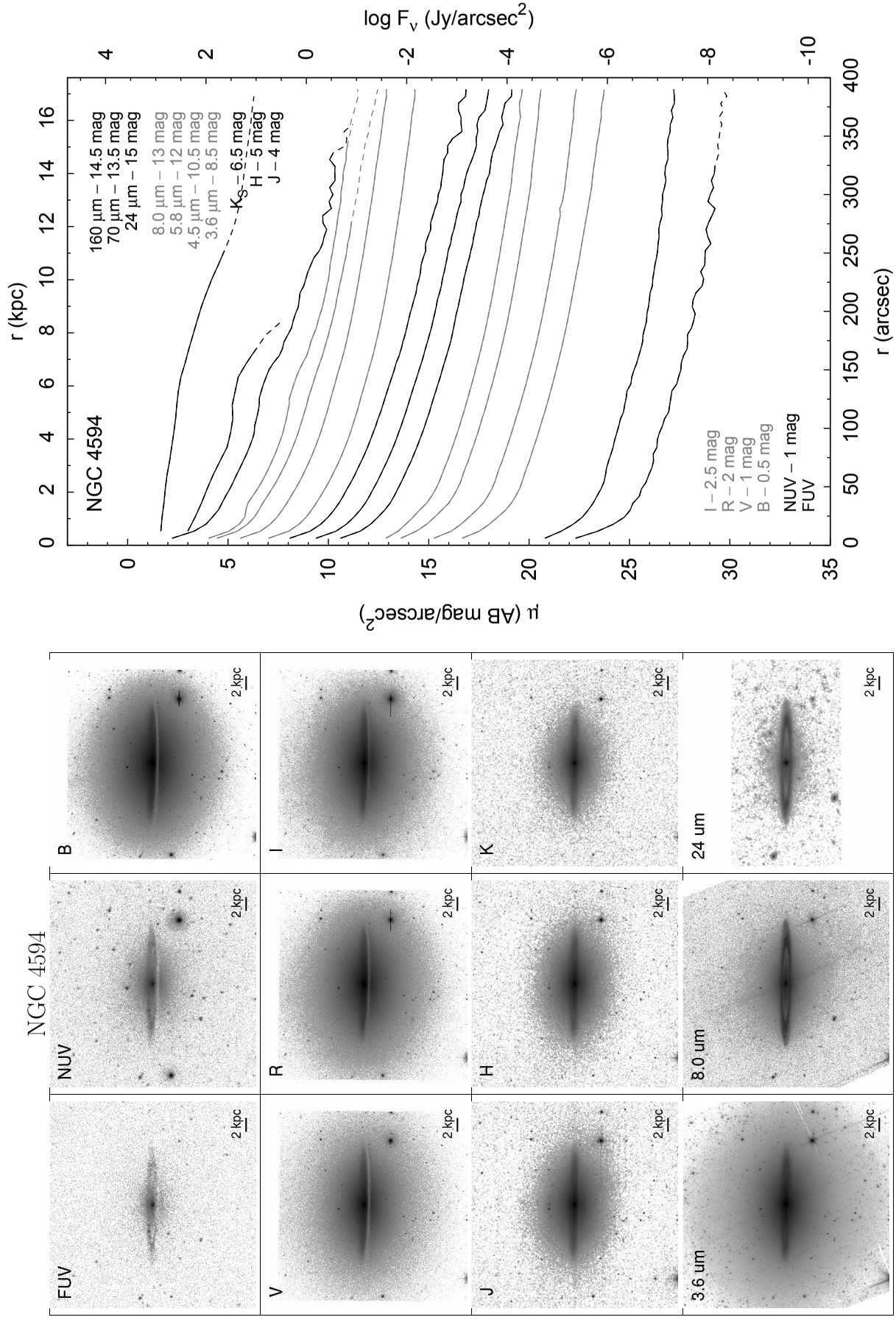
NGC 4594
FUV
NUV
B
V
R
I
J
H
K
3.6 um
8.0 um
24 um
2 kpc
μ (AB mag/arcsec²)
log F_ν (Jy/arcsec²)
r (kpc)
r (arcsec)
NGC 4594
160 μm – 14.5 mag
70 μm – 13.5 mag
24 μm – 15 mag
8.0 μm – 13 mag
5.8 μm – 12 mag
4.5 μm – 10.5 mag
3.6 μm – 8.5 mag
K_S – 6.5 mag
H – 5 mag
J – 4 mag
I – 2.5 mag
R – 2 mag
V – 1 mag
B – 0.5 mag
NUV – 1 mag
FUV

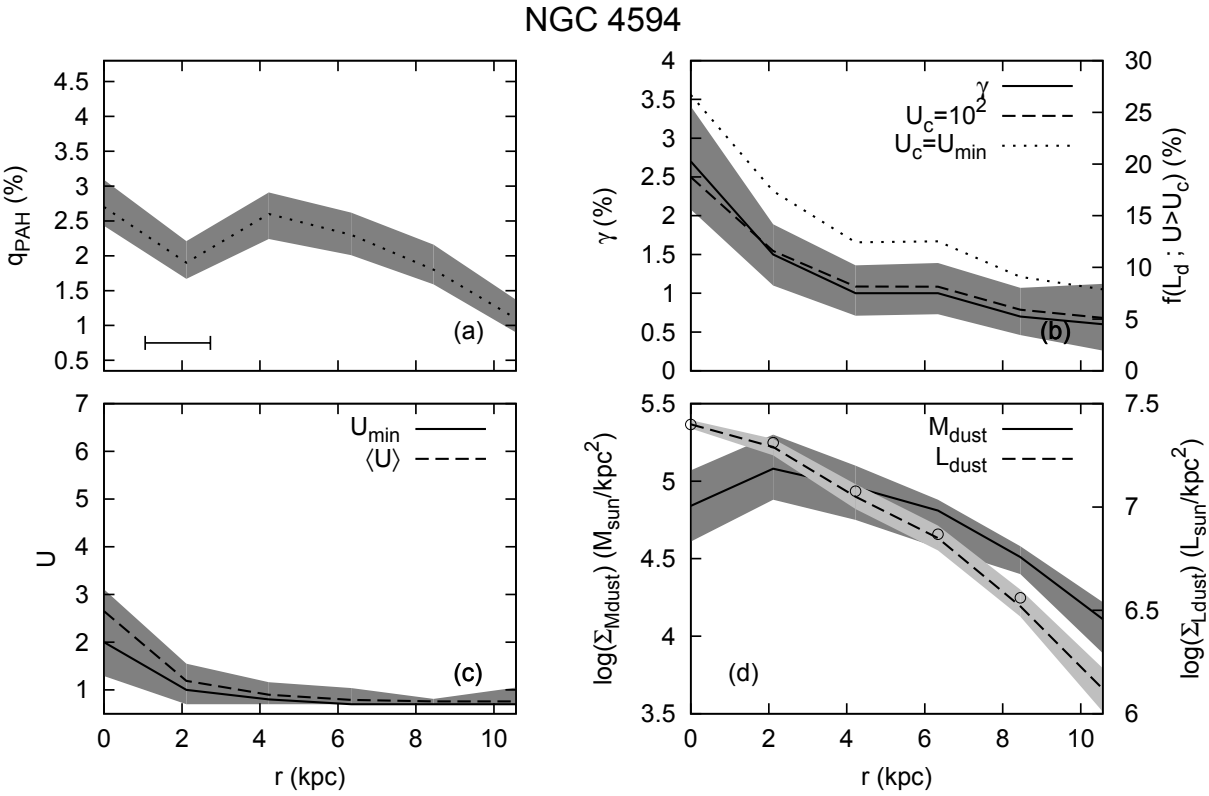
NGC 4594
q_{PAH} (%)
(a)
γ
$U_c=10^2$
$U_c=U_{min}$
γ (%)
$f(L_d\ ;\ U>U_c)$ (%)
(b)
U_{min}
$\langle U \rangle$
U
(c)
r (kpc)
M_{dust}
L_{dust}
$\log(\Sigma_{Mdust})$ (M_{sun}/kpc^2)
$\log(\Sigma_{Ldust})$ (L_{sun}/kpc^2)
(d)
r (kpc)

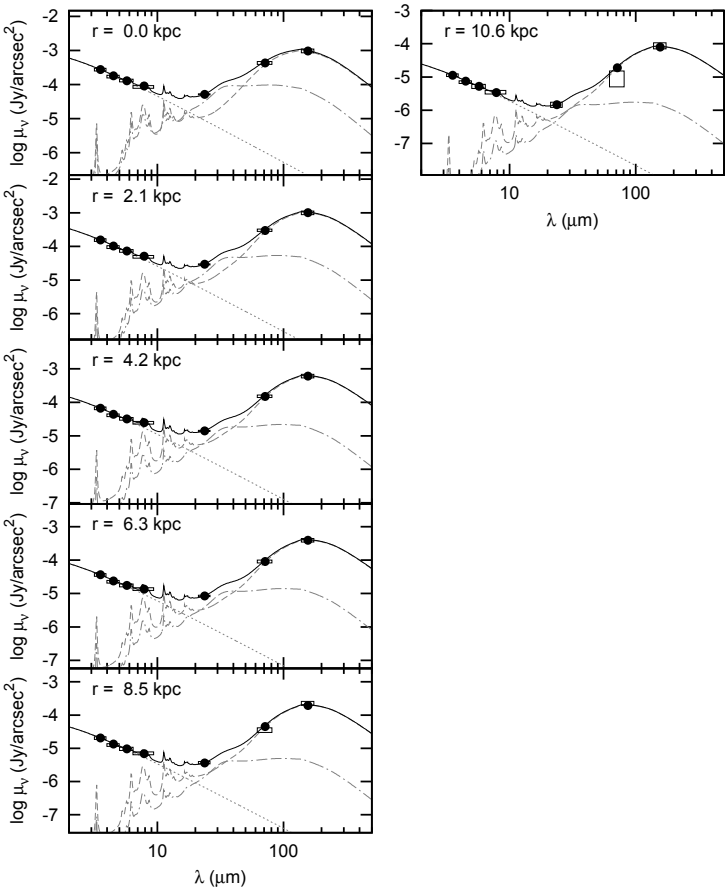
r = 0.0 kpc
r = 10.6 kpc
r = 2.1 kpc
r = 4.2 kpc
r = 6.3 kpc
r = 8.5 kpc
log μ_ν (Jy/arcsec^2)
λ (μm)

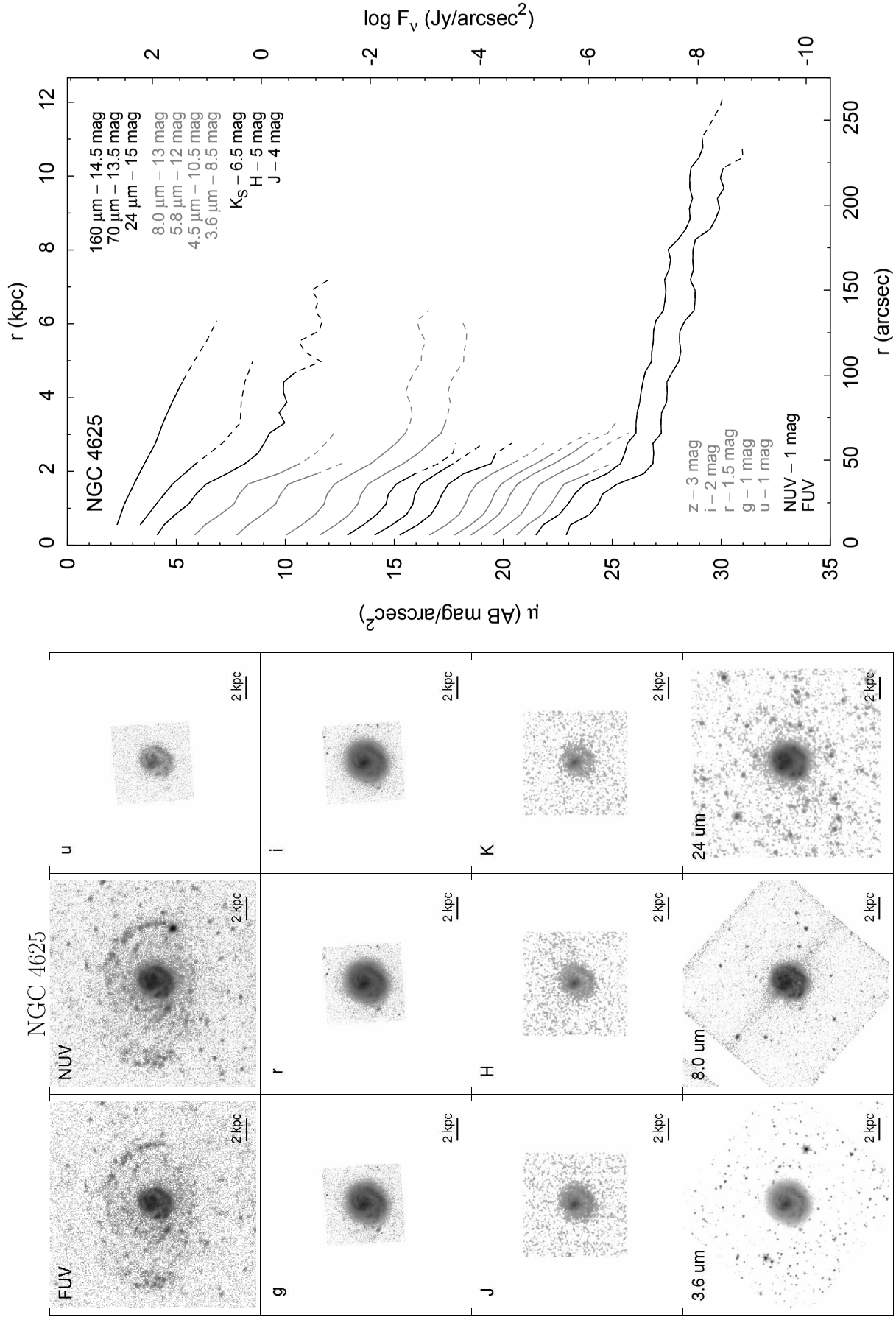
NGC 4625
FUV
NUV
u
g
r
i
J
H
K
3.6 um
8.0 um
24 um
2 kpc
μ (AB mag/arcsec²)
r (kpc)
log F_ν (Jy/arcsec²)
r (arcsec)
NGC 4625
160 μm – 14.5 mag
70 μm – 13.5 mag
24 μm – 15 mag
8.0 μm – 13 mag
5.8 μm – 12 mag
4.5 μm – 10.5 mag
3.6 μm – 8.5 mag
K_S – 6.5 mag
H – 5 mag
J – 4 mag
z – 3 mag
i – 2 mag
r – 1.5 mag
g – 1 mag
u – 1 mag
NUV – 1 mag
FUV

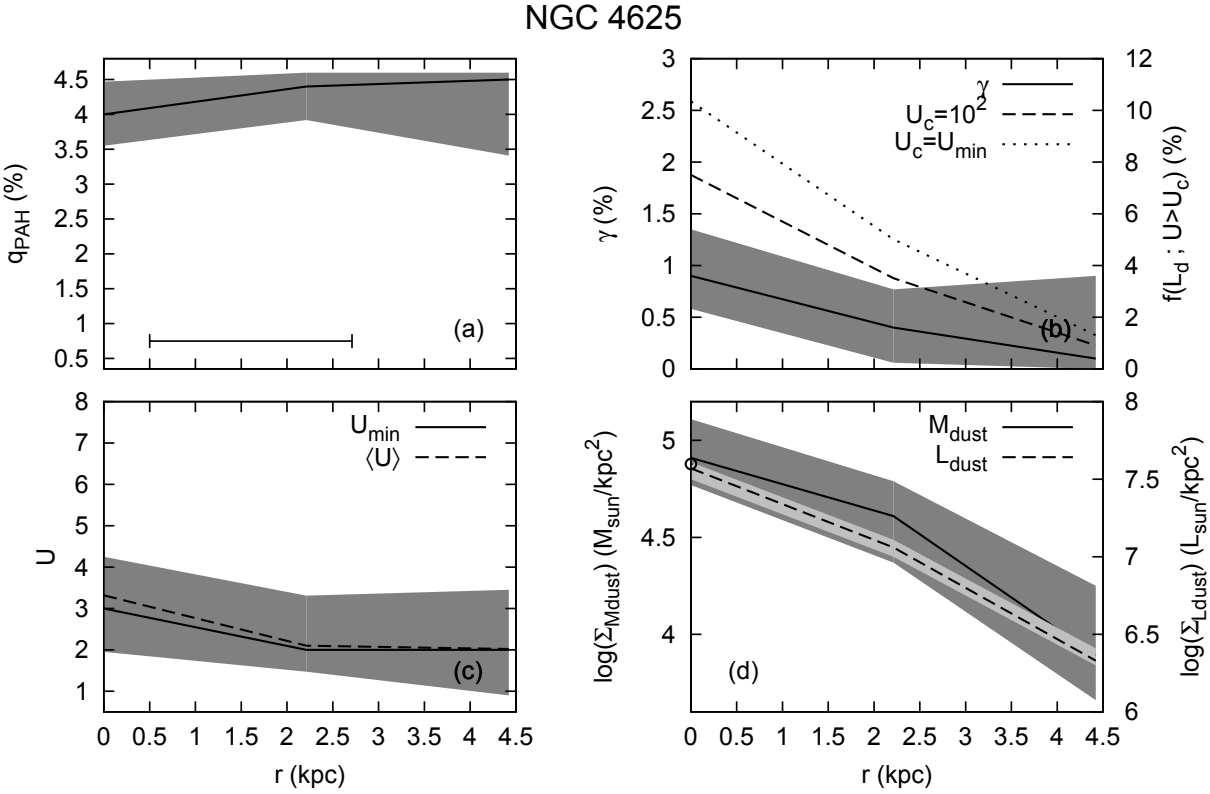
NGC 4625
q_{PAH} (%)
(a)
γ
$U_c=10^2$
$U_c=U_{min}$
γ (%)
$f(L_d ; U>U_c)$ (%)
(b)
U_{min}
⟨U⟩
U
(c)
r (kpc)
M_{dust}
L_{dust}
$\log(\Sigma_{Mdust})$ (M_{sun}/kpc^2)
$\log(\Sigma_{Ldust})$ (L_{sun}/kpc^2)
(d)
r (kpc)

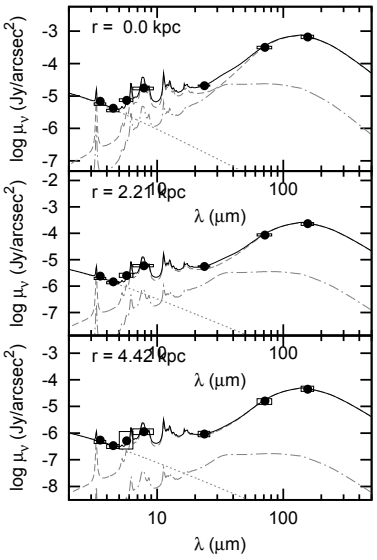
r = 0.0 kpc
r = 2.21 kpc
r = 4.42 kpc
log μ_ν (Jy/arcsec^2)
λ (μm)

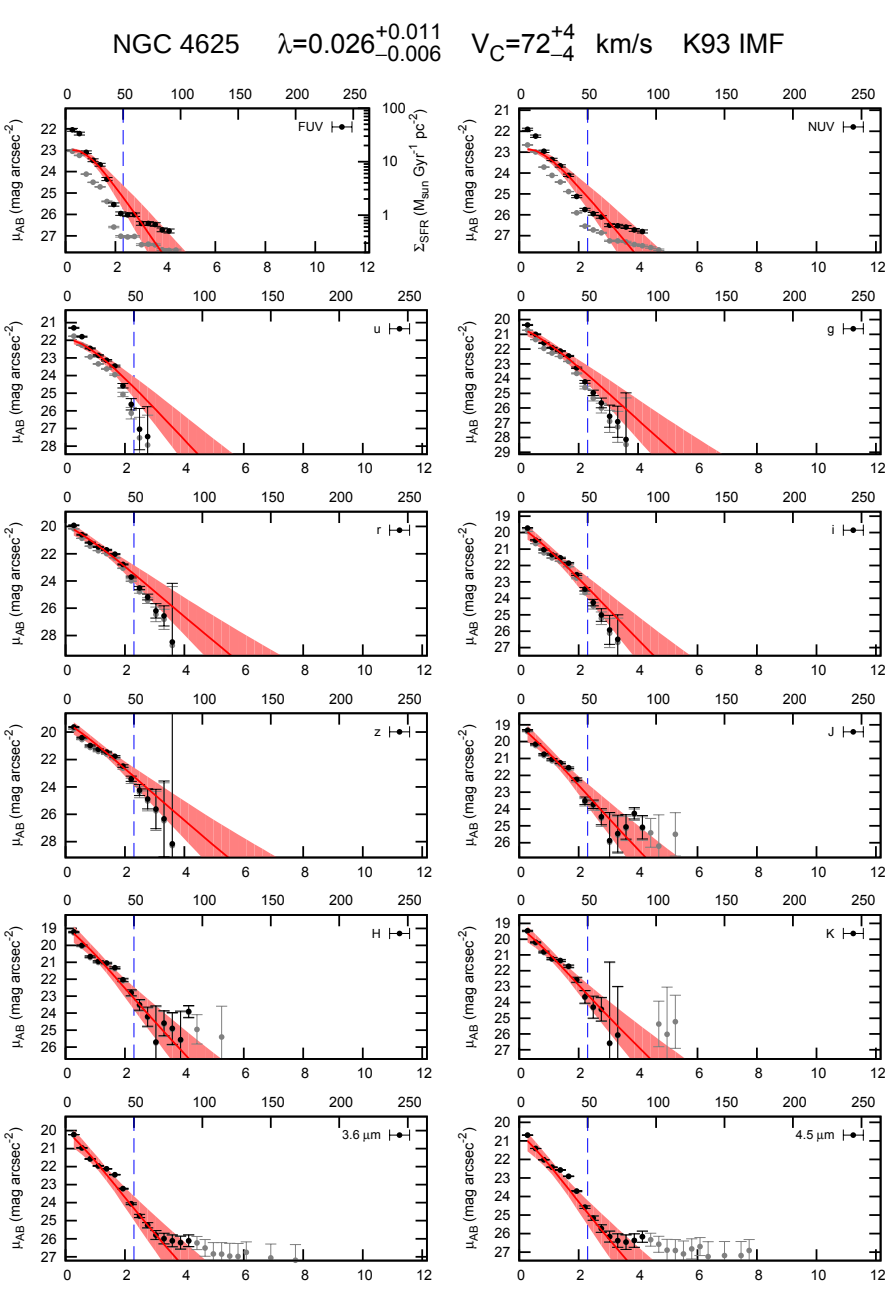
NGC 4625 λ=0.026+0.011−0.006 VC=72+4−4 km/s K93 IMF
FUV
NUV
u
g
r
i
z
J
H
K
3.6 μm
4.5 μm
μAB (mag arcsec−2)
ΣSFR (Msun Gyr−1 pc−2)

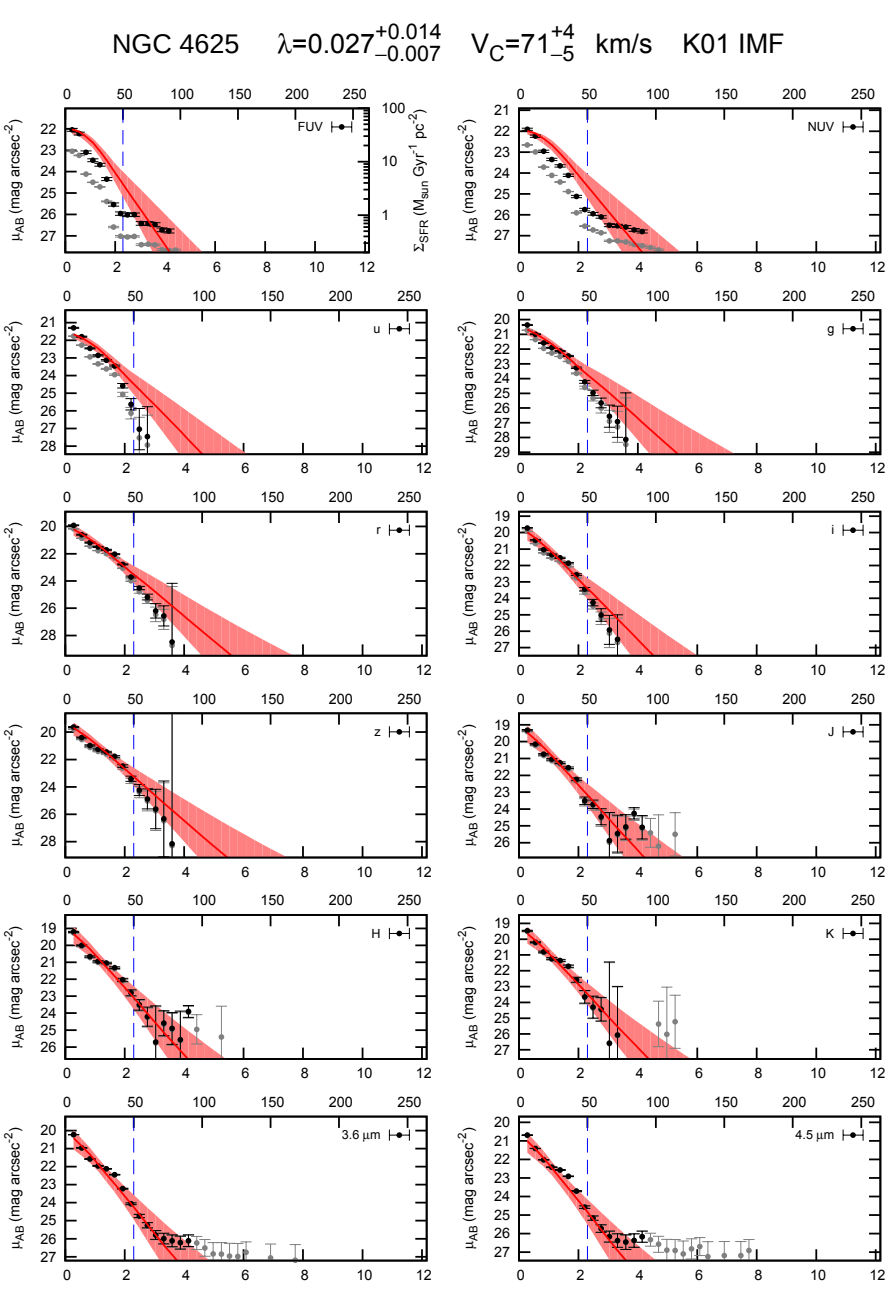
NGC 4625 λ=0.027+0.014−0.007 VC=71+4−5 km/s K01 IMF
FUV
NUV
u
g
r
i
z
J
H
K
3.6 μm
4.5 μm
μAB (mag arcsec−2)
ΣSFR (Msun Gyr−1 pc−2)

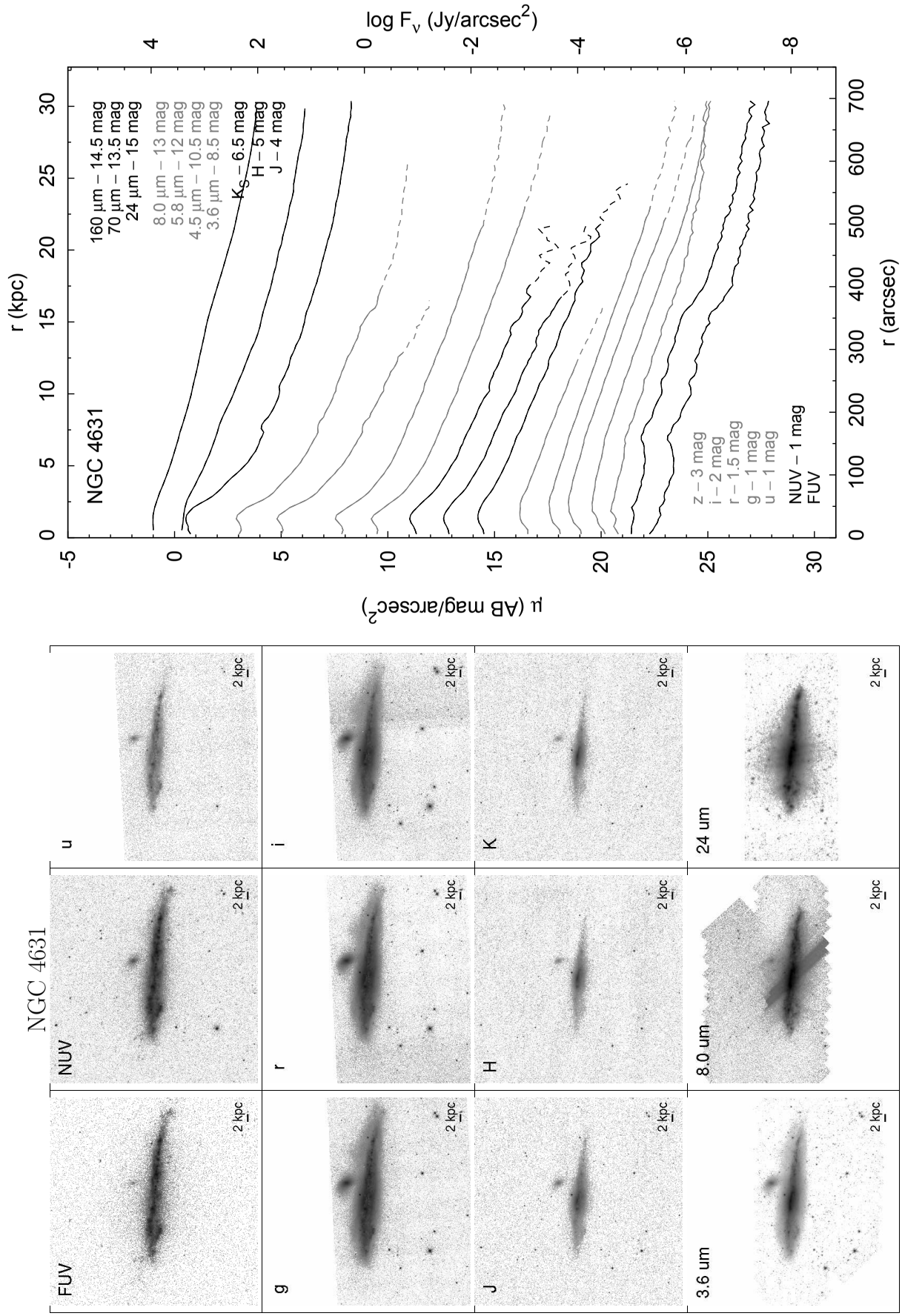
NGC 4631
FUV
NUV
u
g
r
i
J
H
K
3.6 um
8.0 um
24 um
2 kpc
μ (AB mag/arcsec²)
log F_ν (Jy/arcsec²)
r (kpc)
r (arcsec)
NGC 4631
160 μm – 14.5 mag
70 μm – 13.5 mag
24 μm – 15 mag
8.0 μm – 13 mag
5.8 μm – 12 mag
4.5 μm – 10.5 mag
3.6 μm – 8.5 mag
K_S – 6.5 mag
H – 5 mag
J – 4 mag
z – 3 mag
i – 2 mag
r – 1.5 mag
g – 1 mag
u – 1 mag
NUV – 1 mag
FUV

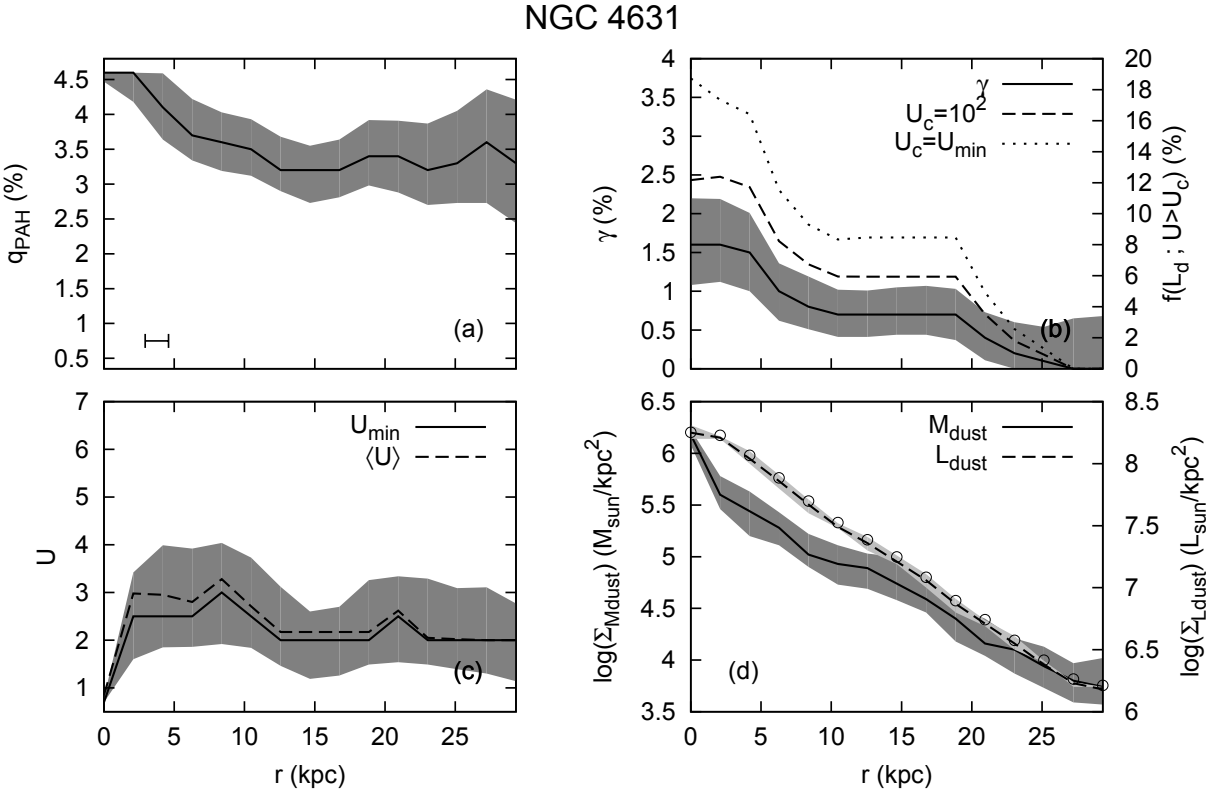
NGC 4631
q_{PAH} (%)
(a)
γ (%)
$U_c=10^2$
$U_c=U_{min}$
$f(L_d\ ;\ U>U_c)$ (%)
(b)
U
U_{min}
$\langle U \rangle$
(c)
r (kpc)
$\log(\Sigma_{Mdust})$ (M_{sun}/kpc^2)
M_{dust}
L_{dust}
$\log(\Sigma_{Ldust})$ (L_{sun}/kpc^2)
(d)
r (kpc)

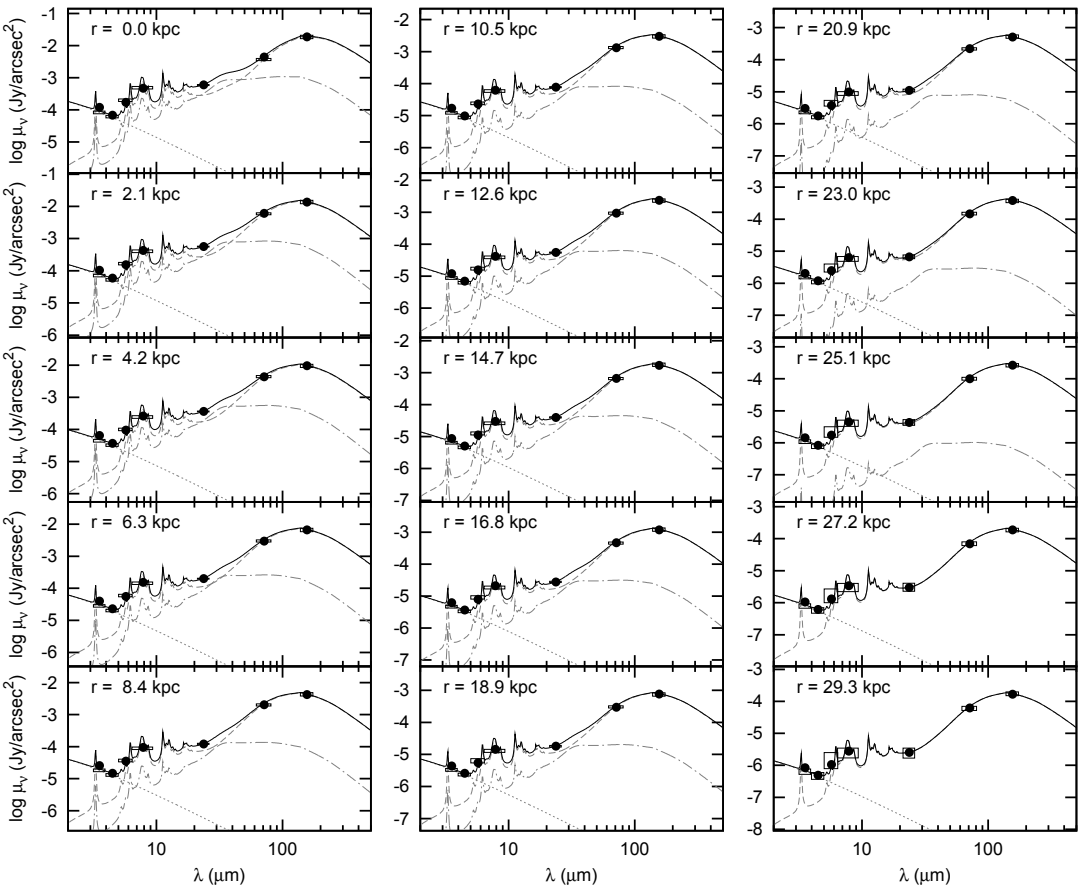
r = 0.0 kpc
r = 2.1 kpc
r = 4.2 kpc
r = 6.3 kpc
r = 8.4 kpc
r = 10.5 kpc
r = 12.6 kpc
r = 14.7 kpc
r = 16.8 kpc
r = 18.9 kpc
r = 20.9 kpc
r = 23.0 kpc
r = 25.1 kpc
r = 27.2 kpc
r = 29.3 kpc
log μ_ν (Jy/arcsec^2)
λ (μm)

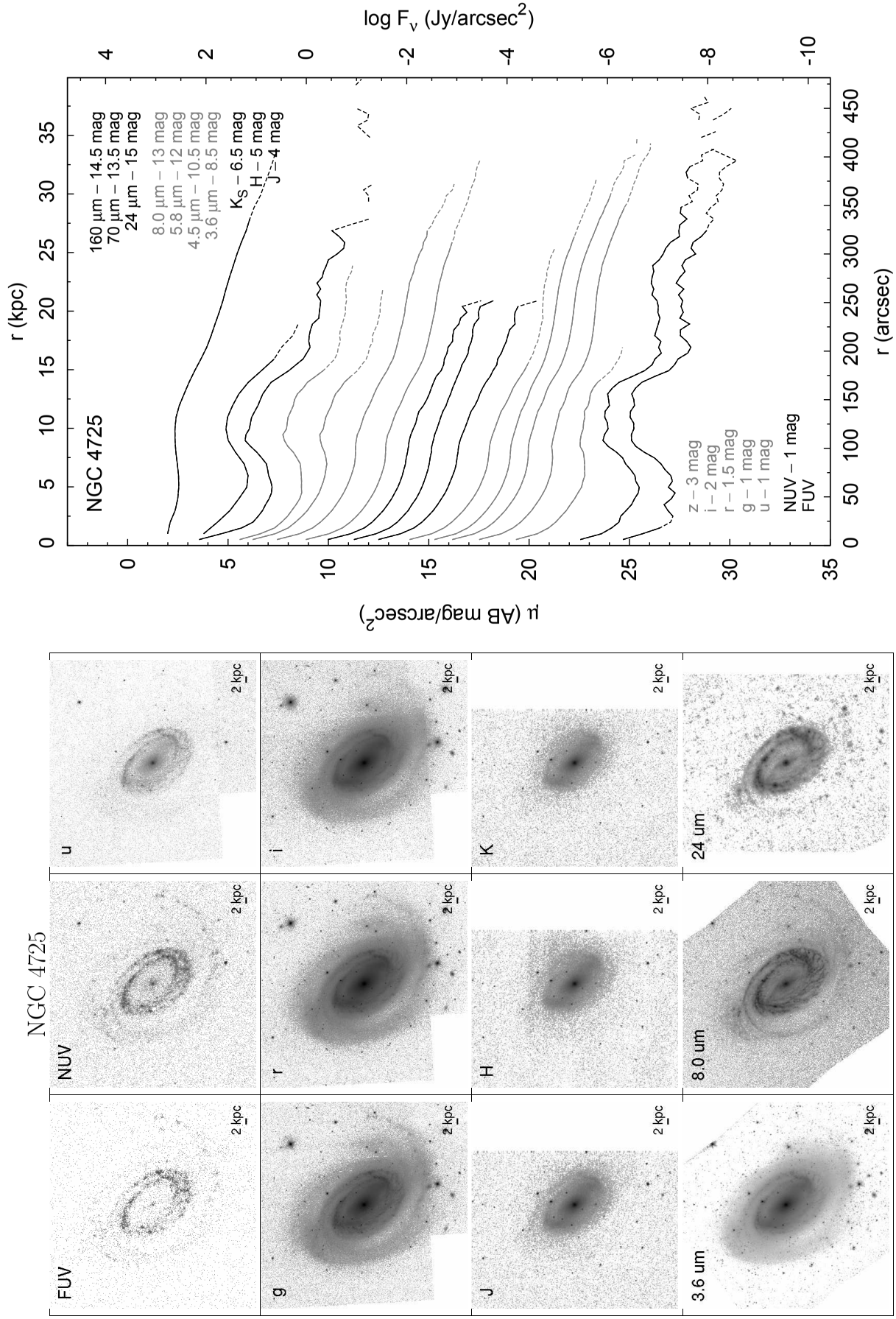
NGC 4725
FUV
NUV
u
g
r
i
J
H
K
3.6 um
8.0 um
24 um
2 kpc
μ (AB mag/arcsec²)
log F_ν (Jy/arcsec²)
r (kpc)
r (arcsec)
NGC 4725
160 μm – 14.5 mag
70 μm – 13.5 mag
24 μm – 15 mag
8.0 μm – 13 mag
5.8 μm – 12 mag
4.5 μm – 10.5 mag
3.6 μm – 8.5 mag
K_S – 6.5 mag
H – 5 mag
J – 4 mag
z – 3 mag
i – 2 mag
r – 1.5 mag
g – 1 mag
u – 1 mag
NUV – 1 mag
FUV

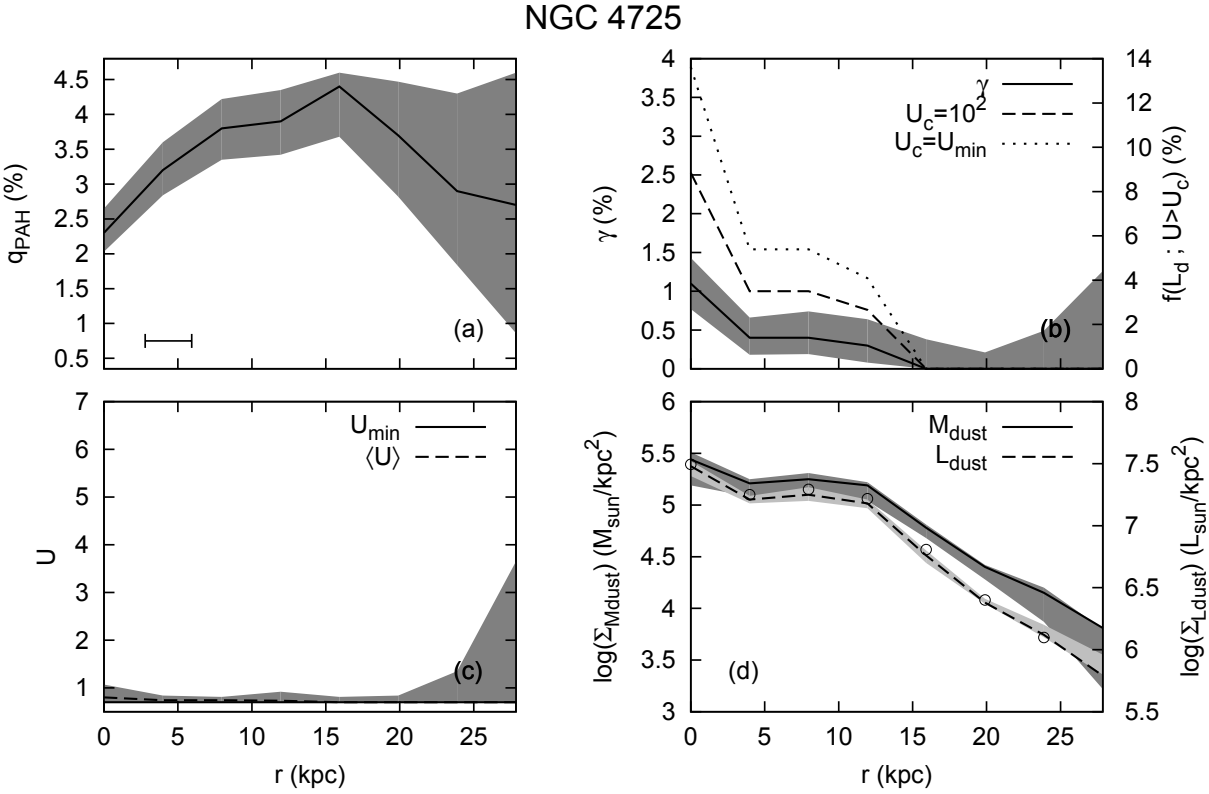
NGC 4725
q_{PAH} (%)
(a)
γ
$U_c=10^2$
$U_c=U_{min}$
γ (%)
$f(L_d ; U>U_c)$ (%)
(b)
U_{min}
⟨U⟩
U
(c)
r (kpc)
M_{dust}
L_{dust}
$\log(\Sigma_{Mdust})$ (M_{sun}/kpc^2)
$\log(\Sigma_{Ldust})$ (L_{sun}/kpc^2)
(d)
r (kpc)

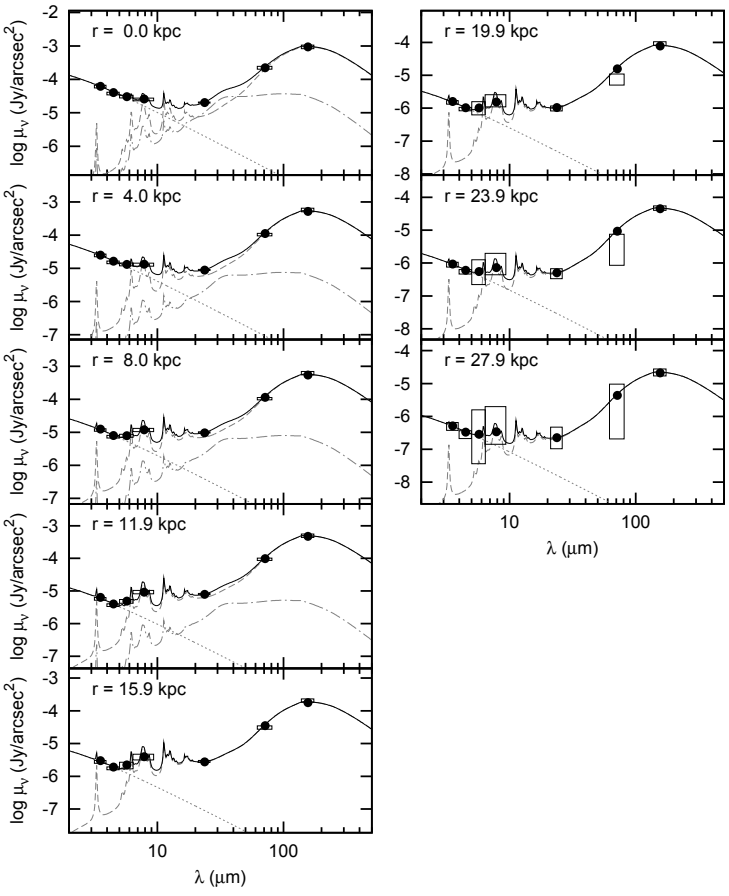
r = 0.0 kpc
r = 4.0 kpc
r = 8.0 kpc
r = 11.9 kpc
r = 15.9 kpc
r = 19.9 kpc
r = 23.9 kpc
r = 27.9 kpc
log μ_ν (Jy/arcsec^2)
λ (μm)

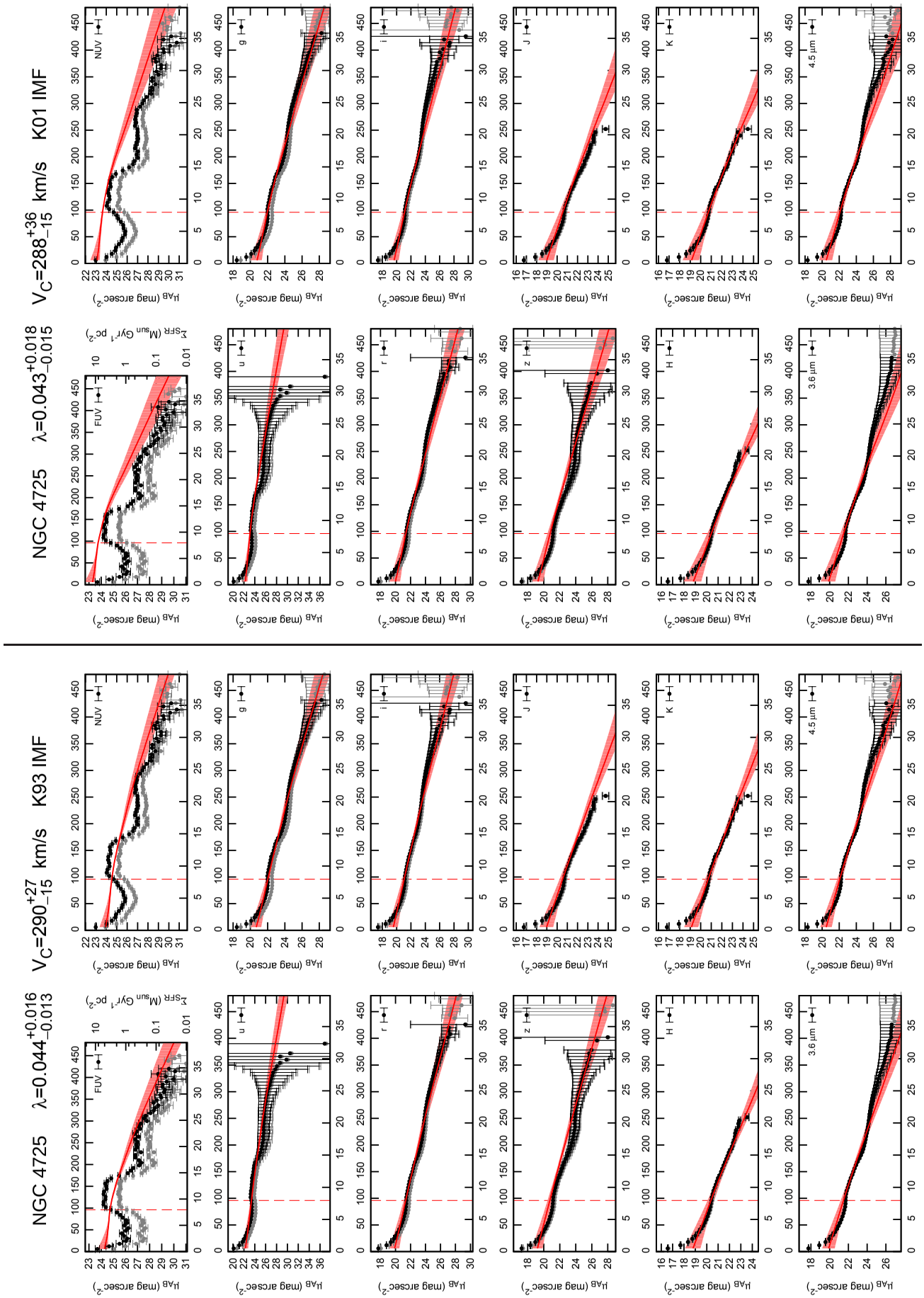
NGC 4725 λ=0.044+0.016−0.013 VC=290+27−15 km/s K93 IMF
NGC 4725 λ=0.043+0.018−0.015 VC=288+36−15 km/s K01 IMF
μAB (mag arcsec-2)
Σ*SFR (Msun Gyr-1 pc-2)
FUV
NUV
u
g
r
i
z
J
H
K
3.6 μm
4.5 μm

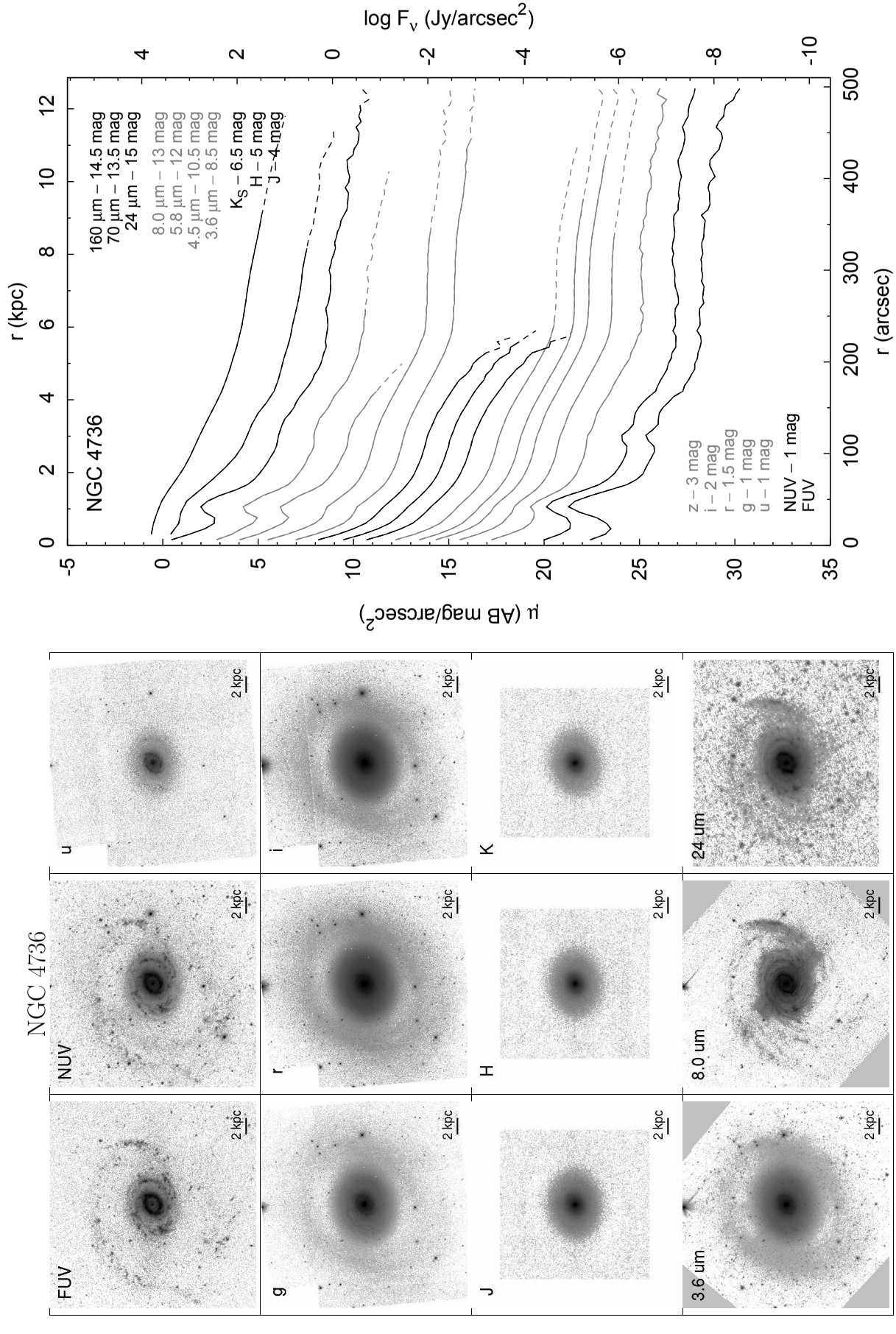
NGC 4736
FUV
NUV
u
g
r
i
J
H
K
3.6 um
8.0 um
24 um
2 kpc
μ (AB mag/arcsec²)
log F_ν (Jy/arcsec²)
r (kpc)
r (arcsec)
NGC 4736
160 μm – 14.5 mag
70 μm – 13.5 mag
24 μm – 15 mag
8.0 μm – 13 mag
5.8 μm – 12 mag
4.5 μm – 10.5 mag
3.6 μm – 8.5 mag
K_S – 6.5 mag
H – 5 mag
J – 4 mag
z – 3 mag
i – 2 mag
r – 1.5 mag
g – 1 mag
u – 1 mag
NUV – 1 mag
FUV

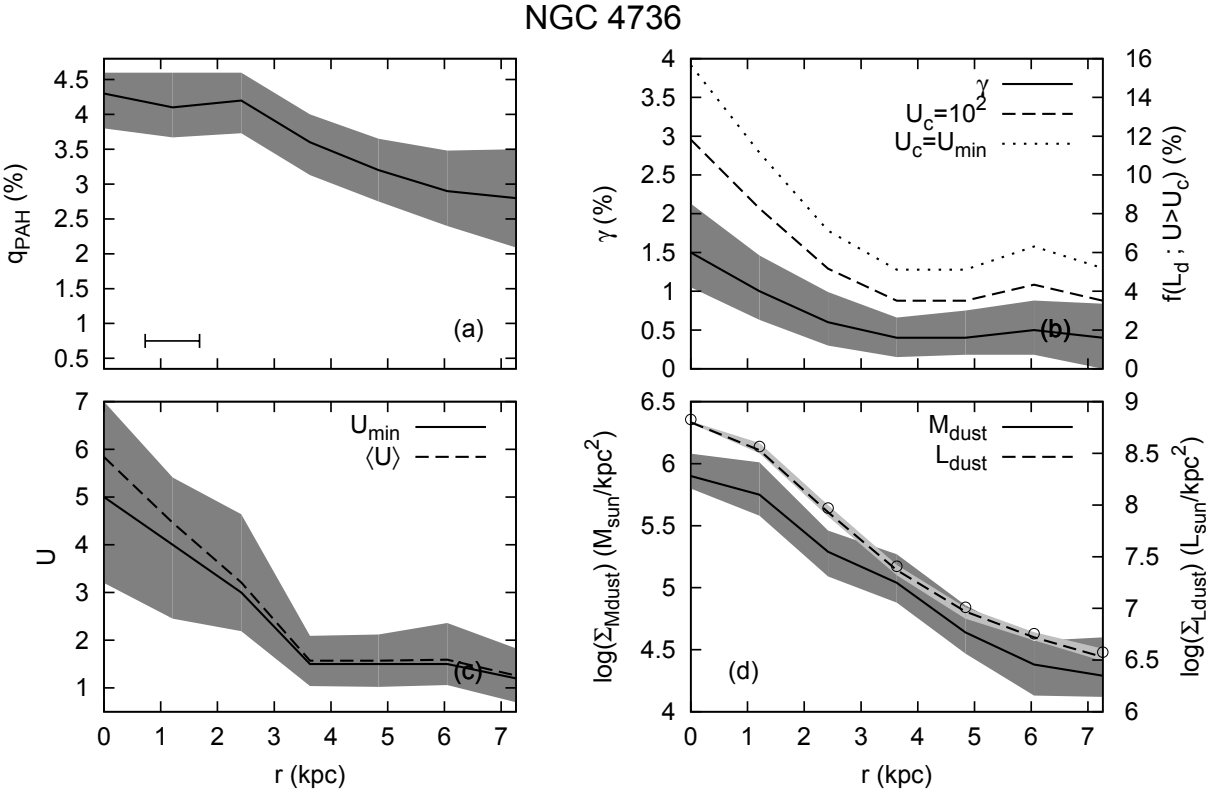
NGC 4736
q_{PAH} (%)
(a)
γ (%)
$f(L_d ; U>U_c)$ (%)
$U_c=10^2$
$U_c=U_{min}$
(b)
U
U_{min}
⟨U⟩
(c)
r (kpc)
$\log(\Sigma_{Mdust})$ (M_{sun}/kpc^2)
$\log(\Sigma_{Ldust})$ (L_{sun}/kpc^2)
M_{dust}
L_{dust}
(d)
r (kpc)

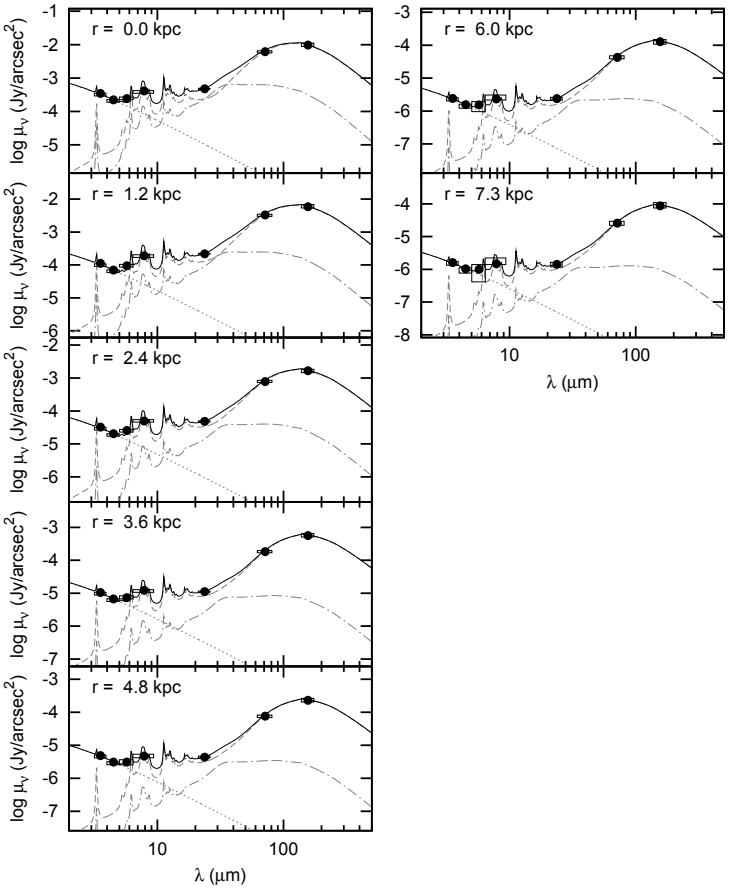
r = 0.0 kpc
r = 1.2 kpc
r = 2.4 kpc
r = 3.6 kpc
r = 4.8 kpc
r = 6.0 kpc
r = 7.3 kpc
log μ_ν (Jy/arcsec^2)
λ (μm)

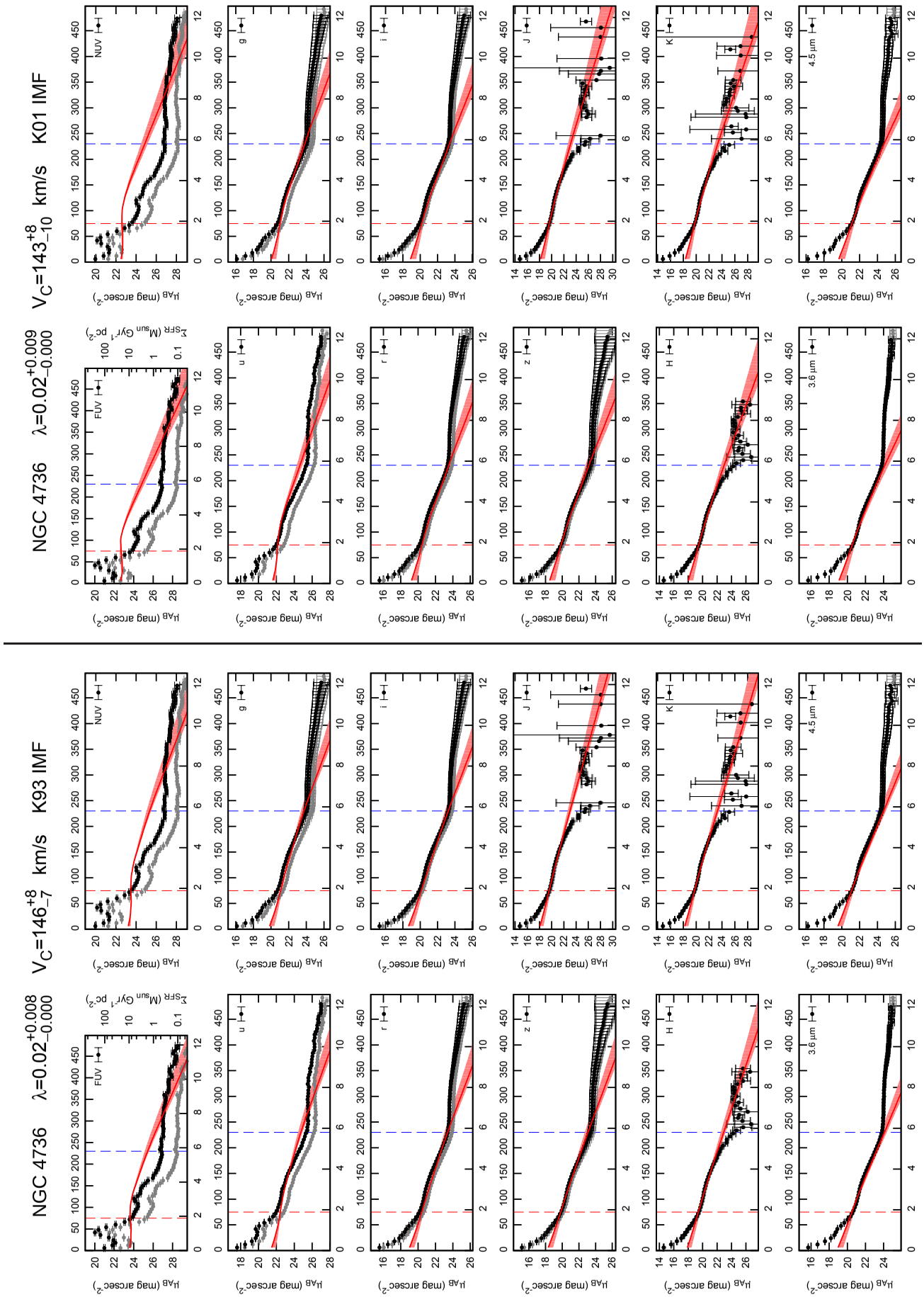
NGC 4736 λ=0.02+0.009−0.000 VC=143+8−10 km/s K01 IMF
NGC 4736 λ=0.02+0.008−0.000 VC=146+8−7 km/s K93 IMF
μAB (mag arcsec-2)
Σ*SFR (Msun Gyr-1 pc-2)
FUV
NUV
u
g
r
i
z
J
H
K
3.6 μm
4.5 μm

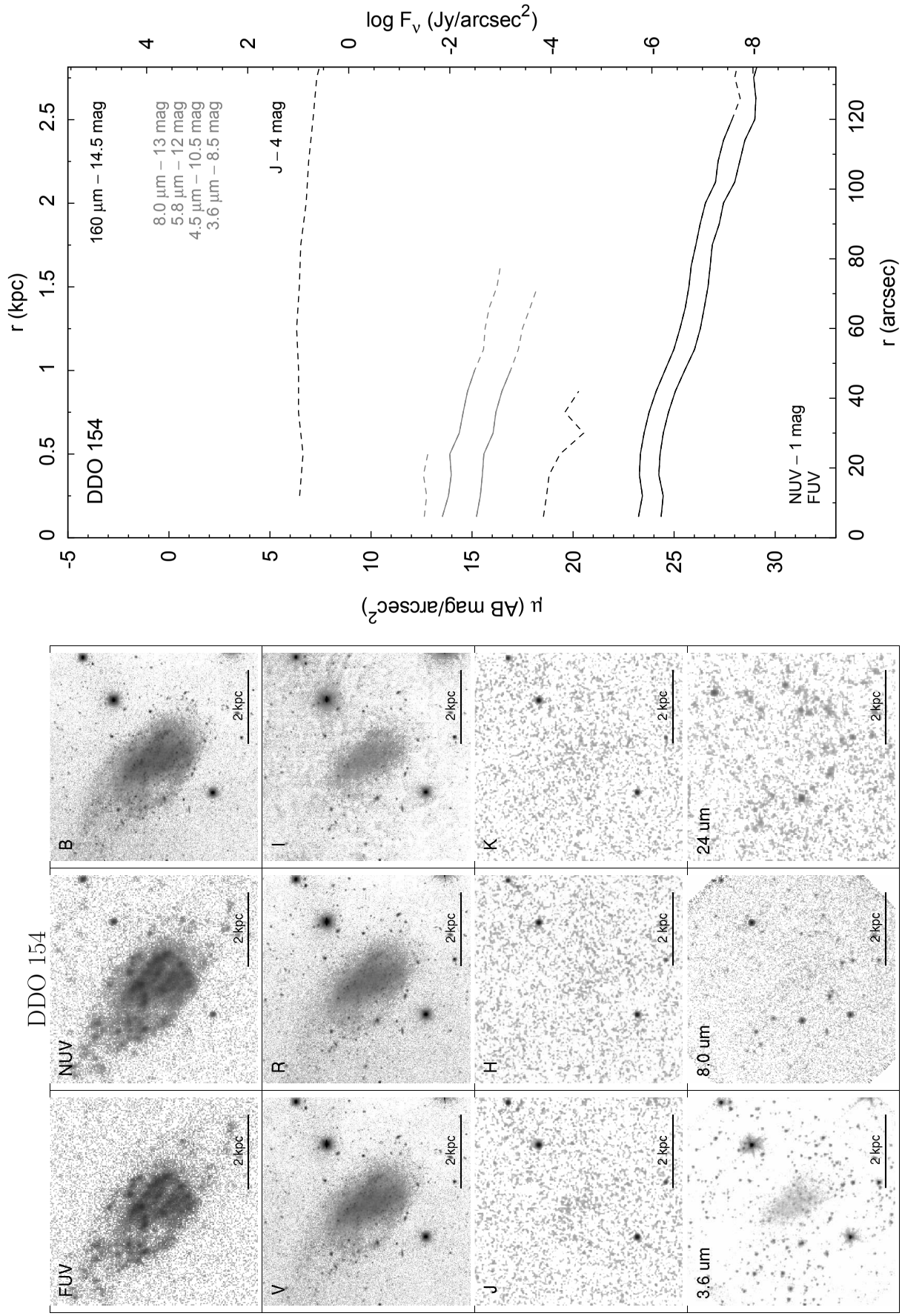
DDO 154
FUV
NUV
B
V
R
I
J
H
K
3.6 um
8.0 um
24 um
2 kpc
μ (AB mag/arcsec²)
log F_ν (Jy/arcsec²)
r (kpc)
r (arcsec)
DDO 154
160 μm – 14.5 mag
8.0 μm – 13 mag
5.8 μm – 12 mag
4.5 μm – 10.5 mag
3.6 μm – 8.5 mag
J – 4 mag
NUV – 1 mag
FUV

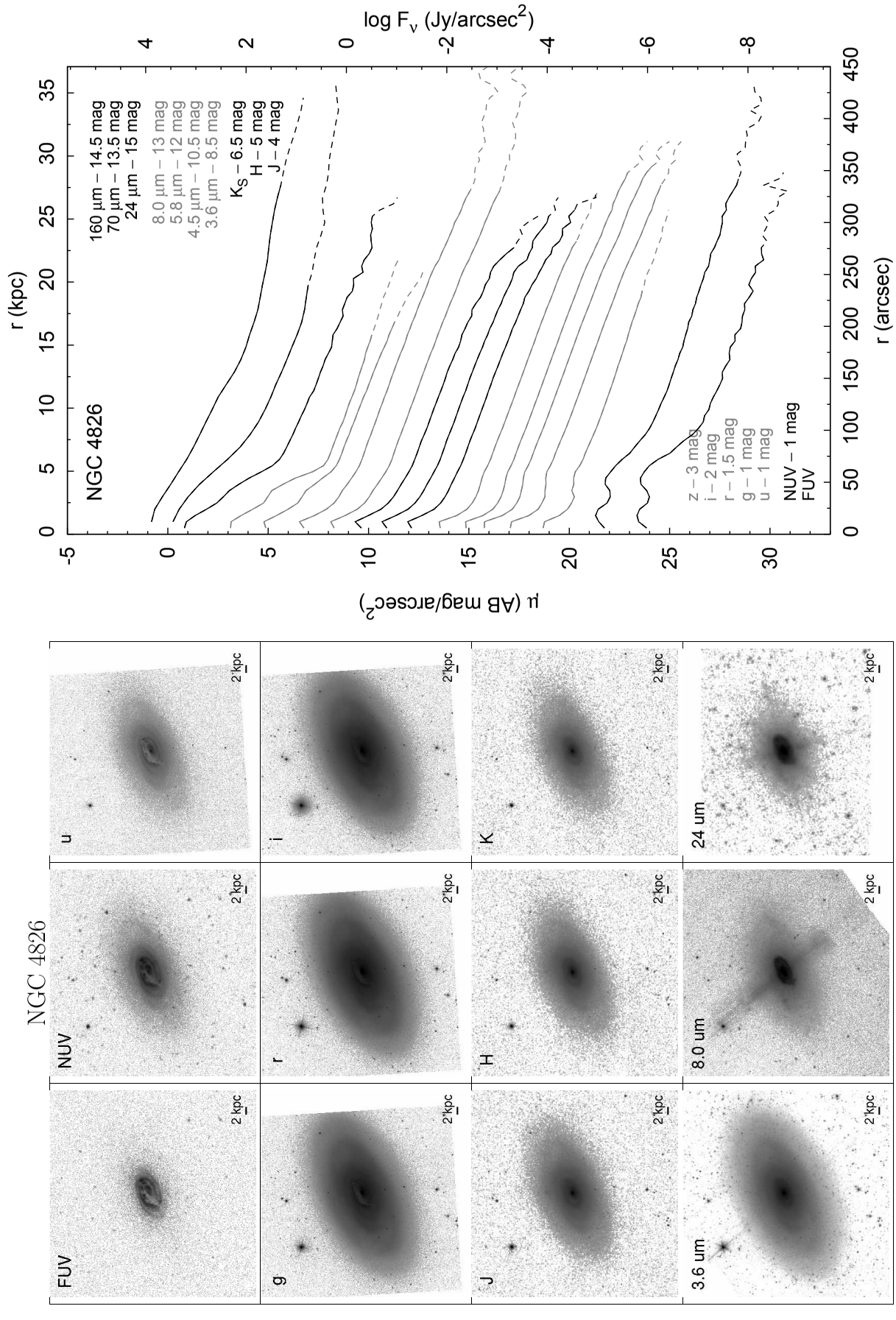
NGC 4826
FUV
NUV
u
g
r
i
J
H
K
3.6 um
8.0 um
24 um
2 kpc
NGC 4826
160 μm – 14.5 mag
70 μm – 13.5 mag
24 μm – 15 mag
8.0 μm – 13 mag
5.8 μm – 12 mag
4.5 μm – 10.5 mag
3.6 μm – 8.5 mag
K_S – 6.5 mag
H – 5 mag
J – 4 mag
z – 3 mag
i – 2 mag
r – 1.5 mag
g – 1 mag
u – 1 mag
NUV – 1 mag
FUV
r (kpc)
r (arcsec)
log F_ν (Jy/arcsec²)
μ (AB mag/arcsec²)

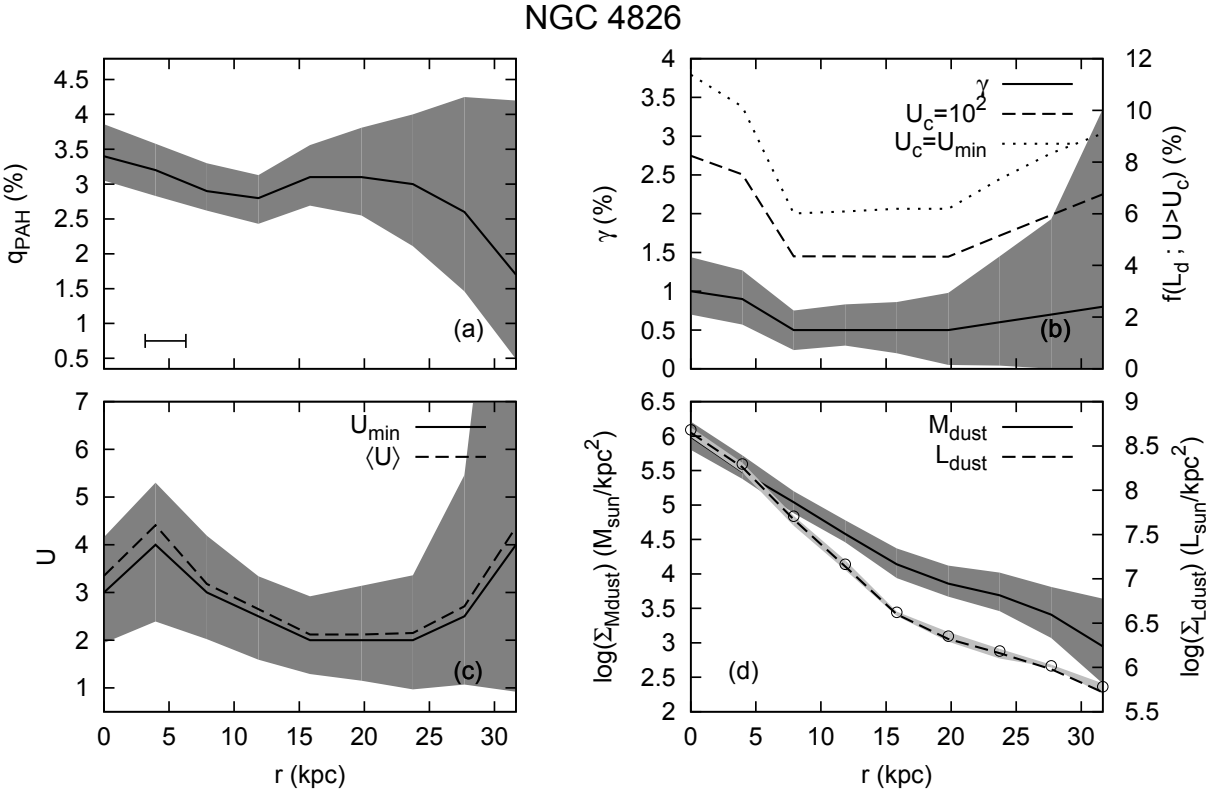
NGC 4826
q_{PAH} (%)
(a)
γ (%)
$U_c=10^2$
$U_c=U_{min}$
$f(L_d ; U>U_c)$ (%)
(b)
U
U_{min}
⟨U⟩
(c)
r (kpc)
$\log(\Sigma_{Mdust})$ (M_{sun}/kpc^2)
M_{dust}
L_{dust}
$\log(\Sigma_{Ldust})$ (L_{sun}/kpc^2)
(d)
r (kpc)

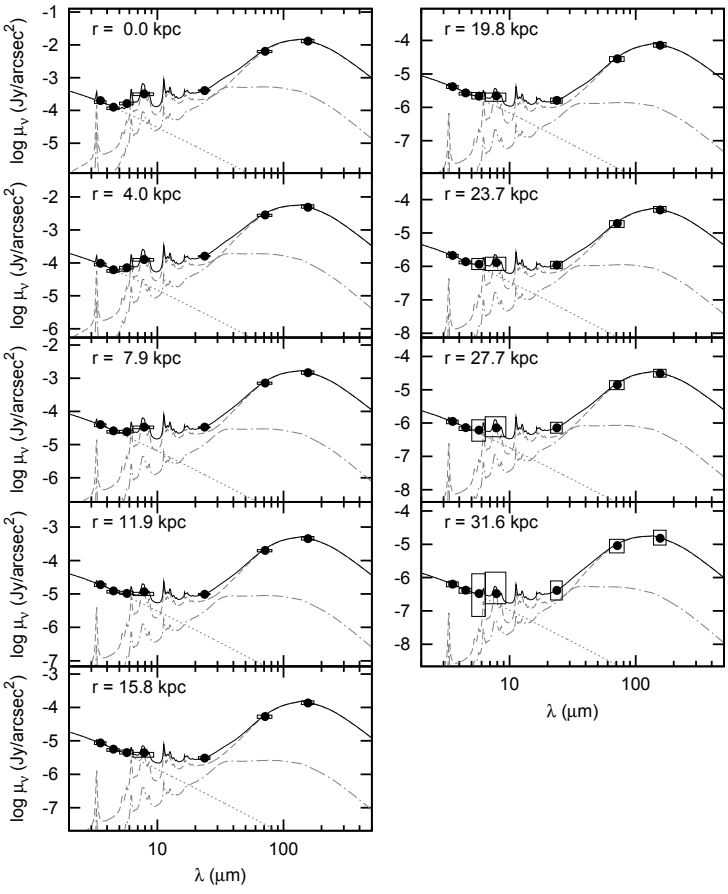
r = 0.0 kpc
r = 4.0 kpc
r = 7.9 kpc
r = 11.9 kpc
r = 15.8 kpc
r = 19.8 kpc
r = 23.7 kpc
r = 27.7 kpc
r = 31.6 kpc
log μν (Jy/arcsec²)
λ (μm)

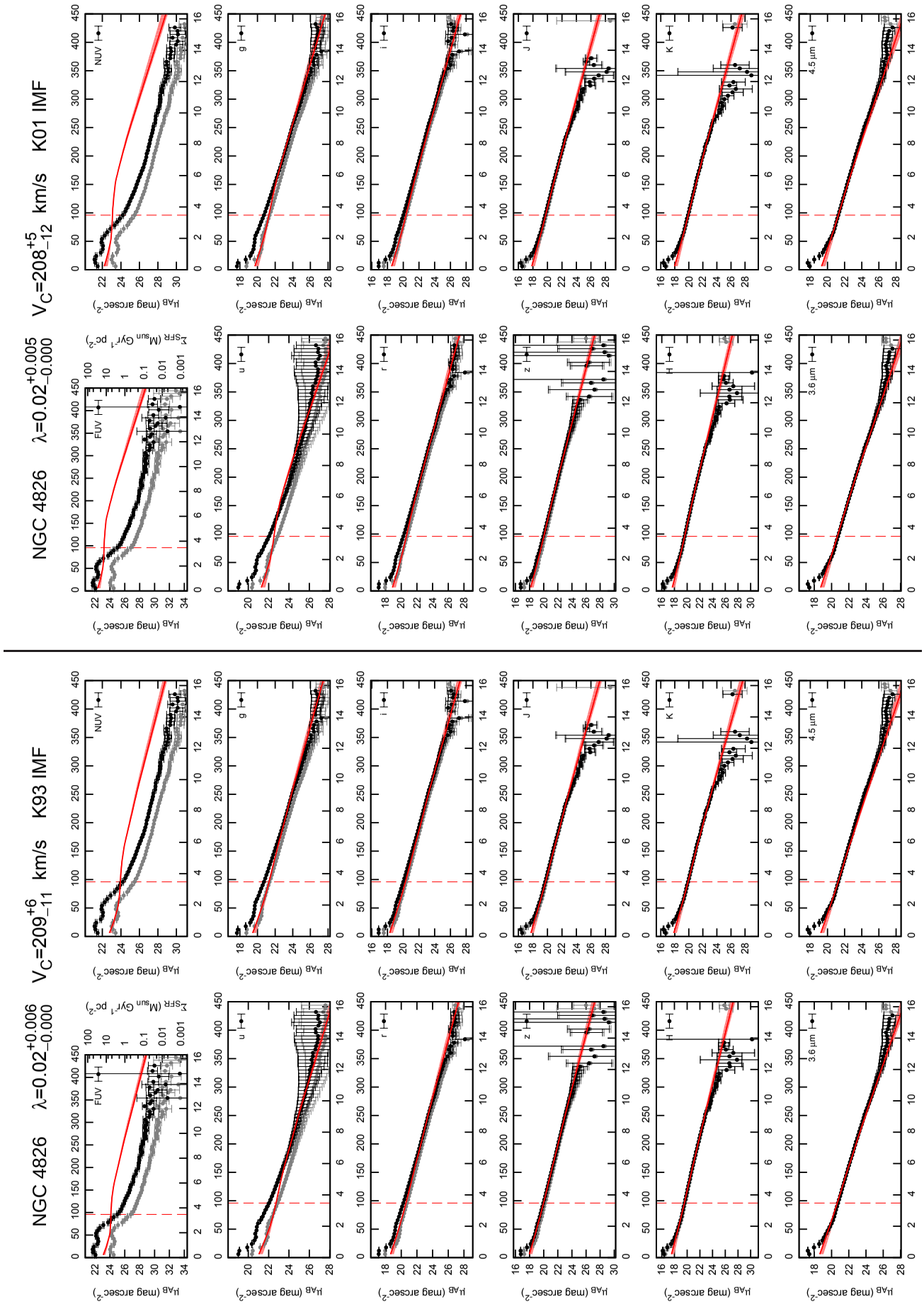
NGC 4826 λ=0.02+0.005−0.000 VC=208+5−12 km/s K01 IMF
NGC 4826 λ=0.02+0.006−0.000 VC=209+6−11 km/s K93 IMF
μAB (mag arcsec-2)
ΣSFR (Msun Gyr-1 pc-2)
FUV
NUV
u
g
r
i
z
J
K
3.6 μm
4.5 μm

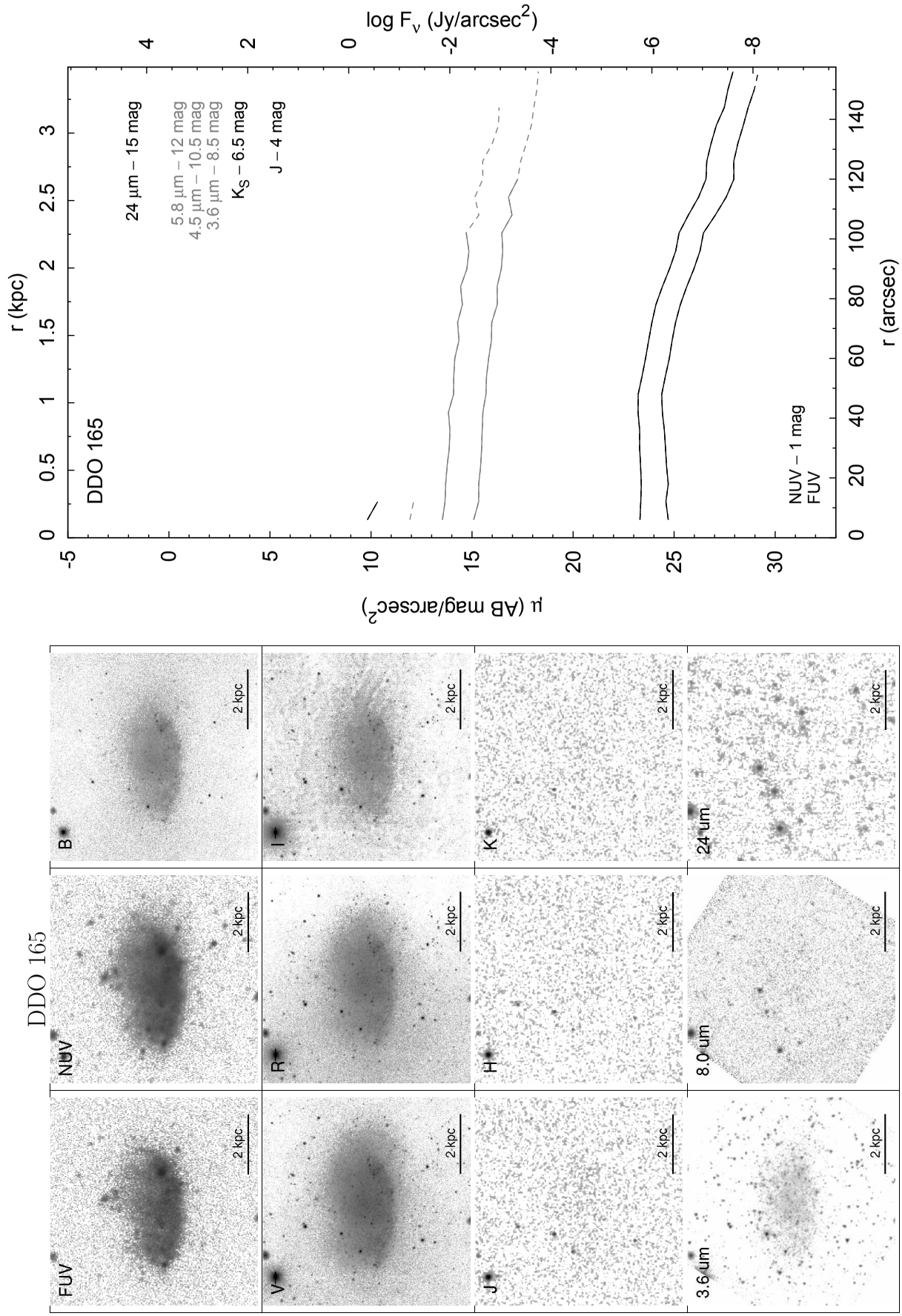
DDO 165
FUV
NUV
B
V
R
I
J
H
K
3.6 um
8.0 um
24 um
2 kpc
μ (AB mag/arcsec²)
log F_ν (Jy/arcsec²)
r (kpc)
r (arcsec)
24 μm – 15 mag
5.8 μm – 12 mag
4.5 μm – 10.5 mag
3.6 μm – 8.5 mag
K_S – 6.5 mag
J – 4 mag
NUV – 1 mag
FUV

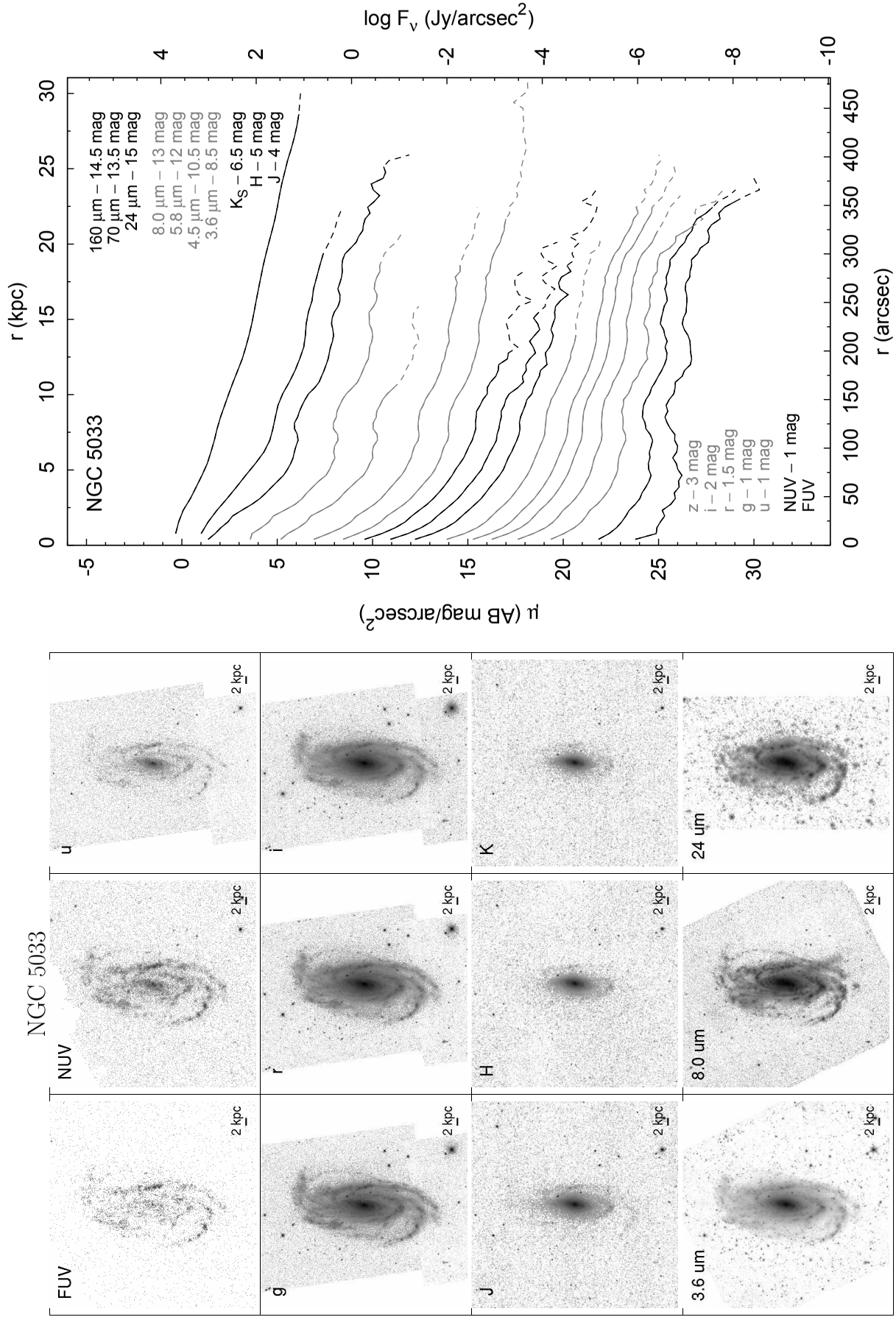
NGC 5033
FUV
NUV
u
g
r
i
J
H
K
3.6 um
8.0 um
24 um
2 kpc
μ (AB mag/arcsec²)
log F_ν (Jy/arcsec²)
r (kpc)
r (arcsec)
NGC 5033
160 μm – 14.5 mag
70 μm – 13.5 mag
24 μm – 15 mag
8.0 μm – 13 mag
5.8 μm – 12 mag
4.5 μm – 10.5 mag
3.6 μm – 8.5 mag
K_S – 6.5 mag
H – 5 mag
J – 4 mag
z – 3 mag
i – 2 mag
r – 1.5 mag
g – 1 mag
u – 1 mag
NUV – 1 mag
FUV

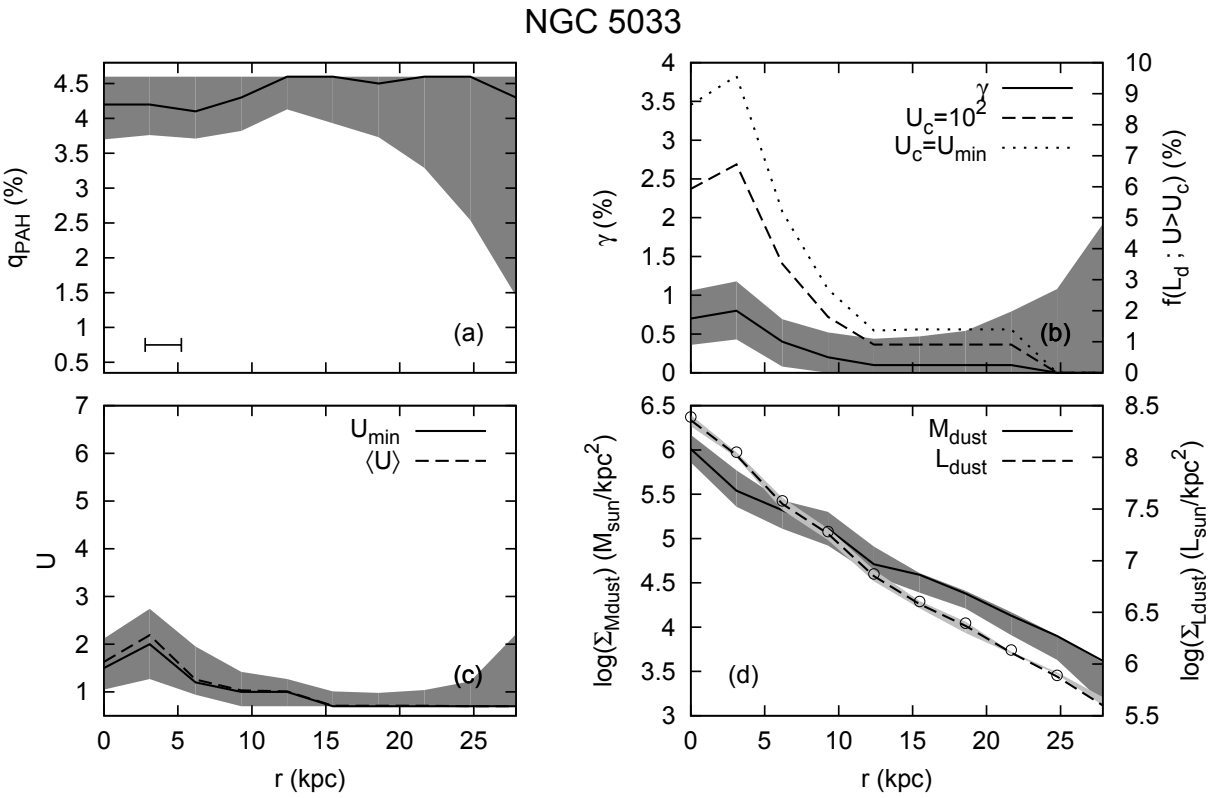
NGC 5033
q_{PAH} (%)
(a)
γ (%)
$U_c=10^2$
$U_c=U_{min}$
$f(L_d ; U>U_c)$ (%)
(b)
U
U_{min}
⟨U⟩
(c)
r (kpc)
$\log(\Sigma_{Mdust})$ (M_{sun}/kpc^2)
M_{dust}
L_{dust}
$\log(\Sigma_{Ldust})$ (L_{sun}/kpc^2)
(d)
r (kpc)

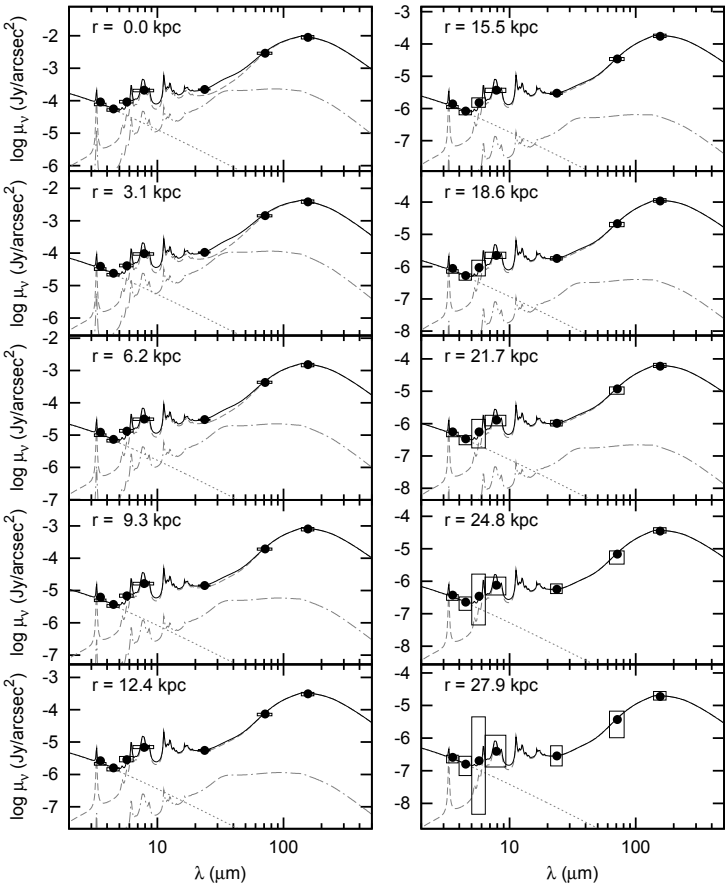
r = 0.0 kpc
r = 3.1 kpc
r = 6.2 kpc
r = 9.3 kpc
r = 12.4 kpc
r = 15.5 kpc
r = 18.6 kpc
r = 21.7 kpc
r = 24.8 kpc
r = 27.9 kpc
log μ_ν (Jy/arcsec^2)
λ (μm)

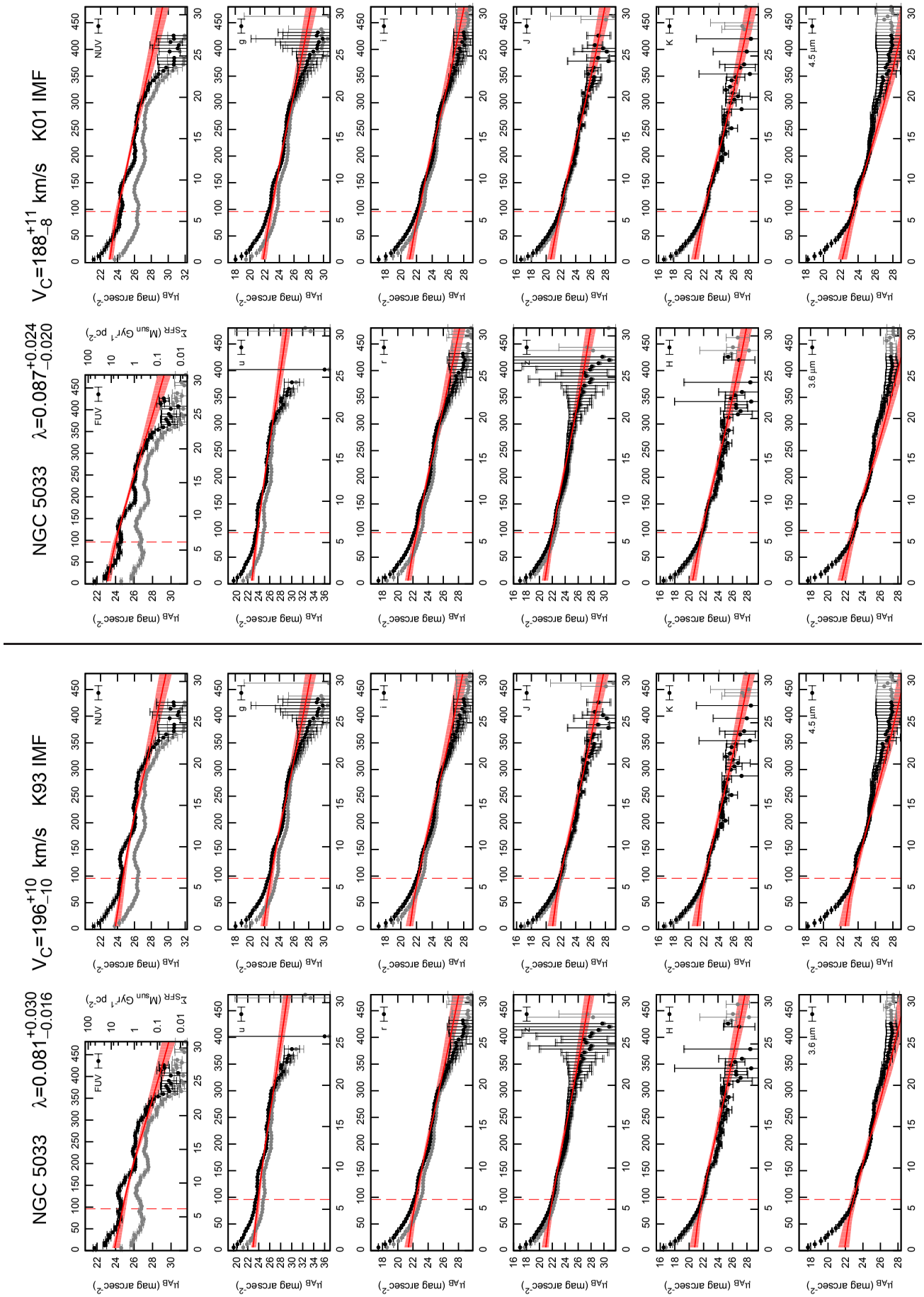
NGC 5033 λ=0.087+0.024−0.020 VC=188+11−8 km/s K01 IMF
NGC 5033 λ=0.081+0.030−0.016 VC=196+10−10 km/s K93 IMF
μAB (mag arcsec-2)
Σ*SFR (Msun Gyr-1 pc-2)
FUV
NUV
u
g
r
i
z
J
H
K
3.6 μm
4.5 μm

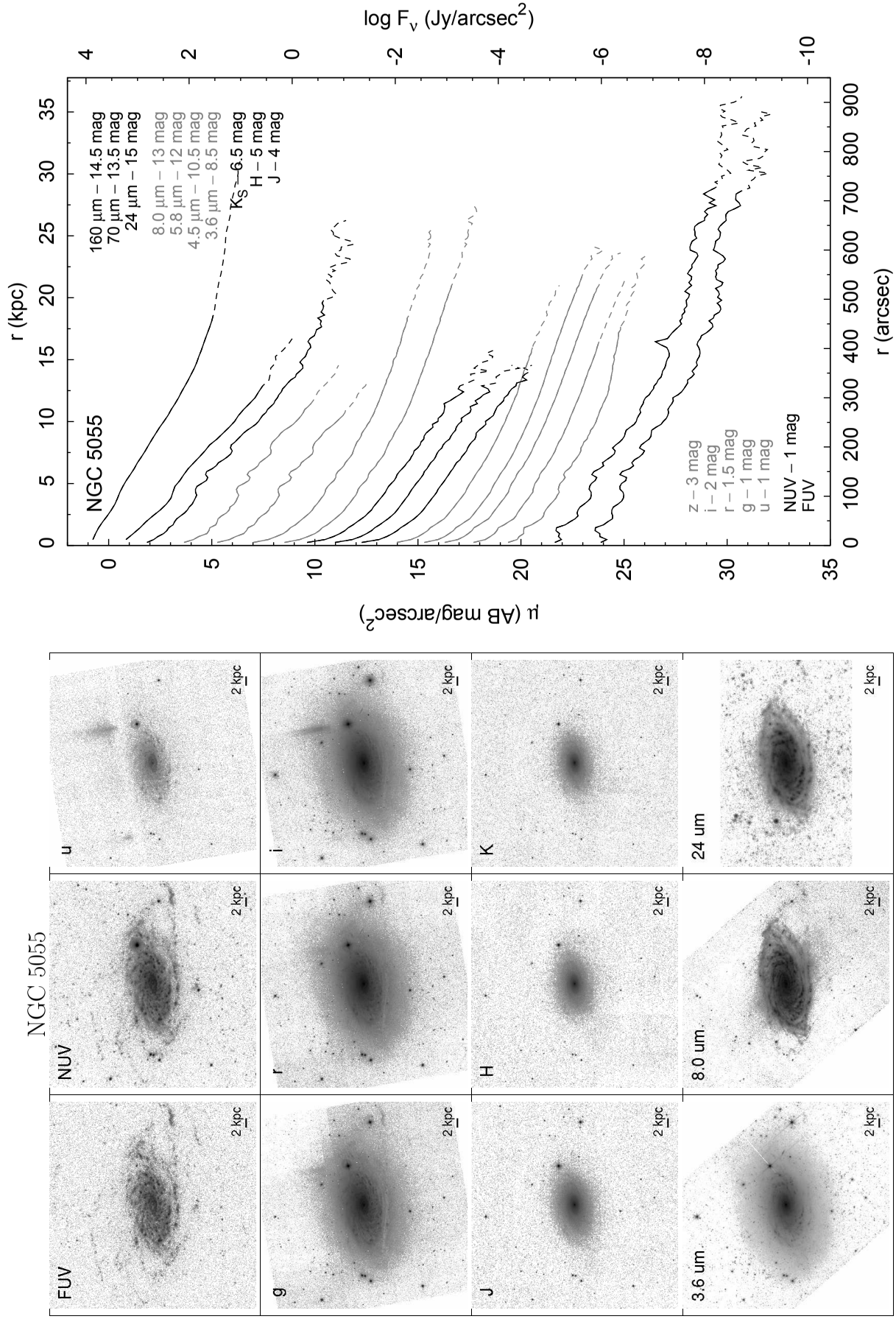
NGC 5055
FUV
NUV
u
g
r
i
J
H
K
3.6 um
8.0 um
24 um
2 kpc
μ (AB mag/arcsec²)
log F_ν (Jy/arcsec²)
r (kpc)
r (arcsec)
NGC 5055
160 μm – 14.5 mag
70 μm – 13.5 mag
24 μm – 15 mag
8.0 μm – 13 mag
5.8 μm – 12 mag
4.5 μm – 10.5 mag
3.6 μm – 8.5 mag
K_S – 6.5 mag
H – 5 mag
J – 4 mag
z – 3 mag
i – 2 mag
r – 1.5 mag
g – 1 mag
u – 1 mag
NUV – 1 mag
FUV

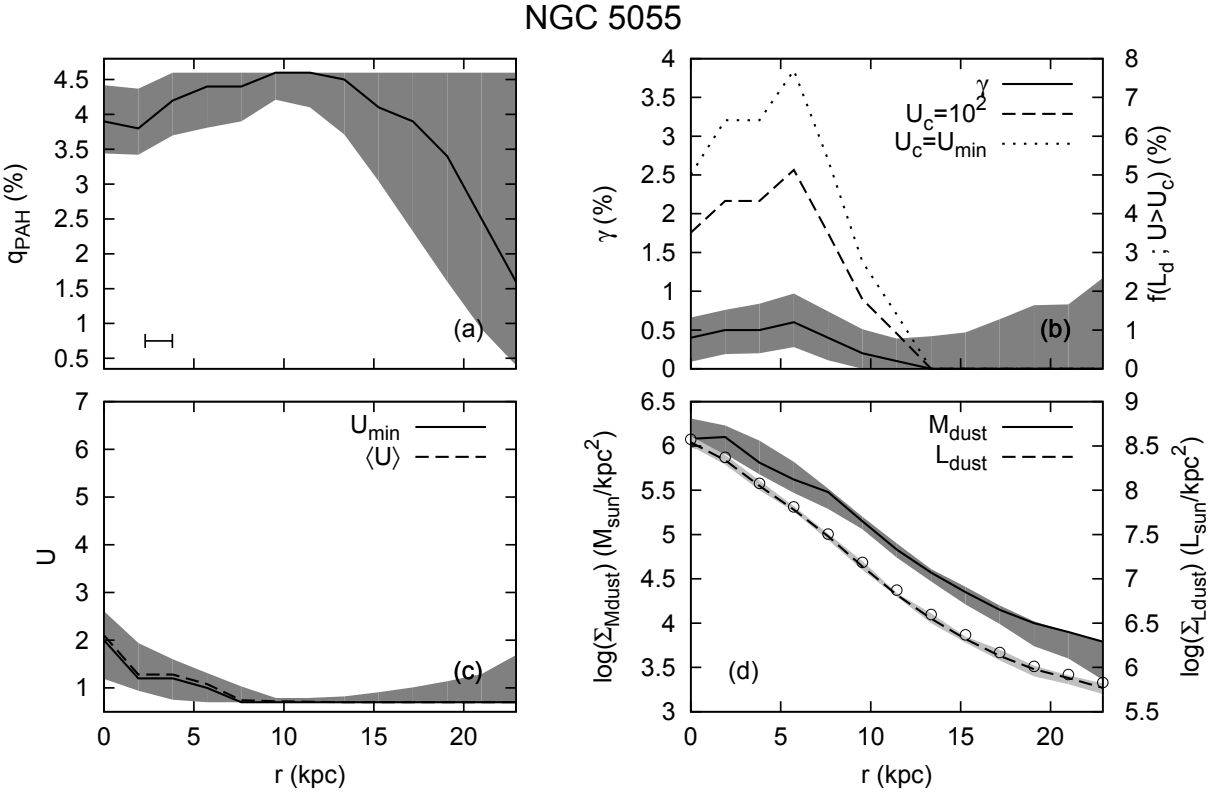
NGC 5055
q_{PAH} (%)
(a)
γ (%)
$f(L_d ; U>U_c)$ (%)
γ
$U_c=10^2$
$U_c=U_{min}$
(b)
U
U_{min}
⟨U⟩
(c)
r (kpc)
$\log(\Sigma_{Mdust})$ (M_{sun}/kpc^2)
$\log(\Sigma_{Ldust})$ (L_{sun}/kpc^2)
M_{dust}
L_{dust}
(d)
r (kpc)

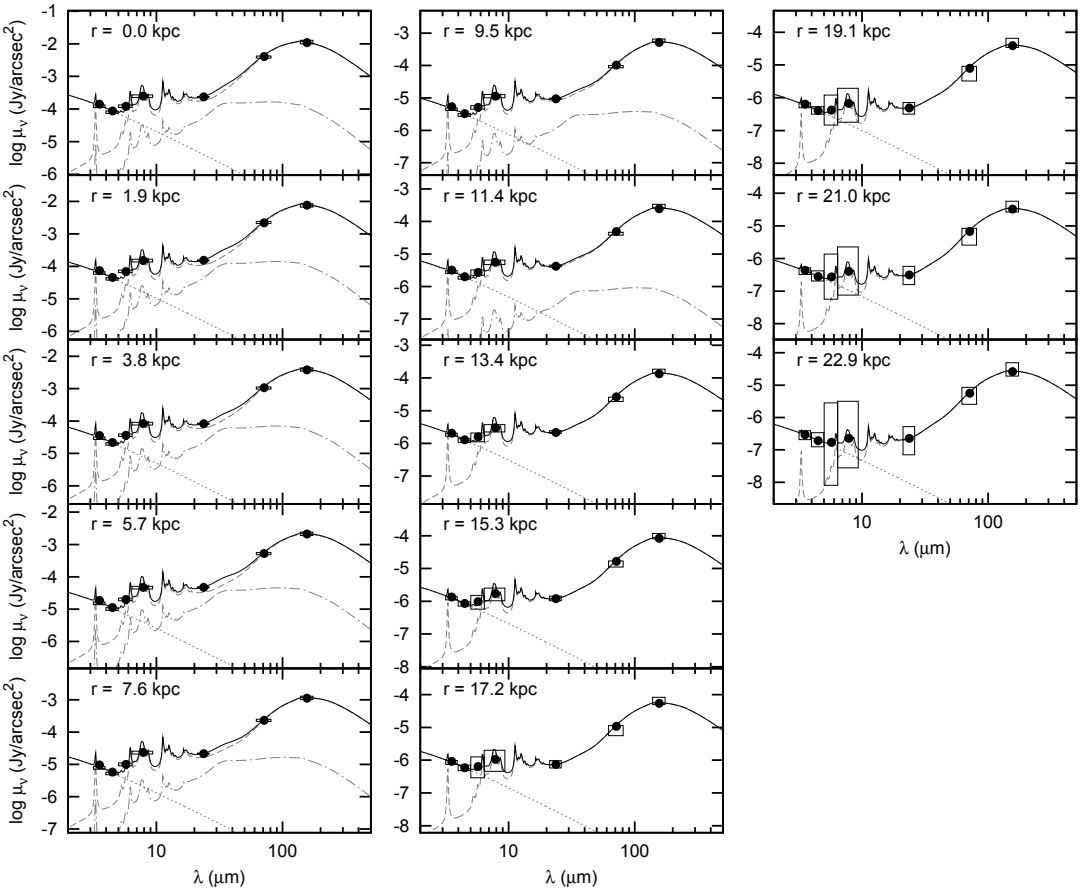
r = 0.0 kpc
r = 1.9 kpc
r = 3.8 kpc
r = 5.7 kpc
r = 7.6 kpc
r = 9.5 kpc
r = 11.4 kpc
r = 13.4 kpc
r = 15.3 kpc
r = 17.2 kpc
r = 19.1 kpc
r = 21.0 kpc
r = 22.9 kpc
log μν (Jy/arcsec^2)
λ (μm)

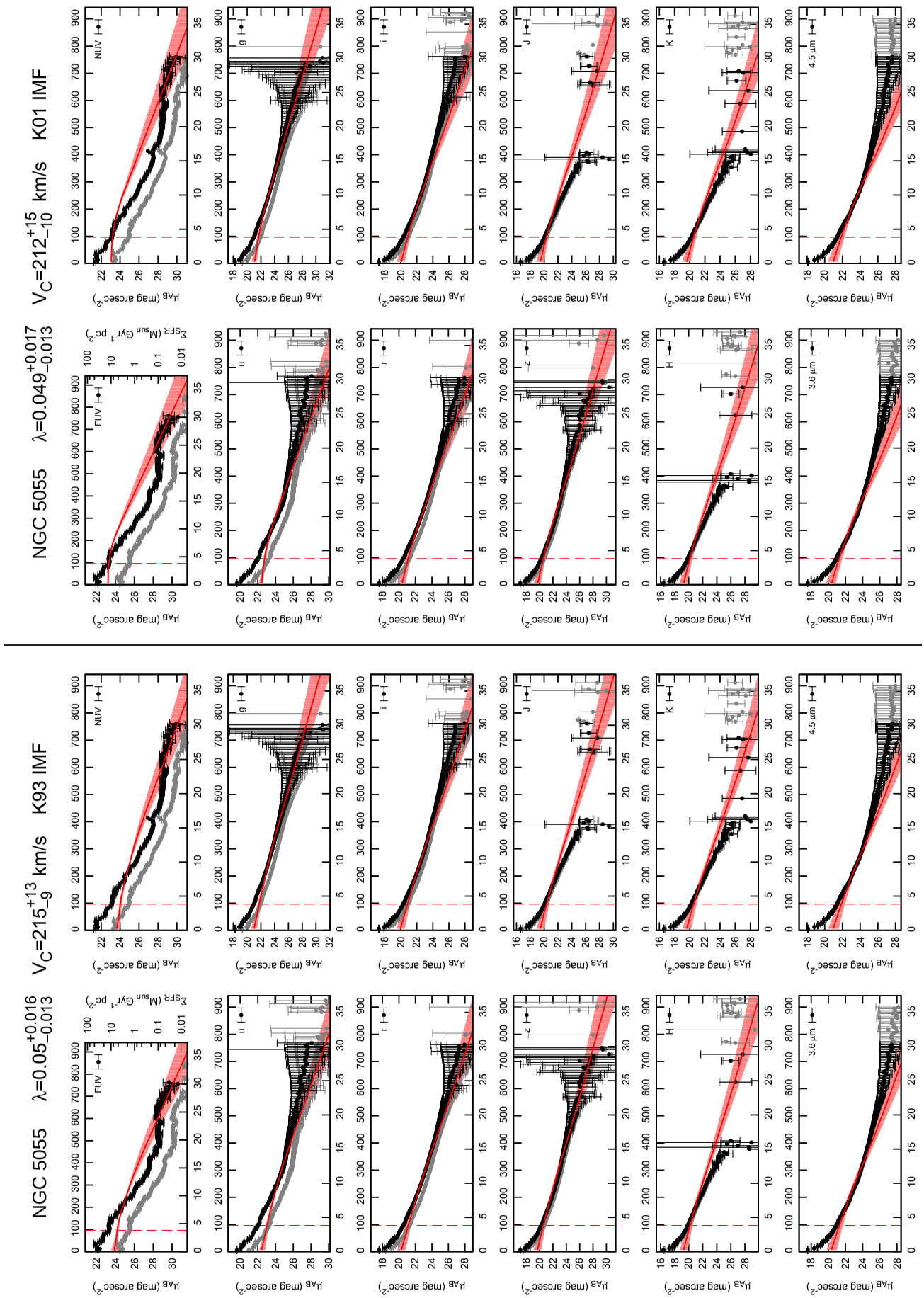
NGC 5055 λ=0.05+0.016−0.013 VC=215+13−9 km/s K93 IMF
NGC 5055 λ=0.049+0.017−0.013 VC=212+15−10 km/s K01 IMF
FUV
NUV
u
g
r
i
z
J
H
K
3.6 μm
4.5 μm
μAB (mag arcsec-2)
ΣSFR (Msun Gyr-1 pc-2)

NGC 5194
FUV
NUV
u
g
r
i
J
H
K
3.6 um
8.0 um
24 um
2 kpc

r (kpc)
0
5
10
15
20
NGC 5194
160 μm – 14.5 mag
70 μm – 13.5 mag
24 μm – 15 mag
8.0 μm – 13 mag
5.8 μm – 12 mag
4.5 μm – 10.5 mag
3.6 μm – 8.5 mag
K_S – 6.5 mag
H – 5 mag
J – 4 mag
z – 3 mag
i – 2 mag
r – 1.5 mag
g – 1 mag
u – 1 mag
NUV – 1 mag
FUV
μ (AB mag/arcsec²)
log F_ν (Jy/arcsec²)
r (arcsec)
0
100
200
300
400
500

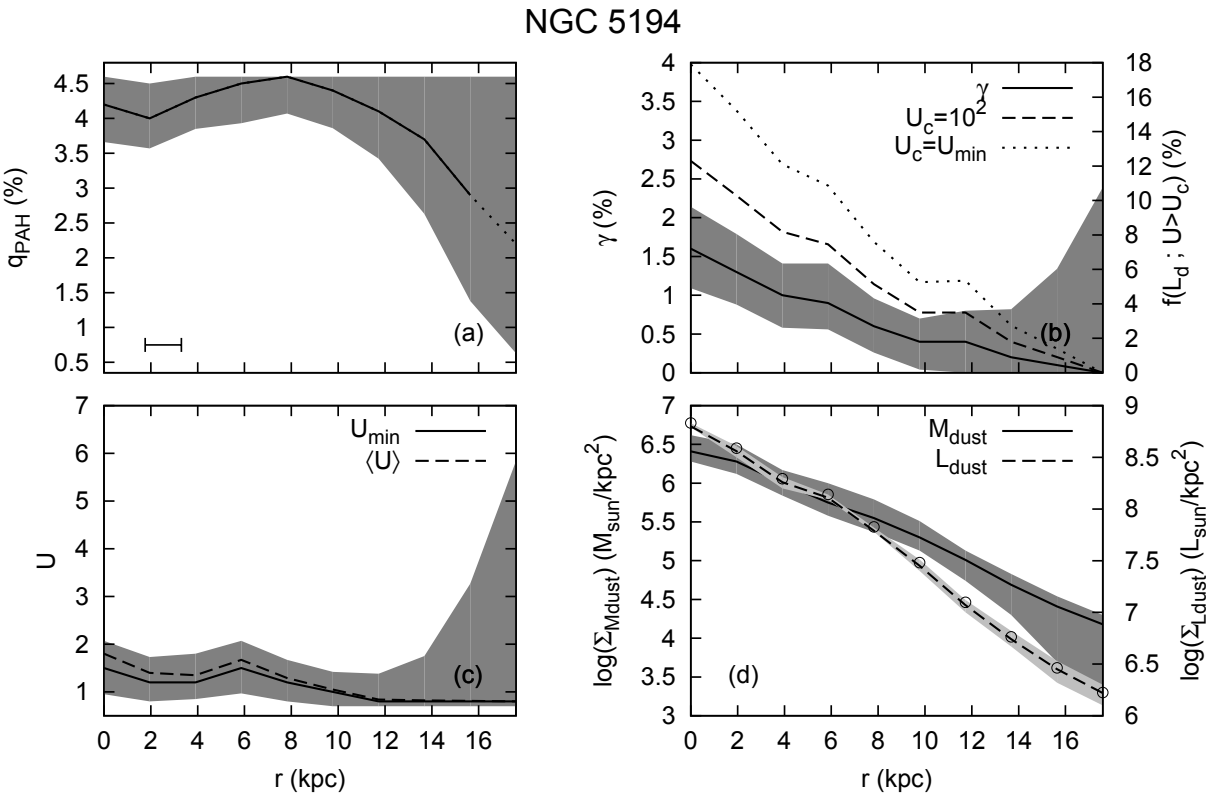
NGC 5194
q_{PAH} (%)
(a)
γ (%)
$U_c=10^2$
$U_c=U_{min}$
$f(L_d\ ;\ U>U_c)$ (%)
(b)
U
U_{min}
⟨U⟩
(c)
r (kpc)
$\log(\Sigma_{Mdust})$ (M_{sun}/kpc^2)
M_{dust}
L_{dust}
(d)
$\log(\Sigma_{Ldust})$ (L_{sun}/kpc^2)
r (kpc)

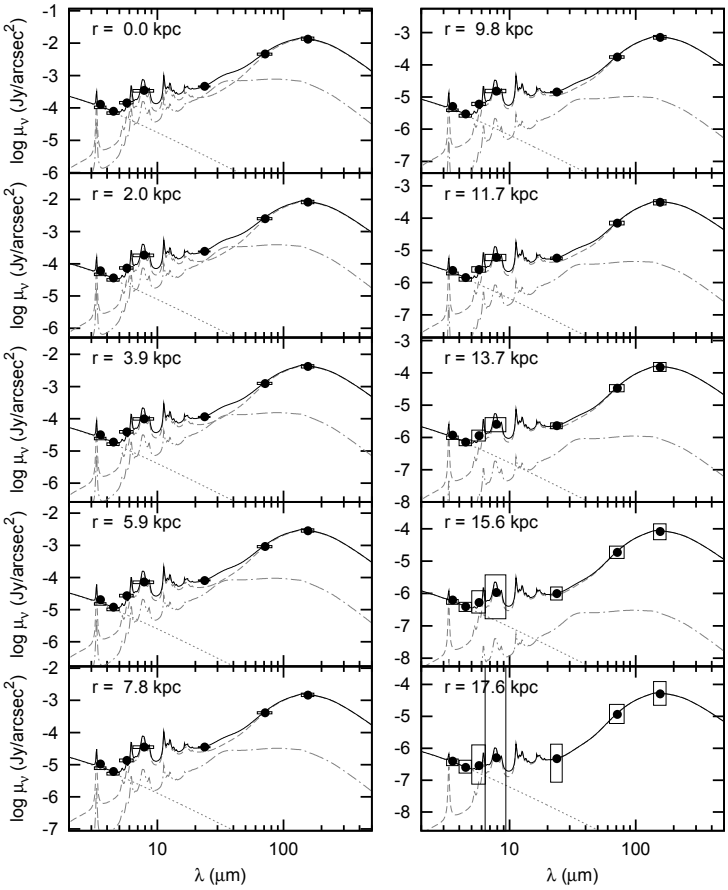
r = 0.0 kpc
r = 2.0 kpc
r = 3.9 kpc
r = 5.9 kpc
r = 7.8 kpc
r = 9.8 kpc
r = 11.7 kpc
r = 13.7 kpc
r = 15.6 kpc
r = 17.6 kpc
log μ_ν (Jy/arcsec^2)
λ (μm)

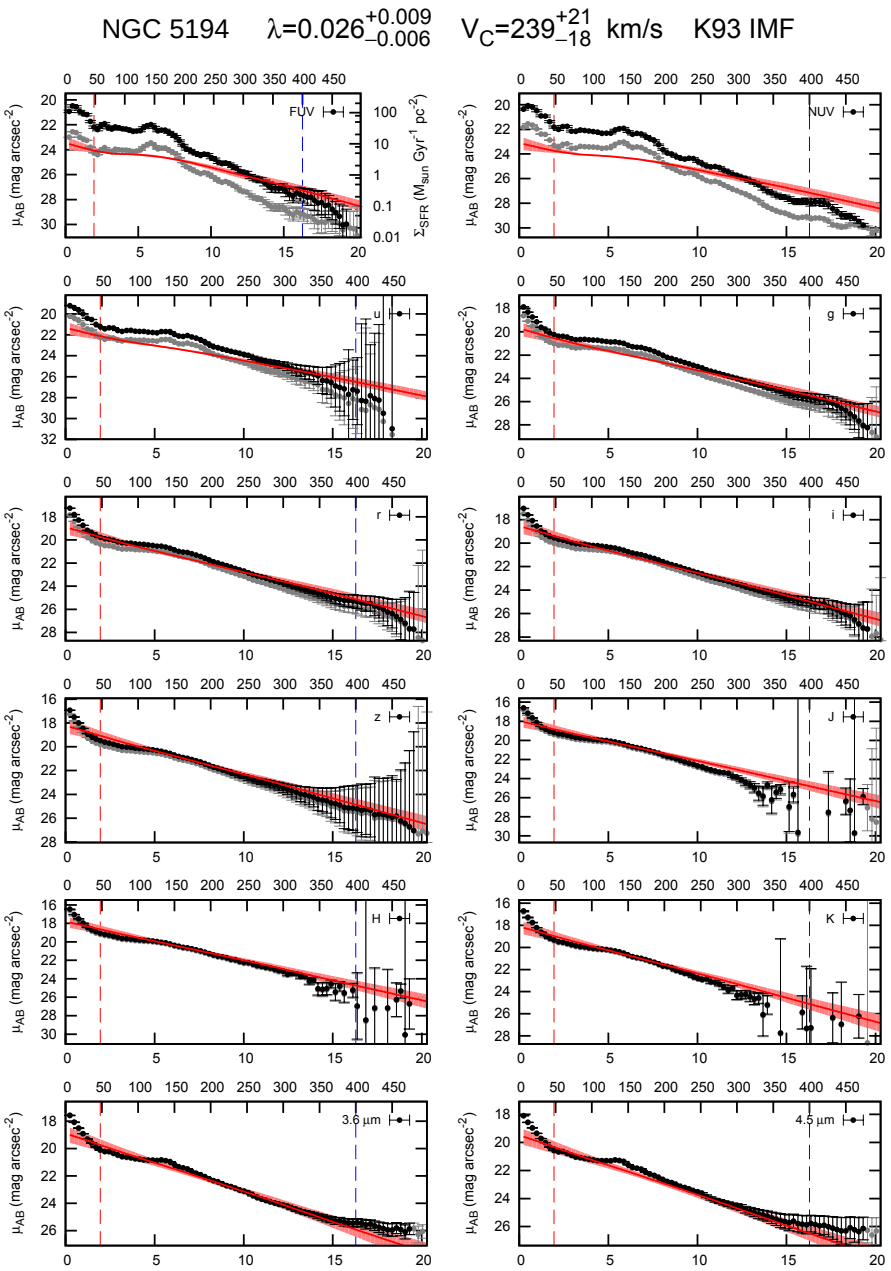
NGC 5194 λ=0.026+0.009−0.006 VC=239+21−18 km/s K93 IMF
FUV
NUV
u
g
r
i
z
J
H
K
3.6 μm
4.5 μm
μAB (mag arcsec−2)
ΣSFR (Msun Gyr−1 pc−2)

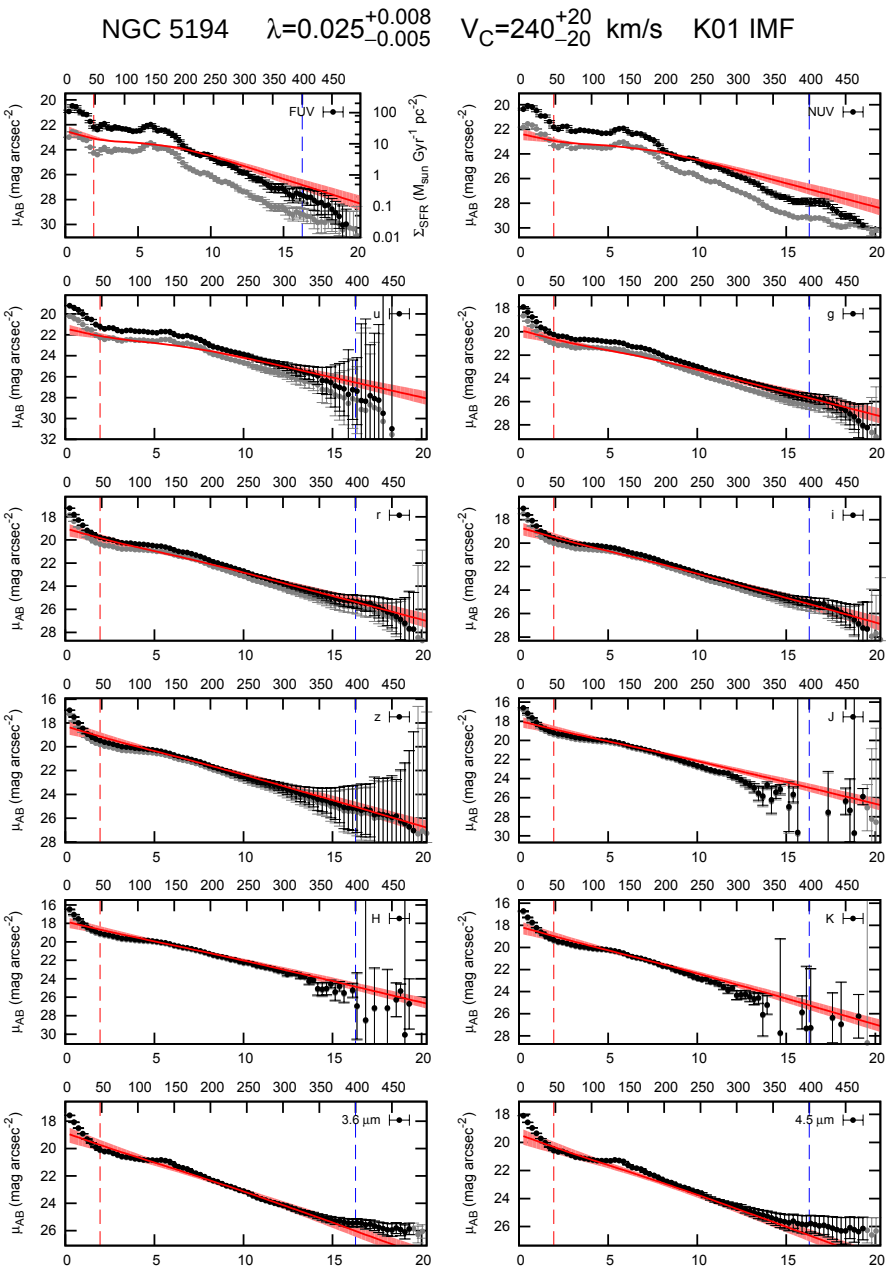
NGC 5194 λ=0.025+0.008−0.005 VC=240+20−20 km/s K01 IMF
FUV
NUV
u
g
r
i
z
J
H
K
3.6 μm
4.5 μm
μAB (mag arcsec−2)
ΣSFR (Msun Gyr−1 pc−2)

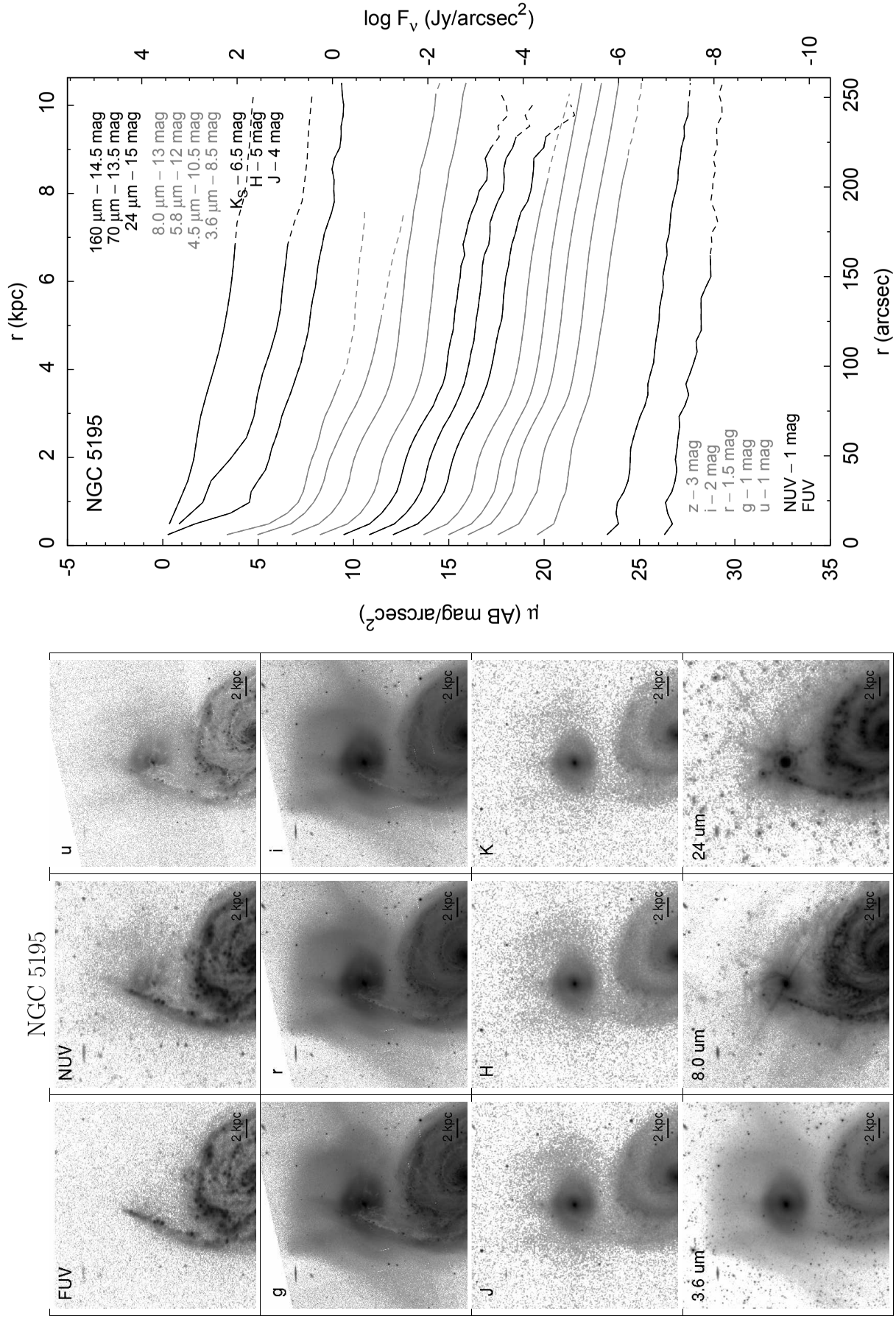
NGC 5195
FUV
NUV
u
g
r
i
J
H
K
3.6 um
8.0 um
24 um
2 kpc
μ (AB mag/arcsec²)
log F_ν (Jy/arcsec²)
r (kpc)
r (arcsec)
NGC 5195
160 μm – 14.5 mag
70 μm – 13.5 mag
24 μm – 15 mag
8.0 μm – 13 mag
5.8 μm – 12 mag
4.5 μm – 10.5 mag
3.6 μm – 8.5 mag
K_s – 6.5 mag
H – 5 mag
J – 4 mag
z – 3 mag
i – 2 mag
r – 1.5 mag
g – 1 mag
u – 1 mag
NUV – 1 mag
FUV

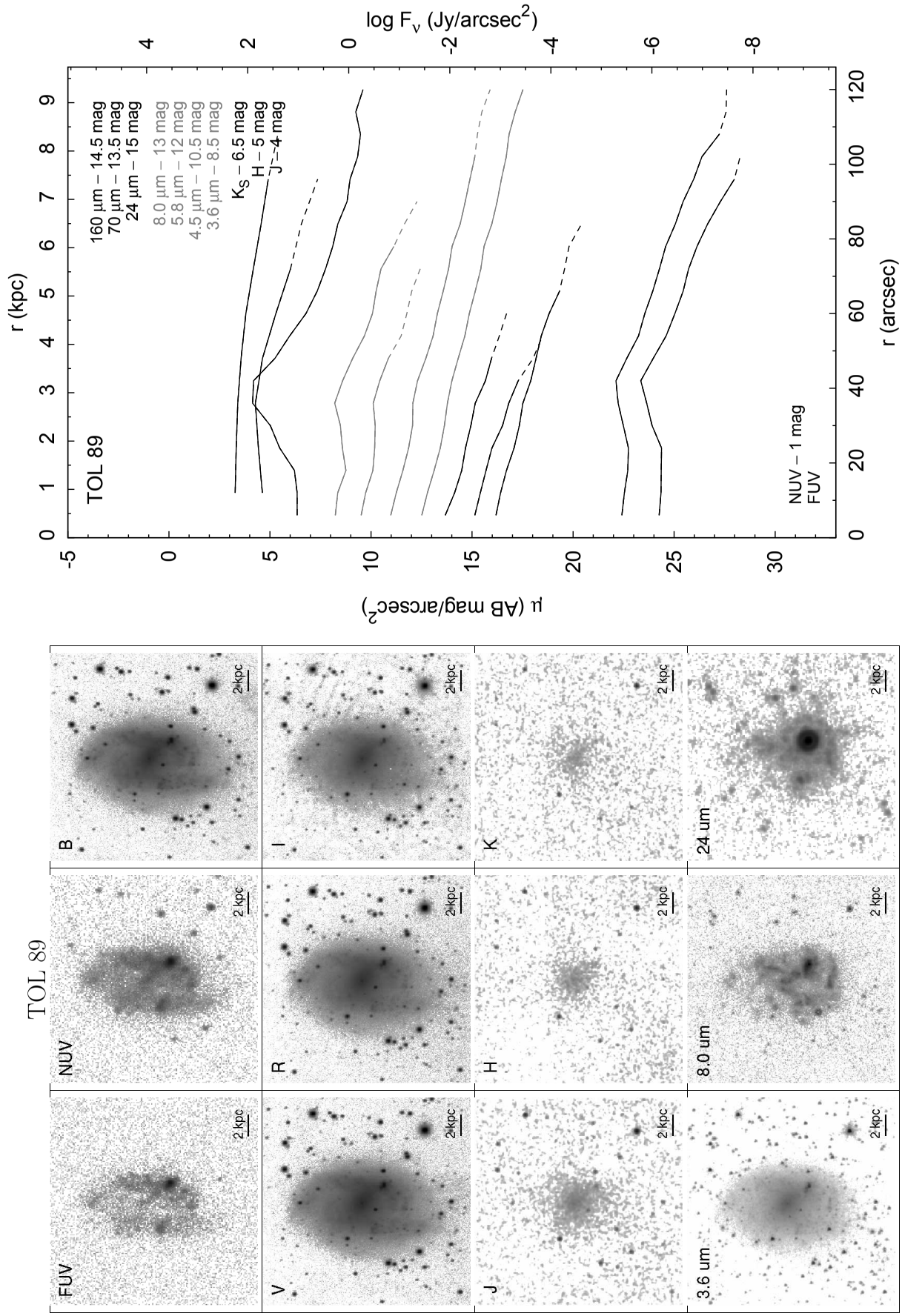
TOL 89
μ (AB mag/arcsec²)
log F_ν (Jy/arcsec²)
r (kpc)
r (arcsec)
TOL 89
160 μm – 14.5 mag
70 μm – 13.5 mag
24 μm – 15 mag
8.0 μm – 13 mag
5.8 μm – 12 mag
4.5 μm – 10.5 mag
3.6 μm – 8.5 mag
K_S – 6.5 mag
H – 5 mag
J – 4 mag
NUV – 1 mag
FUV
FUV
NUV
B
V
R
I
J
H
K
3.6 um
8.0 um
24 um
2 kpc

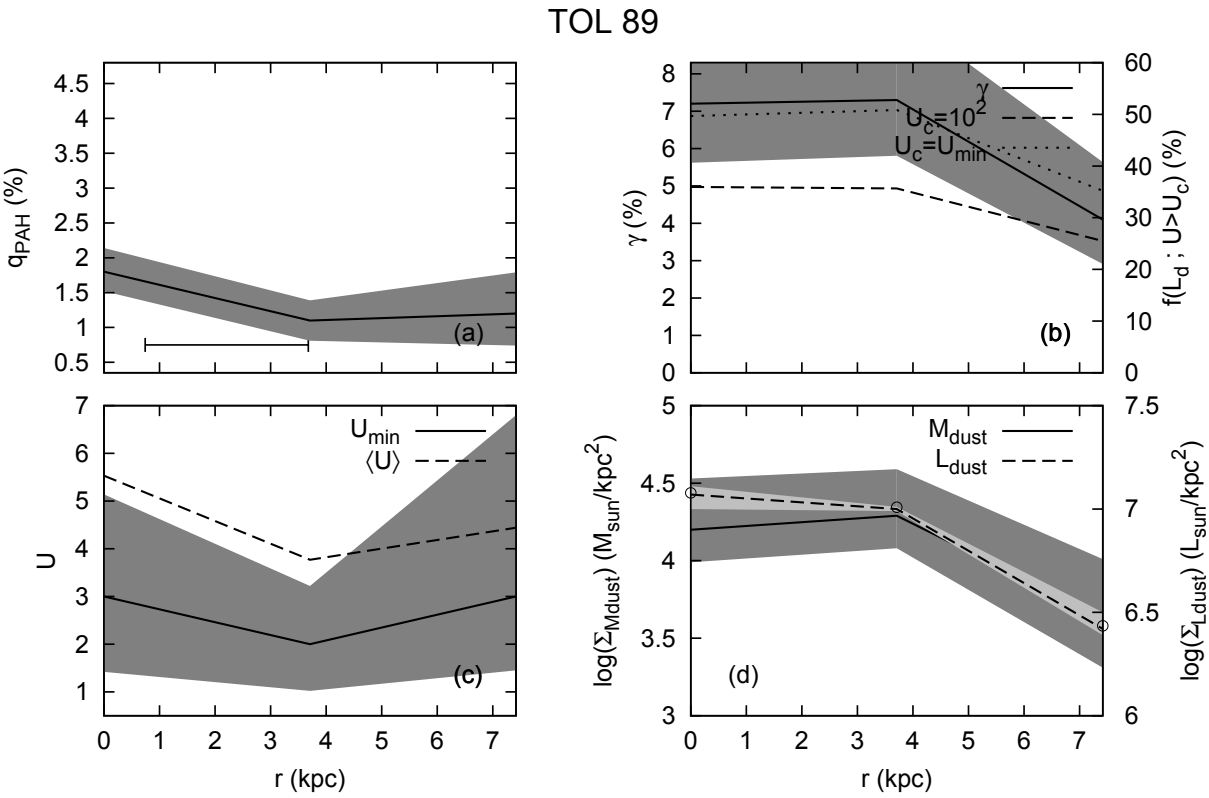
TOL 89
q_{PAH} (%)
(a)
γ (%)
$f(L_d ; U>U_c)$ (%)
γ
$U_c=10^2$
$U_c=U_{min}$
(b)
U
U_{min}
⟨U⟩
(c)
r (kpc)
$\log(\Sigma_{Mdust})$ (M_{sun}/kpc^2)
$\log(\Sigma_{Ldust})$ (L_{sun}/kpc^2)
M_{dust}
L_{dust}
(d)
r (kpc)

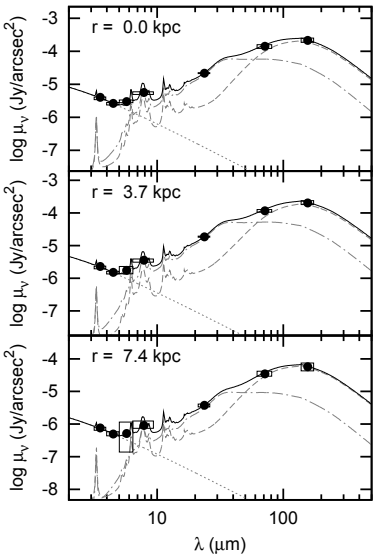
r = 0.0 kpc
r = 3.7 kpc
r = 7.4 kpc
log μ_ν (Jy/arcsec^2)
λ (μm)

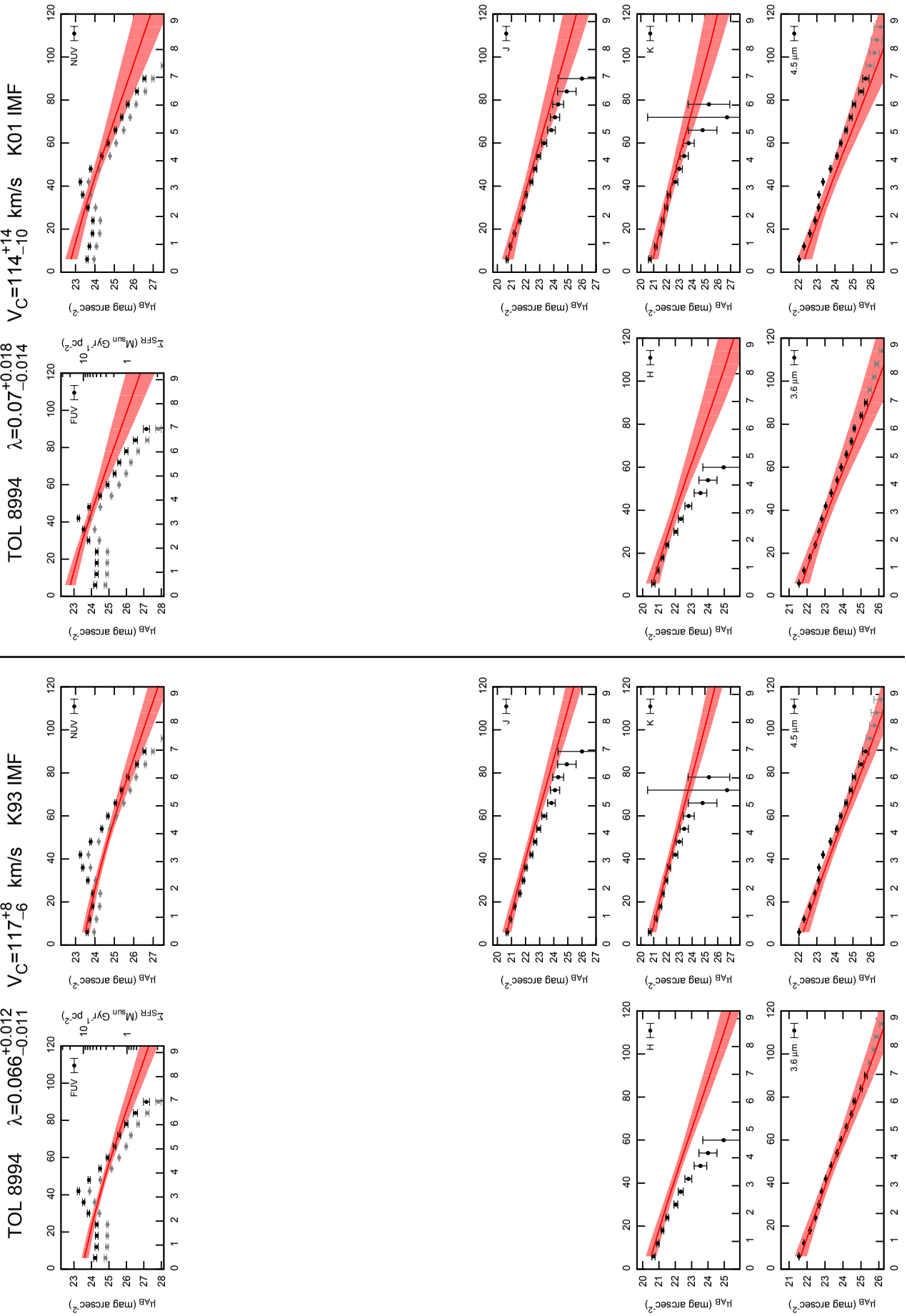
TOL 8994 λ=0.07+0.018−0.014 VC=114+14−10 km/s K01 IMF
TOL 8994 λ=0.066+0.012−0.011 VC=117+8−6 km/s K93 IMF
NUV
FUV
J
K
H
4.5 μm
3.6 μm
μAB (mag arcsec-2)
ΣSFR (Msun Gyr-1 pc-2)

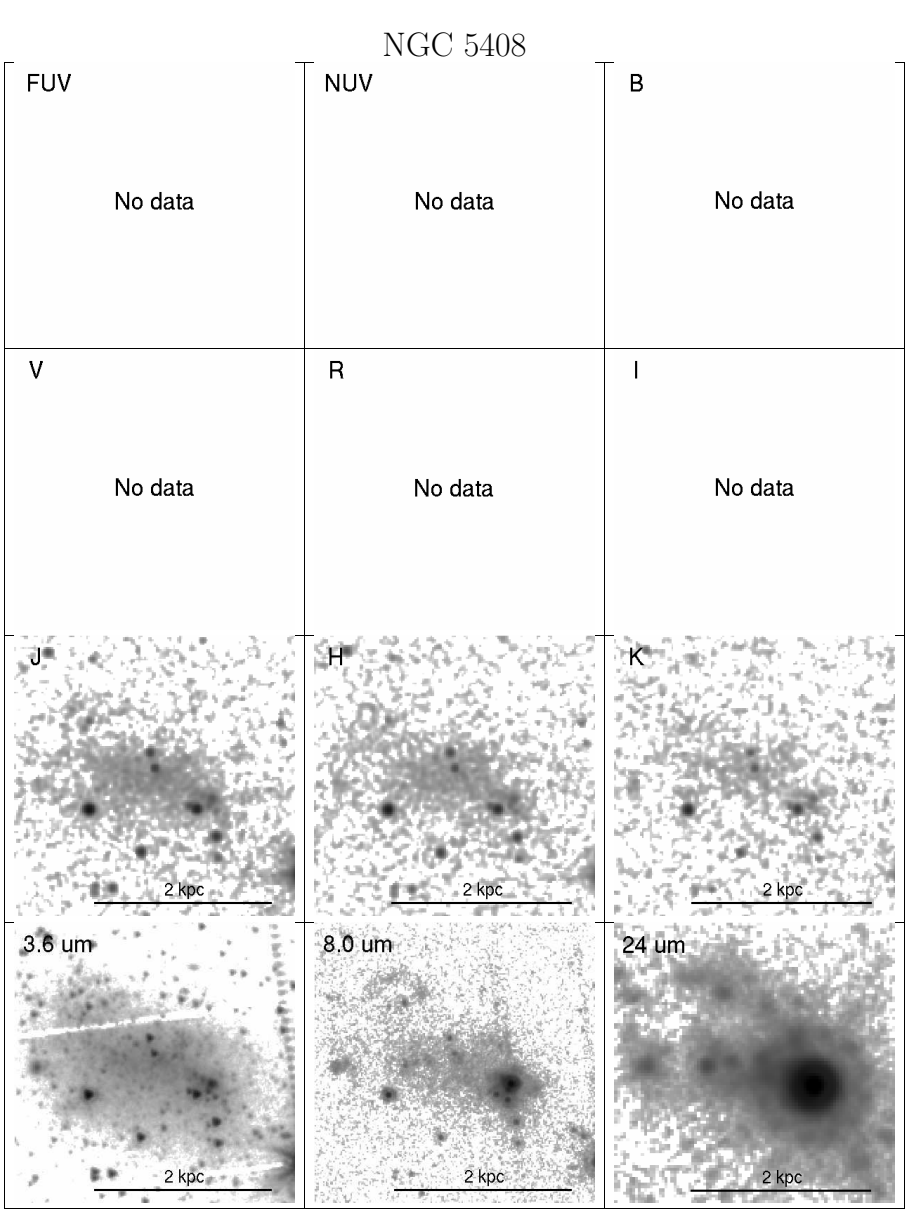
NGC 5408
FUV
No data
NUV
No data
B
No data
V
No data
R
No data
I
No data
J
2 kpc
H
2 kpc
K
2 kpc
3.6 um
2 kpc
8.0 um
2 kpc
24 um
2 kpc

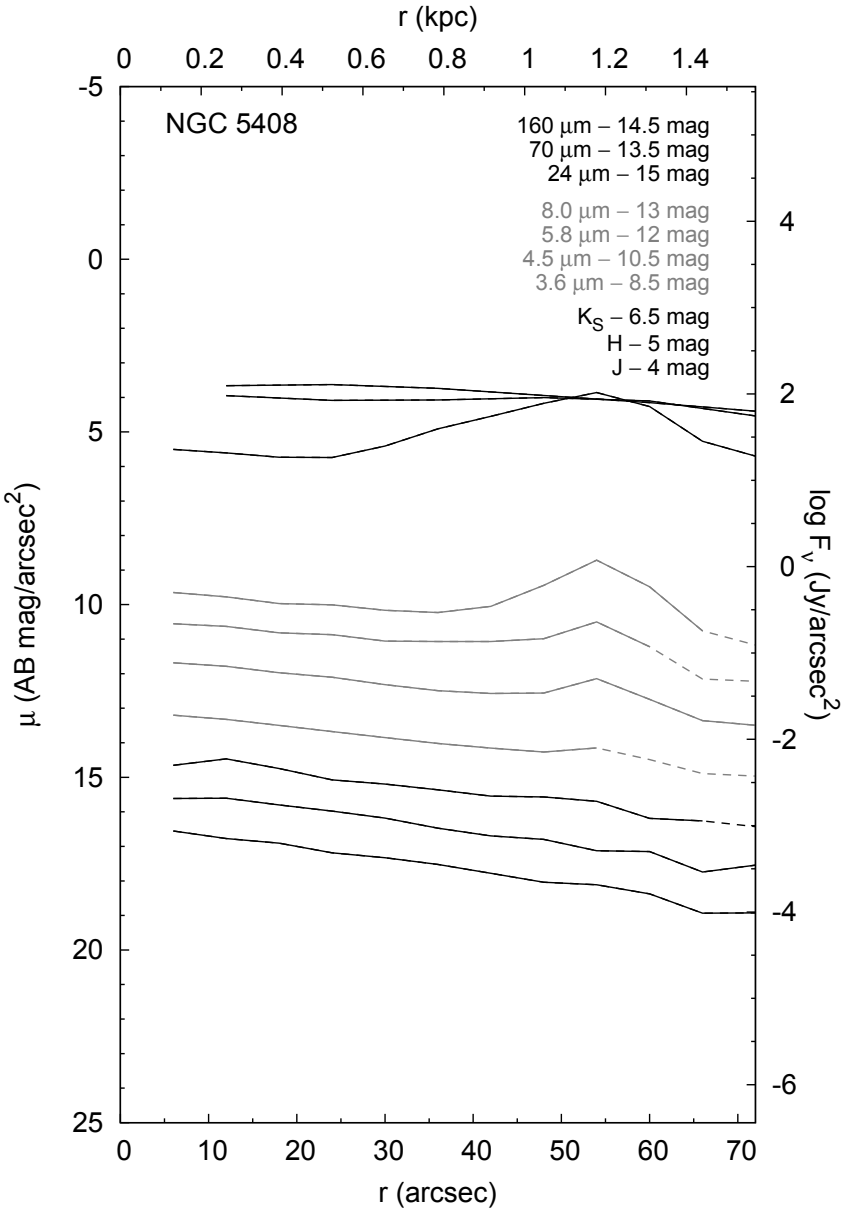
r (kpc)
0
0.2
0.4
0.6
0.8
1
1.2
1.4
NGC 5408
160 μm – 14.5 mag
70 μm – 13.5 mag
24 μm – 15 mag
8.0 μm – 13 mag
5.8 μm – 12 mag
4.5 μm – 10.5 mag
3.6 μm – 8.5 mag
K_S – 6.5 mag
H – 5 mag
J – 4 mag
μ (AB mag/arcsec²)
log F_ν (Jy/arcsec²)
r (arcsec)
0
10
20
30
40
50
60
70
-5
0
5
10
15
20
25
4
2
0
-2
-4
-6

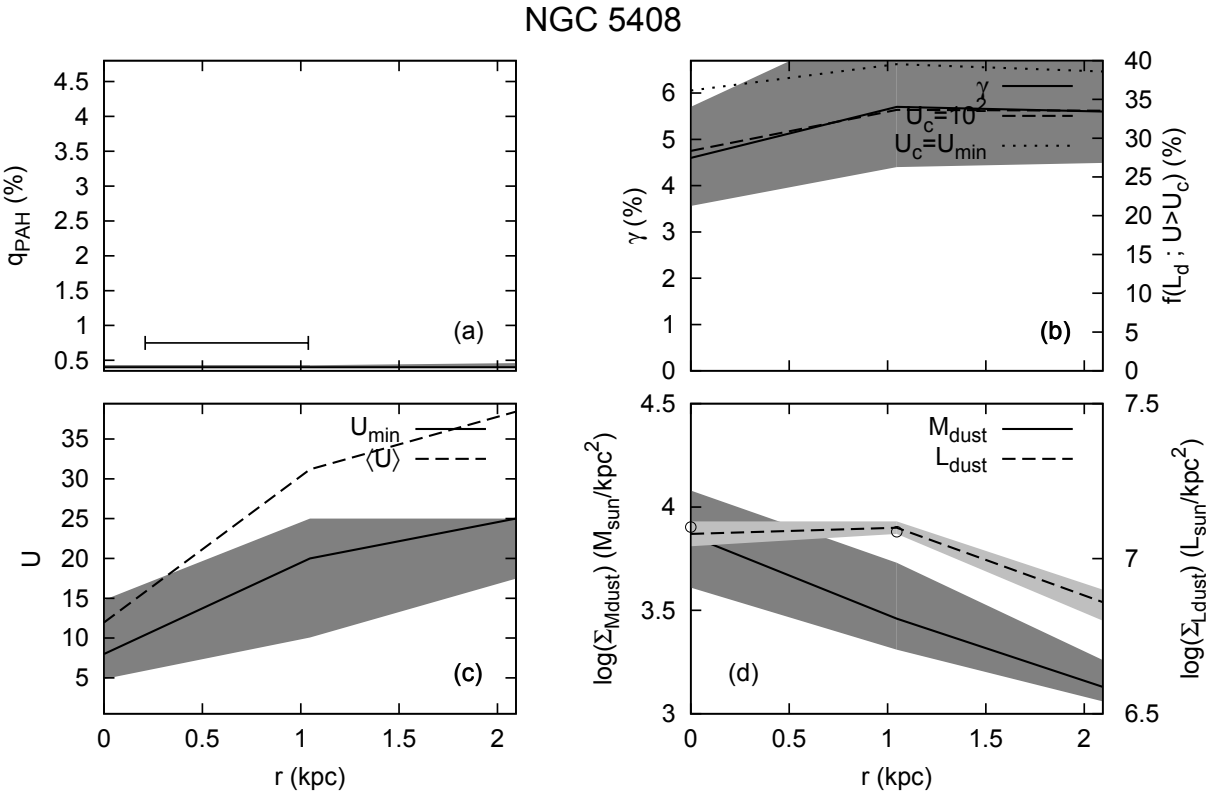
NGC 5408
q_{PAH} (%)
(a)
γ
U_c=10
U_c=U_{min}
γ (%)
$f(L_d ; U>U_c)$ (%)
(b)
U_{min}
⟨U⟩
U
(c)
r (kpc)
M_{dust}
L_{dust}
$\log(\Sigma_{Mdust})$ (M_{sun}/kpc^2)
$\log(\Sigma_{Ldust})$ (L_{sun}/kpc^2)
(d)
r (kpc)

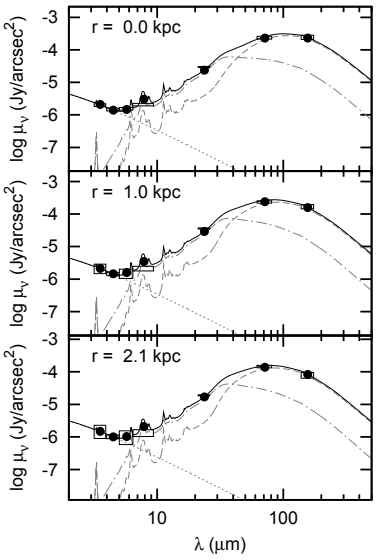
r = 0.0 kpc
r = 1.0 kpc
r = 2.1 kpc
log μ_ν (Jy/arcsec^2)
λ (μm)

NGC 5474
FUV
NUV
u
g
r
i
J
H
K
3.6 um
8.0 um
24 um
2 kpc

r (kpc)
NGC 5474
160 μm – 14.5 mag
70 μm – 13.5 mag
24 μm – 15 mag
8.0 μm – 13 mag
5.8 μm – 12 mag
4.5 μm – 10.5 mag
3.6 μm – 8.5 mag
K_S – 6.5 mag
H – 5 mag
J – 4 mag
z – 3 mag
i – 2 mag
r – 1.5 mag
g – 1 mag
u – 1 mag
NUV – 1 mag
FUV
μ (AB mag/arcsec²)
log F_ν (Jy/arcsec²)
r (arcsec)

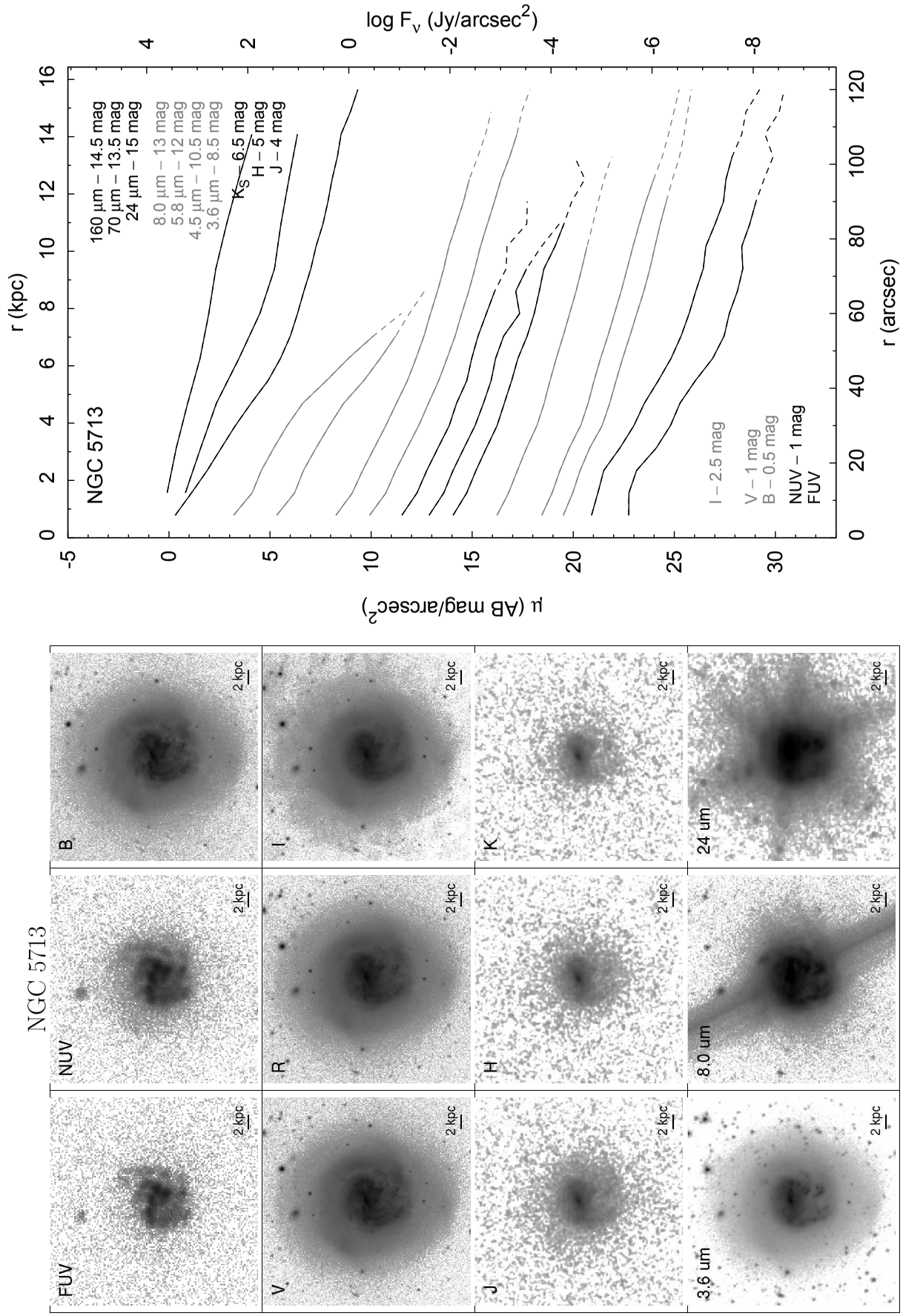
NGC 5713
FUV
NUV
B
V
R
I
J
H
K
3.6 um
8.0 um
24 um
2 kpc
μ (AB mag/arcsec²)
r (kpc)
r (arcsec)
log F_ν (Jy/arcsec²)
NGC 5713
160 μm – 14.5 mag
70 μm – 13.5 mag
24 μm – 15 mag
8.0 μm – 13 mag
5.8 μm – 12 mag
4.5 μm – 10.5 mag
3.6 μm – 8.5 mag
K_S – 6.5 mag
H – 5 mag
J – 4 mag
I – 2.5 mag
V – 1 mag
B – 0.5 mag
NUV – 1 mag
FUV

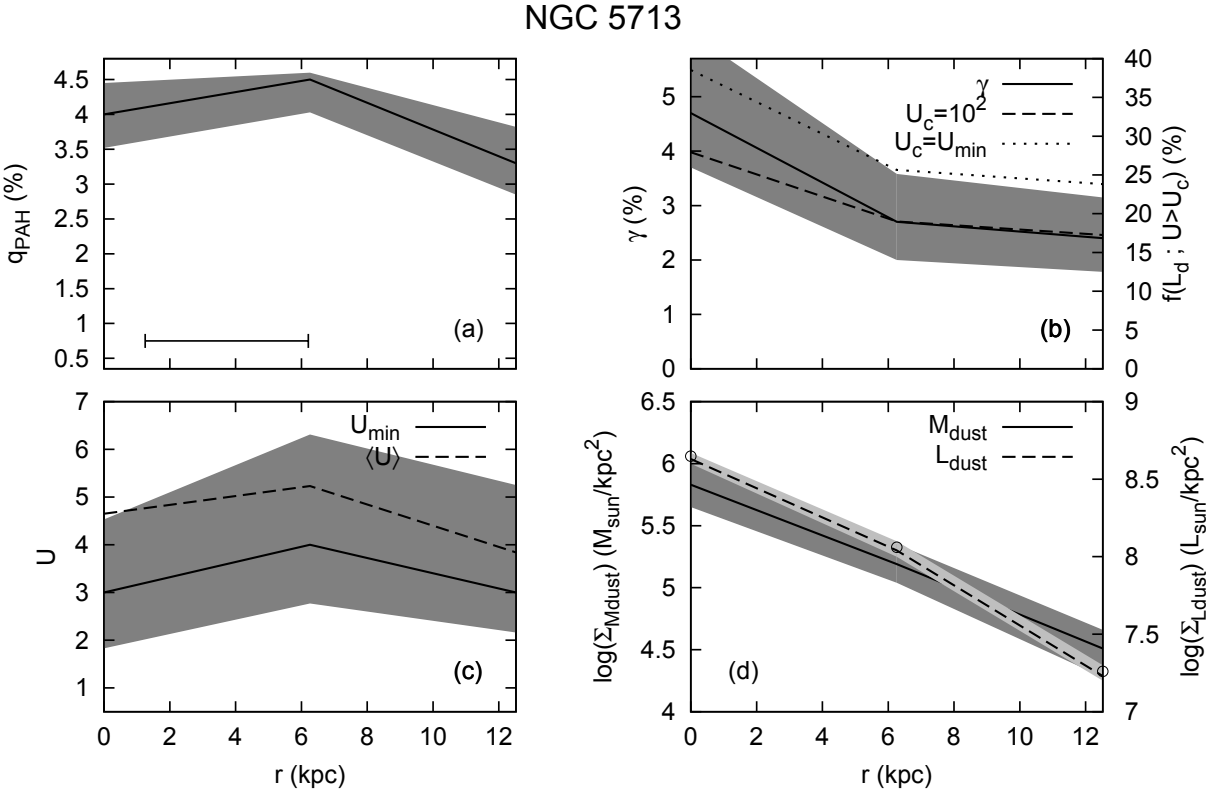
NGC 5713
q_{PAH} (%)
(a)
γ
$U_c=10^2$
$U_c=U_{min}$
γ (%)
$f(L_d ; U>U_c)$ (%)
(b)
U_{min}
⟨U⟩
U
(c)
r (kpc)
M_{dust}
L_{dust}
$\log(\Sigma_{Mdust})$ (M_{sun}/kpc^2)
$\log(\Sigma_{Ldust})$ (L_{sun}/kpc^2)
(d)
r (kpc)

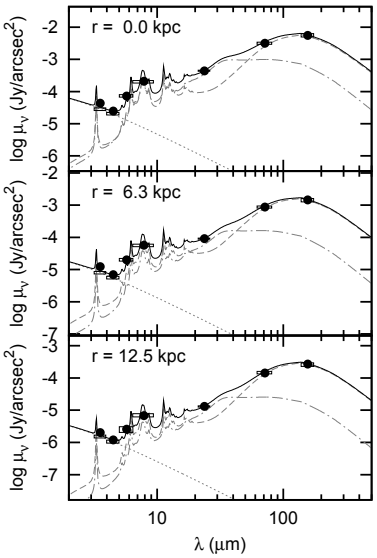
r = 0.0 kpc
r = 6.3 kpc
r = 12.5 kpc
log μ_ν (Jy/arcsec^2)
λ (μm)

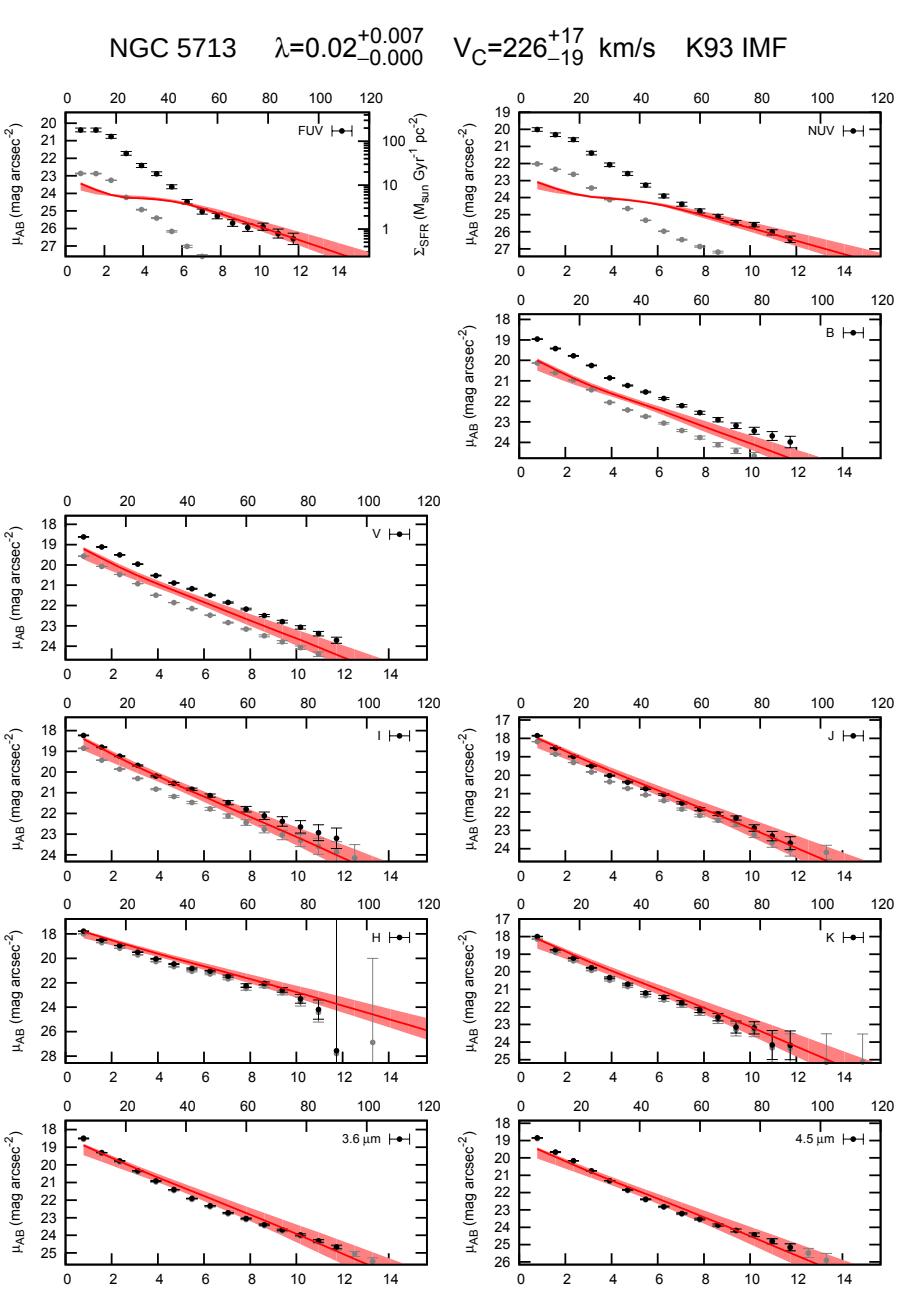
NGC 5713 λ=0.02+0.007−0.000 VC=226+17−19 km/s K93 IMF
FUV
NUV
B
V
I
J
H
K
3.6 μm
4.5 μm
μAB (mag arcsec−2)
ΣSFR (Msun Gyr−1 pc−2)

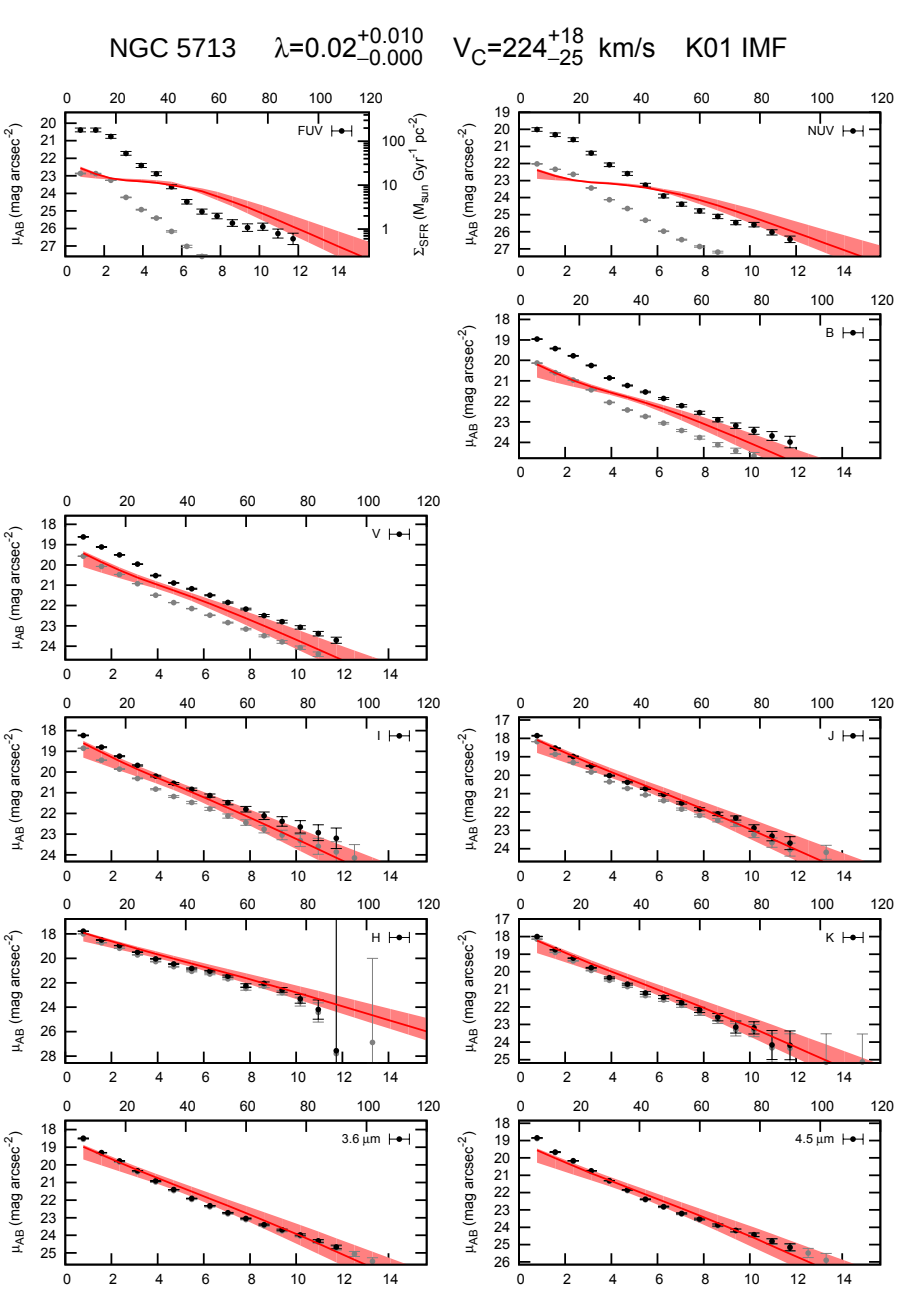
NGC 5713 λ=0.02+0.010−0.000 VC=224+18−25 km/s K01 IMF
FUV
NUV
B
V
I
J
H
K
3.6 μm
4.5 μm
μAB (mag arcsec−2)
ΣSFR (Msun Gyr−1 pc−2)

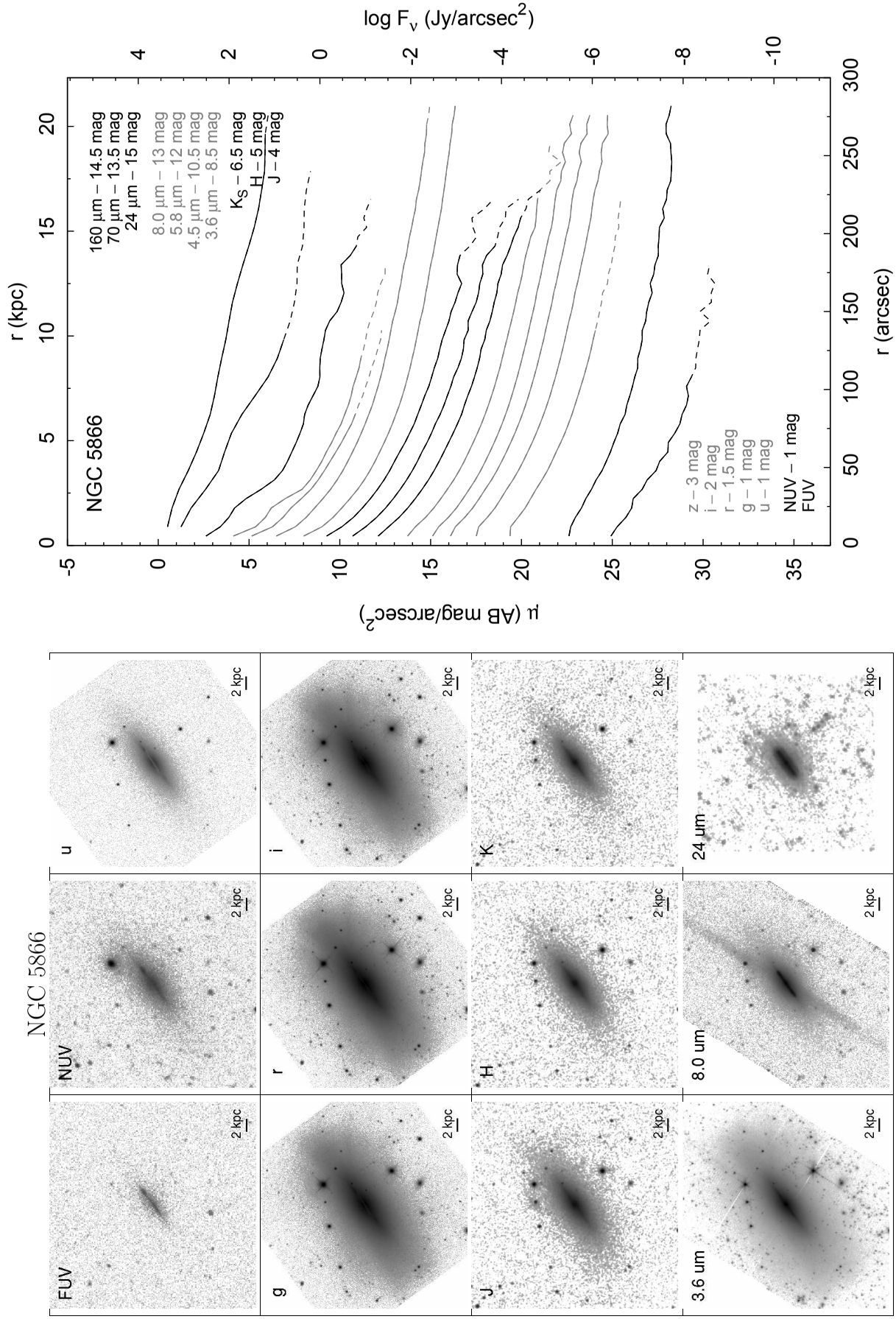
NGC 5866
FUV
NUV
u
g
r
i
J
H
K
3.6 um
8.0 um
24 μm
2 kpc
μ (AB mag/arcsec²)
log F_ν (Jy/arcsec²)
r (kpc)
r (arcsec)
160 μm – 14.5 mag
70 μm – 13.5 mag
24 μm – 15 mag
8.0 μm – 13 mag
5.8 μm – 12 mag
4.5 μm – 10.5 mag
3.6 μm – 8.5 mag
K_S – 6.5 mag
H – 5 mag
J – 4 mag
z – 3 mag
i – 2 mag
r – 1.5 mag
g – 1 mag
u – 1 mag
NUV – 1 mag
FUV

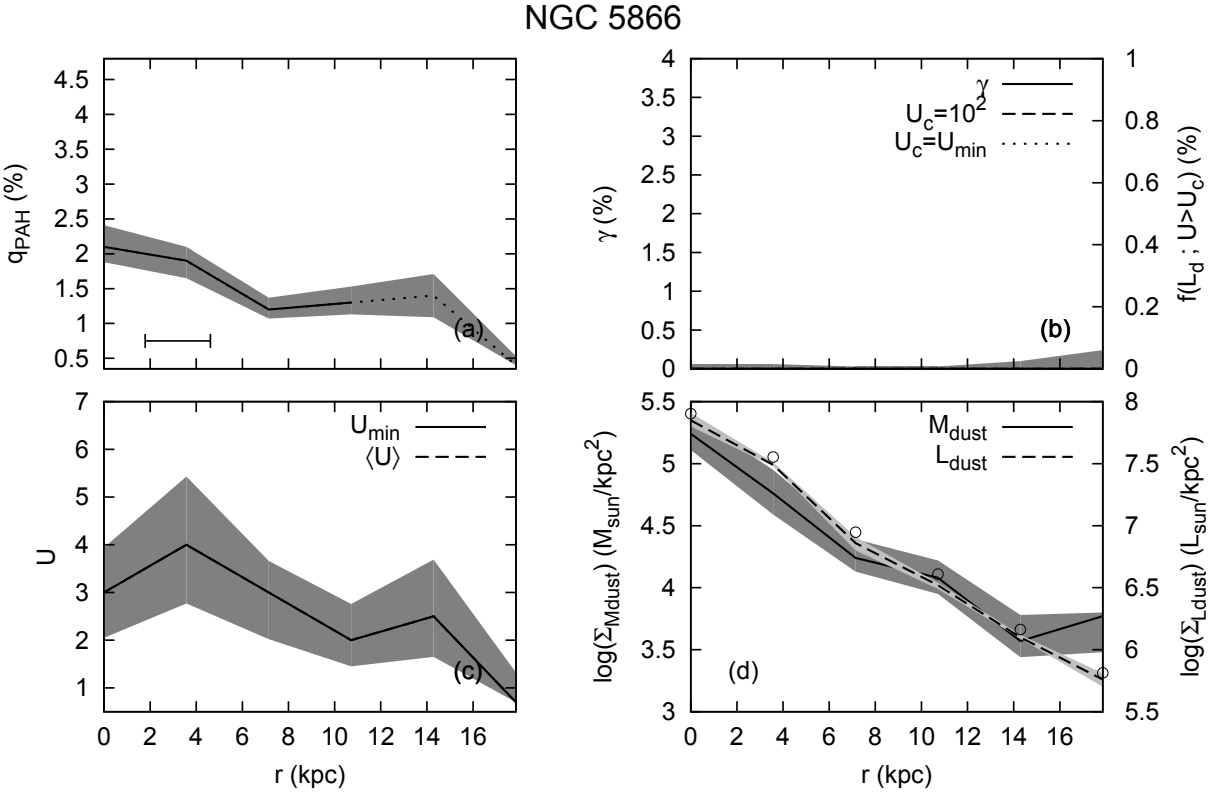
NGC 5866
q_{PAH} (%)
(a)
γ
$U_c=10^2$
$U_c=U_{min}$
γ (%)
$f(L_d ; U>U_c)$ (%)
(b)
U_{min}
⟨U⟩
U
(c)
r (kpc)
M_{dust}
L_{dust}
$\log(\Sigma_{Mdust})$ (M_{sun}/kpc^2)
$\log(\Sigma_{Ldust})$ (L_{sun}/kpc^2)
(d)
r (kpc)

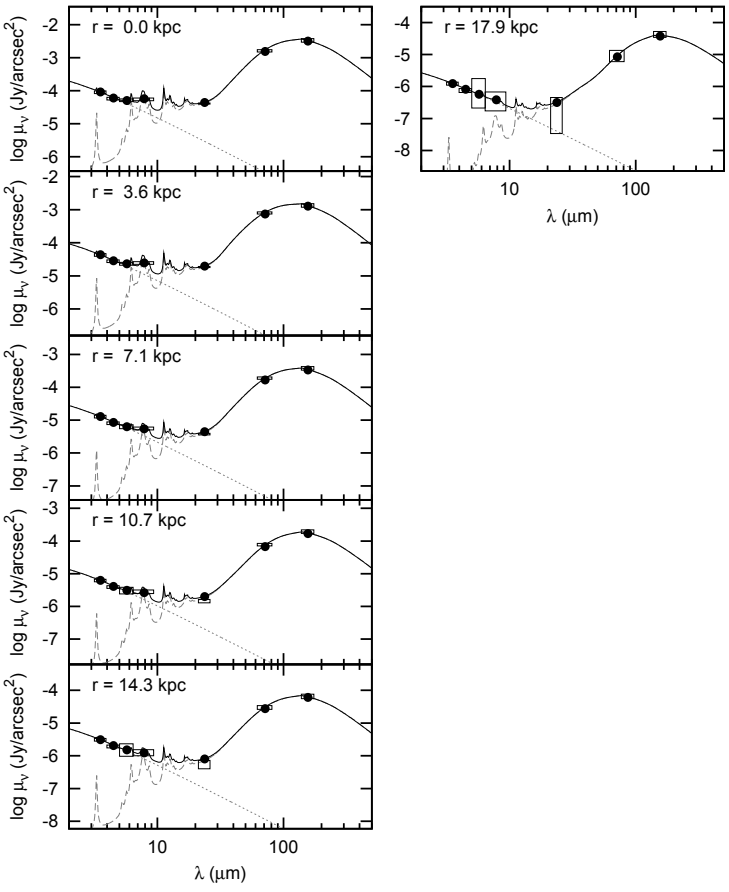
r = 0.0 kpc
r = 3.6 kpc
r = 7.1 kpc
r = 10.7 kpc
r = 14.3 kpc
r = 17.9 kpc
log μ_ν (Jy/arcsec^2)
λ (μm)

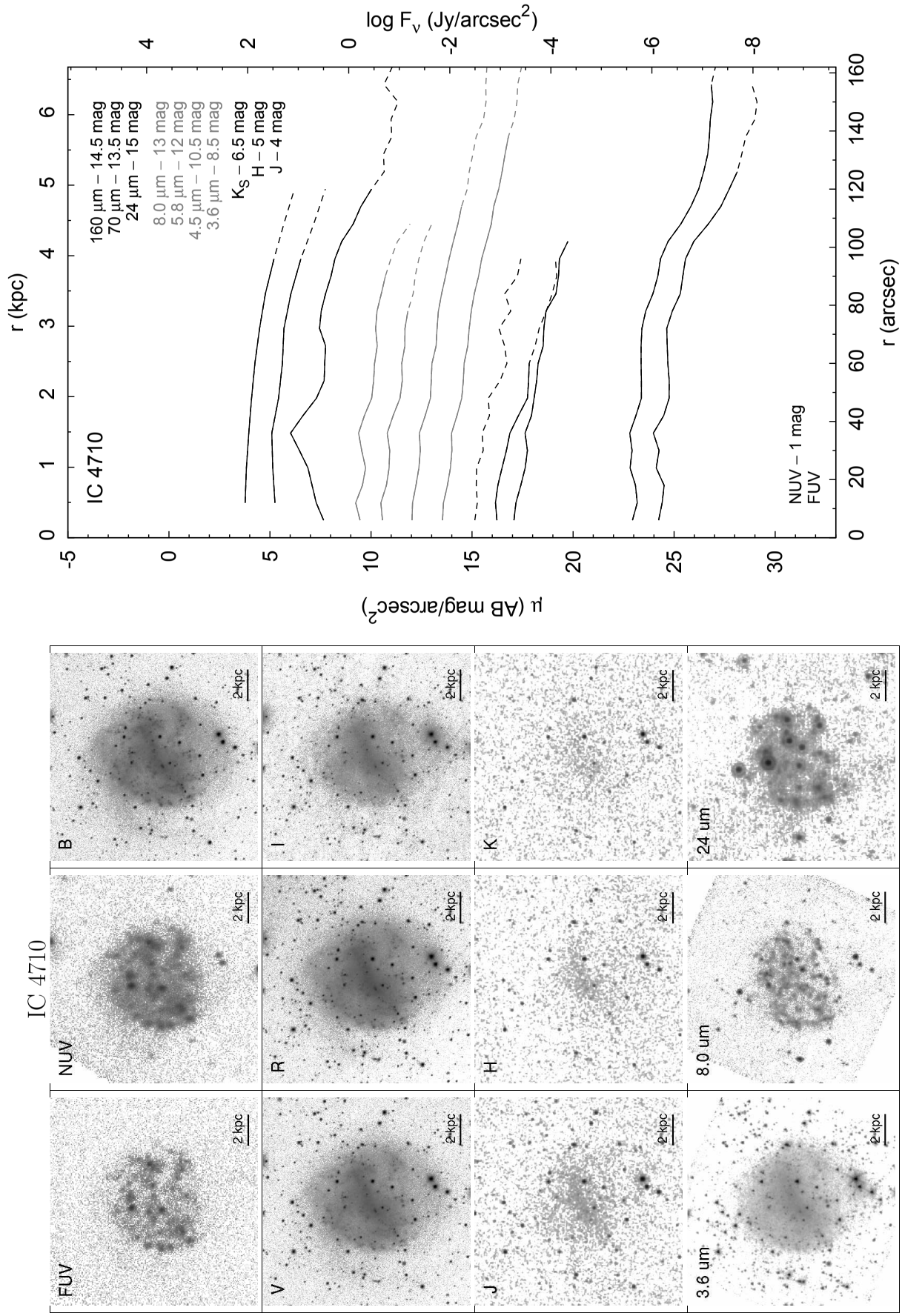
IC 4710
160 μm – 14.5 mag
70 μm – 13.5 mag
24 μm – 15 mag
8.0 μm – 13 mag
5.8 μm – 12 mag
4.5 μm – 10.5 mag
3.6 μm – 8.5 mag
K_S – 6.5 mag
H – 5 mag
J – 4 mag
NUV – 1 mag
FUV
r (kpc)
r (arcsec)
log F_ν (Jy/arcsec^2)
μ (AB mag/arcsec^2)
FUV
NUV
B
V
R
I
J
H
K'
3.6 um
8.0 um
24 um
2 kpc

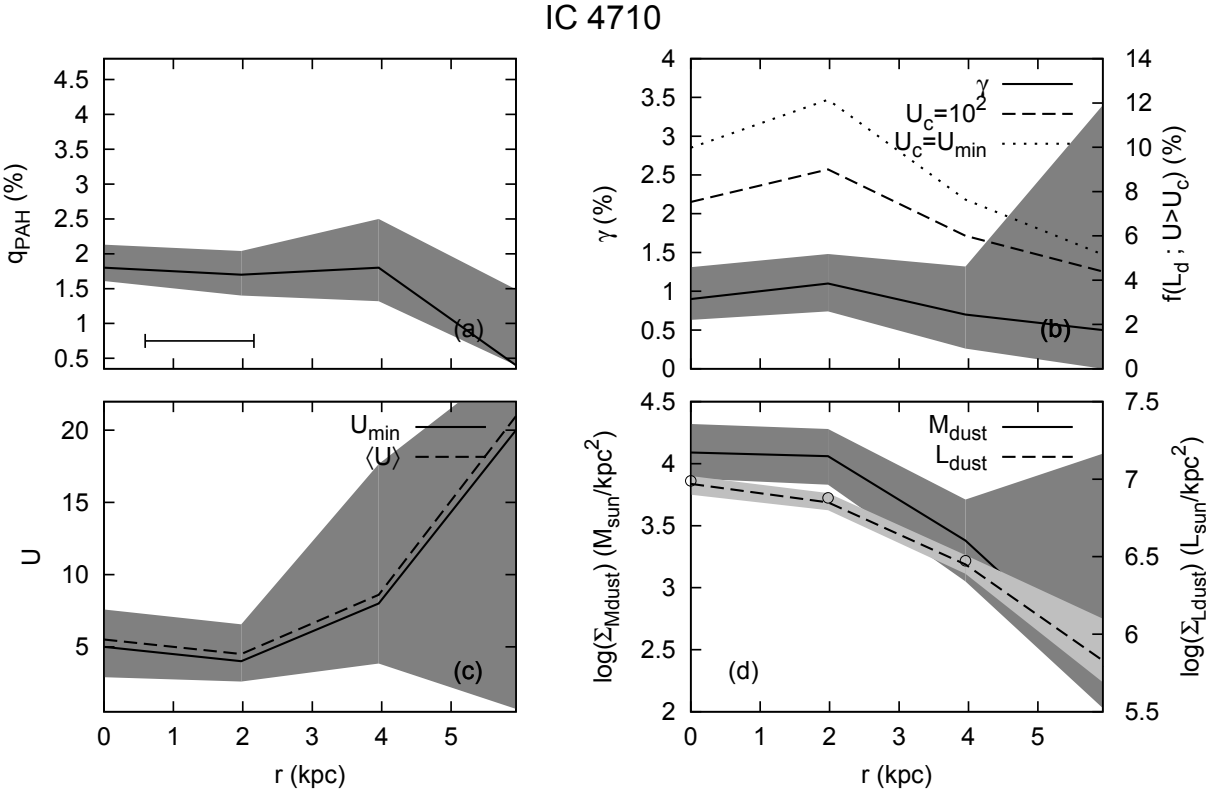
IC 4710
q_{PAH} (%)
(a)
γ
$U_c=10^2$
$U_c=U_{min}$
γ (%)
$f(L_d ; U>U_c)$ (%)
(b)
U_{min}
⟨U⟩
U
(c)
M_{dust}
L_{dust}
$\log(\Sigma_{Mdust})$ (M_{sun}/kpc^2)
$\log(\Sigma_{Ldust})$ (L_{sun}/kpc^2)
(d)
r (kpc)
r (kpc)

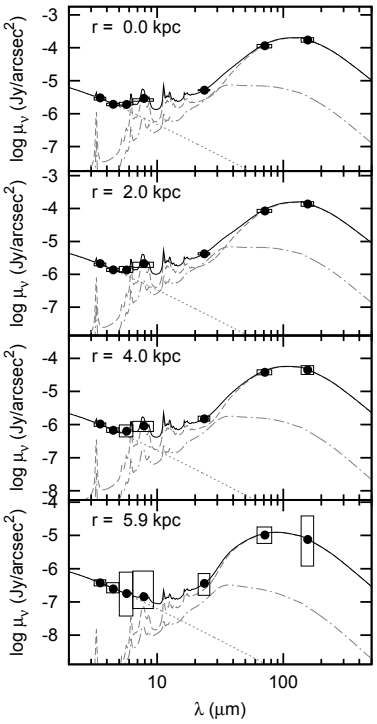
r = 0.0 kpc
r = 2.0 kpc
r = 4.0 kpc
r = 5.9 kpc
log μ_ν (Jy/arcsec^2)
λ (μm)

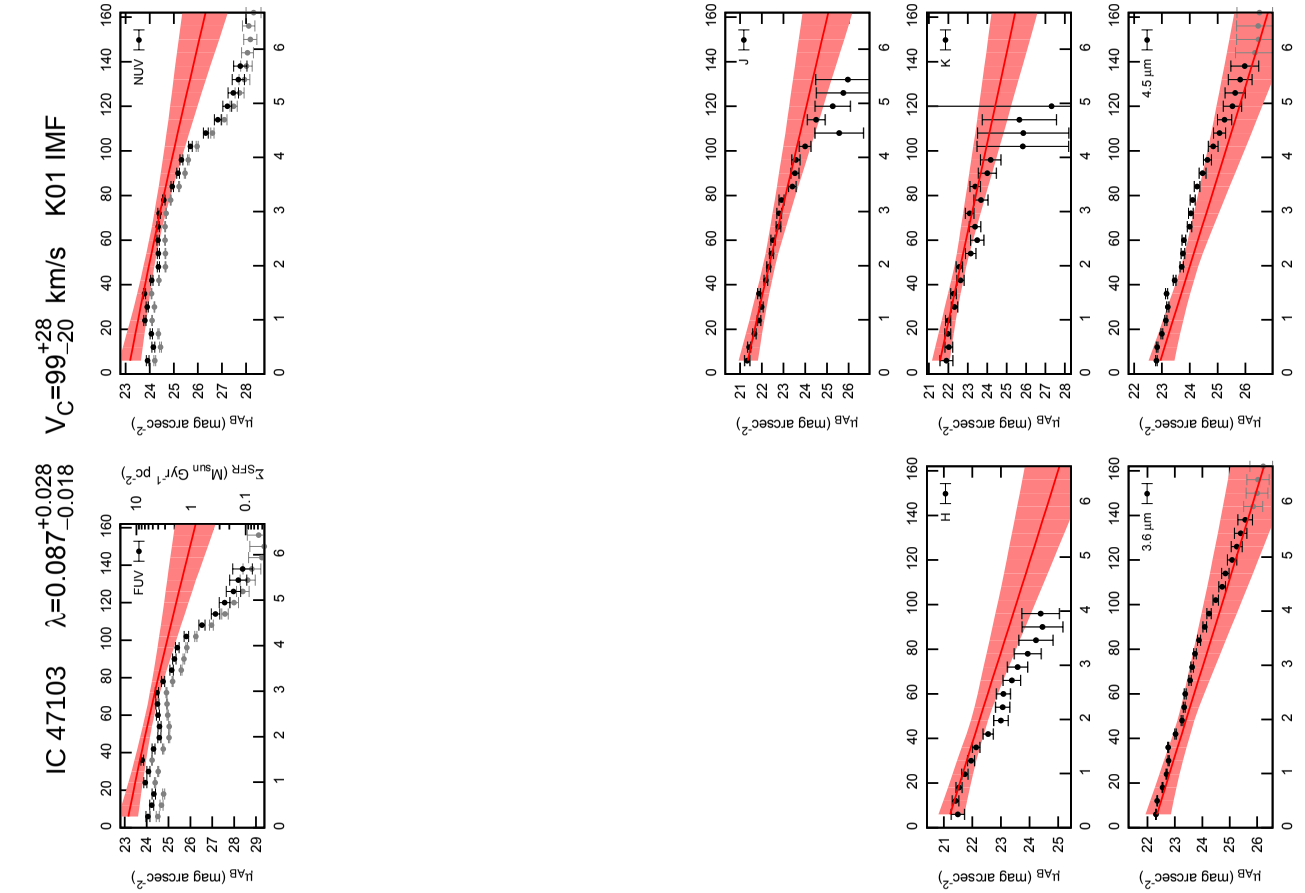
IC 47103 λ=0.087+0.028−0.018 VC=99+28−20 km/s K01 IMF
NUV
FUV
J
H
K
4.5 μm
3.6 μm
μAB (mag arcsec-2)
ΣSFR (Msun Gyr-1 pc-2)

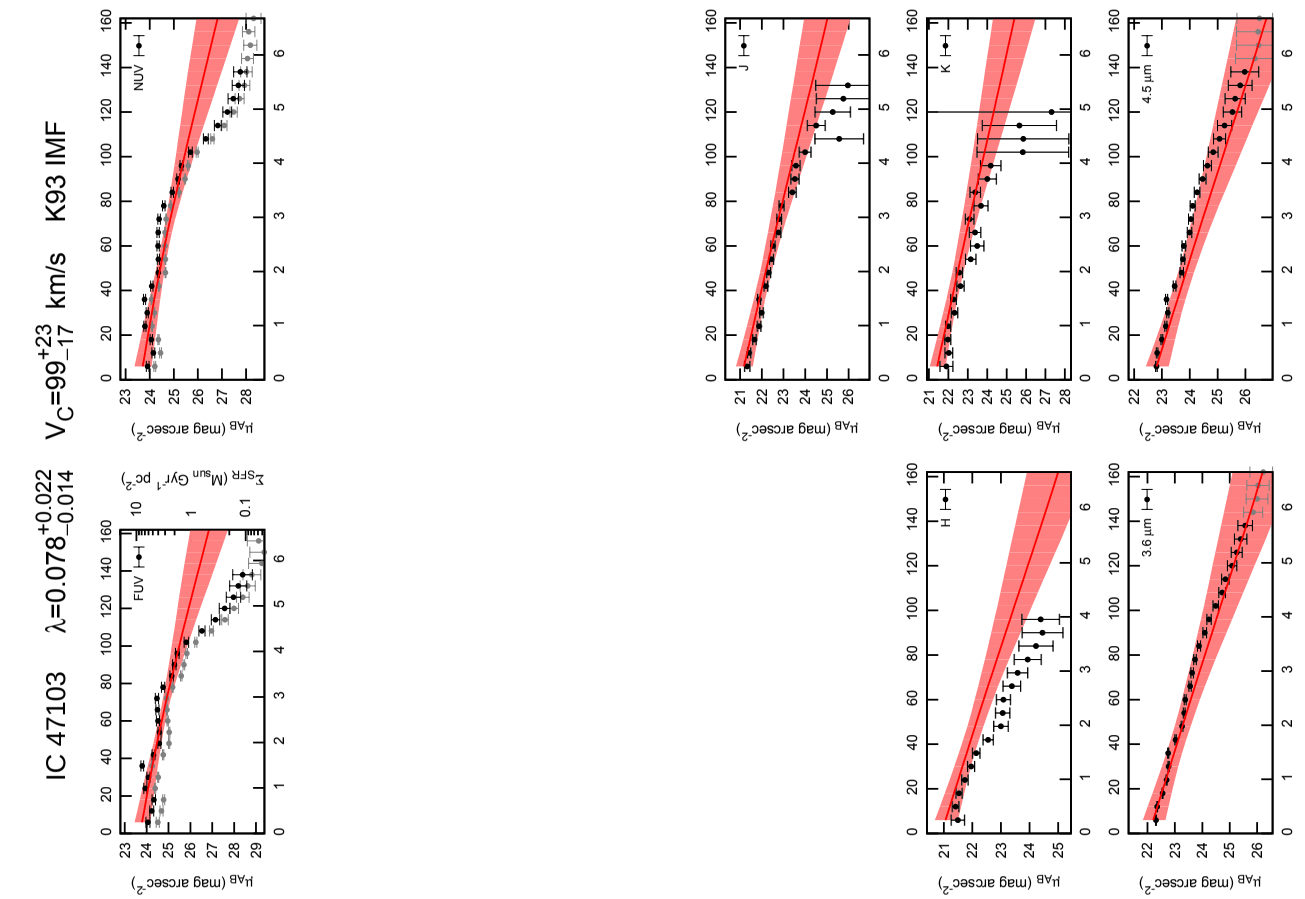
IC 47103 λ=0.078+0.022−0.014 VC=99+23−17 km/s K93 IMF
NUV
FUV
J
H
K
4.5 μm
3.6 μm
μAB (mag arcsec-2)
ΣSFR (Msun Gyr-1 pc-2)

NGC 6822
FUV
NUV
B
V
R
I
J
H
K
3.6 um
8.0 um
24 um
2 kpc

r (kpc)
0
0.5
1
1.5
2
NGC 6822
160 μm – 14.5 mag
70 μm – 13.5 mag
24 μm – 15 mag
8.0 μm – 13 mag
5.8 μm – 12 mag
4.5 μm – 10.5 mag
3.6 μm – 8.5 mag
K_S – 6.5 mag
H – 5 mag
J – 4 mag
NUV – 1 mag
FUV
μ (AB mag/arcsec²)
log F_ν (Jy/arcsec²)
r (arcsec)
0
100
200
300
400
500
600
700
800
-5
0
5
10
15
20
25
30
4
2
0
-2
-4
-6
-8

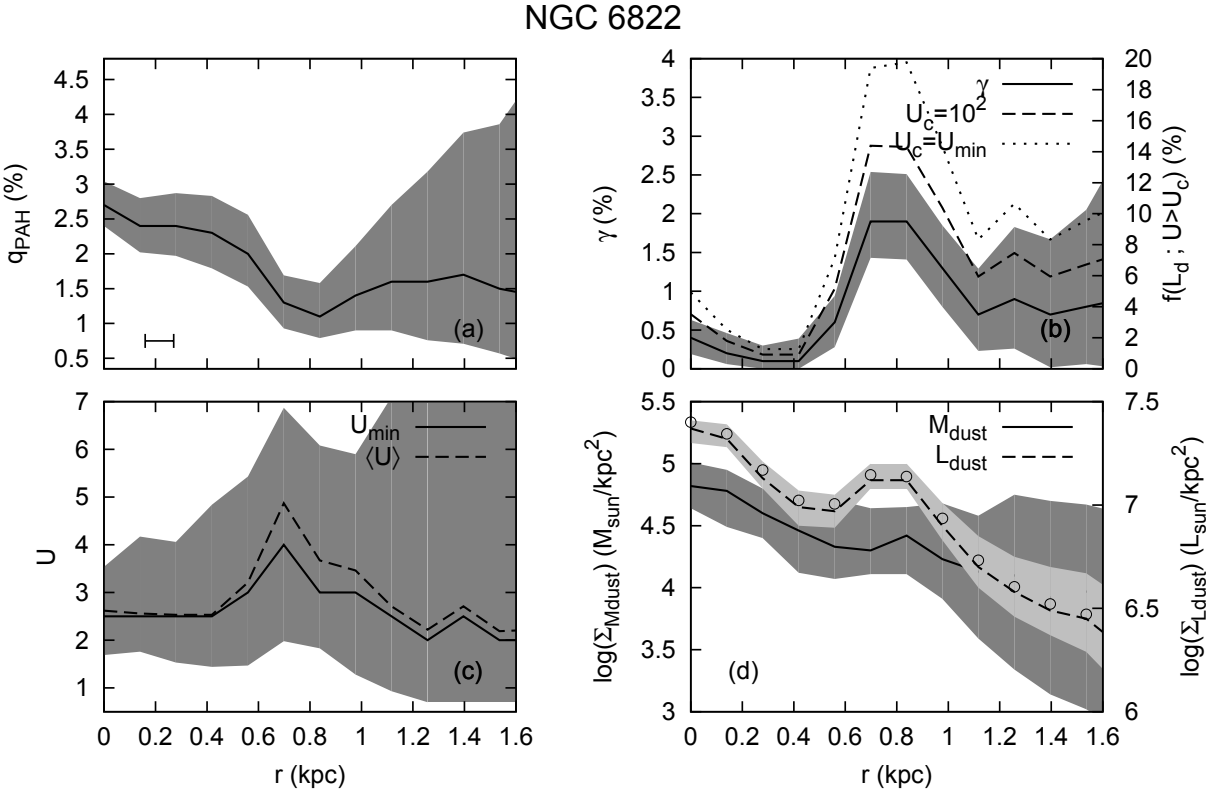
NGC 6822
q_{PAH} (%)
(a)
γ (%)
$U_c=10^2$
$U_c=U_{min}$
$f(L_d ; U>U_c)$ (%)
(b)
U
U_{min}
⟨U⟩
(c)
$\log(\Sigma_{Mdust})$ (M_{sun}/kpc^2)
M_{dust}
L_{dust}
$\log(\Sigma_{Ldust})$ (L_{sun}/kpc^2)
(d)
r (kpc)

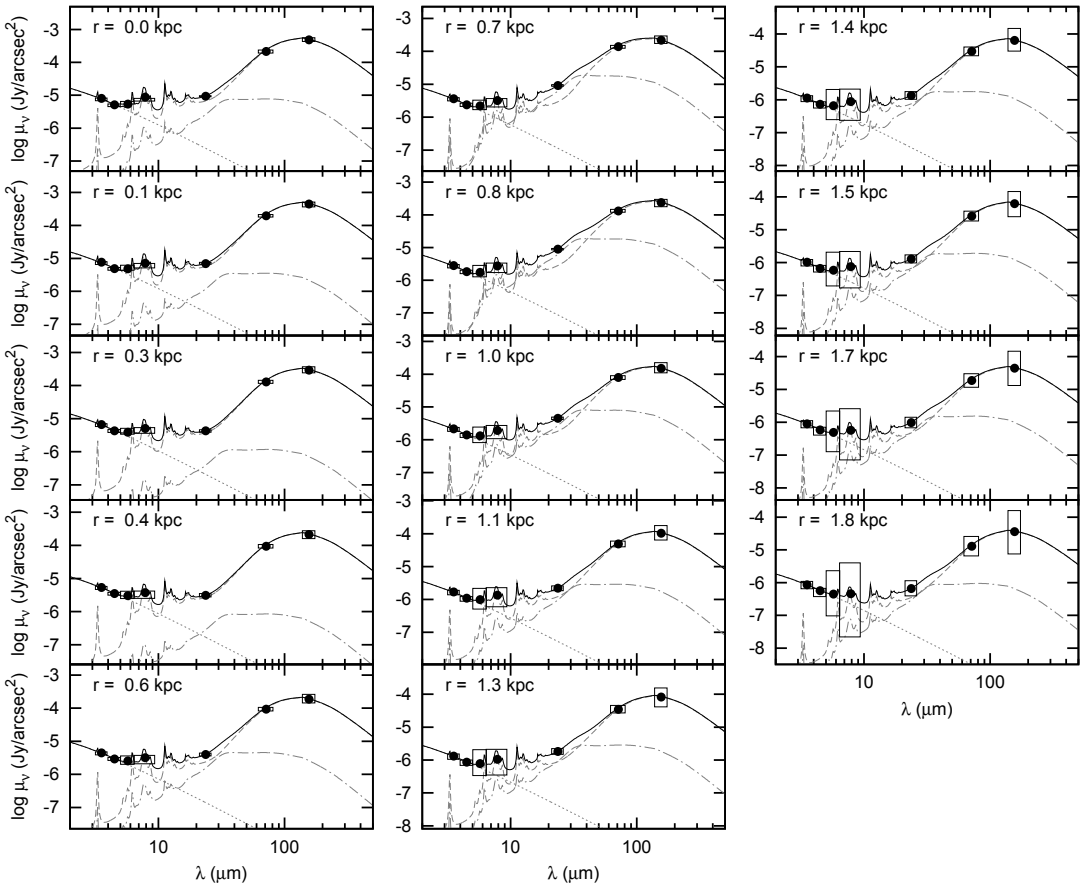
r = 0.0 kpc
r = 0.1 kpc
r = 0.3 kpc
r = 0.4 kpc
r = 0.6 kpc
r = 0.7 kpc
r = 0.8 kpc
r = 1.0 kpc
r = 1.1 kpc
r = 1.3 kpc
r = 1.4 kpc
r = 1.5 kpc
r = 1.7 kpc
r = 1.8 kpc
log μ_ν (Jy/arcsec^2)
λ (μm)

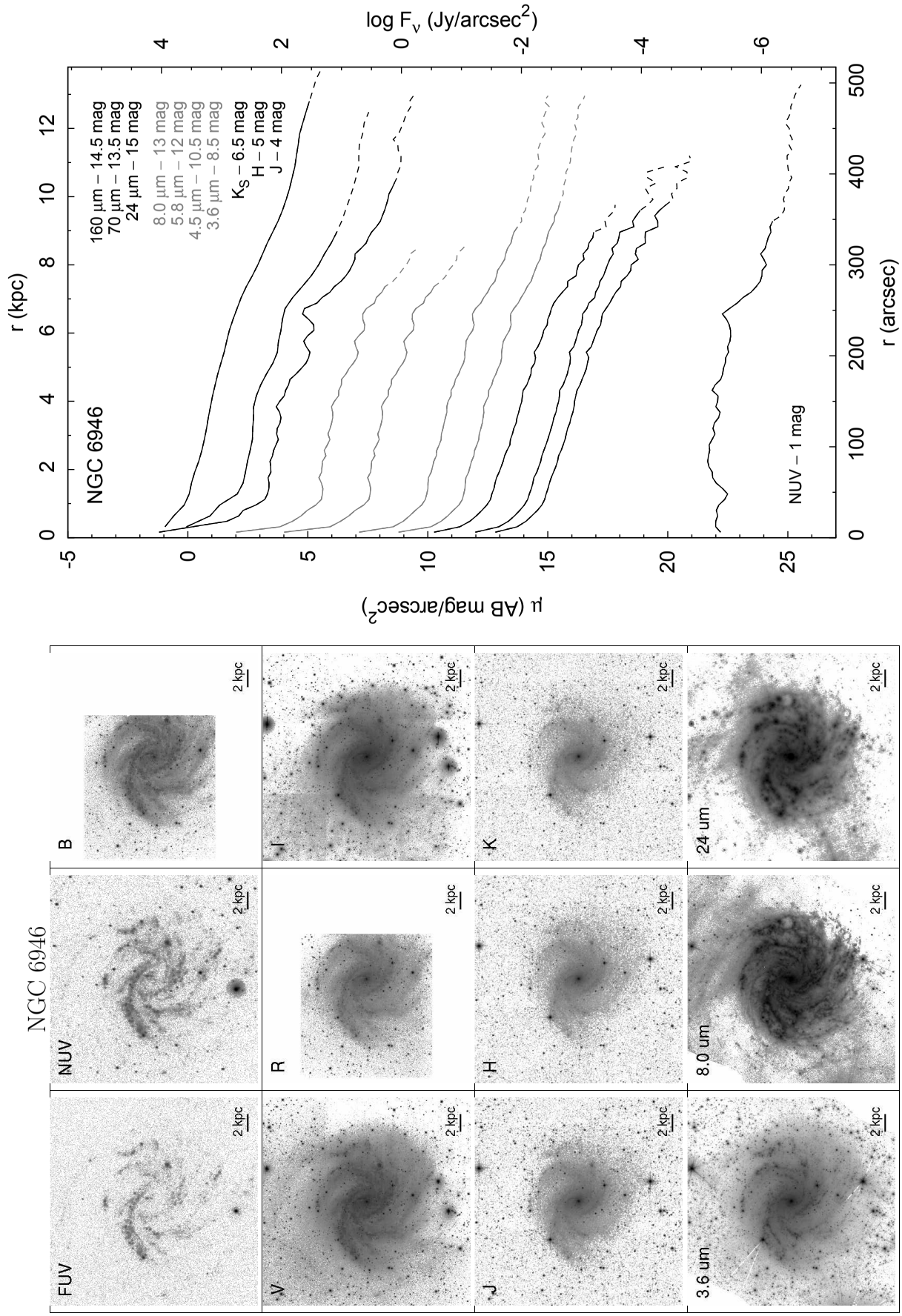
NGC 6946
FUV
NUV
B
V
R
I
J
H
K
3.6 um
8.0 um
24 um
2 kpc
NGC 6946
160 μm – 14.5 mag
70 μm – 13.5 mag
24 μm – 15 mag
8.0 μm – 13 mag
5.8 μm – 12 mag
4.5 μm – 10.5 mag
3.6 μm – 8.5 mag
K_S – 6.5 mag
H – 5 mag
J – 4 mag
NUV – 1 mag
r (kpc)
r (arcsec)
log F_ν (Jy/arcsec^2)
μ (AB mag/arcsec^2)

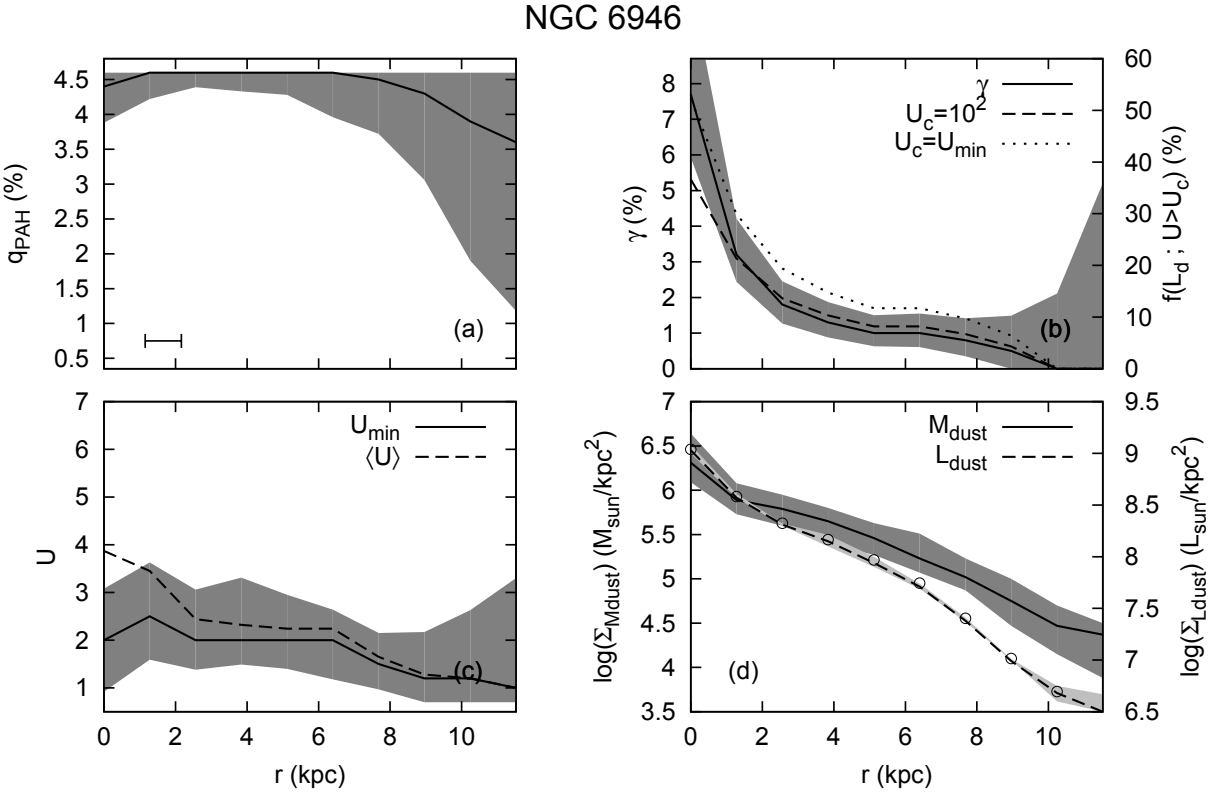
NGC 6946
q_{PAH} (%)
(a)
γ
$U_c=10^2$
$U_c=U_{min}$
γ (%)
$f(L_d ; U>U_c)$ (%)
(b)
U_{min}
⟨U⟩
U
(c)
r (kpc)
M_{dust}
L_{dust}
$\log(\Sigma_{Mdust})$ (M_{sun}/kpc^2)
$\log(\Sigma_{Ldust})$ (L_{sun}/kpc^2)
(d)
r (kpc)

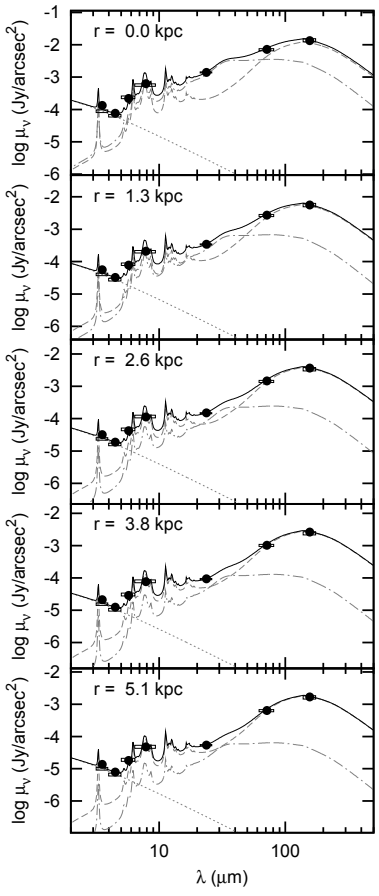
r = 0.0 kpc
r = 1.3 kpc
r = 2.6 kpc
r = 3.8 kpc
r = 5.1 kpc
log μ_ν (Jy/arcsec^2)
λ (μm)

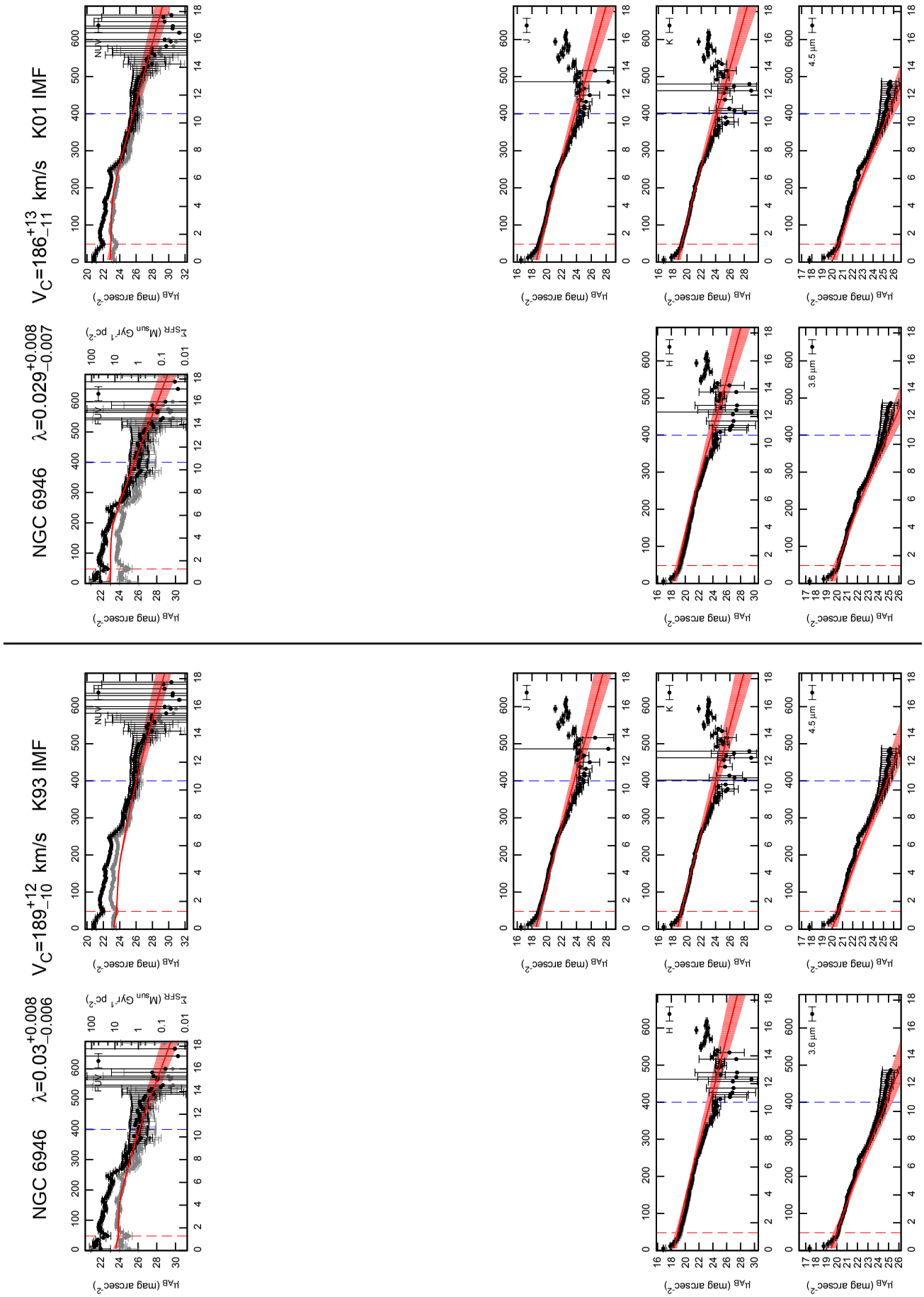
NGC 6946 λ=0.029+0.008−0.007 VC=186+13−11 km/s K01 IMF
NGC 6946 λ=0.03+0.008−0.006 VC=189+12−10 km/s K93 IMF
μAB (mag arcsec-2)
ΣSFR (Msun Gyr-1 pc-2)
NUV
FUV
J
H
K
3.6 μm
4.5 μm

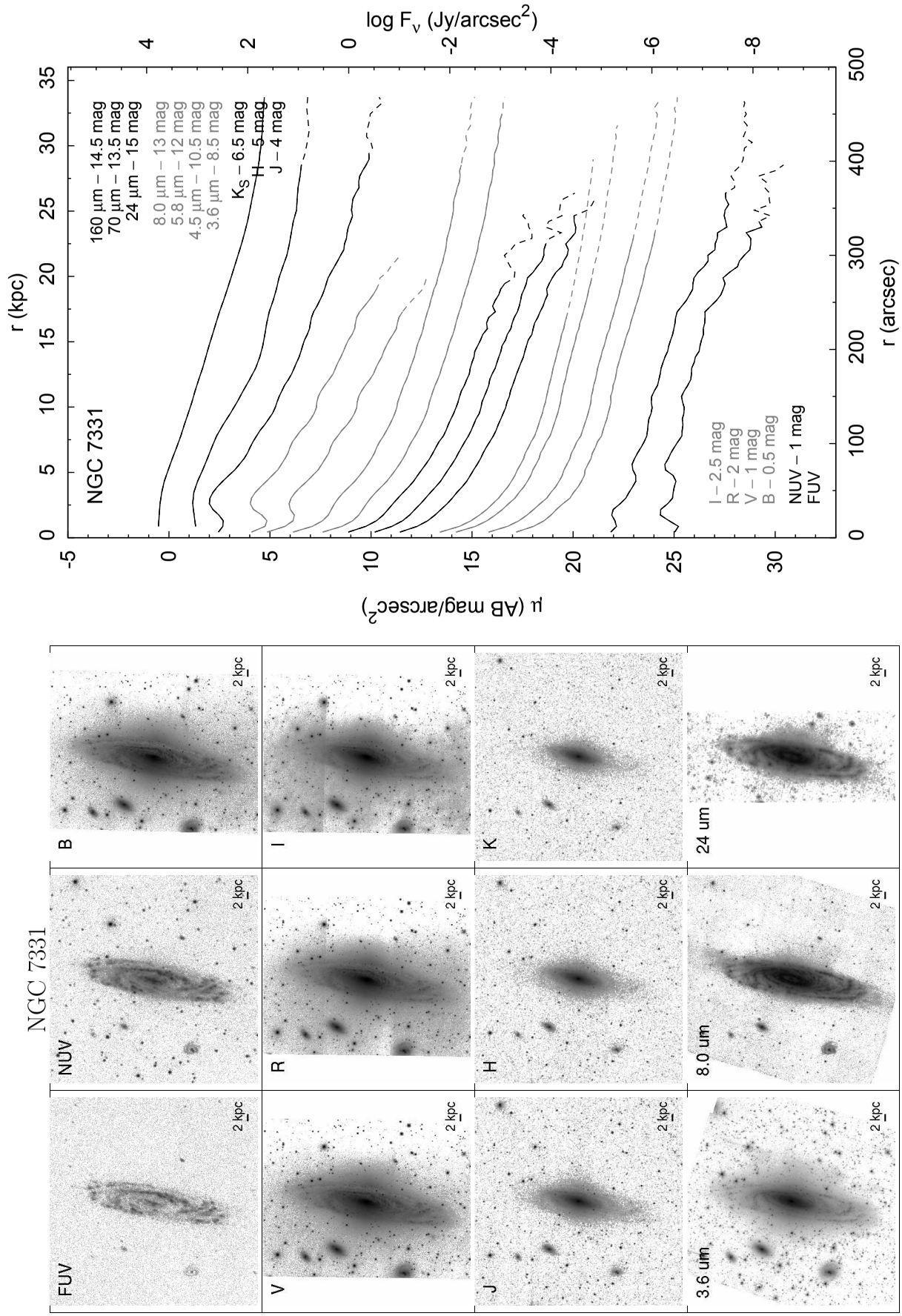
NGC 7331
160 µm – 14.5 mag
70 µm – 13.5 mag
24 µm – 15 mag
8.0 µm – 13 mag
5.8 µm – 12 mag
4.5 µm – 10.5 mag
3.6 µm – 8.5 mag
K_S – 6.5 mag
H – 5 mag
J – 4 mag
I – 2.5 mag
R – 2 mag
V – 1 mag
B – 0.5 mag
NUV – 1 mag
FUV
r (kpc)
r (arcsec)
log F_ν (Jy/arcsec^2)
µ (AB mag/arcsec^2)
FUV
NUV
B
I
R
V
K
H
J
24 um
8.0 um
3.6 um
2 kpc

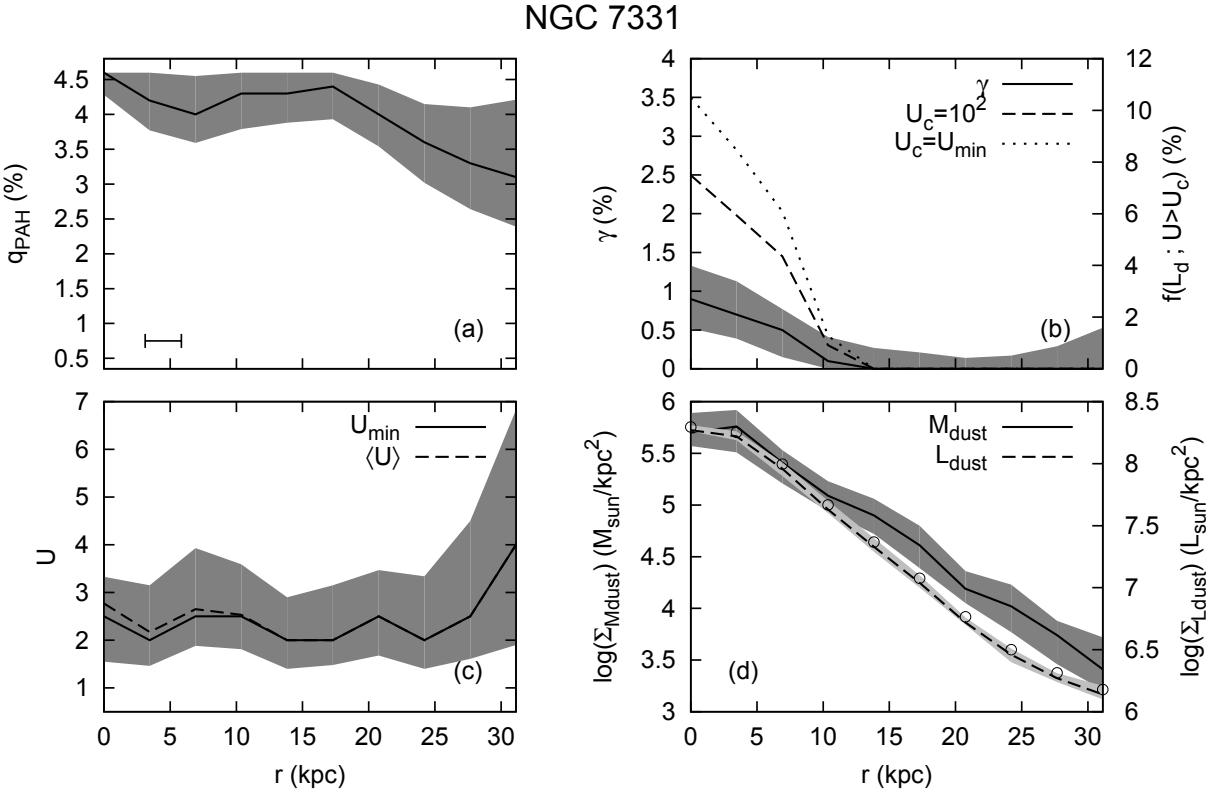
NGC 7331
(a)
(b)
(c)
(d)
γ
U_c=10^2
U_c=U_min
U_min
⟨U⟩
M_dust
L_dust
r (kpc)
r (kpc)

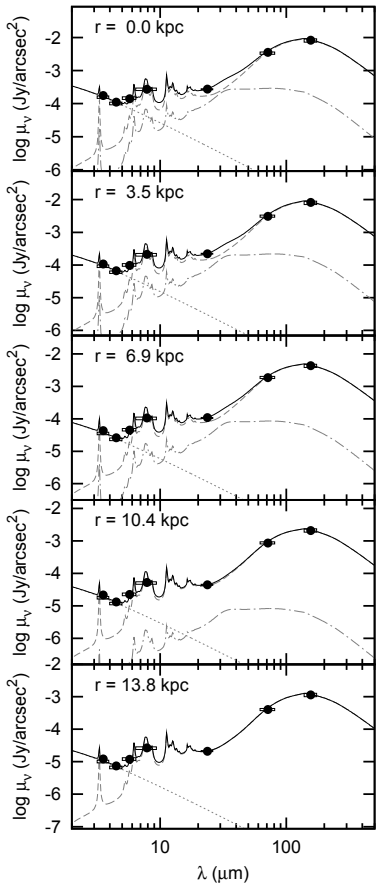
r = 0.0 kpc
r = 3.5 kpc
r = 6.9 kpc
r = 10.4 kpc
r = 13.8 kpc
λ (μm)

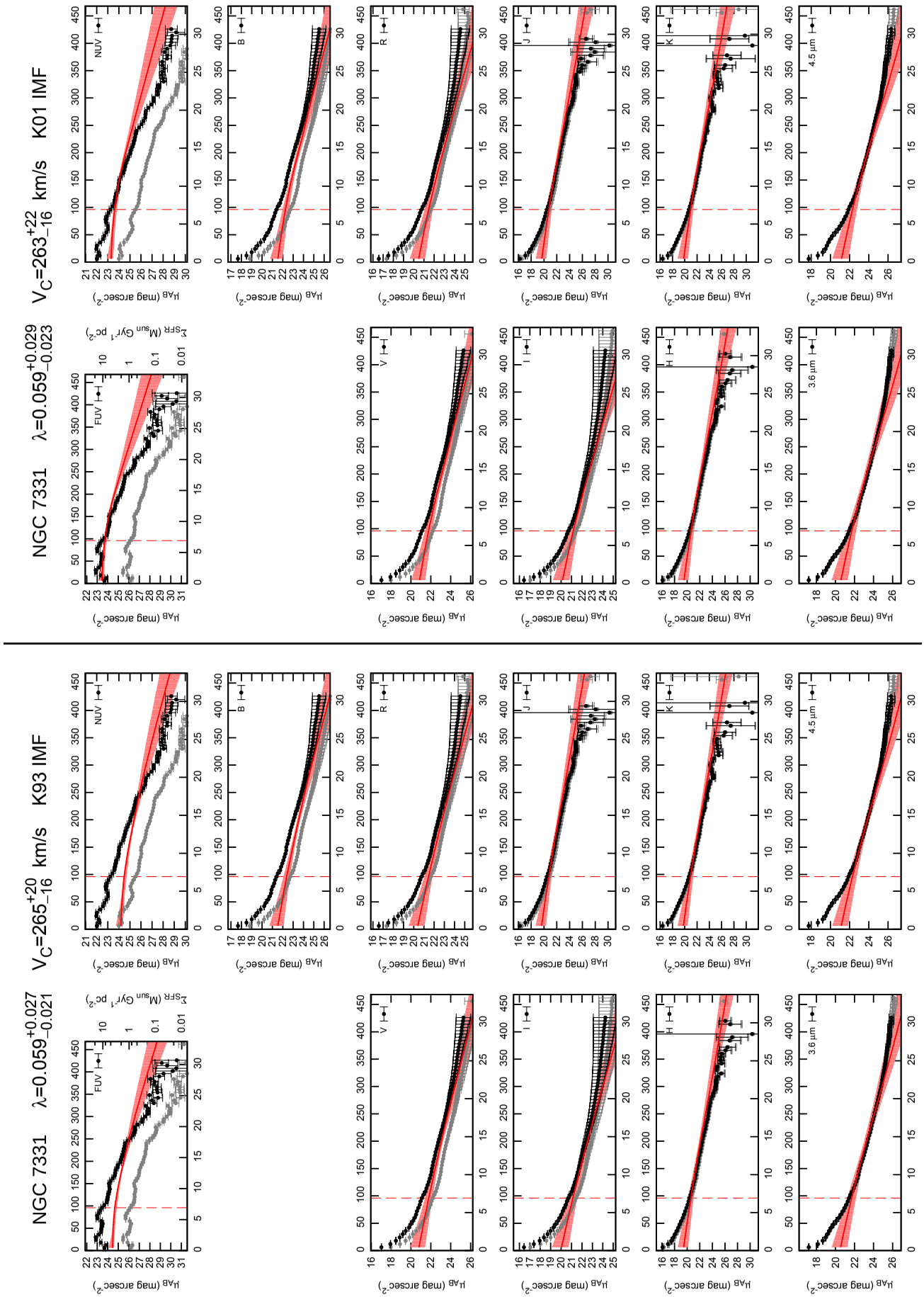
NGC 7331 λ=0.059+0.029−0.023 VC=263+22−16 km/s K01 IMF
NGC 7331 λ=0.059+0.027−0.021 VC=265+20−16 km/s K93 IMF
μAB (mag arcsec-2)
ΣSFR (Msun Gyr-1 pc-2)
NUV
FUV
B
V
R
I
J
H
K
3.6 μm
4.5 μm

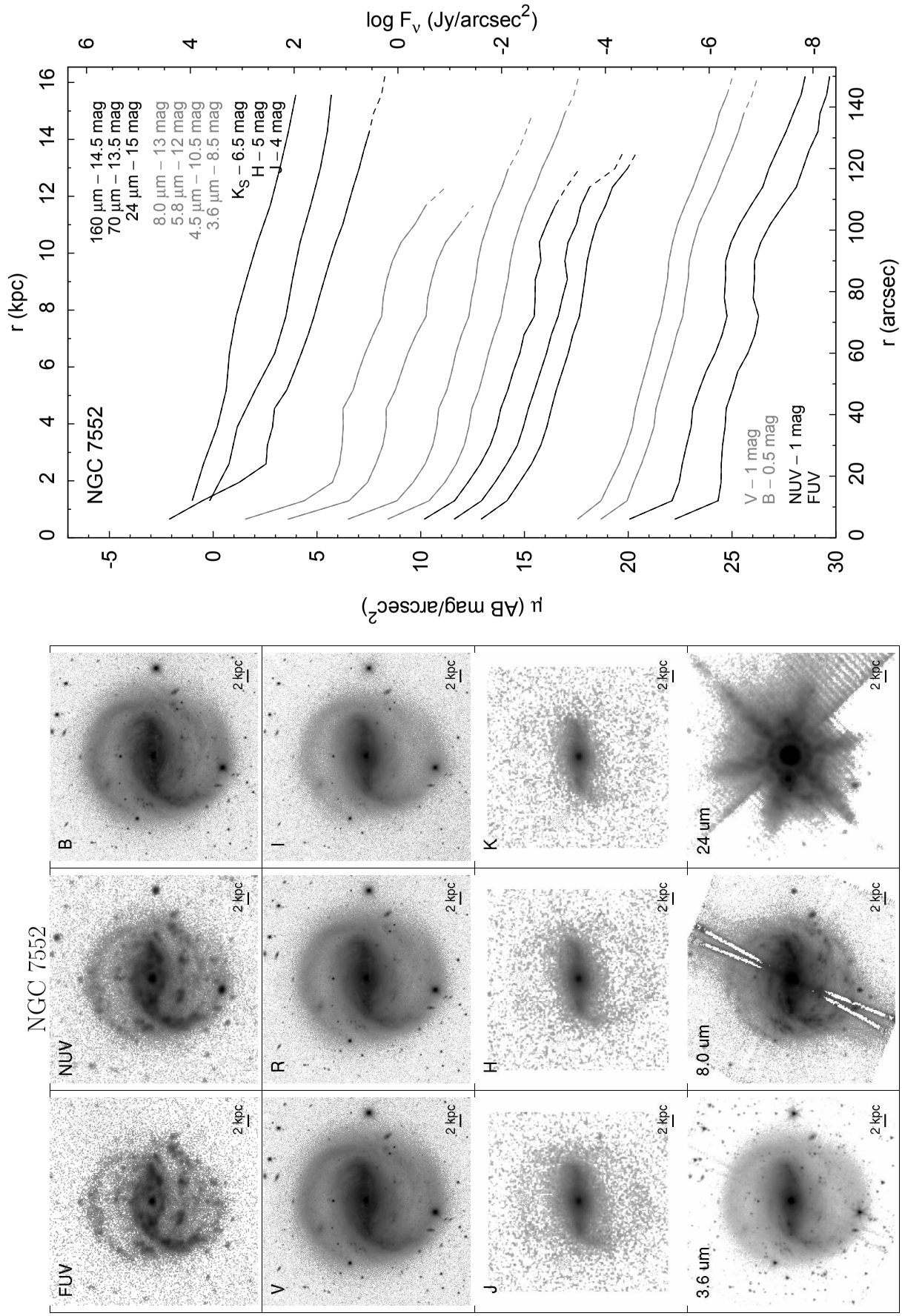
NGC 7552
FUV
NUV
B
V
R
I
J
H
K
3.6 um
8.0 um
24 um
2 kpc
μ (AB mag/arcsec²)
log F_ν (Jy/arcsec²)
r (kpc)
r (arcsec)
160 μm – 14.5 mag
70 μm – 13.5 mag
24 μm – 15 mag
8.0 μm – 13 mag
5.8 μm – 12 mag
4.5 μm – 10.5 mag
3.6 μm – 8.5 mag
K_S – 6.5 mag
H – 5 mag
J – 4 mag
V – 1 mag
B – 0.5 mag
NUV – 1 mag
FUV

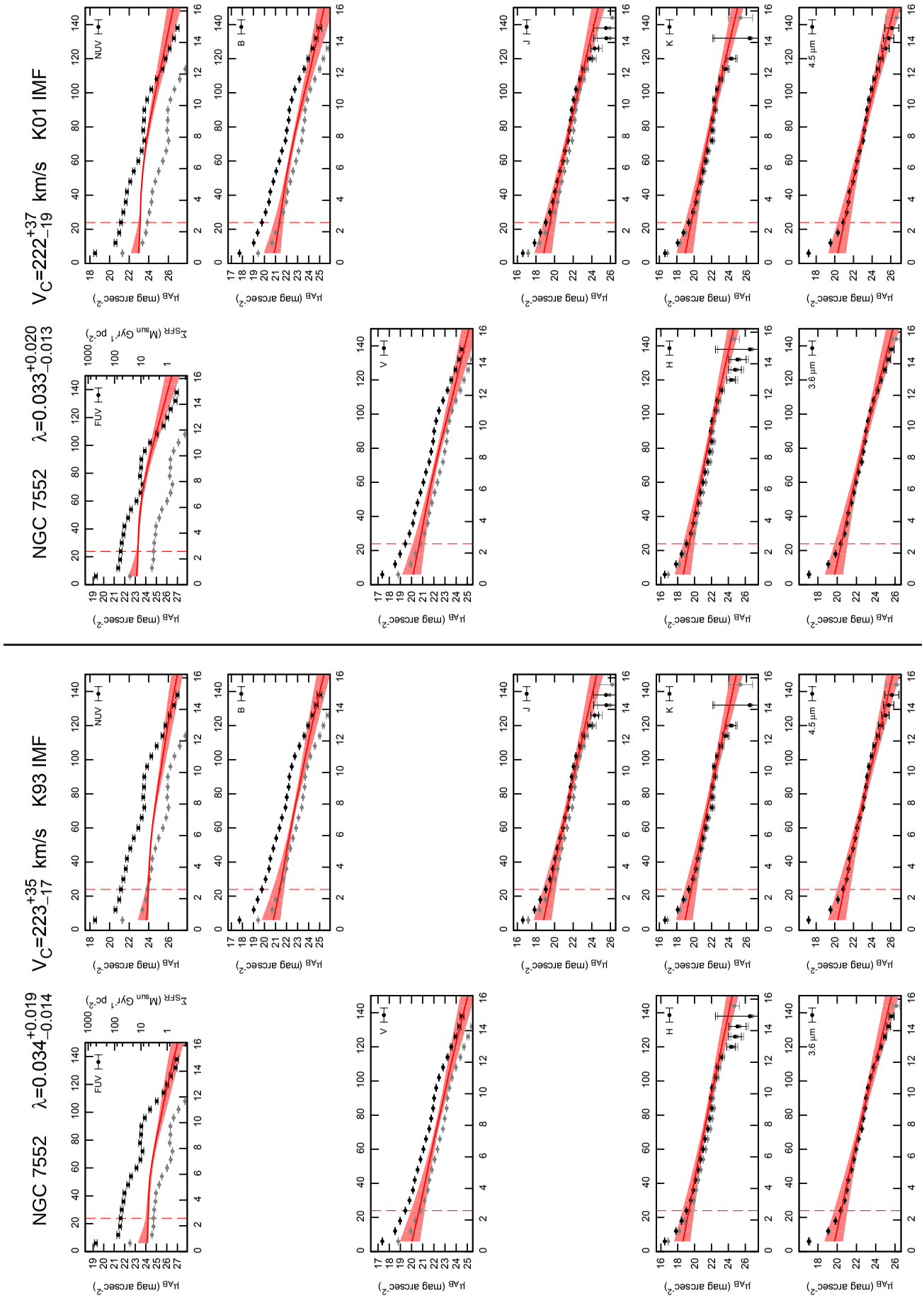
NGC 7552 λ=0.033+0.020−0.013 VC=222+37−19 km/s K01 IMF
NGC 7552 λ=0.034+0.019−0.014 VC=223+35−17 km/s K93 IMF
FUV
NUV
B
V
H
J
K
3.6 μm
4.5 μm
μAB (mag arcsec-2)
ΣSFR (Msun Gyr-1 pc-2)

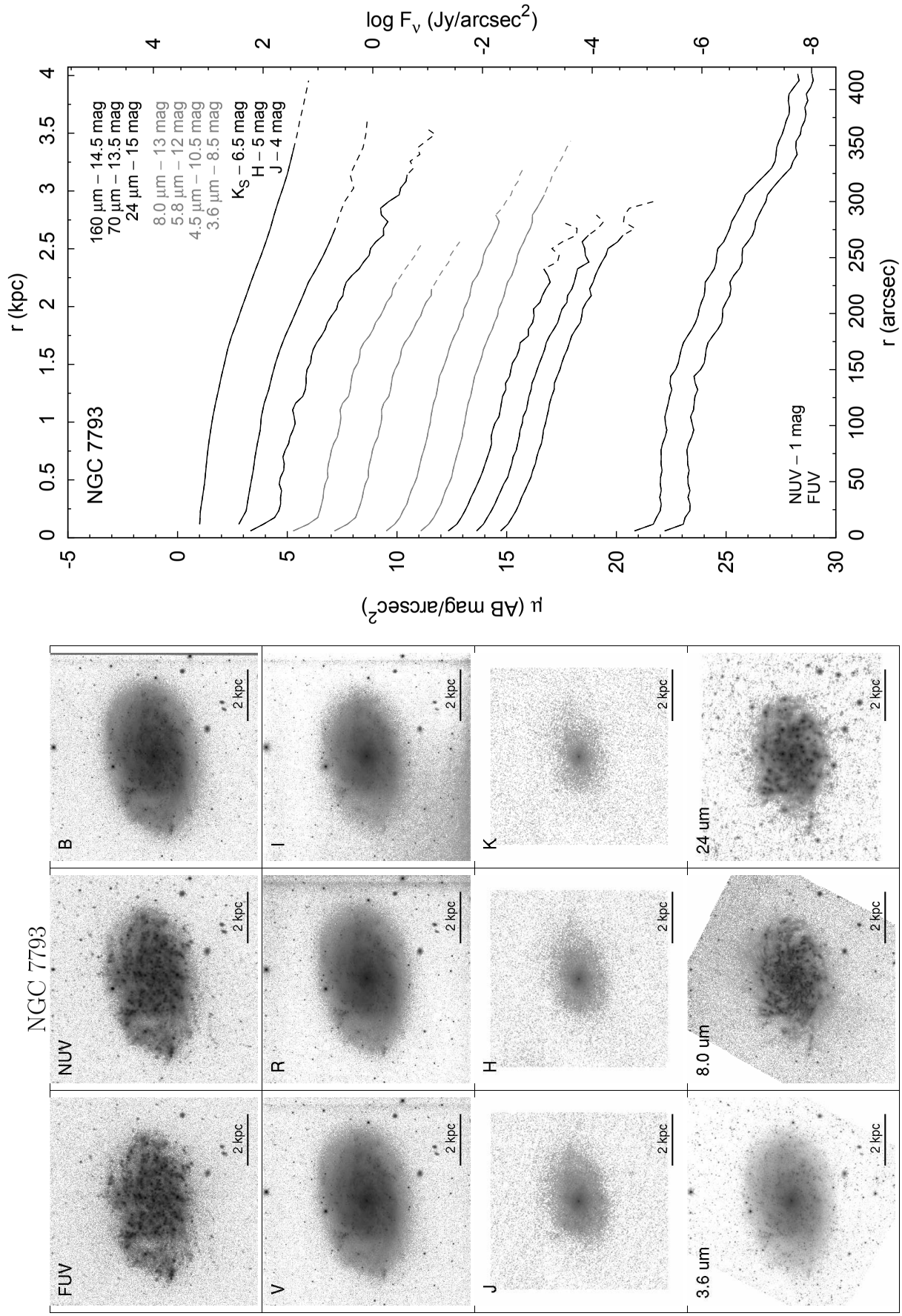
NGC 7793
FUV
NUV
B
V
R
I
J
H
K
3.6 um
8.0 um
24 um
2 kpc
μ (AB mag/arcsec²)
log F_ν (Jy/arcsec²)
r (kpc)
r (arcsec)
NGC 7793
160 μm – 14.5 mag
70 μm – 13.5 mag
24 μm – 15 mag
8.0 μm – 13 mag
5.8 μm – 12 mag
4.5 μm – 10.5 mag
3.6 μm – 8.5 mag
K_S – 6.5 mag
H – 5 mag
J – 4 mag
NUV – 1 mag
FUV

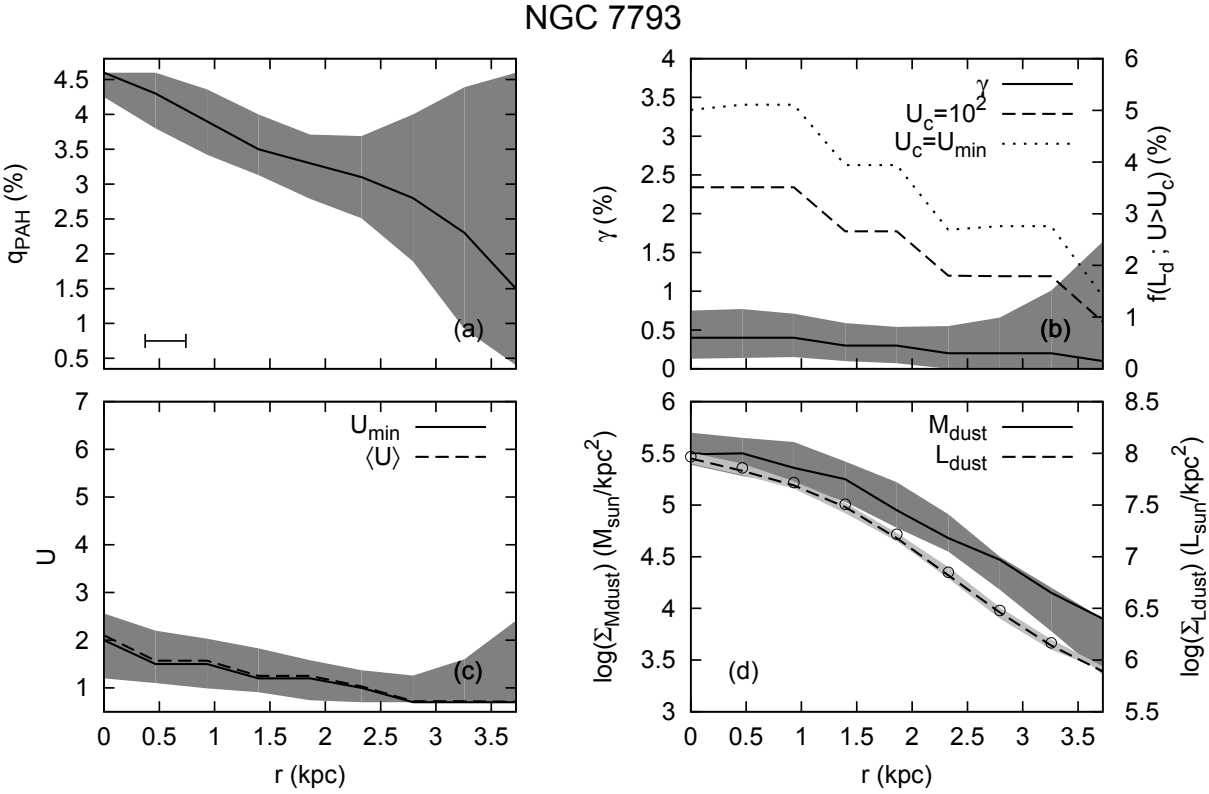
NGC 7793
(a)
(b)
(c)
(d)
q_{PAH} (%)
γ (%)
$f(L_d ; U>U_c)$ (%)
U
U_{min}
⟨U⟩
γ
$U_c=10^2$
$U_c=U_{min}$
M_{dust}
L_{dust}
$\log(\Sigma_{Mdust})$ (M_{sun}/kpc^2)
$\log(\Sigma_{Ldust})$ (L_{sun}/kpc^2)
r (kpc)

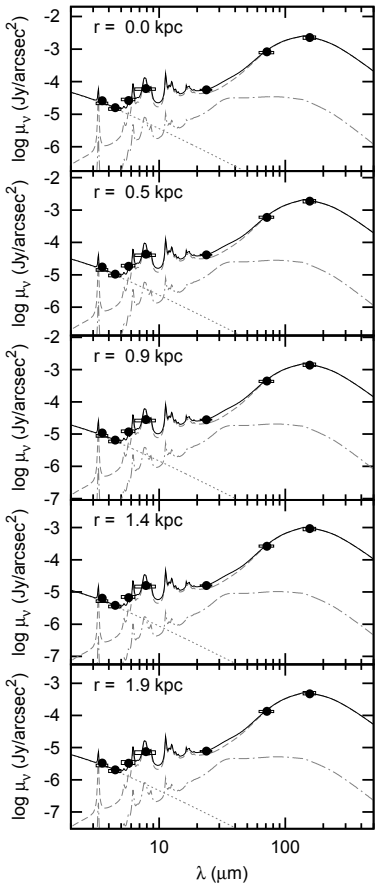
r = 0.0 kpc
r = 0.5 kpc
r = 0.9 kpc
r = 1.4 kpc
r = 1.9 kpc
log μ_ν (Jy/arcsec^2)
λ (μm)

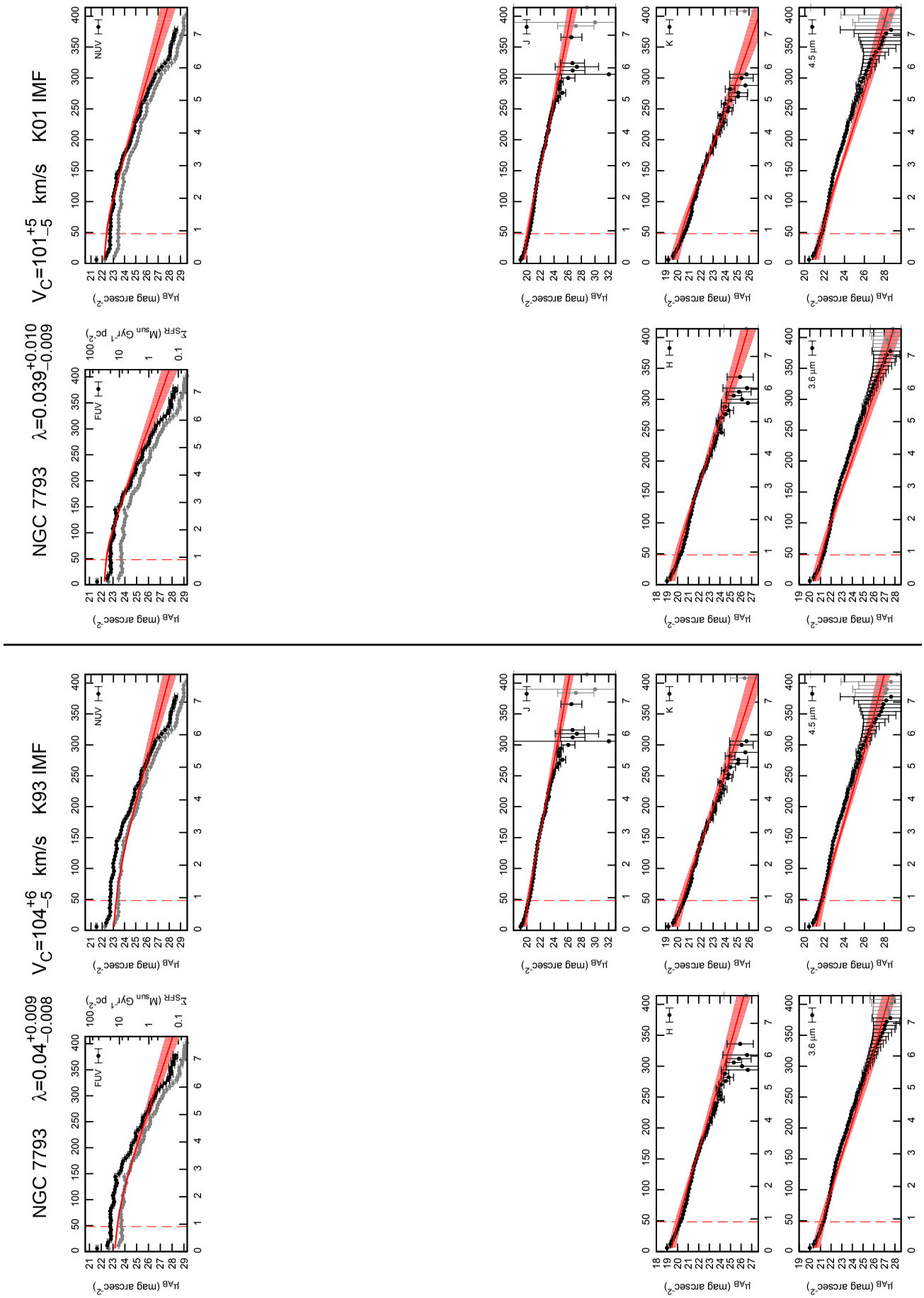
NGC 7793 λ=0.039+0.010−0.009 VC=101+5−5 km/s K01 IMF
NGC 7793 λ=0.04+0.009−0.008 VC=104+6−5 km/s K93 IMF
NUV
FUV
J
K
H
4.5 μm
3.6 μm
μAB (mag arcsec-2)
ΣSFR (Msun Gyr-1 pc-2)

B

Morphological estimators

In this appendix we provide the non-parametric morphological estimators described in chapter 3 for the whole SINGS sample. For each galaxy we quote the oncentration index (C_{42}), the asymmetry (A), the Gini coeff ent (G) and the normalized second-order moment of the brightest 20% to the total galaxy f ux ($\overline{M}_{20}$) at different wavelengths. Below each galaxy's name we provide the full description of its morphological type, together with the corresponding numerical stage along the Hubble sequence T.

When the inner radius r_{20} needed to compute C_{42} is smaller than the innermost point in our prof les (or the PSF size, in the case of the 70 μm and 160 μm bands), the quoted values are just lower limits for the actual concentration indices. These values are therefore marked with a 'greater than' symbol ($>$). Values of A, G and $\overline{M}_{20}$ marked with a dagger (†) should be taken with caution, since at the particular distance of each galaxy, the FWHM of the PSF of the affected bands does not allow resolving structures smaller than 0.5 kpc.

Galaxy		FUV	NUV	B	V	R	I	u	g	r	i	z	J	H	K_S	3.6 μm	4.5 μm	5.8 μm	8.0 μm	24 μm	70 μm	160 μm
NGC 0024	C_{42}	2.58	2.57	2.71	2.81	2.85	2.92	···	···	···	···	···	2.94	3.02	2.87	3.05	3.07	2.66	2.64	2.90	2.83	2.69
SA(s)c	A	0.241	0.163	0.091	0.072	0.063	0.052	···	···	···	···	···	0.021	0.010	0.019	0.082	0.078	0.054	0.109	0.133	0.082†	0.172†
$T = 5$	G	0.562	0.533	0.538	0.550	0.559	0.553	···	···	···	···	···	0.568	0.556	0.533	0.594	0.594	0.631	0.693	0.646	0.554†	0.454†
	$\overline{M}_{20}$	−1.17	−1.35	−1.67	−1.74	−1.77	−1.71	···	···	···	···	···	−1.82	−1.85	−1.85	−1.75	−1.72	−1.60	−1.52	−1.23	−1.70†	−1.55†
NGC 0337	C_{42}	1.93	2.02	2.22	2.37	2.44	2.52	···	···	···	···	···	2.58	2.66	2.63	2.69	2.70	2.57	2.68	2.29	2.37	> 2.25
SB(s)d	A	0.369†	0.310†	0.228	0.190	0.179	0.149	···	···	···	···	···	0.084	0.080	0.055	0.197	0.205	0.287	0.343	0.429†	0.331†	0.335†
$T = 7$	G	0.659†	0.635†	0.616	0.612	0.613	0.605	···	···	···	···	···	0.584	0.586	0.529	0.646	0.653	0.682	0.707	0.721†	0.515†	0.340†
	$\overline{M}_{20}$	−0.96†	−1.08†	−1.24	−1.38	−1.46	−1.57	···	···	···	···	···	−1.64	−1.65	−1.71	−1.59	−1.54	−1.44	−1.41	−1.23†	−1.49†	−1.55†
NGC 0584	C_{42}	4.72	4.44	4.53	4.55	4.56	4.50	···	···	···	···	···	4.65	5.02	4.82	4.75	4.71	4.56	4.74	4.29	···	···
E4	A	0.023†	0.085†	0.041	0.043	0.021	0.034	···	···	···	···	···	0.014	0.013	0.016	0.030	0.028	0.000	0.000	0.021†	0.077†	··· †
$T = -5$	G	0.359†	0.622†	0.727	0.736	0.736	0.730	···	···	···	···	···	0.731	0.710	0.718	0.751	0.751	0.729	0.722	0.625†	0.481†	··· †
	$\overline{M}_{20}$	−2.44†	−2.46†	−2.72	−2.75	−2.77	−2.72	···	···	···	···	···	−2.69	−2.75	−2.65	−2.76	−2.73	−2.60	−2.38	−2.28†	−1.95†	··· †
NGC 0628	C_{42}	2.13	2.24	2.73	2.96	2.94	3.06	···	···	···	···	···	3.16	3.18	3.11	3.09	3.03	2.28	2.17	1.99	2.20	2.28
SA(s)c	A	0.423	0.346	0.144	0.092	0.105	0.057	···	···	···	···	···	0.027	0.010	0.039	0.139	0.138	0.199	0.333	0.341	0.254†	0.116†
$T = 5$	G	0.625	0.606	0.579	0.607	0.644	0.636	···	···	···	···	···	0.565	0.550	0.494	0.659	0.650	0.639	0.649	0.714	0.630†	0.534†
	$\overline{M}_{20}$	−0.80	−0.85	−1.34	−1.67	−1.70	−1.92	···	···	···	···	···	−2.11	−2.11	−2.04	−1.61	−1.47	−1.00	−0.96	−0.82	−1.09†	−1.51†
NGC 0855	C_{42}	> 3.23	4.32	···	···	···	···	···	···	···	···	···	3.81	3.75	3.83	4.22	4.25	> 4.33	> 2.77	3.12	3.05	> 2.23
E	A	0.209	0.116	···	···	···	···	···	···	···	···	···	0.015	0.026	0.013	0.085	0.080	0.087	0.121	0.116	0.077†	0.113†
$T = -5$	G	0.803	0.765	···	···	···	···	···	···	···	···	···	0.628	0.612	0.583	0.660	0.669	0.711	0.831	0.837	0.631†	0.454†
	$\overline{M}_{20}$	−1.70	−2.31	···	···	···	···	···	···	···	···	···	−2.25	−2.11	−2.31	−2.37	−2.36	−2.39	−2.00	−1.80	−1.88†	−1.79†
NGC 0925	C_{42}	2.55	2.63	2.84	2.90	2.99	3.14	···	···	···	···	···	3.07	3.02	3.05	3.27	3.25	3.40	3.51	3.14	3.01	2.52
SAB(s)d	A	0.404	0.350	0.176	0.109	0.133	0.095	···	···	···	···	···	0.015	0.010	0.000	0.149	0.123	0.134	0.260	0.309	0.224†	0.205†
$T = 7$	G	0.648	0.619	0.551	0.516	0.550	0.530	···	···	···	···	···	0.516	0.482	0.467	0.600	0.599	0.616	0.676	0.692	0.615†	0.509†
	$\overline{M}_{20}$	−0.90	−0.95	−1.21	−1.41	−1.42	−1.64	···	···	···	···	···	−1.75	−1.75	−1.58	−1.56	−1.41	−1.27	−1.28	−0.85	−1.15†	−1.62†
NGC 1097	C_{42}	2.67	3.58	4.37	4.60	4.77	4.75	···	···	···	···	···	4.84	4.95	4.96	5.61	5.77	5.55	5.50	4.43	4.09	3.47
SB(s)b	A	0.463	0.389	0.196	0.145	0.132	0.084	···	···	···	···	···	0.039	0.034	0.026	0.114	0.110	0.136	0.185	0.113	0.134†	0.204†
$T = 3$	G	0.680	0.674	0.616	0.639	0.662	0.668	···	···	···	···	···	0.694	0.686	0.654	0.725	0.733	0.767	0.826	0.899	0.782†	0.615†
	$\overline{M}_{20}$	−1.00	−1.43	−2.14	−2.54	−2.64	−2.73	···	···	···	···	···	−2.76	−2.79	−2.80	−2.83	−2.78	−2.64	−2.58	−2.39	−2.42†	−2.16†
NGC 1266	C_{42}	2.70	2.71	3.00	3.14	3.35	3.41	···	···	···	···	···	> 3.68	> 3.45	> 3.62	> 3.57	> 3.26	> 2.25	···	> 2.08	> 2.17	> 0.91
(R')SB0(rs) pec	A	0.000†	0.079†	0.053	0.043	0.043	0.041	···	···	···	···	···	0.020	0.039	0.032	0.058	0.083	0.075	0.112	0.139†	0.384†	0.374†
$T = -2$	G	0.393†	0.511†	0.549	0.560	0.571	0.561	···	···	···	···	···	0.603	0.648	0.622	0.631	0.696	0.773	0.876	0.875†	0.477†	0.445†
	$\overline{M}_{20}$	··· †	−1.66†	−1.88	−2.01	−2.10	−2.12	···	···	···	···	···	−2.09	−2.02	−1.94	−2.58	−2.95	−2.81	−2.51	−2.32†	−1.78†	−1.49†
NGC 1291	C_{42}	2.60	3.82	5.25	5.39	5.43	5.39	···	···	···	···	···	4.95	4.62	5.01	5.78	5.72	5.61	5.80	5.49	5.55	3.00
(R)SB(s)0/a	A	0.193	0.164	0.036	0.026	0.010	0.021	···	···	···	···	···	0.019	0.019	0.016	0.034	0.027	0.000	0.000	0.062	0.121†	0.127†
$T = 0$	G	0.476	0.583	0.637	0.660	0.671	0.678	···	···	···	···	···	0.743	0.763	0.725	0.680	0.678	0.698	0.675	0.636	0.696†	0.365†
	$\overline{M}_{20}$	−0.87	−1.39	−2.80	−2.86	−2.85	−2.86	···	···	···	···	···	−2.86	−2.83	−2.90	−2.92	−2.90	−2.84	−2.90	−2.84	−2.65†	−1.94†
NGC 1316	C_{42}	4.85	5.01	5.02	5.09	5.21	4.98	···	···	···	···	···	3.72	3.62	3.74	5.63	5.61	5.60	5.37	6.33	3.28	> 2.83
SAB(s)0 pec	A	0.000†	0.097†	0.048	0.046	0.049	0.034	···	···	···	···	···	0.058	0.057	0.042	0.038	0.035	0.016	0.000	0.019†	0.158†	0.149†
$T = -2$	G	0.376†	0.622†	0.669	0.685	0.692	0.710	···	···	···	···	···	0.746	0.745	0.711	0.706	0.703	0.713	0.734	0.720†	0.779†	0.778†
	$\overline{M}_{20}$	−2.10†	−2.42†	−2.67	−2.74	−2.77	−2.80	···	···	···	···	···	−2.31	−2.27	−2.33	−2.90	−2.89	−2.79	−2.83	−3.25†	−2.61†	−1.86†
NGC 1377	C_{42}	···	···	2.96	2.97	3.28	3.33	···	···	···	···	···	3.40	3.53	3.49	> 3.10	> 1.29	···	···	> 2.17	> 2.49	> 0.81
S0	A	··· †	··· †	0.055	0.032	0.028	0.035	···	···	···	···	···	0.022	0.029	0.014	0.061	0.110	0.217	0.154	0.158†	0.278†	0.311†
$T = -2$	G	··· †	··· †	0.606	0.646	0.623	0.630	···	···	···	···	···	0.664	0.661	0.639	0.765	0.878	0.915	0.933	0.888†	0.571†	0.469†
	$\overline{M}_{20}$	··· †	··· †	−1.94	−2.08	−2.11	−2.15	···	···	···	···	···	−2.23	−2.28	−2.06	−3.10	−2.93	−2.80	−2.90	−2.35†	−1.83†	−1.75†

Galaxy		FUV	NUV	B	V	R	I	u	g	r	i	z	J	H	K_S	3.6 μm	4.5 μm	5.8 μm	8.0 μm	24 μm	70 μm	160 μm
NGC 1404	C_{42}	> 4.67	4.55	4.73	4.67	4.69	4.59	···	···	···	···	···	4.40	4.41	4.51	5.02	5.00	4.86	4.92	3.86	···	···
E1	A	0.112†	0.088†	0.025	0.029	0.032	0.031	···	···	···	···	···	0.037	0.038	0.031	0.023	0.026	0.007	0.000	0.000†	··· †	··· †
$T = -5$	G	0.625†	0.692†	0.702	0.713	0.712	0.708	···	···	···	···	···	0.763	0.771	0.755	0.727	0.722	0.685	0.720	0.667†	··· †	··· †
	$\overline{M}_{20}$	−2.68†	−2.55†	−2.63	−2.63	−2.64	−2.62	···	···	···	···	···	−2.54	−2.60	−2.42	−2.63	−2.62	−2.56	−2.55	−2.33†	··· †	··· †
NGC 1482	C_{42}	3.01	3.35	3.74	3.88	4.09	4.39	···	···	···	···	···	> 3.91	> 3.30	> 3.20	> 2.21	> 1.93	> 1.35	> 1.33	> 2.42	> 2.60	> 1.96
SA0$^+$ pec	A	0.146†	0.185†	0.154	0.134	0.129	0.116	···	···	···	···	···	0.085	0.059	0.050	0.053	0.076	0.074	0.118	0.078†	0.222†	0.407†
$T = -0.8$	G	0.500†	0.586†	0.529	0.595	0.642	0.649	···	···	···	···	···	0.762	0.786	0.786	0.868	0.880	0.893	0.921	0.900†	0.635†	0.506†
	$\overline{M}_{20}$	−1.40†	−1.79†	−2.21	−2.29	−2.29	−2.34	···	···	···	···	···	−2.08	−2.53	−2.42	−2.57	−2.59	−2.42	−2.28	−2.31†	−1.88†	−1.65†
NGC 1512	C_{42}	3.50	3.83	4.19	4.24	4.14	4.21	···	···	···	···	···	4.13	4.21	4.24	4.95	4.90	5.06	5.09	5.18	3.98	3.22
SB(r)a	A	0.347	0.278	0.079	0.052	0.054	0.041	···	···	···	···	···	0.013	0.010	0.003	0.068	0.052	0.033	0.091	0.126	0.091†	0.079†
$T = 1$	G	0.697	0.699	0.697	0.721	0.744	0.724	···	···	···	···	···	0.648	0.622	0.570	0.748	0.749	0.680	0.776	0.775	0.778†	0.634†
	$\overline{M}_{20}$	−1.42	−1.55	−2.19	−2.56	−2.62	−2.60	···	···	···	···	···	−2.57	−2.58	−2.61	−2.73	−2.75	−2.25	−2.78	−2.54	−2.47†	−1.53†
NGC 1566	C_{42}	3.17	3.28	3.58	3.59	3.86	4.05	···	···	···	···	···	3.87	3.91	4.01	4.18	4.40	2.69	2.43	2.45	2.58	2.74
SAB(s)bc	A	0.414†	0.349†	0.155	0.095	0.111	0.069	···	···	···	···	···	0.023	0.031	0.009	0.119	0.125	0.193	0.265	0.312	0.215†	0.225†
$T = 4$	G	0.731†	0.729†	0.691	0.668	0.695	0.713	···	···	···	···	···	0.669	0.634	0.606	0.765	0.774	0.784	0.829	0.848	0.772†	0.649†
	$\overline{M}_{20}$	−1.25†	−1.32†	−1.63	−2.03	−2.06	−2.32	···	···	···	···	···	−2.53	−2.47	−2.53	−2.15	−2.03	−1.26	−1.15	−1.05	−1.24†	−1.76†
NGC 1705	C_{42}	> 2.04	> 2.35	> 3.70	> 4.11	> 4.17	4.50	···	···	···	···	···	> 3.69	> 3.37	> 3.57	> 4.26	> 4.34	> 3.04	> 3.13	2.51	> 2.33	> 2.00
SA0- pec	A	0.204	0.207	0.303	0.313	0.301	0.287	···	···	···	···	···	0.122	0.108	0.072	0.276	0.252	0.163	0.242	0.146	0.314	0.378†
$T = 11$	G	0.902	0.864	0.763	0.702	0.679	0.654	···	···	···	···	···	0.625	0.609	0.554	0.681	0.689	0.664	0.709	0.731	0.495	0.354†
	$\overline{M}_{20}$	−2.59	−2.10	−2.16	−2.23	−2.25	−2.25	···	···	···	···	···	−2.26	−2.11	−2.21	−2.15	−2.27	−1.89	−1.63	−1.28	−1.49	−1.42†
NGC 2403	C_{42}	2.71	2.74	···	2.90	2.96	3.33	···	···	···	···	···	2.78	2.82	2.79	3.27	3.21	2.70	2.63	2.44	2.55	2.44
SAB(s)cd	A	0.447	0.381	···	0.107	0.122	0.098	···	···	···	···	···	0.033	0.023	0.007	0.183	0.178	0.179	0.322	0.414	0.228	0.147†
$T = 6$	G	0.724	0.717	···	0.694	0.725	0.698	···	···	···	···	···	0.626	0.587	0.528	0.738	0.738	0.738	0.792	0.822	0.769	0.687†
	$\overline{M}_{20}$	−1.04	−1.10	···	−1.56	−1.61	−1.87	···	···	···	···	···	−1.32	−1.38	−1.24	−1.82	−1.69	−1.45	−1.24	−1.08	−1.40	−1.72†
Holmberg II	C_{42}	2.43	2.41	2.40	2.52	2.39	2.31	···	···	···	···	···	2.20	1.94	2.04	2.57	2.59	2.08	2.86	2.44	2.55	2.56
Im	A	0.494	0.428	0.210	0.151	0.171	0.208	···	···	···	···	···	0.025	0.130	0.029	0.313	0.274	0.084	0.131	0.420	0.349	0.167†
$T = 10$	G	0.640	0.615	0.541	0.526	0.530	0.490	···	···	···	···	···	0.439	0.421	0.427	0.632	0.597	0.474	0.490	0.696	0.604	0.447†
	$\overline{M}_{20}$	−0.93	−0.94	−1.11	−1.20	−1.15	−1.33	···	···	···	···	···	−0.91	−0.84	−0.74	−0.89	−0.92	−0.59	−1.08	−0.71	−0.85	−1.12†
M81 Dwa	C_{42}	1.84	1.98	2.27	2.90	2.32	2.13	···	···	···	···	···	···	···	···	2.33	2.72	···	···	···	···	···
I?	A	0.346	0.244	0.148	0.065	0.108	0.015	···	···	···	···	···	···	···	···	0.263	0.163	···	···	···	···	··· †
$T = 10$	G	0.588	0.548	0.463	0.430	0.419	0.448	···	···	···	···	···	···	···	···	0.516	0.518	···	···	···	···	··· †
	$\overline{M}_{20}$	−0.97	−1.00	−1.01	−0.84	−0.86	−0.71	···	···	···	···	···	···	···	···	−0.71	−0.70	···	···	···	···	··· †
DDO 053	C_{42}	3.25	3.22	2.82	2.76	2.58	1.49	···	···	···	···	···	···	···	···	3.08	3.11	> 2.74	> 3.55	> 4.03	> 2.86	···
Im	A	0.614	0.557	0.372	0.267	0.338	0.095	···	···	···	···	···	···	···	···	0.336	0.306	0.074	0.170	0.159	0.215	0.138†
$T = 10$	G	0.688	0.637	0.449	0.386	0.488	0.343	···	···	···	···	···	···	···	···	0.534	0.602	0.522	0.580	0.765	0.439	0.252†
	$\overline{M}_{20}$	−1.56	−1.47	−1.20	−1.14	−1.08	−0.93	···	···	···	···	···	···	···	···	−1.12	−1.74	−1.36	−1.80	−2.42	−1.84	−0.94†
NGC 2798	C_{42}	> 3.59	> 3.99	> 4.30	4.21	> 4.30	4.19	···	···	···	···	···	> 4.12	> 3.90	> 3.65	3.53	3.56	> 1.62	> 1.39	> 3.08	> 3.06	> 2.14
SB(s)a pec	A	0.292†	0.245†	0.165	0.158	0.171	0.147	···	···	···	···	···	0.094	0.096	0.093	0.131	0.156	0.055	0.089	0.099†	0.173†	0.402†
$T = 1$	G	0.813†	0.821†	0.753	0.722	0.752	0.726	···	···	···	···	···	0.758	0.764	0.763	0.738	0.767	0.882	0.921	0.904†	0.668†	0.507†
	$\overline{M}_{20}$	−2.17†	−2.52†	−2.53	−2.47	−2.64	−2.42	···	···	···	···	···	−2.50	−2.32	−2.48	−2.03	−2.01	−2.65	−2.54	−2.34†	−1.81†	−1.72†
NGC 2841	C_{42}	2.28	2.36	3.77	3.93	3.93	3.89	3.33	3.84	3.92	3.91	3.96	3.84	3.84	3.84	3.95	3.83	3.12	2.00	1.82	1.90	2.15
SA(r)b	A	0.289	0.213	0.107	0.082	0.065	0.052	0.084	0.098	0.070	0.054	0.031	0.009	0.008	0.000	0.027	0.018	0.022	0.086	0.084	0.041†	0.081†
$T = 3$	G	0.586	0.586	0.595	0.606	0.610	0.605	0.566	0.611	0.626	0.629	0.647	0.666	0.662	0.667	0.648	0.645	0.633	0.601	0.612	0.610†	0.444†
	$\overline{M}_{20}$	−1.02	−1.15	−2.42	−2.47	−2.45	−2.51	−2.16	−2.48	−2.53	−2.55	−2.61	−2.58	−2.55	−2.57	−2.56	−2.54	−2.03	−1.09	−0.99	−1.02†	−1.04†

Galaxy		FUV	NUV	B	V	R	I	u	g	r	i	z	J	H	K_S	3.6 μm	4.5 μm	5.8 μm	8.0 μm	24 μm	70 μm	160 μm
NGC 2915	C_{42}	>2.91	3.22	···	3.28	3.38	3.16	···	···	···	···	···	3.31	3.45	3.42	3.38	3.45	3.09	2.75	3.08	2.33	···
I0	A	0.158	0.162	···	0.103	0.119	0.079	···	···	···	···	···	0.034	0.043	0.028	0.125	0.126	0.092	0.143	0.166	0.239	0.283†
$T=90$	G	0.814	0.766	···	0.596	0.549	0.503	···	···	···	···	···	0.530	0.507	0.513	0.500	0.505	0.536	0.606	0.686	0.427	0.321†
	$\overline{M}_{20}$	-1.93	-1.99	···	-1.85	-1.85	-1.77	···	···	···	···	···	-1.80	-1.85	-1.69	-1.82	-1.81	-1.76	-1.39	-1.69	-1.54	-1.40†
Holmberg I	C_{42}	1.72	1.93	2.39	2.35	2.13	2.25	···	···	···	···	···	···	···	···	2.26	2.27	···	1.95	···	1.32	1.77
IAB(s)m	A	0.439	0.338	0.132	0.112	0.148	0.120	···	···	···	···	···	···	···	···	0.325	0.243	0.057	0.025	0.035	0.230	0.289†
$T=10$	G	0.594	0.531	0.373	0.349	0.443	0.432	···	···	···	···	···	···	···	···	0.544	0.521	0.425	0.429	0.447	0.453	0.386†
	$\overline{M}_{20}$	-0.72	-0.71	-0.83	-0.85	-0.78	-0.80	···	···	···	···	···	···	···	···	-0.78	-0.78	-0.29	-0.70	-0.84	-0.75	-0.81†
NGC 2976	C_{42}	1.58	1.70	2.42	2.56	2.56	2.64	1.94	2.29	2.33	2.38	2.43	2.25	2.21	2.22	2.29	2.26	1.73	1.54	1.11	1.71	2.36
SAc pec	A	0.386	0.316	0.132	0.098	0.082	0.071	0.127	0.111	0.084	0.064	0.044	0.024	0.024	0.019	0.104	0.111	0.187	0.255	0.361	0.197	0.160†
$T=5$	G	0.793	0.686	0.558	0.529	0.520	0.508	0.590	0.561	0.545	0.535	0.538	0.555	0.556	0.537	0.575	0.582	0.641	0.719	0.773	0.614	0.417†
	$\overline{M}_{20}$	-0.76	-0.80	-1.18	-1.31	-1.33	-1.42	-0.92	-1.24	-1.30	-1.44	-1.41	-1.41	-1.39	-1.21	-1.00	-0.94	-0.68	-0.60	-0.65	-0.63	-0.88†
NGC 3049	C_{42}	···	>4.58	3.85	3.48	3.52	3.30	>4.67	3.70	3.60	3.29	3.31	3.46	3.23	3.42	4.33	>4.58	>4.07	>3.92	>2.74	>2.32	>1.82
SB(rs)ab	A	··· †	0.184†	0.164	0.118	0.106	0.070	0.098	0.101	0.090	0.056	0.000	0.006	0.016	0.000	0.101	0.111	0.152	0.176	0.209†	0.307†	0.322†
$T=2$	G	··· †	0.650†	0.499	0.489	0.517	0.505	0.580	0.515	0.521	0.504	0.519	0.527	0.526	0.493	0.555	0.584	0.678	0.754	0.852†	0.618†	0.359†
	$\overline{M}_{20}$	··· †	-2.40†	-2.32	-2.12	-2.19	-1.96	-2.57	-2.22	-2.17	-1.98	-2.01	-2.04	-2.03	-2.12	-2.22	-2.31	-2.69	-2.75	-2.60†	-1.97†	-1.67†
NGC 3031	C_{42}	1.35	1.56	···	···	···	···	3.66	4.02	4.08	4.10	4.18	4.24	4.26	4.31	4.26	4.27	4.06	2.74	2.95	2.51	1.90
SA(s)ab	A	0.405	0.335	···	···	···	···	0.053	0.066	0.045	0.034	0.015	0.015	0.013	0.008	0.049	0.049	0.086	0.227	0.246	0.191	0.142†
$T=2$	G	0.653	0.624	···	···	···	···	0.552	0.725	0.753	0.749	0.736	0.750	0.728	0.719	0.761	0.760	0.701	0.665	0.717	0.691	0.559†
	$\overline{M}_{20}$	-0.79	-0.81	···	···	···	···	-1.70	-2.41	-2.50	-2.53	-2.59	-2.74	-2.73	-2.75	-2.68	-2.68	-2.14	-1.07	-0.93	-1.03	-0.96†
NGC 3034	C_{42}	3.52	3.18	2.58	2.66	2.82	2.94	2.54	2.65	2.88	2.89	3.08	3.49	3.85	4.23	···	···	···	···	···	···	···
I0	A	0.325	0.327	0.221	0.177	0.145	0.127	0.198	0.199	0.150	0.115	0.109	0.092	0.079	0.080	···	···	···	···	···	···	··· †
$T=90$	G	0.623	0.646	0.727	0.742	0.758	0.773	0.673	0.729	0.751	0.766	0.797	0.824	0.841	0.858	···	···	···	···	···	···	··· †
	$\overline{M}_{20}$	-1.29	-1.23	-1.32	-1.45	-1.60	-1.66	-1.29	-1.37	-1.64	-1.65	-1.74	-2.15	-2.28	-2.54	···	···	···	···	···	···	···	··· †
Holmberg IX	C_{42}	2.66	2.62	2.87	2.72	2.58	2.81	···	···	···	···	···	···	···	···	1.61	1.59	···	···	···	···	···
Im	A	0.213	0.173	0.300	0.320	0.330	0.316	···	···	···	···	···	···	···	···	0.390	0.250	···	···	···	···	··· †
$T=10$	G	0.448	0.407	0.544	0.566	0.563	0.554	···	···	···	···	···	···	···	···	0.600	0.545	···	···	···	···	··· †
	$\overline{M}_{20}$	-0.99	-1.05	-0.81	-0.75	-0.70	-0.66	···	···	···	···	···	···	···	···	-0.62	-0.64	···	···	···	···	··· †
M81 Dwb	C_{42}	1.79	2.20	3.06	2.86	2.79	2.60	···	···	···	···	···	···	···	···	2.61	2.59	2.27	2.93	2.77	2.40	···
Im	A	0.345	0.197	0.113	0.098	0.088	0.058	···	···	···	···	···	···	···	···	0.109	0.114	0.025	0.132	0.170	0.186	··· †
$T=10$	G	0.606	0.506	0.326	0.304	0.274	0.278	···	···	···	···	···	···	···	···	0.258	0.291	0.425	0.427	0.486	0.220	··· †
	$\overline{M}_{20}$	-0.62	-0.75	-1.06	-1.02	-1.01	-1.04	···	···	···	···	···	···	···	···	-0.88	-0.89	-0.80	-0.88	-0.71	-1.22	··· †
NGC 3190	C_{42}	2.95	3.16	3.70	3.99	4.20	4.14	3.90	4.00	4.15	4.13	4.11	4.12	4.10	4.21	4.44	4.40	4.11	3.85	3.62	2.93	3.05
SA(s)a pec	A	0.171†	0.226†	0.260	0.213	0.180	0.148	0.178	0.247	0.211	0.172	0.119	0.062	0.052	0.043	0.080	0.064	0.073	0.131	0.160	0.202†	0.227†
$T=1$	G	0.486†	0.592†	0.675	0.693	0.701	0.714	0.621	0.688	0.710	0.723	0.746	0.758	0.769	0.762	0.773	0.769	0.755	0.808	0.788	0.706†	0.479†
	$\overline{M}_{20}$	-1.58†	-1.92†	-2.67	-2.73	-2.71	-2.70	-2.45	-2.74	-2.73	-2.77	-2.80	-2.77	-2.57	-2.68	-2.75	-2.58	-2.54	-2.00	-2.28	-2.07†	-1.69†
NGC 3184	C_{42}	1.73	1.78	2.22	2.35	2.44	2.56	2.03	2.27	2.41	2.51	2.56	2.62	2.70	2.63	2.55	2.51	2.03	1.89	2.06	2.05	2.12
SAB(rs)cd	A	0.537	0.400	0.163	0.104	0.093	0.068	0.153	0.143	0.121	0.089	0.042	0.026	0.011	0.008	0.137	0.125	0.186	0.293	0.294	0.200†	0.085†
$T=6$	G	0.771	0.598	0.490	0.492	0.513	0.520	0.509	0.510	0.525	0.531	0.532	0.518	0.496	0.483	0.553	0.562	0.591	0.640	0.662	0.592†	0.486†
	$\overline{M}_{20}$	-0.84	-0.90	-1.26	-1.43	-1.50	-1.62	-0.94	-1.31	-1.45	-1.59	-1.62	-1.73	-1.72	-1.60	-1.47	-1.39	-0.98	-0.94	-0.98	-1.14†	-1.45†
NGC 3198	C_{42}	2.07	2.05	2.56	3.03	3.34	3.43	2.76	2.54	2.63	2.74	2.84	2.82	2.87	2.88	2.86	2.87	2.74	2.65	5.10	2.73	2.51
SB(rs)c	A	0.397	0.302	0.121	0.127	0.123	0.138	0.105	0.115	0.091	0.066	0.031	0.036	0.043	0.049	0.095	0.089	0.148	0.194	0.220	0.164†	0.228†
$T=5$	G	0.598	0.569	0.584	0.568	0.570	0.591	0.530	0.618	0.653	0.661	0.624	0.592	0.545	0.534	0.713	0.712	0.696	0.756	0.802	0.666†	0.531†
	$\overline{M}_{20}$	-0.79	-0.85	-1.39	-1.55	-1.62	-1.74	-1.09	-1.39	-1.57	-1.72	-1.77	-1.86	-1.89	-1.80	-1.64	-1.59	-0.78	-1.23	-1.59	-1.53†	-1.59†

Galaxy		FUV	NUV	B	V	R	I	u	g	r	i	z	J	H	K_S	3.6 μm	4.5 μm	5.8 μm	8.0 μm	24 μm	70 μm	160 μm
IC 2574	C_{42}	1.43	1.61	2.30	2.35	2.38	2.36	···	···	···	···	···	2.66	1.72	2.96	2.55	2.54	2.58	2.97	1.27	1.45	2.03
SAB(s)m	A	0.574	0.501	0.326	0.211	0.274	0.266	···	···	···	···	···	0.000	0.006	0.004	0.337	0.335	0.047	0.113	0.428	0.521	0.330†
$T = 9$	G	0.711	0.617	0.520	0.487	0.479	0.481	···	···	···	···	···	0.422	0.421	0.422	0.542	0.527	0.449	0.468	0.630	0.587	0.419†
	$\overline{M}_{20}$	−0.63	−0.61	−0.69	−0.77	−0.83	−0.86	···	···	···	···	···	−0.63	−0.27	−0.57	−0.74	−0.70	−0.63	−0.60	−0.59	−0.57	−0.69†
NGC 3265	C_{42}	> 1.32	> 1.59	> 2.16	> 2.06	> 2.03	> 2.33	···	···	···	···	···	> 2.12	> 1.90	> 1.91	> 1.54	> 1.49	> 0.79	> 0.42	> 1.64	> 1.90	> 0.97
E	A	0.140†	0.160†	0.102	0.056	0.063	0.024	···	···	···	···	···	0.041	0.023	0.040	0.075	0.058	0.043	0.056	0.190†	0.309†	0.441†
$T = -5$	G	0.838†	0.844†	0.812	0.820	0.818	0.782	···	···	···	···	···	0.777	0.777	0.741	0.835	0.834	0.852	0.875	0.850†	0.485†	0.371†
	$\overline{M}_{20}$	−2.24†	−2.17†	−2.55	−2.42	−2.42	−2.36	···	···	···	···	···	−2.24	−2.02	−2.16	−2.43	−2.45	−2.35	−2.36	−2.08†	−1.88†	−1.31†
MRK 33	C_{42}	> 0.82	> 1.31	> 2.04	> 3.06	> 4.03	> 3.33	···	···	···	···	···	> 3.73	> 3.87	> 4.24	> 2.17	> 2.12	> 0.55	> 0.11	> 1.73	> 1.64	> 1.32
Im pec	A	0.175†	0.160†	0.085	0.124	0.087	0.081	···	···	···	···	···	0.045	0.030	0.047	0.076	0.058	0.110	0.079	0.162†	0.310†	0.251†
$T = 10$	G	0.911†	0.864†	0.807	0.760	0.735	0.706	···	···	···	···	···	0.692	0.664	0.671	0.771	0.778	0.827	0.841	0.827†	0.432†	0.307†
	$\overline{M}_{20}$	−2.24†	−2.08†	−2.48	−2.54	−2.55	−2.51	···	···	···	···	···	−2.24	−2.33	−1.92	−2.48	−2.48	−2.32	−2.34	−2.09†	−1.67†	−1.30†
NGC 3351	C_{42}	2.31	5.40	3.91	3.96	4.01	3.99	4.63	3.96	4.02	4.02	4.16	4.20	4.37	4.42	4.78	4.94	5.74	6.10	5.47	3.69	2.96
SB(r)b	A	0.367	0.255	0.100	0.071	0.052	0.042	0.031	0.043	0.032	0.025	0.016	0.007	0.007	0.010	0.044	0.036	0.042	0.100	0.120	0.160†	0.181†
$T = 3$	G	0.627	0.637	0.586	0.603	0.597	0.622	0.559	0.613	0.626	0.629	0.639	0.637	0.638	0.601	0.651	0.653	0.642	0.693	0.831	0.786†	0.531†
	$\overline{M}_{20}$	−1.30	−2.62	−2.23	−2.41	−2.44	−2.48	−1.91	−2.38	−2.49	−2.54	−2.58	−2.59	−2.63	−2.62	−2.77	−2.81	−3.00	−2.96	−2.71	−2.41†	−1.99†
NGC 3521	C_{42}	2.41	2.72	3.70	3.98	3.96	3.95	3.33	3.89	3.99	4.07	4.19	3.96	4.03	3.99	3.96	3.86	2.56	2.30	2.26	2.45	2.84
SAB(rs)bc	A	0.321	0.259	0.221	0.192	0.201	0.149	0.175	0.180	0.149	0.123	0.110	0.057	0.036	0.021	0.068	0.072	0.134	0.171	0.172	0.092†	0.085†
$T = 4$	G	0.614	0.664	0.689	0.703	0.694	0.712	0.641	0.679	0.687	0.694	0.716	0.740	0.726	0.706	0.759	0.765	0.778	0.822	0.832	0.773†	0.644†
	$\overline{M}_{20}$	−1.15	−1.51	−2.28	−2.51	−2.49	−2.48	−1.94	−2.38	−2.42	−2.48	−2.57	−2.53	−2.56	−2.56	−2.42	−2.37	−1.57	−1.34	−1.22	−1.50†	−1.74†
NGC 3621	C_{42}	3.32	3.47	3.95	3.41	3.39	3.38	···	···	···	···	···	2.84	2.92	2.87	3.50	3.36	2.60	2.34	2.23	2.53	2.74
SA(s)d	A	0.379	0.330	0.151	0.139	0.119	0.110	···	···	···	···	···	0.016	0.001	0.000	0.126	0.117	0.173	0.240	0.302	0.249†	0.107†
$T = 7$	G	0.669	0.672	0.721	0.728	0.749	0.742	···	···	···	···	···	0.681	0.675	0.595	0.763	0.768	0.771	0.837	0.837	0.789†	0.683†
	$\overline{M}_{20}$	−0.99	−1.21	−1.67	−1.73	−1.81	−1.88	···	···	···	···	···	−1.91	−1.87	−1.94	−1.94	−1.83	−1.49	−1.31	−1.15	−1.56†	−1.68†
NGC 3627	C_{42}	1.93	2.11	3.20	3.47	3.55	3.61	3.21	3.38	3.57	3.67	3.75	3.69	3.75	3.80	3.66	3.54	2.26	1.95	1.73	2.22	2.39
SAB(s)b	A	0.487	0.400	0.203	0.163	0.144	0.128	0.166	0.171	0.135	0.115	0.094	0.085	0.077	0.070	0.157	0.170	0.292	0.359	0.410	0.218†	0.193†
$T = 3$	G	0.791	0.775	0.631	0.636	0.648	0.637	0.625	0.628	0.636	0.640	0.654	0.695	0.690	0.692	0.697	0.700	0.754	0.805	0.837	0.746†	0.605†
	$\overline{M}_{20}$	−1.03	−1.06	−1.85	−2.09	−2.16	−2.23	−1.51	−1.98	−2.16	−2.24	−2.29	−2.37	−2.41	−2.42	−1.91	−1.68	−1.01	−0.93	−0.93	−1.06†	−1.27†
NGC 3773	C_{42}	> 0.75	> 1.44	> 3.32	> 3.42	> 3.47	> 3.51	···	···	···	···	···	> 3.65	> 3.01	> 3.31	> 3.65	> 3.32	> 2.22	> 1.36	> 1.79	> 1.97	···
SA0	A	0.283	0.222	0.100	0.088	0.082	0.076	···	···	···	···	···	0.055	0.065	0.032	0.082	0.073	0.127	0.181	0.160	0.253†	0.181†
$T = -2$	G	0.942	0.861	0.684	0.630	0.607	0.575	···	···	···	···	···	0.571	0.596	0.546	0.600	0.637	0.732	0.808	0.826	0.479†	0.312†
	$\overline{M}_{20}$	−1.91	−2.17	−2.40	−2.47	−2.44	−2.42	···	···	···	···	···	−2.15	−2.07	−1.86	−2.34	−2.34	−2.23	−2.11	−1.95	−1.77†	−1.20†
NGC 3938	C_{42}	···	2.46	2.74	2.93	2.99	3.09	2.73	2.78	2.92	3.02	3.10	3.10	3.12	3.17	3.15	3.10	2.42	2.28	2.45	2.48	2.41
SA(s)c	A	···	0.354	0.184	0.135	0.116	0.091	0.165	0.159	0.123	0.090	0.050	0.026	0.016	0.014	0.130	0.125	0.173	0.250	0.273	0.151†	0.138†
$T = 5$	G	···	0.571	0.560	0.569	0.591	0.596	0.546	0.572	0.604	0.613	0.617	0.614	0.575	0.571	0.644	0.645	0.644	0.686	0.691	0.619†	0.496†
	$\overline{M}_{20}$	···	−0.94	−1.50	−1.80	−1.90	−2.01	−1.10	−1.54	−1.77	−1.97	−1.99	−2.10	−2.00	−2.09	−1.84	−1.69	−1.21	−1.14	−0.84	−1.65†	−1.71†
NGC 4125	C_{42}	···	4.48	4.12	4.30	4.34	4.32	4.21	4.63	4.71	4.75	4.78	4.40	4.38	4.36	5.17	5.10	5.00	5.10	5.18	> 2.92	> 1.86
E6 pec	A	··· †	0.104†	0.106	0.098	0.087	0.172	0.000	0.016	0.015	0.011	0.000	0.030	0.023	0.025	0.036	0.033	0.000	0.000	0.025†	0.108†	0.162†
$T = -5$	G	··· †	0.610†	0.713	0.701	0.712	0.723	0.629	0.659	0.672	0.672	0.696	0.727	0.726	0.711	0.686	0.684	0.650	0.696	0.652†	0.741†	0.625†
	$\overline{M}_{20}$	··· †	−2.32†	−2.52	−2.58	−2.60	−1.56	−2.47	−2.55	−2.60	−2.59	−2.65	−2.48	−2.48	−2.53	−2.67	−2.67	−2.58	−2.62	−2.43†	−2.36†	−1.77†
NGC 4236	C_{42}	1.94	2.01	2.51	2.59	2.62	2.83	···	···	···	···	···	2.57	2.34	2.44	3.19	3.19	2.73	3.62	1.75	1.95	2.30
SB(s)dm	A	0.442	0.371	0.179	0.131	0.104	0.153	···	···	···	···	···	0.000	0.000	0.000	0.218	0.173	0.124	0.131	0.347	0.242	0.125†
$T = 8$	G	0.684	0.661	0.588	0.583	0.550	0.553	···	···	···	···	···	0.434	0.428	0.424	0.610	0.578	0.445	0.500	0.680	0.635	0.580†
	$\overline{M}_{20}$	−0.78	−0.80	−1.08	−1.17	−1.26	−1.37	···	···	···	···	···	−0.68	−0.49	−0.39	−1.03	−0.89	−0.85	−0.89	−0.67	−0.78	−0.90†

Galaxy		FUV	NUV	B	V	R	I	u	g	r	i	z	J	H	K_S	3.6 μm	4.5 μm	5.8 μm	8.0 μm	24 μm	70 μm	160 μm
NGC 4254	C_{42}	···	2.38	2.95	3.14	3.25	3.36	2.76	2.99	3.19	3.29	3.38	3.38	3.42	3.48	3.41	3.34	2.85	2.75	2.73	2.68	2.47
SA(s)c	A	···	0.431	0.263	0.217	0.187	0.162	0.275	0.249	0.202	0.158	0.129	0.084	0.066	0.064	0.209	0.214	0.276	0.320	0.299	0.275†	0.307†
$T = 5$	G	···	0.655	0.602	0.607	0.611	0.630	0.607	0.619	0.634	0.642	0.657	0.648	0.648	0.623	0.687	0.693	0.665	0.695	0.708	0.633†	0.495†
	$\overline{M}_{20}$	···	−0.98	−1.48	−1.68	−1.80	−1.89	−1.13	−1.50	−1.70	−1.83	−1.84	−2.14	−2.16	−2.17	−1.90	−1.83	−1.43	−1.42	−1.49	−1.75†	−1.72†
NGC 4321	C_{42}	···	2.41	2.64	2.78	2.84	2.86	2.52	2.69	2.88	2.97	3.08	3.18	3.38	3.41	3.26	3.28	3.63	3.54	4.50	3.27	2.45
SAB(s)bc	A	··· †	0.315†	0.145	0.120	0.103	0.099	0.165	0.141	0.110	0.086	0.067	0.024	0.035	0.011	0.125	0.124	0.201	0.270	0.269	0.220†	0.145†
$T = 4$	G	··· †	0.675†	0.550	0.545	0.536	0.507	0.539	0.544	0.547	0.547	0.550	0.580	0.577	0.571	0.595	0.601	0.656	0.692	0.745	0.693†	0.523†
	$\overline{M}_{20}$	··· †	−1.39†	−1.44	−1.62	−1.71	−1.86	−1.26	−1.48	−1.69	−1.88	−1.91	−2.05	−2.12	−2.14	−1.75	−1.68	−1.38	−1.43	−2.20	−2.08†	−1.63†
NGC 4450	C_{42}	···	2.55	3.68	3.82	3.87	3.85	3.76	3.69	3.82	3.85	···	3.85	3.95	3.92	4.09	4.07	3.90	3.26	3.66	2.78	2.39
SA(s)ab	A	···	0.217	0.054	0.035	0.031	0.023	0.047	0.042	0.033	0.026	···	0.010	0.003	0.012	0.035	0.024	0.008	0.095	0.133	0.112†	0.138†
$T = 2$	G	···	0.567	0.581	0.594	0.590	0.613	0.536	0.608	0.613	0.616	···	0.643	0.625	0.627	0.627	0.626	0.624	0.659	0.657	0.686†	0.510†
	$\overline{M}_{20}$	···	−1.29	−2.31	−2.40	−2.42	−2.41	−2.13	−2.38	−2.42	−2.43	···	−2.45	−2.44	−2.41	−2.48	−2.47	−2.19	−1.70	−1.96	−1.69†	−1.68†
NGC 4536	C_{42}	1.94	2.00	2.64	2.94	3.22	3.48	2.47	2.78	3.30	3.52	3.96	4.65	5.36	5.52	6.65	> 6.75	> 5.74	> 5.78	4.89	3.79	3.22
SAB(rs)bc	A	0.467	0.361	0.145	0.121	0.113	0.135	0.092	0.148	0.107	0.082	0.037	0.029	0.028	0.038	0.112	0.104	0.127	0.160	0.138	0.210†	0.303†
$T = 4$	G	0.613	0.566	0.501	0.520	0.532	0.553	0.506	0.549	0.585	0.597	0.608	0.627	0.642	0.595	0.737	0.743	0.818	0.854	0.905	0.782†	0.581†
	$\overline{M}_{20}$	−0.77	−0.85	−1.51	−1.79	−1.98	−2.25	−1.09	−1.58	−1.94	−2.18	−2.48	−2.99	−3.09	−3.33	−3.40	−3.39	−3.33	−3.12	−2.97	−2.35†	−2.15†
NGC 4552	C_{42}	> 6.35	6.10	5.47	5.50	5.58	5.34	4.90	5.02	5.09	5.02	5.10	4.92	4.94	4.92	6.00	5.84	5.40	5.68	4.96	> 1529.38	···
E0	A	0.078	0.081	0.015	0.006	0.013	0.024	0.000	0.012	0.011	0.011	0.002	0.024	0.017	0.014	0.023	0.027	0.000	0.000	0.000	0.085†	··· †
$T = -5$	G	0.548	0.658	0.682	0.701	0.688	0.700	0.624	0.730	0.735	0.729	0.749	0.771	0.767	0.765	0.720	0.720	0.710	0.685	0.580	0.457†	··· †
	$\overline{M}_{20}$	−3.07	−2.98	−2.88	−2.89	−2.92	−2.83	−2.79	−2.90	−2.93	−2.85	−2.93	−2.84	−2.65	−2.84	−2.98	−2.93	−2.77	−2.77	−2.79	−2.21†	··· †
NGC 4559	C_{42}	2.59	2.58	2.83	2.98	3.02	3.09	2.61	2.79	2.92	2.99	3.11	2.95	2.98	2.99	3.20	3.17	2.68	2.69	2.58	2.77	2.71
SAB(rs)cd	A	0.401	0.334	0.169	0.136	0.119	0.113	0.166	0.155	0.129	0.099	0.040	0.030	0.018	0.013	0.139	0.135	0.152	0.239	0.305	0.174†	0.238†
$T = 6$	G	0.660	0.650	0.650	0.654	0.663	0.670	0.610	0.660	0.667	0.663	0.616	0.594	0.555	0.549	0.716	0.707	0.710	0.780	0.764	0.694†	0.595†
	$\overline{M}_{20}$	−1.03	−1.09	−1.59	−1.79	−1.93	−2.02	−1.18	−1.61	−1.82	−1.98	−2.01	−2.07	−2.07	−2.07	−1.94	−1.76	−1.46	−1.35	−1.01	−1.63†	−1.76†
NGC 4569	C_{42}	4.30	4.34	···	···	···	···	3.30	3.28	3.32	3.54	3.74	3.76	3.80	3.87	4.04	4.04	3.89	3.45	4.85	2.47	2.50
SAB(rs)ab	A	0.256	0.194	···	···	···	···	0.118	0.106	0.095	0.084	0.063	0.043	0.037	0.033	0.084	0.079	0.115	0.236	0.172	0.249†	0.349†
$T = 2$	G	0.567	0.641	···	···	···	···	0.541	0.601	0.632	0.653	0.677	0.681	0.657	0.656	0.719	0.716	0.761	0.859	0.898	0.842†	0.776†
	$\overline{M}_{20}$	−2.24	−2.52	···	···	···	···	−1.95	−2.09	−2.15	−2.35	−2.54	−2.56	−2.49	−2.58	−2.29	−2.17	−1.52	−1.27	−2.79	−1.25†	−1.40†
NGC 4579	C_{42}	1.53	1.74	3.89	4.07	4.19	4.13	3.63	3.95	4.13	4.17	4.23	4.17	4.31	4.28	4.51	4.65	4.04	2.37	4.11	2.71	2.16
SAB(rs)b	A	0.304	0.247	0.068	0.045	0.047	0.033	0.027	0.055	0.042	0.030	0.024	0.040	0.029	0.041	0.047	0.038	0.054	0.151	0.173	0.154†	0.097†
$T = 3$	G	0.655	0.687	0.603	0.608	0.611	0.626	0.568	0.619	0.630	0.628	0.645	0.651	0.642	0.632	0.649	0.661	0.656	0.699	0.742	0.714†	0.535†
	$\overline{M}_{20}$	−1.02	−1.07	−2.41	−2.51	−2.56	−2.52	−2.16	−2.45	−2.54	−2.56	−2.59	−2.60	−2.57	−2.61	−2.66	−2.72	−2.09	−1.20	−1.81	−1.54†	−1.32†
NGC 4594	C_{42}	4.50	4.30	4.21	4.31	4.33	4.14	···	···	···	···	···	4.01	3.98	3.95	4.51	4.43	3.99	3.38	3.24	2.46	2.03
SA(s)a	A	0.166	0.148	0.117	0.098	0.087	0.071	···	···	···	···	···	0.048	0.038	0.027	0.017	0.015	0.006	0.019	0.022	0.046†	0.108†
$T = 1$	G	0.589	0.603	0.644	0.653	0.650	0.649	···	···	···	···	···	0.691	0.701	0.713	0.666	0.666	0.650	0.699	0.722	0.708†	0.502†
	$\overline{M}_{20}$	−2.17	−2.21	−2.42	−2.41	−2.39	−2.19	···	···	···	···	···	−2.44	−2.48	−2.48	−2.42	−2.43	−2.29	−1.67	−1.14	−0.92†	−0.76†
NGC 4625	C_{42}	4.40	4.42	4.73	4.86	5.30	3.91	2.58	2.67	2.72	2.76	2.79	2.86	2.90	2.78	3.10	3.57	2.64	2.68	2.60	> 2.75	> 1.90
SAB(rs)m pec	A	0.351	0.289	0.243	0.219	0.209	0.198	0.166	0.227	0.222	0.195	0.140	0.117	0.072	0.065	0.242	0.233	0.258	0.296	0.246	0.136†	0.252†
$T = 9$	G	0.716	0.701	0.660	0.638	0.627	0.640	0.598	0.690	0.684	0.669	0.617	0.588	0.555	0.531	0.676	0.675	0.692	0.743	0.721	0.602†	0.354†
	$\overline{M}_{20}$	−1.58	−1.64	−1.76	−1.83	−1.84	−1.78	−1.45	−1.74	−1.78	−1.78	−1.77	−1.91	−1.90	−1.82	−1.77	−1.72	−1.50	−1.47	−1.48	−1.71†	−1.57†
NGC 4631	C_{42}	2.20	2.12	2.32	2.38	2.48	2.65	2.36	2.38	2.49	2.63	2.63	2.94	3.03	3.22	3.56	3.58	3.29	3.33	3.48	3.20	2.92
SB(s)d	A	0.415	0.360	0.218	0.187	0.178	0.157	0.206	0.214	0.188	0.164	0.162	0.117	0.117	0.123	0.235	0.240	0.240	0.260	0.294	0.251†	0.325†
$T = 7$	G	0.701	0.671	0.578	0.566	0.570	0.592	0.583	0.577	0.589	0.587	0.605	0.647	0.649	0.664	0.751	0.760	0.792	0.824	0.817	0.683†	0.577†
	$\overline{M}_{20}$	−0.72	−0.72	−1.12	−1.32	−1.53	−1.88	−0.80	−1.12	−1.36	−1.71	−1.86	−2.01	−1.96	−2.08	−2.02	−1.95	−1.78	−1.77	−1.78	−1.94†	−1.97†

Galaxy		FUV	NUV	B	V	R	I	u	g	r	i	z	J	H	K_S	3.6 μm	4.5 μm	5.8 μm	8.0 μm	24 μm	70 μm	160 μm
NGC 4725	C_{42}	1.58	1.72	···	3.82	3.92	3.91	2.89	3.61	3.82	3.89	4.07	3.91	3.78	3.89	4.12	4.01	3.14	1.66	1.30	1.40	1.85
SAB(r)ab pec	A	0.257	0.267	···	0.067	0.064	0.055	0.000	0.078	0.058	0.043	0.017	0.024	0.029	0.015	0.067	0.060	0.076	0.204	0.198	0.201†	0.122†
$T = 2$	G	0.764	0.565	···	0.619	0.636	0.636	0.544	0.624	0.654	0.655	0.683	0.676	0.633	0.634	0.689	0.695	0.645	0.662	0.677	0.679†	0.549†
	$\overline{M}_{20}$	−0.85	−0.88	···	−2.46	−2.51	−2.49	−1.29	−2.21	−2.46	−2.51	−2.62	−2.56	−2.48	−2.55	−2.58	−2.50	−1.31	−0.91	−0.91	−0.82†	−0.93†
NGC 4736	C_{42}	2.40	3.07	4.67	4.69	4.81	4.84	4.55	5.30	5.21	5.21	5.26	4.72	4.77	4.75	6.02	5.73	3.83	3.52	3.18	2.81	3.34
(R)SA(r)ab	A	0.265	0.211	0.099	0.090	0.105	0.041	0.096	0.056	0.050	0.036	0.023	0.021	0.017	0.019	0.040	0.045	0.071	0.127	0.127	0.122	0.227†
$T = 2$	G	0.881	0.881	0.843	0.850	0.834	0.813	0.749	0.818	0.814	0.823	0.827	0.837	0.818	0.801	0.829	0.840	0.856	0.872	0.902	0.865	0.733†
	$\overline{M}_{20}$	−1.33	−1.40	−2.80	−2.77	−2.79	−2.81	−2.43	−2.92	−2.94	−2.94	−2.98	−2.87	−2.91	−2.91	−2.96	−2.99	−2.27	−1.73	−1.61	−1.85	−2.03†
DDO 154	C_{42}	2.66	2.67	0.29	0.38	> 0.32	> 0.39	···	···	···	···	···	2.22	···	···	3.28	3.24	···	···	···	···	···
IB(s)m	A	0.376	0.310	0.202	0.143	0.110	0.040	···	···	···	···	···	0.000	···	···	0.183	0.058	···	···	···	···	··· †
$T = 10$	G	0.625	0.603	0.589	0.575	0.552	0.527	···	···	···	···	···	0.439	···	···	0.569	0.503	···	···	···	···	··· †
	$\overline{M}_{20}$	−1.06	−1.12	−1.15	−1.24	−1.28	−1.23	···	···	···	···	···	−0.10	···	···	−0.97	−0.96	···	···	···	···	··· †
NGC 4826	C_{42}	2.07	2.75	2.89	3.03	3.12	3.22	3.00	2.92	3.12	3.24	3.38	3.53	3.65	3.72	3.91	3.97	4.04	3.10	2.88	2.91	> 2.69
(R)SA(rs)ab	A	0.412	0.360	0.115	0.107	0.129	0.113	0.110	0.132	0.131	0.122	0.115	0.096	0.101	0.109	0.155	0.162	0.174	0.299	0.269	0.203†	0.092†
$T = 2$	G	0.744	0.783	0.681	0.678	0.706	0.682	0.640	0.678	0.688	0.692	0.700	0.724	0.727	0.724	0.737	0.739	0.783	0.881	0.912	0.876†	0.795†
	$\overline{M}_{20}$	−1.23	−1.47	−1.92	−2.01	−2.10	−2.15	−1.89	−1.95	−2.08	−2.16	−2.27	−2.37	−2.44	−2.47	−2.49	−2.50	−2.48	−2.31	−2.33	−1.99†	−1.98†
DDO 165	C_{42}	1.70	1.79	2.50	2.26	2.34	2.18	···	···	···	···	···	2.01	···	2.36	2.25	2.22	1.98	···	···	···	···
Im	A	0.457	0.380	0.103	0.142	0.127	0.105	···	···	···	···	···	0.000	0.000	0.000	0.237	0.214	0.065	···	···	···	··· †
$T = 10$	G	0.519	0.468	0.392	0.356	0.337	0.370	···	···	···	···	···	0.418	0.418	0.422	0.414	0.459	0.425	···	···	···	··· †
	$\overline{M}_{20}$	−0.81	−0.93	−0.98	−1.02	−1.03	−0.98	···	···	···	···	···	−0.69	−0.62	−0.22	−0.76	−0.73	−0.68	···	···	···	··· †
NGC 5033	C_{42}	1.82	2.35	4.28	4.60	···	4.68	3.99	4.43	4.67	4.83	4.92	4.80	4.77	4.75	5.22	5.24	4.52	4.45	4.24	3.75	3.38
SA(s)c	A	0.461	0.352	0.233	0.159	···	0.209	0.132	0.172	0.141	0.109	0.054	0.038	0.032	0.036	0.106	0.102	0.144	0.217	0.189	0.178†	0.145†
$T = 5$	G	0.797	0.580	0.615	0.635	···	0.744	0.531	0.661	0.709	0.735	0.692	0.718	0.706	0.688	0.810	0.810	0.774	0.802	0.822	0.789†	0.648†
	$\overline{M}_{20}$	−0.70	−0.91	−2.31	−2.54	···	−2.80	−1.71	−2.58	−2.81	−2.89	−2.94	−2.85	−2.97	−2.83	−2.95	−2.96	−2.43	−2.30	−2.40	−2.23†	−2.09†
NGC 5055	C_{42}	2.71	3.15	···	···	···	···	3.61	3.62	3.77	3.85	3.90	3.57	3.57	3.68	4.01	3.98	3.20	2.93	2.83	3.00	2.86
SA(rs)bc	A	0.356	0.276	···	···	···	···	0.095	0.133	0.105	0.072	0.072	0.037	0.031	0.021	0.068	0.068	0.140	0.210	0.200	0.144†	0.093†
$T = 4$	G	0.677	0.704	···	···	···	···	0.587	0.615	0.627	0.631	0.657	0.708	0.684	0.681	0.694	0.696	0.723	0.763	0.781	0.787†	0.643†
	$\overline{M}_{20}$	−1.03	−1.31	···	···	···	···	−1.77	−2.15	−2.26	−2.29	−2.36	−2.40	−2.36	−2.45	−2.45	−2.39	−1.62	−1.43	−1.31	−2.06†	−1.89†
NGC 5194	C_{42}	1.65	2.06	2.60	2.85	2.98	3.12	2.41	2.66	2.95	3.09	3.21	3.39	3.44	3.53	3.38	3.37	3.05	2.85	3.16	2.94	2.71
SA(s)bc pec	A	0.435	0.398	0.196	0.158	0.140	0.129	0.165	0.171	0.130	0.099	0.050	0.041	0.028	0.011	0.147	0.154	0.237	0.286	0.263	0.234†	0.143†
$T = 4$	G	0.724	0.743	0.664	0.661	0.649	0.664	0.635	0.649	0.663	0.659	0.660	0.687	0.659	0.660	0.702	0.705	0.718	0.750	0.773	0.688†	0.593†
	$\overline{M}_{20}$	−0.88	−1.00	−1.41	−1.63	−1.75	−1.99	−1.25	−1.48	−1.71	−1.93	−2.06	−2.33	−2.33	−2.36	−1.86	−1.74	−1.29	−1.24	−1.29	−1.64†	−1.85†
NGC 5195	C_{42}	2.87	3.26	3.84	4.18	4.53	4.07	3.21	3.96	4.45	4.63	4.91	4.79	4.97	5.12	5.77	5.93	> 5.54	> 7.82	> 4.98	> 4.03	3.30
SB0 pec	A	0.038	0.111	0.159	0.144	0.111	0.074	0.089	0.156	0.123	0.093	0.052	0.027	0.020	0.011	0.086	0.088	0.063	0.122	0.181	0.330†	0.448†
$T = 90$	G	0.403	0.476	0.540	0.592	0.590	0.529	0.503	0.566	0.612	0.620	0.668	0.705	0.700	0.715	0.693	0.700	0.734	0.767	0.869	0.744†	0.490†
	$\overline{M}_{20}$	−0.80	−1.60	−2.15	−2.34	−2.48	−2.41	−1.73	−2.19	−2.44	−2.51	−2.67	−2.74	−2.79	−2.90	−2.87	−2.92	−2.96	−3.37	−3.22	−2.42†	−1.93†
TOL 89	C_{42}	1.31	1.55	2.32	2.45	2.56	2.64	···	···	···	···	···	2.68	2.41	2.46	2.74	2.66	2.01	1.74	0.87	1.65	2.10
(R')SB(s)dm pec	A	0.498	0.416	0.181	0.150	0.116	0.078	···	···	···	···	···	0.000	0.000	0.000	0.134	0.149	0.236	0.428	0.829	0.598†	0.251†
$T = 8.1$	G	0.619	0.566	0.479	0.478	0.470	0.472	···	···	···	···	···	0.505	0.473	0.460	0.485	0.502	0.553	0.614	0.854	0.587†	0.283†
	$\overline{M}_{20}$	−0.99	−1.00	−1.37	−1.41	−1.47	−1.62	···	···	···	···	···	−1.55	···	−1.10	−1.47	−1.34	−1.06	−1.03	−0.86	−0.96†	−1.08†
NGC 5408	C_{42}	···	···	···	···	···	···	···	···	···	···	···	2.40	2.19	2.19	2.10	1.88	1.57	1.00	0.84	0.95	0.94
IB(s)m	A	···	···	···	···	···	···	···	···	···	···	···	0.013	0.000	0.000	0.151	0.155	0.167	0.200	0.777	0.528	0.372†
$T = 9.7$	G	···	···	···	···	···	···	···	···	···	···	···	0.438	0.417	0.428	0.402	0.437	0.503	0.538	0.753	0.423	0.278†
	$\overline{M}_{20}$	···	···	···	···	···	···	···	···	···	···	···	−0.80	−0.85	−0.80	−0.82	−0.78	−0.61	−0.61	−0.62	−0.63	−0.92†

Galaxy		FUV	NUV	B	V	R	I	u	g	r	i	z	J	H	K_S	3.6 μm	4.5 μm	5.8 μm	8.0 μm	24 μm	70 μm	160 μm
NGC 5474	C_{42}	2.48	2.55	2.85	2.91	2.96	2.97	2.76	2.86	2.96	3.00	3.03	3.13	3.02	3.18	3.12	3.11	3.41	3.13	2.93	2.67	2.36
SA(s)cd pec	A	0.524	0.467	0.385	0.399	0.365	0.309	0.223	0.377	0.398	0.355	0.249	0.131	0.094	0.043	0.435	0.392	0.288	0.380	0.329	0.399†	0.364†
$T = 6$	G	0.619	0.576	0.555	0.585	0.565	0.535	0.526	0.588	0.604	0.600	0.562	0.500	0.471	0.450	0.628	0.620	0.534	0.611	0.601	0.542†	0.398†
	$\overline{M}_{20}$	−0.82	−0.90	−1.43	−1.60	−1.65	−1.72	−1.01	−1.39	−1.56	−1.73	−1.67	−1.70	−1.46	−1.23	−1.52	−1.32	−1.30	−1.21	−1.05	−1.68†	−1.31†
NGC 5713	C_{42}	2.39	2.54	3.13	3.15	3.24	3.29	···	···	···	···	···	3.27	3.25	3.32	3.43	3.46	3.29	> 3.26	3.05	> 2.29	> 1.65
SAB(rs)bc pec	A	0.394†	0.325†	0.186	0.163	0.146	0.121	···	···	···	···	···	0.094	0.089	0.070	0.216	0.226	0.297	0.314	0.304†	0.277†	0.266†
$T = 4$	G	0.791†	0.802†	0.655	0.640	0.637	0.624	···	···	···	···	···	0.653	0.641	0.628	0.734	0.749	0.819	0.868	0.869†	0.693†	0.456†
	$\overline{M}_{20}$	−1.40†	−1.51†	−1.79	−1.85	−1.90	−1.96	···	···	···	···	···	−2.03	−2.04	−2.12	−2.01	−1.93	−1.86	−1.80	−2.01†	−1.74†	−1.71†
xNGC 5866	C_{42}	3.78	3.95	3.84	3.87	4.05	4.11	3.53	3.65	3.77	3.84	3.84	3.72	3.78	3.97	4.65	4.65	4.11	3.63	3.29	2.89	> 2.71
SA0	A	0.118	0.109	0.033	0.024	0.020	0.039	0.000	0.027	0.023	0.021	0.019	0.028	0.028	0.036	0.038	0.035	0.030	0.039	0.080	0.233†	0.186†
$T = -1$	G	0.486	0.608	0.630	0.645	0.641	0.651	0.635	0.644	0.657	0.657	0.685	0.713	0.737	0.748	0.721	0.725	0.743	0.821	0.834	0.801†	0.604†
	$\overline{M}_{20}$	−1.41	−1.66	−2.02	−2.13	−2.20	−2.24	−1.94	−2.08	−2.20	−2.22	−2.29	−2.33	−2.38	−2.49	−2.50	−2.52	−2.14	−1.77	−1.75	−2.02†	−1.79†
IC 4710	C_{42}	1.88	1.91	2.15	2.28	2.34	2.43	···	···	···	···	···	2.19	2.48	2.27	2.52	2.46	2.24	2.02	2.03	2.03	1.93
SB(s)m	A	0.375	0.288	0.168	0.137	0.139	0.102	···	···	···	···	···	0.000	0.014	0.000	0.158	0.140	0.089	0.248	0.401	0.203†	0.173†
$T = 9$	G	0.543	0.493	0.408	0.417	0.425	0.430	···	···	···	···	···	0.445	0.430	0.431	0.407	0.409	0.443	0.506	0.588	0.411†	0.370†
	$\overline{M}_{20}$	−0.79	−0.83	−1.02	−1.10	−1.14	−1.14	···	···	···	···	···	−0.99	−0.64	−0.67	−1.12	−1.07	−0.90	−0.77	−0.96	−0.87†	−1.10†
NGC 6822	C_{42}	2.11	2.32	2.27	2.30	2.32	2.44	···	···	···	···	···	2.31	2.29	2.32	3.12	2.94	2.86	2.37	1.21	1.95	2.18
IB(s)m	A	0.212	0.390	0.342	0.310	0.347	0.402	···	···	···	···	···	0.197	0.182	0.123	0.394	0.402	0.195	0.268	0.656	0.436	0.442
$T = 10$	G	0.554	0.621	0.632	0.613	0.622	0.615	···	···	···	···	···	0.520	0.507	0.472	0.571	0.590	0.497	0.535	0.748	0.544	0.420
	$\overline{M}_{20}$	−0.71	−0.73	−0.63	−0.62	−0.62	−0.64	···	···	···	···	···	−0.68	−0.68	−0.70	−0.77	−0.76	−0.79	−0.73	−0.73	−0.68	−0.80
NGC 6946	C_{42}	1.81	1.93	···	2.54	···	2.70	···	···	···	···	···	2.83	2.91	2.97	2.91	2.96	3.11	3.05	5.68	3.05	2.54
SAB(rs)cd	A	0.139	0.264	···	0.161	···	0.122	···	···	···	···	···	0.076	0.065	0.057	0.186	0.197	0.286	0.334	0.330	0.295	0.194†
$T = 6$	G	0.569	0.588	···	0.495	···	0.515	···	···	···	···	···	0.580	0.554	0.566	0.590	0.609	0.655	0.699	0.767	0.639	0.512†
	$\overline{M}_{20}$	−0.68	−0.72	···	−1.05	···	−1.26	···	···	···	···	···	−1.54	−1.69	−1.67	−1.37	−1.31	−1.18	−1.19	−2.16	−1.46	−1.74†
NGC 7331	C_{42}	2.18	2.60	4.20	4.49	4.71	5.00	···	···	···	···	···	4.05	3.95	3.86	4.09	3.95	2.76	2.59	2.53	2.92	2.91
SA(s)b	A	0.341	0.322	0.223	0.196	0.174	0.134	···	···	···	···	···	0.060	0.037	0.029	0.086	0.083	0.147	0.189	0.181	0.206†	0.145†
$T = 3$	G	0.579	0.604	0.649	0.676	0.676	0.673	···	···	···	···	···	0.770	0.774	0.759	0.774	0.773	0.756	0.784	0.806	0.700†	0.595†
	$\overline{M}_{20}$	−0.94	−1.39	−2.17	−2.28	−2.32	−2.51	···	···	···	···	···	−2.56	−2.56	−2.51	−2.58	−2.51	−1.74	−1.57	−1.46	−1.64†	−1.74†
NGC 7552	C_{42}	4.16	> 5.44	4.47	4.31	4.44	4.41	···	···	···	···	···	4.86	> 4.89	> 4.83	> 4.88	> 4.55	> 3.82	> 3.86	> 2.85	3.03	> 1.73
(R')SB(s)ab	A	0.368†	0.247†	0.162	0.106	0.092	0.070	···	···	···	···	···	0.045	0.043	0.049	0.093	0.141	0.126	0.138	0.118†	0.179†	0.365†
$T = 2$	G	0.696†	0.720†	0.681	0.677	0.688	0.681	···	···	···	···	···	0.738	0.761	0.747	0.790	0.826	0.831	0.858	0.910†	0.683†	0.481†
	$\overline{M}_{20}$	−1.81†	−2.85†	−2.55	−2.55	−2.54	−2.65	···	···	···	···	···	−2.63	−2.56	−2.52	−2.87	−2.82	−2.93	−2.84	−2.47†	−1.98†	−1.88†
NGC 7793	C_{42}	2.04	2.07	2.37	2.53	2.58	2.63	···	···	···	···	···	2.68	2.73	2.72	2.67	2.65	2.44	2.36	2.26	2.19	2.24
SA(s)d	A	0.396	0.334	0.176	0.120	0.114	0.076	···	···	···	···	···	0.036	0.032	0.026	0.134	0.126	0.164	0.256	0.284	0.181	0.110
$T = 7$	G	0.594	0.567	0.519	0.522	0.535	0.539	···	···	···	···	···	0.546	0.526	0.488	0.557	0.567	0.598	0.654	0.652	0.554	0.455
	$\overline{M}_{20}$	−0.90	−0.95	−1.30	−1.56	−1.61	−1.68	···	···	···	···	···	−1.84	−1.86	−1.74	−1.60	−1.52	−1.24	−1.17	−1.06	−1.39	−1.60

C

Two-dimensional distribution of χ^2 values of the disk evolution models

When fitting multi-wavelength profiles with the disk evolution models of Boissier & Prantzos (2000), one must bear in mind the the circular velocity and the spin may not act as completely independent parameters. Depending on the particular shape of a galaxy's profile at different wavelengths, variations in one parameter might be compensated by variations in the other one while still providing an acceptably good fit.

In order to depict the possible internal degeneracies between λ and $V_{\rm C}$, in this appendix we present the two-dimensional χ^2 distributions obtained for each galaxy in our sample. Even though we keep track of the individual χ^2 distributions corresponding to each particular band for each galaxy, the plots presented here show the distribution of total χ^2 values taking into account all bands. The best fitting model is marked with a white dot, and the area encompassing all models with $\chi \leq 2\chi_{\rm min}$ has been delimited with a white closed line. The same range in λ and $V_{\rm C}$ is displayed in all panels, except for the small subset of galaxies requiring larger spins and/or lower circular velocities than those in our initial grid. For the sake of clarity, those galaxies have been grouped together at the end.

In general, some galaxies exhibit some degree of anticorrelation between both parameters for low and intermediate values of λ, since the increment in the radial scale-length caused by augmenting λ can be partly compensated by decreasing $V_{\rm C}$. In some other objects, the χ^2 distribution around the best fitting model does not show any significant degeneracy. Finally, for large values of the spin the correlation is possitive: further incrementing λ significantly decreases the central surface brightness, which can be compensated to some extent by increasing $V_{\rm C}$ −even though this tends to aument the radial scale-length as well.

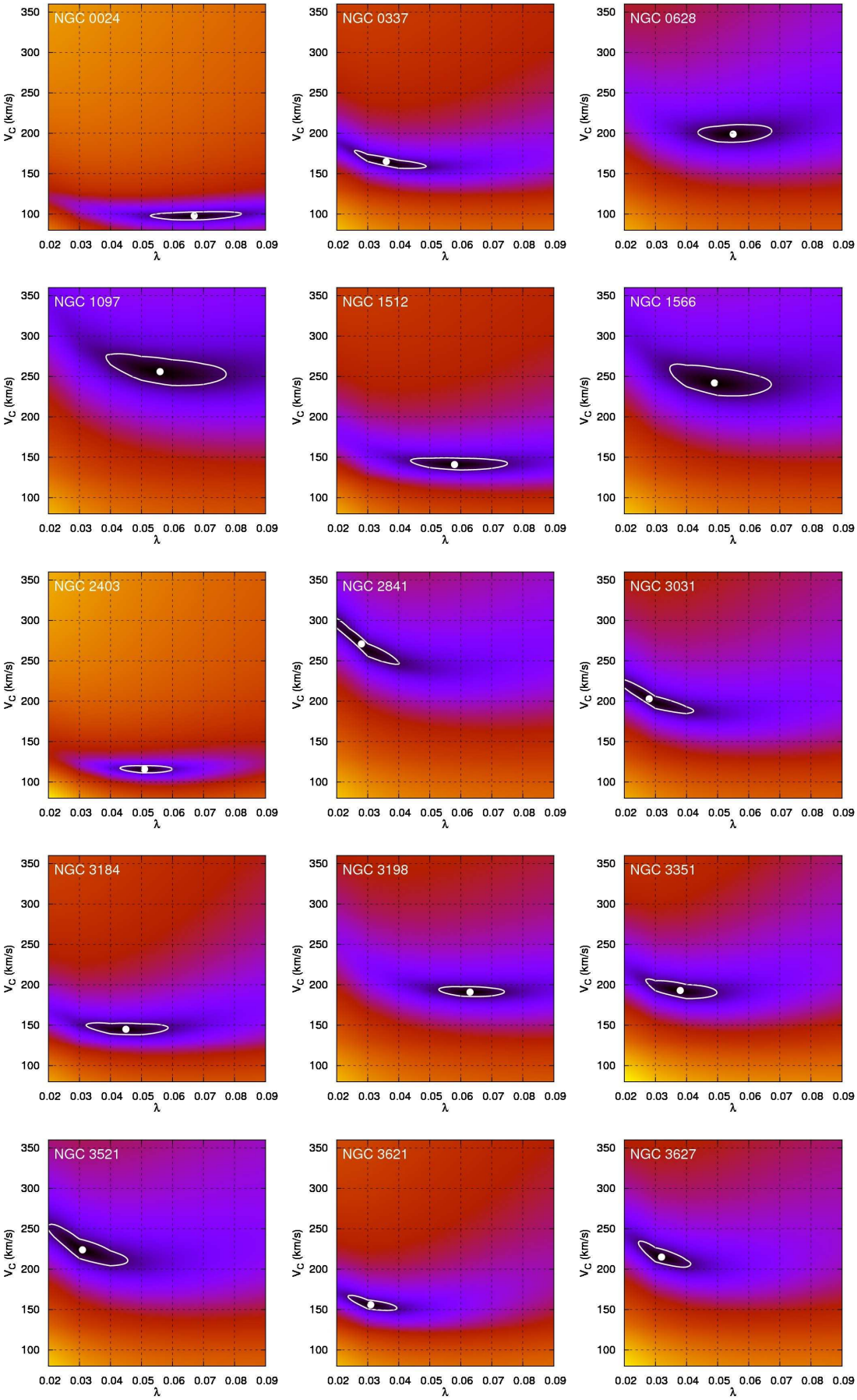
NGC 0024
NGC 0337
NGC 0628
NGC 1097
NGC 1512
NGC 1566
NGC 2403
NGC 2841
NGC 3031
NGC 3184
NGC 3198
NGC 3351
NGC 3521
NGC 3621
NGC 3627
V_C (km/s)
λ
100
150
200
250
300
350
0.02 0.03 0.04 0.05 0.06 0.07 0.08 0.09

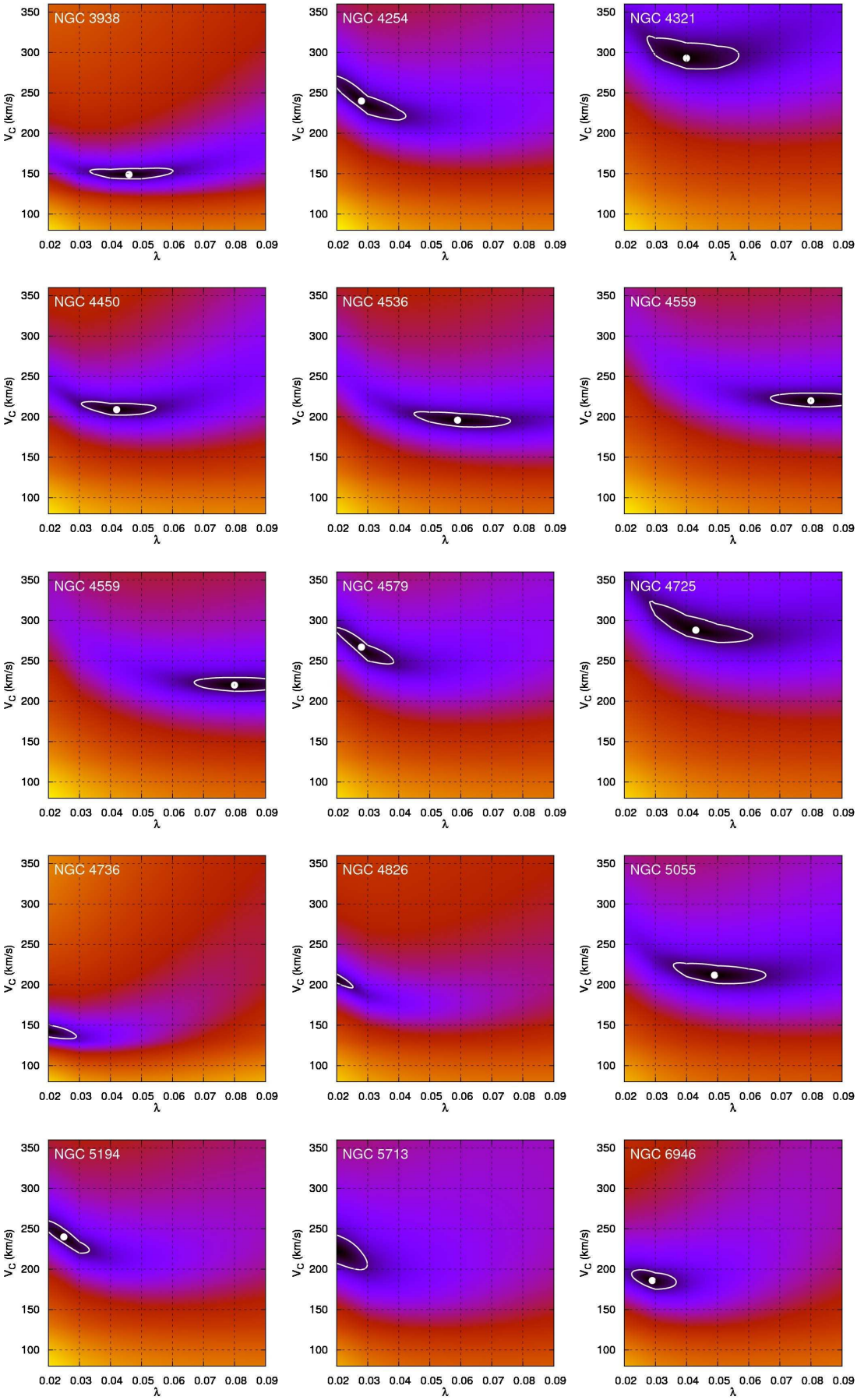
NGC 3938
NGC 4254
NGC 4321
NGC 4450
NGC 4536
NGC 4559
NGC 4559
NGC 4579
NGC 4725
NGC 4736
NGC 4826
NGC 5055
NGC 5194
NGC 5713
NGC 6946
V_C (km/s)
λ
350
300
250
200
150
100
0.02 0.03 0.04 0.05 0.06 0.07 0.08 0.09

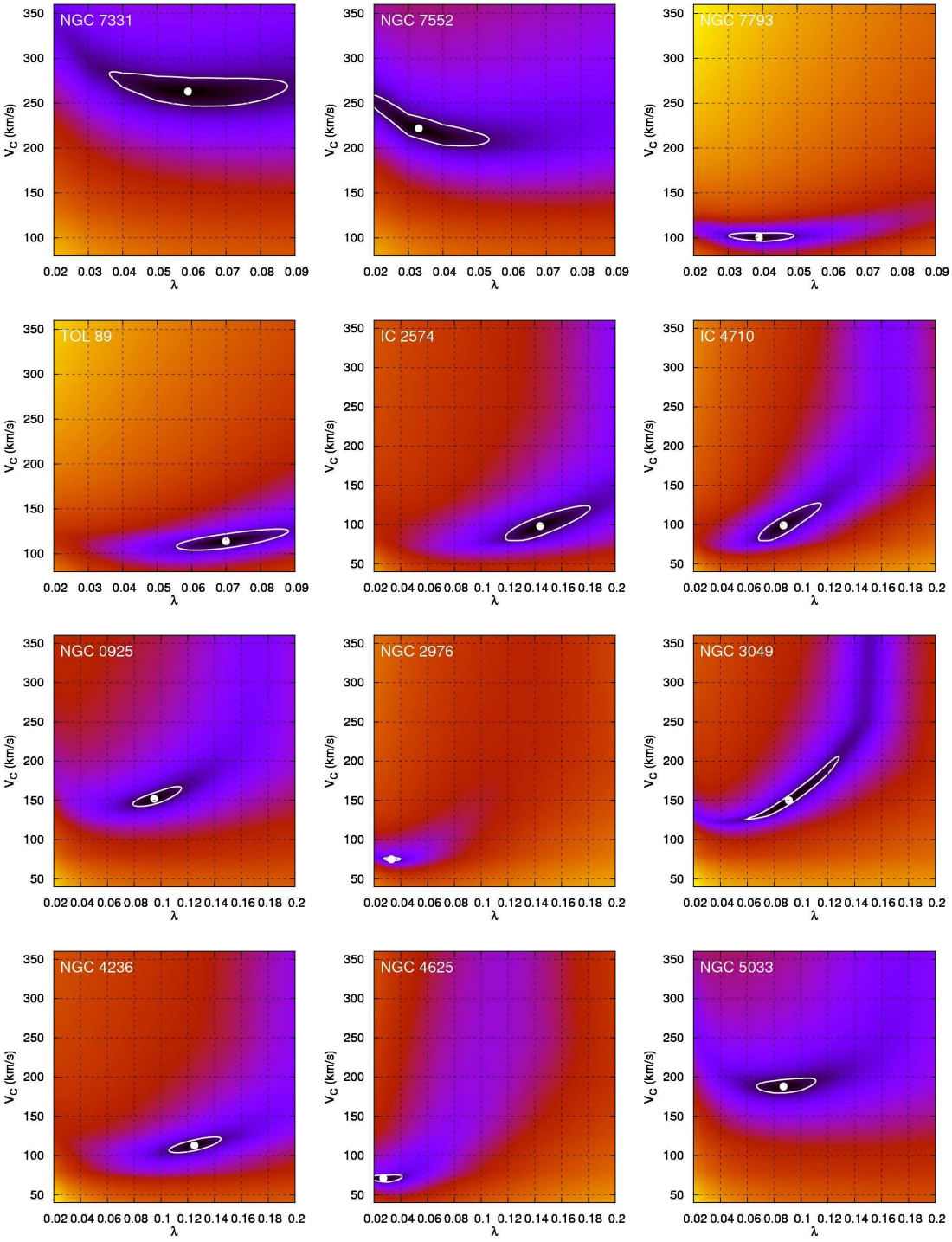
NGC 7331
NGC 7552
NGC 7793
TOL 89
IC 2574
IC 4710
NGC 0925
NGC 2976
NGC 3049
NGC 4236
NGC 4625
NGC 5033
V_C (km/s)
λ

Glossary

2MASS Two Micron All Sky Survey. Survey of the whole sky in the J, H and K_S bands (1.2 μm, 1.6 μm and 2.2 μm, respectively).

AGB Asymptotic Giant Branch. A late stage in stellar evolution undertaken by low- to intermediate-mass stars.

AGN Active Galactic Nucleus. Very luminous and compact source in the center of a galaxy, possibly hosting a supermassive black hole.

ALMA Atacama Large Millimeter/Submillimeter Array. Interferometer being built in the Atacama desert (Chile), that will observe in the spectral range between 0.3 mm to 9.6 mm.

B/D Bulge-to-disk ratio. Ratio between the bulge and disk luminosities of a spiral galaxy.

CARMA Combined Array for Research in Millimeter Astronomy. Millimeter interferometer resulting from the combination of the Berkeley Illinois Maryland Association interferometer (BIMA) and the Owens Valley Radio Observatory (OVRO).

CDS Centre de Donées Astronomiques de Strasbourg. Strasbourg Astronomical Data Center.

CTIO Cerro Tololo Inter-American Observatory.

DDO David Dunlap Observatory Catalogue.

E3D Euro3D. Software tool for visualizing and analyzing integral f eld spectroscopy data.

ESO European Southern Observatory (also ESO/Uppsala Survey of the ESO(B) Atlas).

EW Equivalent Width. In a spectral feature, width of a rectangle whose height is equal to the continuum level, and whose area is the same as that encompassed by the spectral feature.

FITS Flexible Image Transport System. Standard image format used in astronomy.

FIR Far-Infrared (from 25-40 μm to 200-350 μm).

FUV Far-Ultraviolet (1350-1750 Å).

FWHM Full Width at Half Maximum. Measurement of the width of a function (such as a spectral line or a PSF), def ned as the difference between the two values of the x variable when the y one is equal to half of its maximum value.

GALEX Galaxy Evolution Explorer. Space telescope that observes in the FUV and NUV bands.

HB Horizontal Branch. A stage in stellar evolution that follows the asymptotic giant branch in the Hertzsprung-Russell diagram.

HST Hubble Space Telescope.

HUDF Hubble Ultra Deep Field. Deepest image of the distant universe taken by the Hubble Space Telescope.

IC Index Catalogue.

IFS Integral Field Spectroscopy. Technique that allows gathering two-dimensional spectra of extended objects simultaneously.

IFU Integral Field Unit. Instrument designed to perform two-dimensional spectroscopy.

IGIMF Integrated Galactic Initial Mass Function. Mass distribution of newly born stars in a whole galaxy, resulting from the combination of the IMFs of all clusters in that galaxy, which follow themselves there own mass function.

IMF Initial Mass Function. Function describing the mass distribution of newly born stars in a single cluster, in terms of number of stars per mass interval.

IPAC Infrared Processing and Analysis Center.

IRAC Infrared Array Camera. Mid-infrared instrument onboard *Spitzer*, providing images at 3.6 μm, 4.5 μm, 5.8 μm and 8.0 μm.

IRAF Image Reduction and Analysis Facility. Software to reduce and analyze astronomical data.

IRAS Infrared Astronomical Satellite. An infrared space observatory that performed an all-sky survey at 12 μm, 25 μm, 60 μm and 100 μm.

IRS Infrared Spectrograph. Instrument onboard *Spitzer* that provides low- and high-resolution mid-infrared spectra from 5.2 μm to 38 μm.

IRX-β Relation between the total-infrared to UV ratio (or infrared excess, IRX) and the slope of the UV spectrum (β).

ISM Interstellar medium. The gas and dust pervading space between stars.

ΛCDM Lambda Cold Dark Matter. Cosmological model that includes dark energy (in the form of a cosmological constant Λ) and non-baryonic dark matter moving at non-relativistic speeds.

KPNO Kitt Peak National Observatory.

KUG Kiso Survey for Ultraviolet-excess Galaxies.

LEDA Lyon-Meudon Extragalactic Database. Database of galaxies now referred to as HyperLeda, after having merged with the Hypercat database.

LGA 2MASS Large Galaxy Atlas. Compilation of the galaxies with the largest apparent sizes observed by 2MASS.

LIRG Luminous Infrared Galaxy. Galaxy whose total infrared luminosity is larger than 10^{11} solar luminosities.

ULIRG Ultra-Luminous Infrared Galaxy. Galaxy whose total infrared luminosity is larger than 10^{12} solar luminosities.

M Messier catalogue.

MIPS Multiband Imaging Photometer. Camera onboard *Spitzer* observing in the far-infrared, at 24 μm, 70 μm and 160 μm.

MIR Mid-Infrared (from 5 μm to 25-40 μm).

MRK Markarian Catalogue.

MW Milky Way.

NASA National Aeronautics and Space Administration.

NED NASA/IPAC Extragalactic Database. Database that compiles positions, basic data and bibliographic references for millions of extragalactic objects.

NGC New General Catalogue.

NIR Near-infrared (from 0.7-1 μm to 5 μm).

NTT New Technology Telescope. A 3.6 m telescope in La Silla (Chile).

NUV Near-Ultraviolet (1750-2750 Å).

PA Position Angle. Angle between a galaxy's major axis and the north celestial pole, measured counterclockwise when north is up and east is left.

PACS Photodetector Array Camera and Spectrometer. One of the instruments onboard the Herschel Space Observatory, that can work either as an imaging photometer or an IFU in the spectral range from 57 μm to 210 μm.

PAH Polycyclic Aromatic Hydrocarbon. Very large and flat molecules consisting of an hexagonal grid of carbon atoms surrounded by hydrogen ones.

PDR Photodissociation Region. Predominantly neutral region of the interstellar medium in which FUV photons regulate the heating and chemistry.

PGC Principal Galaxies Catalogue.

PINGS PPAK IFS Nearby Galaxies Survey. Two-dimensional spectroscopic survey of 17 nearby galaxies, performed with the PPAK instrument.

PPAK PMAS fiber pack. An off-axis fiber bundle of PMAS, the Postdam Multi-Aperture Spectrophotometer mounted on the 3.5 m telescope in Calar Alto observatory. It provides integral field spectroscopy observations in the optical range.

PSF Point Spread Function. Image of a point source yielded by an optical system.

R3D Software package for reducing f ber-based integral f eld spectroscopy data.

RC3 Third Reference Catalogue of Bright Galaxies. Catalog of thousands of nearby galaxies in the optical range.

SCUBA Submillimeter Common-User Bolometer Array. Submillimeter array detector at 450 μm and 850 μm, operating at the James Clerk Maxwell Telescope.

SDSS Sloan Digital Sky Survey. Photometric and spectroscopic survey of more than a quarter of the sky in the optical range.

SED Spectral Energy Distribution. Variation with wavelength of an object's luminosity.

SFH Star Formation History. Temporal evolution of the star formation rate.

SFR Star Formation Rate. Mass of gas transformed into stars per unit of time.

SINGS Spitzer Infrared Nearby Galaxies Survey. Mid- and far-IR survey of 75 representative nearby galaxies, complemented with ground-based optical images.

S/N Signal-to-noise ratio.

SPH Smoothed Particle Hydrodynamics. Numerical method that simulates f uids as made of discrete and smoothed elements.

sSFR Specif c Star Formation Rate. Ratio of the SFR and the total stellar mass.

THINGS The HI Nearby Galaxies Survey. Survey of 34 nearby galaxies performed with the Very Large Array at the 21 cm hydrogen line.

TIR Total Infrared (3-1100 μm).

TF Tully-Fisher. Empirical relation between a galaxy's luminosity and its rotational velocity.

TOL Tololo Catalogue.

UGC Uppsala General Catalogue.

VIMOS Visible Multi-Object Spectrograph. Imager, multi-object spectrograph and integral f eld unit in the optical range, mounted on one of the telescopes (unit 3) of the Very Large Telescope facility.

VLA Very Large Array. Radio interferometer in New Mexico.

VLT Very Large Telescope. Array of four f xed 8.2 m telescopes and four movable 1.8 m ones at Cerro Paranal (Chile).

VV Vorontsov-Velyaminov catalogue of interacting galaxies.

XSC 2MASS Extended Source Catalog.

XUV Extended Ultraviolet emission found in some spirals beyond their optical size.

Bibliography

Abraham, R. G., Tanvir, N. R., Santiago, B. X., Ellis, R. S., Glazebrook, K., & van den Bergh, S. 1996a, MNRAS, 279, 47

Abraham, R. G., van den Bergh, S., Glazebrook, K., Ellis, R. S., Santiago, B. X., Surma, P., & Griff ths, R. E. 1996b, ApJS, 107, 1

Abraham, R. G.; van den Bergh, S., & Nair, P. 2003, ApJ, 588, 218

Adelman-McCarthy, J. K., et al. 2008, ApJS, 175, 297

Avni, Y. 1976, ApJ, 210, 642

Baggett, W. E., Baggett, S. M., & Anderson, K. S. J. 1998, AJ, 116, 1626

Bajaja, E., Wielebinski, R., Reuter, H. P., Harnett, J. I., & Hummel, E. 1995, A&A, 114, 147

Bakos, J., Trujillo, I., & Pohlen, M. 2008, ApJ, 683, 103

Balogh, M. L., Baldry, I. K., Nichol, R., Miller, C., Bower, R., & Glazebrook, K. 2004, ApJ, 615, 101

Barden, M. et al. 2005, ApJ, 635, 959

Barnes, J., & Efstathiou, G. 1987, ApJ, 319, 575

Bell, E. F. 2002, ApJ, 577, 150

Bell, E. F., & de Jong, R. S. 2000, MNRAS, 312, 497

Bell, E. F., & de Jong, R. S. 2001, ApJ, 550, 212

Bell, E. F., McIntosh, D. H., Katz, N., & Weinberg, M. D. 2003, ApJS, 149, 289

Bendo, G. J., et al. 2006, ApJ, 645, 134

Bendo, G. J., et al. 2007, MNRAS, 380, 1313

Bendo, G. J., et al. 2008, MNRAS, 389, 629

Bershady, M. A., Jangren, A., & Conselice, C. J. 2000, AJ, 119, 2645

Bertin, E., & Arnouts, S. 1996, A&AS, 117, 393

Block, D. L., Freeman, K. C., Jarrett, T. H., Puerari, I., Worthey, G., Combes, F., & Groess, R. 2004, A&A, 425, L37

Boissier, S., Boselli, A., Buat, V., Donas, J., & Milliard, B. 2004, A&A, 424, 465

Boissier, S., & Prantzos, N. 1999, MNRAS, 307, 857

Boissier, S., & Prantzos, N. 2000, MNRAS, 312, 398

Boissier, S., & Prantzos, N. 2001, MNRAS, 325, 321

Boissier, S., et al. 2005, ApJ, 619, 83

Boissier, S. et al. 2007, ApJS, 173, 524

Boselli, A., Boissier, S., Cortese, L., Gil de Paz, A., Seibert, M., Madore, B. F., Buat, V., & Martin, D. C. 2006, ApJ, 651, 811

Boselli, A., & Gavazzi, G. 2006, PASP, 118, 517

Boselli, A., Gavazzi, G., Donas, J., & Scodeggio, M. 2001, AJ, 121, 753

Boselli, A., Gavazzi, G., & Sanvito, G. 2003, A&A, 402, 37

Boselli, A., Lequeux, J., & Gavazzi, G. 2002, A&A, 384, 33

Boselli, A., Tuffs, R. J., Gavazzi, G., Hippelein, H., & Pierini, D. 1997, A&AS, 121, 507

Boselli, A., et al. 1998, A&A, 335, 53

Boselli, A., et al. 2005, ApJ, 629, 29

Boselli, A., et al. 2010, PASP, 122, 261

Brinchmann, J., Charlot, S., White, S. D. M., Tremonti, C., Kauffmann, G., Heckman, T., & Brinkmann, J. 2004, MNRAS, 351, 1151

Brook, C. B., Kawata, D., Martel, H., Gibson, B. K., & Bailin, J. 2006, ApJ, 639, 126

Bruzual, G., & Charlot, S. 2003, MNRAS, 344, 1000

Buat, V., & Xu, C. 1996, A&A, 306, 61

Buat, V. et al. 2005, ApJ, 619, 51

Bullock, J. S., Dekel, A., Kolatt, T. S., Kravtsov, A. V., Klypin, A. A., Porciani, C., & Primack, J. R. 2001, ApJ, 555, 240

Burgarella, D., Buat, V., Donas, J., Milliard, B., & Chapelon, S. 2001, A&A, 369, 421

Burgarella, D., Buat, V., & Iglesias-Páramo, J. 2005, MNRAS, 360, 1413

Burstein, D., Bertola, F., Buson, L. M., Faber, S. M., & Lauer, T. R. 1988, ApJ, 328, 440

Bush, S. J., Cox, T. J., Hernquist, L., Thilker, D., & Younger, J. D. 2008, ApJ, 683, 13

Byun, Y. I., & Freeman, K. C. 1995, ApJ, 448, 563

Cairós, L. M., Caon, N., Vílchez, J. M., González-Pérez, J. N., & Muñoz-Tuñón, C. 2001, ApJS, 136, 393

Calzetti, D. 2001, PASP, 113, 1449

Calzetti, D., Kinney, A. L., & Storchi-Bergmann, T. 1994, ApJ, 429, 582

Calzetti, D., et al. 2005, ApJ, 633, 871

Cardelli, J. A., Clayton, G. C., & Mathis, J. S. 1989, ApJ, 345, 245

Cardiel, N. 2009, MNRAS, 396, 680

Chiappini, C., Matteucci, F., & Gratton, R. 1997, ApJ, 477, 765

Cohen, M., Wheaton, Wm. A., & Megeath, S. T. 2003, AJ, 126, 1090

Conselice, C. J., Bershady, M. A., & Jangren, A. 2000, ApJ 529, 886

Cortese, L., Boselli, A., Franzetti, P., Decarli, R., Gavazzi, G., Boissier, S., & Buat, V. 2008, MNRAS, 386, 1157

Cortese, L., et al. 2006, ApJ, 637, 242

Curtis, H. D. 1918, *Publications of Lick Observatory*, 13, 9

Cutri, R. M., et al. 2003, *Explanatory Supplement to the 2MASS All Sky Data Release and Extended Mission Products*, `http://www.ipac.caltech.edu/2mass/releases/allsky/doc/explsup.html`

da Cunha, E., Charlot, S., & Elbaz, D. 2008, MNRAS, 388, 1595

Dale, D. A., & Helou, G. 2002, ApJ, 576, 159

Dale, D. A., Helou, G., Contursi, A., Silbermann, N. A., & Kolhatkar, S. 2001, ApJ, 549, 215

Dale, D. A., et al. 2007, ApJ, 655, 863

de Jong, R. S. 1996, A&A, 313, 377

de Vaucouleurs, G. 1948, AnAp, 11, 247

de Vaucouleurs, G. 1958, ApJ, 128, 465

de Vaucouleurs, G. 1959, *Handbuch der Physik*, 53, 275

de Vaucouleurs, G. 1977, *Evolution of galaxies and stellar populations*, ed. R. B. Larson, & B. M., Tynsley, Yale Univ. Obs., New Haven, 43

de Vaucouleurs, G., de Vaucouleurs, A., Corwin, H. G., Buta, R. J., Paturel, G., & Fouqué, P. 1991, *Third Reference Catalogue of Bright Galaxies* (RC3) (Springer-Verlag)

Dellenbusch, K. E., Gallagher, J. S., III, & Knezek, P. M. 2007, ApJ, 655, 29

Draine, B. T. 2009, ASP Conf. Ser. *Cosmic Dust – Near and Far*, eds. Henning, T., Grün, E., & Steinacker, J. (astro-ph/0903.1658)

Draine, B. T., & Li, A. 2007, ApJ, 657, 810

Draine, B. T., et al. 2007, ApJ, 663, 866

Drozdovsky, I. O., & Karachentsev, I. D. 2000, A&AS, 142, 425

Dwek, E., Galliano, F., & Jones, A. 2008, ASP Conf. Ser. *Cosmic Dust – Near and Far*, eds. Henning, T., Grün, E., & Steinacker, J. (astro-ph/0903.0006)

Edmunds, M. G. 2001, MNRAS, 328, 223

Engelbracht, C. W., Gordon, K. D., Rieke, G. H., Werner, M. W., Dale, D. A., & Latter, W. B. 2005, ApJ, 628, 29

Engelbracht, C. W., Rieke, G. H., Gordon, K. D., Smith, J. D. T., Werner, M. W., Moustakas, J., Willmer, C. N. A., & Vanzi, L. 2008, ApJ, 678, 804

Engelbracht, C. W., et al. 2007, PASP, 119, 994

Erwin, P., Pohlen, M., & Beckman, J. E. 2008, AJ, 135, 20

Fall, S. M., & Efstathiou, G. 1980, MNRAS, 193, 189

Fazio, G. G., et al. 2004, ApJS, 154, 10

Ferguson, A. M. N., & Clarke, C. J. 2001, MNRAS, 325, 781

Freeman, K. C. 1970, ApJ, 160, 811

Fukugita, M., Shimasaku, K., & Ichikawa, T. 1995, PASP, 107, 945

Galliano, F., Dwek, E., & Chanial, P. 2008, ApJ, 672, 214

García-Lario, P. 2006, in *Planetary Nebulae in our Galaxy and Beyond*, IAU symp. 234, ed. M. J. Barlow & R. H. Méndez, Cambridge University Press, 63

Gardner, J. P. 2001, ApJ, 557, 616

Gavazzi, G., Bonfanti, C., Sanvito, G., Boselli, A., & Scodeggio, M. 2002, ApJ, 576, 135

Gavazzi, G., Boselli, A., Donati, A., Franzetti, P., & Scodeggio, M. 2003, A&A, 400, 451

Gil de Paz, A., & Madore, B. F. 2005, ApJS, 156, 345

Gil de Paz, A., et al. 2005, ApJ, 627, 29

Gil de Paz, A., et al. 2007a, ApJS, 173, 185

Gil de Paz, A., et al. 2007b, ApJ, 661, 115

Gini, C. 1912, reprinted in *Memorie di Metodologia Statistica*, ed. E. Pizetti & T. Salvemini (1955; Rome: Libreria Eredi Virgilio Veschi)

Gonzalez, A. H., Williams, K. A., Bullock, J. S., Kolatt, T. S., & Primack, J. R. 2000, ApJ, 528, 145

Gordon, K. D., Clayton, G. C., Misselt, K. A., Landolt, A. U., & Wolff, M. J. 2003, ApJ, 594, 279

Gordon, K. D., Clayton, G. C., Witt, A. N., & Misselt, K. A. 2000, ApJ, 533, 236

Gordon, K. D., Engelbracht, C. W., Rieke, G. H., Misselt, K. A., Smith, J. D. T., & Kennicutt, R. C., Jr. 2008, ApJ, 682, 336

Gordon, K. D., et al. 2007, PASP, 119, 1019

Governato, F., Willman, B., Mayer, L., Brooks, A., Stinson, G., Valenzuela, O., Wadsley, J., & Quinn, T. 2007, MNRAS, 374, 1479

Graham, A. W., Driver, S. P., Petrosian, V., Conselice, C. J., Bershady, M. A., Crawford, S. M., & Goto, T. 2005, AJ, 130, 1535

Guthrie, B. N. G. 1992, A&AS, 93, 255

Heckman, T. M., Robert, C., Leitherer, C., Garnett, D. R., & van der Rydt, F. 1998, ApJ, 503, 646

Heckman, T. M. et al. 1995, ApJ, 452, 549

Helou, G., et al. 2004, ApJS, 154, 253

Heyer, M. H., Corbelli, E., Schneider, S. E., & Young, J. S. 2004, ApJ, 602, 723

Hirashita, H., Tajiri, Y. Y., & Kamaya, H. 2002, A&A, 388, 439

Hogg, D. W., Tremonti, C. A., Blanton, M. R., Finkbeiner, D. P., Padmanabhan, N,, Quintero, A. D., Schlegel, D. J., & Wherry, N. 2005, ApJ, 624, 162

Holwerda, B. W., Gonzalez, R. A., Allen, R. J., & van der Kruit, P. C. 2005, AJ, 129, 1396

Hubble, E. P. 1925, ApJ, 62, 409

Hubble, E. P. 1926a, ApJ, 63, 236

Hubble, E. P. 1926b, ApJ, 64, 321

Hubble, E. P. 1929, ApJ, 69, 103

Hubble, E. P. 1936, *The Realm of the Nebulae* (New Haven: Yale University Press)

Hunt, L., Bianchi, S., & Maiolino, R. 2005, A&A, 434, 849

Issa, M. R., MacLaren, I., & Wolfendale, A. W. 1990, A&A, 236, 237

James, A., Dunne, L., Eales, S., & Edmunds, M. G. 2002, MNRAS, 335, 753

James, P. A. et al. 2004, A&A, 414, 23

Jarrett, T. H., Chester, T., Cutri, R., Schneider, S. E., & Huchra, J. P. 2003, AJ, 125, 525

Jarrett, T. H., Chester, T., Cutri, R., Schneider, S., Skrutskie, M., & Huchra, J. P. 2000, AJ, 119, 2498

Kenney, J., & Young, J. 1988, ApJS, 66, 261

Kennicutt, R. C., Jr. 1998, ARA&A, 36, 189

Kennicutt, R. C., Jr., et al. 2003, PASP, 115, 928

Kent, S. M. 1985, ApJS, 59, 115

Kobulnicky, H. A., & Kewley, L. J. 2004, ApJ, 617, 240

Koda, J., et al. 2009, ApJ, 700, 132

Kong, X., Charlot, S., Brinchmann, J., & Fall, S. M. 2004, MNRAS, 349, 769

Kormendy, J. 1977, ApJ, 217, 406

Kroupa, P., 2001, MNRAS, 322, 231

Krumholz, M. R., & McKee, C. F. 2008, Nature, 451, 1082

Kroupa, P., Tout, C. A., & Gilmore, G. 1993, MNRAS, 262, 545

Kuchinski, L. E., Madore, B. F., Freedman, W. L., & Trewhella, M. 2001, AJ, 122, 729

Kuchinski, L. E., et al. 2000, ApJS, 131, 441

Lauger, S., Burgarella, D., & Buat, V. 2005, A&A, 434, 77

Lee, J., et al. 2009, ApJ, 706, 599

Leitherer, C. et al. 1999, ApJS, 123, 3

Leroy, A. K., Walter, F., Brinks, E., Bigiel, F., de Blok, W. J. G., Madore, B. F., & Thornley, M. D. 2008, AJ, 136, 2782

Li, A., & Draine, B. T. 2001, ApJ, 554, 778

Lisenfeld, U., & Ferrara, A. 1998, ApJ, 496, 145

López-Sanjuan, C., et al. 2009 ApJ, 694, 643

Lorenz, M. O. 1905, J. Am. Stat. Assoc., 9, 209

Lotz, J. M., Primack, J., & Madau, P. 2004, AJ, 128, 163

MacArthur, L. A, Courteau, S., Bell, E., & Holtzman, J. A. 2004, ApJS, 152, 175

Madau, P., Pozzetti, L., & Dickinson, M. 1998, ApJ, 498, 106

Madden, S. C. 2000, NewAR, 44, 249

Madden, S. C., Galliano, F., Jones, A. P., Sauvage, M. 2006, A&A, 446, 877

Marcelin, M., et al. 2008, *Ground-based and Airborne Instrumentation for Astronomy II*, eds. McLean, I. S., & Casali, M. M., Proceedings of the SPIE, 7014, 701455

Marcum, P. M., et al. 2001, ApJS, 132, 129

Martin. D., et al. 2005, ApJ, 619 1

Mathis, J. S., Mezger, P. G., & Panagia, N. 1983, A&A, 128, 212

Matteucci, F., & François, P. 1989, MNRAS, 239, 885

Meurer, G. R., Heckman, T.M., & Calzetti, D. 1999, ApJ, 521, 64

Meurer, G. R., Heckman, T. M., Leitherer, C., Kinney, A., Robert, C., & Garnett, D. R. 1995, AJ, 110, 2665

Mo, H. J., Mao, S., & White, S. D. M. 1998, MNRAS, 295, 319

Moustakas, J., & Kennicutt, R. C., Jr. 2006, ApJ, 651, 155

Muñoz-Mateos, J. C., et al. 2007, ApJ, 658, 1006

Muñoz-Mateos, J. C., et al. 2009a, ApJ, 703, 1569

Muñoz-Mateos, J. C., et al. 2009b, ApJ, 701, 1965

Noll, S., Burgarella, D., Giovannoli, E., Buat, V., Marcillac, D., & Muñoz-Mateos, J. C. 2009, A&A, 507, 1793

Ochsenbein, F., Bauer, P., & Marcout, J. 2000, A&AS, 143, 23

O'Connell, R. W. 1999, ARA&A, 37, 603

Ohl, R. G., et al. 1998, ApJ, 505, 11

Oke, J. B. 1974, ApJS, 27, 21

Paglione, T. A. D., et al. 2001, ApJS, 135, 183

Panuzzo, P., Granato, G. L., Buat, V., Inoue, A. K., Silva, L., Iglesias-Páramo, J., & Bressan, A. 2007, MNRAS, 375, 640

Paturel, G., Petit, C., Prugniel, P., Theureau, G., Rousseau, J., Brouty, M., Dubois, P., & Cambrésy, L. 2003, A&A, 412, 45

Peimbert, M., & Torres-Peimbert, S. 1981, ApJ, 245, 845

Peletier, R. F., & Balcells, M. 1996, AJ, 111, 2238

Pérez-González, P. G., Gil de Paz, A., Zamorano, J., Gallego, J., Alonso-Herrero, A., & Aragón-Salamanca, A. 2003, MNRAS, 338, 525

Pérez-González, P. G., et al. 2006, ApJ, 648, 987

Petrosian, V. 1976, ApJ, 209, 1

Pilyugin, L. S., & Thuan, T. X. 2005, ApJ, 631, 231

Pf amm-Altenburg, J., Weidner, C., & Kroupa, P. 2007, ApJ, 671, 1550

Pf amm-Altenburg, J., Weidner, C., & Kroupa, P. 2009, MNRAS, 395, 394

Phookun, B., & Mundy, L. G. 1995, ApJ, 453, 154

Pohlen, M., & Trujillo, I. 2006, A&A, 454, 759

Pohlen, M., et al. 2008, in ASP Conf. Ser. 396, *Formation and Evolution of Galaxy Disks*, ed. Funes, J. G., & Corsini, E. M. (San Francisco, CA: ASP), 183

Popescu, C. C., Misiriotis, A., Kylaf s, N. D., Tuffs, R. J., & Fischera, J. 2000, A&A, 362, 138

Popescu, C. C., et al. 2005, ApJ, 619, 75

Portinari, L., Sommer-Larsen, J., & Tantalo, R. 2004, MNRAS, 347, 691

Prantzos, N., & Boissier, S. 2000, MNRAS, 313, 338

Prescott, M. K. M., et al. 2007, ApJ, 668, 182

Press, W. H., Teukolsky, S. A., Vetterling, W. T., & Flannery, B. P. 1992, *Numerical recipes in C. The art of scientific computing* (Cambridge: University Press)

Prugniel, Ph., & Heraudeau, Ph. 1998, A&AS, 128, 299

Reach, W. T., et al. 2005, PASP, 117, 978

Regan, M. W., Thornley, M. D., Helfer, T. T., Sheth, K., Wong, T., Vogel, S. N., Blitz, L., & Bock, D. C. J. 2001, ApJ, 561, 218

Rieke, G. H., et al. 2004, ApJS, 154, 25

Robin, A. C., et al. 2007, ApJS, 172, 545

Rosales-Ortega, F. F., Kennicutt, R. C., Sánchez, S. F., Díaz, A. I., Pasqualli, A., Johnson, B. D., & Hao, C. N. 2010, MNRAS, in press (astro-ph/1002.1946)

Rŏskar, R., Debattista, V. P., Stinson, G. S., Quinn, T. R., Kaufmann, T., & Wadsley, J. 2008, ApJ, 675, 65

Roussel, H., Gil de Paz, A., Seibert, M., Helou, G., Madore, B. F., & Martin, C. 2005 ApJ, 632, 227

Rubin, R. H., et al. 2008, MNRAS, 387, 45

Sage, L. J. 1993, A&A, 272, 123

Salpeter, E. E. 1955, ApJ, 121, 161

Samland, M., & Gerhard, O. E. 2003, A&A, 399, 961

Sánchez, S. F. 2004, AN, 325, 167

Sánchez, S. F. 2006, AN, 327, 580

Sánchez-Blázquez, P., Courty, S., Gibson, B. K., & Brook, C. B. 2009, MNRAS, 398, 591

Sandage, A. 1961, *The Hubble Atlas of Galaxies* (Washington, D.C.: Carnegie Institution)

Sandage, A. 1975, *Galaxies and the Universe*, ed. A. Sandage, M. Sandage and J. Kristian, University of Chicago Press, (*Stars and Stellar Systems*. Volume 9)

Sandage, A. R. 1986, A&A, 161, 89

Scalo, J. M. 1986, Fundamentals of Cosmic Physics, 11, 1

Scarlata, S., et al. 2007, ApJS, 172, 406

Schade, D., Lilly, S. J., Crampton, D., Hammer, F., Le Fevre, O., & Tresse, L. 1995, ApJ, 451, 1

Schlegel, D. J., Finkbeiner, D. P., & Davis, M. 1998, ApJ, 500, 525

Seibert, M., et al. 2005, ApJ, 619, 55

Sellwood, J. A., & Wilkinson, A. 1993, RPPh, 56, 173

Sérsic, J. L., 1968, *Atlas de Galaxias Australes* (Córdoba, Argentina: Observatorio Astronómico)

Smith, J. D. T.. et al. 2007, ApJ, 656, 770

Sommer-Larsen, J., Götz, M., & Portinari, L. , 2003, ApJ, 596, 47

Springel, V., et al. 2005, Nature, 435, 629

Stansberry, J. A., et al. 2007, PASP, 119, 1038

Sturm, E., Lutz, D., Tran, D., Feuchtgruber, H., Genzel, R., Kunze, D., Moorwood, A. F. M., & Thornley, M. D. 2000, A&A, 358, 481

Taylor, V. A., Jansen, R. A., Windhorst, R. A., Odewahn, S. C., & Hibbard, J. E. 2005, ApJ, 630, 784

Taylor-Mager, V. A., Conselice, C. J., Windhorst, R. A., & Jansen, R. A. 2007, ApJ, 659, 162

Thilker et al. 2005, A&A, ApJ, 619, L79

Thilker, D. A., et al. 2007a, ApJS, 173, 538

Thilker, D. A., et al. 2007b, ApJS, 173, 572

Trujillo, I., & Pohlen, M. 2005, ApJ, 630, 17

Trujillo, I. et al. 2004, ApJ, 604, 521

Trujillo, I. et al. 2006, ApJ, 650, 18

Tully, R. B., & Fisher, J. R. 1977, A&A, 54, 661

van den Bergh, S. 1960a, ApJ, 131, 215

van den Bergh, S. 1960b, ApJ, 131, 558

van den Bergh, S. 1976, ApJ, 206, 883

van der Kruit, P. C. 1979, A&AS, 38, 15

Verheijen, M. A. W. 2001, ApJ, 563, 694

Vitvitska, M., Klypin, A. A., Kravtsov, A. V., Wechsler, R. H., Primack, J. R., & Bullock, J. S. 2002, ApJ, 581, 799

Wadadekar, Y., Robbason, B., & Kembhavi, A. 1999, AJ, 117, 1219

Walter, F., Brinks, E., de Blok, W. J. G., Bigiel, F., Kennicutt, R. C., Jr., Thornley, M. D., & Leroy, A. K. 2008, AJ, 136, 2563

Walter, F., et al. 2007, ApJ, 661, 102

Warren, M. S., Quinn, P. J., Salmon, J. K., & Zurek, W. H. 1992, ApJ, 399, 405

Weidner, C., & Kroupa, P. 2005, ApJ, 625, 754

Weidner, C., & Kroupa, P. 2006, ApJ, 365, 1333

Weidner, C., Kroupa, P., & Larsen, S. S. 2004, MNRAS, 350, 1503

Weingartner, J. C., & Draine, B. T. 2001, ApJ, 548, 296

Werner, M. W., et al. 2004, ApJS, 154, 1

White, S. D. M., & Frenk, C. S. 1991, ApJ, 379, 52

Witt, A. N., & Gordon, K. D. 2000, ApJ, 528, 799

Wong, T., & Blitz, L. 2002, ApJ, 569, 157

Worthey, G. 1994, ApJS, 95, 107

Wu, Y., Charmandaris, V., Hao, L., Brandl, B. R., Bernard-Salas, J., Spoon, H. W. W., & Houck, J. R. 2006, ApJ, 639, 157

Xilouris, E. M., Byun, Y. L., Kylaf s, N. D., Paleologou, E. V., Papamastorakis, & J. 1999, A&A, 344, 868

York, D., et al. 2000, AJ, 120, 1579

Yoshii, Y., & Sommer-Larsen, J. 1989, MNRAS, 236, 779

Young, J. S., & Scoville, N. 1982, ApJ, 260, 41

Young, J. S., et al. 1995, ApJS, 98, 219